



**HAL**  
open science

# Comportement des roches sous sollicitations thermiques et circulation de fluides (FLUTE)

Thomas Junique

► **To cite this version:**

Thomas Junique. Comportement des roches sous sollicitations thermiques et circulation de fluides (FLUTE). Sciences de la Terre. URCA - GEGENAA, 2021. Français. NNT : . tel-03482532

**HAL Id: tel-03482532**

**<https://hal.univ-reims.fr/tel-03482532v1>**

Submitted on 12 Nov 2023

**HAL** is a multi-disciplinary open access archive for the deposit and dissemination of scientific research documents, whether they are published or not. The documents may come from teaching and research institutions in France or abroad, or from public or private research centers.

L'archive ouverte pluridisciplinaire **HAL**, est destinée au dépôt et à la diffusion de documents scientifiques de niveau recherche, publiés ou non, émanant des établissements d'enseignement et de recherche français ou étrangers, des laboratoires publics ou privés.

UNIVERSITÉ DE REIMS CHAMPAGNE-ARDENNE  
ÉCOLE DOCTORALE SCIENCES FONDAMENTALES - SANTÉ N°619

# THÈSE

Pour obtenir le grade de  
DOCTEUR DE L'UNIVERSITÉ DE REIMS CHAMPAGNE-ARDENNE

*Discipline* : SCIENCES DE L'UNIVERS

*Spécialité* : Géosciences de l'environnement

Présentée et soutenue publiquement par

**THOMAS JUNIQUE**

Le 1er juillet 2021

---

## Comportement des roches sous sollicitations thermiques et circulation de fluides

---

Thèse co-dirigée par Patricia VAZQUEZ et Yves GERAUD

### JURY

Mme Sara Vandycke,	Professeur,	Université de Mons (Belgique),	<b>Rapporteur</b>
M. Patrick Baud,	Professeur,	Université de Strasbourg,	<b>Rapporteur</b>
M. Philippe Cosenza,	Professeur,	Université de Poitiers,	<b>Examineur</b>
M. Philippe Robion,	Maître de Conférences HDR,	Université de Cergy-Pontoise,	<b>Examineur</b>
Mme Patricia Vazquez,	Maître de Conférences HDR,	Université de Reims Champagne Ardenne,	<b>Directrice de thèse</b>
M. Yves Géraud,	Professeur,	Université de Lorraine,	<b>Co-Directeur de thèse</b>
Mme Céline Thomachot-Schneider,	Maître de Conférences HDR,	Université de Reims Champagne Ardenne,	<b>Co-encadrante</b>





“滴水穿石 – Constant dripping wears away a stone.”

“No matter how hard or impossible it is, never lose sight of your goal.”

尾田 栄一郎 – Eiichiro Oda



# REMERCIEMENTS

*Ce travail n'aurait jamais été tel qu'il est présenté dans cette thèse sans le soutien et l'aide de plusieurs personnes.*

*Je voudrais avant tout remercier mes directeurs de thèse, Patricia Vazquez et Yves Géraud. Un grand merci tout d'abord à Patricia, qui a suivi ma thèse au jour le jour et a toujours su se rendre disponible quand j'en avais besoin. Je te remercie également de m'avoir soutenu durant la totalité de cette thèse quelque soit mon état d'esprit et c'est d'ailleurs aussi pour cela que j'espère pouvoir travailler encore à tes côtés. Merci également à Yves, qui m'a beaucoup appris, et très souvent aidé et conseillé. Merci de m'avoir accueilli dans ton laboratoire, et merci à toutes les personnes du laboratoire GeoRessources de Nancy.*

*Je souhaite remercier Céline Thomachot-Schneider qui s'est énormément investi dans ce projet et qui a dirigé mes travaux avec beaucoup de justesse. Merci pour tes différents points de vue et conseils qui m'ont beaucoup aidé et sans eux, ce travail n'aurait pas pu aboutir.*

*Je souhaite remercier vivement Vincent Barbin, directeur du GEGENAA qui m'a accueilli au sein de son laboratoire. Merci d'avoir suivi de très près le déroulement de ce travail de thèse.*

*Je souhaite ensuite exprimer ma reconnaissance à Madame Sara Vandycke, Professeure de l'université de Mons, et Monsieur Patrick Baud, Professeur de l'université de Strasbourg, qui ont accepté d'être rapporteurs de cette thèse et je tiens sincèrement à les remercier pour l'intérêt qu'ils ont porté à ce travail.*

*Merci à Phillipe Robion, de l'Université de Cergy – Pontoise et Philippe Cosenza de l'université de Poitiers d'avoir fait partie des membres de mon comité et jury de thèse.*

*Merci à David Benavante, chef du groupe de pétrologie appliquée et membre du département des sciences de la terre et de l'environnement de l'Université d'Alicante en Espagne qui m'a accueilli durant trois mois au sein de son laboratoire. Merci de m'avoir tant appris et si bien guidée à mon arrivé.*

*De façon général, je voudrais également dire un grand Merci à toute l'équipe du GEGENAA, que j'ai pu côtoyer quotidiennement pendant toutes ces années et qui ont participé de près ou de loin à cette thèse : Gilles, Stéphanie, Julien, Alexandra, Maxime, Benjamin, Xavier.D, Jessy, Sébastien, Norman, Pauline, Xavier.M, Robin, Marie, Béatrice, Jean-Paul ...ainsi que tous les thésards, postdoctorants et aux stagiaires de passage qui m'ont accompagnée dans cette*

*aventure et auprès desquels j'ai beaucoup appris tant sur le plan scientifique qu'humain : Emilie, Feifei, Sarah, Quayhn, Safa, Soizic, Bachirou, Lucie, Haram, Mirlène, Issra, Dania, Sésil, Léna...*

*A titre plus personnel, je voudrais aussi exprimer toute ma gratitude à mes amis, pour leur soutien sans faille durant toute ces années : Caillou, Matou, mrChalmin, David, Clément, Gautier, Florian (Massedeleau), Adri, Arta...*

*Enfin, Je tiens à remercier du fond du cœur toute ma famille, mes parents, pour m'avoir donné la chance d'arriver jusqu'ici, je m'estime aujourd'hui extrêmement chanceux d'avoir reçu autant d'amour et de soutien de leur part. Je remercie également ma sœur Laura et mon frère Lucas qui m'ont soutenu pendant cette thèse, que j'admire énormément et que j'aime de tout mon cœur.*





# TABLE DES MATIERES

REMERCIEMENTS.....	5
TABLE DES MATIERES.....	9
COMMUNICATIONS SCIENTIFIQUES .....	13
LISTE DES FIGURES .....	17
LISTE DES TABLEAUX.....	25
INTRODUCTION GÉNÉRALE .....	27
<b>I. CHAPITRE : Introduction.....</b>	<b>31</b>
I.1. Contexte.....	32
I.1.1. Exploitation pétrolière .....	32
I.1.2. Géothermie .....	33
I.1.3. Stockage des déchets radioactifs .....	36
I.2. Effet thermique et hydrique.....	36
I.2.1. Craie.....	38
I.2.2. Granite.....	40
I.2.3. Grès .....	46
<b>II. CHAPITRE : Matériels et méthodes .....</b>	<b>49</b>
II.1. Matériels.....	50
II.1.1. Cadre géographique et géologique.....	50
II.1.2. Pétrographie et minéralogie des roches et description de leur porosité .....	53
II.2. Méthodes.....	58
II.2.1. Caractérisation à multi-échelles du réseau poreux .....	58
II.2.2. Classification des pores .....	59
II.2.3. Méthodes d'observation et de quantification .....	61
II.2.4. Analyses pétrophysiques.....	67
<b>III. CHAPITRE : Caractérisation et comportement de la craie de Châlons face à des sollicitations thermiques et hydriques.....</b>	<b>101</b>

III.1.	Article#1 : Characterization of the microstructure of the Châlons chalk and statistical relationship between its petrophysical parameters. ....	109
III.1.1.	INTRODUCTION .....	110
III.1.2.	MATERIAL .....	112
III.1.3.	METHODOLOGY.....	113
III.1.4.	RESULTATS AND DISCUSSION.....	121
III.1.5.	CONCLUSION .....	140
III.2.	Article#2 : Behavior of Chalk under fluid flows at Contrasting Temperatures. ....	141
III.2.1.	INTRODUCTION .....	142
III.2.2.	MATERIAL .....	146
III.2.3.	METHODOLOGY.....	147
III.2.4.	RESULTS .....	158
III.2.5.	DISCUSSION .....	168
III.2.6.	CONCLUSION .....	172
<b>IV.</b>	<b>CHAPITRE : Comportement thermo-hydrigue du granite.....</b>	<b>175</b>
IV.1.	Article#3: Microstructural Evolution of Granitic Stones Exposed to Different Thermal Regimes Analysed by Infrared Thermography.....	183
IV.1.1.	INTRODUCTION .....	185
IV.1.2.	MATERIALS .....	186
IV.1.3.	METHODOLOGY.....	189
IV.1.4.	RESULTS.....	196
IV.1.5.	DISCUSSION .....	208
IV.1.6.	CONCLUSION .....	216
IV.2.	Article#4: Experimental Investigation of the Effect of Quenching Cycles on the Physico-chemical Properties of Granites.....	219
IV.2.1.	INTRODUCTION .....	221
IV.2.2.	MATERIALS .....	224
IV.2.3.	METHODOLOGY.....	227
IV.2.4.	RESULTS.....	235

IV.2.5. DISCUSSION .....	251
IV.2.6. CONCLUSION .....	262
<b>V. CHAPITRE : Changements microstructuraux de 3 roches réservoirs : craie, granite et grès</b>	<b>265</b>
V.1. Article #5: The Use of Infrared Thermography on the Measurement of Microstructural Changes of Reservoir Rocks Induced by Temperature. ....	271
V.1.1. INTRODUCTION .....	273
V.1.2. MATERIALS .....	276
V.1.3. METHODOLOGY.....	277
V.1.4. RESULTS.....	281
V.1.5. DISCUSSION .....	294
V.1.6. CONCLUSION .....	303
<b>DISCUSSION GÉNÉRALE.....</b>	<b>307</b>
<b>CONCLUSION GÉNÉRALE .....</b>	<b>319</b>
<b>BIBLIOGRAPHIE.....</b>	<b>323</b>



# COMMUNICATIONS SCIENTIFIQUES

## Publications scientifiques

Junique, T., Vazquez, P., Thomachot-Schneider, C., Hassoun, I., Jean-Baptiste, M., & Géraud, Y. (2021). **The Use of Infrared Thermography on the Measurement of Microstructural Changes of Reservoir Rocks Induced by Temperature.** Applied Sciences, 11(2), 559.

\*

Junique, T., Vazquez, P., Géraud, Y., Thomachot-Schneider, C., & Sidibé, H. (2021). **Microstructural evolution of granitic stones exposed to different thermal regimes analysed by infrared thermography.** Engineering Geology, 106057.

\*

Junique, T., Vazquez, P., Benavente, D., Thomachot-Schneider, C., & Géraud, Y. (2021). **Experimental Investigation of the Effect of Quenching Cycles on the Physico-chemical Properties of Granites.** Geothermics, 102235.

\*

Junique, T., Géraud, Y., Vazquez, P., & Thomachot-Schneider, C., **Characterization of the microstructure of Châlons chalk and statistical relationship between its petrophysical parameters.**

2021, Engineering Geology [à soumettre]

\*

Junique, T., Géraud, Y., Vazquez, P., & Thomachot-Schneider, C., **Behavior of Chalk under the fluids flow at Contrasting Temperatures.**

2021, Journal of Petroleum Science and Engineering [à soumettre]

\*\*\*

### Communications orales et par voie d'affiche

Vazquez, P., Junique, T., Can, S., Ageorges, L., & Benkara, D., **Influence of porosity and mineralogy on Infrared Thermography measurements.** JpGU-AGU Online Meeting 2021, Japan Geoscience Union Meeting 2021.

\*

Junique, T., Vazquez, P., Thomachot-Schneider, C., Jean Baptiste, M., & Hassoun, I., **Coupled capillary water uptake and Infrared Thermography to assess crack evolution.** JpGU-AGU Meeting 2020, Jul 2020, Chiba, Japan. (hal-02961557)

\*

Junique, T., Vazquez, P., Géraud, Y., Thomachot-Schneider, C., Sidibé, H., & Hassoun, I., **Experimental evaluation of the texture evolution of geothermal system rocks exposed to different thermal regimes.** 36th International Geological Congress, 2-8 Mars 2020, Delhi, Inde. Abstract et bourse complète acceptés (**congrès annulé**).

\*

Junique, T., Vazquez, P., Thomachot-Schneider, C., & Géraud, Y., **Comportement de la craie sous la circulation de fluides à températures contrastées.** Réunion des Sciences de la Terre, Oct 2018, Lille, France. (hal-02961698)

Junique, T., **Comportement des roches sous sollicitations thermiques et circulation de fluides,** Challenge de vulgarisation scientifique « Ma thèse en 180 secondes », Université de Reims Champagne-Ardenne, Sélection régionale (2018)

\*

Junique, T., Vazquez, P., Thomachot-Schneider, C., & Géraud, Y., **Comportement des roches sous sollicitations thermiques et circulations de fluides.** 1ère journée doctorale transfrontalière, 2018, Reims, France. (hal-02981461)







# LISTE DES FIGURES

FIGURE I-1. SCHEMA DU DISPOSITIF DE BASE D'UNE CENTRALE GEOTHERMIQUE DE TYPE EGS. ....	35
FIGURE I-2. SENSIBILITE THERMIQUE DES ROCHES EN FONCTION DE LEUR MICROSTRUCTURE (D'APRES HOMAND ET AL., 2000). ....	37
FIGURE I-3. L'ACTION PHYSIQUE ET LES REACTIONS CHIMIQUES POUR LE CHAUFFAGE DU GRANITE EN FONCTION DE LA TEMPERATURE. (W. ZHANG ET AL., 2018) .....	41
FIGURE II-1. CONTEXTE GEOLOGIQUE ET GEOGRAPHIQUE. A. CRAIE DE CHALONS (C). B. GRANITES IBERIQUES (A, GA, GS, SM) DANS LE DIAGRAMME DU MACIZO IBERICO. C. GRES DE FONTAINEBLEAU (FS). ADAPTE DE VAZQUEZ ET AL. (2018A) ET THIRY ET AL. (1988). ....	51
FIGURE II-2. ROCHES SELECTIONNEES. PHOTOGRAPHIES REALISEES AU MICROSCOPE BINOCULAIRE, OPTIQUE (LUMIERE POLARISEE) ET ELECTRONIQUE A BALAYAGE (MEB). (QZ : QUARTZ ; AFS : FELDSPATH ALCALIN ; PL : PLAGIOCLASE ; M : MICA).....	54
FIGURE II-3. GAMMES DES METHODES DE CARACTERISATION MULTI-EHELLES DU RESEAU POREUX (MODIFIE DE MEYER ET AL. (1994) ET ROBERT, (2004)). ....	59
FIGURE II-4. REPRESENTATION SCHEMATIQUE 2D DES DIFFERENTES POROSITES PRESENTENT DANS UN MATERIEL ROCHEUX. ....	60
FIGURE II-5. SCHEMA IDEALISE DES FISSURES INTERGRANULAIRES, INTRAGRANULAIRES ET TRANSGRANULAIRES IDENTIFIEES DANS UN GRANITE. ....	60
FIGURE II-6. CLASSIFICATION DES PORES PROPOSEE PAR L'IUPAC ( <i>INTERNATIONAL UNION OF PURE AND APPLIED CHEMISTRY</i> ) ET CLASSIFICATION ADOPTEE POUR CETTE ETUDE SELON FRONTEAU, 2000 ET ROBERT, 2004.....	61
FIGURE II-7. MICROSCOPE OPTIQUE (OLYMPUS BX51).....	62
FIGURE II-8. DIMENSION ET NOMBRE DES ECHANTILLONS ETUDIES EN MICROTOMOGRAPHIE.....	64
FIGURE II-9. PHOTOGRAPHIE DU TOMOGRAPHE PHOENIX NANOTOM S <sup>®</sup> UTILISE. ....	64
FIGURE II-10. PRINCIPE DE LA MICROTOMOGRAPHIE A RAYONS X ALLANT DE LA RECONSTRUCTION D'IMAGE A LA VISUALISATION 3D.....	65
FIGURE II-11. EXEMPLES DE COUPES MICROTOMOGRAPHIQUES OBTENUES SUR LA CRAIE ET UN GRANITE. ....	66
FIGURE II-12. PHOTOGRAPHIE DU DISPOSITIF DE MESURE DE LA POROSITE TOTALE A L'EAU SOUS VIDE. ....	69
FIGURE II-13. SCHEMA DU DISPOSITIF DE MESURE DE LA MASSE HYDROSTATIQUE D'UN ECHANTILLON SATURE. ....	69
FIGURE II-14. A. POROSIMETRE MERCURE AUTOPORE IV 950 ANALYSER DE MICROMERITICS AVEC DANS LA PARTIE HAUTE, LES PORTS DE MESURE A BASSE PRESSION ET DANS LA PARTIE INFERIEURE, LA CELLULE HAUTE PRESSION. B. EXEMPLE DE PENETROMETRE ET SA REPRESENTATION SCHEMATIQUE.....	72
FIGURE II-15. EXEMPLES DE COURBES OBTENUES A PARTIR DE LA POROSIMETRIE AU MERCURE POUR UN ECHANTILLON DE CRAIE. A. COURBES D'INTRUSION ET D'EXTRUSION CUMULEES EXPRIMEES EN FONCTION DES RAYONS D'ACCES AUX PORES. B. INCREMENT DE VOLUME DE MERCURE INJECTE EN FONCTION DES RAYONS D'ACCES AUX PORES. ....	74
FIGURE II-16. SCHEMA DU DISPOSITIF DE PYCNOMETRIE A L'HELIUM. ....	75
FIGURE II-17. SCHEMA DU DISPOSITIF UTILISE POUR LES TESTS D'ABSORPTION CAPILLAIRE. ....	79
FIGURE II-18. EXEMPLE DE COURBE CARACTERISTIQUE DE RESTITUTION DES TESTS D'IMBIBITION CAPILLAIRE AVEC LA DETERMINATION DES COEFFICIENTS C1 DE PRISE DE POIDS ET C2 DE REMONTEE DE LA FRANGE HUMIDE.....	80
FIGURE II-19. SCHEMA MONTRANT LA MISE EN PLACE EXPERIMENTALE DE LA METHODE DE MESURE AUTOMATIQUE DE L'ABSORPTION D'EAU PAR CAPILLARITE. ....	81

FIGURE II-20. ILLUSTRATION DES ETAPES DE SUIVI DU REFROIDISSEMENT PAR UNE CAMERA IRT. 1. PHASE DE CHAUFFAGE DE L'ÉCHANTILLON DANS UN FOUR (40 °C) 2. SYSTEME D'ACQUISITION PAR LA CAMERA THERMIQUE 3. ÉTAPE DE TRAITEMENT DES DONNEES D'UN THERMOGRAMME MONTRANT LA FACE DE L'ÉCHANTILLON (COULEURS CHAUDES) ET LES OUTILS DE MESURE DISPONIBLES POUR L'ESTIMATION DE LA TEMPERATURE DE SURFACE. 4. ÉTUDE DES COURBES DE REFROIDISSEMENT. ....	85
FIGURE II-21. CONFIGURATION EXPERIMENTALE DU SUIVI PAR IRT DU REFROIDISSEMENT D'UN ECHANTILLON SOUMIS A UNE IMBIBITION CAPILLAIRE.....	86
FIGURE II-22. A. REPRESENTATION SCHEMATIQUE DE L'INDICE DE REFROIDISSEMENT (CRI10) A LA SURFACE D'UN ECHANTILLON. B. VALEURS DE CRI10 LE LONG DU PROFIL VERTICAL AB. LA LIGNE POINTILLEE ROUGE EST POSITIONNEE SUR LA RUPTURE DE PENTE. SA POSITION EST AFFINEE GRACE AUX ISOLIGNES A LA SURFACE DE L'ECHANTILLON. ....	87
FIGURE II-23. DISPOSITIF EXPERIMENTAL DE MESURE DES VITESSES DE PROPAGATION DES ONDES ACOUSTIQUES.....	89
FIGURE II-24. SCHEMA DE LA TRANSMISSION DES ONDES ULTRASONORES AVEC UN EXEMPLE DE SIGNAUX REÇUS DANS UN ECHANTILLON AU STADE INITIAL ET APRES DES CYCLES DE VIEILLISSEMENT. ....	91
FIGURE II-25. PROPRIETES MAGNETIQUES DES NOYAUX D'HYDROGENE (PROTONS). (MODIFIE DE VINCENT ET AL., 2011). ....	93
FIGURE II-26. SCHEMA EXPLICATIF DE LA RELAXATION DE SURFACE EN RMN. LORSQUE LES PORES SONT DE PETITES TAILLES, LA PROBABILITE D'ENTRER EN COLLISION AVEC LA SURFACE DES GRAINS EST FORTE ET LA RELAXATION EST RAPIDE. LORSQUE LES PORES SONT DE GRANDES TAILLES, LA PROBABILITE D'ENTRER EN COLLISION AVEC LA SURFACE DES GRAINS EST FAIBLE ET LA RELAXATION EST LENTE. ....	94
FIGURE II-27. APPAREIL RMN MINISPEC ET ORDINATEUR DE CONTROLE. ÉCHANTILLON SATURE DANS UN RECIPIENT EN VERRE.....	95
FIGURE II-28. RESUME DE L'UTILISATION DE LA RMN DANS L'ANALYSE DES ROCHES POREUSES. A. SCHEMA 2D D'UNE FISSURE, LES CERCLES BLEUS SONT DETECTES PAR RMN. B. COURBE DE DECROISSANCE DE L'AIMANTATION TRANSVERSALE. C. COURBE DE DISTRIBUTION DU TEMPS DE RELAXATION TRANSVERSALE (T2) CONSTRUITE PAR UN PROCESSUS D'INVERSION MATHEMATIQUE. ....	96
FIGURE II-29. RELATION ENTRE LE RAYON DE PORE ( $\mu\text{m}$ ) ET LE T2 MESURE AVEC $p = 2 \mu\text{m/s}$ A PARTIR DE L'EQUATION (II. 29). ....	97
FIGURE III-1. SCHEMA DES 4 DISPOSITIFS REALISES POUR SIMULER DES CYCLES DE CIRCULATION DE FLUIDES A TEMPERATURES CONTRASTEES. ....	105
FIGURE III-2. GEOLOGICAL AND GEOGRAPHICAL SETTINGS OF THE CHALK SAMPLING SITE (RED STAR). MODIFIED FROM RICHARD ET AL. (1997). ....	113
FIGURE III-3. METHOD FOR MEASURING THE SIZE OF PORES AND COCCOLITHS USING THE J.MICROVISION SOFTWARE. A. EXAMPLE OF POROSITY THRESHOLDING (SELECTED IN RED). B. DISTRIBUTION CURVE OF THE PORE LENGTH (DISTRIBUTION INTERVAL: 0.25 $\mu\text{m}$ ) OF THE EXAMPLE IMAGE (A). C. EXAMPLE OF MEASURING THE MAXIMUM LENGTH OF COCCOLITHS (RED LINE). D. DISTRIBUTION CURVE OF THE LENGTH OF THE COCCOLITHS (DISTRIBUTION INTERVAL: 0.25 $\mu\text{m}$ ) OF THE EXAMPLE IMAGE (C). ....	118
FIGURE III-4. PRINCIPLE OF X-RAY MICROTOMOGRAPHY, IMAGE RECONSTRUCTION, AND 2D AND 3D VISUALIZATION. ....	120
FIGURE III-5. SIZE RANGE ASSESSED ACCORDING TO THE PORE CHARACTERIZATION TECHNIQUES USED (ZHANG ET AL., 2018; JAFFEL, 2006; MEYER ET AL., 1994).....	123
FIGURE III-6. SEM IMAGE OF NANNOFACIES (PUNCTIC STRUCTURE) OF THE CHALONS CHALK. A. COCCOLITHS OF A FEW MICRONS AS THE MAIN CONSTITUENTS OF THE ROCK. B. INTERPARTICLE PORES OF SMALL SIZES COMING FROM THE SPACES BETWEEN THE	

GRAINS AND OF THE EMPTY IMPRINT OF THE DISSOLVED ORGANISM. C. VIEW OF A MACROPORE FROM THE DISSOLUTION OF A BIOCLAST. D. LARGE DIAMETER INTRAPARTICLE PORE. ....	124
FIGURE III-7. DISTRIBUTION OF THE SIZE OF A. THE COCCOLITHS AND B. THE PORES USING THE J.MICROVISION SOFTWARE ON 478 INDIVIDUALS FOR THE COCCOLITHS AND 5907 INDIVIDUALS FOR THE PORES (DISTRIBUTION INTERVAL: 0.25 MM). ....	125
FIGURE III-8. QUALITATIVE AND QUANTITATIVE DATA EXTRACTED FROM X-RAY CT MEASUREMENTS. A. X-RAY MICROTOMOGRAPHY 2D IMAGES AND FOCUS ON A FORAMINIFERA PRINT. B. RECONSTRUCTION OF THE 3D POROUS NETWORK. C. PORE DIAMETER DISTRIBUTION (DISTRIBUTION RANGE: 20 MM). D. RELATIONSHIP BETWEEN SPHERICITY AND PORE DIAMETER.....	127
FIGURE III-9. CURVES OBTAINED FROM MERCURY POROSIMETRY. A. INCREMENTAL DISTRIBUTION OF THE MIP THROAT SIZE. B. MIP POROSITY (%) AND THE VALUE OF THE MEDIAN RADIUS ( $\mu\text{M}$ ).....	128
FIGURE III-10. A. INCREMENTAL NMR OBTAINED BY INVERSION OF THE RELAXATION CURVE. B. DISTRIBUTION OF THE TRANSVERSE RELAXATION TIME T2 (MS) (DISTRIBUTION INTERVAL: 2 MS). ....	129
FIGURE III-11. A. COMPARISON OF THE SIZE DISTRIBUTION OF THE INTERPARTICLE VOIDS BY NMR AND MIP. THE NMR DISTRIBUTION WAS CONVERTED INTO THE DISTRIBUTION OF THE RADIUS OF THE SIZE OF THE VOIDS USING THE CALIBRATION OF THE LARGE VOIDS DETERMINED BY X-RAY TOMOGRAPHY. B. SCHEMATIC REPRESENTATION OF THE CHALK MICROSTRUCTURE WITH THE CHARACTERISTICS OF EACH FAMILY OF PORES.....	129
FIGURE III-12. A. WEIGHT GAIN RELATIVE TO THE SAMPLE AREA ( $\Delta W / S$ ) AS A FUNCTION OF THE SQUARE ROOT OF TIME ( $\sqrt{t}$ ). B EFFECTIVE RADII AS A FUNCTION OF THE CAPILLARY COEFFICIENTS.....	131
FIGURE III-13. BOXPLOT ON PETROPHYSICAL PROPERTIES OF THE CHALK. THE LIMITS OF THE BOX REPRESENT 25% AND 75% OF THE DISTRIBUTION (QUANTILES Q1 AND Q3), THE LINE INSIDE THE BOX REPRESENTS THE MEDIAN VALUE (50% OF SAMPLES). THE CENTRAL RED CROSS REPRESENTS THE MEAN VALUE. THE EXTREME POINTS REPRESENT THE MINIMA AND MAXIMA. ....	133
FIGURE III-14. RELATIONSHIP BETWEEN TOTAL POROSITY AND YOUNG'S MODULUS E FROM DIFFERENT STUDIES (DATA: BELL, 1977; ENGSTRØM, 1992; MONJOIE AND SCHROEDER, 1989; SHITRIT ET AL., 2016; SIWAK, 1994).....	134
FIGURE III-15. A. DATA VISUALIZATION FOR THE FIRST TEST WITH 33 SAMPLES. B. CORRELATION CIRCLES (DIM1×DIM2) OF THE PRINCIPAL COMPONENT ANALYSIS (PCA). RELATIONSHIP BETWEEN C THE CAPILLARY COEFFICIENT AND THE PORE SIZE (NMR), D. THE FREE POROSITY AND THE PERMEABILITY, E. THE CAPILLARY COEFFICIENT AND MEDIAN PORE RADIUS (MIP) (N=33)...	138
FIGURE III-16. A. VISUALIZATION OF MISSING DATA, B. CORRELATION CIRCLES (DIM1×DIM2) OF THE PCA ON VARIABLES OF ALL SAMPLES WITHOUT THE MISSING DATA. WEIGHT CLOUDS REPRESENT THE CONFIDENCE ZONES OF SEVERAL IMPUTED DATA SETS. RELATIONSHIP BETWEEN C. THE FREE POROSITY AND THE P- WAVES PROPAGATION VELOCITY, D. THE CAPILLARY COEFFICIENT AND THE P- WAVES PROPAGATION VELOCITY (N=445).....	139
FIGURE III-17. A. GEOLOGICAL AND GEOGRAPHICAL SETTINGS OF THE CHALK SAMPLING SITE (RED STAR). MODIFIED FROM RICHARD ET AL. (1997). B. SAMPLING OUTCROP AND CORE PLUG SAMPLES.....	147
FIGURE III-18. EXPERIMENTAL SETUP OF A SAMPLE SUBMITTED TO CAPILLARY ABSORPTION AT CONTRASTED TEMPERATURE. ....	149
FIGURE III-19. TEMPERATURE MONITORING DURING THE HR-CF EXPERIMENT AND INSTRUMENTED SAMPLE.....	150
FIGURE III-20. SETUP DESIGNED FOR THERMAL SHOCK TS TESTING. ....	150
FIGURE III-21. EXPERIMENTAL DEVICE FOR THE SIMULATION OF CONTINUOUS FLUID FLOW. A. C-R-F TEST AT ROOM TEMPERATURE. B. C-HR-CF / C-CR-HF TESTS AT CONTRASTED TEMPERATURE. ....	151
FIGURE III-22. SUMMARY OF THE USE OF NMR IN THE ANALYSIS OF POROUS ROCKS. A. PHOTOGRAPH OF MINISPEC MQ-SERIES INSTRUMENT AND THE HERMETIC SUPPORT CONTAINING THE SAMPLE. B. SEM IMAGE OF THE CHALK TO VISUALISE PORES, THE	

BLUE CIRCLES ARE DETECTED BY NMR. C. THE TRANSVERSE MAGNETISATION DECAY CURVE. D. THE TRANSVERSE RELAXATION TIME ( $T_2$ ) DISTRIBUTION CURVE CONSTRUCTED BY A MATHEMATICAL INVERSION PROCESS (THE CURVE REFLECTS A DISTRIBUTION OF PORE, SURFACE TO VOLUME RATIOS $V/S$ ).	156
FIGURE III-23. SUMMARY OF THE USE OF X-RAY MICRO-TOMOGRAPHY IN THE ANALYSIS OF POROUS ROCKS.	157
FIGURE III-24. POROSITY BY MERCURY INJECTION $\Phi_{MIP}$ (%) (FREE AND TRAPPED) AND THE VALUE OF THE MEDIAN RADIUS ( $\mu\text{M}$ ). INITIAL STATE $N = 10$ AND FOR THE REMAINDER $N = 1$ .	160
FIGURE III-25. RELATIONSHIP BETWEEN THE NUMBER OF CYCLES AND THE CAPILLARY COEFFICIENT (C) FOR CAPILLARY IMBIBITION FLUID FLOW TESTS.	161
FIGURE III-26. RELATIONSHIP BETWEEN THE NUMBER OF CYCLES AND THE CAPILLARY COEFFICIENT (C) FOR CONTINUOUS FLUID FLOW TESTS.	162
FIGURE III-27. RELATIONSHIP BETWEEN THE NUMBER OF CYCLES AND P-WAVES PROPAGATION VELOCITIES AND THE YOUNG'S DYNAMIC MODULUS (E) FOR CAPILLARY IMBIBITION FLUID FLOW TESTS.	163
FIGURE III-28. INCREMENTAL NMR OBTAINED BY INVERSION OF THE RELAXATION CURVE ON FLUID FLOW TESTS BY CAPILLARY IMBIBITION.	165
FIGURE III-29. INCREMENTAL NMR OBTAINED BY INVERSION OF THE RELAXATION CURVE ON CONTINUOUS FLUID FLOW TESTS AT INITIAL STATE AND AFTER 10 LITERS.	165
FIGURE III-30. DISTRIBUTION OF THE PORE RADIUS ( $\mu\text{M}$ ) (DISTRIBUTION INTERVAL: $2 \mu\text{M}$ ) AND RECONSTRUCTION OF THE 3D POROUS NETWORK.	167
FIGURE III-31. A. CUMULATIVE DISTRIBUTION OF THE PORE RADIUS OF THE TOTAL INTERPARTICLE VOIDS AND DISTRIBUTION OF THE PORE RADIUS ( $\mu\text{M}$ ) (DISTRIBUTION INTERVAL: $1 \mu\text{M}$ ) BETWEEN 0 AND $20 \mu\text{M}$ FOR THE HR-CF AND CR-HF TEST.	168
FIGURE IV-1. SCHEMA DES DIFFERENTS TAUX DE REFROIDISSEMENT D'UN RESERVOIR CHAUD LORS D'UNE INJECTION DE FLUIDE.	178
FIGURE IV-2. MACROSCOPIC AND MICROSCOPIC PHOTOGRAPHS (POLARISED LIGHT OPTICAL MICROSCOPY) OF THE STUDIED GRANITE: ALBERO (A); GRIS ALBA (GA); GOLDEN SKI (GS); SILVESTRE MORENO (SM). (QZ: QUARTZ; AFS: ALKALI FELDSPAR; PL: PLAGIOCLASE; M: MICA).	187
FIGURE IV-3. EXPERIMENTAL SETUP OF INFRARED THERMOGRAPHY (IRT) MONITORING OF A SAMPLE SUBMITTED TO CAPILLARY ABSORPTION.	193
FIGURE IV-4. A. SCHEMATIC REPRESENTATION OF THE COOLING RATE INDEX (CRI10) ON THE SURFACE OF THE SAMPLES. B. CRI10 VALUES ALONG THE VERTICAL PROFILE AB. THE RED DOTTED LINE IS POSITIONED IN THE CENTRE OF THIS AREA. ITS POSITION IS REFINED THANKS TO THE ISOLINES ON THE SURFACE OF THE SAMPLE. COOLING RATE INDEX (CRI10) REPRESENTING THE TEMPERATURE VARIATION PER UNIT OF TIME (10 MIN).	196
FIGURE IV-5. SAMPLE SURFACES BEFORE AND AFTER 5 CYCLES OF HEAT TREATMENT OF EXP2. ALBERO (A); GRIS ALBA (GA); GOLDEN SKI (GS); SILVESTRE MORENO (SM). INITIALLY, THE YELLOW-BROWN COLOUR IS DUE TO FELDSPAR WEATHERING TO CLAY MINERALS. A RED COLOUR CHANGE AT CRYSTAL BOUNDARIES WAS OBSERVED AT $200(5)^\circ\text{C}$ DUE TO THE IRON OXIDATION OF THOSE CLAYS.	197
FIGURE IV-6. PORE ACCESS SIZE DISTRIBUTION CURVES FOR EXP1 AND EXP2. THE CURVES SHOW THE GRANITES TESTED AT ROOM TEMPERATURE (INITIAL STATE), $90^\circ\text{C}$ , $130^\circ\text{C}$ , $200(1)^\circ\text{C}$ AND $200(5)^\circ\text{C}$ . (A-A') ALBERO, (B-B'), GRIS ALBA, (C-C') GOLDEN SKI, (D-D') SILVESTRE MORENO.	198

FIGURE IV-7. OPTICAL POLARISING MICROSCOPY (POL) AND SCANNING ELECTRON MICROSCOPY (SEM) ILLUSTRATING THE MINERALOGY (QZ: QUARTZ; AFS: ALKALI FELDSPAR; PL: PLAGIOCLASE; M: MICA) AND THE MICROCRACKING OF THE FOUR GRANITES BEFORE AND AFTER ONE THERMAL TREATMENT AT 200 °C (200(1) °C). ALBERO (A), GRIS ALBA (GA), GOLDEN SKI (GS), AND SILVESTRE MORENO (SM). .....	201
FIGURE IV-8. EVOLUTION OF THE CAPILLARY COEFFICIENT (C) DURING THE 2 HEAT TREATMENTS (EXP1 IN BLUE AND EXP2 IN RED). THE FULL LINE CORRESPONDS TO SAMPLE 1 AND THE DOTTED LINE TO SAMPLE 2. ....	203
FIGURE IV-9. EVOLUTION OF THE CRI10 MEASURED AT THE TOP OF THE SAMPLE (AIR COOLING-SPOT C5) AND THE BOTTOM (WATER COOLING-SPOT C1) THROUGH EXP2. ....	205
FIGURE IV-10. EXAMPLE OF CRI10 MAPPING (A) AND ASSOCIATED PROFILES (B) OBTAINED BY INFRARED THERMOGRAPHY (IRT) MONITORING ON GA BEFORE AND AFTER ONE THERMAL CYCLE AT 200 °C (200(1) °C) AND FIVE THERMAL CYCLES (200(5) °C): THE DOT BLUE LINE CORRESPONDS TO THE TRANSITION ZONE AND IS ASSUMED TO CORRESPOND TO THE POSITION OF THE CAPILLARY FRINGE. ....	207
FIGURE IV-11. HEIGHT OF THE CAPILLARY FRINGE AFTER THE FIRST 10 MINUTES (H) OF CAPILLARY ABSORPTION OF THE FOUR GRANITES BEFORE AND AFTER THERMAL CYCLES AT 200 °C (EXP2). ....	208
FIGURE IV-12. A. THERMAL DILATION CURVE ( $\Delta L$ ) OF THE FOUR GRANITES SUBMITTED TO HEATING-COOLING CYCLES OVER A RANGE OF 20 TO 90 °C. RESIDUAL STRAIN (RS) EXPRESSED IN MM / M. B. RELATIONSHIP BETWEEN THE Qz / F RATIO AND AVERAGE RESIDUAL STRAIN OF A, GA, GS, AND SM (VAZQUEZ ET AL., 2010, 2011, 2015). ....	210
FIGURE IV-13. SIZE DISTRIBUTION OF THE VOIDS. ON THE TOP OF EACH COLUMN, THE POROSITY BY MIP IS DETAILED. ....	212
FIGURE IV-14. DIAGRAM OF THE PARAMETER EVOLUTION DURING EXP2: MERCURY INTRUSION POROSIMETRY (MIP), THE COOLING RATE INDEX (CRI10 (C1); CRI10 (C5)) TO SPOT C1 AND C5, THE CAPILLARY COEFFICIENT (C) AND THE HEIGHT OF THE CAPILLARY FRINGE DETECTED WITH AN INFRARED THERMOGRAPHY CAMERA (H). EXCEPT FOR MIP, THE PARAMETERS WERE MEASURED ON THE SAME SAMPLES. ....	215
FIGURE IV-15. A. GEOLOGICAL AND GEOGRAPHICAL SETTINGS OF THE IBERIAN GRANITES STUDIED WITHIN THE DIAGRAM OF THE MACIZO IBERICO: ALBERO (A), GRIS ALBA (GA), GOLDEN SKI (GS), AND SILVESTRE MORENO (SM) GRANITES. B. TERNARY DIAGRAM WITH QUARTZ (Q), POTASSIUM FELDSPAR (FK), AND PLAGIOCLASE (P) REPRESENTING GRANITES OF THIS STUDY (RED) AND GRANITES FROM GLOBAL EGS SITES (YELLOW). (ALT-EPPING ET AL., 2013 <sup>1</sup> ; KOVAC ET AL., 2004 <sup>2</sup> ; LUTZ ET AL., 2004 <sup>3</sup> ; MARSHALL ET AL., 2010 <sup>4</sup> ; STUSSI ET AL., 2002 <sup>5</sup> ; UEDA ET AL., 2005 <sup>6</sup> ; VAZQUEZ ET AL., 2018A <sup>7</sup> ; ZHOU ET AL., 2016 <sup>8</sup> ). ....	224
FIGURE IV-16. MACROSCOPIC AND MICROSCOPIC PHOTOGRAPHY OF THE STUDIED GRANITE: GRIS ALBA (GA), SILVESTRE MORENO (SM), GOLDEN SKI (GS), AND ALBERO (A). ....	226
FIGURE IV-17. A. EXPERIMENTAL METHODOLOGY. B. DETAIL OF SAMPLING DURING THE CYCLES (C). ....	228
FIGURE IV-18. DIAGRAM OF THE TRANSMISSION OF ULTRASONIC WAVES WITH AN EXAMPLE OF SIGNALS RECEIVED AS A FUNCTION OF THE DEGRADATION OF THE ROCK. ....	231
FIGURE IV-19. SUMMARY OF THE USE OF NMR IN THE ANALYSIS OF POROUS ROCKS. A. DIAGRAM OF THE ENLARGED 2D X-RAY CT VIEW OF THE SM GRANITE TO VISUALISE THE CRACKS, THE BLUE CIRCLES ARE DETECTED BY NMR. B. THE TRANSVERSE MAGNETISATION DECAY CURVE (EXAMPLE OF MEASUREMENT ON THE SM GRANITE). C. THE TRANSVERSE RELAXATION TIME (T2) DISTRIBUTION CURVE CONSTRUCTED BY A MATHEMATICAL INVERSION PROCESS (THE CURVE REFLECTS A DISTRIBUTION OF PORE, SURFACE TO VOLUME RATIOS V / S). ....	232
FIGURE IV-20. PRINCIPLE OF X-RAY MICROTOMOGRAPHY GOING FROM IMAGE RECONSTRUCTION TO 3D VISUALISATION. ....	234

FIGURE IV-21. RELATIONSHIP BETWEEN THE NUMBER OF THERMAL CYCLES AND THE CONNECTED POROSITY ( $\Phi_c$ ) FOR THE TWO QUENCHING TESTS AT 200 °C AND 400 °C. ....	237
FIGURE IV-22. RELATIONSHIP BETWEEN THE NUMBER OF THERMAL CYCLES AND THE CAPILLARY COEFFICIENT (C) FOR THE TWO QUENCHING TESTS AT 200 °C AND 400 °C. ....	238
FIGURE IV-23. RELATIONSHIP BETWEEN THE NUMBER OF THERMAL CYCLES AND THE PERCENTAGE CHANGE IN THE P-WAVES VELOCITY ( $V_p$ ) AND THE AMPLITUDE COEFFICIENT (A) WITH THE INITIAL STATE. SOLID AND DASHED BLACK LINES REPRESENT THE TREND FOR 200 °C AND 400 °C, RESPECTIVELY. ....	241
FIGURE IV-24. RELATIONSHIP BETWEEN THE NUMBER OF THERMAL CYCLES AND THE YOUNG'S MODULUS (E) FOR THE TWO QUENCHING TESTS. ....	242
FIGURE IV-25. EVOLUTION OF THE TRANSVERSE RELAXATION TIME (T2) DISTRIBUTION CURVES AFTER 1 AND 35 CYCLES. THE INITIAL AND FINAL STATE CORRESPONDING TO THE SAME SAMPLES. ....	243
FIGURE IV-26. RELATIONSHIP BETWEEN THE NUMBER OF THERMAL CYCLES AND THE TRANSVERSE RELAXATION TIME (T2) FOR THE TWO QUENCHING TESTS. ....	244
FIGURE IV-27. HORIZONTAL X-RAY CT SLIDES OF GA AND SM INITIAL AND FINAL STATE (CYCLE 35) FOR THREE DIFFERENT ELEVATIONS. THE PORES AND CRACKS ARE PRESENTED IN RED COLOR. ....	246
FIGURE IV-28. QUALITATIVE AND QUANTITATIVE DATA EXTRACTED FROM X-RAY CT MEASUREMENTS BEFORE AND AFTER THE QUENCHING TEST (CYCLE 35). A-A'. RECONSTRUCTION OF THE 3D POROUS NETWORK. B-B'. RELATIONSHIP BETWEEN VOLUME AND DIAMETER OF PORES. C-C'. PORE SIZE-FREQUENCY DISTRIBUTION. ....	248
FIGURE IV-29. CUMULATIVE CURVES OF THE CONCENTRATION (PPB) IN AL, FE, K, MG, CA, AND NA IN THE SOLUTIONS AS A FUNCTION OF THE NUMBER OF CYCLES FOR THE TWO QUENCHING TESTS. ....	250
FIGURE IV-30. RELATIONSHIP BETWEEN THE INITIAL POROSITY OF THE GRANITE AND THEIR CAPILLARY COEFFICIENT, MAXIMUM AMPLITUDE OF THE P-WAVES, AND YOUNG MODULUS. ....	252
FIGURE IV-31. EVOLUTION OF THE PARAMETERS MEASURED FOR THE TWO QUENCHING TESTS. C: CAPILLARY COEFFICIENT; $V_p$ : P-WAVE PROPAGATION VELOCITY; $V_s$ : S-WAVE PROPAGATION VELOCITY; A: AMPLITUDE COEFFICIENT; E: YOUNG'S MODULUS; T2: TRANSVERSE RELAXATION TIME AND $\Phi_c$ : CONNECTED POROSITY. ....	255
FIGURE IV-32. SYNTHESIS OF MICROSTRUCTURAL AND OBSERVATIONS. $\uparrow$ : INCREASE; $\downarrow$ : DECREASE; C: CAPILLARY COEFFICIENT; $V_p$ : P-WAVE PROPAGATION VELOCITY; $V_s$ : S-WAVE PROPAGATION VELOCITY; A: AMPLITUDE COEFFICIENT; E: YOUNG'S MODULUS; T2: TRANSVERSE RELAXATION TIME AND $\Phi_c$ : CONNECTED POROSITY.....	257
FIGURE IV-33. EVOLUTION OF THE PERMEABILITY K AND THE DAMAGE FACTOR DE AS A FUNCTION OF THE NUMBER OF CYCLES. SAMPLES PREHEATED AT 200 °C AND 400 °C ARE REPRESENTED BY CIRCLES AND TRIANGLES, RESPECTIVELY. THE RED AND PURPLE ARROWS REPRESENT THE DIRECTION OF THE EVOLUTION OF THE 2 PARAMETERS. THE BASE OF ARROWS WAS POSITIONED ON THE AVERAGE VALUE OF 3 INITIAL SAMPLES AND HAVING REACHED THE AVERAGE VALUE OF 3 SAMPLES OF THE FINAL CYCLE. ....	259
FIGURE V-1. SELECTED ROCKS. PHOTOGRAPHS MADE UNDER A BINOCULAR MICROSCOPE. A. CHALONS CHALK (CC); B. FONTAINEBLEAU SANDSTONE (FS); C. GRIS ALBA GRANITE (GA); D. GOLDEN SKI GRANITE (GS).....	276
FIGURE V-2. EXPERIMENTAL SETUP OF CAPILLARY UPTAKE CONTROLLED BY AUTOMATIC WEIGHT AND IRT MONITORING. ....	279

FIGURE V-3. IRT SETUP. A. SCHEMA OF THE SAMPLE AND THE MEASUREMENTS CARRIED OUT. B. IRT IMAGE IN FALSE COLOUR. C. IMAGE AFTER THE APPLICATION OF A SUBTRACTION AND AN ADVANCED PLATEAU EQUALISATION (APE) SCALE. D. COOLING CURVES. E. INTERPRETATION OF THE IRT IMAGE. ....	280
FIGURE V-4. SEM OBSERVATIONS OF THE CHALONS CHALK (A. CC), THE FONTAINEBLEAU SANDSTONE (B. FS), THE GRIS ALBA GRANITE (C. GA), AND THE GOLDEN SKI GRANITE (D. GS), IN THEIR INITIAL STATE AND AFTER HEATING TREATMENT. (TT: THRESHOLD TEST AND TF: THERMAL FATIGUE TEST). ....	283
FIGURE V-5. PORE ACCESS SIZE DISTRIBUTION CURVES OF SAMPLES BEFORE AND AFTER THE FIRST HEATING CYCLE AND AT THE END OF THE TT (THRESHOLD TEST) AND TF (THERMAL FATIGUE TEST). CC: CHALONS CHALK; FS: FONTAINEBLEAU SANDSTONE; GA: GRIS ALBA GRANITE; GS: GOLDEN SKI GRANITE.....	286
FIGURE V-6. SUBTRACTED IRT IMAGES OF CC (CHALONS CHALK) AND FS (FONTAINEBLEAU SANDSTONE) AT THEIR INITIAL STATE (A–D; K–N) AND AFTER 5 CYCLES OF TF (THERMAL FATIGUE TEST) (200(5) °C) (F–I; P–S) OBTAINED BY SUBTRACTING THERMOGRAMS AT 1, 5, 10, AND 30 MIN FROM THE INITIAL STATE. VERTICAL TEMPERATURE PROFILES ARE PLOTTED FROM THE IRT IMAGES (E,J,O,T). ....	290
FIGURE V-7. SUBTRACTED IRT IMAGES OF GA (GRIS ALBA GRANITE) AND GS (GOLDEN SKI GRANITE) AT THEIR INITIAL STATE (A–D; K–N) AND AFTER 5 CYCLES OF TF (THERMAL FATIGUE TEST) (200(5) °C) (F–I; P–S) OBTAINED BY SUBTRACTING THERMOGRAMS AT 1, 5, 10, AND 30 MIN FROM THE INITIAL STATE. VERTICAL TEMPERATURE PROFILES ARE PLOTTED FROM THE IRT IMAGES (E,J,O,T). ....	292
FIGURE V-8. VARIATIONS OF THE CAPILLARY COEFFICIENT (C), THE COOLING RATE INDEX (CRI), AND THE POROSITY (MIP) ALONG THE THERMAL THRESHOLD TEST (TT). ....	295
FIGURE V-9. DIAGRAM OF THE EVOLUTION OF THE POROUS 2D NETWORK OF THE CHALONS CHALK (A), FONTAINEBLEAU SANDSTONE (B), AND GRIS ALBA (C) ACCORDING TO THE TEMPERATURE. ....	298
FIGURE V-10. RELATIONSHIP BETWEEN THE CAPILLARY COEFFICIENT (C), THE COOLING RATE INDEX (CRI), AND THE MIP POROSITY FOR THE THERMAL FATIGUE TEST (TF). ....	300
FIGURE V-11. FLUID CIRCULATION IN POROUS MEDIA. A. GRANULAR ROCK. B. POLYCRYSTALLINE ROCK. ....	302
FIGURE V-12. ÉVOLUTION DE LA POROSITE DES GRANITES SELON LES DIFFERENTS TRAITEMENTS THERMIQUES APRES 1 CYCLE.....	313





# LISTE DES TABLEAUX

TABLEAU II-1. RESUME DES PRINCIPALES CARACTERISTIQUES DES ROCHES. ....	55
TABLEAU II-2. TAILLES DES ECHANTILLONS EN FONCTION DE LA METHODE PETROPHYSIQUE UTILISEE. ....	67
TABLEAU III-1. RESULTS OF THE SET OF PROPERTIES MEASURED. ....	122
TABLEAU III-2. LIST OF EXPERIMENT AND SPECIFICATION OF MEASUREMENT CONDITIONS.....	148
TABLEAU III-3. CONNECTED POROSITY $\phi_c$ (%) .....	158
TABLEAU III-4. P- AND S-WAVES PROPAGATION VELOCITIES AND THE YOUNG'S DYNAMIC MODULUS (E) FOR CONTINUOUS FLUID FLOW TESTS. ....	163
TABLEAU III-5. GEOMETRICAL PARAMETERS OF INDIVIDUAL PORES DERIVED FROM X-RAY CT DATA.....	167
TABLEAU III-6. INITIAL AND FINAL PETROGRAPHIC PARAMETERS. ....	169
TABLEAU IV-1. MAIN CHARACTERISTICS OF THE SELECTED GRANITOIDS: TRADE NAME, MINERAL PROPORTION, IUGS CLASSIFICATION (LE MAITRE, 2002), Qz / F RATIO (Qz: QUARTZ; F: ALKALI FELDSPAR + PLAGIOCLASE) AND CRYSTAL SIZE (VAZQUEZ ET AL., 2018A).....	188
TABLEAU IV-2. SPECIFICATION OF THE MEASUREMENT CONDITIONS FOR SAMPLES SUBJECTED TO THE TWO-HEAT TREATMENTS (EXP1 AND EXP2). THE RED SAMPLES WERE USED CONTINUOUSLY THROUGH EACH EXP, WHILE THE GREEN ONES WERE USED ONLY ONCE, DUE TO THE DESTRUCTIVE NATURE OF THE MEASUREMENTS CARRIED OUT.....	190
TABLEAU IV-3. TOTAL POROSITY DETERMINED BY MIP (%) OF THE 4 GRANITES BEFORE AND AFTER TREATMENT AT DIFFERENT TEMPERATURES. UNDERLINED VALUES MEAN LOWER VALUES THAN THE FRESH ROCK, IN BOLD THE HIGHER VALUES AND BOLD RED THE FIRST HIGHER VALUE STATED AS THE MICROCRACKING THRESHOLD. ....	197
TABLEAU IV-4. SOME PREVIOUS RESEARCHES ON THE THERMAL MICROCRACKING THRESHOLD. ....	208
TABLEAU IV-5. CHARACTERISTICS OF THE SELECTED GRANITOIDS. TRADE NAME, MINERAL PROPORTION (STUDIED USING OPTICAL POLARISATION MICROSCOPY), IUGS CLASSIFICATION (LE MAITRE, 2002) AND THE CRYSTAL SIZE OF THE STUDIED GRANITES (VAZQUEZ ET AL., 2018A). (AVG: AVERAGE; Q: QUARTZ; FK: ALKALI FELDSPAR; P: PLAGIOCLASE; M: MICA).....	226
TABLEAU IV-6. VALUES OF PHYSICAL PROPERTIES. $\phi_c$ : CONNECTED POROSITY C: CAPILLARY COEFFICIENT; $V_p$ : P-WAVE PROPAGATION VELOCITY; AMP: MAXIMUM AMPLITUDE OF THE P-WAVES; $V_s$ : S-WAVE PROPAGATION VELOCITY; E: YOUNG'S MODULUS AND T2: TRANSVERSE RELAXATION TIME. ....	236
TABLEAU IV-7. CHEMICAL COMPOSITION OF THE MAJOR ELEMENTS EXPRESSED IN PERCENT.....	249
TABLEAU IV-8. MAXIMUM TANGENTIAL TENSILE STRESS GENERATED AT THE SURFACE OF THE GRANITES DURING THE QUENCHING AFTER THE TWO PREHEATING TREATMENTS AND EXPERIMENTAL TENSILE STRENGTH TEST (VAZQUEZ ET AL., 2018A <sup>1</sup> ). ....	253
TABLEAU V-1. SPECIFICATION OF THE MEASUREMENT CONDITIONS FOR SAMPLES SUBJECTED TO THE TWO THERMAL TREATMENTS: THRESHOLD TEST (TT) AND THERMAL FATIGUE TEST (TF).....	278
TABLEAU V-2. POROSITY MIP (%) OF THE 4 ROCKS BEFORE AND AFTER TREATMENT AT DIFFERENT TEMPERATURES (IN BLUE, VALUES LOWER THAN THE INITIAL VALUE, IN RED, VALUES HIGHER THAN THE INITIAL VALUE). ....	285
TABLEAU V-3. CAPILLARY COEFFICIENT (C) ( $G \cdot M^{-2} \cdot S^{-1/2}$ ) BEFORE AND AFTER HEAT TREATMENTS (IN BLUE, VALUES LOWER THAN THE INITIAL VALUES, IN RED, VALUES HIGHER THAN THE INITIAL VALUES). ....	287
TABLEAU V-4. COOLING RATE INDEXES ( $^{\circ}C \cdot MIN^{-1}$ ) OF THE 4 ROCKS BEFORE AND AFTER TREATMENT AT DIFFERENT TEMPERATURES (IN BLUE, VALUES LOWER THAN THE INITIAL VALUES, IN RED, VALUES HIGHER THAN THE INITIAL VALUES). ....	293

TABLEAU V-5. PRINCIPALES CONCLUSIONS DU COMPORTEMENT THERMIQUE DES ROCHES ETUDIEES..... 309

# INTRODUCTION GÉNÉRALE

L'approfondissement des connaissances du **comportement des roches sous sollicitations thermiques et sous circulation de fluides** intéresse de nombreux domaines de la géologie comme la géothermie, le stockage des résidus liquides radioactifs, le captage-stockage du CO<sub>2</sub> ou encore l'activité pétrolière. Afin de garantir le bon développement de ces applications, la connaissance plus générale de roches types et notamment d'un point de vue de la déformation thermique, est indispensable pour identifier les lois de comportement. Il existe encore des questions non résolues autour des déformations et des fracturations des roches par sollicitations thermiques et circulation de fluides. La circulation des fluides affecte les roches de façon chimique par dissolution ou altération, mais aussi de façon mécanique par les contraintes engendrées par les différences de température entre le fluide et la roche encaissante. Cette thèse abordera des principes fondamentaux sur le comportement thermique et comparera l'influence de la température et de la circulation de fluides sur trois roches analogues à celles utilisées comme réservoir ou matériau de stockage. Ces roches sont **la craie, le granite et le grès**. Elles ont été choisies en fonction de leurs **réseaux poreux** différents (type nano- microporeux, fissural et micro- macroporeux, respectivement), leurs **volumes de pores** différents, environ 40-50%, 1-5%, 5-20% respectivement, leurs **minéralogies** et **tailles de grains** différentes, homogènes et monominérales pour la craie et le grès, hétérogène et polyminérale pour le granite. Lorsque la roche est soumise à des sollicitations thermiques, la minéralogie, la texture et la présence d'eau dans la roche jouent un rôle essentiel. Pour comprendre les mécanismes mis en jeu, une étude à petite échelle a été nécessaire. Le suivi des variations texturales produites a été effectué avec des techniques d'imagerie en laboratoire de haute résolution pour ce type de processus et de matériaux (**résonance magnétique nucléaire, microtomographie à rayon X**). D'autres techniques et méthodes comme l'observation directe (**microscopie optique, microscopie électronique à balayage**), les mesures de **porosité (à l'eau ou par injection de mercure)**, **l'absorption d'eau par capillarité** et **l'auscultation ultrasonique** ont été déterminantes dans la description des propriétés de transferts et des propriétés mécaniques des matériaux. Les techniques mises en

œuvres ont permis à la fois d'obtenir des informations sur le volume des différents éléments qui composent le réseau poreux, mais aussi sur leurs dimensions, géométries et connectivités. L'**analyse statistique** des résultats, incluant l'ACP et la représentation en boîte à moustaches, a été réalisée en utilisant le code R (fondation R). Des statistiques descriptives et des régressions linéaires, coefficient de détermination ont été réalisées avec le logiciel xlstat (extension d'Excel). Des tests innovants en laboratoire basés sur la **thermographie infrarouge**, ont été mis en place afin de mettre en évidence les différences et les caractéristiques particulières liées à la structure des roches à l'échelle minérale. La thermographie infrarouge est un outil émergent dans l'étude des roches, utilisé pour détecter les masses d'eau ou déterminer les propriétés thermiques. Le transfert d'eau au sein de la roche a pu être suivi avec cette technique non-destructive. Une **partie expérimentale** a été menée sur les processus de déformation, fracturation et dissolution de roches dans des conditions similaires à celles rencontrées dans le domaine de la géothermie, du stockage et de l'extraction de fluides. Les roches ont été comparées afin d'identifier les différences qui pourraient éventuellement être relevées concernant leurs caractéristiques (poreuses, minérales) et leurs propriétés. Les techniques de mesure ont été **combinées et corrélées** afin de contrôler et d'estimer la répétabilité et l'exactitude des résultats. Cette étude était centrée sur la détermination des valeurs et des variations des paramètres de **structure poreuse** des roches et des **propriétés de transport** des fluides.

Dans ce contexte, l'**objectif principal** de ce projet de thèse **FLUTE**, « **Comportement des roches sous sollicitations thermiques et circulation des fluides** », est d'approfondir les connaissances des variations texturales des roches rencontrées dans le domaine du stockage, de la géothermie et des hydrocarbures (craie, granite, grès) soumis à des contraintes thermiques et à de la circulation de fluides. Cela présente des enjeux majeurs comme l'optimisation de l'extraction et du stockage des ressources naturelles et à la minimisation des risques dans ces roches hôtes.

En outre, **les objectifs** ont été (1) de caractériser en détail la structure de la craie et d'établir les principales relations entre ses propriétés hydriques et le réseau poreux, (2) de déterminer l'effet de la température et de la circulation de l'eau sur l'évolution du réseau de pores de la craie, (3) d'évaluer l'évolution du réseau de pores du granite et l'influence de la porosité lorsque cette roche est exposée à différents traitements thermiques, (4) de déduire le seuil

de fissuration thermique irréversible et l'effet de la fatigue thermique sur la craie, le granite et le grès, (5) et de tirer les informations sur le transport de l'eau par imbibition capillaire qui découlent des tests thermiques.

Afin de répondre à la problématique, la structuration du manuscrit a été établie comme suit :

Le **chapitre 1** (Introduction) présente le contexte global de l'étude. Une synthèse bibliographique des études traitant de l'influence de la température et de la circulation de fluides dans les roches réservoirs a été présentée.

Le **chapitre 2** (Matériels et méthodes) détaille les roches et sites étudiés. Il a été rappelé quelques définitions liées aux milieux poreux. Ensuite, les méthodes expérimentales d'analyses employées ont été décrites.

Le **chapitre 3** traite de l'étude expérimentale menée sur la craie. La microstructure de la craie a été soumise à une étude pétrographique multi-échelle et une caractérisation pétrophysique (propriétés du réseau poreux, hydrauliques et élastiques de la roche) avant traitement thermique. Ensuite, le comportement de la craie soumise à de la contrainte thermique et de la circulation de fluides a été étudié grâce à une analyse multi-paramètres.

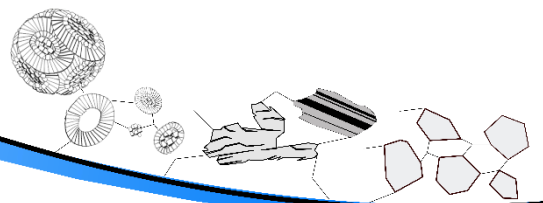
Le **chapitre 4** est consacré à la présentation et l'interprétation des résultats de l'étude expérimentale menée sur quatre granites. Différents traitements thermiques (chauffage lent suivi d'un refroidissement lent ou d'une trempe rapide) ont été réalisés sur les échantillons. Dans un premier temps, ces roches ont été soumises à des sollicitations thermiques faibles pour étudier leur déformation et leur résistance à la fatigue. Dans un second temps, ces roches ont été soumises à des cycles de trempe afin d'étudier l'influence sur les propriétés mécaniques et microstructurales.

Le **chapitre 5** reprend les résultats des précédentes parties en intégrant un grès. Ces roches ont été soumises à des tests de températures croissantes et de fatigues thermiques afin d'étudier leurs impacts sur la porosité et la microstructure et d'établir les relations existantes entre les caractéristiques du réseau poreux et le cheminement des fluides à travers la roche.

La **discussion générale** synthétise les travaux présentés, et expose les perspectives qui en découlent.



# I. CHAPITRE : Introduction





### I.1. Contexte

La contrainte thermique ajoutée à la circulation de fluides intervient dans de nombreuses applications géologiques, telle que l'injection intermittente d'eau froide dans un réservoir chaud pendant la production de pétrole, la production géothermique ou l'injection de CO<sub>2</sub> supercritique pour le stockage du carbone. L'effet du refroidissement induit lors de l'injection d'un grand volume de fluide peut modifier l'état de contrainte du réservoir et ainsi dégrader thermiquement la formation entourant un puits d'injection (Perkins and Gonzalez, 1985). De plus, les variations de température peuvent également influencer le comportement fragile ou ductile de la roche, en fonction de facteurs tels que les caractéristiques minérales et structurales de la roche, et la plage de température (Jaeger et al., 2007).

#### I.1.1. Exploitation pétrolière

Les roches carbonatées représentent entre 50 et 60% des réservoirs mondiaux de pétrole (Burchette, 2012). Parmi les carbonates, la craie est connue pour héberger d'énormes quantités d'hydrocarbures (*e.g.* la mer du Nord). Les interactions réservoir de craie-fluide ont fait l'objet d'une grande attention dans les communautés scientifiques (Delage et al., 1996; Gutierrez et al., 2000; Nermoen et al., 2016; Nguyen, 2009; Risnes et al., 2005) en raison des phénomènes d'affaissement des fonds marins détectés dans les années 1980 dans les gisements de pétrole de la mer du Nord (Addis, 1987; Johnson et al., 1988) entraînant une baisse rapide de la production (Simon et al., 1982). L'effondrement des pores (« pore collapse ») peut se produire au cours de l'injection d'eau, qui est une méthode visant à améliorer la rentabilité du réservoir (Blanton, 1981; Keszthelyi et al., 2016). Des controverses subsistent quant aux causes de son origine et à la dépendance à l'égard des facteurs physico-chimiques (Heggheim et al., 2005; Schroeder, 1995). De nombreuses études ont montré que la force de la craie dépend beaucoup du fluide saturant (Risnes, 2001). Monjoie and Schroeder, (1989) montrent que l'eau a un effet affaiblissant sur la craie. Ce mécanisme est connu sous le nom de «water weakening» et induit une baisse significative de la résistance mécanique (Madland, 2005). Nadah (2010), décrit ce phénomène comme instantané et réversible. Il montre que la force compressive de la craie diminue après avoir été saturée de quelques pourcents d'eau. D'autres mécanismes font appel à la dissolution chimique comme mécanisme d'affaiblissement (Heggheim et al., 2005; Heugas and Charlez, 1990; Nermoen et

al., 2015; Newman, 1983). Toutefois, la solubilité très faible de la calcite et la grande surface spécifique de la craie, font qu'il est peu probable que la résistance mécanique de la craie soit causée par de la dissolution (Andersen, 1992; Rhett, 1990). Des expériences de solution sous pression sont prises en compte dans les tests de fluage à long terme (Hellmann et al., 2002b) et favorise localement la dissolution de la calcite. Toutefois, ce phénomène lent n'est pas compatible avec l'affaiblissement rapide de la craie (Schroeder et al., 1998).

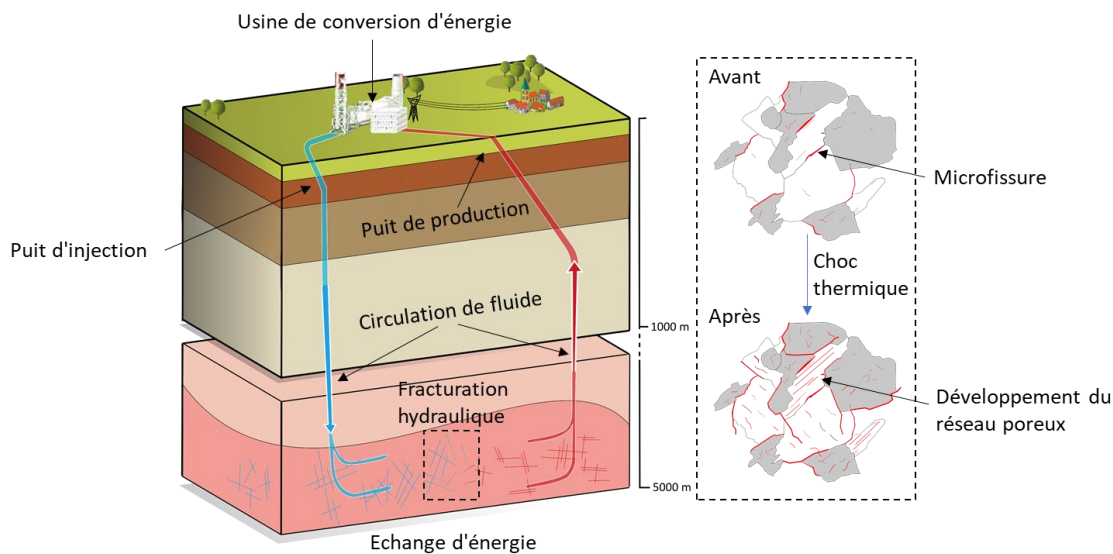
L'affaiblissement est le plus souvent attribué à des interactions physiques pures entre les grains. Les forces capillaires sont importantes pour induire une cohésion entre les particules de la craie (Delage et al., 1996). Lors d'une inondation, le ménisque d'eau encore présent dans la craie sèche (Lord et al., 1998) disparaît et affaiblit la roche. L'action de l'eau peut briser les contacts entre les grains par absorption grâce à ce qu'on appelle l'effet Rhebinder qui dépend de la surface d'énergie libre (Rehbinder and Lichtman, 1957). Risnes et al. (2003) indiquent que l'activité de l'eau dans un fluide (saumures ou glycol-eau) est un paramètre clé de l'affaiblissement par l'eau. Il s'agit d'un mécanisme physico-chimique complexe dans lequel les grains de craie sont dégradés par les forces d'adsorption des molécules liquides à la surface de la calcite.

### **I.1.2. Géothermie**

La géothermie vise à l'exploitation de la chaleur profonde. Cette ressource est développée grâce à la circulation de fluides à travers les défauts de la roche. Les systèmes géothermiques améliorés (Enhanced Geothermal System, EGS) anciennement connus sous le nom de systèmes de roches sèches chaudes (Hot Dry Rock, HDR), sont des réservoirs artificiels créés par des puits de forage dans des roches à faible perméabilité. Le fluide traverse les voies perméables faites dans la roche, collectant la chaleur au fur et à mesure, puis est extrait via des puits de production. La vapeur d'eau chaude atteignant la surface est transformée par une turbine pour produire de l'électricité. L'eau après refroidissement est retournée au puits d'injection pour être réchauffée, ce qui soumet le réservoir à des cycles répétés de chauffage / refroidissement (cycles thermiques). Lorsque l'eau froide est injectée dans la roche sèche chaude tel que le granite, les fractures sont soumises à une importante contrainte thermique. Une telle contrainte thermique soudaine pourrait endommager l'intégrité du réseau de fractures dans les EGS.

Les EGS reposent sur des techniques visant à augmenter la perméabilité du réservoir afin d'améliorer la récupération de l'énergie d'une source de chaleur profonde. Ceci peut être atteint par différentes approches, telles que la stimulation thermique, la stimulation hydraulique et ou chimique, voire la fracturation hydraulique.

La stimulation thermique, par exemple, est provoquée par l'injection d'eau froide dans un réservoir à haute température (Flores et al., 2005; Grant et al., 1982; Jeanne et al., 2017; Siratovich et al., 2011; Tarasovs and Ghassemi, 2012). L'effet bénéfique de ce processus est dû à l'initiation et à la propagation de fractures hydrauliques créées artificiellement dans la roche (Kumari et al., 2018). L'injection d'eau froide dans la masse rocheuse profonde à haute température, peut entraîner un réseau de microfissures plus dense dans la masse rocheuse (Figure I-1). La circulation de fluides est améliorée, ce qui permet d'augmenter la production d'énergie thermique. Les fissures formées dans les réservoirs peuvent se développer et entraîner des changements dans les propriétés physiques et mécaniques des roches environnantes. Lorsque la propagation des fissures atteint un certain degré, la stabilité du puits peut changer et être réduite (Bérard and Cornet, 2003; De Simone et al., 2013; Siratovich et al., 2016). Les mécanismes mis en jeu lors des stimulations hydrauliques peuvent modifier localement les contraintes pouvant être à l'origine de microsismicité. Entre juin et juillet 2000, une expérience de stimulation hydraulique a eu lieu sur le site géothermique EGS de Soultz-sous-Forêts (Alsace, France) et plus de 7200 événements microsismiques ont été localisés dans la gamme de magnitude  $-0,9$  à  $2,6$  (Cuenot et al., 2008). En 2006, le projet de géothermie de Bâle (Suisse) a été arrêté en raison d'un événement sismique de magnitude supérieure à  $2,0$  ayant provoqué quelques dommages sur des bâtiments (Catalli et al., 2016).



**Figure I-1. Schéma du dispositif de base d'une centrale géothermique de type EGS.**

Ces systèmes géothermiques montrent une grande variété dans leur environnement (température, hydrologie, géomécanique ou pétrologie). Le granite est la roche mère la plus appropriée dans les EGS (Breede et al., 2013). Dans certaines régions au sous-sol granitique, le gradient thermique peut-être élevé et atteindre les  $100\text{ }^{\circ}\text{C.km}^{-1}$  (Baldeyrou et al., 2003). Par exemple, les EGS sont généralement des systèmes avec des températures d'environ  $200\text{ }^{\circ}\text{C}$ , bien que certaines températures de puits comme le plus grand champ géothermique du monde : *The Geysers* (Californie), soient mesurées à  $400\text{ }^{\circ}\text{C}$  (Garcia et al., 2012; Heuze, 1983; Olasolo et al., 2016). Selon la température de la formation, le granite aura un comportement mécanique différent (fracturation, transformation texturale et minéralogique). Il est donc fondamental d'évaluer ces changements dans la roche.

En raison de sa porosité élevée, la craie est également un réservoir intéressant. En effet, le potentiel géothermique se développe en Europe, dans le nord de la Belgique (Berckmans and Vandenberghe, 1998; Loveless et al., 2014), dans le sud-est de l'Angleterre (Headon et al., 2009; Law, 2010), en sous-sol Danois (Poulsen et al., 2017; Weibel et al., 2020), en République Serbe (Duric, 2013) ou en France en Champagne-Ardenne (France) (Chabart et al., 2012; Maget and Rambaud, 1980). Cependant, peu de recherches ont été menées sur la manière dont le réservoir chaud réagira à l'injection d'eau froide à court et à long terme.

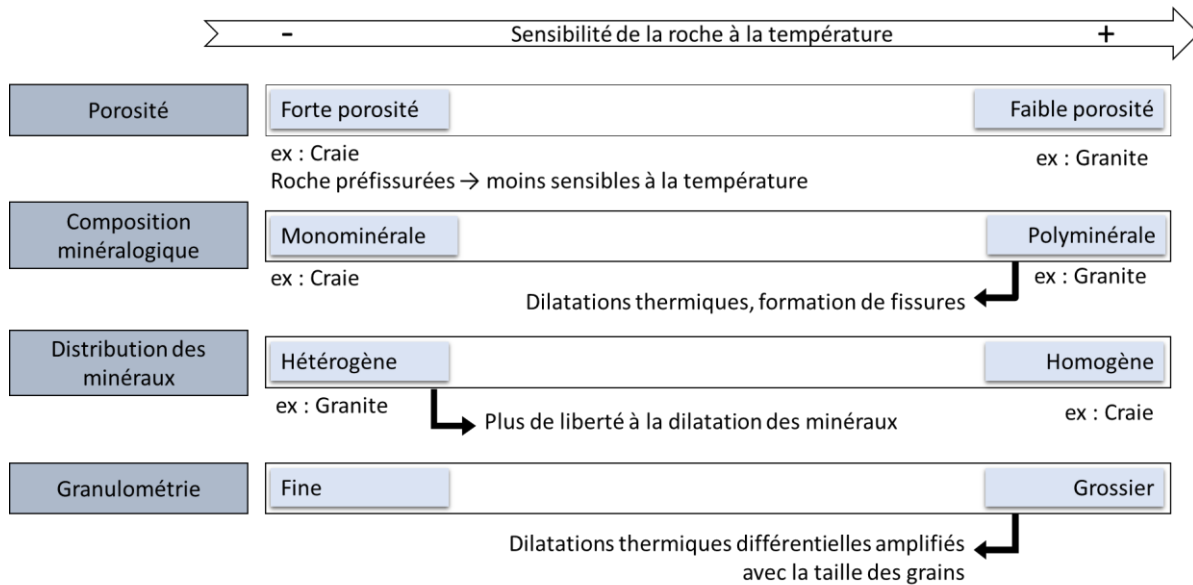
### **I.1.3. Stockage des déchets radioactifs**

Les installations de stockage nucléaire géologique à grande profondeur doivent s'intéresser à l'effet de la température sur des matériaux rocheux comme les granites (matériaux peu poreux et peu perméables). L'évolution des techniques de stockage prévoit un élargissement du type des massifs rocheux, comme des roches carbonatées (Tran et al., 2020). Ces installations montrent des températures importantes, généralement supérieur à 200 °C. Ces températures peuvent atteindre plus de 1000 °C lors de la décomposition des substance radioactives (Gibb, 2000). Avec ces niveaux de température, un déséquilibre entre les propriétés élastiques et thermiques des grains de la roche encaissante peut avoir lieu. Des fissures peuvent alors être générées et cela peut avoir des conséquences dramatiques sur l'évolution de la perméabilité d'un stockage de déchets nucléaires.

## **I.2. Effet thermique et hydrique**

Lors d'une augmentation de température, la fissuration thermique comprend à la fois la création de nouveaux vides ainsi que l'élargissement des vides préexistants, ce qui implique une augmentation de la porosité. La dilatation des grains dans les vides initiaux lors de cette élévation de la température (Somerton, 1992) peut en revanche provoquer une diminution de la porosité par déformation résiduel des grains. Ces deux phénomènes contradictoires expliquent pourquoi, selon la roche étudiée, le comportement en fonction de la température peut être varié.

Plusieurs paramètres liés à la microstructure initiale des roches vont influencer leur sensibilité à la température (Homand et al., 2000). La Figure I-2 indique la sensibilité des roches en fonction de leur microstructure.



**Figure I-2. Sensibilité thermique des roches en fonction de leur microstructure (d'après Homand et al., 2000).**

La **porosité initiale** et la **densité des fissures** existantes peuvent influencer l'altération thermique des roches. L'étude de Tuğrul and Zarif, (1999) a révélé que l'influence des caractéristiques texturales sur les propriétés physiques semble plus importante que la minéralogie. Plus la porosité est faible et plus les roches sont sensibles à la température. Les roches poreuses comme la craie ou le grès sont peu sensibles à la température puisque la dilatation thermique des constituants peut s'effectuer assez librement. La dilatation minérale des roches à haute porosité serait « absorbée », réduisant les contraintes internes induites (Sousa et al., 2005). Au contraire, les roches fissurales comme le granite sont plus sensibles à la température, et le seront d'autant plus si les fissures initiales sont faibles (Vazquez et al., 2011, 2016). Géraud et al. (1992) ont montré que les granites à forte porosité de fissure seraient plus disposés à se fermer et présenteraient des modifications plus importantes dans leur réseau poreux que les granites à faible porosité de fissure. Les roches à structure serrée empêchent les changements de longueur et présentent une faible déformation résiduelle (Gräf et al., 2013).

La **composition minérale** est également un paramètre qui influence le comportement thermique des roches. Les roches sont constituées de minéraux le plus souvent anisotropes, dont les coefficients de dilatation thermique peuvent varier en fonction de l'axe considéré.

Lors d'une augmentation de température, des phénomènes d'incompatibilité entre les minéraux voisins se produisent lorsque l'ordre de grandeur des dilatations thermiques est différent. C'est ce qu'on appelle la dilatation différentielle. Dans les roches présentant plusieurs types de minéraux (polyminérales), des contraintes thermiques différentielles peuvent conduire à de la microfissuration. Par exemple, la calcite et le quartz sont des minéraux dont la dilatation thermique anisotrope est marquée. Les minéraux se dilatent avec la température, mais parfois, ils ne retrouvent pas leur position initiale après refroidissement, donnant à la roche une déformation résiduelle. Pour certains granites, après refroidissement, cela conduit à une diminution de la densité de vides qui implique que la roche peut devenir plus compacte avec une plus grande résistance mécanique (Yin et al., 2015). Certaines modifications minéralogiques peuvent avoir lieu sous température comme le changement de phase du quartz, la déshydratation des minéraux argileux ou la décarbonatation.

Pour la **distribution des minéraux** des roches, plus elle est homogène et plus la fissuration se développe. Les granites à texture hétérogène sont moins sensibles puisque celle-ci offre plus de liberté à la dilatation des minéraux.

La **granulométrie** est un paramètre également à prendre en compte. Les roches à grains grossiers peuvent amplifier les phénomènes de dilatation thermique. Ainsi, les pierres présentant de grandes différences de tailles minérales peuvent subir des contraintes amplifiées en raison des différences de dilatation thermique (Gómez-Heras et al., 2006; Vazquez et al., 2011). Au contraire, les roches à grains fins seraient moins sensibles à la température.

A noter que des phénomènes physico-chimiques peuvent également se produire lorsqu'un fluide saturant n'est pas inerte vis-à-vis de la roche (Somerton, 1992).

### I.2.1. Craie

L'effet de la température sur la craie peut avoir un impact sur le comportement du matériau. Le réservoir pétrolier Valhall (mer du Nord) a une température de 92 °C, cette température peut être plus élevée dans certaine formation comme Ekofisk (mer du Nord) à 130 °C (Nermoen et al., 2016). Ces niveaux de température sont d'ailleurs identiques à ceux des fluides rencontrés dans le domaine de la géothermie entre basse et profonde énergie. La température élevée des réservoirs peut avoir une influence considérable sur le comportement

du système fluide-roche induisant des changements conséquents comme la modification de la porosité ou de la perméabilité (Uribe-Patiño et al., 2017). Le chauffage et le refroidissement cycliques des roches peuvent causer des dommages permanents, en particulier sur les roches composées de minéraux à dilatation thermique anisotrope comme la calcite. Le cristal de calcite a un axe trigonal de symétrie, avec un coefficient thermique de dilatation moyen de  $23,8 \times 10^{-6} \text{ K}^{-1}$  et  $-5,2 \times 10^{-6} \text{ K}^{-1}$  dans les directions parallèles et perpendiculaires à l'axe trigonal, respectivement (Rosenholtz and Smith, 1949). Cette dilatation thermique hautement anisotrope des cristaux de calcite induit sur les craies, qui ont subi des fluctuations de température, une contrainte thermique qui se traduit par une accumulation de déformation irréversible, mais qui n'a aucune influence significative sur le module d'élasticité (Voake et al., 2019).

Les variations de température peuvent affecter les propriétés du réservoir. Par exemple, la géométrie des pores peut être modifiée avec l'augmentation de la température, ce qui peut affecter la distribution du fluide et les performances d'écoulement. Le nombre d'études sur le comportement thermique de la craie reste néanmoins faible et leurs conclusions ne sont pas totalement cohérentes. Par exemple, le module de Young n'était pas affecté par le changement de température (température ambiante à 130 °C) pour la craie sèche et saturée du réservoir des formations d'Ekofisk et de Tor (DaSilva et al., 1985). En revanche, une légère diminution du module de Young a été observée sur les craies étudiées par Brignoli et al. (1994) lors d'une augmentation de la température entre 20 et 100 °C. La température n'a eu aucun effet significatif dans des tests de déformation uniaxiale (Addis, 1989). Charlez et al. (1992) ont montré que les paramètres thermo-poro-élastiques n'étaient pas affectés par la température et que la rupture par cisaillement était indépendante de la température sur des craies à 40,5% de porosité, saturée en huile et testées à 20 °C, 90 °C et 120 °C. Nadah et al. (2009) ont étudié les effets de la température sur le comportement mécanique d'une craie du Nord de la France. Ils montrent une augmentation de la résistance à la rupture lorsque l'on dépasse 105 °C. En effet, le chauffage, même à très hautes températures, n'a pas modifié les paramètres élastiques, mais a eu un impact sur l'apparition des premières déformations plastiques. Le chauffage provoquerait donc, a priori, un retard du phénomène de « pore collapse », prolongeant ainsi la phase élastique du matériau. Ce phénomène a souvent été expliqué par l'écrasement des hypothétiques ponts de calcite présents entre les grains. Cette



explication est néanmoins remise en question, car si les ponts mécaniques étaient la seule raison, il ne devrait pas y avoir de résistance après la rupture de ces ponts. Or, en phase plastique, la craie reste assez résistante (Nadah et al., 2009). Plus récemment, il a été montré que la résistance de la craie augmente avec l'augmentation de la température due à la croissance des cristaux de calcite, l'évaporation de l'eau et l'agglomération de grains de calcite (Lipin and Trufanov, 2019).

L'effet des cycles répétés du refroidissant d'un réservoir initialement chaud par l'injection d'eau froide a moins été étudié. Voake et al. (2019) ont étudié l'effet de la variation de température sur la résistance à la traction de deux types de craie. Ils ont montré que la présence d'eau et la dilatation thermique anisotrope de la calcite sont les principaux mécanismes d'affaiblissement lorsque la craie est exposée à des cycles thermiques, en revanche en conditions sèches, les craies n'ont montré aucun affaiblissement causé par les cycles de température. Il a été montré que la température du fluide injecté et la différence de température entre le fluide injecté et la température du réservoir affectaient le taux de récupération (Hamouda and Karoussi, 2008), avec une amélioration de la production de pétrole lors d'une augmentation de la température d'injection d'eau à 80 °C.

### **I.2.2. Granite**

Sun et al. (2013) ont découvert dans leurs études sur les modèles de dommages thermiques du granite, que la forme d'eau existante dans le granite changerait pendant le chauffage. L'eau absorbée, l'eau liée et l'eau cristalline s'échapperait du granite à des températures différentes. La perte d'eau absorbée apparaîtrait à environ 100 °C, l'eau liée s'échapperait entre 100 et 300 °C, l'eau cristalline s'échapperait en dessous de 400 °C ; et l'eau structurelle du minéral s'échapperait au-dessus de 300 °C. La structure du réseau cristallin peut être endommagée par la perte de l'eau cristalline et structurelle provoquant une augmentant des défauts. La Figure I-3 répertorie les actions physiques et réactions chimiques qui peuvent des produire à des températures supérieures à 400 °C.

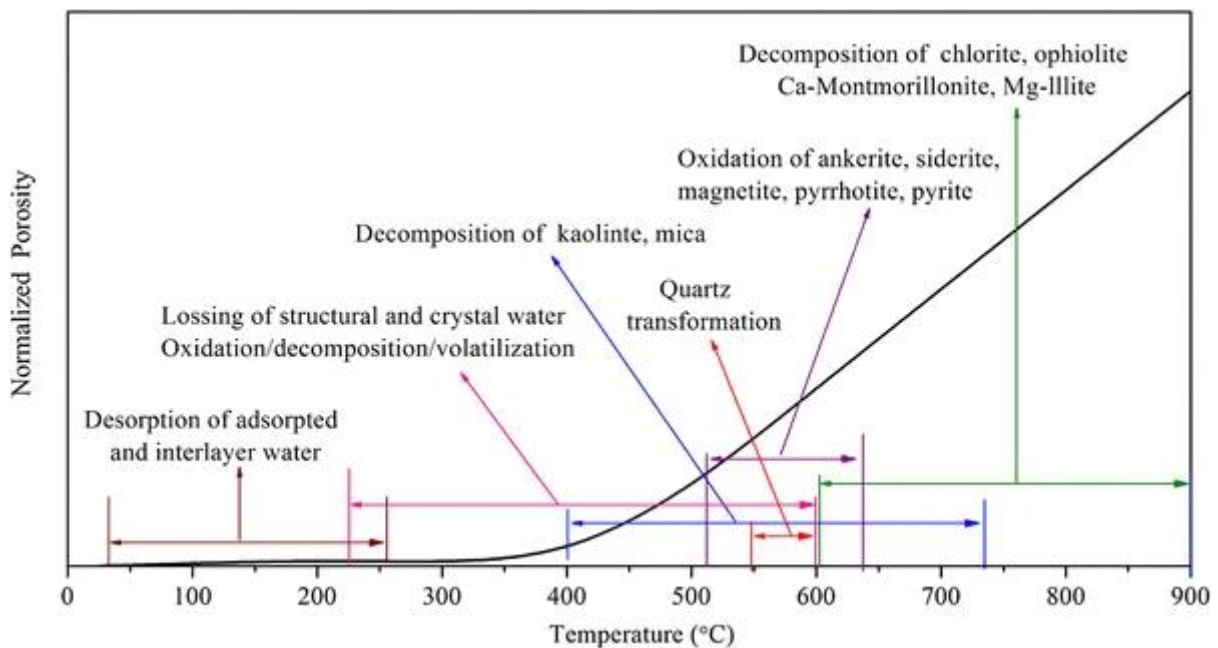


Figure I-3. L'action physique et les réactions chimiques pour le chauffage du granite en fonction de la température. (W. Zhang et al., 2018)

### I.2.2.1. Comportement thermique

Les microfissurations thermiques sont causées par des changements de température dans le temps et l'espace. De nombreuses études ont travaillé sur les variations des propriétés physiques et mécaniques des granites à haute température. Pour la plupart, les granites ont été chauffés à une température donnée, mais les expériences de suivi ont été faites à température ambiante (Chaki et al., 2008; Fan et al., 2017; Gautam et al., 2018; Géraud and Gaviglio, 1990; Jin et al., 2019; Kant et al., 2017; Kumari et al., 2018; Reuschlé et al., 2006; Xu et al., 2008; Zhang et al., 2009). Certaines études réalisent la surveillance pendant le chauffage en utilisant, par exemple, les émissions acoustiques ou des mesures in-situ de la vitesse des ondes P ( $V_p$ ) (Glover et al., 1995; Griffiths et al., 2018).

Lors de l'augmentation de la température, les minéraux formant la roche se dilatent et des fissures irréversibles sont générées une fois qu'un seuil thermique est atteint (Argandoña et al., 1985; Géraud et al., 1992; Gómez-Heras et al., 2006; Menéndez et al., 1999; Miskovsky et al., 2004). Lorsque le seuil de microfissure est dépassé, la porosité totale (et connectée) augmente grâce à la connexion de nouvelles discontinuités créées (Géraud et al., 1992).

En raison de la complexité minérale du granite, le seuil de température de fissuration est aléatoire. Certains chercheurs ont montré que des fissures se produiraient dans le granite en

dessous de 150 °C, et même lorsque la roche est chauffée à 70 °C (Lin, 2002). Yong and Wang, (1980) montrent l'existence d'une température seuil de 60 à 70 °C dans le granite de Westerly grâce à l'utilisation de la technologie d'émission acoustique. En revanche, Fredrich and Wong, (1986) ont chauffé trois roches crustales dont un granite (Westerly), et ont observé et quantifié les microfissures induit thermiquement. Ils ont montré que le seuil de microfissure était produit lorsque des échantillons étaient chauffés à des températures de l'ordre de 100 à 165 °C. À 250 °C, les fissures étaient concentrées à la limite des grains. Jansen et al. (1993) montrent des microfissures dans leur granite à des températures supérieures à 80 °C. Dans les travaux de Géraud et al. (1992), deux granites à faible porosité de fissure génèrent de nouvelles fissures à basse température, entre 50 et 100 °C. Leur observation par microscope électronique à balayage a montré qu'à partir de 50 °C, de nombreux grains de biotite se sont ouverts et que les limites de grain de quartz étaient déjà fissurées. Dwivedi et al. (2008) chauffent un granite à des températures allant de 30 °C à 160 °C. Ils observent au microscope électronique à balayage un élargissement des microfissures préexistantes à 65 °C, suivies d'une fermeture à des températures comprises entre 100 °C et 125 °C. Une étude sur la granodiorite de Gondomar a montré une température seuil de 110-115 °C (Argandoña et al., 1985). Darot et al. (1992) chauffent le granite de La Peyratte entre 123 et 646 °C. Ils observent qu'à des températures supérieures à 123 °C, les dommages thermiques résiduels induits se traduisent par une augmentation progressive de la porosité et de la perméabilité. Lin, (2002) observe que le seuil d'élargissement des microfissures apparaît à des températures comprises entre 100 °C et 125 °C. Takarli and Prince-Agbodjan, (2008) suggèrent une nouvelle fissuration potentielle causée par la décohésion des grains entre 105-200 °C. Q. L. Yu et al. (2015) ont travaillé sur un granite de la province de Dandong Liaoning en Chine et considèrent que la température seuil pour la fissuration thermique est de 100 °C. Guo et al. (2018) montre que la dilatation des minéraux dans la roche a déclenché des microfissures entre 60 °C et 90 °C. Au-delà de ces températures, une nouvelle fermeture se produit due au réarrangement des particules. Entre 120 et 150 °C, une augmentation notable des dégâts se produit.

Dans la littérature, de nombreuses études indiquent que la température critique de la fissuration du granite se situe à des températures plus élevées encore, comprises entre 200 et 400 °C (Homand-Etienne and Houpert, 1989; Kumari et al., 2017a; Meredith and Atkinson, 1985; Sun et al., 2015; Yin et al., 2015). Chen et al. (1999) ont effectué une mesure de la

perméabilité sur un granite et ont observé que la température seuil induit par le craquage thermique serait supérieure à 200 °C. Liu and Xu (2014) ont montré que le granite Qinling à biotite subit une légère augmentation de la vitesse des ondes longitudinales à 100 °C et une diminution avec la hausse de la température à 200 °C. Feng et al. (2018) ont étudié l'évolution de la perméabilité en temps réel sur le granite de Luhui craqué thermiquement, et ont constaté que 300 °C était la température seuil de changement de perméabilité. Ils observent que la quantité de microfissures commence à augmenter à 50 °C et atteint la valeur maximale à 100–150 °C.

### 1.2.2.2. Fatigue thermique

La fatigue thermique est également un mécanisme important d'altération dans les granites. Lin (2002) a effectué de 5 à 9 cycles à la même température max (variant de la température ambiante à 600 °C) et a observé qu'à une température de 200 °C, toutes les fissures sont produites au cours des deux premiers cycles de chauffage et refroidissement lent. C'est à partir des températures maximales supérieures à 300 °C que les fissures thermiques continuent de se développer même après le deuxième cycle, bien qu'elles deviennent de moins en moins importantes avec les cycles. Feng et al. (2020) soumettent un granite à 20 cycles thermiques dans un four entre 100 °C et 300 °C et montrent que le cyclage thermique est plus propice à diminuer la stabilité mécanique de la roche et permet aux réseaux de fissures de se former plus facilement. De plus l'interconnexion des fissures intragranulaires et intergranulaires provoquent la fragmentation de la structure du granite et plus de risques de dégradation.

Gómez-Heras et al. (2006) ont sélectionné 4 granites et les ont soumis à des cycles de chauffage en contrôlant les différences de dilatation thermique entre les minéraux constitutifs. Ils montrent que la fatigue thermique semble être un facteur critique pour favoriser la dégradation, plutôt que l'amplitude de la plage de température. Freire-Lista et al. (2016) ont soumis des monzo- et leucogranites de la région de Madrid en Espagne à 42 cycles thermiques de chauffage et refroidissement continu (105-20 °C). La micro-fissuration générée a été principalement quantifiée par l'analyse pétrographique et a montré que l'effet cyclique thermique provoque la production de microfissurations et la fusion de microfissures préexistantes. Les cycles répétés de chauffage et refroidissement (105-25 °C) ont révélé que

la dilatation thermique dans les différents minéraux du granite génère des variations dans le réseau de fissures et, selon la roche, même une ouverture de fissure (Vazquez et al., 2018a).

### I.2.2.3. Choc thermique

Le choc thermique induit par des cycles thermiques provoque des changements brusques de température, ce qui conduit à la fissuration dans les roches à faible conduction thermique, comme le granite. Les fractures thermiquement induites permettent d'améliorer la circulation de fluides à travers la roche (Chaki et al., 2008; Siratovich et al., 2015).

Au cours des dernières années, de nombreuses études se sont concentrées sur les changements de propriétés dans la roche après avoir subi un refroidissement rapide (Fan et al., 2020; Feng et al., 2020; Isaka et al., 2018; Jin et al., 2019; Kumari et al., 2018; Wu et al., 2019; Yu et al., 2020). Isaka et al. (2018) ont étudié les propriétés mécaniques du granite sous refroidissement naturel et refroidissement par eau et ont démontré que la dégradation thermique sous refroidissement rapide était sensiblement plus élevée que sous refroidissement lent. L'augmentation de la densité de fissures au cours de ces traitements de trempe entraîne une réduction significative des paramètres élastiques du granite ainsi que des propriétés physiques.

Par exemple, le granite de Pedras Salgadas (Portugal) initialement chauffé à 200 °C présente une diminution de 18% de la résistance à la flexion lorsqu'il est refroidi avec de l'eau (Lam dos Santos et al., 2011). La résistance à la compression et le module d'Young ont tendance à diminuer après des traitements de chauffage et de refroidissement par eau (Kumari et al., 2017a; Li et al., 2020; Shao et al., 2015; Wu et al., 2019; Zhang et al., 2017). Wu et al. (2019) montrent que les échantillons refroidis à l'eau présentent une grande diminution de la vitesse des ondes P et un grand nombre de fissures nouvellement générées à la surface de l'échantillon. Les fortes contraintes thermiques réparties dans le granite favorisent la croissance des microfissures et induisent une nouvelle génération de fissures thermiques (Kim et al., 2014).

Après avoir soumis un granite à une succession de trempes, il a été montré que la résistance à la traction est anti-corrélée avec la température et le nombre de cycles de trempe (Dong et al., 2020; Xu and Sun, 2018). Une baisse plus rapide de la résistance à la traction se produit à des températures supérieures à 450 °C (Xu and Sun, 2018). Les dommages accumulés dans le

granite abaissent le seuil de température critique des dommages aux roches à 350 °C, et même à 250 °C (Dong et al., 2020). Li et al. (2019) indiquent une température seuil au-dessus de laquelle la détérioration des paramètres mécaniques est devenue significative à 300 °C pour le granite étudié.

Les expériences de Zhu et al. (2020) montrent une réduction de la vitesse des ondes P d'environ 40% à 400% au cours de 30 cycles de refroidissement avec une diminution significative par rapport au premier cycle. Pour Fellner and Supancic (2002), les chocs thermiques ont engendré des contraintes en traction sur la surface des échantillons et ont élargi les microfissures induites thermiquement. La température critique pour laquelle la perméabilité du granite augmente considérablement est fixée à 400 °C (Jin et al., 2019; Yangsheng Zhao et al., 2017). Fan et al. (2020) ont effectué des chocs thermiques entre 200 et 800 °C et montrent que les dommages à proximité de la surface sont plus importants qu'à l'intérieur de l'échantillon. Yu et al. (2020) ont réalisé 20 cycles thermiques à 300 °C et ont montré une diminution progressive de la résistance maximale et du module élastique avec l'augmentation du cycle de choc thermique. Avec des cycles croissants, les dommages à la surface de l'échantillon de granite sont plus concentrés, entraînant la nucléation de microfissures de surface.

### 1.2.2.4. Interaction fluide-granite

Les réactions fluide-roche peuvent influencer la porosité et la perméabilité par dissolution minérale et / ou précipitation (Sausse et al., 2001). Lors de l'interaction fluide-granite, divers changements chimiques se produisent dans la composition interne de la roche. Si de nombreuses études suivent les propriétés physiques ou mécaniques du granite, seules quelques études ont intégré l'interaction géochimique dans la caractérisation des processus de fissuration (Alt-Epping et al., 2013; Baldeyrou et al., 2004).

Les études d'altération chimique après une interaction fluide-roche sont souvent des expériences réalisées sur une seule phase minérale, et peu d'études caractérisent les changements de la minéralogie totale dans les roches cristallines (Drüppel et al., 2020; Schmidt et al., 2018).

Les concentrations en éléments majeurs et en oligo-éléments des fluides sont liées à la composition et à la stabilité des minéraux dans les roches et peuvent être directement liées

aux processus de dissolution. Les données de lixiviation et d'altération de Drüppel et al. (2020) indiquent que la quantité de dissolution dépend principalement de la température, de la composition du fluide réactif et de la minéralogie du type de roches.

Dans le granite, l'interaction eau-roche est dominée par la dissolution du plagioclase, du K-feldspath et du quartz en mobilisant les éléments Si, Al, K, Ca, Na, Ba, Sc, Pb, Sr, Rb et Eu et par la dissolution de la biotite et de chlorite en mobilisant K, Cl, Fe, Mn, Mg, Cu, Zn, Cr, Sc, V et Li dans le fluide.

Le calcium peut être trouvé dans le fluide saturant par la dégradation et la dissolution des plagioclases (Wogelius et al., 2020). En effet, les microfissures minéralisées en calcite, transgranulaires et intragranulaires sont particulièrement fréquentes dans les cristaux de plagioclase, qui présentent généralement des figures d'exsolution ou de zonation lors de leur cristallisation.

L'enrichissement en Fe de la solution peut être dû à la dégradation du fer de la biotite (Vazquez et al., 2016) et les traces de K, Mg, Mn, Ti dans le fluide peuvent provenir de l'ouverture des clivages de la biotite lors d'une augmentation de la température (Vazquez et al., 2015).

### **I.2.3. Grès**

L'effet de haute température peut déclencher chez le grès des effets tels qu'un écrasement des grains, de la fracturation, un changement dans la perméabilité, de la dilatation thermique ou encore de la rupture de cohésion minérale (Rosenbrand et al., 2014; Somerton et al., 1981; Wang and Dusseault, 2003). La grande diversité des grès peut montrer une grande variété dans les résultats des expériences en laboratoire (Uribe-Patiño et al., 2017).

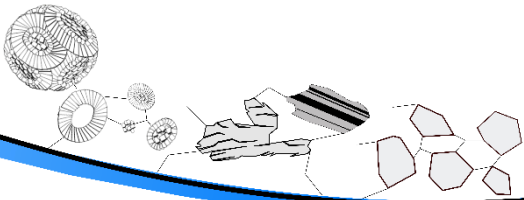
Par exemple, Agar et al. (1987) effectuent des essais triaxiaux sur des grès de sables bitumineux d'Athabasca non cimenté sur des températures variant de 20 °C à 200 °C. Les auteurs observent peu de modifications dans la résistance au cisaillement avec l'accroissement des températures. Toutefois, l'augmentation de la température à 200 °C augmente la rigidité de la roche. Zhang et al. (2009) étudient les propriétés mécaniques de grès bien cimentés soumis à des températures allant de la température ambiante à 800 °C et à pression non confinée à partir d'essais uniaxiaux. Entre la température ambiante et 200 °C, la résistance maximale du grès montre une tendance à la baisse. Ils montrent qu'entre 200 et

600 °C les grès présentent une augmentation de la résistance et peu de variation pour le module élastique. À plus de 600 °C, une diminution abrupte de la résistance à la compression se produit. Rao et al. (2007) utilisent 3 techniques destructives (essai brésilien, test de compression axiale et test de flexion en trois points) pour évaluer les propriétés mécaniques de grès bien cimentés soumis à des températures comprises entre la température ambiante et 300 °C. Ils montrent que la résistance à la traction et à la compression en environnement non confiné augmente de façon linéaire avec la température en dessous de 200 °C-250 °C puis diminue au-dessus de ces températures. J. Yu et al. (2015) réalisent des essais triaxiaux des échantillons de grès rouge de Jiangxi en Chine. Leurs échantillons sont au préalable chauffés avant les tests à des températures allant de 20 °C à 600 °C. De 20 °C à 200 °C, la résistance et le module d'Young augmentent et la perméabilité diminue. Les auteurs attribuent ce changement à la fermeture de pores. En revanche entre 200 °C et 600 °C, de la dégradation thermique est observée avec une diminution de la résistance et du module d'élasticité et une augmentation de la perméabilité. Rosenbrand et al. (2014) étudient le grès de Berea provenant des carrières de Cleveland (grès argileux) soumis à des températures de 20 à 200 °C et montrent une réduction de la porosité avec l'augmentation de la température. Les auteurs suggèrent que cette réduction est due à la mobilisation de la kaolinite, réversible à court terme. Ils indiquent que la dilatation thermique a un effet plus important sur des roches à faible porosité (en raison du plus grand volume de solide qui se dilate par rapport au faible volume de porosité). Les grès de Flechtinger (Allemagne) bien cimenté et résistant, étudié par Hassanzadegan (2013) montre que la montée de température sous des contraintes de confinement élevées crée de nouvelles fissures. A l'inverse l'étude des grès non cimentés suggèrent que la réponse inélastique du grès peut s'accompagner de réarrangement des grains de sable (Buitrago and Alejandro, 2015). Des essais de compression hydrostatique ont été réalisés par Berest et al. (1989) sur les grès de Fontainebleau pré-fissurés thermiquement. Ils ont montré que la fraction volumique de la porosité fissurale augmentait à partir de 200 °C.





# II. CHAPITRE : Matériels et méthodes

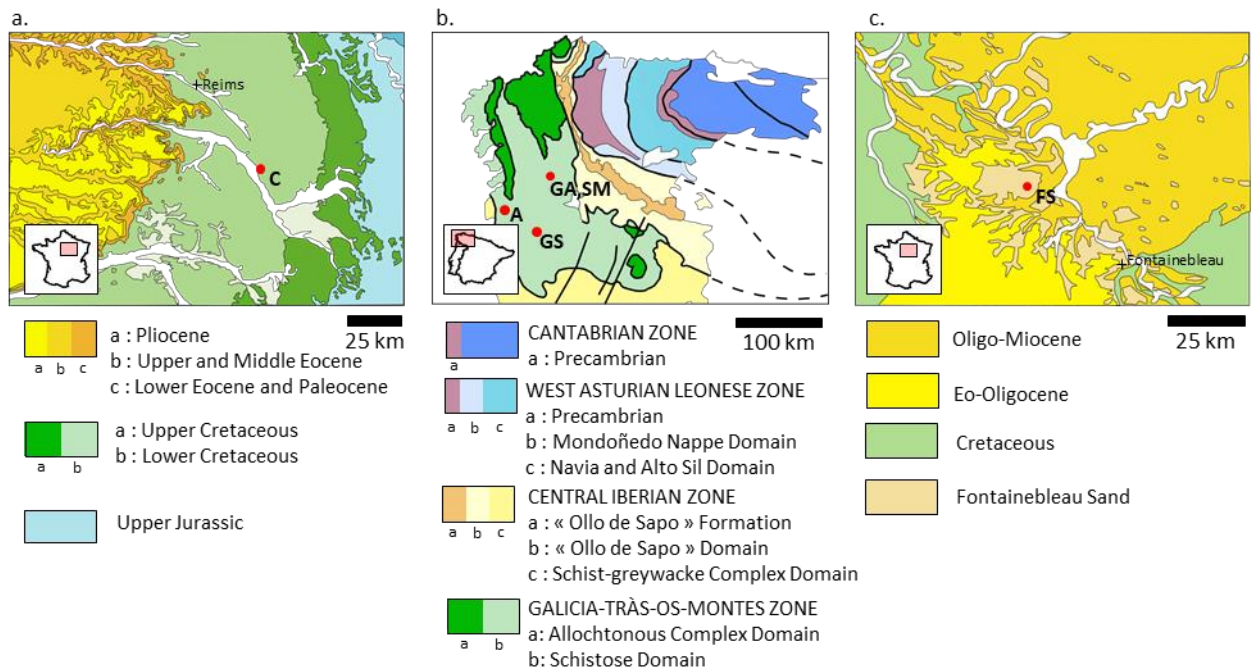


## **II.1. Matériels**

### **II.1.1. Cadre géographique et géologique**

Trois roches ont été retenues pour cette étude ; une craie (craie de Châlons), quatre granitoïdes (Albero, Golden ski, Gris alba et Silvestre moreno) et un grès (grès de Fontainebleau), en raison de leurs différents réseaux poreux : de type nano microporeux pour la craie, fissural pour le granite et micro- macroporeux pour le grès.

Le contexte géologique et géographique est présenté en Figure II-1. Les échantillons de craie ont été extraits dans le bassin parisien le long d'un affleurement daté du Crétacé supérieur (Coniacien). Les granitoïdes proviennent des carrières situées dans la région galicienne au nord-ouest de l'Espagne. Les grès étudiés proviennent de la formation de Fontainebleau dans le bassin parisien datée du Stampien (Oligocène). Les échantillons ont été orientés en carrière perpendiculairement à la stratification (craie, grès) et à la principale famille de fractures (granite). Les échantillons ont été préparés à l'aide d'une carotteuse équipée d'un foret diamanté de diamètre adapté. Afin de réduire la carotte à la taille voulue et de rectifier les bases, une scie avec lame diamantée a été utilisée.



**Figure II-1. Contexte géologique et géographique. a. Craie de Châlons (C). b. Granites ibériques (A, GA, GS, SM) dans le diagramme du Macizo Ibérico. c. Grès de Fontainebleau (FS). Adapté de Vazquez et al. (2018a) et Thiry et al. (1988).**

### II.1.1.1. Craie

La craie de Châlons étudiée est une craie blanche, provenant de la région d'Omey (Bassin parisien, France). Nos échantillons ont été prélevés proche des carrières de Marson exploitées par Omya S.A.S (producteur international de charges minérales de carbonate de calcium pour l'industrie).

Les échantillons de craie ont été prélevés dans la carrière du Grand Mont (Saint-Germain-la-Ville) le long d'un affleurement présentant une zone de craie coniacienne. Des études de terrain ont montré que cette craie est hydrofracturée, liée au développement de fentes de tension verticales et à une faille normale (Coulon and Lamotte, 1988; Richard et al., 1997). En effet dans ces carrières, il a été constaté de nombreux phénomènes d'hydro-fracturation de la craie. Des analyses microtectoniques réalisées dans la carrière de la région d'Omey par Richard, (1996) ont permis de distinguer trois épisodes tectoniques successifs. L'histoire tectonique débute avec un épisode décrochant, à l'Éocène avec un raccourcissement horizontal N-S. L'Oligocène est marqué par un épisode extensif pluri-directionnel SE-NW à E-W, NE-SW, N-S. Les derniers épisodes tectoniques datent du Miocène avec un

raccourcissement NW-SW. Ces réseaux, plus ou moins complexes de fentes de tension, se créent lors de l'épisode à l'Oligocène extensif et multidirectionnel (Richard, 1996).

Le prélèvement à la craie a été réalisé dans une zone où la déformation tectonique est très faible. Les échantillons proviennent des bancs caractérisés par une craie blanche à *Micraster*, relativement tendre et microgrenue sur cassure fraîche (Allouc and Le Roux, 1995).

### II.1.1.2. Granites

Les granites sont situés géologiquement dans le massif ibérique au niveau de l'affleurement le plus occidental situé dans la ceinture orogénique hercynienne. Les granites de notre étude sont issus des carrières situées dans la région galicienne (nord-ouest de l'Espagne). L'ensemble des granites se trouve dans la zone dite de Galicia-Trás-Os-Montes, déterminée par Farias et al. (1987). Ce sont des granitoïdes hercyniens post-cinématiques et syn-cinématiques.

La région s'organise séquentiellement en trois groupes en fonction de leurs compositions et des critères structuraux (Vera, 2004); les « Calc-alkaline syn-kinematic granitoïdes », « Peraluminous syn and post-kinematic granitoïdes » et « Calc-alkaline post-kinematic granitoïdes ». Les variétés Albero (A), Gris Alba (GA), Golden Ski (GS) et Silvestre Moreno (SM) appartiennent au groupe des « Peraluminous syn and post-kinematic granitoïdes ». Ce groupe inclut les granitoïdes liés temporellement au processus de métamorphisme régional et aux processus d'anatexie crustale Hercynienne.

**Albero** se trouve dans l'alignement de Donón-Tomiño. Cette zone est caractérisée par une faible déformation qui confère une orientation aux minéraux. Donón-Tomiño représente une masse allongée d'environ 56 km de longueur et 12 km de largeur, parallèle aux directions générales de l'hercynien.

Le granitoïde de la variété **Golden Ski** provient du sud de Pontevedra (Espagne), dans l'alignement granitique Salvaterra-A Cañiza-Cerdedo, représenté par un allongement de l'axe longitudinal, parallèle aux directions générales de l'hercynien. Ce massif a une forme plus ou moins elliptique et mesure environ 7,5 km de longueur sur 4 km de largeur.

L'Institut Espagnol de Géologie et d'exploitation Minière (IGME, 2004a, 2004b) décrit les variétés **Gris Alba** et **Silvestre Moreno** comme des « granitoïdes à deux micas très

leucocratiques ». Ils se situent dans l'alignement Salvaterra-A Cañiza-Cerdedo qui appartient au batholite de Faro de Avión.

### II.1.1.3. Grès

Les grès de Fontainebleau proviennent de la formation du Stampian (Oligocène) dans le bassin parisien. La carrière de grès de Fontainebleau se situe dans la forêt de Fontainebleau à 60 Km au sud-est de Paris, dans la commune de Moigny-sur-Ecole, région de l'Île de France et couvre près de 5000 m<sup>2</sup> (Figure II-1). La couche géologique a une épaisseur de 50 à 80 m (Thiry and Maréchal, 2001). Ces grès sont des arénites de quartz pur (plus de 99,5% de SiO<sub>2</sub>) déposé principalement dans un environnement marin (Thiry et al., 1988). Il a trois faciès diagenétiques différents selon la position géomorphologique (Thiry et al., 1988). Sous la nappe phréatique, se trouve le faciès d'une sédimentation primaire. Les sables sont noirs ou gris dus à la présence de feldspaths, glauconite, carbonates, pyrite et matière organique. Au-dessus ce trouve des sables beiges, verdâtres ou ocres. On retrouve des argiles (smectite et illite) et des traces de feldspaths et de glauconite. Ce faciès résulte de l'oxydation et de l'altération des faciès sombres par les eaux souterraines et eaux de recharge. Les faciès proches de l'affleurement sont des sables avec exclusivement du quartz. Les grès sont parfois profondément cimentés par des excroissances de quartz dues à la migration de l'eau. Bourbie and Zinsner, (1985) indiquent que la variation de porosité peut être importante, et passer de 2% à 30% sans faire varier la taille des grains. Cette silicification extensive a induit le développement de corps de grès homogènes au sein des masses de sable. Les grès de Fontainebleau n'ont pas été enfouis profondément. La profondeur est estimée à 100 m par Thiry and Maréchal, (2001). Cette profondeur exclut une élévation de la pression et de la température lors de la diagenèse (Thiry et al., 1988). C'est le réseau hydrographique qui a érodé une partie des sables de Fontainebleau.

### II.1.2. Pétrographie et minéralogie des roches et description de leur porosité

Les roches étudiées sont présentées sur la Figure II-2 et leurs principales caractéristiques pétrographiques sont présentées dans le Tableau II-1.

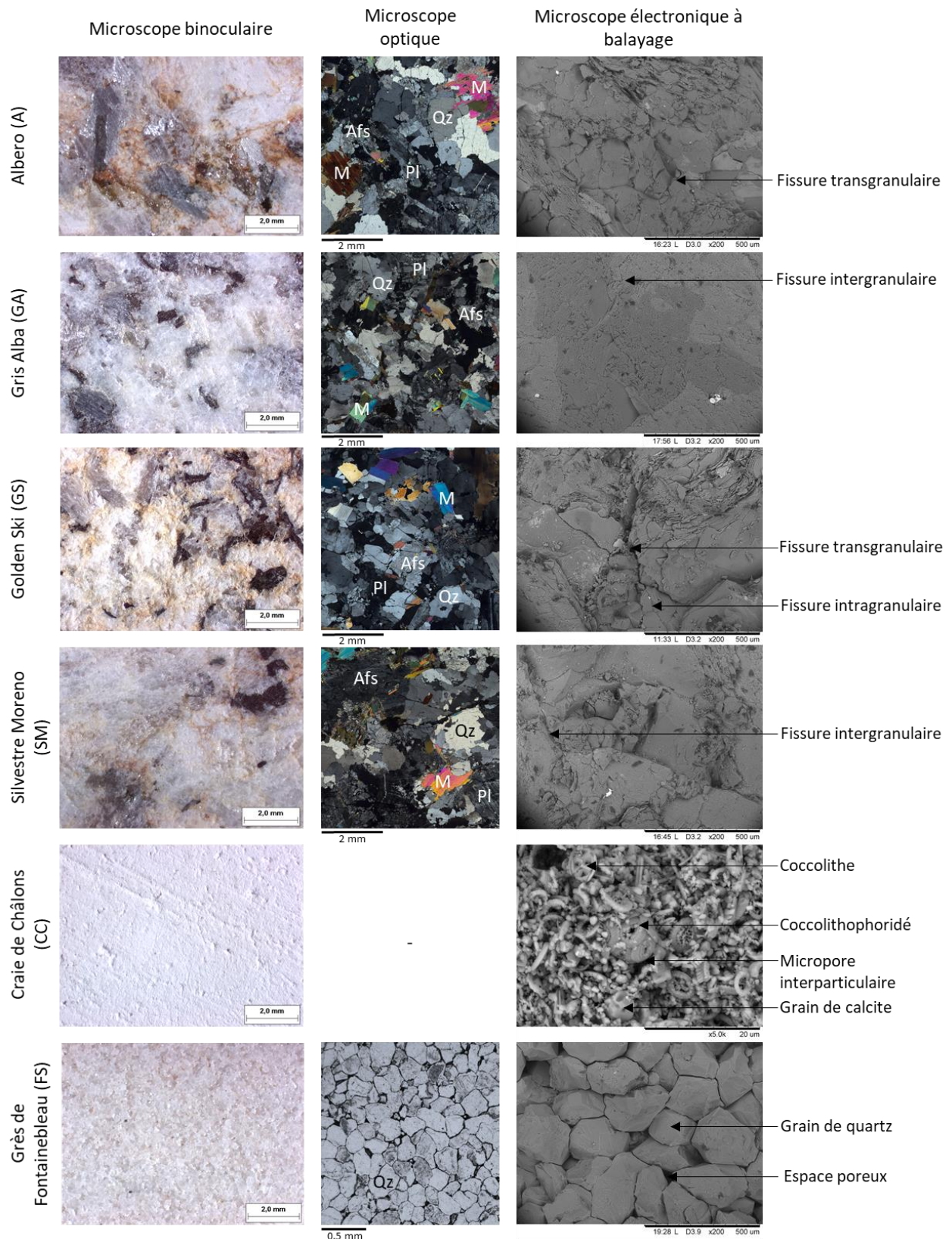
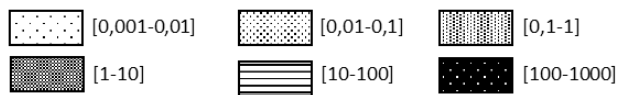


Figure II-2. Roches sélectionnées. Photographies réalisées au microscope binoculaire, optique (lumière polarisée) et électronique à balayage (MEB). (Qz : quartz ; Afs : feldspath alcalin ; Pl : plagioclase ; M : mica).

Tableau II-1. Résumé des principales caractéristiques des roches.

Nom de la roche	Type de roche	Principales caractéristiques de la structure minérale		Principales caractéristiques de la structure poreuse			Propriétés de transport des fluides (Imbibition d'eau capillaire)
		Composition minérale	Caractéristique textural	Porosité	Classe de pore	Taille d'accès aux pores	
Albero (A)	Granodiorite	Quartz Feldspath alcalin Plagioclase Mica	Grains moyens-fins (5 mm) Présence d'argile Fissures transgranulaire ouvertes	5,4%	Nano-microporosité macroporosité	Distribution hétérogène Distribution principale comprise entre environ 0,01 µm et 1–10 µm Distribution secondaire supérieur à 10 µm	Imbibition d'eau à travers les fissures
Gris Alba (GA)	Monzogranite		Grains fins (4 mm) Minéraux subautomorphes à xénomorphes	1,0%			
Golden Ski (GS)			Grains fins (4 mm) Présence d'argile Quartz et feldspath subautomorphe Muscovite automorphe	3,8%			
Silvestre Moreno (SM)			Grains moyens-fins (5 mm) Présence d'argile Minérale est subautomorphe	2,0%			
Craie de Châlons (CC)	-	Calcite	Bien trié Coccolithes (4 µm) bien conservés Micrites xénomorphe Calcite rhomboédriques à sous-rhombodriques Absence de ciment	38%	Nano-microporosité	Distribution unimodale centrée autour de 0,26 µm	Imbibition d'eau dans les pores interparticulaires bien interconnectée et uniformément répartie dans l'échantillon.
Grès de Fontainebleau (FS)	Quartzarénite	Quartz	Bien trié Quartz de 200 µm automorphe Zones partiellement cimenté	4,3%	Nano-microporosité	distribution unimodale centrée sur 1 µm	Imbibition d'eau dans les gorges et pores

Taille d'accès aux pores (µm)





**Albero (A)** : c'est une granodiorite homogène à grains moyens-fins (5 mm). Il a la teneur en feldspath alcalin la plus faible parmi les quatre granitoïdes étudiés (10%, Vazquez et al., 2018a). Il a en revanche une forte proportion en micas (25%, Vazquez et al., 2018a) avec un rapport similaire pour les deux types de micas. Il contient des minéraux xénomorphes (cristal dont aucune face cristalline n'est décelable) allongés et orientés suivant la foliation. La teinte jaunâtre du granitoïde est due à une altération initiale marquée par la présence d'argile. Il a la porosité la plus élevée des granitoïdes étudiés. Ce granitoïde est caractérisé par des fissures transgranulaires ouvertes.

**Gris Alba (GA)** : c'est un monzogranite homogène à grain fin (4 mm). Ces minéraux sont subautomorphes (cristal dont les faces cristallines sont imparfaitement exprimées) à xénomorphes avec des limites irrégulières dans le quartz. La proportion de muscovite / biotite est d'environ 2 : 1. Les fissures sont principalement intergranulaires suivant les limites des micas.

**Golden Ski (GS)** : c'est un monzogranite homogène à grains fins (4 mm). Il présente une orientation évidente du mica et une teneur plus élevée en quartz qu'en feldspaths. Le quartz et les feldspaths sont subautomorphes, tandis que la muscovite est automorphe (cristal dont les faces cristallines sont parfaitement exprimées). Il est caractérisé par une altération initiale marquée par présence d'argiles et par des fissures intragranulaires et transgranulaires, principalement présentent dans les plagioclases.

**Silvestre Moreno (SM)** : c'est un monzogranite homogène de taille fine (5 mm). La forme minérale est subautomorphe en général et montre une orientation. La teneur en quartz est l'une des plus élevées parmi les granitoïdes étudiés (45%, Vazquez et al., 2018a). Il présente de larges fissures intra, inter et transgranulaires.

Les courbes de porosimétrie au mercure (MIP) des quatre granites peuvent être divisées en deux parties : i) une distribution principale entre environ 0,01  $\mu\text{m}$  et 1-10  $\mu\text{m}$  avec une forme unimodale ; ii) et une distribution hétérogène pour l'accès aux rayons de rayons supérieurs.

**Craie de Châlons** : D'un point de vue minéralogique, la craie de Châlons apparaît comme constituée presque exclusivement de carbonate de calcium (98.5% de  $\text{CaCO}_3$ ) (Ballif et al., 1995). Les principaux composants de la roche sont des fragments de coccolithes bien

conservés avec des micrites xénomorphes et des cristaux de calcite rhomboédriques à sous-rhomboédriques. Les coccolithes ont montré différentes formes bien que la majorité soient elliptiques sans orientation privilégiée. Cela définit une structure punctique (Richard et al., 1997). La longueur des coccolithes est d'environ 4  $\mu\text{m}$  en moyenne. Certaines particules peuvent être plus grosses (jusqu'à 8  $\mu\text{m}$ ) ou plus petites (environ 0,5  $\mu\text{m}$ ). En raison cette structure très fine, les microfissures n'ont pas été observées. La porosité été principalement composée d'une microporosité ouverte sur les images au MEB. La porosité interparticulaire entre les fragments, a un diamètre moyen de 1,3  $\mu\text{m}$ . Des traces de dissolution sont révélées par des formes plus lisses et par la trace de bioclastes dissouts. Les vides intraparticulaires dans les cellules des nannofossiles sont de petit diamètre (<1  $\mu\text{m}$ ), tandis que les vides intraparticulaires de fragments fossiles présentent une plus grande variété de diamètre s'étendant entre 10 et 60  $\mu\text{m}$ . La présence de coquilles vides de bio-organismes et de squelettes de grand diamètre est détectée en microtomographie à rayon X. La répartition des macropores varie entre environ 20 et 600  $\mu\text{m}$  de diamètre, bien que la majorité soit inférieure à environ 200  $\mu\text{m}$ . Les plus grands pores sont principalement des éléments isolés. Cette roche microporeuse présente une porosité totale moyenne d'environ 38%. Les résultats de porosité par injection de mercure (MIP) montrent une distribution unimodale des rayons d'accès aux pores comprise entre 0,04 et 0,40  $\mu\text{m}$  avec un mode d'environ 0,28  $\mu\text{m}$ . La forme des courbes MIP témoignent de l'existence de nanopores bien interconnectés et uniformément répartis dans l'échantillon.

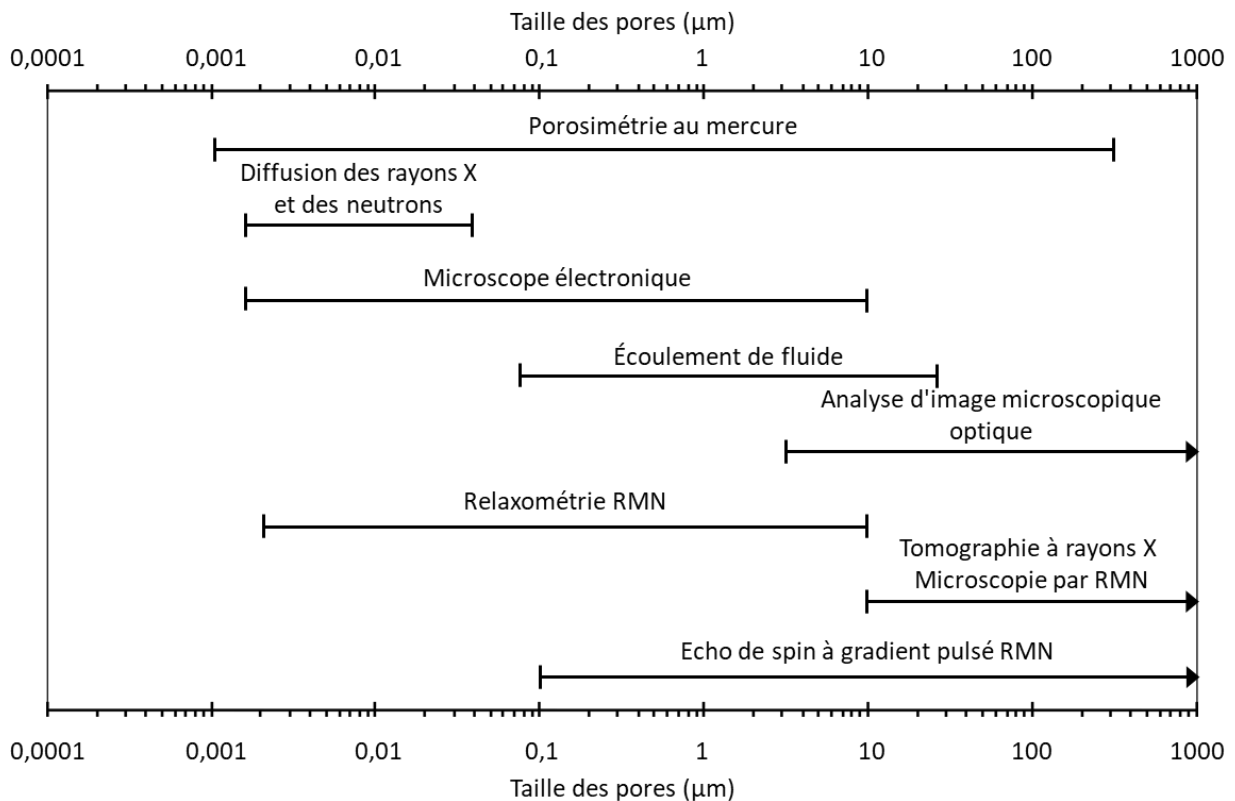
**Grès de Fontainebleau :** Le grès de Fontainebleau une quartzarénite (Folk, 1974) composée de grains de quartz subautomorphe et automorphe (> 99%) très bien triés et à granulométrie constante. Les grains de quartz ont un diamètre compris entre 100 et 300  $\mu\text{m}$ . Les contacts entre les grains se font principalement par faces et les pores ont des formes polyédriques typiques. L'observation au MEB montre que la forme des espaces poreux libres est constituée de pores intergranulaires dont la largeur s'étend de 5 à 30  $\mu\text{m}$ , même si certains peuvent atteindre 60  $\mu\text{m}$ . Certaines zones du grès sont fortement cimentées et responsables de l'hétérogénéité de l'espace poreux observé en lame mince. Le grès de Fontainebleau a une porosité d'environ 4%, avec une large distribution unimodale centrée sur 1  $\mu\text{m}$  (MIP). Certains pores sont accessibles par de grands diamètres (10 à 100  $\mu\text{m}$ ), mais représentent un faible volume du réseau poreux total.

## II.2. Méthodes

### II.2.1. Caractérisation à multi-échelles du réseau poreux

Il existe des mesures purement quantitatives qui donnent la valeur globale de la porosité ou des mesures descriptives qui fournissent des indications sur la morphologie de l'espace poreux. Des comparaisons et des corrélations entre les méthodes permettent de caractériser la structure poreuse des roches avec des informations à des échelles complémentaires (Figure II-3).

L'étude de la structure des roches poreuses implique des méthodologies adaptées. Ces méthodes sont en évolution constante et permettent d'avoir une définition précise de la microstructure de la roche. La microtomographie aux rayons X permet d'imager de plus en plus précisément la composition et la structure des matériaux étudiés. La porosimétrie au mercure est une méthode souvent utilisée pour apporter des précisions sur les familles de pores qui composent une structure poreuse. Cette technique reflète uniquement le volume accessible à une pression donnée. C'est la connectivité physique de l'échantillon poreux qui reflète la distribution observée. Une distribution sera faussée si la connexion des grands pores n'est accessible que par des petites ouvertures par exemple (pas d'information sur la topologie des pores). La résonance magnétique nucléaire, en revanche permet de caractériser la taille réelle du pore. Cette technique est considérée comme un outil complémentaire à la porosimétrie au mercure.

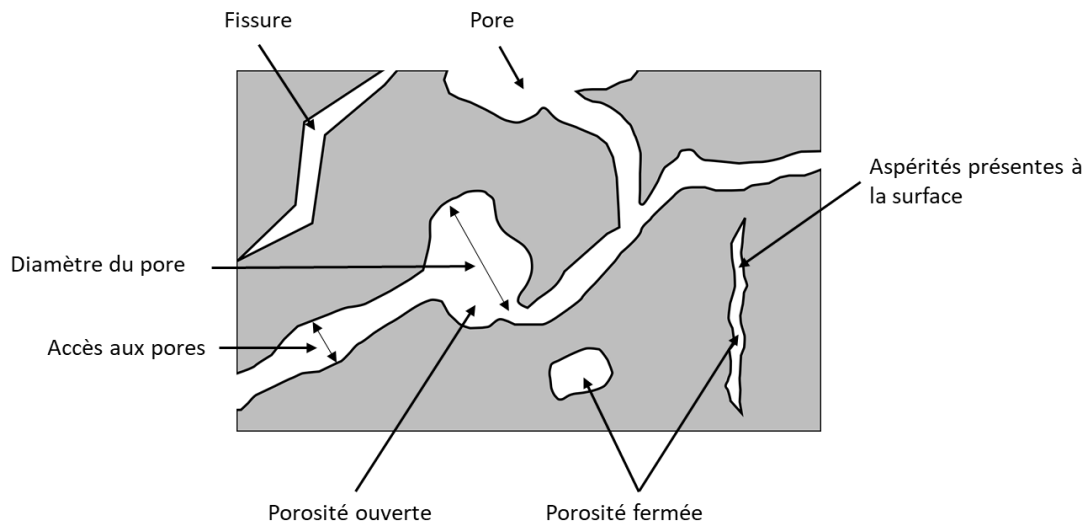


**Figure II-3. Gammes des méthodes de caractérisation multi-échelles du réseau poreux (Modifié de Meyer et al. (1994) et Robert, (2004)).**

## II.2.2. Classification des pores

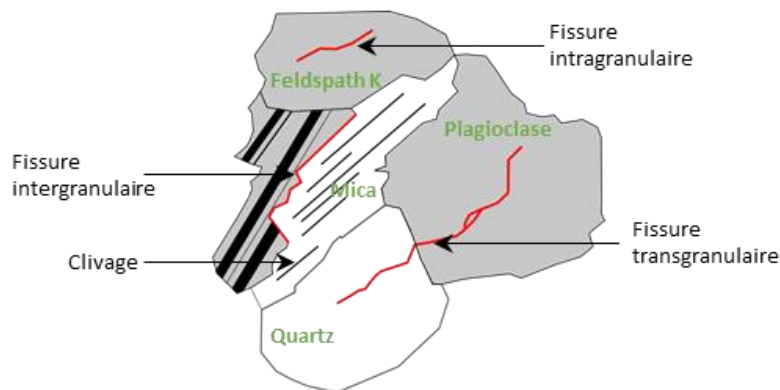
La porosité est l'ensemble des volumes de petite taille pouvant être occupé par des fluides (gaz, eau, pétrole) à l'intérieur d'une roche (Foucault and Raoult, 2010). Selon la forme et la dimension, les vides de l'espace poreux peuvent être désignés comme des pores ou des fissures. Les pores ont des formes plutôt convexes, alors que les fissures sont préférablement des vides anguleux, des discontinuités planes et allongé de faible épaisseur qui évoluent en fonction des conditions auxquelles est soumise la roche. Leur développement est d'origine thermique et / ou mécanique. La circulation de fluides à travers les pores et fissures peut induire des échanges entre minéraux et conduire à des phénomènes de dissolution ou recristallisation.

La porosité liée au réseau poreux connecté à l'extérieur de l'échantillon, représente la porosité ouverte. La porosité liée à des pores non connectés, est appelée porosité fermée (Figure II-4). Cette dernière ne contribue pas à la circulation des fluides.



**Figure II-4. Représentation schématique 2D des différentes porosités présentes dans un matériel rocheux.**

Les microfissures dans le granite, par exemple, peuvent être divisées en trois groupes (Kranz, 1979) : les fissures intergranulaires qui se propagent le long des joints de grains, les fissures intragranulaires qui commencent et disparaissent totalement en un seul grain, et les fissures transgranulaires qui traversent plus d'un grain (Figure II-5).



**Figure II-5. Schéma idéal des fissures intergranulaires, intragranulaires et transgranulaires identifiées dans un granite.**

L'étude de la porosité consiste à examiner la taille des pores et des étranglements de pores y donnant accès. Cet examen nécessite de clarifier la terminologie de la taille des pores. L'union internationale de chimie pure et appliquée (International Union of Pure and Applied Chemistry, IUPAC) définit les macropores comme les pores supérieurs à 50 nm, les mésopores comme les pores entre 2 et 50 nm et les micropores comme les pores inférieurs à 2 nm (Sing,

1985). Cette classification est indépendante du choix du matériau poreux, du type de pores ou de l'emplacement réel des pores. En géosciences, de nombreux auteurs ont choisi différentes limites entre les macropores et les micropores. Cette séparation dépend de l'observateur et des méthodes d'étude. Par exemple, Bousquié et al. (1979) a proposé une limite de diamètre des pores entre les macropores et les micropores à 10  $\mu\text{m}$  grâce à l'observation au microscope optique et à 2  $\mu\text{m}$  grâce à la porosimétrie par injection de mercure. Robert, (2004) et Fronteau, (2000) ont également choisi 15  $\mu\text{m}$  comme diamètre limite entre la macroporosité et la microporosité définie grâce aux diamètres des pores accessibles à pression atmosphérique par porosimétrie au mercure. Cette thèse a adopté cette même classification (Figure II-6). La nanoporosité a été définie comme étant inférieur à 1  $\mu\text{m}$  de diamètre, ce qui correspond à la taille maximale d'accès de la famille majoritaire mesurée en porosimétrie au mercure pour la craie étudiée.

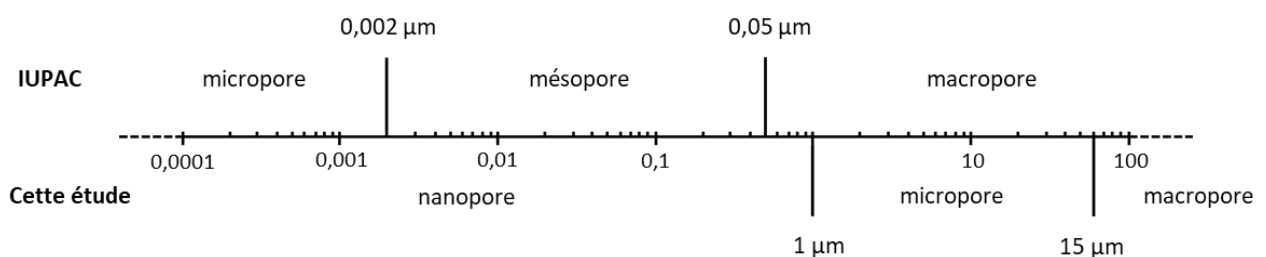


Figure II-6. Classification des pores proposée par l'IUPAC (*International Union of Pure and Applied Chemistry*) et classification adoptée pour cette étude selon Fronteau, 2000 et Robert, 2004.

### II.2.3. Méthodes d'observation et de quantification

L'analyse pétrographique et minéralogique de chaque roche a été réalisée par diverses techniques qui ont permis une étude multi-échelle complémentaire de la minéralogie et de la structure poreuse.

#### II.2.3.1. Loupe binoculaire

La caractérisation à la loupe binoculaire (Olympus SZH-ILLB) a été réalisée comme première approche afin de relever les hétérogénéités à grande échelle (millimètre-centimètre). Les observations ont été réalisées avec l'appareil loupe binoculaire pouvant atteindre un grossissement de x80, qui a permis d'apprécier des aspects tels que la couleur, minéralogie, inclusions fossiles, les macrofissures, la granulométrie ou la texture.

### II.2.3.2. Microscope optique

Les lames minces ont été observées qualitativement sous un microscope optique Olympus BX51 (Figure II-7) muni d'une caméra QICAM Fast 1394 couplée à un ordinateur équipé du logiciel Microvision Image Analysis. Grâce à ce dispositif, des images ont été enregistrées pour l'ensemble des lames minces avec des grossissements allant de x20 à x80.



**Figure II-7. Microscope optique (Olympus BX51).**

### II.2.3.3. Microscope électronique à balayage

L'imagerie par microscopie électronique à balayage (MEB) a été utilisée afin de visualiser le réseau poreux et pour étudier les caractéristiques texturales à l'échelle du micromètre. Des esquilles à cassure fraîche ont été préparées pour chacune des roches

Les observations ont été effectuées sur un microscope Hitachi TM-1000 équipé d'un spectromètre à dispersion d'énergie (EDS). La tension d'accélération était fixée à 15 kV et la distance de travail à 6 mm. L'image enregistrée avait un grossissement de 100 à 20 000 fois. Ce type de microscope ne requiert pas la métallisation des échantillons.

### II.2.3.4. Traitement des données obtenues en microscopie

Les observations microscopiques ont permis de réaliser une caractérisation qualitative des différentes roches. Après enregistrement des images, une quantification des grains et / ou des pores a été réalisée à l'aide du logiciel JMicroVision élaboré par Roduit, (2007). L'analyse d'images numériques permet de déterminer la porosité, la morphologie des pores et la distribution granulométrique. La méthode de seuillage en niveaux de gris a permis de sélectionner les éléments désignés.

### II.2.3.5. Micotomographie à rayons X

Développée dans le domaine médical, la microtomographie à rayons X (X-ray CT) permet de créer des reconstructions 2D ou 3D de la structure interne d'un objet à haute résolution. Le premier scanner assisté par ordinateur (X-ray CT) fut conçu et réalisé par Hounsfield (1972). En géosciences, cette technique a été largement mise en œuvre dans de nombreuses études (Bera et al., 2011; De Kock et al., 2015; Fan et al., 2018; Géraud et al., 1999; Gibeaux et al., 2018; Isaka et al., 2019; Kumari et al., 2017a; Robert, 2004; Sepúlveda et al., 2020; Yun et al., 2013). Cette technique donne de nombreuses caractéristiques sur la structure interne de la roche (porosité, taille des pores, connectivité, tortuosité). Cette technique est réalisée sans préparation d'échantillon ni fixation chimique. En conséquence, les caractéristiques naturelles des informations minéralogiques et du réseau poreux sont conservées.

#### II.2.3.5.1. Choix de la taille de l'échantillon

La taille de l'échantillon influence le temps de mesure et la résolution spatiale. Plus l'échantillon sera de petite taille, plus les caractéristiques du réseau poreux seront précises. Néanmoins, le volume doit être assez important pour être représentatif de l'échantillon. Des échantillons de craie et granite ont été mesurés (Figure II-8). Selon la taille de l'échantillon, la résolution était comprise entre 4,5-16  $\mu\text{m}$  pour 1 voxel. La limitation de la résolution de la microtomographie peut rendre difficile et empêcher la description d'une large gamme de pores de faibles tailles.



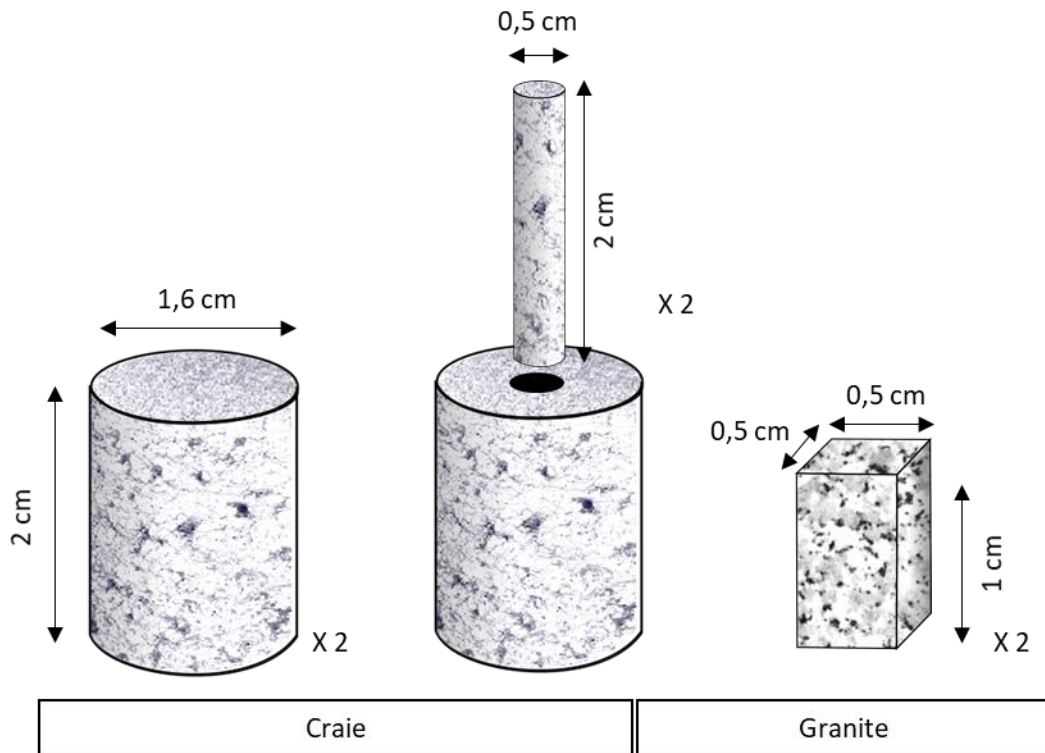


Figure II-8. Dimension et nombre des échantillons étudiés en microtomographie.

#### II.2.3.5.2. Principe

L'imagerie par microtomographie aux rayons X a été réalisée sur un Phoenix Nanotom S<sup>®</sup> (Figure II-9).

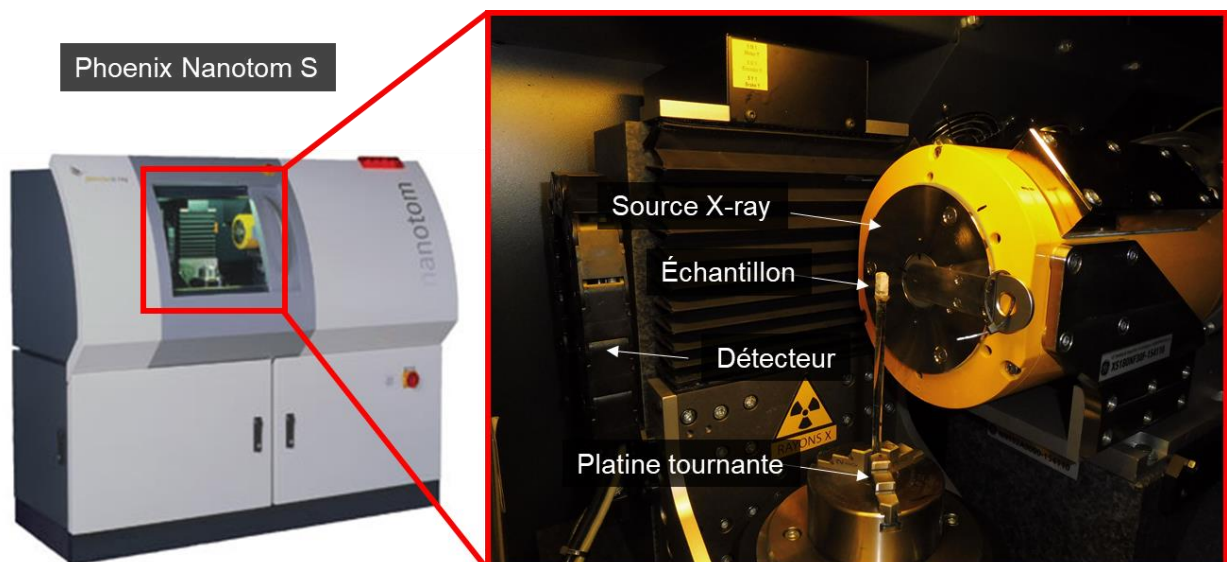
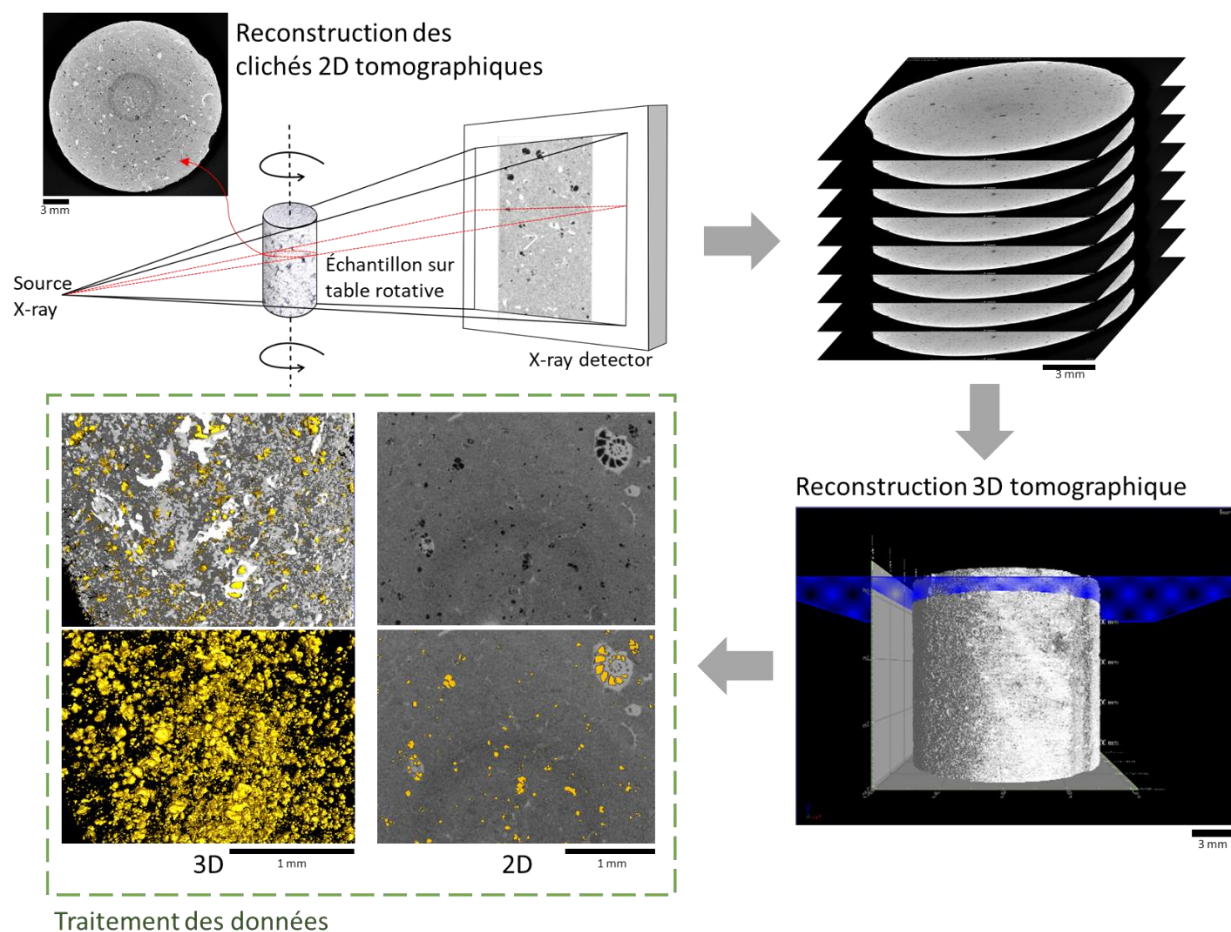


Figure II-9. Photographie du tomographe Phoenix Nanotom S<sup>®</sup> utilisé.

Les rayons X sont une forme de rayonnement électromagnétique à haute fréquence dont l'énergie de photons va de quelques électron-volts (eV) à plusieurs MeV. La tension maximale que ce microtomographe peut fournir est de 180KV / 15W. Une source de rayons X génère des faisceaux qui traversent l'échantillon placé sur une platine rotative à 360 °, laissant des projections d'ombre sur le détecteur et acquérant plusieurs images d'absorption de rayons X 2D (Figure II-10). La microtomographie utilise le fait que les rayons X sont atténués lorsqu'ils traversent un objet.



**Figure II-10. Principe de la microtomographie à rayons X allant de la reconstruction d'image à la visualisation 3D.**

La mesure de l'atténuation des rayons X est proportionnelle à la densité apparente locale de l'objet si la composition chimique de l'objet est uniforme. Les valeurs de densité sont représentées par des niveaux de gris, le noir équivaut à l'air tandis que le blanc est réglé sur la densité minérale la plus élevée.

Pour la craie, le carbonate de calcium représente une nuance de gris et la porosité apparaît en noir. Pour le granite, les minéraux de feldspath, de quartz et de biotite ont des densités moyennes de  $2\,560\text{ kg}\cdot\text{m}^3$ ,  $2\,648\text{ kg}\cdot\text{m}^3$  et  $3\,090\text{ kg}\cdot\text{m}^3$ , respectivement. Par conséquent, la biotite apparaît en couleur claire sur les images numérisées par microtomographie aux rayons X, et les minéraux de quartz et de feldspath ont des couleurs plus foncées. La faible différence de densité entre le quartz et le feldspath rend leur identification plus difficile (Figure II-11).

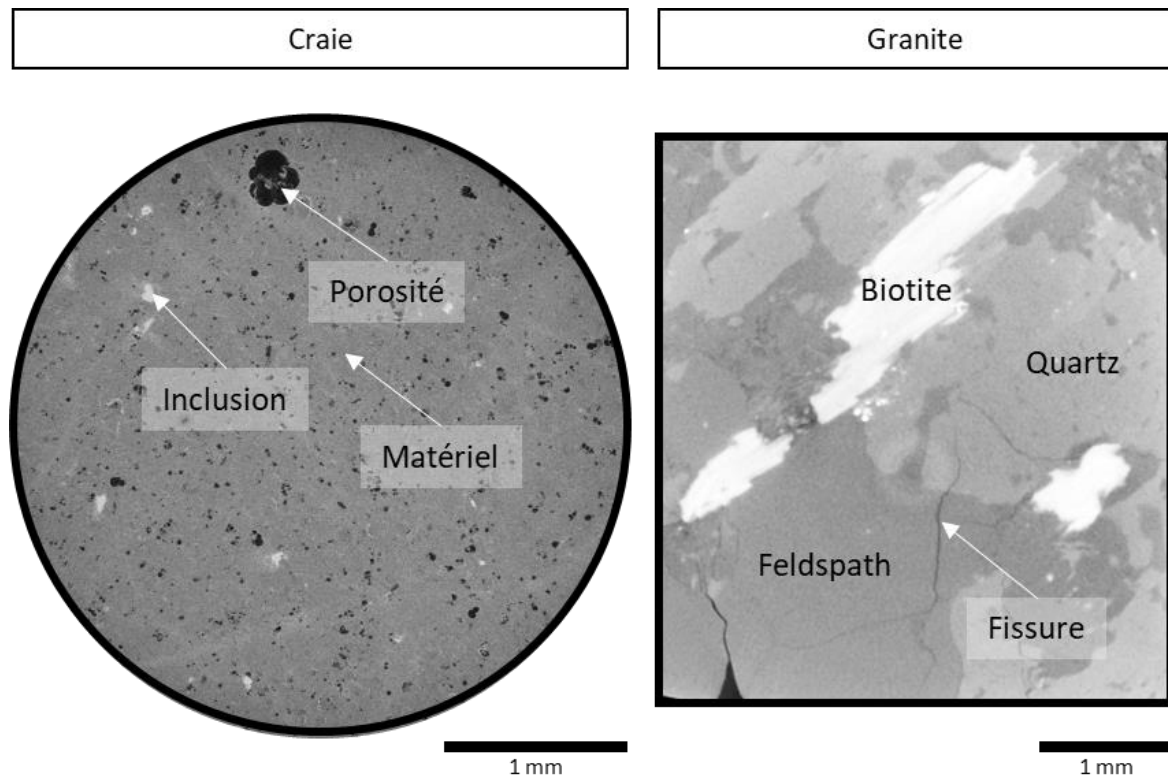


Figure II-11. Exemples de coupes microtomographiques obtenues sur la craie et un granite.

### II.2.3.5.3. Traitement des données

À l'issue du processus d'acquisition, le logiciel VGStudio MAX 2.2 © (Volume Graphics) a été utilisé pour réaliser la reconstruction du réseau poreux et son analyse qualitative et quantitative. Tout d'abord, les défauts de volume associés à l'acquisition ont été éliminés. Les régions d'intérêt (ROI) ont été créées en respectant la capacité de l'ordinateur utilisé et étant la plus représentative de l'ensemble de l'échantillon. Le même ROI a été sélectionné sur les échantillons avant et après traitement. La segmentation des images a permis de séparer la phase minérale de la porosité de la fissure en attribuant à chaque voxel de l'image la phase correspondante en fonction de sa nuance de gris. Les valeurs de porosité des lames ont été fortement influencées par le choix du seuil de binarisation. Pour cette raison, les paramètres

d'ajustement sont restés les mêmes tout au long de l'analyse. Différentes propriétés des voxels (volume, diamètre, sphéricité, etc.) ont été obtenues à l'aide d'un outil de détection de défauts.

L'hétérogénéité de la distribution des microfissures le long de la hauteur z a été évaluée. À partir de la porosité des images de microtomographie aux rayons X, des coupes transversales dans les plans x-y, le coefficient de variation appelé coefficient d'hétérogénéité ( $U_z$ ) par (Fan et al., 2018) a été calculé tel que :

$$U_z = \frac{1}{\underline{D}_{xy}} \sqrt{\frac{1}{n} \sum_{j=1}^n (D_{xy,j} - \underline{D}_{xy})^2} \quad (\text{II. 1})$$

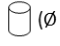
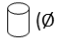



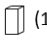
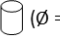
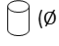


Avec  $D_{xy,j}$  désigne la porosité de la section transversale j et  $\underline{D}_{xy} = \frac{1}{n} \sum_{j=1}^n D_{xy,j}$  désigne la section de porosité moyenne dans le plan x-y.  $n$  est le nombre d'images en microtomographie aux rayons X utilisées pour l'analyse.

### II.2.4. Analyses pétrophysiques

#### II.2.4.1. Réalisation des échantillons

Pour réaliser les mesures pétrographiques et pétrophysiques, il est nécessaire d'adapter la taille des échantillons à la méthode utilisée (Tableau II-2). Lorsque c'était possible, un maximum d'analyses pétrophysiques a été réalisé sur le même échantillon. Cela a permis de corréler les différents paramètres et éviter les éventuelles hétérogénéités du matériel.

**Tableau II-2. Tailles des échantillons en fonction de la méthode pétrophysique utilisée.**

Technique de mesure	Craie	Granite	Grès
Porosimétrie à l'eau	 ( $\varnothing = 1,6 \text{ cm}$ ; $h = 2 \text{ cm}$ )	 ( $\varnothing = 1,6 \text{ cm}$ ; $h = 1,6 \text{ cm}$ )	
Mesure des cinétiques d'imbibition capillaire	 (1 cm x 4 cm x 4 cm)	 (1 cm x 4 cm x 4 cm)	 (1 cm x 4 cm x 4 cm)
Porosimétrie au mercure			 (1 cm x 1 cm x 1,5 cm)
Mesure des vitesses de propagation des ondes acoustiques	 ( $\varnothing = 1,6 \text{ cm}$ ; $h = 2 \text{ cm}$ )	 ( $\varnothing = 1,6 \text{ cm}$ ; $h = 1,6 \text{ cm}$ )	-
Résonance magnétique nucléaire			-
Mesure de perméabilité au gaz	 ( $\varnothing = 3 \text{ cm}$ ; $h = 4 \text{ cm}$ )	-	-
La thermographie infrarouge		 (1 cm x 4 cm x 4 cm)	

$\varnothing$  = diamètre, h = hauteur.

### II.2.4.2. Porosité

#### II.2.4.2.1. Porosité totale

La porosité totale ( $\varphi_t$ ) est définie comme le rapport du volume des vides connectés au volume total de roche :

$$\varphi_t = \frac{V_{vide}}{V_{solide} + V_{vide}} \times 100 = \frac{V_{vide}}{V_{tot}} \times 100 \quad (\text{II. 2})$$

où  $\varphi_t$  est la porosité totale en %,  $V_{vide}$  le volume de vide,  $V_{solide}$  le volume du squelette et  $V_{tot}$  le volume total de la roche.

La porosité totale une grandeur sans dimension, généralement exprimée en pourcentages. Elle correspond à la partie de la porosité dans laquelle le fluide pourra circuler. Dans cette thèse, la porosité a été mesurée par deux méthodes : (1) mesure de la porosité à l'eau ou dite de triple pesée (2) mesure de la porosité par injection de mercure.

#### II.2.4.2.2. Porosimétrie à l'eau

Le protocole expérimental qui a été suivi pour déterminer la porosité ouverte à l'eau est celui indiqué sur la norme NF EN 1936, (2007). Le but de la manipulation a été de déterminer la masse volumique apparente et la porosité ouverte de nos échantillons par absorption d'eau sous vide et pesée hydrostatique.

Après séchage dans une étuve à 40 °C jusqu'à masse constante, les échantillons ont été refroidis à température ambiante dans une boîte hermétique qui contient du « gel silica » pour empêcher les échanges avec l'extérieur. Ils ont ensuite été pesés ( $m_{sec}$ ). Les échantillons ont ensuite été placés dans un dessiccateur où la pression est abaissée progressivement à  $(2,0 \pm 0,7)$  kPa =  $(15 \pm 5)$  mm Hg à l'aide d'une pompe à vide. Le vide est maintenu pendant 2h afin d'éliminer tout l'air contenu dans les pores. Dans un second dessiccateur, de l'eau distillée est brassée à l'aide d'un agitateur magnétique et dégazée à l'aide d'une pompe à vide pendant 6 heures (Figure II-12).

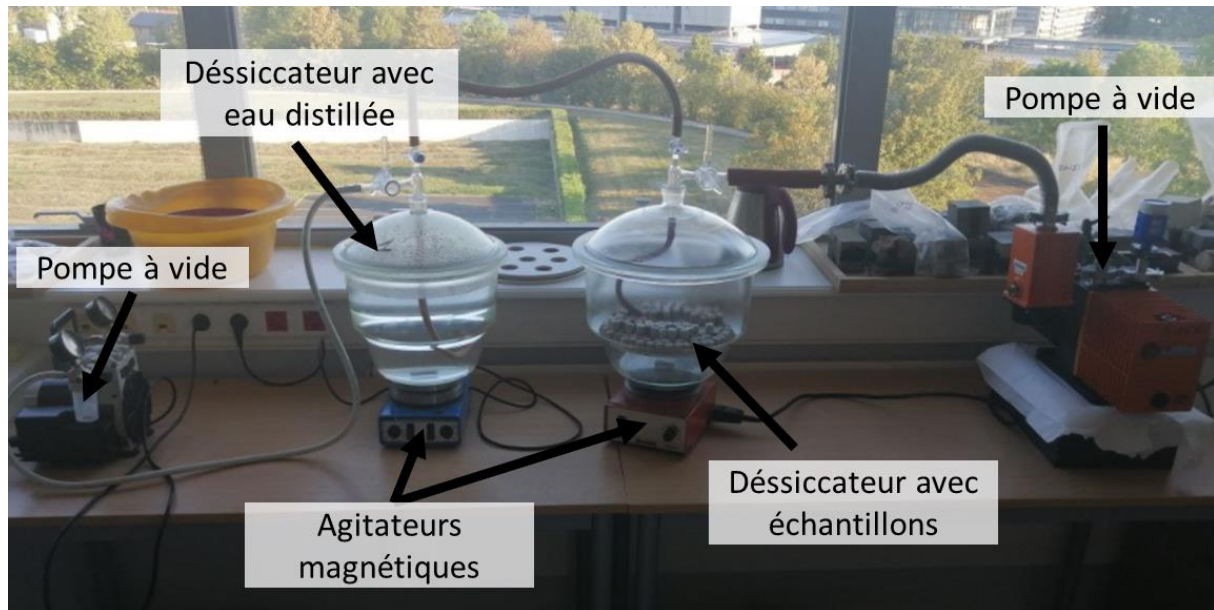


Figure II-12. Photographie du dispositif de mesure de la porosité totale à l'eau sous vide.

Après dégazage du dessiccateur rempli d'eau, l'eau distillée est ensuite introduite progressivement dans le dessiccateur contenant les échantillons. L'eau est imbibée depuis la base de l'échantillon. La pression est maintenue pendant l'imbibition. La vitesse de remontée d'eau est ajustée afin de suivre la frange capillaire. Une fois que les échantillons sont immergés totalement, et après une heure, le vide est cassé et la pression atmosphérique est rétablie. Les échantillons sont laissés à saturation pendant 24 heures pour assurer une saturation complète. Deux types de pesées sont ensuite réalisées ; masse saturée ( $m_s$ ) et masse hydrostatique ( $m_h$ ) de l'échantillon (Figure II-13).

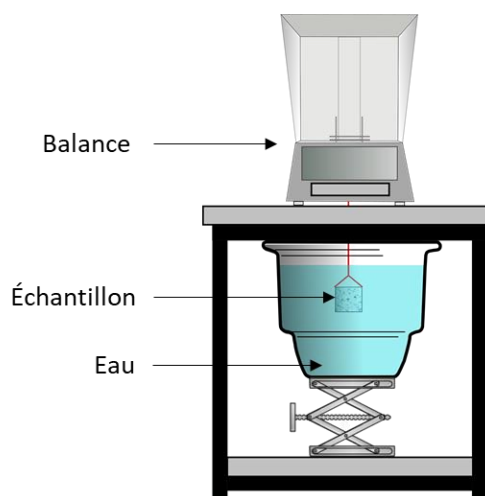


Figure II-13. Schéma du dispositif de mesure de la masse hydrostatique d'un échantillon saturé.

La masse des éprouvettes sèches  $m_{sec}$  ainsi que la masse saturée  $m_s$  permet de calculer le volume des pores ouverts  $V_o$  (ml) :

$$V_o = \frac{m_s - m_{sec}}{\rho r h} \times 1000 \quad (\text{II. 3})$$

Avec  $\rho r h$ , la masse volumique de l'eau, en  $\text{kg}\cdot\text{m}^3$ . Elle est égale à  $998 \text{ kg}\cdot\text{m}^3$  à  $20^\circ\text{C}$

La masse obtenue grâce à la pesé hydrostatique  $m_h$  et la masse de l'échantillon saturée, a permis de calculer le volume apparent (ml) :

$$V_o = \frac{m_s - m_h}{\rho r h} \times 1000 \quad (\text{II. 4})$$

La masse volumique apparente a été calculé grâce au rapport entre la masse sèche de l'éprouvette et son volume apparent :

$$\rho b = \frac{m_{sec}}{m_s - m_h} \times \rho r h \quad (\text{II. 5})$$

Enfin, la porosité ouverte a été calculée grâce au rapport entre le volume des pores ouverts et le volume apparent de l'éprouvette :

$$\phi_o = \frac{m_s - m_{sec}}{m_s - m_h} \times 100 \quad (\text{II. 6})$$

### II.2.4.3. Porosimétrie au mercure

C'est avec Washburn, (1921) que le mercure va être utilisé pour caractériser le réseau poreux sur un matériel rocheux. Cette technique a ensuite été utilisée pour la première fois dans le domaine pétrolier par Purcell en 1949.

La porosité par injection de mercure (Mercury Injection capillary Pressure, MIP) est un outil utile pour étudier l'hétérogénéité au niveau des pores et consiste à injecter du mercure liquide dans un échantillon en augmentant progressivement la pression exercée sur le mercure (Purcell, 1949; Ritter and Drake, 1945). Cet appareil a été couramment utilisé en géosciences pour évaluer la porosité totale et pour calculer la distribution de la porosité en fonction de la taille des pores sur des roches carbonatées, granite ou grès (*e.g.* David et al., 1999; Dessandier et al., 1997; Zhang et al., 2016). Certains facteurs peuvent influencer les résultats des mesures MIP comme les différences dans la procédure de mesure (Ma, 2014).

### II.2.4.3.1. Principe

Cette technique destructive, est basée sur la loi des pressions capillaire de Laplace, (1806) et de Young, (1805) qui détermine les angles de contact entre trois phases non-miscibles (solide-liquide-gaz) :

$$P = \frac{2\sigma \cos \theta}{R} \quad (\text{II. 7})$$

Où  $P$  est la pression d'injection,  $\sigma$  la tension superficielle du mercure ( $0,486 \text{ N.m}^{-1}$  à  $25^\circ\text{C}$ ),  $\theta$  l'angle de contact entre les 3 phases (compris entre  $139$  et  $191^\circ$  pour la plupart des minéraux et en pratique :  $\theta = 140^\circ$ ), et  $R$  le rayon du pore.

Cette relation, qui relie un rayon d'accès aux pores à une pression appliquée est définie pour un modèle de pores cylindriques. Compte tenu de la présence dans le système de mercure sous forme liquide et sous forme de vapeur, la pression capillaire  $P_c$ , est définie comme la différence de pression entre le fluide mouillant et le fluide non-mouillant, telle que :

$$P_c = P_{Hg} - P_{vap} \quad (\text{II. 8})$$

Où  $P_{Hg}$  est la pression externe appliquée sur le mercure, et  $P_{vap}$  la pression de vapeur saturante du mercure.

Néanmoins, la pression de vapeur saturante du mercure qui est de  $0,002$  Torr (environ  $0,27 \text{ Pa}$ ) à température ambiante ( $25^\circ\text{C}$ ), est négligeable par rapport à celle appliquée sur le mercure ( $0,0029$  à  $200 \text{ MPa}$ ). Ainsi, la pression de mercure liquide injecté  $P_{Hg}$ , peut être assimilée à la pression capillaire  $P_c$ , et directement reliée à une taille de rayon d'accès aux pores, telle que :

$$P_{Hg} = \frac{7,5}{r} \quad (\text{II. 9})$$

Où  $P_{Hg}$  est la pression capillaire (en bar), et  $r$  le rayon du tube capillaire (en  $\mu\text{m}$ ).

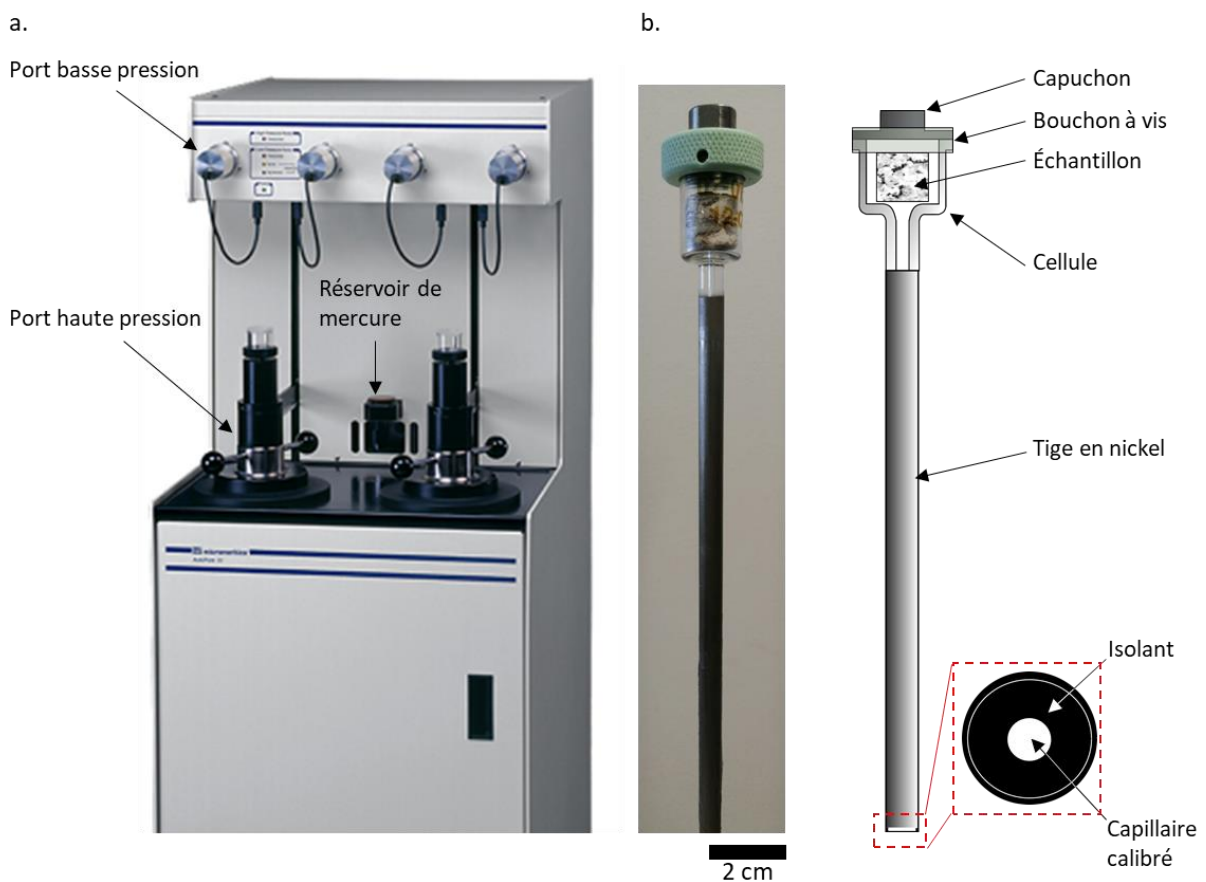
La porosimétrie par intrusion de mercure ne fournit pas la taille des pores mais celle de leurs accès. Lors de l'injection de mercure, la pression induite permet de franchir les étranglements fins qui donnent accès à des pores beaucoup plus grands. Plus la pression sera forte, plus la saturation du mercure sera grande.



### II.2.4.3.2. Acquisition

La méthode consiste à injecter du mercure à une pression donnée croissante dans une enceinte initialement sous vide quasi-parfait ( $\approx 2,6$  Pa). Chaque pression appliquée sur le mercure liquide est associée à une taille de rayon d'accès aux pores et à un volume de mercure injecté.

Les mesures ont été réalisées grâce à l'appareil AutoPore IV 9500, Analyser distribué par la société Micromeritics, disposant d'une cellule pour la mesure à basse pression et d'une cellule pour la mesure à haute pression (Figure II-14).



**Figure II-14. a. Porosimètre mercure AutoPore IV 950 Analyser de Micromeritics avec dans la partie haute, les ports de mesure à basse pression et dans la partie inférieure, la cellule haute pression. b. Exemple de pénétromètre et sa représentation schématique.**

Les échantillons utilisés sont des micro-carottes d'environ  $1,5 \text{ cm}^3$ , séchées au préalable jusqu'à masse constante. Ils sont placés dans un pénétromètre hermétiquement clos, servant de cellule de confinement où sera injecté le mercure sous pression (Figure II-14).

Ce pénétromètre est prolongé d'un capillaire en nickel, entouré d'un manchon isolant, dont le volume est calibré. Il existe différents pénétromètres dont le volume de la cellule et du capillaire change. Le choix se fait sur la base de la taille de l'échantillon et de sa porosité.

La phase d'intrusion du mercure est réalisée en deux temps (mesures en basse et haute pression). Pour chaque pas de pression, le volume de mercure injecté est mesuré après stabilisation du système. Les réglages du temps d'équilibre étaient de 30 s pour les cellules basse et haute pression.

Dans un premier temps, l'échantillon est placé dans l'unité basse pression du porosimètre. Le mercure est introduit jusqu'à remplissage complet de la cellule capillaire contenu dans la tige et la pression est amenée à 0,034 MPa. Ensuite, le mercure envahit progressivement le milieu poreux jusqu'à atteindre une pression d'injection de 0,2 MPa. La pénétration n'étant pas instantanée, le porosimètre laisse le temps au mercure liquide de pénétrer. À ce stade, les pores dont le rayon d'accès est supérieur ou égal à 7,5  $\mu\text{m}$  sont envahis. L'ensemble du dispositif (pénétromètre + échantillon) est pesé.

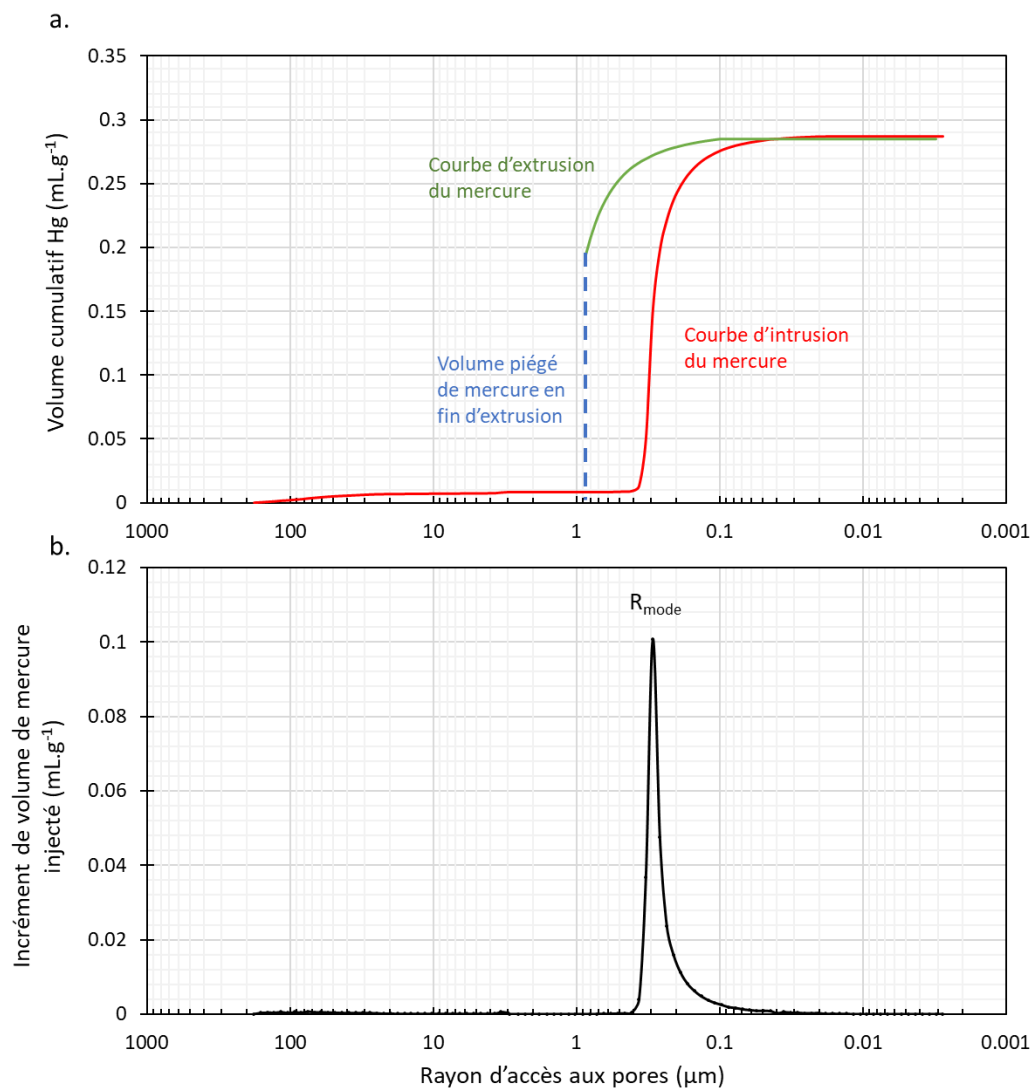
Dans un second temps, l'ensemble du dispositif est placé dans le port de hautes pressions afin de pouvoir appliquer progressivement les pressions supérieures à la pression atmosphérique et jusqu'à 228 MPa. Cet intervalle de pressions permet d'étudier les pores dont le rayon d'accès aux pores est compris entre 0,0025 et 3  $\mu\text{m}$ .

À la fin du cycle d'intrusion, la pression du mercure est progressivement relâchée (phase d'extrusion) et le mercure quitte le réseau poreux progressivement en commençant par les capillaires les plus fins. Le volume de mercure ressorti est également mesuré par palier de pression. L'espace poreux ainsi libéré représente la porosité dite libre et la partie du mercure n'ayant pas été évacuée représente la porosité dite piégée.

### II.2.4.3.3. Traitement des données

Les résultats de l'intrusion et de l'extrusion permettent de représenter graphiquement le volume de mercure injecté en fonction du rayon d'accès aux pores équivalent en échelle logarithmique. L'axe des ordonnées peut être utilisé pour représenter la courbe du volume cumulé de mercure injecté (Figure II-15 a) ou de l'incrément de volume de mercure injecté (Figure II-15 b) en fonction des rayons d'accès aux pores. Plusieurs paramètres peuvent être

extraits de ces courbes, tels que le rayon d'accès aux pores principal ( $R_{mode}$ ) correspondant au pic principal sur la courbe incrémentale ou encore le volume de mercure piégé lors du retrait.



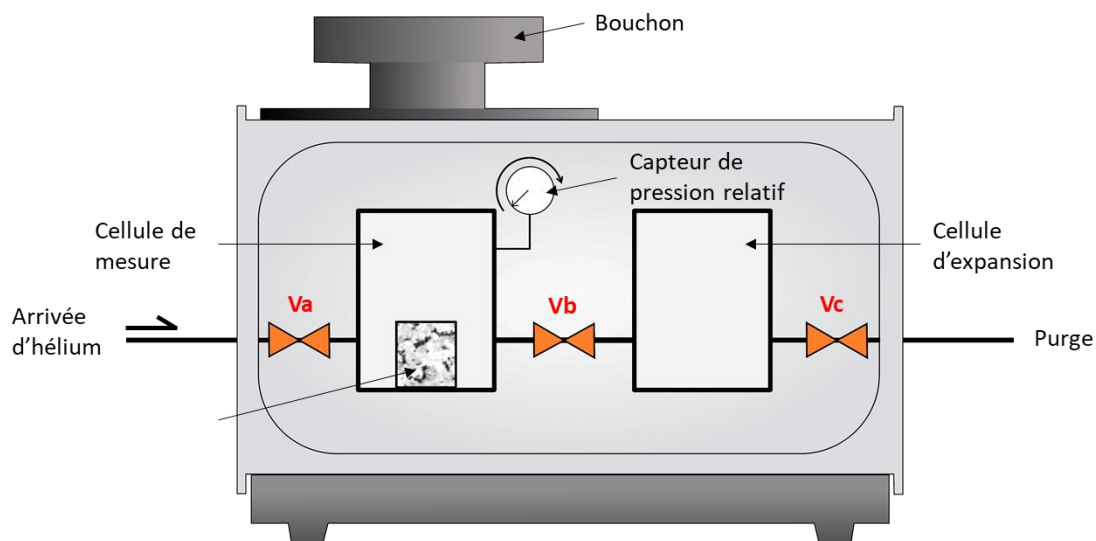
**Figure II-15. Exemples de courbes obtenues à partir de la porosimétrie au mercure pour un échantillon de craie. a. Courbes d'intrusion et d'extrusion cumulées exprimées en fonction des rayons d'accès aux pores. b. Incrément de volume de mercure injecté en fonction des rayons d'accès aux pores.**

#### II.2.4.4. Densité de phase solide

L'acquisition par pycnométrie à l'hélium permet d'obtenir le volume solide  $V_{solide}$  de l'échantillon. Les mesures ont été réalisées à partir d'un pycnomètre AccuPyc II 1340 de Micromeritics. Les échantillons ont été séchés préalablement et il n'a pas été nécessaire d'effectuer une correction sur le volume d'eau occupé dans l'éprouvette (Raynal, 2005).

Le principe de l'appareil est basé sur la loi de compressibilité des gaz parfaits (Boyle-Mariotte). L'utilisation de gaz permet la pénétration dans les pores de très petite taille. C'est l'hélium qui est utilisé, car il a l'avantage d'être un gaz inerte et n'engendre aucune modification physico-chimique avec nos échantillons.

L'appareil est constitué de deux cellules de volumes connus (Figure II-16). Le principe de mesure va être d'injecter le gaz à une pression donnée dans une enceinte de référence (utilisation de la chambre standard de 10 cm<sup>3</sup>).



**Figure II-16. Schéma du dispositif de pycnométrie à l'hélium.**

Dans un premier temps, les vannes Va, Vb et Vc sont fermées et les deux cellules sont mises à une pression d'hélium équivalente à la pression atmosphérique.

Une fois que l'échantillon a été mis dans la cellule, la première phase consiste à ouvrir puis fermer la cellule Va afin que l'hélium pénètre dans la chambre prévue à cet effet. La pression diminue alors jusqu'à stabilisation. La vanne Vb est pour l'instant fermée. La valeur de la pression dans la cellule augmente jusqu'à atteindre la pression  $P_1$ . Les lois des gaz parfaits sont respectées dans ces conditions et la quantité d'hélium dans la cellule est donc à l'équilibre (Raynal, 2005).

La deuxième phase consiste à ouvrir la vanne Vb afin que le gaz circule dans la deuxième chambre. L'hélium se répartit dans la cellule de mesure, la pression  $P_1$  diminue puis se stabilise pour atteindre la valeur de la pression  $P_2$ . Enfin la vanne Vc est ensuite ouverte remettant le système à pression atmosphérique.

La loi des gaz parfaits indique :

$$P_1 \times (V_{cell} - V_{solide}) = nRT = P_2 \times (V_{cell} - V_{solide} + V_{exp}) \quad (\text{II. 10})$$

Il peut être écrit alors :

$$V_{solide} = V_{cell} - \frac{P_2}{P_1 - P_2} V_{exp} \quad (\text{II. 11})$$

Où  $V_{cell}$  est le volume de la cellule de mesure où se trouve l'échantillon,  $V_{solide}$  le volume solide de l'échantillon,  $V_{exp}$  le volume de la cellule d'expansion,  $P_1$  la pression mesurée à la fin de la première phase et  $P_2$  la pression mesurée à la fin de la deuxième phase.

La densité de la phase solide ( $d_{solide}$ ) peut alors être déterminée par l'équation :

$$d_{solide} = \frac{m_{sec}}{V_{solide}} \quad (\text{II. 12})$$

### II.2.4.5. Mesure des cinétiques d'imbibition capillaire

Les tests d'imbibition capillaire sont souvent utilisés comme estimateur de dégradation de la roche (Benavente et al., 2004; Çelik and Kaçmaz, 2016; Fronteau et al., 2010; Sengun et al., 2014). La connaissance du mouvement de l'eau à l'intérieur de la roche est une manière simple d'évaluer la porosité de la roche (Fronteau et al., 2010). L'apparence des courbes d'absorption capillaire fournit des informations sur les types de réseau poreux caractéristiques de la roche (Thomachot-Schneider et al., 2008). Grâce à l'analyse pétrographique, il a été mis en évidence que la composition, la structure, la texture et le système de pores étaient des caractéristiques importantes pour l'absorption d'eau (Tomašić et al., 2011). Benavente et al. (2015) montre une forte relation entre le coefficient d'absorption d'eau par capillarité et la perméabilité à l'eau. Ainsi, le coefficient d'absorption capillaire quantifie les mécanismes d'écoulement influencés par la tortuosité, la structure de pores interconnectés, l'interconnectivité des pores et la migration du fluide (Benavente et al., 2002; Cai and Yu, 2011; Çelik and Kaçmaz, 2016; Hammecker et al., 1993). Cependant, le comportement d'absorption capillaire de l'eau peut parfois montrer des résultats anormaux. Ioannou et al. (2009) observent que la présence de grands pores réduit l'absorption capillaire contrairement à la présence de pores fins qui conduisent à une absorption capillaire lente mais plus importante dans un calcaire (Vuggy).

### II.2.4.5.1. Théorie

La capillarité sur une pierre naturelle est une propriété intrinsèque et représente sa capacité à absorber l'eau sous l'effet de la force capillaire. Cette propriété est directement liée au réseau poreux comme la taille, forme des pores ou connexion du réseau (Hammecker et al., 1993).

#### Loi de Hagen-Poiseuille

Dans les conditions atmosphériques, la théorie de l'imbibition capillaire dans l'eau est basée sur les principes hydrodynamiques et l'expression de la pression capillaire. La loi de Poiseuille, (1844) exprime l'écoulement d'un fluide newtonien en régime permanent dans un tube cylindrique. En considérant une vitesse maximale du fluide  $V_{max}$ , le débit du fluide  $Q$  dans le tube de section transversale  $s$  s'écrit :

$$Q = \int V_{max} ds \quad (\text{II. 13})$$

Sous une pression différentielle  $\Delta P$ , la vitesse maximale d'écoulement est proportionnelle au carré du rayon du capillaire  $r$  selon :

$$V_{max} = \frac{\Delta P r^2}{L 4 \eta} \quad (\text{II. 14})$$

Où  $L$  est la longueur du tube et  $\eta$  la viscosité dynamique du fluide.

Ainsi, plus un capillaire est large, plus le fluide se déplace rapidement lors de l'imbibition capillaire.

Remplacer la vitesse par son expression dans la première relation conduit à la loi de Hagen-Poiseuille à travers la relation :

$$Q = \frac{\pi r^4 \Delta P}{8 \eta L} \quad (\text{II. 15})$$

#### L'équation de Washburn

Dans le cas de l'absorption d'eau capillaire dans un pore cylindrique vertical, le débit d'eau est régi par la pression capillaire et la gravité selon la loi de Laplace :

$$\Delta P = \frac{2\sigma \cos \alpha}{r} - \rho g L \quad (\text{II. 16})$$

Où  $\Delta P$  est le gradient de pression,  $\sigma$  la tension superficielle,  $\alpha$  l'angle de contact,  $r$  le rayon du capillaire,  $\rho$  la masse volumique,  $g$  l'accélération de la pesanteur et  $L$  la longueur du tube.

L'injection de l'équation précédente dans la loi de Hagen-Poiseuille permet d'obtenir la formulation générale de l'équation de Washburn :

$$Q = \frac{\pi r^4 \left( \frac{2\sigma \cos \alpha}{r} - \rho g L \right)}{8\eta L} \quad (\text{II. 17})$$

Sachant que l'expression du volume peut s'écrire  $Q = \frac{dV}{dt} = \pi r^2 \frac{dL}{dt}$ , la loi de Washburn peut s'écrire de la manière suivante :

$$\frac{dL}{dt} = \frac{r^2 \left( \frac{2\sigma \cos \alpha}{r} - \rho g L \right)}{8\eta L} \quad (\text{II. 18})$$

Dans un tube horizontal ou de faible hauteur, les forces gravitaires deviennent négligeable et l'on peut écrire l'expression suivante, après intégration :

$$L = r^{\frac{1}{2}} \sqrt{\frac{\sigma \cos \alpha}{2\eta}} t^{\frac{1}{2}} \quad (\text{II. 19})$$

Cette relation permet de calculer la position du niveau d'eau dans le tube au cours de l'imbibition pour tout temps  $t$ .

En posant le coefficient  $C2$  comme propre au fluide et à la géométrie du tube, telle que :

$$L = C2 t^{\frac{1}{2}} \text{ avec } C2 = r^{\frac{1}{2}} \sqrt{\frac{\sigma \cos \alpha}{2\eta}} \quad (\text{II. 20})$$

Ce coefficient  $C2$  est appelé coefficient de migration linéaire de la frange capillaire.

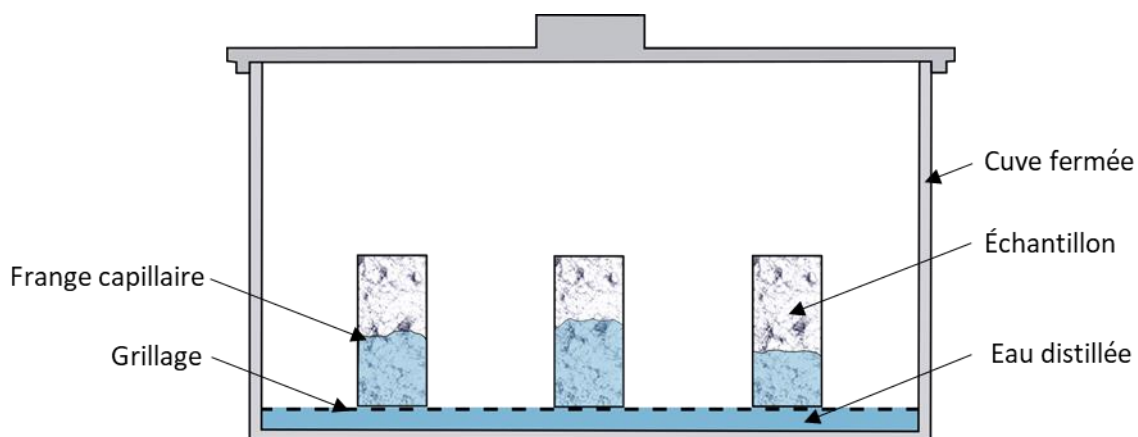
Le coefficient de cinétique de l'imbibition capillaire  $C1$ , représente le volume d'eau absorbé par unité de temps. Ainsi, le volume de liquide  $V$  imbibant le tube sera :

$$V = C1 t^{\frac{1}{2}} \text{ avec } C1 = \pi r^{\frac{5}{2}} \sqrt{\frac{\sigma \cos \alpha}{2\eta}} \quad (\text{II. 21})$$

Ces deux relations attestent de la proportionnalité de la hauteur de la frange capillaire et de la prise de masse en eau de l'échantillon en fonction de la racine carrée du temps.

### II.2.4.5.2. Mesure

Le protocole préconisé par la norme NF EN 1925, (1999) a été utilisé. Les échantillons sont séchés à  $40 \pm 5$  °C avant chaque test jusqu'à stabilisation de leurs masses. Les échantillons peuvent alors être placés dans un bac fermé hermétiquement afin de maintenir une hygrométrie proche de la saturation et donc d'éviter la superposition de phénomènes d'évaporation (Figure II-17). Au cours de l'expérience, un volume constant d'eau distillée (1 mm de profondeur) permet l'imbibition du bas de l'échantillon. Une grille plastique est placée entre l'échantillon et le fond de la cuve afin d'assurer une bonne conduction hydraulique. Afin de ne pas modifier la tension de surface air-eau et la viscosité de l'eau dépendante de la température (Mertz, 1991), les mesures sont donc réalisées à température ambiante. La manipulation a pour principe de mettre en contact notre solide poreux avec de l'eau. Ainsi le fluide dit non-mouillant (air) initialement dans les pores est remplacé par le fluide mouillant (eau distillée) sans pression extérieure appliquée. Les pesées de l'échantillon sont effectuées à des intervalles de temps croissants.



**Figure II-17. Schéma du dispositif utilisé pour les tests d'absorption capillaire.**

Deux phases en ressortent (Hammecker et al., 1993; Hammecker and Jeannette, 1994). La première phase est le remplissage progressif par la force capillaire de l'eau dans la porosité libre. La deuxième phase débute après la rupture de pente. Elle se caractérise par la diffusion et la dissolution de l'air dans l'eau. La pente de la section droite de la courbe représente le coefficient de capillarité  $C_1$  (Roels et al., 2000). Il représente le volume d'eau pénétré par



capillarité dans la roche par unité de temps (en  $\text{g}\cdot\text{m}^{-2}\cdot\text{s}^{-1/2}$ ). Sur ces courbes les interceptions ne sont pas forcément les mêmes à zéro. C'est la faible submersion nécessaire pour assurer le contact entre l'échantillon et l'eau qui affecte de manière minimale cette valeur. Le coefficient C2, appelé coefficient de remontée de la frange capillaire, représente la migration de la frange capillaire par unité de temps (en  $\text{m}\cdot\text{s}^{-1/2}$ ). L'évolution de la frange capillaire (L en m) et la prise de masse en eau par rapport à la surface de l'échantillon ( $dW/S$  en  $\text{g}\cdot\text{m}^{-2}$ ) sont reportées graphiquement (Figure II-18), en fonction de la racine carrée du temps ( $\sqrt{t}$  en  $\text{s}^{-1/2}$ ). Représenter l'abscisse en racine carrée du temps, est justifié par le fait que la cinétique d'imbibition capillaire dans les roches est du même type que celle décrite par la relation de Washburn. Ainsi, pour ce type de représentation, les courbes apparaissent comme des segments de droite, sur lesquels sont définis la pente des deux droites, C1 et C2.

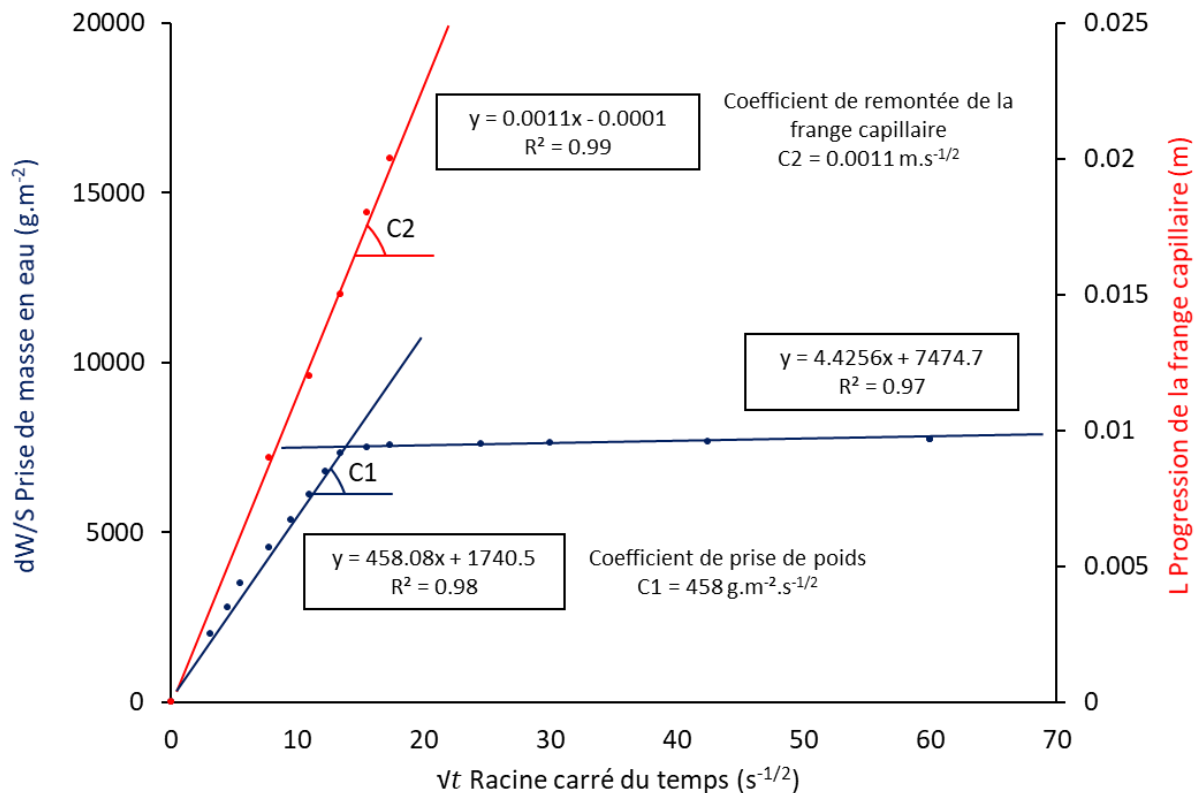


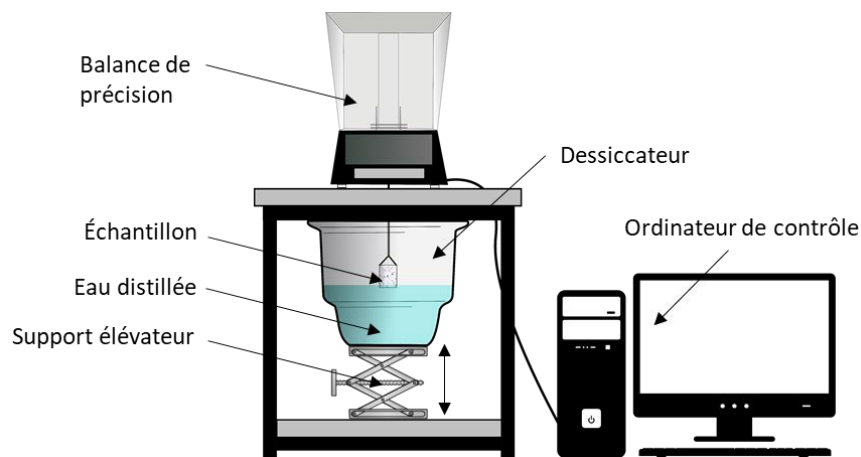
Figure II-18. Exemple de courbe caractéristique de restitution des tests d'imbibition capillaire avec la détermination des coefficients C1 de prise de poids et C2 de remontée de la frange humide.

### II.2.4.5.3. Automatisation de l'expérience

Une méthode d'absorption automatisée jugée plus pratique et précise (Al-Naddaf, 2018; Lu et al., 2020) a été mise en place. Cette technique consiste à enregistrer automatiquement le poids

de l'échantillon tout au long des tests d'imbibition capillaire (Gao and Hu, 2012) sans manipulation de l'échantillon, ce qui réduit l'erreur de fonctionnement.

Le schéma du montage expérimental est présenté sur la Figure II-19. Les échantillons sont suspendus sur la partie inférieure d'une balance de précision électronique, avec une lisibilité de 0,1 mg, à l'aide d'un crochet. La partie inférieure de l'échantillon est plate et usinée horizontalement et l'échantillon était situé à l'intérieur d'un dessiccateur (en verre). Le récipient contenant de l'eau est posé sur un support élévateur. Le récipient et l'échantillon sont confinés afin que l'hygrométrie soit proche de 100%. Les phénomènes d'évaporation sont alors évités. La température de la salle est maintenue à température ambiante. Le récipient peut alors être ajusté verticalement afin de mettre l'échantillon en contact avec l'eau du réservoir à une profondeur constante d'environ 1 mm.



**Figure II-19. Schéma montrant la mise en place expérimentale de la méthode de mesure automatique de l'absorption d'eau par capillarité.**

L'avantage de cette méthode est que l'appareil est facile à utiliser. La masse de l'échantillon est mesurée automatiquement juste après avoir été placée sur le plateau, ce qui garantit la précision de la mesure et réduit les manipulations. L'efficacité est supérieure à la méthode d'essai standard notamment pour les roches à faible porosité comme les granites ou pour des échantillons de petites tailles. Néanmoins, cette méthode présente l'inconvénient de tester qu'un seul échantillon à la fois par balance, alors que pour la méthode standard, plusieurs échantillons peuvent être testés en même temps.

### II.2.4.6. Thermographie infrarouge

La thermographie infrarouge (IRT) est une technique permettant de déterminer la température de la surface d'un objet en exploitant le rayonnement thermique émis. La loi de Stephan-Boltzmann permet d'estimer l'énergie thermique émise au moyen d'une caméra thermique (Chrysochoos et al., 1989), capable de produire des images numériques. Chaque pixel va contenir l'information de la température de surface. Cette loi de proportionnalité s'écrit :

$$j = \varepsilon \sigma T^4 \quad (\text{II.22})$$

Avec  $J$ , l'énergie totale émise par le corps.  $\varepsilon$  représente l'émissivité (aptitude d'un matériau à absorber puis à réémettre de l'énergie par rayonnement). L'émissivité est une valeur sans unité, comprise entre 0 et 1. Plus l'émissivité est forte, plus l'énergie rayonnée sera forte et plus la température mesurée sera faible (Watson, 1975). Elle se situe entre 0,80 et 0,90 pour les roches poreuses naturelles (Vlcek, 1982). La constante de Stefan-Boltzmann est représentée par  $\sigma$ . Enfin la température de surface du corps est notée  $T$ .

L'utilisation de l'IRT a été largement adoptée au cours des dernières années dans de nombreux domaines (médecine, la chimie et la sécurité). Elle est largement utilisée dans le génie civil et l'architecture ou l'archéométrie (Avdelidis and Moropoulou, 2004; Meola, 2007). Par exemple, Datcu et al. (2005) utilisent l'IRT afin d'améliorer la lecture de la température du mur d'un bâtiment. Cette technique a permis la détection en laboratoire de l'humidité et des sels (Thomachot-Schneider et al., 2016). Par exemple, Vazquez et al. (2018b) étudient par le moyen de l'IRT, les phases de cristallisation de gouttes de solution salines que l'on peut retrouver dans les murs et pouvant contribuer à la détérioration des bâtiments qui appartiennent au patrimoine culturel d'une ville.

L'IRT a permis avec succès d'étudier le comportement mécanique des roches en tant que technique de surveillance non-destructive (Chicco et al., 2019; Sun et al., 2017). Par exemple, Luong (1990) a étudié le développement de microfissures dans des expériences de fatigue, fracturation et d'endommagement sur un béton. Wu et al. (2005) utilisent l'IRT pour détecter des grottes érodées derrière des pentes protégées par du béton. L'IRT a été utilisé par Mineo et al. (2015) pour réaliser une enquête sur les zones instable d'une zone de pente rocheuse en Sicile.

L'IRT permet de quantifier la cinétique thermique des roches directement liée à la porosité (Grinzato et al., 2004) ou à l'état de dégradation (Thomachot-Schneider et al., 2019). La relation entre le comportement thermique d'une roche et sa fracturation a été étudiée par Pappalardo et al. (2016) avec l'analyse des anomalies thermiques d'une pente rocheuse. Le refroidissement naturel de la roche a été exprimé par l'indice de vitesse de refroidissement (CRI) et montre une corrélation directe entre le degré de fracturation et la cinétique de refroidissement de la roche. Plus récemment, Mineo et Pappalardo (2019) utilisent l'IRT pour surveiller le refroidissement de roches en laboratoire. Ces tests ont permis d'estimer indirectement la porosité d'une roche. Les roches poreuses montrent un refroidissement rapide et inversement, les roches non fissurées seraient de mauvais conducteur thermique et le refroidissement serait plus lent.

L'IRT permet également de visualiser l'écoulement du fluide (Forestieri and Buergo, 2018; Fang Zhang et al., 2018). Par exemple, Ludwig et al. (2018) visualisent grâce à l'IRT la diffusion de l'eau dans le réseau poreux de 3 roches (grés, calcarénite et marbre) à partir de taches d'eau absorbées et caractérisent ainsi la typologie des pores.

Dans le projet présenté ici, le suivi de l'endommagement thermique et les mouvements hydriques ont été suivis grâce à l'utilisation d'une méthode utilisant la thermographie infrarouge. Cette technique d'observation directe de la variation de température a l'avantage d'être non-destructive, rapide et précise.

### II.2.4.6.1. Caméra thermique et logiciel de traitement

La caméra thermique infrarouge (IRT) est une FLIR SC655. Elle fonctionne dans les longueurs d'onde comprises entre 7,5 et 14  $\mu\text{m}$ , avec une température de détection comprise entre -40 et 150 °C et une sensibilité de 0.1 °C. Le détecteur est un réseau de microbolomètres non refroidis. Elle est capable de construire des images en utilisant le rayonnement infrarouge. Une fois l'acquisition réalisée, la donnée obtenue est une image avec échelle de couleur. Chaque pixel représente une valeur de température (surface). La taille de l'image est de 640 x 480 pixels et le signal de bruit est d'environ 40 mK. Le signal enregistré est appelé thermosignal (TS). Le TS dépend de la température et de l'émissivité du corps observé et est exprimé en unités isothermiques (UI). Les mesures ont été effectuées en mode IRT actif, c'est-à-dire avec changement de stimulus externe (chauffage et refroidissement). L'instrument a

été réglé en considérant une émissivité à 0,90. Les risques liés aux variations environnementales ont été minimisés (contrôle de la température et de l'humidité, éclairage des pièces éteint).

Les images ont été traitées et analysées avec le logiciel ResearchIR (FLIR). Ce logiciel est spécialement conçu pour l'édition et l'analyse de thermogramme. Chaque pixel du thermosignal contient une valeur de température spécifique. L'analyse de l'image thermique peut être effectuée dans différentes zones : en un seul pixel (fonction « spotmeter »), en une zone définie du thermogramme (fonction « Area ») ou le long d'une ligne (fonction « Line »).

### II.2.4.6.2. Protocole de mesure

Deux informations ont été obtenues à partir des données de l'IRT : l'indice de vitesse de refroidissement de la roche après 10 minutes ( $CRI_{10}$ , Pappalardo et al., 2016), et le suivi de la circulation de l'eau à travers les échantillons.

La procédure d'estimation de ces paramètres est décrite dans la Figure II-20.

La montée d'eau se fait sur des échantillons de taille 40 x 40 x 10 mm. Dans un premier temps, les échantillons ont été chauffés pendant 24 heures à 40 °C afin que la température soit uniforme dans l'entièreté de la roche.

Les échantillons chauffés ont été placés devant la caméra thermique à une distance de d'environ 15 cm dans une pièce à température contrôlée ( $23 \pm 1$  °C). Les thermogrammes ont été pris à intervalles de temps réguliers à la cadence d'une image toutes les 10 secondes. La caméra a été activée 1 minute après le début de l'expérience pour éviter les larges variations de signal pendant l'étalonnage initial. La roche débute alors sa phase de refroidissement à l'air pour le haut de l'échantillon et à l'eau pour le bas de l'échantillon.

Chaque acquisition dure environ 30 minutes et est réalisée sur un échantillon à la fois. La température au temps ( $t_0$ ), correspond à la température maximale ( $T_0$ ) atteinte par la roche au début de l'expérience. Une courbe décroissante de la température en fonction du temps est alors obtenue. Une fois la température de surface évaluée, l'indice de vitesse de refroidissement ( $CRI$ ) des échantillons sur les 10 premières minutes ( $t_{10}$ ) (Pappalardo et al., 2016) est calculé selon :

$$CRI_{10} = \frac{\Delta T}{\Delta t} = \frac{(T_{10} - T_0)}{(t_{10} - t_0)} \quad (\text{II. 23})$$

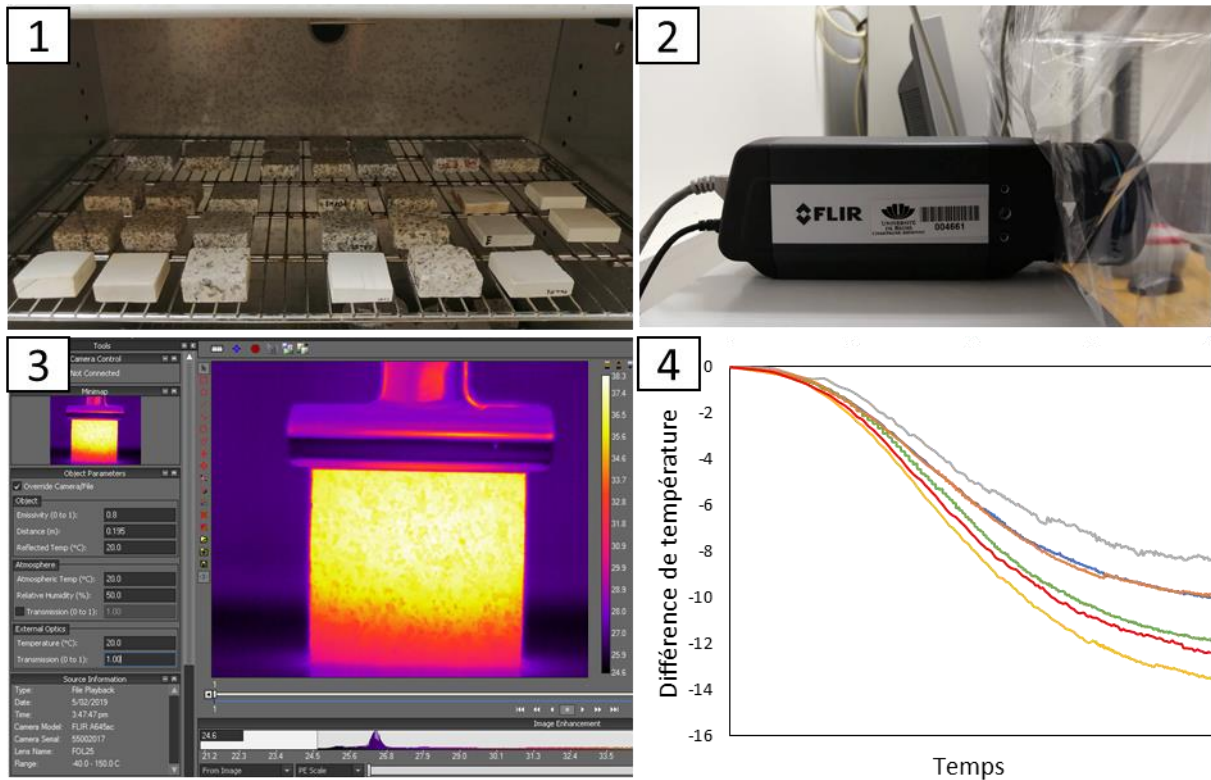
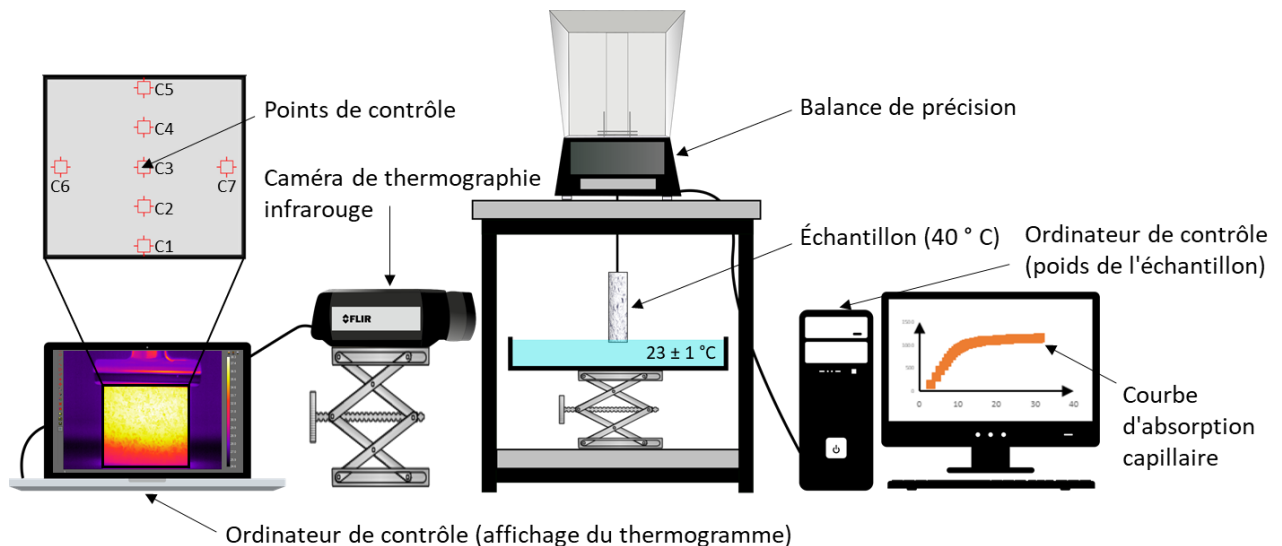


Figure II-20. Illustration des étapes de suivi du refroidissement par une caméra IRT. 1. Phase de chauffage de l'échantillon dans un four (40 °C) 2. Système d'acquisition par la caméra thermique 3. Étape de traitement des données d'un thermogramme montrant la face de l'échantillon (couleurs chaudes) et les outils de mesure disponibles pour l'estimation de la température de surface. 4. Étude des courbes de refroidissement.

### II.2.4.6.3. Suivi de la frange capillaire

La cinétique d'imbibition capillaire pendant le refroidissement a été suivie par IRT. La configuration expérimentale est illustrée sur la Figure II-21.



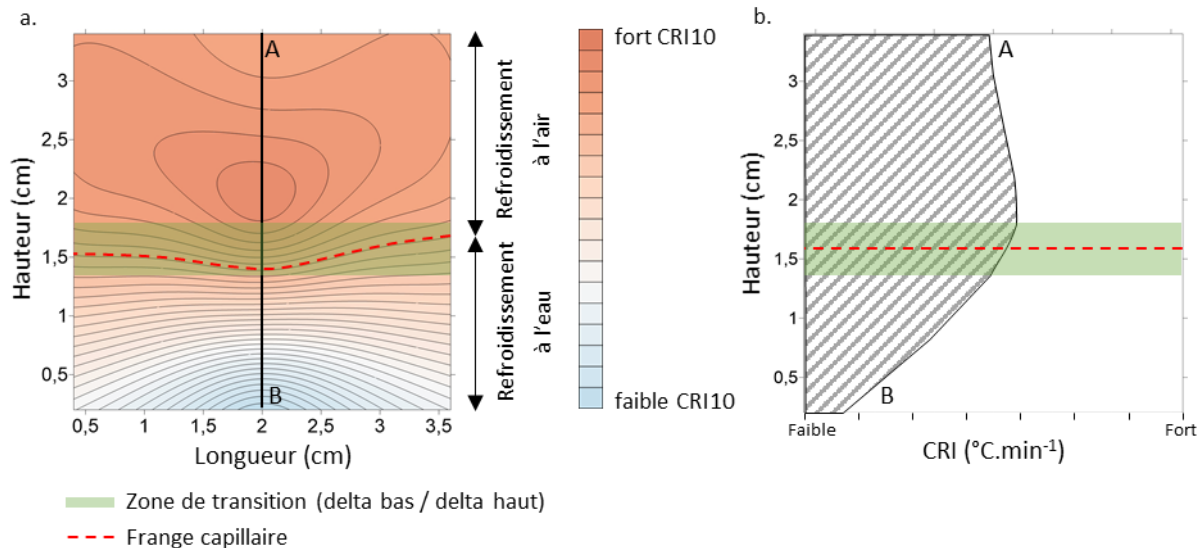
**Figure II-21. Configuration expérimentale du suivi par IRT du refroidissement d'un échantillon soumis à une imbibition capillaire.**

Le récipient et l'échantillon ont été confinés de manière à ce que l'hygrométrie soit proche de 100% afin d'éviter les phénomènes d'évaporation. Le principe de l'expérience a été de mettre l'échantillon en contact avec de l'eau distillée à une profondeur d'environ 1 mm.

L'échantillon a été suspendu par le dessous d'une balance de précision électronique à l'aide d'un crochet afin de suivre la cinétique d'imbibition capillaire. La masse a été automatiquement enregistrée toutes les 10 secondes sur l'ordinateur de contrôle. La température de la pièce a été maintenue à  $23 \pm 1 \text{ }^\circ\text{C}$ . La hauteur de la frange capillaire de l'échantillon a été suivie par la caméra IRT.

Sur le logiciel de traitement ResearchIR (FLIR), l'outil "temporal plot" a permis de mesurer la température moyenne contenue dans un carré de  $3 \times 3$  pixels en fonction du temps. 5 curseurs ont été verticalement centrés et 2 autres ont été placés dans la longueur de l'échantillon. À  $T_0$ , la température des curseurs a enregistré la température maximale à la surface de l'échantillon atteinte pendant la phase de chauffage. Le logiciel SURFER a été utilisé pour faciliter la visualisation 2D de la vitesse de refroidissement à la surface de l'échantillon. La cartographie des indices de refroidissement sur toute la surface de l'échantillon est obtenue. De plus, le logiciel permet d'extrapoler les 7 points de mesure afin d'étendre les données sur l'échantillon total. Une zone où la valeur sera élevée correspondra à une partie de l'échantillon refroidie rapidement et inversement.

La Figure II-22 montre la distribution schématique de l'indice de refroidissement à la surface de l'échantillon. Les axes X et Y des grilles représentent les dimensions de l'échantillon en centimètres.



**Figure II-22. a. Représentation schématique de l'indice de refroidissement (CRI10) à la surface d'un échantillon. b. Valeurs de CRI10 le long du profil vertical AB. La ligne pointillée rouge est positionnée sur la rupture de pente. Sa position est affinée grâce aux isolignes à la surface de l'échantillon.**

Les images de la distribution des pentes des courbes de refroidissement ont permis de distinguer le refroidissement par l'eau et le refroidissement par l'air. Cette limite est représentée par la ligne pointillée rouge.

La partie haute de l'échantillon a permis de quantifier l'évolution du refroidissement à l'air à partir du CRI10 mesuré au niveau du curseur 5 (Figure II-21).

Le refroidissement de la roche, la frange capillaire et les détails de l'image étaient de moins en moins nets avec le temps. Pour cette raison, un filtre de soustraction a été appliqué, afin de soustraire le thermogramme initial et augmenté les détails des variations de températures.

### II.2.4.7. Mesure de perméabilité au gaz

La perméabilité d'un milieu poreux est caractérisée par son aptitude à laisser circuler un fluide (liquide ou gaz) au sein de son espace poreux. Sa valeur dépend de la structure interne du réseau poreux et de la connectivité des éléments qui le compose. La perméabilité représente le rapport entre une force (gradient de pression) imposée à un fluide pour traverser le milieu



et le débit résultant. Elle se rapporte au milieu poreux indépendamment des caractéristiques du fluide. Elle peut être mesurée à l'échelle de l'échantillon en laboratoire, à l'échelle de l'affleurement sur le terrain ou peut être évaluée en modélisant la circulation des fluides dans un milieu poreux dont la microstructure est connue.

Les mesures de perméabilité ont été réalisées en laboratoire à l'aide d'un perméamètre à azote. Cette technique non-destructive est principalement composée d'une cellule Hassler dans laquelle l'échantillon a été introduit revêtu d'un manchon étanche et flexible afin qu'il adhère parfaitement à la surface de l'échantillon. Le fluide est introduit à la surface de l'échantillon à une pression donnée, le traverse et en ressort avec une nouvelle pression. Une pression de confinement de 1,5 MPa est appliquée latéralement sur le manchon d'étanchéité pour empêcher les écoulements le long des bords de l'échantillon. Des manomètres de différentes sensibilités permettent de contrôler les différentes pressions. Au moins 4 niveaux de pression de tête ont été mesurés par échantillon. Les perméabilités mesurées ont été corrigées pour l'effet Klinkenberg (Klinkenberg, 1941). Dans le système international, la perméabilité est exprimée en  $m^2$ , mais cette unité ne convient pas aux valeurs mesurées dans les roches. Les résultats ont été estimés en millidarcy (mD), ce qui équivaut à  $10^{-15} m^2$ .

### II.2.4.8. Mesure des vitesses de propagation des ondes acoustiques

La vitesse des ondes P et S dans un milieu poreux dépend à la fois de la minéralogie et du volume poral. Ces vitesses seront perturbées par la modification des propriétés microstructurales et l'altération du matériau. La mesure de ces vitesses est par conséquent un bon outils pour étudier le vieillissement, estimer les caractéristiques élastiques ou quantifier le comportement anisotrope des roches (Benavente et al., 2020; Vazquez et al., 2018a).

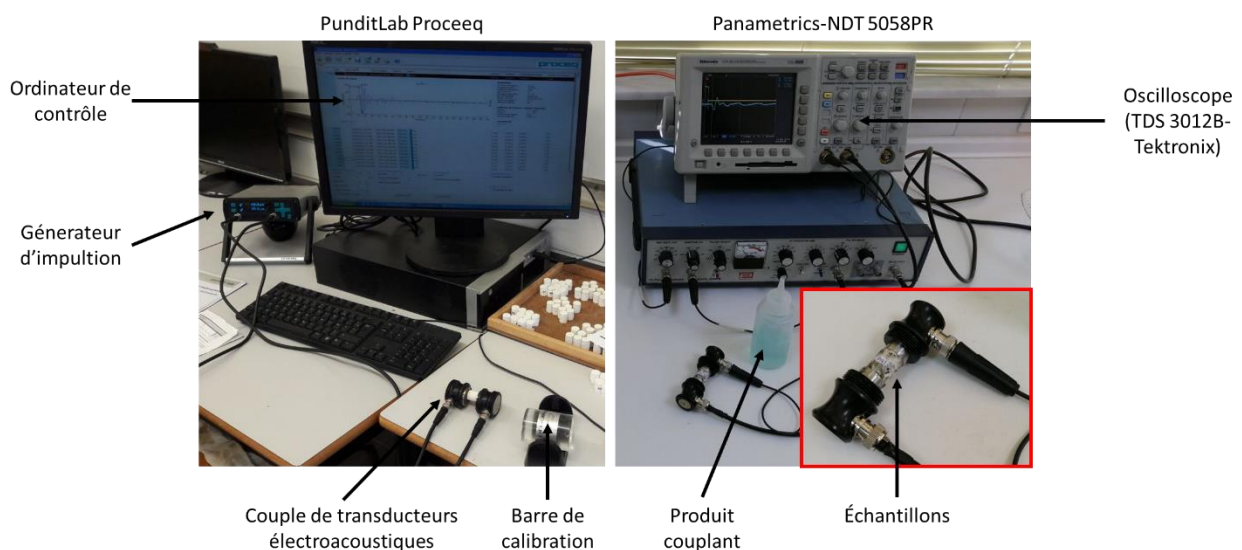
La vitesse des ondes de compression  $V_p$  (P=primaire) permet d'estimer les défauts de texture induits sur la roche (Martínez-Martínez et al., 2011). Ce paramètre a tendance à varier en fonction du contenu minéralogique (Homand et al., 2000), la présence de grains allongés ou de fissures orientées (Vazquez et al., 2018a). En effet la porosité et la taille des pores et des fissures sont des paramètres déterminant dans la vitesse des ondes des roches.

La vitesse des ondes élastiques de cisaillement  $V_s$  (S=secondaire) est mesurée principalement en combinaison des ondes P afin de calculer les propriétés élastiques (coefficient de Young,

module de Poisson) et déduire les propriétés mécaniques (Homand et al., 2000). Son estimation expérimentale est moins simple que pour la vitesse des ondes P (Wang et al., 2009). L'onde P pourrait masquer l'onde S ce qui rendrait sa génération et son acquisition difficile (Benavente et al., 2020).

L'analyse de l'amplitude (*Amp*) de l'onde enregistrée permet de caractériser l'atténuation d'énergie (*A*). La quantification de l'atténuation spatiale permet d'estimer les défauts de texture induits sur la roche. L'amplitude du signal d'onde ultrasonore reçu est atténuée lors du passage à travers les fissures et les vides (Martínez-Martínez et al., 2011). De plus, cette caractéristique est plus sensible aux défauts individuels que la vitesse de l'onde.

Les mesures de vitesses de propagation des ondes  $V_p$  et  $V_s$  ont été réalisées avec un testeur PunditLab Proceeq et des transducteurs de 250 kHz pour les études consacrées à la craie et avec un équipement de réception de signaux non émetteurs (Panametrics-NDT 5058PR) couplé à un oscilloscope (TDS 3012B-Tektronix) et des transducteurs centrés sur 2,5 MHz pour les ondes P et 1 MHz pour les ondes S pour les études consacrées aux granites (Figure II-23).



**Figure II-23. Dispositif expérimental de mesure des vitesses de propagation des ondes acoustiques.**

Les mesures  $V_p$  et  $V_s$  ont été réalisées sur des échantillons séchés à l'étuve à 60 °C et remis à la température ambiante. Les deux transducteurs en céramique piézo-électrique (émetteur et récepteur) sont placés d'un bout à l'autre de l'échantillon. Pour assurer la transmission de l'énergie ultrasonore entre les transducteurs et la surface de l'échantillon, un coupleur visco-élastique a été utilisé. Une pression constante est systématiquement appliquée entre les

transducteurs et l'échantillon. L'appareil mesure le temps ( $t$  en  $\mu\text{s}$ ) de parcours des ondes acoustiques entre les deux extrémités de l'échantillon. Connaissant la longueur ( $L$ ) du plug, la vitesse  $V$  est calculé telle que :

$$V = \frac{L}{t} \quad (\text{II. 24})$$

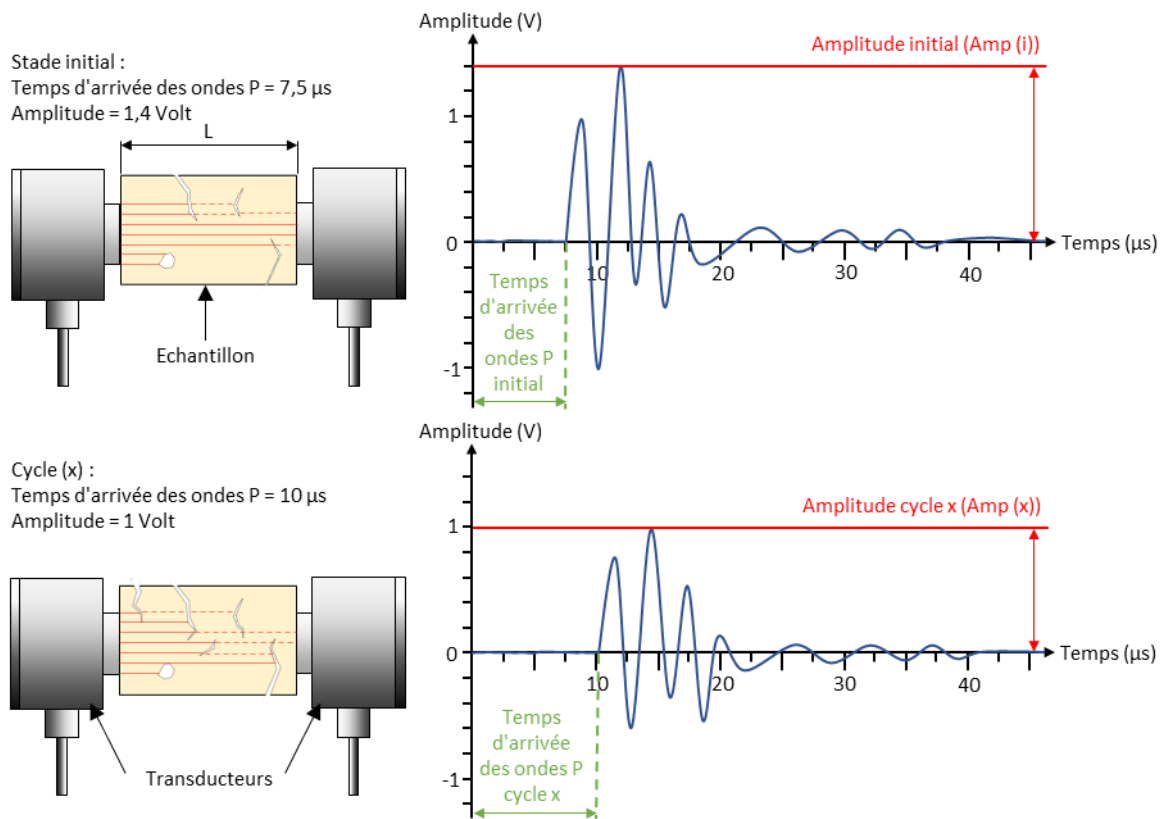
Le module de Young dynamique ( $E$ ) et le coefficient de Poisson ( $\nu$ ) ont été calculés comme suit (Homand et al., 2000) :

$$E = \rho \frac{V_p^2(1+\nu)(1-2\nu)}{1-\nu} \quad (\text{II. 25})$$

$$\nu = \frac{\frac{1}{2} - \left(\frac{V_s}{V_p}\right)^2}{1 - \left(\frac{V_s}{V_p}\right)^2} \quad (\text{II. 26})$$

Où  $\rho$  est la masse volumique apparente déterminée par la mesure directe des poids séchés et des dimensions des échantillons.

En plus de  $V_p$  et  $V_s$ , le coefficient d'amplitude ( $A$ ) a été obtenu. Il a été défini comme le rapport entre l'ampli (x) et l'ampli (i). Amp est l'amplitude maximale (en valeurs absolues) mesurée sur la forme de l'onde du signal reçu : Amp (i) correspond à la valeur de l'échantillon initiale et Amp (x) après (x) test. L'atténuation de l'amplitude du signal (Figure II-24) dépend des caractéristiques texturales de la roche et des défauts individuels mais est moins sensible à la taille et à la porosité des cristaux comme peut l'être  $V_p$  (Martínez-Martínez et al., 2011). La présence d'une fracture ouverte entraîne une forte diffusion des ondes ultrasonores et induit une diminution du coefficient  $A$ .



**Figure II-24. Schéma de la transmission des ondes ultrasonores avec un exemple de signaux reçus dans un échantillon au stade initial et après des cycles de vieillissement.**

### II.2.4.9. Résonance magnétique nucléaire

La résonance magnétique nucléaire (RMN) est un outil rapide, pratique et non-destructif permettant de caractériser les milieux poreux complexes. Entre les années 1960 et 1980 la méthode de relaxation par résonance magnétique était largement utilisée pour l'analyse pétrophysique et la diaggraphie de puits dans l'exploitation pétrolière (Timur, 1969, 1972). Récemment, cette méthode se développe afin de caractériser les propriétés du réseau poreux dans des roches réservoir (porosité, perméabilité). La RMN est basée sur la désintégration par aimantation du noyau hydrogène de l'eau et est utile pour la déduction de certaines informations sur la structure des pores (distribution des pores) (Liu et al., 2017; Tian et al., 2020; Weng et al., 2018).

Le signal RMN dépend de plusieurs paramètres comme la relaxation de surface des micropores ou de la diffusivité des fluides mais, ne repose pas sur la connectivité (Anand and Hirasaki, 2007). La forme des pores affecte également de façon importante le signal de RMN (Kenyon, 1997). Plusieurs études ont utilisé la RMN dans l'analyse de la distribution de la taille

des pores dans les réservoirs (Brigaud et al., 2014; Cai et al., 2014; Fleury, 1998; Yousef et al., 2011). Sur la base des mesures RMN, il est possible de déterminer indirectement la perméabilité estimée grâce à la porosité et la distribution des tailles de pores (Westphal et al., 2005). Néanmoins, le phénomène de couplage des pores peut impacter le signal et perturber les calculs de perméabilité (Vincent et al., 2011). Dans les roches, la présence de minéraux à forte susceptibilité magnétique peut perturber le signal RMN et conduire à une sous-estimation de la taille des vides (Keating and Knight, 2012). Par exemple, la concentration et la forme minéralogique du fer modifient le comportement de relaxation RMN (Keating and Knight, 2006).

### II.2.4.9.1. Principe

La résonance magnétique nucléaire fait référence au principe physique de la réponse des noyaux à un champ magnétique. L'eau et les hydrocarbures présents dans l'espace poreux contiennent l'hydrogène qui possède un moment magnétique relativement grand. Les protons d'hydrogène se comportent comme de petits aimants, de sorte que leurs orientations peuvent être contrôlées par des champs magnétiques. Ce sont des dipôles magnétiques qui ont une orientation aléatoire en l'absence de champ magnétique externe (Figure II-25). Si l'outil d'enregistrement RMN est accordé à la fréquence de résonance magnétique de l'hydrogène, le signal est maximisé et peut être mesuré.

La première étape d'une mesure RMN est d'aligner les protons à l'aide de puissants aimants permanents. Un champ magnétique  $B_1$  est alors généré afin d'incliner l'aimantation dans une direction perpendiculaire au champ magnétique statique  $B_0$ . L'alignement ne prend que quelques secondes et a un axe parallèle à la direction  $B_0$ . Afin d'avoir une bonne efficacité  $B_1$  doit osciller à une fréquence précise.

Le champ  $B_1$  est donc activé sur une période très courte, s'arrête puis le noyau d'hydrogène essaye de retrouver son état d'équilibre, c'est-à-dire son alignement initial sur  $B_0$  grâce à des mouvements de précession.

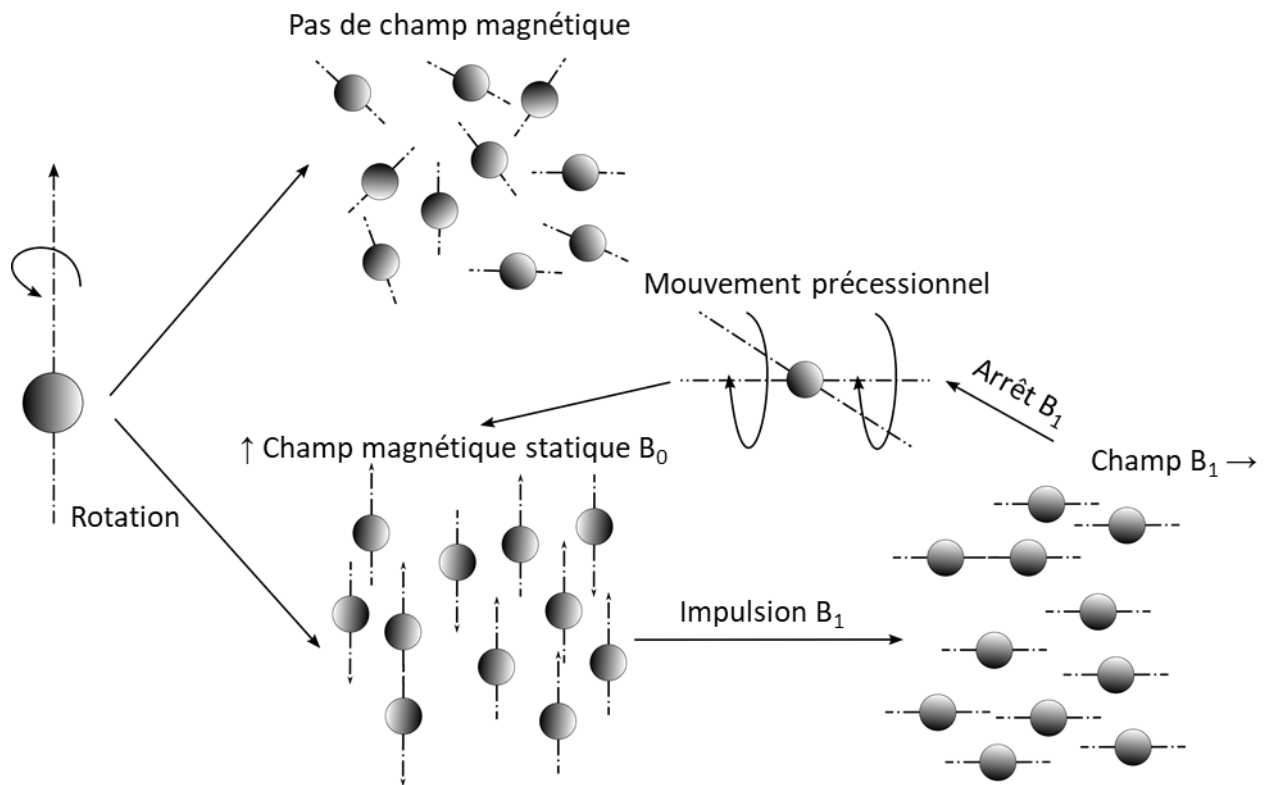


Figure II-25. Propriétés magnétiques des noyaux d'hydrogène (protons). (Modifié de Vincent et al., 2011).

#### II.2.4.9.2. Précession et déphasage

Lorsque les protons sont inclinés perpendiculairement à la direction  $B_0$ , une précession lui est exercée, agissant comme des gyroscopes dans un champ de gravitation. Dans un premier temps, la précession se fait à l'unisson. Cependant, le champ magnétique n'étant pas parfaitement homogène, la précession des protons se fait à des fréquences légèrement différentes. La synchronisation se perd petit à petit, ce qui les déphase et provoque la relaxation du signal (Figure II-25).

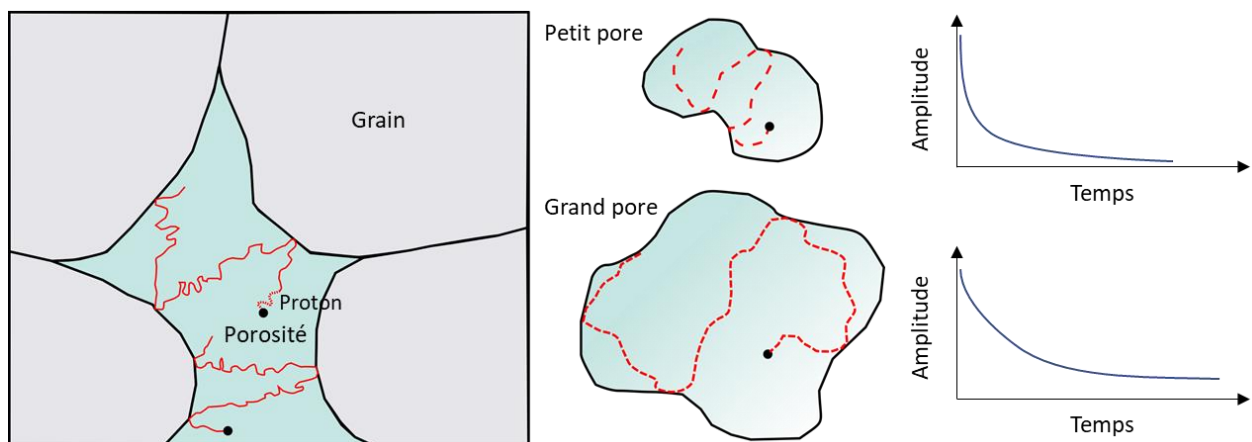
Il existe 2 types de temps de relaxation :

- $T_1$  = temps de relaxation longitudinal. C'est le temps de relaxation nécessaire pour que la composante longitudinale de l'aimantation retrouve sa valeur initiale.
- $T_2$  = temps de relaxation transverse selon un plan perpendiculaire à  $B_0$

Il a été constaté que le  $T_1$  est souvent égal à 1,5  $T_2$  mais peut varier lors de la présence d'autres fluides au sein de la roche (Kleinberg et al., 1993).

### II.2.4.9.3. Fonctionnement

Les protons qui se déplacent dans l'espace des pores, entrent en collision avec d'autres protons ou avec les surfaces de grain. A chaque collision avec la surface d'un grain une interaction de relaxation peut se produire. La relaxation de la surface du grain est le processus le plus important affectant les temps de relaxation T1 et T2. Les plus grands pores qui contiennent plus facilement des fluides, permettent des temps de relaxation plus lent (Figure II-26). En revanche, les pores de petites tailles ont une probabilité de collision avec la surface de grain plus forte et présentent des temps de relaxation plus rapide.



**Figure II-26. Schéma explicatif de la relaxation de surface en RMN. Lorsque les pores sont de petites tailles, la probabilité d'entrer en collision avec la surface des grains est forte et la relaxation est rapide. Lorsque les pores sont de grandes tailles, la probabilité d'entrer en collision avec la surface des grains est faible et la relaxation est lente.**

Ainsi, le signal RMN provenant de la répartition des temps de relaxation est une mesure de la distribution de la taille des pores. D'autres paramètres pétrophysiques peuvent être déduits du temps de relaxation comme la perméabilité ou la saturation irréductible de l'eau (Kleinberg et al., 2003; Knight et al., 2016; Ren et al., 2019).

### II.2.4.9.4. Mesure

Les mesures RMN ont été effectuées à l'aide de l'instrument Minispec série mq (Figure II-27). Le Minispec a été exploité à une fréquence de résonance de 9,95 MHz et a été maintenu à 40 °C. Toutefois, les différences de fréquence n'affectent pas significativement les mesures pour les roches carbonatées.

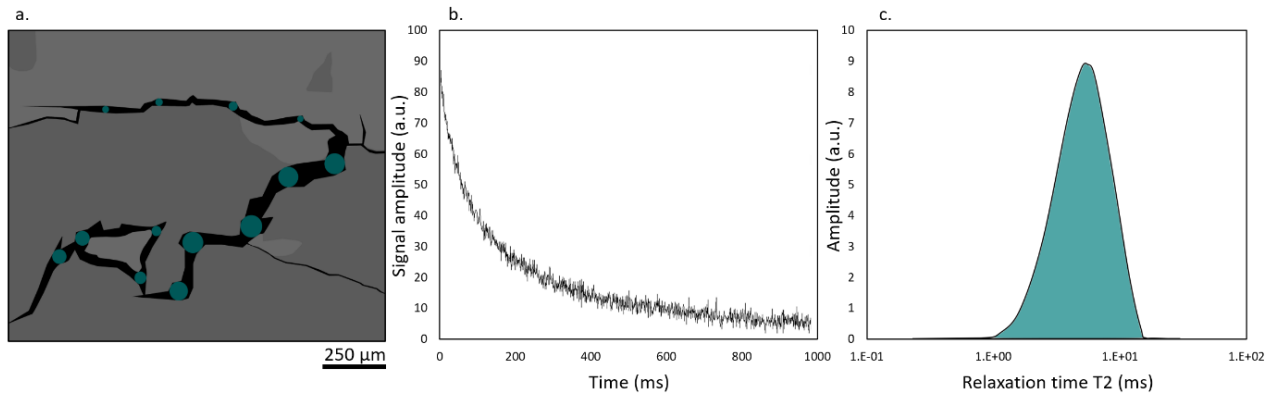
Les échantillons de roche ont été mis sous vide pendant 24h, puis immergés dans l'eau pendant 24h afin de saturer les pores. Lors de la mesure, l'échantillon a été sorti de l'eau et instantanément intégré dans un support hermétique. Cela a maintenu la saturation pendant toutes les mesures.



**Figure II-27. Appareil RMN Minispec et ordinateur de contrôle. Échantillon saturé dans un récipient en verre.**

Le temps de relaxation transverse ( $T_2$ ) est mesuré avec une séquence Carr-Purcell-Meiboom-Gill (CPMG), à intervalles de temps réguliers  $TE$  (ou  $2\tau$ ) de  $100 \mu s$ . La courbe de désintégration de la magnétisation transversale (Figure II-28b) est la somme de tous les signaux de désintégration générés par les protons dans le volume de pores. Le logiciel Dynamics Center (Version : 2.5.5) a été utilisé pour représenter la distribution des temps de relaxation (les amplitudes en fonction de  $T_2$ ) obtenue par une transformation mathématique (inverse de Laplace). La zone sous la courbe de distribution représente la porosité.





**Figure II-28. Résumé de l'utilisation de la RMN dans l'analyse des roches poreuses. a. Schéma 2D d'une fissure, les cercles bleus sont détectés par RMN. b. Courbe de décroissance de l'aimantation transversale. c. Courbe de distribution du temps de relaxation transversale (T2) construite par un processus d'inversion mathématique.**

L'effet de surface est la propriété physique qui domine la relaxation magnétique nucléaire en milieux poreux. La relation fondamentale pour un seul pore est retranscrit dans l'équation (Fleury, 1998), comme suit :

$$\frac{1}{T_2} = \frac{1}{T_{2b}} + \rho \frac{S}{V} + \frac{1}{12} (TE\gamma G)^2 D \quad (\text{II. 27})$$

Où  $T_2$  (s) représente le temps de relaxation transverse,  $\rho$  ( $\mu\text{m}\cdot\text{s}^{-1}$ ) est la relaxation de surface homogène à une vitesse (de l'ordre de  $1\text{-}30 \mu\text{m}\cdot\text{s}^{-1}$  pour les milieux poreux naturels).  $T_{2b}$  (s) représente le temps de relaxation du fluide saturant l'espace poreux (2700 ms pour l'eau à  $30^\circ\text{C}$ ),  $S$  ( $\text{m}^2$ ) est la surface et  $V$  ( $\text{m}^3$ ) le volume du pore considéré,  $TE$  (s) est le temps inter-écho de la séquence CPMG (Carr-Purcell-Meiboom-Gill) ; fixé à  $100 \mu\text{s}$ ,  $G$  ( $\text{G}\cdot\text{cm}^{-1}$ ) est le gradient de champ magnétique local moyen,  $\gamma$  ( $\text{Hz}\cdot\text{T}^{-1}$ ) est le rapport gyromagnétique et  $D$  ( $\text{m}^2\cdot\text{s}^{-1}$ ) est le coefficient de diffusion du fluide.

Le temps d'écho  $TE$  est choisi petit pour pouvoir négliger le terme de diffusion de l'équation (II. 27).

Une hypothèse sur la géométrie de nos pores doit être émise. Dans le cas monophasique, les pores sphériques ont un rapport de surface de :

$$\frac{S}{V} = \frac{3}{r} \quad (\text{II. 28})$$

Où  $r$  est le rayon des pores. En considérons que nos pores sont sphériques, l'équation peut être simplifiée comme suit :

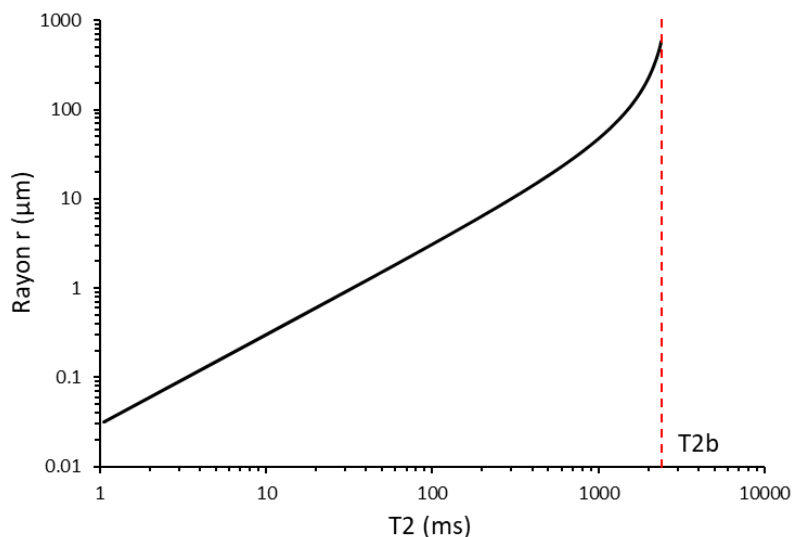
$$\frac{1}{T_2} = \frac{1}{T_{2b}} + \rho \frac{3}{r} \quad (\text{II. 29})$$

Pour les échantillons dont le réseau poreux est occupé uniquement par de l'eau, le terme  $T_{2b}$  reflète la relaxation de l'eau libre. Uniquement les interactions entre protons au sein de la phase liquide sont considérées. L'influence des effets de surface de grains, qui réduisent les temps de relaxation est exprimée par le terme  $\rho \frac{3}{r}$ . Ainsi, la distribution  $T_2$  reflète les informations sur la taille des pores, et plus la valeur  $T_2$  est petite, plus la taille des pores est petite.

### II.2.4.9.5. Étalonnage des mesures $T_2$ en rayon de pore

Afin de convertir de la distribution des  $T_2$  en distribution de taille de pores, il peut y avoir deux possibilités :

L'équation (II. 29) peut être utilisée si la relaxation de surface de la roche mesurée est connue. La limite supérieure pour la détection de grands pores est donnée par la valeur  $T_{2b}$  (Figure II-29).



**Figure II-29. Relation entre le rayon de pore ( $\mu\text{m}$ ) et le  $T_2$  mesuré avec  $\rho = 2 \mu\text{m/s}$  à partir de l'équation (II. 29).**

La conversion peut également se faire grâce à la calibration des pores mesurés en microtomographie aux rayons X (X-ray CT) avec les temps de relaxation. La X-ray CT est un

moyen fiable d'interpréter la distribution RMN. Bossennec et al. (2018) ont converti le T2 RMN en diamètre de pore équivalent en superposant la distribution des tailles de pores donnée par l'analyse de la X-ray CT avec la distribution des T2. Également, Kruschwitz et al. (2020) transfèrent la distribution T2 à la taille des pores après étalonnage avec la X-ray CT. Yixin Zhao et al. (2017) proposent une méthode pour déterminer la relaxation de surface en ajustant les distributions cumulatives du volume des pores en fonction de la taille des pores, déterminée par RMN et X-ray CT. Le premier pic, représentant les temps de relaxation les plus longs, reflète les plus grands pores observés par X-ray CT.

### II.2.4.10. Analyse chimique

#### II.2.4.10.1. Fluorescence X (XRF)

L'analyse chimique a été réalisée sur des échantillons de granite mis en poudre (fraction fine <2  $\mu\text{m}$ ) à l'aide d'un spectromètre séquentiel à rayons X (appareil Philips Magix Pro), qui a fourni des informations sur les éléments majeurs et traces.

#### II.2.4.10.2. Spectrométrie de masse à plasma à couplage inductif (ICP)

La réactivité géochimique de l'interaction eau-craie ou eau-granite a été réalisée en analysant l'eau résultante / lixiviée après les tests thermiques. De l'acide nitrique ( $\text{HNO}_3$ ) a été ajouté avant l'analyse pour stabiliser les solutions.

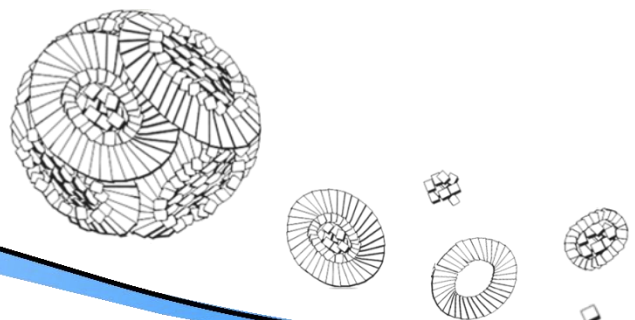
Pour la craie, les teneurs en Ca dissous ont été déterminées par spectrométrie d'émission atomique plasma à couplage inductif (ICP-AES, Iris Advantage, Thermo Fisher Scientific).

Pour le granite, les teneurs en Al, Ca, Fe, Mg, Mn, Na, K et Ti dissous ont été déterminées en utilisant la spectrométrie de masse à plasma à couplage inductif (ICP) (VG PQ-ExCell, THERMO ELEMENTAL).





# **III. CHAPITRE : Caractérisation et comportement de la craie de Châlons face à des sollicitations thermiques et hydriques**



**Résumé étendu et conclusions principales de l'articles #1 « Caractérisation de la microstructure de la craie de Châlons et relation statistique entre ses paramètres pétrophysiques » et de l'article #2 « Comportement de la craie sous la circulation de fluides à températures contrastées ».**

En plus d'être une roche réservoir importante, **la craie** en elle-même est un matériau granulaire fascinant avec un réseau poreux complexe. Elle se présente sous la forme d'un matériau nano- microporeux à texture désordonnée généralement caractérisé par une porosité totale élevée (> 40%) (Faÿ-Gomord et al., 2016; Nadah et al., 2009; Risnes et al., 2005). Sa microstructure est formée d'une matrice solide composée principalement de fragments aléatoirement enchevêtrés. En général, la roche est composée presque exclusivement de carbonate de calcium, organisé principalement sous forme de cristaux de calcite, avec des diamètres allant de 0,17 à 2,8  $\mu\text{m}$  et des restes squelettiques de *Coccolithophoridae*, coccolithe, avec des diamètres allant de 1 à 20  $\mu\text{m}$  (Betson et al., 2004). D'autres restes biogéniques peuvent être inclus dans la roche comme des foraminifères ou des coquilles bivalves, mais restent en petites quantités.

La compréhension des caractéristiques du **réseau poreux** de la craie est importante à prendre en compte pour un large éventail de domaines scientifiques. Bien que sa composition chimique et les propriétés physiques de ses constituants jouent un rôle important dans le contrôle des voies d'écoulement et des propriétés mécaniques, la compréhension de la géométrie de l'espace poreux reste le paramètre de contrôle essentiel (Le Roux, 1973).

La variabilité de la porosité de la craie peut être due à la variation de sa granulométrie, de sa texture, de l'importance des traces de fossiles et de sa teneur en argile et en silice (Frykman, 2001). En revanche, la perméabilité de la craie est très faible en raison de son caractère microporeux. Les propriétés physiques des corps microporeux et peu perméables comme la craie sont complexes. Par exemple, la craie de la mer du Nord présente une large variabilité faciologique (Fabricius, 2003; Fabricius and Borre, 2007; Gommesen et al., 2007; Japsen et al., 2004; Røgen et al., 2005; Schroeder, 2002). Il est nécessaire de caractériser précisément sa microstructure pour un développement efficace et rentable de l'énergie géothermique, du stockage des déchets radioactifs ou une avancée dans la compréhension des mécanismes régissant l'affaiblissement de la craie par l'eau.

Pour comprendre les réservoirs de carbonate comme la craie, il faut une étude pétrographique multi-échelles et une caractérisation pétrophysique fine (Regnet et al., 2015). La combinaison et la comparaison entre les méthodes de mesure sont nécessaires dans l'interprétation des résultats. L'objectif de **l'article #1 : « Caractérisation de la microstructure de la craie de Châlons et relation statistique entre ses paramètres pétrophysiques »**, est de décrire qualitativement et quantitativement les propriétés du réseau poreux de la craie de Châlons avec une résolution micrométrique. La craie étudiée provient des carrières du Grand Mont (Saint-Germain-la-Ville, France).

Cette étude est basée sur un **large éventail de techniques** (porosité de l'eau, porosité par injection de mercure, tests d'imbibition d'eau par capillarité, perméabilité, vitesses de propagation des ondes P et S, microscope électronique à balayage). De plus, les progrès considérables réalisés dans l'imagerie 3D non-destructive et haute résolution (microtomographie aux rayons X, résonance magnétique nucléaire) ont permis de déterminer rapidement la géométrie des pores. La microtomographie à rayons X à haute résolution a été utilisée pour calibrer le signal mesuré par résonance magnétique nucléaire et les observations ont été confirmés par microscopie électronique à balayage.

La craie est caractérisée par une porosité élevée (environ 40%) et une faible perméabilité (environ 5 mD), une faible taille d'accès des pores ( $<0,3 \mu\text{m}$ ), une taille de pores interparticulaires comprise entre 1 et  $20 \mu\text{m}$  et des macropores minoritaires avec peu de connexion. Ainsi, la combinaison et la comparaison des paramètres ont montré que si les mesures d'injection de mercure suggèrent que toute la craie est nanoporeuse ( $< 1 \mu\text{m}$ ), les mesures d'autres paramètres pétrophysiques montrent une porosité microporeuse (entre 1 et  $15 \mu\text{m}$ ) et macroporeuse ( $> 15 \mu\text{m}$ ).

Les résultats de cette caractérisation fine du réseau poreux de la craie de Châlons ont été utilisés pour étudier le comportement de la craie soumise à un écoulement de fluides sous contraintes thermiques. Cela a fait l'objet d'un **second article #2 : « Comportement de la craie sous la circulation de fluides à températures contrastées »**.

Le comportement des roches soumises à un écoulement de fluides peut être influencé par la nature de la contrainte appliquée, la structure de la roche et la nature du fluide injecté. Les **interactions craie-fluide** ont fait l'objet d'une grande attention dans les communautés



scientifiques (Gutierrez et al., 2000; Nermoen et al., 2016; Nguyen, 2009; Risnes et al., 2005). L'effet sur les interactions craie-eau n'est cependant pas clair. Et en raison de la durée des différents phénomènes physicochimiques qui influencent le comportement de la craie, il est difficile de tirer des conclusions sur les effets de la température grâce à des tests de compression triaxiaux ou uniaxiaux standard assez rapides effectués dans de nombreuses études. Les variations du comportement thermique de la craie pourraient être dues aux différentes températures entre la roche et le fluide saturant.

Dans cet **article #2**, des expériences de circulation de fluides à températures contrastées (roche froide-eau chaude / roche chaude-eau froide) ont été menées afin de caractériser la **variation microtexturale** de la craie, composant majeur de la croûte supérieure de Champagne-Ardenne. Un ensemble de 130 échantillons a été testé dans 4 dispositifs (Figure III-1) afin de produire une circulation de fluides:

- i) 150 cycles d'imbibition d'eau par capillarité ont été réalisés sur des craies chauffées à 80 °C, à température ambiante ou à 8 °C, avec de l'eau à 80 °C, à température ambiante ou à 8 °C.
- ii) 150 cycles d'endommagement par choc thermique ont été obtenus par trempe des échantillons à 80 °C dans une eau à 0 °C.
- iii) un transfert continu d'eau (10 L) à 80 °C ou à température ambiante a été réalisé au moyen d'un dispositif utilisant l'appel d'air exercé par des dessiccateurs placés sous vide.
- iv) 10 L d'eau ont été mis en circulation dans des échantillons témoins (sans contrainte thermique) grâce à la conception d'un perméamètre à charge constante.

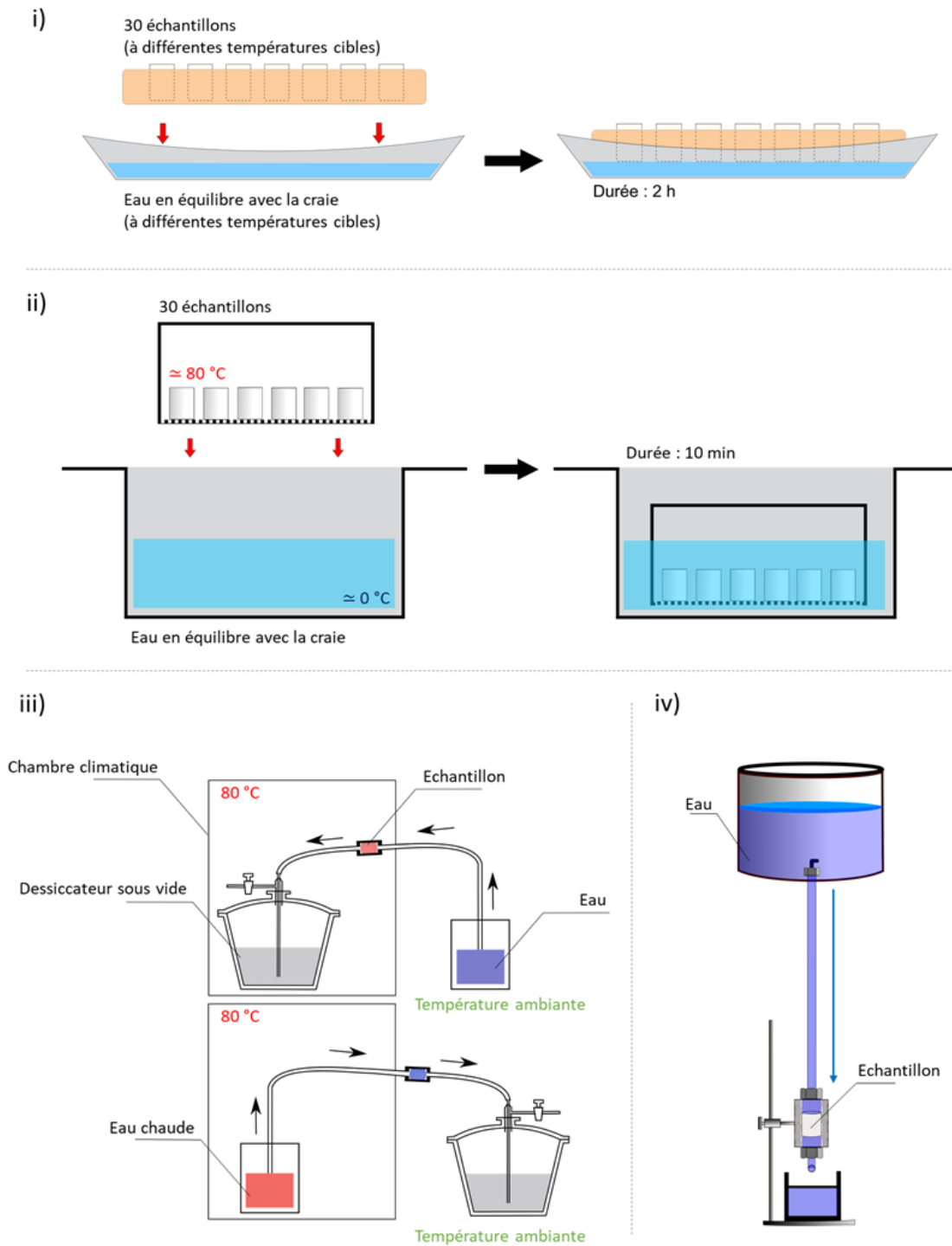


Figure III-1. Schéma des 4 dispositifs réalisés pour simuler des cycles de circulation de fluides à températures contrastées.

L'évolution du réseau poreux a été quantifiée à l'échelle des grains après chaque expérience.

L'évolution des propriétés du réseau poreux a été analysée par imbibition capillaire,

porosimétrie par injection de mercure, résonance magnétique nucléaire, auscultation ultrasonique et microtomographie aux rayons X.

Le fluide utilisé dans cette thèse était de l'eau en équilibre chimique avec les constituants de la craie (en grande partie  $\text{CaCO}_3$ ). Par conséquent, les échantillons n'ont pas été affectés par les **phénomènes de dissolution** lors du passage du fluide d'injection. Cette variable n'a donc pas été prise en compte dans notre interprétation.

De nombreux chercheurs proposent les forces de capillarité et les effets de saturation comme le principal **mécanisme physique de l'affaiblissement de la craie par l'eau**. C'est de la tension entre l'interface solide-fluide que surviennent les forces de capillarité. La force de capillarité est inversement proportionnelle à la taille des pores. Après saturation, l'eau dans les petits pores forment des ménisques de capillarité qui lient les grains ensemble avec une pression de contact. La cohésion créée par cette pression **n'a pas suffi pour détruire les liens de capillarité** entre les grains pour nos expériences. En effet, il n'y a pas eu de différence nette entre les valeurs des perméabilités lors des cycles d'injection de fluide à températures contrastées. La **structure punctique, la grande porosité et les macropores** présents dans la craie ont permis de réduire l'endommagement. Les pores ont pu se réorganiser sous l'effet des faibles contraintes induites par la circulation de l'eau évitant la création de fissures.

Les tests de circulation de fluides (par imbibition capillaire et en continu) ont montré que les phénomènes d'affaiblissement par l'eau ne **sont pas irréversibles** et les essais à températures contrastées n'ont pas affecté de façon significative le réseau poreux pour induire des dommages internes. Il a été montré que la **circulation d'une eau froide dans une craie préchauffé à 80 °C** induit une réduction de la connectivité hydrique. Cette réduction a été interprétée comme étant due à la recristallisation des ions  $\text{Ca}^{2+}$  et  $\text{CO}_3^{2-}$  saturant le fluide lors des phases de chauffage cyclique. En revanche, la recristallisation n'entraîne pas nécessairement une réduction du volume des pores (Maliva and Dickson, 1992), comme l'ont indiqué nos valeurs de porosité. Si les cycles de la circulation n'affectent que très peu le réseau poreux de la craie, ce sont les **conditions expérimentales** (cycle de chauffage après expérience) qui influencent le comportement de la craie. En effet, à la fin de chaque cycle, la craie était séchée et chauffée à 80 °C avant d'effectuer un nouveau cycle. Pendant ce séchage / chauffage au four, les ions dissous (du fluide d'équilibre) dans les pores ont pu précipiter à des températures plus élevées en raison de l'évaporation du volume d'eau. Lors de l'exécution

d'un nouveau cycle, l'écoulement de l'eau froide serait ralenti. Cela pourrait expliquer pourquoi l'augmentation du nombre de cycles peut entraîner une diminution de la connectivité hydrique progressive. Pour les expériences avec une circulation continue, la circulation de fluides a été encore plus réduite. Le flux continu de liquide augmente la probabilité qu'un grain se détache de son emplacement et pénètre dans un pore, redistribuant ainsi l'espace poreux.

Il a été également montré que la taille des pores était inférieure à celle des essais de **circulation d'eau chaude dans une roche froide**. Les conséquences de la fermeture de l'espace poreux avec l'augmentation de la température ne sont pas encore entièrement définies. **L'expansion thermique** à l'échelle des pores pourrait être responsable de la fermeture des pores (Katende et al., 2020). Le chauffage à 80 °C serait alors suffisant pour provoquer une expansion thermique des grains de calcite et fermerai les pores.

Toutes les expériences ont abouti à la conclusion que les effets des transferts cycliques d'eau jouent un rôle très mineur dans les variations du volume des pores. L'expansion thermique anisotropique de la calcite est le principal mécanisme de variation des paramètres pétrophysiques mesurées dans cette étude lorsque la craie est exposée aux cycles thermiques. En résumé, il a été démontré que ni les cycles de circulation par imbibition capillaires, ni le transfert continu à basse température (80 °C) n'induisent d'effets affaiblissants la craie de Châlons.



### **III.1. Article#1 : Characterization of the microstructure of the Châlons chalk and statistical relationship between its petrophysical parameters.**

Cet article sera soumis, à la revue de rang A, *Engineering Geology*.

Junique<sup>1</sup>, T., Géraud<sup>2</sup>, Y., Vazquez<sup>1</sup>, P., & Thomachot-Schneider<sup>1</sup>, C. (2021). Characterization of the microstructure of the Châlons chalk and statistical relationship between its petrophysical parameters. *Engineering Geology*.

<sup>1</sup>GEGENAA EA 3795, University of Reims Champagne-Ardenne, 2, esplanade Roland Garros, 51100 Reims, France

<sup>2</sup>GeoRessources Laboratory UMR 7359, University of Lorraine, F54505 Vandoeuvre les Nancy

### III.1.1. INTRODUCTION

The chalk is a microporous stone with a disordered texture composed mainly by fragments of coccolithophorids, randomly entangled. The texture of the chalk plays an important role in its properties (Le Roux, 1973). The microstructure and porosity control the fluid flow paths and determine the mechanical strength of the chalk.

Due to its high porosity, chalk is an interesting reservoir. Moreover, the geothermal potential is developing in Europe, in the north of Belgium (Berckmans and Vandenberghe, 1998; Loveless et al., 2014), in the south-east of England (Headon et al., 2009; Law, 2010) in Danish subsoil (Poulsen et al., 2017; Weibel et al., 2020), in Republic of Srpska (Duric, 2013) or in France with the Champagne-Ardenne area (France) (Chabart et al., 2012; Maget and Rambaud, 1980).

The interactions chalk-fluid have been the subject of great attention in the scientific communities (Gutierrez et al., 2000; Nermoen et al., 2016; Nguyen, 2009; Risnes et al., 2005) due to the seabed subsidence phenomena detected in the 1980s in the North Sea oil deposits (Addis, 1987; Johnson et al., 1988) causing a rapid decline in the production (Simon et al., 1982). These modifications can occur during the water injection, aimed at improving the reservoir's profitability up to the "pore collapse" (Blanton, 1981; Keszthelyi et al., 2016). This mechanism is known as "water weakening effect" and induces a significant drop in the mechanical resistance (Madland, 2005). Several factors can be at the origin of this modification. Chemical dissolution would be responsible for the sensitivity of chalk to water (Heggheim et al., 2005; Heugas and Charlez, 1990; Nermoen et al., 2015), causing a reduction in the elasticity strength and an increase in the compressibility and induce mechanical failures (Hellmann et al., 2002b; Newman, 1983; Sylte et al., 1999). However, these solution-pressure phenomena, taken into account in long-term creep tests, are not compatible with the rapid weakening of chalk (Schroeder et al., 1998). Dissolution of calcium carbonate in weakened chalk has been questioned by Rhett (1990) due to the different stress responses of water-saturated and hydrocarbon-saturated chalk. In addition, due to the small amount of dissolved chalk and its large specific surface area, weakening is most often attributed to pure physical interactions between grains (Andersen, 1992; Rhett, 1990). The mechanical stability of chalk has often been linked to the existence of forces of physical origin. Capillary forces are important in chalk to induce cohesion between particles (Delage et al., 1996). Nadah (2010)

describes the phenomenon of “water weakening effect” as instantaneous and reversible. They show that the compressive strength of chalk drops after being saturated with a few percent of water. During a water flood, the meniscus of water, still present in dry chalk (Lord et al., 1998), disappears and weakens the rock. The action of water can break the contacts between the grains by absorption thanks to the so-called Rhebinder effect which depends on the free energy surface (Rehbinder and Lichtman, 1957; Risnes et al., 2005). The adsorption pressure model described by Risnes et al. (2003) is a complex physicochemical mechanism in which the chalk grains are degraded by the attraction of water molecules.

For an effective development of the geothermal energy and an advance in understanding the mechanisms governing the weakening of chalk by water, it is first necessary to precisely characterize the chalk microstructure. Understanding carbonate reservoirs such as chalk requires a multiscale petrographic study and petrophysical characterization (Regnet et al., 2015). Previous studies have shown that the physical properties and microporous features of chalk are complex with wide facies variability. The North Sea chalk has been the most studied one (Fabricius, 2003; Fabricius and Borre, 2007; Gommesen et al., 2007; Japsen et al., 2004; Røgen et al., 2005; Schroeder, 2002). Studies on chalks are often carried out at a small scale (Andreassen, 2011; Faÿ-Gomord et al., 2017; Hellmann et al., 2002b) sometimes by scanning electron microscopy (SEM) and image analysis (Hjuler and Fabricius, 2009; Meyer et al., 2019; Nadah et al., 2013). The chalk is generally characterized by a high total porosity (> 40%) (Faÿ-Gomord et al., 2016; Nadah et al., 2009; Risnes et al., 2005). The variability of this porosity may be due to the variation in particle size, texture, traces of fossils, or the content of clay and silica (Frykman, 2001). For example, the microporosity of chalk from the Omeÿ region (France), concerns pores having a dominant pore access diameter of 0.7  $\mu\text{m}$  (Richard et al., 1997), given by the morphology and size of the micrite particles and the arrangement of detrital and biogenic minerals. The Tuffeau chalk (Paris basin, France) has a macroporous domain between the access radii of 1 to 8  $\mu\text{m}$ , microporous between 0.025 to 1  $\mu\text{m}$ , and infraporous between 0.001 to 0.025  $\mu\text{m}$  (Dessandier et al., 1997). Despite high porosity, the chalk exhibits a low permeability which can range from about 1 mD to 10 mD (Andreassen and Fabricius, 2010; Robert, 2004). These values vary according to the different lithologies of the chalk due to its microporous character.

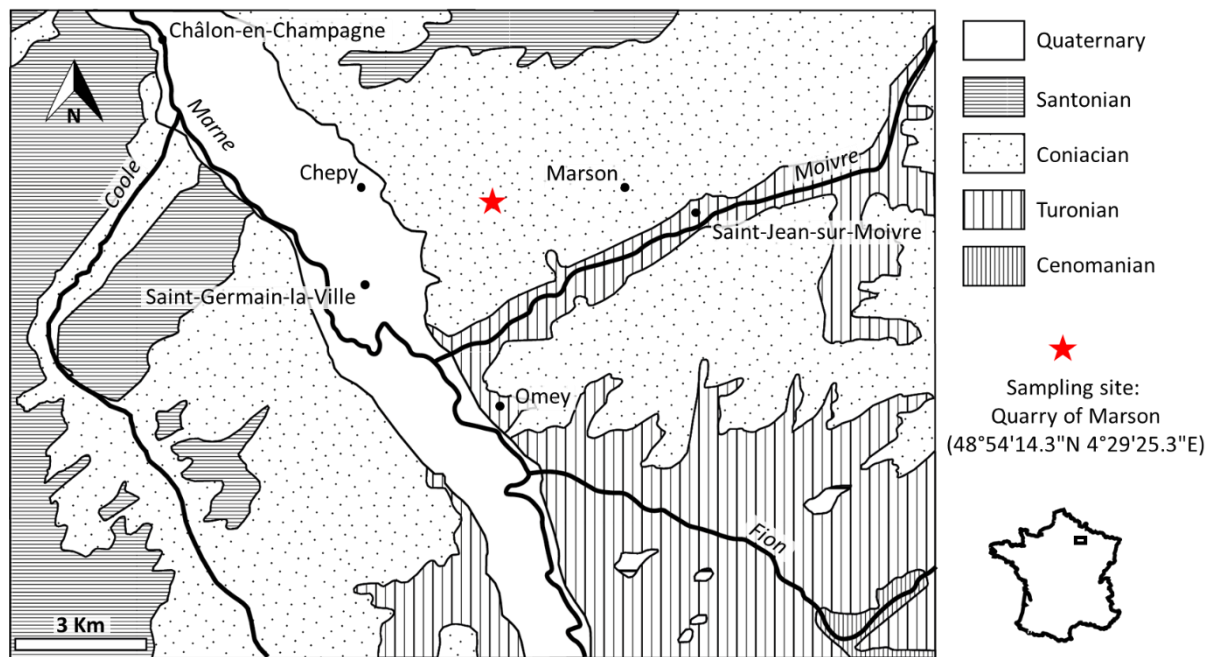


Understanding the porous structure is possible in the laboratory thanks to the combination of different analysis tools (water porosity, propagation velocities of P and S-waves, capillary water uptake tests (CWUT), porosity by mercury injection (MIP), nuclear magnetic resonance (NMR), imagery and X-ray tomography (X-ray CT). The Scanning Electron Microscope (SEM) is used to determine the grain morphology, size, and arrangement (Richard, 2008, 2014; Saïag, 2016; Schroeder, 2002). The non-destructive NMR method provides an overview of the pore structures and fluid phase distributions in porous chalk media (Faÿ-Gomord et al., 2016; Li et al., 2014; Liaw et al., 1996; Megawati et al., 2012). The interpretation of NMR data associated with MIP and X-ray CT observations provides detailed information regarding the petrographic and petrophysical characteristics (Bossennec et al., 2018).

The objective of this study is to characterize in detail the structure of the Châlons chalk and to establish the main relationships between its properties and the porous network, in order to predict its behaviour during water transfer. For that purpose, a model of the rock porous network was developed, integrating MIP, NMR and X-ray CT measurements. Cross-use of these three devices was complementary in identifying pore size distribution. The acquisition of the SEM images allowed to confirm the data obtained from the model. The petrophysical properties measured on the samples were correlated with each other, in order to understand the global relationships that existed between these parameters.

### **III.1.2. MATERIAL**

The white chalk of Châlons samples were extracted from the Grand Mont quarry (Saint-Germain-la-Ville, Paris Basin, France) (Figure III-2) along an outcrop dated from the Coniacian (Upper Cretaceous).



**Figure III-2. Geological and geographical settings of the chalk sampling site (red star). Modified from Richard et al. (1997).**

The selected chalk was quarried from an area with a very slight tectonic deformation, mainly during tertiary (Coulon and Lamotte, 1988; Richard, 1996; Richard et al., 1997) and presented a homogeneous appearance. This white rock is relatively tender and contains *Micraster* echinoids (Allouc and Le Roux, 1995). From a mineralogical point of view, the Châlons chalk consists almost exclusively of calcium carbonate (98.5% de  $\text{CaCO}_3$ ) (Ballif et al., 1995). The nanofacies observed with SEM reveals an accumulation of well-preserved coccoliths (Allouc and Le Roux, 1995), with a regular outline that were arranged without a privileged orientation and that defined a punctic structure (Richard et al., 1997).

### III.1.3. METHODOLOGY

#### III.1.3.1. Pore classification

The study of porosity consists of examining the size of the pores and throats giving access to them. This review requires clarifying the terminology of the pore size. The International Union of Pure and Applied Chemistry (IUPAC) defines the macropores as the pores greater than 50 nm, the mesopores as the pores between 2 and 50 nm, and the micropores as the pores less than 2 nm (Sing, 1985). This classification is independent of the choice of the porous material, the type of pores, or where the pore is actually located. In geosciences, many authors have chosen different limits between macropores and micropores. This separation depends on the

observer and the study methods. For example, Bousquié et al. (1979) proposed a pore diameter limit between macropores and micropores of 10  $\mu\text{m}$  by observation under an optical microscope and 2  $\mu\text{m}$  by porosimetry by injection of mercury. Robert (2004), Fronteau (2000) also chose 15  $\mu\text{m}$  as the limiting diameter between macroporosity and microporosity defined thank to the diameters of the pores accessible by mercury porosimetry under atmospheric pressure. We have adopted this same classification. Moreover, this limit corresponds to the resolution of X-ray CT (16  $\mu\text{m}$ ), that is, all the pores observed with this technique are considered as macropores. The nanoporosity was defined to be less than 1  $\mu\text{m}$  in diameter, which corresponds to the maximum access size of the majority family measured at the MIP for the chalk studied.

### III.1.3.2. Samples preparation

Complementary techniques have been used to characterize the complete porous structure of Châlons chalk. This study was carried out on cylinders of 1.6 cm in diameter and 2 cm in height, except the samples used in the nitrogen permeameter which were cylinders 3 cm in diameter and 4 cm high, sampled in a single specific layer of the quarry and with the height perpendicular to the bedding. The number of samples (Tableau III-1) was chosen according to the technique in order to have a stable mean and minimum standard deviation. The samples were dried at  $40 \pm 5$  °C before each test until their masses stabilized, except for NMR measurements which required saturated samples. The operations were carried out at a controlled temperature of 25 °C.

### III.1.3.3. Porosity measurement

Porosity was determined by different methods:

The *total porosity*  $\varphi_T$  was calculated thanks to the relation (III. 1) between the bulk and the grain densities ( $\rho_b$  and  $\rho_g$ , respectively):

$$\varphi_T = \frac{\left(\frac{1}{\rho_b} - \frac{1}{\rho_g}\right)}{\frac{1}{\rho_b}} \quad (\text{III. 1})$$

The *bulk density* was determined by direct measurement of the dimensions of 406 dry samples. A helium pycnometer (AccuPyc II 1340 Pycnometer) was used to obtain the grain density (Lin et al., 2015). The mineralogical composition of chalk consists mainly of a single

mineral (calcium carbonate), in this case, the *grain density* of the rock is equal to the mineral density. Therefore, this value changed very little from one sample to another with a standard deviation of  $0.004 \text{ g}\cdot\text{cm}^{-3}$ . The value of  $\rho_g$  in equation (III. 1) was fixed and represented the average of the measurements carried out.

The mass of the saturated samples was obtained by following standard NF EN 1936, (2007). The samples were placed in a desiccator where the pressure was gradually lowered to  $2.0 \pm 0.7 \text{ kPa}$  using a vacuum pump. The vacuum was maintained for 1 hour in order to remove all the air contained in the pores. In a second desiccator, water was degassed for 2 hours. The two desiccators were connected in order to gradually introduce the degassed distilled water into the desiccator containing the samples. The water was soaked from the base of the sample. The pressure was maintained at  $(2.0 \pm 0.7) \text{ kPa}$  during the imbibition. The climb speed was set in such a way that the sample cover did not exceed 15 min. Once the samples were completely submerged, the vacuum was broken and atmospheric pressure was restored. The samples were left underwater for 24 hours and were weighed. The free porosity ( $\varphi_f$ ) was calculated using equation (III. 2) which does not use hydrostatic weighing but only double weighing and grain density. The measurement principle was equivalent to the triple weighing one.

$$\varphi_f = \frac{ms - me}{ms - me \left(1 - \frac{\rho_w}{\rho_g}\right)} \quad (\text{III. 2})$$

with,  $me$  = mass of the dry sample,  $ms$  = mass of the saturated sample,  $\rho_w$  = density of water,  $\rho_g$  = grain density.

*Porosity*  $\varphi_{\text{MIP}}$  and pore radii access distribution was determined by MIP thanks to a micromeritics AutoPore IV 950. The mercury intrusion is performed in two stages (low- and high-pressure measurements). Mercury injection pressures ranged from 0.004 to 228 MPa, giving corresponding pore access radii of 180 to  $0.003 \mu\text{m}$ , respectively. Equilibrium time settings were 30 s for low- and high-pressure steps.

### III.1.3.4. Capillary water uptake tests (CWUT)

The non-destructive test allows determining the connectivity and the homogeneity of the porous network. The capillarity on a natural stone is an intrinsic property and represents its capacity to absorb water under the effect of capillary forces. The capillary coefficient ( $C$ ) was

calculated based on standard NF EN 1925, (1999). The temperature of the room was kept at  $23 \pm 1$  °C. The principle of the experiment was to put a bit of previously dried chalk in contact with a light film of distilled water to reach the chemical equilibrium and avoid acid dissolution (a few millimeters). Thus, the non-wetting fluid (air), initially in the pores, is replaced by the wetting fluid (distilled water) without external pressure applied. Two phases emerged (Hammecker et al., 1993; Hammecker and Jeannette, 1994). The first phase consists of the progressive filling by the capillary force of the water in the free porosity. The second phase begins after the slope has broken and is characterized by the diffusion and dissolution of air in the water. The slope of the curve of the first phase represents the capillary coefficient (C) (Roels et al., 2000). It represents the volume of water that penetrate by capillary action in the rock per unit of time ( $\text{g}\cdot\text{m}^{-2}\cdot\text{s}^{-1/2}$ ).

Washburn, (1921) and Lucas, (1918) propose a simple model, based on the Hagen-Poiseuille and Laplace equations in laminar flow, describe the phenomenon of imbibition in a porous medium. This law represents a set of small parallel cylindrical tubes of the same radius and whose imbibition height and mass as a function of time follow the relation of  $t^{1/2}$ . However, it should be noted that the Lucas-Washburn law does not take into account parameters such as the geometric shape of the pores, the gravity, or the tortuosity of the capillary and fractal dimensions of the porous media. Benavente et al. (2002) and Cai and Yu, (2011) improved this law to take into account the geometry of non-cylindrical capillaries and tortuosity. The capillary radius is replaced by an effective capillary radius which defines the hydraulic conductance and the topology of the water uptake. The improvement of the Washburn equation leads Benavente et al. (2002) to equation (III. 3):

$$C = \varphi \rho \sqrt{\frac{r_{eff} \delta \gamma \cos \theta}{2 \tau \eta}} \quad (\text{III. 3})$$

With  $\varphi$  the porosity,  $\rho$  the density of the fluid ( $998 \text{ kg}\cdot\text{m}^{-3}$  for water at 20 °C),  $\delta$  the pore shape factor (between 1 and 0. If  $\delta = 1$ , the cross section of the pore is a perfect circle),  $\gamma$  the interfacial tension ( $0.0728 \text{ N}\cdot\text{m}^{-1}$  for water at 20 °C),  $\theta$  the contact angle (in general to be considered zero),  $\tau$  the tortuosity,  $\eta$  the viscosity of the fluid ( $1.003 \times 10^{-3} \text{ Pa}\cdot\text{s} = \text{kg}\cdot\text{m}^{-1}\cdot\text{s}^{-1}$  for water at 20 °C).

### III.1.3.5. Permeability (k coefficient)

The permeability measurements were carried out on 4 cylindrical samples of 3 cm in diameter and 4 cm in height. The measurement was made using a nitrogen permeameter (N<sub>2</sub> k). This non-destructive technique was mainly composed of a Hassler cell into which the sample has been introduced coated with a tight and flexible sleeve. A confining pressure of 1.5 MPa was applied laterally on the sealing sleeve to prevent flows along the edges of the sample. At least 4 head pressure steps were measured per sample. The measured permeabilities were corrected for the Klinkenberg effect (Klinkenberg, 1941). The results were estimated in millidarcy (mD) which is equivalent to 10<sup>-15</sup> m<sup>2</sup>.

### III.1.3.6. Elastic rock properties and deduced mechanical properties

P and S wave propagation velocities measurements ( $V_p$  and  $V_s$ ) were carried out with a PunditLab Proceeq tester and 250 kHz transducers. The Young's dynamic modulus ( $E$ ) and the Poisson's ratio ( $\nu$ ) were calculated following the equations (III. 4 and III. 5):

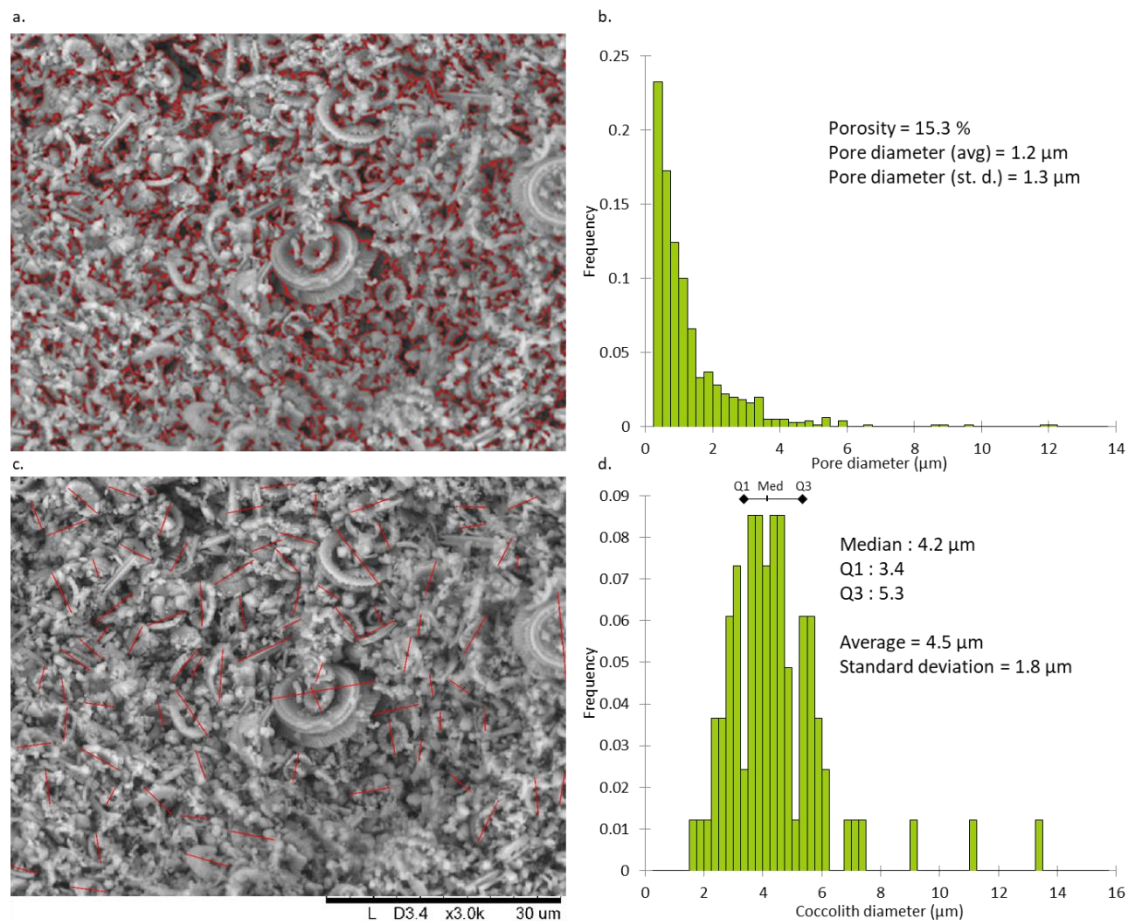
$$\nu = \frac{\frac{1}{2} - \left(\frac{V_s}{V_p}\right)^2}{1 - \left(\frac{V_s}{V_p}\right)^2} \quad (\text{III. 4})$$

$$E = \rho g \frac{V_p^2(1 + \nu)(1 - 2\nu)}{1 - \nu} \quad (\text{III. 5})$$

### III.1.3.7. Scanning electron microscope (SEM)

The observation of the structure of the chalk matrix requires the use of optical tools suitable for studying very small particles, so that a scanning electron microscope (SEM) was preferred. The samples were observed on a Hitachi TM1000 SEM. The depth of field offered by SEM allowed to better quantify the size of the microporosities and the shape of the particles. The digital image analysis allows determining porosity, pore morphology, and grain size distribution (Røgen et al., 2001). The quantification of the coccolith and pore sizes was carried out using the JMicroVision software developed by Roduit, (2007), (Figure III-3). The greyscale thresholding method enables to select of the porosity on 10 SEM images. The darker areas between the grains corresponding to microporosity. The maximum elongation of the coccoliths was measured at various magnifications (x3000, x4000, x5000). Particles masked by others or not parallel to the plane of the SEM image were not taken into account. The median

and quartiles Q1 (25%) and Q3 (75%) were used to characterize the size distribution of the coccoliths. To have a representative sampling, between 400 and 900 pores were selected and between 25 and 100 coccoliths were measured for each of the images, which represent approximately 6000 pores and 500 particles measured for this study.



**Figure III-3. Method for measuring the size of pores and coccoliths using the J.Microvision software. a. Example of porosity thresholding (selected in red). b. Distribution curve of the pore length (distribution interval: 0.25 μm) of the example image (a). c. Example of measuring the maximum length of coccoliths (red line). d. Distribution curve of the length of the coccoliths (distribution interval: 0.25 μm) of the example image (c).**

### III.1.3.8. Nuclear Magnetic Resonance (NMR) relaxometry

The NMR measurements were carried out using the Minispec mq-Series instrument. The rock samples were vacuumed and saturated for 24 h and were then soaked in water for 24 h in order to fill the rock material with water. During the measurement, the sample is taken out of the water and instantly integrated into the airtight support before being placed in the NMR,

so that the rock sample is kept saturated during the NMR measurements. NMR is based on the decay by magnetization of the hydrogen nucleus of water. A more detailed description of the method is found in Dunn et al. (2002). The transverse relaxation time (T2) was measured with a Carr-Purcell-Meiboom-Gill (CPMG) sequence. Dynamics Center software (Version: 2.5.5) was used to represent the distribution of T2 relaxation times (the amplitudes  $A_i$  as a function of  $T2_i$ ) obtained thanks to an inverse of Laplace transformation. These are the surface effects and the physical properties that are used in nuclear magnetic relaxation in porous media. Each T2 is linked to the porous space of the sample, in particular the ratio surface / volume (S/V). This link is transcribed in equation (III. 6):

$$\frac{1}{T2} = \frac{1}{T2b} + \rho \frac{S}{V} + \frac{1}{12} (TE\gamma G)^2 D \quad (\text{III. 6})$$

Where T2 represents the transverse relaxation time,  $\rho$  is the specific surface relaxivity (of the order of 1-30  $\mu\text{m}\cdot\text{s}^{-1}$  for natural porous media). T2b represents the relaxation time of the fluid saturating the porous space (2700 ms for water at 30 °C), S is the surface and V the volume of the pore considered, TE is the inter-echo time of the CPMG sequence; we set it at 100  $\mu\text{s}$ , G is the average local magnetic field gradient,  $\gamma$  is the gyromagnetic ratio and D is the auto-diffusion coefficient of the fluid. The term of diffusion can be neglected in equation (III. 6) because T2 is independent of the inter-echo time (very weak in this experiment).

The pore size distribution was calculated by making certain assumptions about the geometry (Fleury, 1998). In the monophasic case, the spherical pores result in:

$$\frac{S}{V} = \frac{3}{r} \quad (\text{III. 7})$$

With r, the pore radius considering spherical pores. The simplified equation (III. 8), is as follows:

$$\frac{1}{T2} = \frac{1}{T2b} + \rho \frac{3}{r} \quad (\text{III. 8})$$

### III.1.3.9. X-ray microtomography (X-ray CT)

X-ray CT is a non-destructive technique that allows visualizing the porous network at high resolution. It enables the internal structure of an object to be reconstituted in three dimensions (3D) from several radiographic images (slices) in two dimensions (2D). These slices



are reconstructed by calculation using the measurements of the X-rays attenuation passing through the sample, that is proportional to the local bulk density of the object if its chemical composition is uniform. Density values are represented by grey levels, black is equivalent to air while white is set to the highest bulk density. In geoscience, this technique has been widely implemented (Bossennec et al., 2018; Géraud et al., 1999; Ji et al., 2015; Robert, 2004).

Each 2D element (pixel) of the image contains the calculated bulk density of a 3D solid element (voxel). The X-ray CT scan resolution is associated with the sample size. X-ray CT imaging was performed on a Phoenix Nanotom S with cylindric samples of 1.6 cm in diameter and 2 cm in height, to obtain a resolution around 1 voxel = 16  $\mu\text{m}$ . The maximum voltage that this microtomograph can provide is 180KV / 15W. The scanner acquires several 2D X-ray absorption images or projections of the sample placed on a 360 ° rotating stage (Figure III-4). The 3D visualization of the sample was processed with VG Studio software (Volume Graphics) to extract the 2D reconstructions of the internal structure.

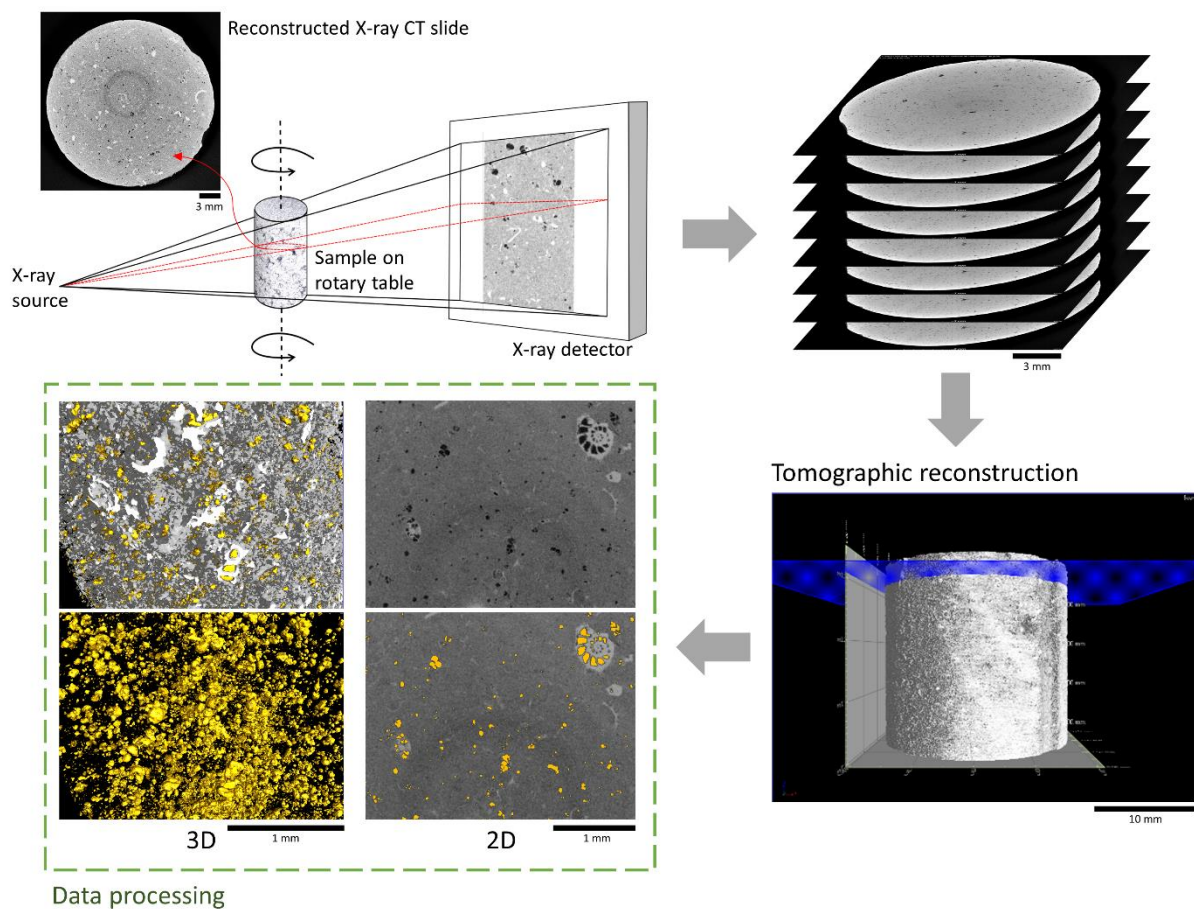


Figure III-4. Principle of X-ray microtomography, image reconstruction, and 2D and 3D visualization.

The analysis and 3D rendering of the X-ray CT data were carried out using VGStudio MAX 2.2 © software. It allows the geometric analysis of porosity, inclusions, and heterogeneities. First of all, acquisition artifacts have been removed from the volume. The sample was separated into three cylindrical areas of interest on which the study was carried out to respect the capacity of the computer and to be representative of the entire sample. The software was used to extract porosity by binarization. This image segmentation permitted to separate the different phases (between biogenic / non-biogenic particles and voids) by assigning to each voxel of the image the corresponding phase according to its shade of grey. The adjustment parameters remained the same throughout the analysis. The porosity zones appear black in the images (open and closed porosity). Various properties of the voxels (volume, diameter, sphericity, etc.) were obtained using a fault detection tool.

### III.1.3.10. Statistical analysis

Statistical analysis of results including PCA and boxplot representation was performed using R code (R foundation). Descriptive statistics and linear regressions were performed with XLstat. The R missMDA package (Josse and Husson, 2016) was used to manage the missing values. It performs single and multiple imputations. All missing data are supplemented with plausible values for analysis by exploratory data analysis methods. The prediction of the values is carried out from a model that takes into account the similarities both between individuals and variables based on principal component analysis (PCA) for continuous variables. MissMDA package allows to impute the missing values by minimizing the loss function (the reconstruction error) on all the non-missing elements, that is without influencing the results of the ACP. The replacement was performed thanks to the iterative PCA algorithm (Kiers, 1997). It consists of fixing the missing entries with an initial value (average of the variable of the observed values), then performing the PCA on all the completed data. The PCA adjusted values are then used instead of the mean values. These two steps (estimation and imputation) are repeated until convergence.

## III.1.4. RESULTATS AND DISCUSSION

Firstly, to understand the role of the porous network morphology, a visual assessment of the petrographic and textural characteristics of the rock was carried out by SEM and X-ray CT. Afterward, the porous network was quantified by these two techniques together with MIP

and NMR. These complementary techniques, working in different size range detection, allowed to obtain an accurate description and quantification of the porous system.

Physical properties such as CWUT, P-waves and S-waves velocity, which gives indirect information about porosity, were also measured. The statistical relationships between them permitted to clarify the dependency among these parameters.

The number of samples (n) used for each analysis, the mean value, the standard deviations, and the maximum and minimum values of all the calculated parameters are exposed in Tableau III-1.

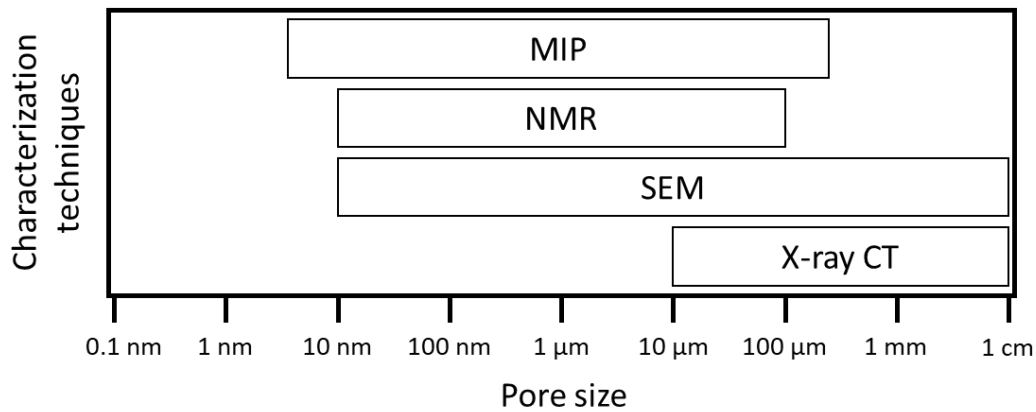
**Tableau III-1. Results of the set of properties measured.**

	$\varphi_T$ (%)	$\varphi_f$ (%)	$\varphi_{MIP}$ (%)	$\rho_g$ ( $\text{g}\cdot\text{cm}^{-3}$ )	T2 NMR (ms)	N2 k (mD)	$V_p$ ( $\text{m}\cdot\text{s}^{-1}$ )	$V_s$ ( $\text{m}\cdot\text{s}^{-1}$ )	C ( $\text{g}\cdot\text{m}^{-2}\cdot\text{s}^{-1/2}$ )
<b>n</b>	406	332	10	82	30	4	386	152	112
<b>Avg.</b>	42.52	39.42	38.33	2.736	40	4.89	2506	1256	415
<b>St.d.</b>	1.79	2.56	4.2	0.004	5	0.22	150	60	72
<b>Maximum</b>	48.86	46.73	42.75	2.749	52	5.22	3203	1444	613
<b>Minimum</b>	34.72	30.6	28.41	2.725	32	4.73	2111	1008	255

n: number of samples; Avg: average; St.d: standard deviation;  $\varphi_T$ : total porosity;  $\varphi_f$ : free porosity;  $\varphi_{MIP}$ : porosity by mercury injection;  $\rho_g$ : grain densities; T2 NMR: relaxation time; N2 k: nitrogen permeameter  $V_p$ ,  $V_s$ : P and S wave propagation velocities C: capillary coefficient.

### III.1.4.1. Analysis of the porous structure (SEM, X-ray CT, MIP, NMR, and CWUT)

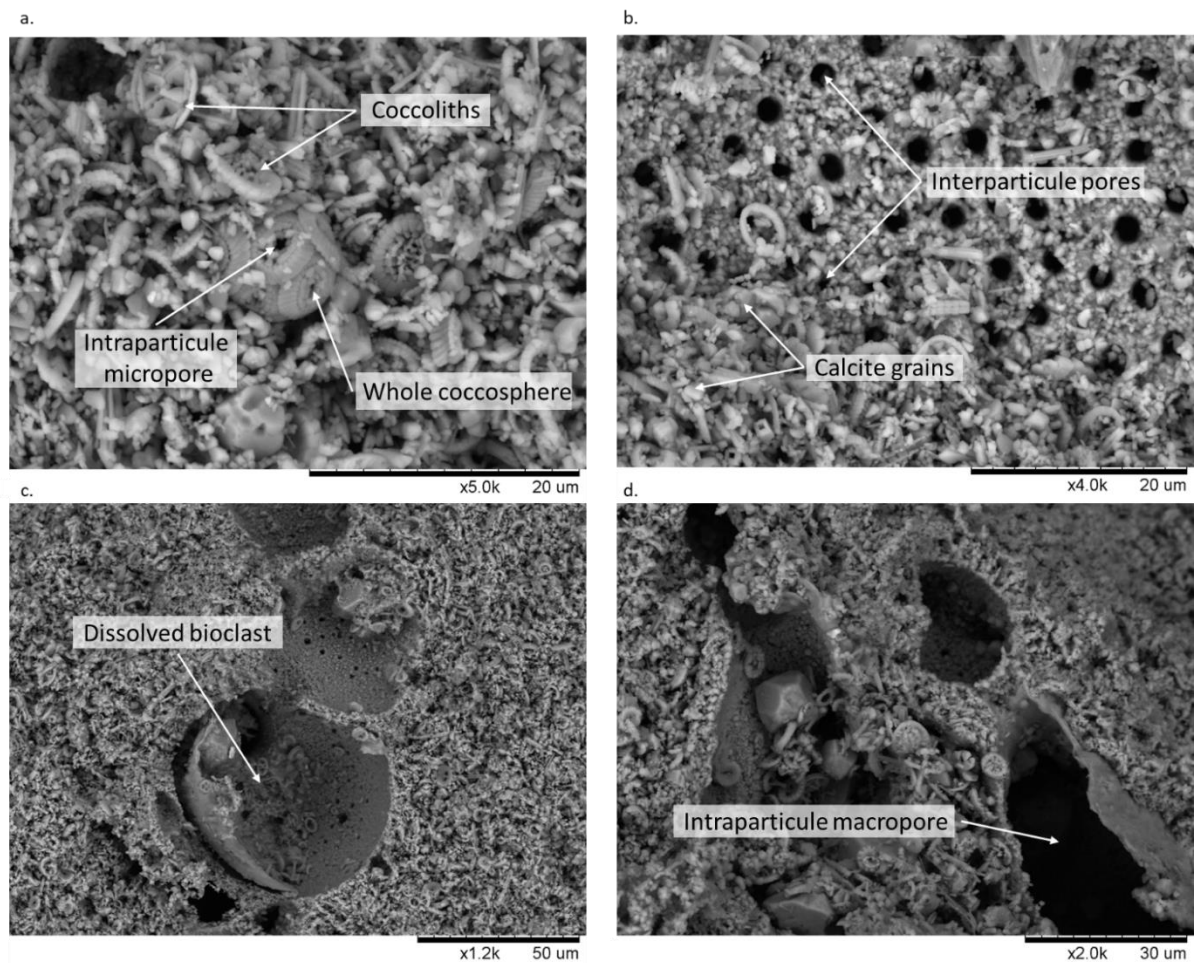
For a complete description of the porous network, the distribution and the pore structure are important parameters to take into account (Li and Zhang, 2018). The existent techniques applied alone did not allow to quantify the whole range of the porous network. Thus, a combination of techniques measuring in different resolution ranges was necessary (Figure III-5). Each of these techniques contributes to the understanding of one or more parts of the porous network (connected or closed porosity, pore size distribution, pores access distribution, tortuosity, connectivity, pore geometry). The coupling of these techniques made it possible to study the full extent of the domain covered by the different pore sizes. Finally, the analysis of the CWUT will be described to complete the results obtained by the techniques mentioned above.



**Figure III-5. Size range assessed according to the pore characterization techniques used (Zhang et al., 2018; Jaffel, 2006; Meyer et al., 1994).**

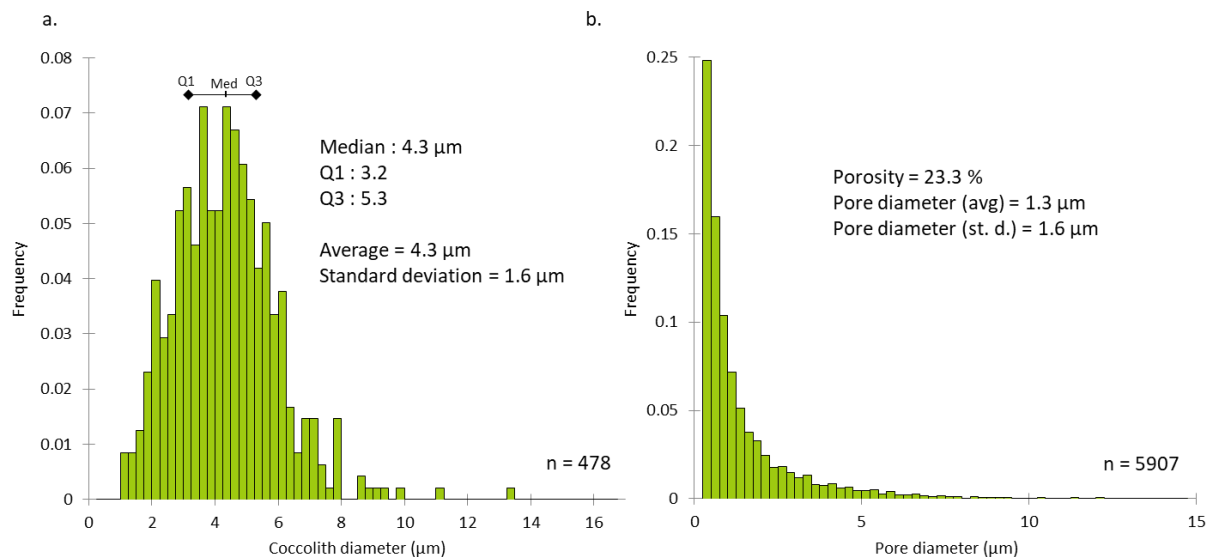
SEM observations permitted to establish the grain shapes and dimensions, and to locate and “characterize” the different pore types. The macropores were visualized and quantified by the X-ray CT .

The main components of the rock were fragments of well-preserved coccoliths with anhedral micrites and rhombohedral to sub-rhombohedral calcite crystals. Cement was scarce (Figure III-6).



**Figure III-6. SEM image of nanofacies (punctic structure) of the Châlons chalk. a. coccoliths of a few microns as the main constituents of the rock. b. interparticle pores of small sizes coming from the spaces between the grains and of the empty imprint of the dissolved organism. c. View of a macropore from the dissolution of a bioclast. d. Large diameter intraparticle pore.**

Coccoliths showed different shapes although the majority were elliptical without a preferred orientation. The distribution of the length of the coccoliths was unimodal (Figure III-7) with a median of 4.3  $\mu\text{m}$  and the interquartile range of about 2  $\mu\text{m}$ . Some particles could be larger (up to 8  $\mu\text{m}$ ) or smaller (about 0.5  $\mu\text{m}$ ). The contacts between the coccolith fragments were mainly punctic as well as between the micrites. Due to the special structure of the chalk, microcracks were not observed.



**Figure III-7. Distribution of the size of a. the coccoliths and b. the pores using the J.Microvision software on 478 individuals for the coccoliths and 5907 individuals for the pores (distribution interval: 0.25 µm).**

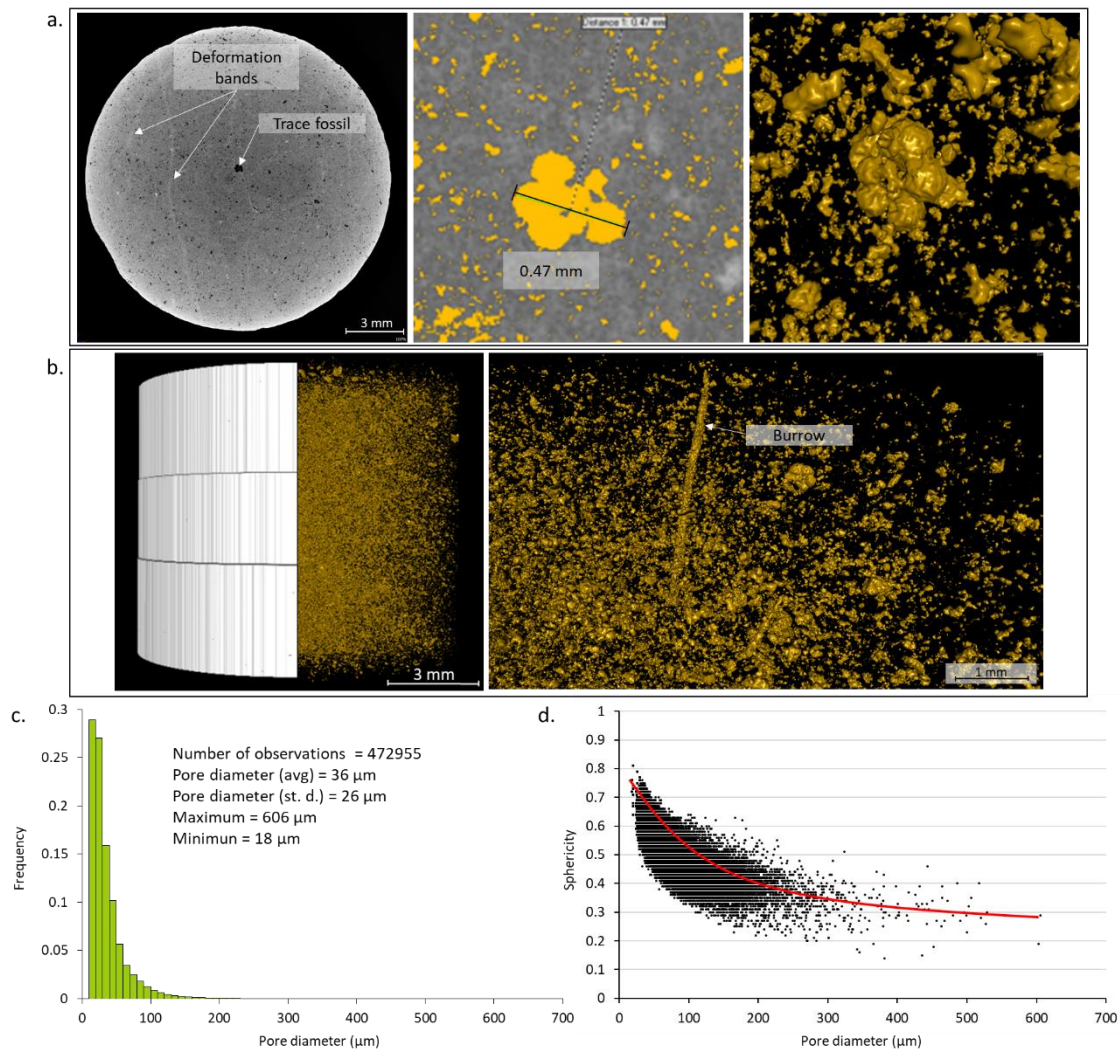
The porosity was mainly composed of an open microporosity on the SEM images. Interparticle porosity appeared between the fragments, with an average diameter of 1.3 µm (Figure III-6 and Figure III-7b). For comparison, Madland, (2005) estimates the size of the pores to be greater than the size of individual grains. Faÿ et al. (2011) observed with SEM an interparticle porosity mainly less than 2 µm in diameter on micritic chalk with well preserved coccoliths. The study by Meyer et al. (2019) estimates for a pure chalk, the pore bodies and throat pores at mean diameters of 4.15 and 0.73 µm, respectively. Traces of dissolution were revealed by smoother shapes and as well as in certain areas of macroporosity formed by the trace of the dissolved bioclasts (Figure III-6c). The intraparticle voids in the nannofossil cells were of small diameter (<1 µm), while the intraparticle voids of fossil fragments presented a greater variety of diameter ranging between 10 and 60 µm (Figure III-6d). The trapped porosity could be placed in these bioclasts but due to their low abundance, it was negligible compared to the high porosity of this chalk.

Few classifications of chalk microtextures have been proposed except that carried out by Saiag, (2016) who classifies pure chalk into seven microtextures according to their degrees of diagenesis. The specific descriptors used in her classification allowed us to relate Châlons chalk to the microtexture corresponding to an anhedral punctic chalk. This chalk group is defined

by an abundant well-preserved biogenic fraction, a well-preserved interparticle porosity, and a poorly cemented sample (Faÿ-Gomord et al., 2016).

Due to its low resolution (Ji et al., 2012; Kelly et al., 2016; Okabe and Blunt, 2007), X-ray CT has been ineffective in describing the whole range of pores observed by SEM or the interconnection between the elements of porosity. To reach a full characterization of the nanoscopic porous network of the chalk by X-ray CT, the resolution would have to be less than 0.025  $\mu\text{m}$  (Müter et al., 2014). In this study the resolution was sufficient to provide details on macropores larger than 10 microns (Figure III-8a). The presence of empty bio-organism shells and skeletons of large-diameter bio-organism was detected. These macropores are responsible for local variations in the porosity noticed also with SEM. The entire porous network was qualitatively observed using the software's 3D visualization (Figure III-8b). The volume rendering of the porous networks showed a homogeneous distribution of the porosity throughout the sample.

The distribution of diameters for macropores varied between 18 and 606  $\mu\text{m}$  although the majority had diameters less than about 200  $\mu\text{m}$  (Figure III-8c). A total of approximately 473,000 macropores were identified through morphological processing. Figure III-8d showed that the sphericity (with the value 1 as a perfect sphere) was negatively correlated with the pore diameter. The sphericity values ranged from 0.14 to 0.81. The largest pores were mainly isolated elements. Tubular-shape voids, very slightly spherical, that can represent bioturbation burrows were observed in the core (Figure III-8b). This heterogeneity could represent a bioturbation burrow located into the core. Wennberg et al. (2018) observed these same bioturbations on chalk from the North Sea; in particular thalassinoids which control the appearance and shape of open fractures. The bands identified in Figure III-8a were deformation bands existent on the high porosity rock described by Wennberg et al. (2013) and they corresponded to areas of grain reorganization formed under strain. However, these structures were relatively rare in the Châlons chalk and were not observed by SEM.



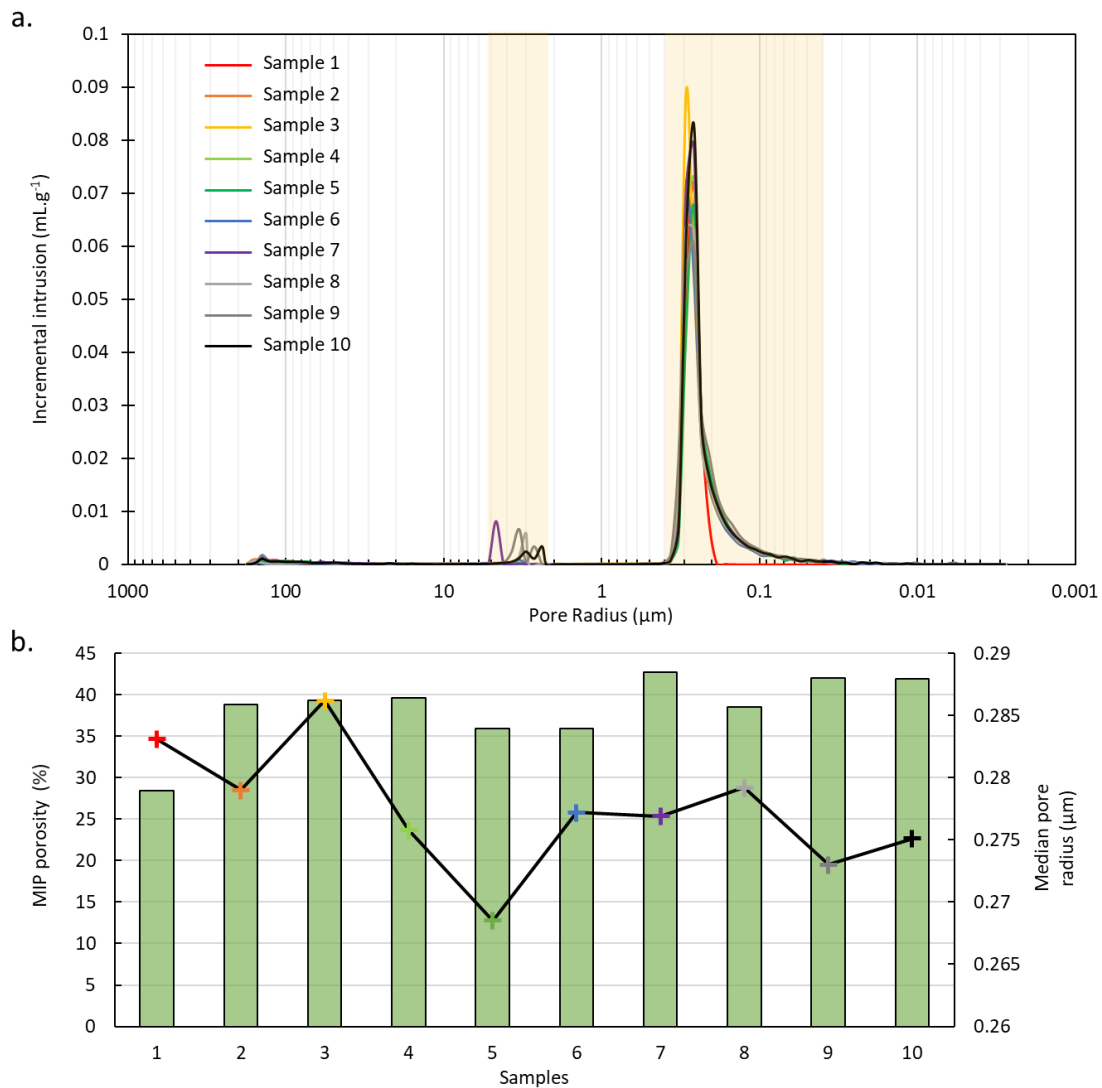
**Figure III-8. Qualitative and quantitative data extracted from X-ray CT measurements. a. X-ray microtomography 2D images and focus on a foraminifera print. b. Reconstruction of the 3D porous network. c. Pore diameter distribution (distribution range: 20 μm). d. Relationship between sphericity and pore diameter.**

These first observations were supplemented by MIP and NMR measurements.

MIP curves (Incremental intrusion relative to the pore access radius) are shown in Figure III-9. This microporous rock presented an average total porosity of  $37.9 \pm 4.2\%$ . The results of the pore access radii evidenced an unimodal distribution of the mean pore access radii from 0.04 to 0.40 μm with a mode of about 0.28 μm (Figure III-9a, b) in agreement with the pore distribution obtained by SEM. This curve shape testified to the existence of well interconnected and uniformly distributed nanopores in the sample. Five of the ten samples showed a second peak between the pore access radii from 2.25 to 5.20 μm. Compared to the



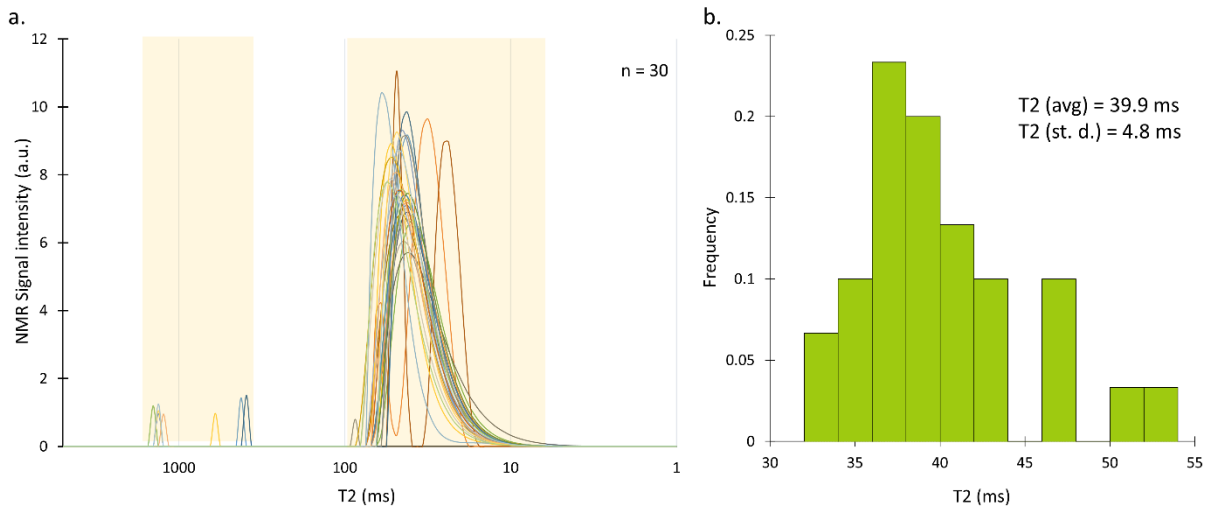
pore size distribution measured by SEM, the MIP porosity overestimated low radii and underestimates wider accesses (Mertz, 1991).



**Figure III-9. Curves obtained from mercury porosimetry. a. Incremental distribution of the MIP throat size. b. MIP porosity (%) and the value of the median radius (μm).**

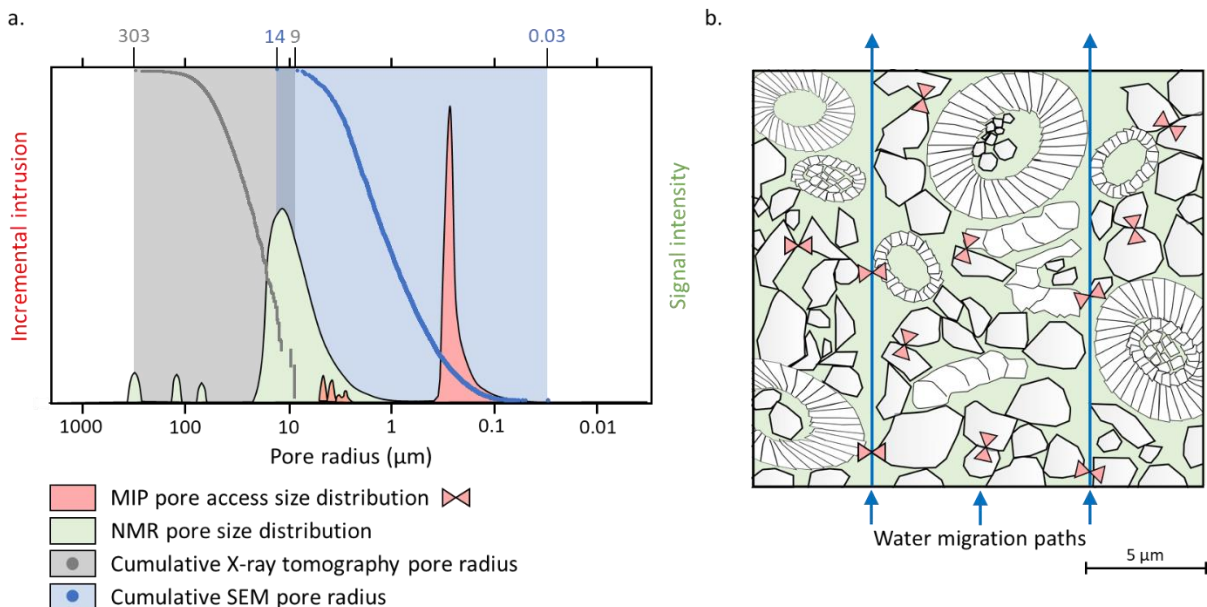
NMR is a technique offering a good description of the microporosity of chalk (Faÿ-Gomord et al., 2016; Li et al., 2014; Megawati et al., 2012; Meyer et al., 2019; Rios et al., 2016). The distribution of the transverse relaxation time (T<sub>2</sub>) of all pores can be considered equivalent to the distribution of the pore sizes of the rock (Kenyon, 1997). The logarithmic mean of the T<sub>2</sub> distribution was 40 ± 5 ms. This tool identifies the pore classes but with less resolution (Vincent et al., 2011). As with the MIP distribution, the T<sub>2</sub> distribution in Figure III-10

presented a unimodal distribution, with a second minor peak of lower intensity between 300 and 1500 ms.



**Figure III-10. a. Incremental NMR obtained by inversion of the relaxation curve. b. Distribution of the transverse relaxation time T2 (ms) (distribution interval: 2 ms).**

To compare the multi-technical and multi-scale results, the distributions of the pores in MIP, NMR, and X-ray CT were put in relation (Figure III-11a) and a schematic representation of the porous network was produced (Figure III-11b).



**Figure III-11. a. Comparison of the Size distribution of the interparticle voids by NMR and MIP. The NMR distribution was converted into the distribution of the radius of the size of the voids using the**

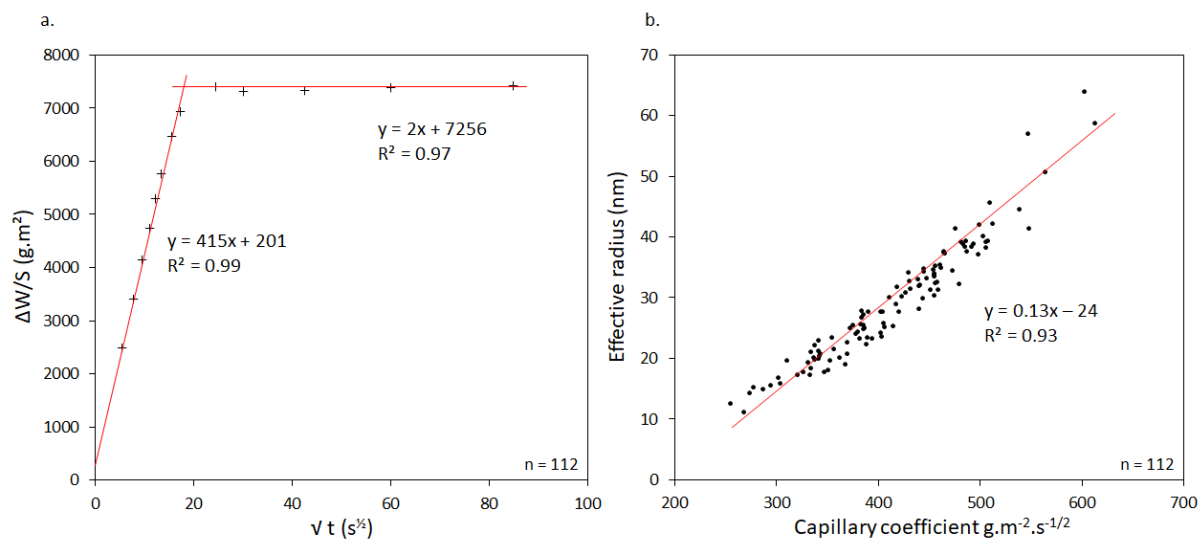
### **calibration of the large voids determined by X-ray tomography. b. Schematic representation of the chalk microstructure with the characteristics of each family of pores.**

The larger macropores observed by X-ray CT had a radius of 303  $\mu\text{m}$ . These larger voids enabled the T2 distribution to be calibrated. X-ray CT is a reliable way to interpret the NMR distribution (Yixin Zhao et al., 2017). The study by Bossennec et al. (2018) calibrated the NMR signal to the size of the voids thanks to the largest pores observed by tomography corresponding to the first NMR peak. Also Kruschwitz et al. (2020) transfer the T2 distribution to pore size after calibration with X-ray CT. Yixin Zhao et al. (2017) provide a method to determine surface relaxivity by adjusting cumulative pore volume distributions as a function of pore size, determined by NMR and X-ray CT both sensitive to pore body radius. In the NMR distribution of the chalk, the majority family corresponded the interparticle porosity between 1 and 20  $\mu\text{m}$ . SEM imaging confirmed this size of the voids. Therefore, water transfers could be controlled by the small pore access radius but also by the pore opening measured by NMR.

The interparticle porosity would be accessible at any time, by a narrow and homogeneous throat as indicated by the unimodal signal in MIP. The finer radii describing the access to the pores were not visible on the NMR distribution. However, secondary peaks (MIP) between 2.25 to 5.20  $\mu\text{m}$  were identified into the NMR distribution. Peaks located in the macropores with a radius greater than 50  $\mu\text{m}$  will reflect the dispersed dissolution pores, quantified by X-ray CT. The presence of these peaks would correspond to the larger pores also observed by SEM. For Faÿ-Gomord et al. (2016), the main peak of the bimodal T2 signal represents the chalk matrix and the second peak the intraparticle pores located in fossils of the large sponge type, fragments of bryozoa, or other bioclasts.

The placement of the NMR distribution in relation to the pore size remained theoretical. The NMR measurement presents certain limitations which explain the differences observed if compared to other techniques. Since the measurement was carried out on a saturated sample, an overestimation of the radii of the pores may occur. Indeed, a skeletal deformation is exerted on the chalk saturated with water causing a mechanical weakening (Duperret et al., 2005). In other words, the loss of cohesion within the chalk causes the particles to "loosen" and the NMR distribution would then be overestimated. In the rest of the text, the NMR pore radius will be calculated from equation (III. 8).

The curve profiles of capillary water uptake that depend on the types of porous networks allowed to confirm the pore distribution previously assessed. The weight gain curves of the samples presented an unimodal porous network with only one slope break, in agreement with MIP and NMR distributions (Figure III-12). This showed that the predominant family of pores was well interconnected and uniformly distributed within the sample. The homogeneity of the porosity over the whole of the sample allowed a regular flow. The isolated unconnected pores, observed under X-ray CT, were very minor and their influences were insignificant (Faÿ-Gomord et al., 2017). This sparse macroporosity did not influence the kinetics of the water uptake.



**Figure III-12. a. Weight gain relative to the sample area ( $\Delta W / S$ ) as a function of the square root of time ( $\sqrt{t}$ ). b Effective radii as a function of the capillary coefficients.**

The effective radius was calculated from equation (III. 3). The contact angle was considered zero and the pore shape spherical. Tortuosity was not taken into account. The radii varied between 11 and 64 nm. When tortuosity is removed from the equation, the complexity of the porous network is not taken into account, and the radius of the capillary is generally many orders of magnitude less than the actual mean radius (Thomachot, 2002). It only allows to reconstruct of a schematic network made up of straight capillaries with known imbibition kinetics (Mertz, 1991) but has no hydraulic significance. By comparing the actual body pores with chalk, the tortuosity parameter can be set.

### III.1.4.2. Tortuosity estimate

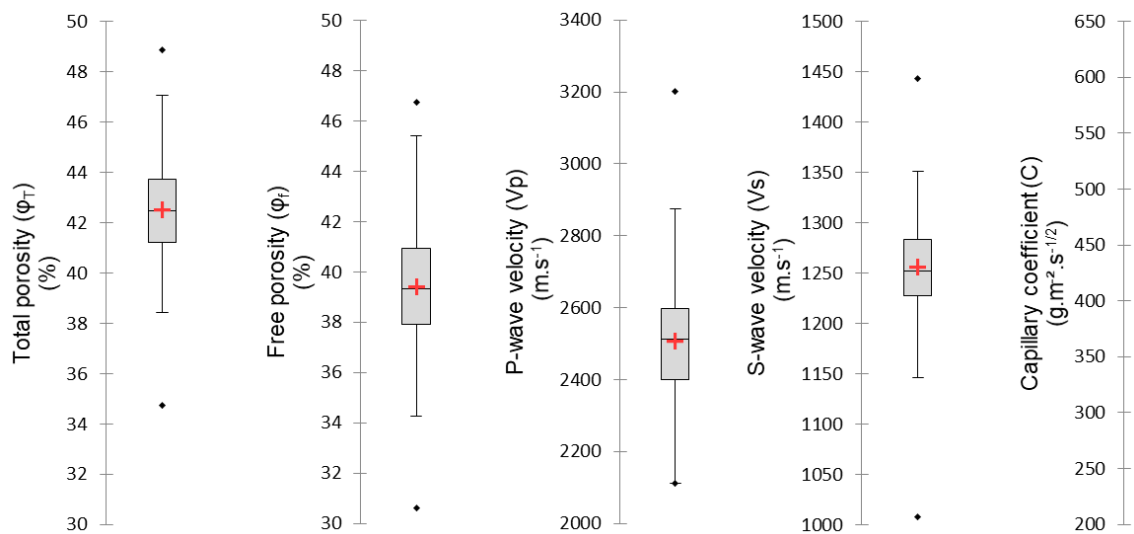
Tortuosity is linked to the topology and the microstructure character of the porous media. The large difference between the capillary radius and the actual pore size, of this study, predicts a significant tortuosity. Tortuosity was calculated from equation (III. 3), from the pore size measured by NMR, and the shape of the pores was based on the mean sphericity observed by X-ray CT. Saïag, (2016) obtains a tortuosity between 1.3 to 31.1 on chalk of different porosity from measurements of electrical conductivity. In our case, if  $\tau = 1$ , it means that the capillary tubes' like would be straight and of the same shape. The calculated values of tortuosity  $\tau$  varied from 14 to 23 with an average of  $18 \pm 2$ . As expected, the tortuosity of the porous networks of the Châlons chalk was remarkable and reflected complex paths which play an important role on the fluid flow.

### III.1.4.3. Relationship between the petrophysical properties

The reservoirs located in the chalk show very wide petrophysical variability. For example, the North Sea chalk (surface and subsurface) has porosities between 5 and 55% for permeabilities between 0.01 and 500 mD (Alam et al., 2011) with the highest permeability for fractured chalk. On average, the matrix permeability for high porosity chalk is between 1 and 5 mD (Sulak and Danielsen, 1988). The nitrogen permeabilities of the chalk studied vary little with an average of  $4.9 \pm 0.2$  mD (Tableau III-1). In this study, despite their high porosity, samples have low permeability due to their microporous character. Static parameters of the porous network (total and free porosity, densities, and mercury porosimeter data), fluid transfer properties (permeability, water uptake), and dynamic properties (wave propagation velocity) were measured. The bulk density was on average  $1.57 \text{ g}\cdot\text{cm}^3 \pm 0.05$  and the grain density was on average  $2.74 \text{ g}\cdot\text{cm}^3 \pm 0.004$  (Tableau III-1). These properties exhibited very limited variability. These values have been attributed to the high mineralogical purity of Châlons chalk and are consistent with the usual values for pure calcite (of the order of  $2.71 \text{ g}\cdot\text{cm}^3$ ).

The quantitative values of the porosity and the parameters related to it are presented in Figure III-13. The mean values of the total and free porosities of the chalks studied were close to the median values with  $42.52 \pm 1.79\%$  and  $39.42 \pm 2.56\%$  respectively. The saturation coefficients are defined as the ratio of the porosity accessible to water and the total porosity (*i.e.*:  $\varphi_f / \varphi_t$ ) (Hirschwald, 1908). On all of our samples, it was between 0.72 and 1. These high values reflect

the fact that the porous network is essentially made up of pores freely accessible to water with little trapped porosity.



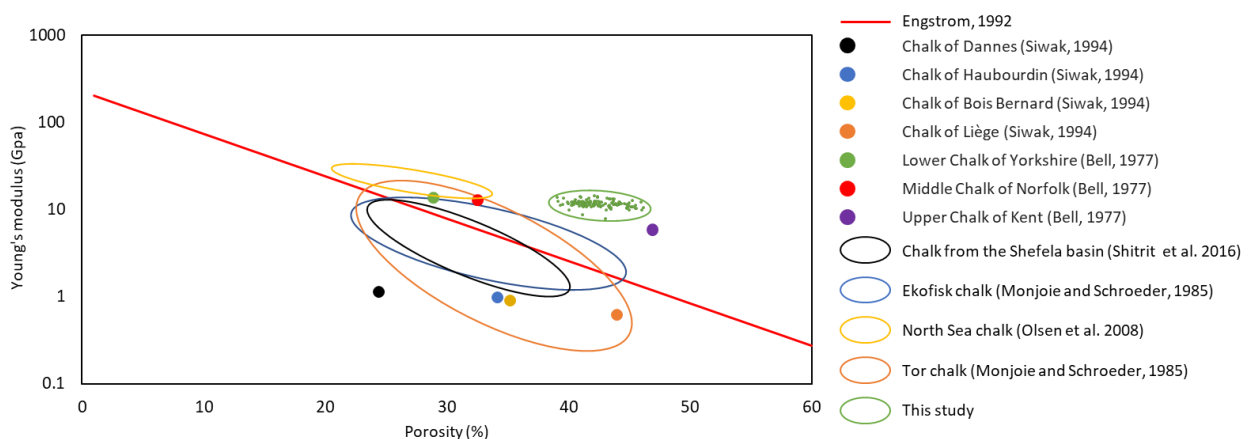
**Figure III-13. Boxplot on petrophysical properties of the chalk. The limits of the box represent 25% and 75% of the distribution (quartiles Q1 and Q3), the line inside the box represents the median value (50% of samples). The central red cross represents the mean value. The extreme points represent the minima and maxima.**

The P-wave propagation velocity measured on the dry samples varied from 2111 to 3203 m·s<sup>-1</sup> with an average of 2506 m·s<sup>-1</sup> and a standard deviation of 150 m·s<sup>-1</sup>. The S-wave propagation velocity measured on the dry samples varied from 1008 to 1444 m·s<sup>-1</sup> with an average of 1256 m·s<sup>-1</sup> and a standard deviation of 60 m·s<sup>-1</sup>. P-wave propagation velocities measurements on a dry sample vary with respect to less dispersive porosity. The velocities variations can be linked to the zones of bioturbations present in these samples oriented perpendicular to the stratification (Saïag, 2016). But it depends above all on the types of contact between the grains constituting it. The P wave propagation velocities of chalks from the Omeÿ region measured by Richard et al. (2002) was 2377 ± 148 m·s<sup>-1</sup>. They interpret the velocities changes as being the modifications of the chalk fabric depending on the contacts between the particles. SEM observations revealed a microtexture consisting of anhedral micrites with punctic contact. Increasing or decreasing the connectivity between grains changes the cohesion and would make the sample more or less favourable to the P wave propagation velocities, as proposed by Regnet et al. (2015).

The elastic properties were calculated on 120 samples from  $V_p$  and  $V_s$  measurements carried out in the same samples. Young's modulus values averaged  $11.5 \pm 1.1$  GPa. The Poisson's ratio showed constant values around the mean of  $0.33 \pm 0.03$ . The Young's modulus as a function of the total porosity is presented in Figure III-14. Several authors studied the relationship between  $E$  and porosity. Engstrøm, (1992) shows a correlation between porosity and Young's modulus (red line in Figure III-14) from a wide range of North Sea chalks with a porosity between 25 and 50%. He defines a statistical relationship such that:

$$E = 225\,000 e^{(-0.112 \varphi)} \quad (\text{III. 9})$$

The resistance of the chalk is attributed to the existence of a capillary force between the calcite grains (Delage et al., 1996; Risnes and Flaageng, 1999). The cohesion of the chalk particles is governed by different types of bonds. The most numerous bonds are those made by the adhesion of two successive particles. Then two close particles can be joined by a calcite bridge (Mata, 2001). The existence of calcite bridges is nevertheless still discussed and has not yet been really demonstrated (Nadah et al., 2009). There are also connections made by coalescence (Nadah, 2010). The results did not show a clear relationship between the two parameters.



**Figure III-14. Relationship between total porosity and Young's modulus  $E$  from different studies (Data: Bell, 1977; Engstrøm, 1992; Monjoie and Schroeder, 1989; Shitrit et al., 2016; Siwak, 1994).**

CWUT was performed to interpret the flow of a fluid in the microporous network. It has been shown that about 5 minutes of experience was sufficient for water capillary absorption to start to stabilize for the 2 cm sample (Figure III-12). The average coefficient  $C$  was  $415 \pm 72 \text{ g}\cdot\text{m}^{-2}\cdot\text{s}^{-1/2}$ . For comparison, on the Mons chalk, Robert, (2004) determines a coefficient of  $487 \pm 13$

$\text{g}\cdot\text{m}^{-2}\cdot\text{s}^{-1/2}$  and Linoir, (2014) obtains a coefficient of  $547 \pm 62 \text{ g}\cdot\text{m}^{-2}\cdot\text{s}^{-1/2}$  on the chalk of Champagne. The chalk of Normandie with a median porosity of 34.7% studied by Saïag, (2016) have a coefficient C of  $257 \text{ g}\cdot\text{m}^{-2}\cdot\text{s}^{-1/2}$ . In addition, they indicate in their study that the coefficient C exhibits little variation for total porosity less than 40% but increases sharply beyond that. That indicated a very fast capillary kinetics, and highly free porosity (Beck et al., 2003; Benavente et al., 2002; Sengun et al., 2014).

Due to the different complexity, duration, and destructive / non-destructive character of the test, the number of samples evaluated was not the same for every measured parameter (Tableau III-1). Two datasets are discussed. First, a restrain dataset of 33 samples having a maximum of measured parameters in common was used to control the correlations between the petrophysic characteristics (Figure III-15a). Second, an increased dataset (Figure III-16a), presenting all the samples with the measurements carried out and used to assess the trends.

#### III.1.4.4. Restricted dataset

The missing data were replaced using the MissMDA package. MissMDA allows to visualize the uncertainty of the different predictions (Josse and Husson, 2016). This assessment was based on multiple imputations called MIPCA which generates different plausible values for each of the missing values. A Principal Component Analysis (PCA) was performed (Figure III-15b) to show the relationships between all the variables carried by the first two main components (Dim 1 and Dim 2). Positively correlated variables were moved away from the center and grouped. Negatively correlated variables were opposite from the origin of the graph. Orthogonal variables were not correlated. The results showed that P wave propagation velocities and the total porosity were negatively correlated ( $R^2=0.7$ ), as expected (Alam et al., 2011; Dvorkin and Alabbad, 2019; Røgen et al., 2005).

##### III.1.4.4.1. Relationship between pore size and capillary coefficient

In order to obtain the pore size radius, the relaxation time T2 should be transformed by using the surface relaxivity  $\rho$  as a scale factor in equation (III. 8). Two hypotheses were stated. Assuming a relaxivity  $\rho$  of  $10 \mu\text{m}/\text{s}$  attributed to carbonate rocks (Hurlimann et al., 1994) and a simple sphere model, the radius obtained corresponded to an unimodal distribution between 0.2 and 3  $\mu\text{m}$ . The interconnection of the pores, measured by the coefficient C, showed a good correlation with the pore size (Figure III-15c). The mechanism of capillary



absorption of water is directly related to the size of the pores and connection of the porous network (Mertz, 1991; Tomašić et al., 2011). The high saturation of the chalk (Bounenni, 2002) assures that the entire microporous network has been taken into account when measuring T2. This positive correlation suggests that the porosity measured by NMR controlled the water flow paths.

PCA analysis showed that the median pore access size and the pore size determined by NMR did not correlate with the porosity. Thus, the variations in porosity could not be interpreted by the enlargement or the narrowing of the size of pore access or the size of the interparticle pores, but would be mainly explained by a variation in the number of micropores. Furthermore, changes in total porosity were not clearly correlated with the C coefficient. This is explained by the fact that coefficient C was mainly controlled by the pore access size (Figure III-15d). In fact, it has been observed that the increase in the C coefficient was negatively correlated with the pore access size. This anomaly in capillary absorption was observed by Ioannou et al. (2009) in their modeling of the capillary water absorption behaviour of porous limestone. They observed that the presence of large pores reduce capillary absorption unlike the presence of finer pores. This is explained by the fact that fine pores have capillary forces greater than gravitational forces, unlike coarse pores.

### III.1.4.4.2. Relationship between permeability and porosity

Several authors have emitted permeability prediction models empirically or from flow laws such as Poiseuille and Darcy's law (Gao and Hu, 2012; Rezaee et al., 2006; Saki et al., 2020). Benavente et al. (2015) use the capillary coefficient, water properties, and microstructural parameters of rock to calculate permeability as (III. 10):

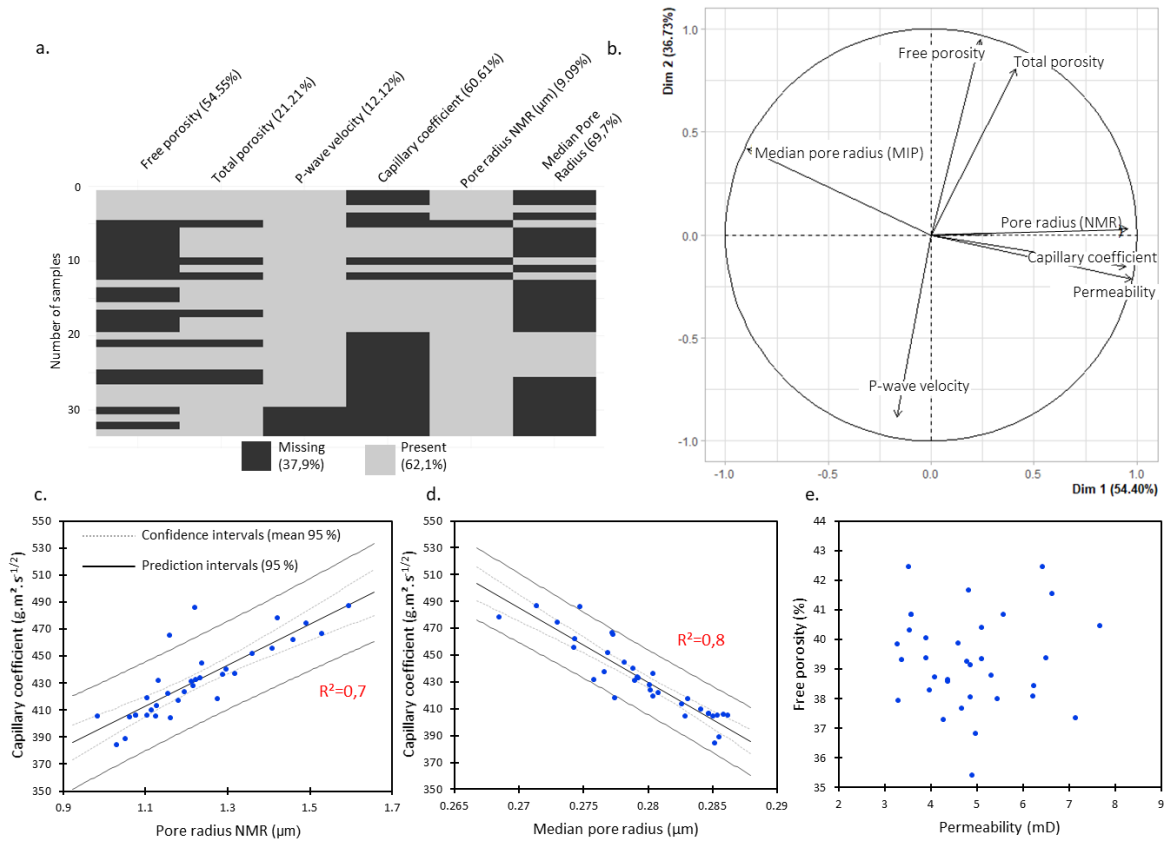
$$k = C^2 \frac{\eta r}{4\phi \rho^2 \gamma \cos\theta} \quad (\text{III. 10})$$

With the water absorption coefficient by capillarity (C), the density ( $\rho$ ) and the viscosity of the water ( $\eta$ ), interfacial tension ( $\gamma$ ), contact angle ( $\theta$ ), pore radius (r) and porosity ( $\phi$ ).

The permeability will be estimated from equation (III. 10). The pore radius measured by NMR was used in the calculation. The permeability values showed better predictions when the wettability was not considered to be complete. Chalk is often defined as a material exhibiting a strong affinity for wetting and the contact angle  $\theta$  is considered null. Some material exhibits

incomplete wetting due to natural contamination of the pore surface which reduces the affinity of the calcite surface for water (Taylor et al., 2000). Considering the different responses chalk could have to water injection, Rhett, (1998) suggested the existence of an organic coating that would protect the matrix from chemical weathering. Such films could change the wettability of the chalk surface and would influence the water weakening effect. On the basis of these observations Benavente et al. (2015) re-estimate the wetting index ( $\beta$ ), indicating a wetting condition between 0 and 1, with 1 corresponding to full wetting conditions. In order to more accurately estimate the wetting of Châlons chalk, the nitrogen permeability was used as a reference value and replaced in equation (III. 10). A wetting index of 0.45 on average was obtained, consistent with the values between 0.2 and 0.5 of some chalk deposits (Andersen, 1995) and with the 0.38 obtained by Benavente et al. (2016) on biocalcarenes containing 70% of calcite grains.

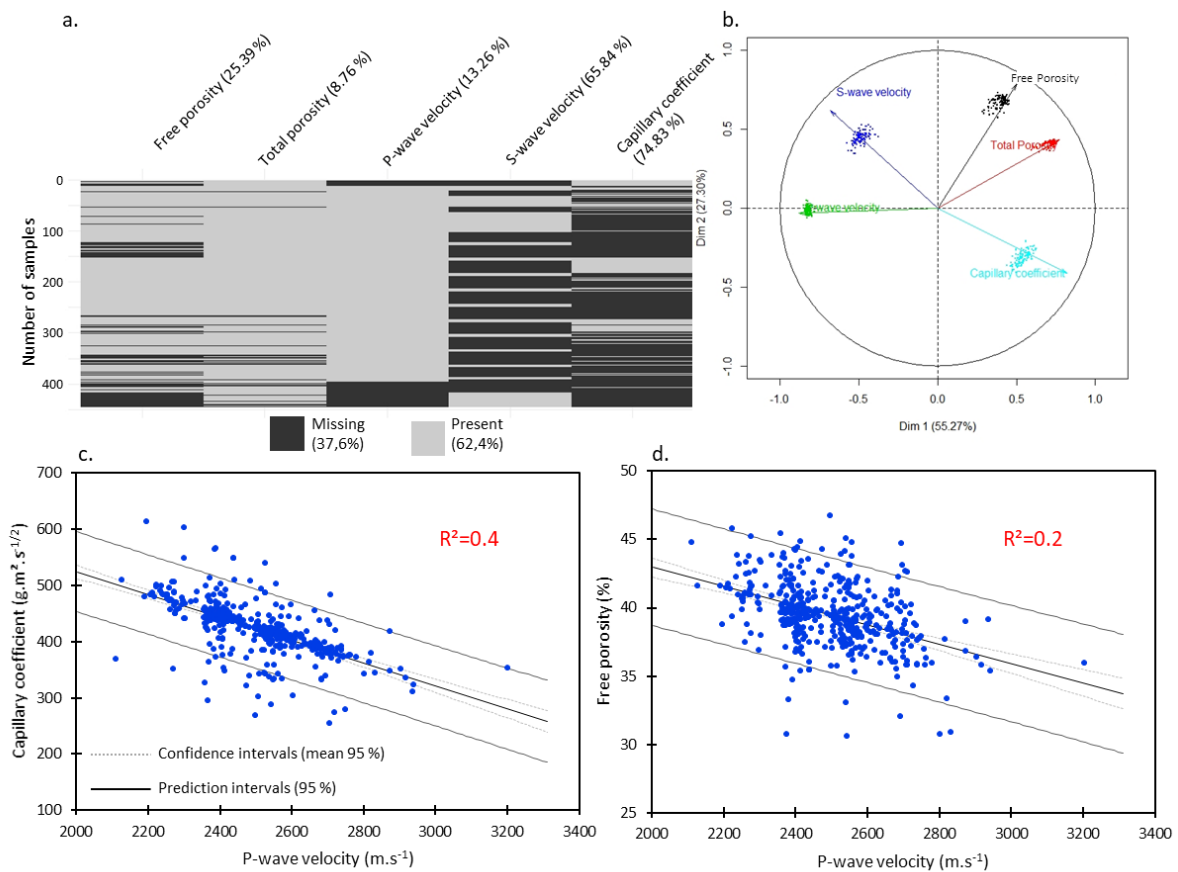
No relationship between porosity and permeability was observed (Figure III-15e) and in agreement with Saïag, (2016) who found a large dispersion of permeability on samples above the porosity of 30%. It has been shown that for porosity values greater than 10%, the permeability values are mainly linked to the size of the pores (Benavente et al., 2015).



**Figure III-15.** a. Data visualization for the first test with 33 samples. b. Correlation circles (Dim1×Dim2) of the Principal Component Analysis (PCA). Relationship between c. the capillary coefficient and the pore size (NMR), d. the free porosity and the permeability, e. the capillary coefficient and median pore radius (MIP) (n=33).

### III.1.4.5. Augmented dataset

In order to check the trends of the collected data set, an augmented data set was created with the 445 samples (Figure III-16a). To replace the missing data, the MISSMDA package was used. To better decipher the interdependence between the characteristics of the porous network, a principal component analysis (PCA) was performed (Figure III-16b).



**Figure III-16. a. Visualization of missing data, b. Correlation circles (Dim1×Dim2) of the PCA on variables of all samples without the missing data. Weight clouds represent the confidence zones of several imputed data sets. Relationship between c. the free porosity and the P- waves propagation velocity, d. the capillary coefficient and the P- waves propagation velocity (n=445).**

The main observations drawn were that total and free porosity was strongly correlated, the C coefficient was negatively correlated with the P-wave propagation velocity (Figure III-16c) and S-wave propagation, and the P- wave propagation velocity was negatively correlated with the free porosity without this correlation being statistically significant (Figure III-16d). Urmos and Wilkens, (1993) also show a difficult correlation between porosity and the P-wave propagation velocity on chalk. The carbonate pore system is complex and the relationship between the P-wave propagation velocity and the porosity can be dispersed (Eberli et al., 2003). Some parts of the interparticle and intercrystalline porosities cannot be discerned on the simple basis of the P-wave propagation velocity. Baechle et al. (2008) indicate that for carbonate rocks the deposition environment and the diagenetic alterations can testify to large propagation velocities ranges at a given porosity. The amount of missing data for the S-wave and the coefficient C can reduce the correlation between certain parameters. In addition, on the

extended data set, samples were compared that had not been tested for the same parameters. To better mark the correlations, it is advisable to restrict the number of samples and to carry out the same measurements on the whole of the data set.

### III.1.5. CONCLUSION

The particular internal structure of chalks makes it difficult to decipher the characteristics of its porous network. This chalk is composed mainly of coccoliths of various morphologies and well preserved. No traces of cement or clay were observed.

The pore access sizes show an unimodal distribution with very small radii ( $<0.3 \mu\text{m}$ ), due to the punctate structure of the chalk, resulting in low nitrogen permeability values. These punctate contacts present in the micrite create a more heterogeneous microtexture with a large number of interfaces and pores, which probably favours the dispersion of P- waves.

If the mercury injection measurements suggest that all the chalk is nanoporous, the measurements carried out in X-ray CT and NMR, indicate that the chalk has microporous and macroporous porosity.

The 3D reconstruction of the microporous network from successive X-ray CT sections revealed the weak connection of the macropores. Large-diameter fossils have been observed by X-ray CT showing empty skeletons responsible for local macroporosity greater than  $100 \mu\text{m}$ . These macropores are responsible for the local variations of porosity also observed by SEM. High-resolution X-ray CT imaging was used to calibrate the signal measured by NMR. The NMR signal shows an interparticle pore size distribution between 1 and  $20 \mu\text{m}$ , consistent with SEM observations.

The relationships between the petrophysical parameters have shown that the hydraulic behaviour (evolution of water uptake by capillarity) of chalk is controlled by the actual size of the pore opening (NMR) and the median access pore size (MIP). Minority macroporosity does not influence the kinetics of water uptake.

The microporous characterization of chalk would be a first step towards a better understanding of the petrophysical and mechanical properties, and therefore of the reservoir qualities of chalk.

## **III.2. Article#2 : Behavior of Chalk under fluid flows at Contrasting Temperatures.**

Cet article sera soumis, à la revue de rang A, *Journal of Petroleum Science and Engineering*.

Junique<sup>1</sup>, T., Géraud<sup>2</sup>, Y., Vazquez<sup>1</sup>, P., & Thomachot-Schneider<sup>1</sup>, C. (2021). Behavior of Chalk under fluid flows at Contrasting Temperatures. *Journal of Petroleum Science and Engineering*.

<sup>1</sup>GEGENAA EA 3795, University of Reims Champagne-Ardenne, 2, esplanade Roland Garros, 51100 Reims, France

<sup>2</sup>GeoRessources Laboratory UMR 7359, University of Lorraine, F54505 Vandoeuvre les Nancy

### III.2.1. INTRODUCTION

The thermal factor added to the fluids flow is involved in many geological applications, such as the intermittent injection of cold water into a hot reservoir during oil production, geothermal production, or the injection of supercritical CO<sub>2</sub> for storage of carbon dioxide. The cooling effect induced during the injection of a large volume of fluid can modify the stress state of the reservoir and thus, thermally degrade the rock surrounding an injection well (Perkins and Gonzalez, 1985). In addition, temperature variations can also influence the brittle or ductile behavior of the rock, depending on factors such as the mineral and structural characteristics of the rock, and the temperature range (Jaeger et al., 2007). For example, enhanced oil recovery (EOR) with hot water (or steam) in reservoirs can lead to increased oil recovery by improving water imbibition in the reservoir (Jabbari et al., 2017).

Carbonate rocks and chalk ones represent between 50 and 60% of the world's oil reservoirs (Burchette, 2012). Chalk is generally characterized by a high total porosity (> 40%) (Faÿ-Gomord et al., 2016; Nadah et al., 2009) with a variability related to the variation in particle size, texture, traces of fossils, and clay and silica content (Frykman, 2001). The permeability of chalk is very low because of its microporous nature. The physical properties of microporous and poorly permeable bodies like chalk are complex and often studied. For example, chalk from the North Sea, which exhibits a wide faciological variability faciological (Fabricius, 2003; Fabricius and Borre, 2007; Gommesen et al., 2007; Japsen et al., 2004; Røgen et al., 2005; Schroeder, 2002). In general, the rock has the chemical quality exclusively consisting of calcium carbonate, organized mainly as calcite crystals, with diameters ranging from 0.17 to 2.8 µm and skeletal remains of Coccolithophoridae, coccoliths, with diameters ranging from 1 to 20 µm (Betson et al., 2004). Other biogenic remains can be included in the rock such as Foraminifera or bivalve shells, but remain in small quantities.

The interactions chalk-fluid have been the subject of great attention in the scientific communities (Delage et al., 1996; Gutierrez et al., 2000; Neramoen et al., 2016; Nguyen, 2009; Risnes et al., 2005) due to the seabed subsidence phenomena detected in the 1980s in North Sea oil deposits (Addis, 1987; Johnson et al., 1988) causing a rapid decline in production (Simon et al., 1982). These modifications can occur during the water injection method, aimed at improving the reservoir's profitability up to the "pore collapse" (Blanton, 1981; Keszthelyi et al., 2016). Controversies remain as to the causes of its behavior and the dependence on

physico-chemical factors (Heggheim et al., 2005; Schroeder, 1995). Numerous studies have shown that the strength of chalk depends a lot on the saturating fluid (Risnes, 2001). Monjoie and Schroeder, (1989) show that water has a weakening effect on chalk. This mechanism is known as “water weakening effect” and induces a significant drop in mechanical resistance (Madland, 2005). Nadah, (2010) describes this phenomenon as instantaneous and reversible. They show that the compressive strength of chalk decreases after being saturated with a few percent water. Chemical dissolution has been proposed as a weakening mechanism (Heggheim et al., 2005; Heugas and Charlez, 1990; Nermoen et al., 2015). However, the very low solubility of calcite and the large specific surface area of chalk make it unlikely that the mechanical strength of chalk is caused by too little dissolution (Andersen, 1992; Rhett, 1990). Pressure solution experiments are taken into account in long-term creep tests (Hellmann et al., 2002b) and locally promote the dissolution of calcite. However, this slow phenomenon is not compatible with the rapid weakening of chalk (Schroeder et al., 1998).

The weakening is most often attributed to pure physical interactions between grains. Capillary forces are important in chalk to induce cohesion between particles (Delage et al., 1996). During a flood, the water meniscus still present in the dry chalk (Lord et al., 1998) disappears and weakens the rock. The action of water can break the contacts between the grains by absorption thanks to the so-called Rhebinder effect which depends on the free energy surface (Rehbinder and Lichtman, 1957). Risnes et al. (2003) indicate that the activity of water in a fluid (brines or glycol-water) is a key parameter in the weakening by water. It is a complex physicochemical mechanism in which the chalk grains are degraded by the adsorption forces of fluid molecules on the surface of calcite. Duperret et al. (2005) studied the impact of tidal-modulated cliff-foot swell by performing a 10-day wetting and drying cycle using fresh and saline water in chalk samples. The disaggregation and salt crystallisation were the main contributors to the decrease in strength.

The effect of temperature on the chalk can have an impact on the behavior of the material. The Valhall Reservoir has a temperature of 92 °C, and this temperature may be higher with the formation of Ekofisk at 130 °C (Nermoen et al., 2016). These temperature levels are also identical to that of the fluids found in the field of geothermal energy between low and deep energy. The high temperature of the reservoirs can have a considerable influence on the behavior of the fluid-rock system. We can find significant changes such as the modification of



porosity and permeability (Uribe-Patiño et al., 2017). Cyclic heating and cooling of rocks can cause permanent damage, especially on rocks composed of anisotropically thermally expanding minerals like calcite. The calcite crystal has a trigonal axis of symmetry, with an average thermal coefficient of expansion of  $23.8 \times 10^{-6} \text{ K}^{-1}$  and  $-5.2 \times 10^{-6} \text{ K}^{-1}$  in the directions parallel and perpendicular to the trigonal axis, respectively (Rosenholtz and Smith, 1949). This highly anisotropic thermal expansion of the calcite crystals induces on the chalks, that have been subjected to temperature fluctuations, a thermal stress which results in an accumulation of irreversible deformation but no significant influence on the elastic modulus (Voake et al., 2019).

Temperature is one of the parameters studied in chalk weakening as these variations can affect the properties of the reservoir. For example, the geometry of the pores can be changed with increasing temperature which can affect the distribution fluid and flow performance. However, the number of studies remains low and their conclusions are not completely consistent. For example, the strain modulus was not affected by the change in temperature (room temperature at 130 °C) for saturated dry and saturated chalk from the reservoir of the Ekofisk and Tor formations (DaSilva et al., 1985). On the other hand, a slight decrease in Young's modulus was observed on the chalks studied by Brignoli et al. (1994) when the temperature increases between 20 and 100 °C. Temperature had no significant effect in uniaxial strain compaction experiments (Addis, 1989). Charlez et al. (1992) showed a clear influence of temperature on the elastoplastic parameters on chalks with 40.5% porosity, saturated with oil and tested at 20 °C, 90 °C and 120 °C with the thermo-poro-elastics parameters unaffected by temperature and temperature independent shear failure mechanism. The temperature of the injected fluid and the temperature difference between the injected fluid and the reservoir temperature have been shown to affect the recovery rate (Hamouda and Karoussi, 2008), with an improvement in oil production increasing by the water injection temperature up to 80 °C. Nadah et al. (2009) study the effects of temperature on the mechanical behavior of chalk from northern France. They show increased tensile strength when exceeding 105 °C. Indeed, heating, even at very high temperatures, did not modify the elastic parameters but had an impact on the appearance of the first plastic deformations. Heating would therefore cause a delay in the pore collapse phenomenon, thus prolonging the elastic phase of the material. This phenomenon has often been explained by the crushing of

the hypothetical calcite bridges present between the grains and has often been given as an explanation for these phenomena. This explanation is nevertheless questioned because if the mechanical bridges were the only reason there should be no resistance after rupture of these bridges. However, in the plastic phase, chalk remains quite resistant (Nadah et al., 2009). It has been shown that the resistance of chalk increases with increasing temperature due to the growth of calcite crystals, the evaporation of water and the agglomeration of calcite grains (Lipin and Trufanov, 2019).

The effect of repeated cooling cycles of an initially hot tank by rapid cold water injection has been less studied. Voake et al. (2019) studied the effect of temperature variation on the tensile strength of two types of chalk. They showed that the presence of water and the anisotropic thermal expansion of calcite are the main weakening mechanisms when chalk is exposed to thermal cycles, in contrast, in dry conditions, chalks have not shown any weakening caused by temperature cycles.

Thus, understanding the behavior of chalk under thermal stress and fluid flow must be based on a multiscale study in which new techniques such as NMR or X-ray CT. Multi-parameter analysis should allow the analysis of petrological characteristics, properties of the porous network and should allow their interactions. Unraveling the variations of physical parameters and rock microstructure then allows a global understanding of the system on a large scale. To obtain an accurate assessment of the microstructure / to understand the microcracking distribution, elastic / mechanical properties and water flow, a wide range of techniques are implemented such as water porosity, absorption tests capillary water (Robert, 2004), mercury porosimetry (Hellmann et al., 2002a), evaluation of the speeds and attenuations of ultrasonic waves (Røgen et al., 2005), nuclear magnetic resonance relaxometry (Faÿ-Gomord et al., 2016), X-ray micro-tomography (Saïag, 2016) and injection fluid analysis (Madland et al., 2011).

The effect on chalk / water interactions is not clear. The differences could be due to the different temperatures between the rock and the injection fluid. And due to the duration of the various physicochemical phenomena which influence the behavior of chalk, it is difficult to draw conclusions on the effects of temperature thanks to fairly rapid standard triaxial or uniaxial compression tests carried out in numerous studies. In the present study, the effect of temperature and water circulation on the evolution of the chalk pore network is investigated

using high resolution techniques. The chalk / water interactions added to thermal stress require a thorough understanding at the laboratory scale in order to become popular at the field scale. Fluids flow and thermal shock tests were performed at contrasting temperatures (cold rock-hot fluid // hot rock-cold fluid). A complementary and high resolution petrophysical characterization of the samples was carried out using techniques specific to the study of rocks (open porosimetry, mercury porosimetry, capillary imbibition kinetics, helium pycnometry, ultrasonic auscultation, NMR, X-ray CT).

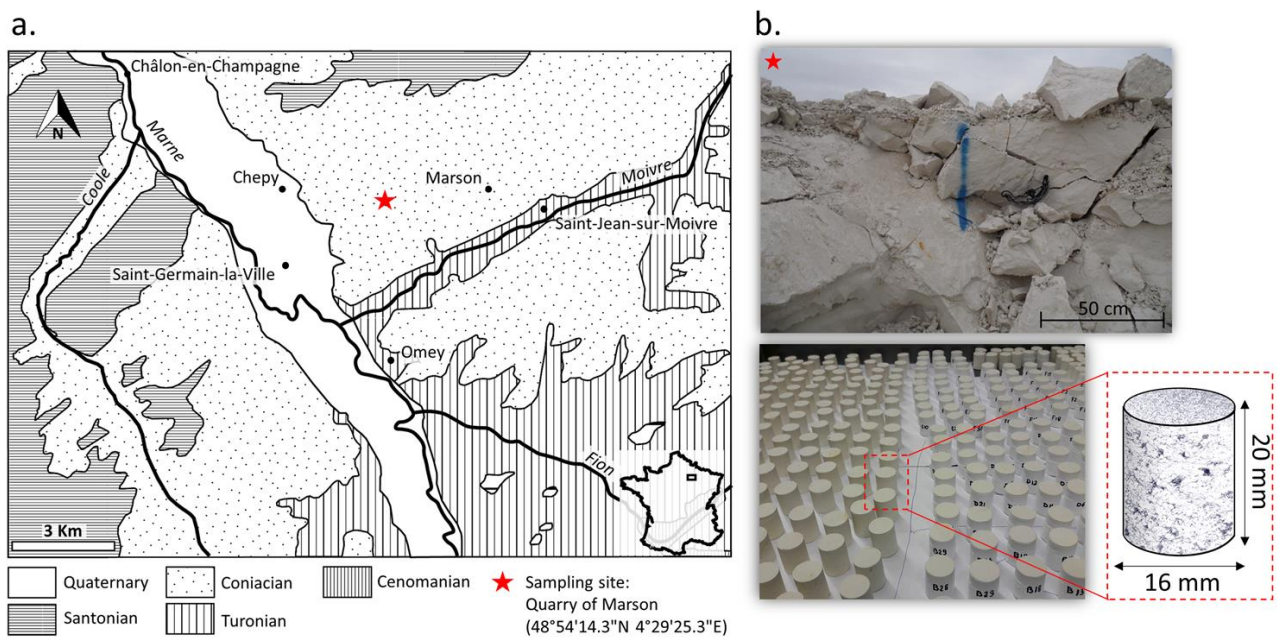
### III.2.2. MATERIAL

The white chalk of Châlons samples was extracted from the Grand Mont quarry (Saint-Germain-la-Ville, Paris Basin, France) (Figure III-17a) along an outcrop dated from the Coniacian (Upper Cretaceous). This chalk is hydrofractured due to the development of vertical tension slots and a normal fault (Coulon and Lamotte, 1988; Richard et al., 1997). To ensure the homogeneity of the samples, the core plug samples were made on the same block and in the same direction (Figure III-17b). Plugs were taken perpendicular to the lamination and were made in the laboratory using a core drill equipped with a diamond drill of the appropriate diameter. Their bases were ground using a chainsaw equipped with diamonds to obtain plugs with very parallel bases. It was made 130 plugs 16 mm in diameter and 20 mm in length.

Thanks to microtectonic analyzes, three successive tectonic episodes have been distinguished in the quarry of the Omev region by (Richard, 1996). The first with an Eocene stalling episode with N-S horizontal shortening. The second in the Oligocene is marked by an extensive multi-directional episode SE-NW to E-W, NE-SW, N-S. The complex networks of tension slots were created during this episode (Richard, 1996). The last tectonic episode date from the Miocene with a shortening NW-SW.

The selected chalk was carried out in an area where the tectonic deformation is very low. This white chalk is characterized by Châlons chalk (micritic chalk, nodular or compact appearance). The thickness of the formation is between 30 and 70 m. This white chalk is relatively tender and presents *Micraster* echinoids (Allouc and Le Roux, 1995). From a mineralogical point of view Châlons chalk appears to consist exclusively of calcium carbonate (98.5% of  $\text{CaCO}_3$ ) (Ballif et al., 1995). The coccoliths observed with SEM appear well preserved (Allouc and Le Roux,

1995) and are arranged without a privileged orientation that defines a punctate structure (Richard et al., 1997).



**Figure III-17. a. Geological and geographical settings of the chalk sampling site (red star). Modified from Richard et al. (1997). b. Sampling outcrop and core plug samples.**

### III.2.3. METHODOLOGY

#### III.2.3.1. Thermal treatment and Analytical procedure

The samples were subjected three sets of different tests. Technical details are listed in Tableau III-2 and sample sizes in Figure III-17b.

The first series of experiments consisted in three capillary water uptake tests at contrasting temperature. For each of the experiments, 150 cycles were performed.

- HR-CF (Hot Rock-Cold fluid) consisted in carrying out capillary water uptake tests with water at low temperatures ( $8 \pm 2 \text{ }^\circ\text{C}$ ) on hot chalk ( $80 \pm 2 \text{ }^\circ\text{C}$ ).

- CR-HF (Cold Rock-Hot Fluid) consisted in carrying out capillary water uptake tests with water at high temperatures ( $80 \pm 2 \text{ }^\circ\text{C}$ ) on a cold chalk ( $8 \pm 2 \text{ }^\circ\text{C}$ ).

- R-F (Rock and fluid at room temperature) consisted in carrying out capillary water uptake tests with water at room temperature on chalk also at room temperature. This test was taken as reference.

The second series of experiments reproduced the three conditions of the first series of experiments but with continuous water flow transfer (10 L).

- C-HR-CF (Continuous-Hot Rock-Cold fluid) consisted in carrying out continuous water flow transfer test with water at low temperatures ( $8 \pm 2$  °C) on hot chalk ( $80 \pm 2$  °C).

-C-CR-HF (Continuous-Cold Rock-Hot Fluid) consisted in carrying out continuous water flow transfer test with water at high temperatures ( $80 \pm 2$  °C) on a cold chalk ( $8 \pm 2$  °C).

- C-R-F (Continuous-Rock and fluid at room temperature) consisted in carrying out continuous water flow transfer test with water at room temperature on chalk also at room temperature. This test was taken as reference.

The third series of experiments consisted in quenching the chalk samples heated to  $80 \pm 2$  °C for 2 hours in water at  $0 \pm 2$  °C for 10 minutes. In this case, also 150 thermal shock cycles (TS) were performed.

**Tableau III-2. List of experiment and specification of measurement conditions**

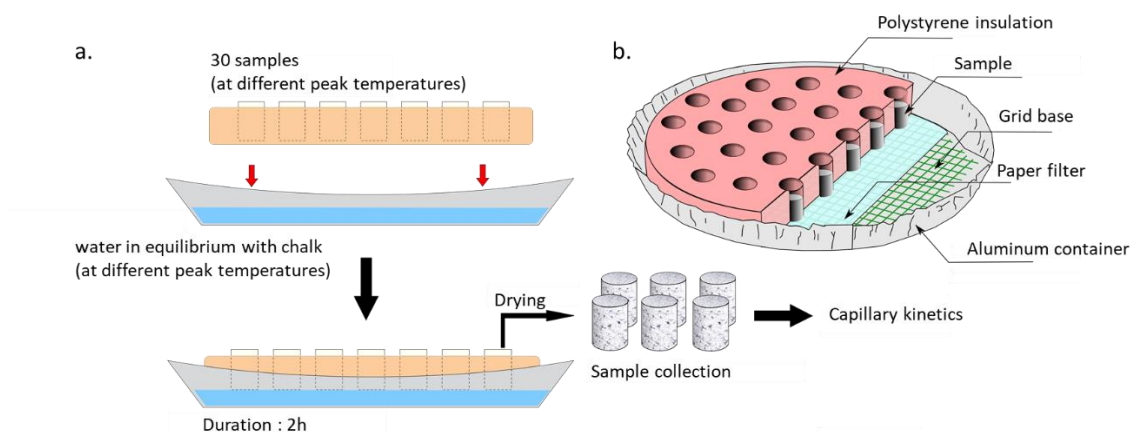
Annotation	Rock	Temperature Fluid	Number of samples (n)	Repetition
<b>Fluid imbibition by capillary action</b>				Number of cycles
HR-CF	$80$ °C ( $\pm 2$ °C)	$8$ °C ( $\pm 2$ °C)	30	150
CR-HF	$8$ °C ( $\pm 2$ °C)	$80$ °C ( $\pm 2$ °C)	30	150
R-F	Room temperature	Room temperature ( $25$ °C)	30	150
<b>Continuous fluid flow</b>				Water volume (L)
C-HR-CF	$80$ °C ( $\pm 2$ °C)	Room temperature ( $25$ °C)	4	10
C-CR-HF	Room temperature	$80$ °C ( $\pm 2$ °C)	4	10
C-R-F	Room temperature	Room temperature ( $25$ °C)	2	10
<b>Thermal shock</b>				
TS	$80$ °C ( $\pm 2$ °C)	$0$ °C ( $\pm 2$ °C)	30	150

### III.2.3.1.1. Fluid imbibition by capillary action (HR-CF / CR-HF / R-F)

The samples were enveloped by Teflon which did not fix water under the experimental conditions applied here and allowed to simulate a unidirectional fluid flow. This experiment required the development of a specific experimental device to ensure that only the bottom area was in contact with the water (Figure III-18). The fluid used in this experiment was water in chemical equilibrium with the constituents of the chalk (largely  $\text{CaCO}_3$ ). The procedure

involves mixing powdered chalk with distilled water to reach saturation. The liquid was chemically close to the composition of the chalk interstitial water, which can be used as injection fluid. This avoided the risk of a major chemical reaction during fluid circulation inside the sample.

Samples and fluids were brought to the set temperature using a *Vötsch* climatic chamber. The samples were then placed in the insulating support at defined locations and so that they only partially rest on their base, no evaporation has taken place from the side surface. Water was added to the aluminium container up to a depth of  $(3 \pm 1)$  mm and the capillary water uptake started. After 2h, enough to reach saturation, the same 6 samples were taken out of the dispositive and a new capillary test was carried out to determine the Capillary coefficient evolution NF EN 1925, (1999). The measuring frequency was as follows: every cycle from cycles 1 to 10, every 2 cycles from 10 to 50, every 5 cycles from 50 to 100 and every 10 cycles of 100 to 150.



**Figure III-18. Experimental setup of a sample submitted to capillary absorption at contrasted temperature.**

During the HR-CF test, the temperature of the sample was monitored by 3 thermocouples inserted into the center of the sample and positioned at three heights, top, middle and bottom of the cylinder (Figure III-19). The cooling kinetics for the first few minutes was  $1\text{ }^{\circ}\text{C} / \text{second}$  for the bottom part and  $0.5\text{ }^{\circ}\text{C} / \text{second}$  for the upper part.

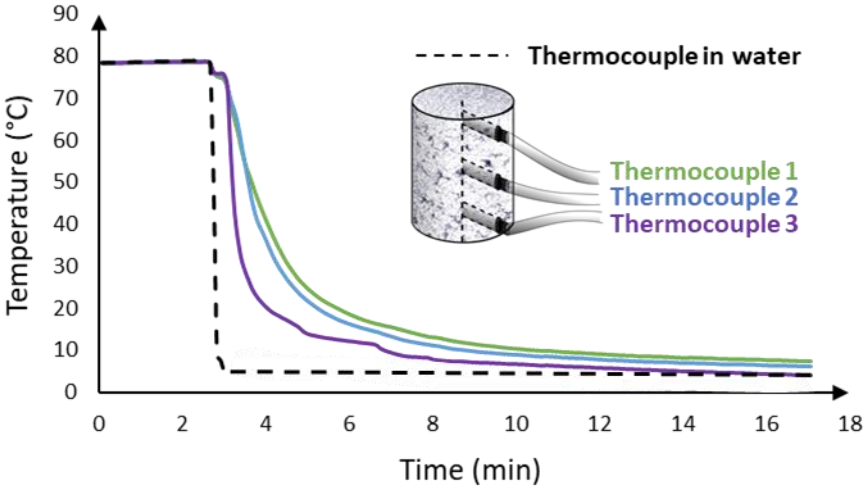


Figure III-19. Temperature monitoring during the HR-CF experiment and instrumented sample.

III.2.3.1.2. Thermal shock (TS)

In order to simulate the rapid cooling in the samples, a succession of quenching were carried out.

They consisted in heating the sample to 80 °C using a *Vötsch* climatic chamber for 2 hours followed by and abrupt immersion in water refrigerated at 0 °C for 10 minutes. The protocol used is the recommended by Standard NF EN 14066, (2013) with neutral pH water. This is adjusted for the heating times compared to the small size of our samples. To assess the evolution, 6 samples were collected in order to determine the coefficient of water absorption by capillarity (C) every 5 cycles (Figure III-20).

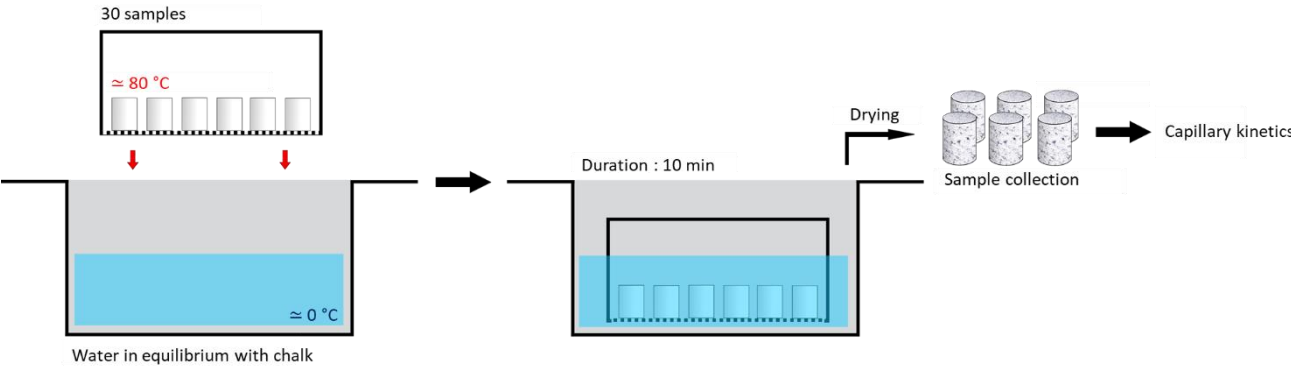


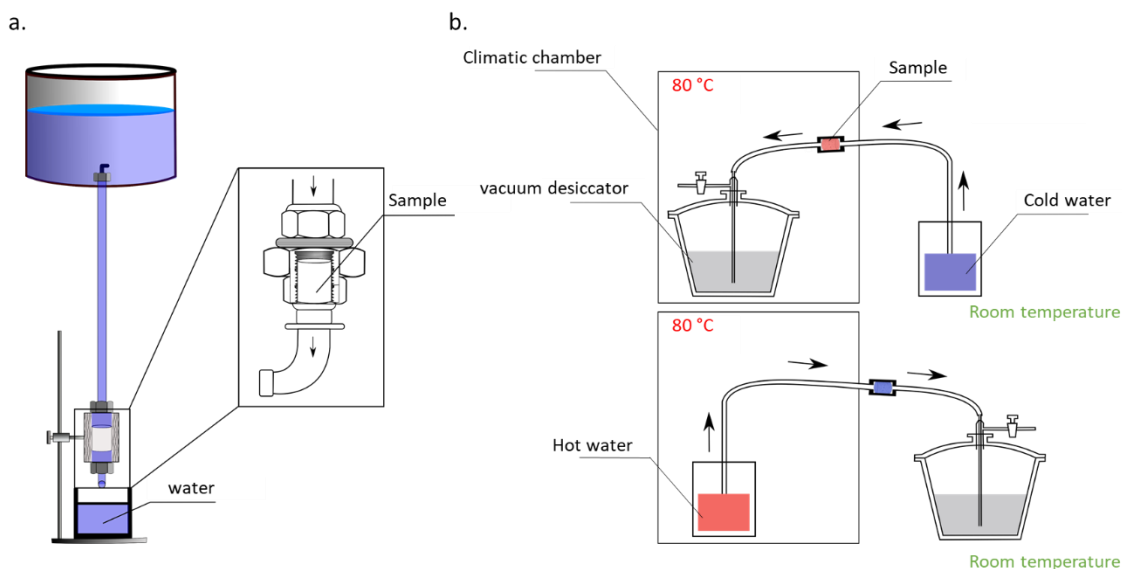
Figure III-20. Setup designed for thermal shock TS testing.

### III.2.3.2. Continuous fluid flow (C-R-F / C-HR-CF / C-CR-HF)

A laboratory device was set up to circulate a fluid continuously through chalk samples (Figure III-21). The fluid used in this experiment was water in chemical equilibrium with the constituents of chalk. A chalk cylinder was confined within the device, surrounded by Teflon and sealed with vacuum grease to prevent side leakage. A pressure gradient was applied to a surface of the sample due to the hydraulic head exerted by the water column. After flow on 10 L of fluid through the sample, water was recovered into a container. These samples were be assessed by capillary imbibition tests in their initial state and after 2 / 4 / 6 / 8 / 10 liters of elapsed water.

This test was carried out at room temperatures for all the composants (Figure III-21a) and also at contrasted temperatures (Figure III-21b).

In the latter, vacuum dryers were used to draw air and allow water to be drawn into the pipe containing the sample. The element that must be heated 80 °C and maintained 2h (water or sample depending on the test C-CR-HF or C-HR-CF) were placed in a climatic chamber at the set temperature (Tableau III-2).



**Figure III-21. Experimental device for the simulation of continuous fluid flow. a. C-R-F test at room temperature. b. C-HR-CF / C-CR-HF tests at contrasted temperature.**



### III.2.3.3. Techniques of evaluation

#### III.2.3.3.1. Porosity

Connected porosity ( $\phi_c$ ) is defined as the ratio of the volume of connected voids to the total volume of rock. In this study, the experimental protocol followed the standard NF EN 1936, (2007). The dried samples were weighed and placed in a desiccator where the pressure was gradually lowered with a vacuum pump to remove any air from the pores. The vacuum was maintained for 1 hour in order to remove all the air contained in the pores. In a second desiccator, water was degassed for 2 hours. The two desiccators were connected in order to gradually introduce the degassed distilled water into the desiccator containing the samples. The ascent speed was set in such a way that it did not exceed 15 min. The samples were left on the water for 24 hours and then the saturated and hydrostatic mass weighed. The porosity was obtained using the triple mass method. All samples were tested in their initial state, after 50 and 150 cycles for the capillary and thermal shock tests and in the initial and final state for continuous circulation tests (Tableau III-2).

Porosity calculated by Mercury Injection Porosimetry ( $\phi_{MIP}$ ) was executed to compute the distribution of porosity versus threshold size thanks to a micromeritics AutoPore IV 950. The mercury intrusion is performed in two stages (low- and high-pressure measurements). Mercury injection pressures ranged from 0.004 to 228 MPa, giving corresponding pore access radii of 180 to 0.003  $\mu\text{m}$ , respectively. Equilibrium time settings were 30 s for low- and high-pressure cells. When the pressure is released, the porous network empties of the mercury with which they were filled, starting with the finest throats. The released pore space represents the free porosity and the volume of mercury that has not been removed represents the trapped porosity. The protocol for this technique requires a small sample size. The small cores of this study allowed to be used without re-dimensioning, which could produce additional damage to the rocks. 10 samples were tested in the initial state and for all of the fluid circulation tests by capillarity (HR-CF / CR-HF / R-F) and thermal shock (TS) 1 samples were tested in the initial state, 50, 100 and 150 cycles.

#### III.2.3.3.2. Capillary water uptake tests (CWUT)

Capillary water uptake is a non-destructive test that allows determining in a simple way the connectivity and the homogeneity of the porous network. The mechanism of capillary

absorption of water is directly related to the porous network (pore size, shape of the pore system and connection of the network) (Mertz, 1991; Tomašić et al., 2011). The water absorption coefficient obtained during the test is often used as an estimator of rock degradation. It is inversely linked to the durability of stone (Benavente et al., 2004; Çelik and Kaçmaz, 2016; Fronteau et al., 2010; Sengun et al., 2014). Knowing the movement of water inside the rock is a simple way to assess the porosity of the rock (Fronteau et al., 2010). Thus rocks characterized by large pores and high connected porosity will exhibit high water absorption coefficient values (Beck et al., 2003; Benavente et al., 2002).

Based on the NF EN 1925, (1999), the samples were dried at  $40 \pm 5$  °C before each test until their weight stabilised. The principle of the experiment was to put the previously dried chalk in contact with a light film of water distilled water. Thus, the non-wetting fluid (air) initially in the pores is replaced by the wetting fluid (distilled water) without external pressure applied. Capillary kinetics are usually characterised by two phases (Hammecker et al., 1993; Hammecker and Jeannette, 1994). The first phase is the progressive filling of the free porosity by the capillary forces of water without external pressure applied. The slope of this curve represents the capillary coefficient (C) (Roels et al., 2000) that is the volume of water penetrated by capillarity into the rock per unit of square root of time according to the Washburn law ( $\text{g}\cdot\text{m}^{-2}\cdot\text{s}^{-1/2}$ ).

### III.2.3.3.3. Elastic rock properties and deduced mechanical properties

The monitoring of the ultrasonic signal is effective in evaluating the characteristics of the pores of the rock because it depends mainly on the size, connectivity, and distribution of the pores, the lithology, and the bedding plans. P- and S-waves propagation velocities ( $V_p$  and  $V_s$  respectively) were measured using equipment for receiving non-transmitting signals (PunditLab ProceeQ tester). The transducer frequency was centered on 2.5 MHz for P-waves and 1 MHz for S-waves. To ensure the optimal transmission of ultrasonic waves between the transducers and the surface of the sample, constant pressure was systematically applied between the transducers and the sample and a visco-elastic coupler was used. All samples were tested in their initial state, after 50 and 150 cycles and in the initial and final state for continuous circulation tests.

The Young's dynamic modulus ( $E$ ) and the Poisson's ratio ( $\nu$ ) were calculated following the equations (III. 11 and III. 12):

$$\nu = \frac{\frac{1}{2} - \left(\frac{V_s}{V_p}\right)^2}{1 - \left(\frac{V_s}{V_p}\right)^2} \quad (\text{III. 11})$$

$$E = \rho g \frac{V_p^2(1 + \nu)(1 - 2\nu)}{1 - \nu} \quad (\text{III. 12})$$

In order to estimate the damage caused by the cycles, two thermal damage variables, related to the Young's modulus and the P- wave velocity were calculated using the equation (III. 13) and (III.14):

$$D_E = 1 - \frac{E_f}{E_i} \quad (\text{III. 13})$$

$$D_v = 1 - \left(\frac{V_{pf}}{V_{pi}}\right)^2 \quad (\text{III. 14})$$

Where  $D_E$  and  $D_v$ , are the thermal damage variables calculated by Young's modulus and the speed of the P wave and  $E_i$  and  $V_{pi}$  are the Young's modulus and P-wave velocity at intiale state, and  $E_f$  and  $V_{pf}$  are the Young's modulus and P-wave velocity at the final state.

### III.2.3.3.4. Nuclear Magnetic Resonance (NMR) relaxometry

Nuclear magnetic resonance in porous media (NMR) is a rapid and non-destructive technique. NMR has become essential in the characterization of the properties of reservoirs. The measurement is useful for characterizing porous structures, going as far as characterizing the distribution of fluids in the pore volume. Between the 1960s and 1980s the magnetic resonance relaxation method was widely used for petrophysical analysis and well logging in petroleum operations (Timur, 1972, 1969). Recently this method has been developed in order to characterize the properties of porous networks in reservoir rocks.

Nuclear Magnetic Resonance (NMR) methods are based on the decay by magnetisation of the hydrogen nucleus of water and useful for the deduction of certain information on the structure of pores (distribution pore) (Liu et al., 2017; Tian et al., 2020; Weng et al., 2018). The NMR measurements were performed using a minispec mq-Series instrument (Figure III-22). The rock samples were vacuumed and saturated for 24 h and were then soaked in water for

24 h to fill the rock material. For the measurement, the sample was taken out from the water and instantly integrated into a hermetic support before being placed in the NMR. That maintained the saturation during the whole analysis.

The transverse relaxation time (T2) was measured with a Carr-Purcell-Meiboom-Gill (CPMG) sequence at regular time intervals  $2\tau$  (or TE) of 100  $\mu\text{s}$ . Dynamics Center software (Version: 2.5.5) was used to represent the distribution of T2 relaxation times (the amplitudes  $A_i$  as a function of T2i) obtained thanks to an inverse of Laplace transformation. These are the surface effects and the physical properties that are used in nuclear magnetic relaxation in porous media.

According to the basic characteristics of NMR measurements in rock, T2 is expressed by:

$$\frac{1}{T2} = \frac{1}{T2b} + \rho \frac{S}{V} + \frac{1}{12} (TE\gamma G)^2 D \quad (\text{III. 15})$$

Where T2 represents the transverse relaxation time,  $\rho$  is the specific surface relaxivity (Assuming a relaxivity  $\rho$  of 10  $\mu\text{m}\cdot\text{s}^{-1}$  attributed to carbonate rocks, Hurlimann et al. (1994). T2b represents the relaxation time of the fluid saturating the porous space (2700 ms for water at 30 °C), S is the surface and V the volume of the pore considered, TE is the inter-echo time of the CPMG sequence; we set it at 100  $\mu\text{s}$ , G is the average local magnetic field gradient,  $\gamma$  is the gyromagnetic ratio and D is the auto-diffusion coefficient of the fluid. The term diffusion can be neglected in equation (III. 15) because T2 is independent of the inter-echo time (very weak in this experiment).

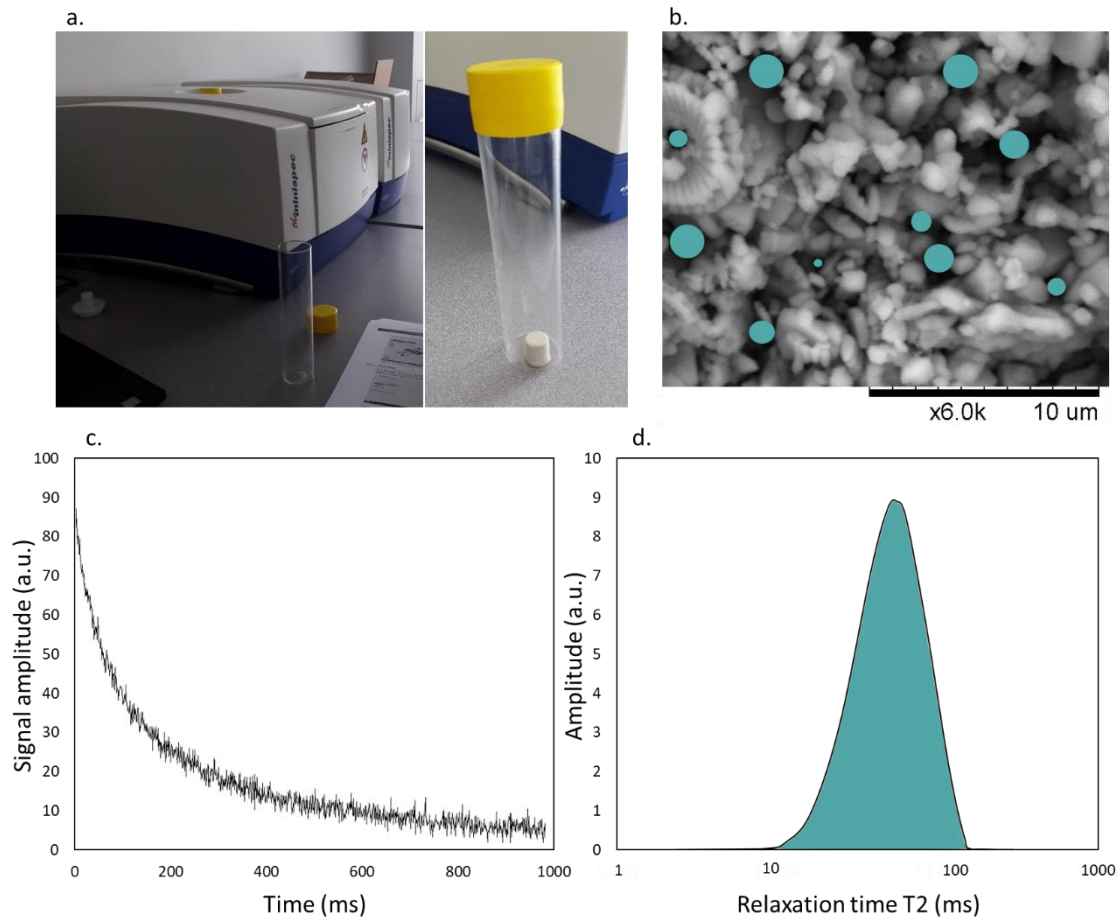
The geometry of our pores must be hypothesised. In the monophasic case, the spherical pores have a surface ratio of:

$$\frac{S}{V} = \frac{3}{r} \quad (\text{III. 16})$$

where r is the pore radius. If the pores are considered spherical, the equation can be simplified as follows (III. 17):

$$\frac{1}{T2} = \frac{1}{T2b} + \rho \frac{3}{r} \quad (\text{III. 17})$$

The values of T2 were taken before and after cycles. The T2 distribution reflects the information on the pore size, the smaller the T2 value, the smaller the pore size.



**Figure III-22. Summary of the use of NMR in the analysis of porous rocks. a. Photograph of minispec mq-Series instrument and the hermetic support containing the sample. b. SEM image of the chalk to visualise pores, the blue circles are detected by NMR. c. The transverse magnetisation decay curve. d. The transverse relaxation time (T<sub>2</sub>) distribution curve constructed by a mathematical inversion process (the curve reflects a distribution of pore, surface to volume ratios  $V / S$ ).**

All samples were tested in their initial and final state and 3 samples were taken at 50 and 100 cycles for analysis.

### III.2.3.3.5. X-ray microtomography (X-ray CT)

X-ray microtomography (X-ray CT) is a non-destructive technique that permits to visualise in 3D the modifications of the porous network at high resolution, without sample preparation or chemical fixation. As a result, the natural characteristics of the mineralogical information and the porous network have been maintained. X-ray tomography imaging was performed on a Phoenix Nanotom S with a maximum voltage of 180KV / 15W. An X-ray source generates

beams which pass through the sample placed on a 360 ° rotating stage, leaving shadow projections on the detector and acquiring several 2D X-ray absorption images (Figure III-23).

A sound sample of the size of 1.6 cm in diameter and 2 cm in height was analyzed with a resolution of approximately 1 voxel = 16 μm. In order to increase the resolution of the potential modifications at the end of the 150 cycles of HR-CF and CR-HF experiments, two samples were cored with a diameter of 0.5 cm on the original ones. The resolution was approximately 1 voxel = 4.5 μm.

At the end of the acquisition process, the VGStudio MAX 2.2 © software (Volume Graphics) was used to perform the reconstruction and its qualitative and quantitative analysis.

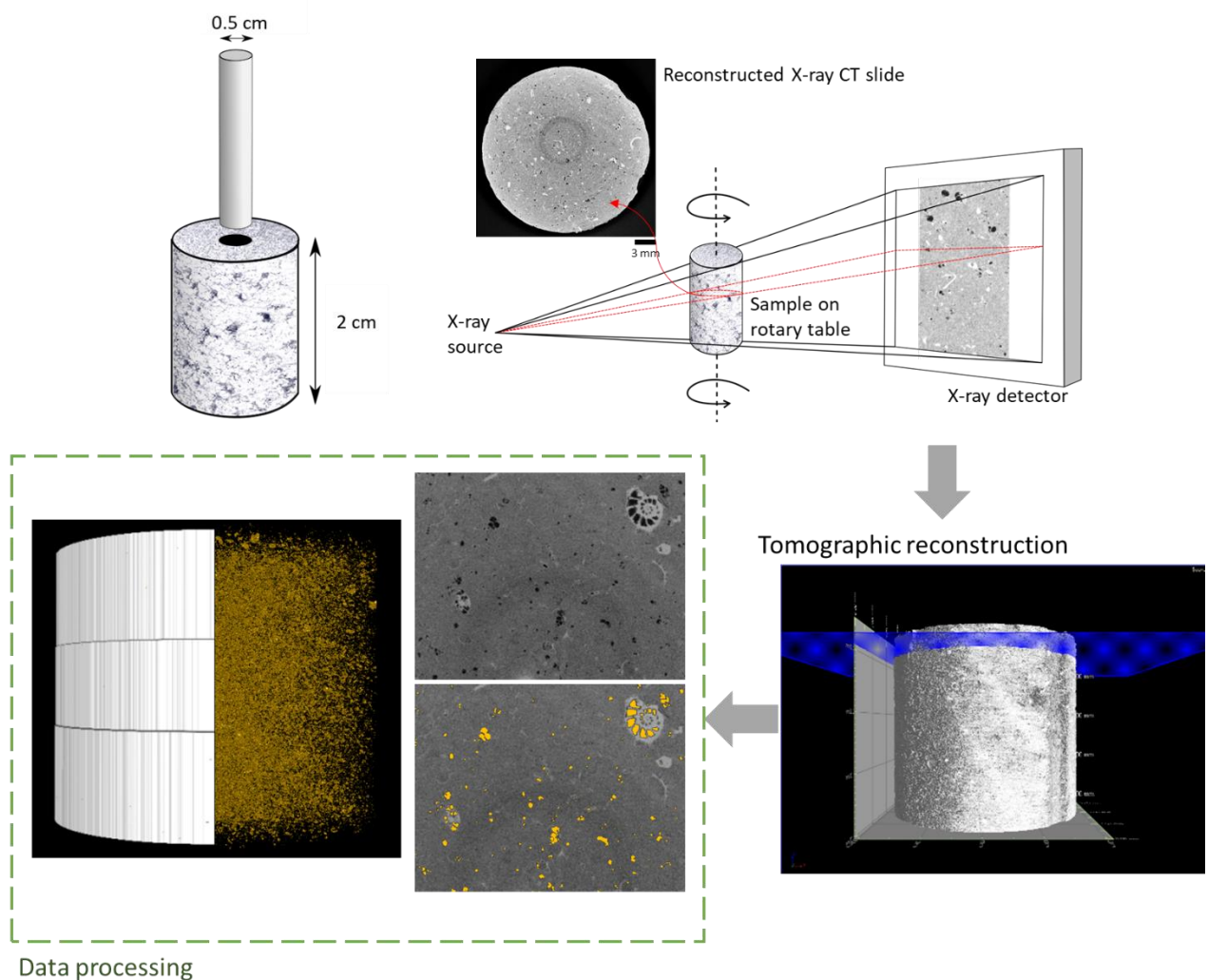


Figure III-23. Summary of the use of X-ray micro-tomography in the analysis of porous rocks.

### III.2.3.3.6. Permeability

The permeability was estimated from equation (III. 18) which uses the capillary coefficient, the water properties and the microstructural parameters of the rock (Benavente et al., 2015):

$$k = C^2 \frac{\eta r}{4\phi \rho^2 \gamma \cos\theta} \quad \text{(III. 18)}$$

With the coefficient of water absorption by capillarity (C), the density ( $\rho$ ) and the viscosity of water ( $\eta$ ), the interfacial tension ( $\gamma$ ), the contact angle ( $\theta$ ), the radius of mean pore (NMR) ( $r$ ) and connected porosity ( $\phi$ ).

Chalk is often defined as a material with a strong affinity for wetting and the contact angle  $\theta$  has been considered zero.

## III.2.4. RESULTS

### III.2.4.1. Porosity (connected porosity $\phi_c$ ; porosity by mercury injection $\phi_{MIP}$ )

The different connected porosity values as a function of the cycles and the different tests are shown in Tableau III-3. It was observed that the pore volume trended to increase slightly in the capillary tests, although the standard deviation did not allow to state a significant change. For the thermal shock the results remained similar.

**Tableau III-3. Connected porosity  $\phi_c$  (%)**

Cycle Test	Initial state		50		150	
	Avg.	St.d	Avg.	St.d	Avg.	St.d
HR-CF (n=30)	39.5	2.8	39.7	2.76	40.4	2.2
CR-HF (n=30)	39.8	1.9	40.0	1.81	40.5	1.3
R-F (n=30)	38.8	2.4	39.1	2.30	39.5	2.0
TS (n=30)	40.2	1.9	40.2	2.09	40.0	1.7

Avg. average, St.d. standard deviation

The MIP porosities are shown in the Figure III-24. The 10 samples measured in the initial state exhibited an average total porosity of  $37.9 \pm 4.2\%$ . The results of the pore access rays showed an unimodal distribution of the threshold pore access rays between 0.04 to 0.40  $\mu\text{m}$  with a median pore of approximately  $0.28 \pm 0.005 \mu\text{m}$ . The trapped porosity was measured from the

MIP extrusion curves of the samples (except for 1 sample from the R-F tests and 2 for the TS tests). This porosity represented approximately 60% of the total porosity in the initial state. The mercury trapping is controlled by the size, shape, surface condition, and roughness of the pores and throat, the coordination number, random and non-random heterogeneities (Wardlaw and McKellar, 1981). The large value of the trapped porosity must have been due to the large difference between the size of the pores and their accesses (Richard et al., 2007). During the mercury extrusion, the capillary end locked the structure. The trapping took place mainly in the macropores of the porous network, access to which was achieved through finer capillaries.

For the hot rock-cold fluid (HR-CF) test the porosity and the median pore radius increased with the number of cycles. The porosity of 43.4% at cycle 100 was the most important porosity measured any test combined.

For the cold rock-hot fluid (CR-HF) test the porosity did not show any noticeable change. In contrast, the median pore radii decreased at cycle 100.

For the room temperature (R-F) test the pore size increased no more than in the other tests.

For thermal shock (TS), the median pore radius increased after 50 cycles, it showed in at the end of the 150 cycles a decrease to 0.27  $\mu\text{m}$ .



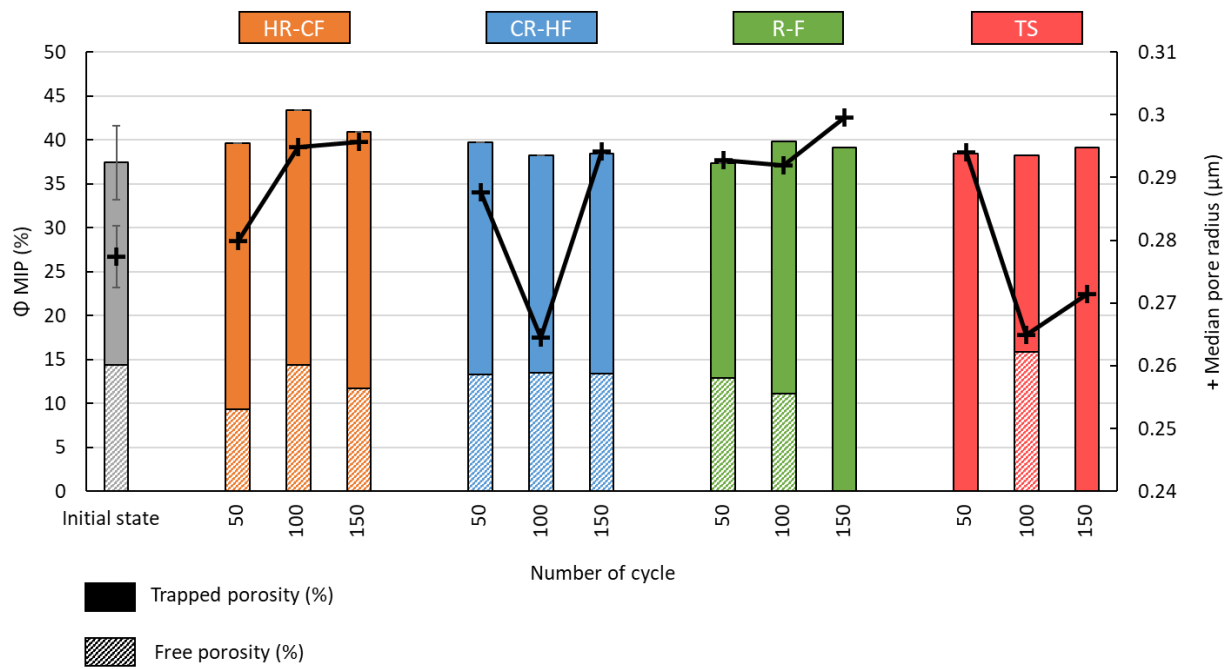
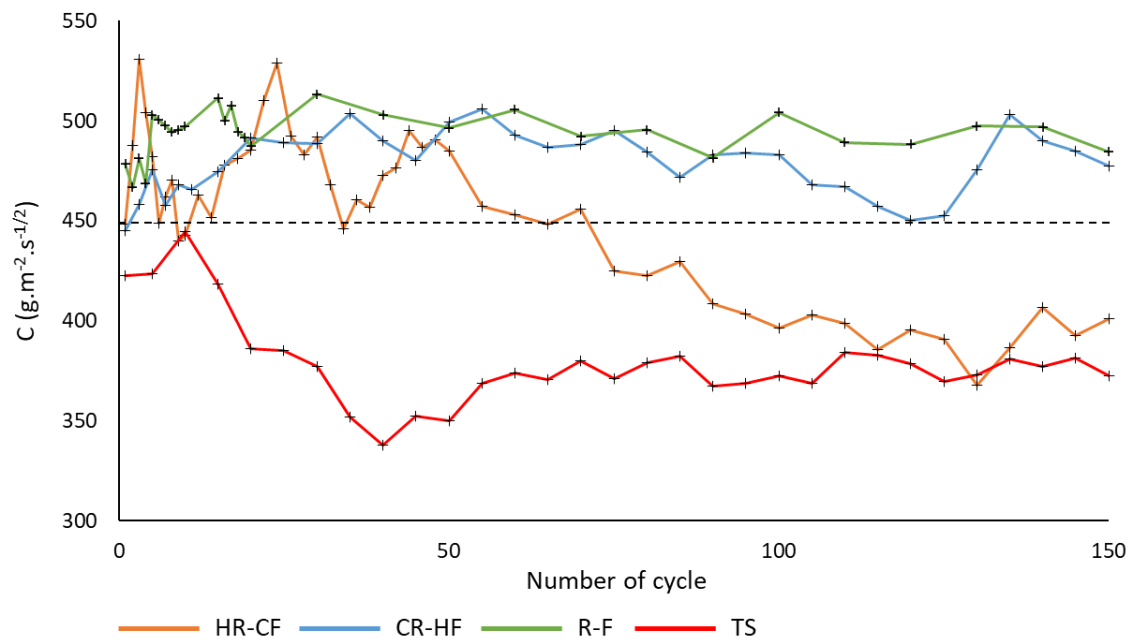


Figure III-24. Porosity by mercury injection  $\phi$ MIP (%) (free and trapped) and the value of the median radius ( $\mu\text{m}$ ). Initial state  $n = 10$  and for the remainder  $n = 1$ .

#### III.2.4.2. Capillary coefficient

Figure III-25 shows the evolution of the capillary coefficient  $C$ . The capillary water uptake test was performed to interpret the flow of a fluid in the microporous network. Due to the small size of the samples, 5 minutes of experience was enough for the capillary absorption to begin to stabilize. The mean capillary coefficient of all samples tested in their initial state was  $448 \text{ g}\cdot\text{m}^{-2}\cdot\text{s}^{-1/2}$ , which was represented by the black dotted line.



**Figure III-25. Relationship between the number of cycles and the capillary coefficient (C) for capillary imbibition fluid flow tests.**

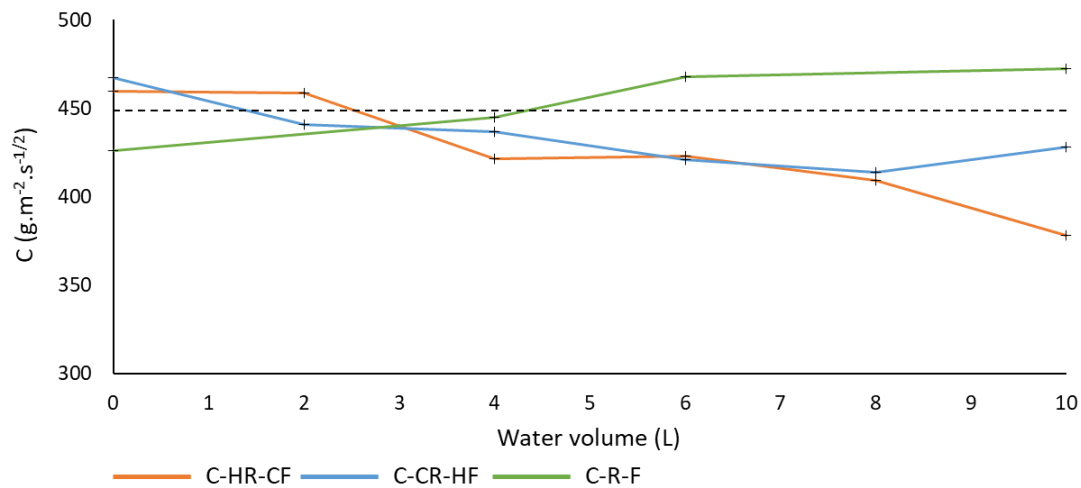
The test (HR-CF) shows a first phase of balancing with significant variations in the 40 first cycles, with a notably increase of 20% in cycle 5 and 25. From cycle 50, the coefficient C decreased progressively until at minus 20% in cycle 130.

For the test (CR-HF), the C coefficients are from the first cycle higher than the initial state. During the cycles there was a maximum increase of 15% after 55 cycles. A decrease was then observed up to cycle 120 to finally show a 15% increase in cycle 135.

After an increase of 7% in cycle 15, the test coefficient (R-F) changed little. It showed variations less than 5% up to cycle 150.

For thermal shocks (TS), after a slight increase of 5% in cycle 10, the coefficient C decreases significantly up to minus 20% in cycle 40. After this rapid decrease, the coefficient increased slowly again until cycle 150.

The change in the coefficient C before and after the continuous circulation of 10 liters of water in rocks with contrasting temperatures is shown in Figure III-26.

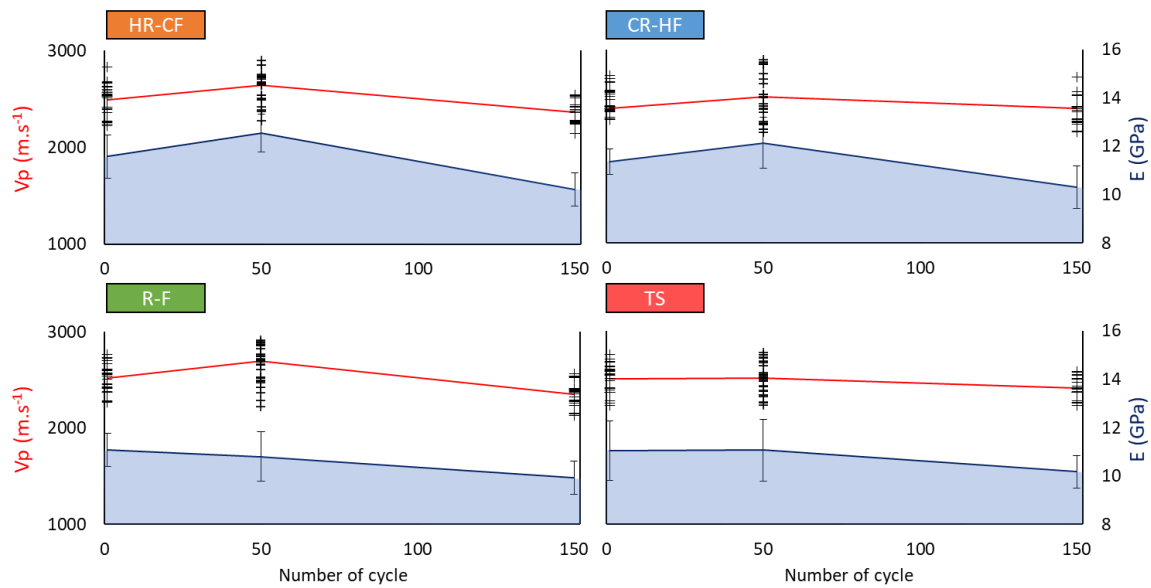


**Figure III-26. Relationship between the number of cycles and the capillary coefficient (C) for continuous fluid flow tests.**

The C-HR-CF and C-CR-HF tests showed a decrease with a similar progression, and at the end of the test the reduction was about 20 and 10%, respectively. The C-R-F test showed the opposite behavior with an increase of 10%.

#### III.2.4.3. P-waves velocities and dynamic elastic moduli

Figure III-27 shows the changes in the mean P wave propagation velocities ( $V_p$ ) and Young's modulus (E) of the capillary imbibition water flow tests. The mean of  $V_p$  and E of all samples tested at baseline were  $2495 \text{ m}\cdot\text{s}^{-1}$  and 11.3 GPa, respectively.



**Figure III-27. Relationship between the number of cycles and P-waves propagation velocities and the Young's dynamic modulus (E) for capillary imbibition fluid flow tests.**

The small variations in  $V_p$  and  $E$  across the cycles are consistent with the small variations in the connected porosity  $\varphi_c$  that were measured. The HR-CR, CR-HF and TS test did not show a significant change in  $V_p$ . In contrast,  $E$  decreased by minus 12%, 10% and 7%, respectively, at the end of the 150 cycles. The R-F test showed a 13% and 10% decrease in  $V_p$  and  $E$ , respectively.

The evolution of  $V_p$  and  $E$  before and after the continuous 10 liters of water flow in rocks with contrasting temperatures is shown in Tableau III-4.

**Tableau III-4. P- and S-waves propagation velocities and the Young's dynamic modulus (E) for continuous fluid flow tests.**

	$V_p$ ( $m \cdot s^{-1}$ )				$V_s$ ( $m \cdot s^{-1}$ )				$E$ (GPa)			
	Initial State		Final State		Initial State		Final State		Initial State		Final State	
	Avg.	St.d	Avg.	St.d	Avg.	St.d	Avg.	St.d	Avg.	St.d	Avg.	St.d
C-HR-CF (n=4)	2471	87	2466	152	1251	19	1228	36	11.4	0.3	11.0	0.7
C-CR-HF (n=4)	2457	79	2492	160	1259	127	1219	106	11.4	1.9	11.0	1.8
C-R-F (n=2)	2621	53	2672	345	1430	116	1321	270	14.3	1.6	13.0	4.9

For the 3 tests the values of  $V_p$  did not change. The E values decreased by 3, 5 and 10% for C-HR-CF, C-CR-HF and C-R-F, respectively.

### III.2.4.4. Nuclear Magnetic Resonance relaxometry

The logarithmic mean of the T2 distribution of the sound samples was  $39.9 \pm 4.8$  ms. The major T2 peak distribution ranged from 8 ms to 88 ms with a mode at 46.5 ms. The measurements of the T2 distribution obtained by inversion of the T2 relaxation curve performed after 50, 100, 150 cycles are shown in Figure III-28. The y axis represents the amplitude of the signal and the x axis is time in milliseconds. For saturated chalk samples, the decay of the T2 magnetization of the CPMG measurement is dominated by a single exponential behavior with a major peak (Megawati et al., 2012). The distribution spectra also show minor peaks of lower intensity (Faÿ-Gomord et al., 2016), here between about 300 and 400 ms.

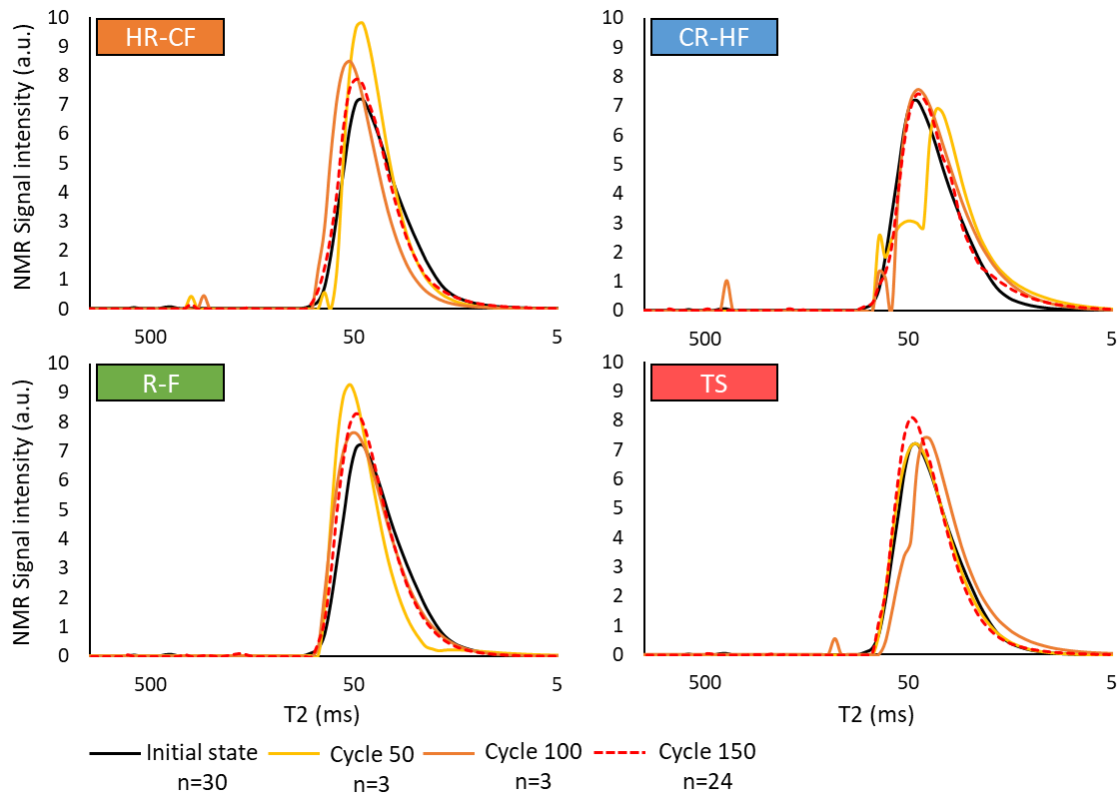
In general, for the circulation tests by capillary imbibition, it was noted important variation of the signal after 50 cycles then gradual return to the initial conditions at 100 and 150. On the other hand the thermal shock tests showed these most important modifications during the last cycle.

For the test (HR-CF), the distribution of samples shifted to the left and showed longer relaxation times. The signal amplitude increased after 50 cycles. After 150 cycles, the major peak mode was 49 ms.

For the test (CR-HF), the distributions resemble those of the initial state. There is a reduction in signal amplitude and relaxation time after 50 cycles and the appearance of a secondary peak at 39.2 ms after 100 cycles.

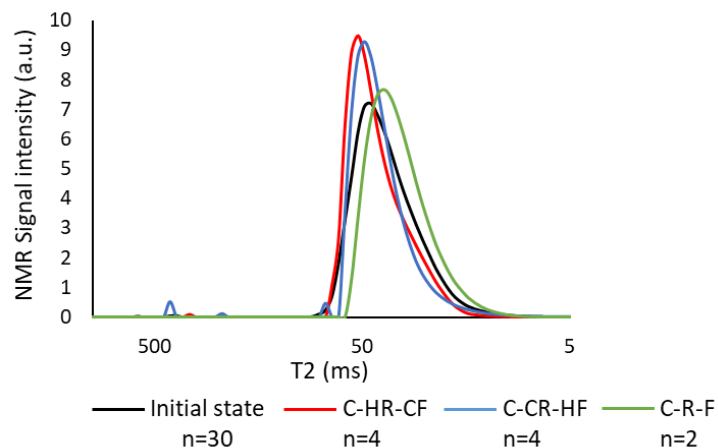
For the test (R-F), the distribution showed longer relaxation times during cycles. The major peak mode was 51 and 49 ms after 50 and 150 cycles, respectively.

For thermal shock (TS), the 50 cycles distributions showed no change. After 100 cycles, faster relaxation times were observed. The final state after 150 cycles showed slightly slower relaxation times with a major peak mode at 47.5 ms.



**Figure III-28. Incremental NMR obtained by inversion of the relaxation curve on fluid flow tests by capillary imbibition.**

The T2 distribution measurements before and after the continuous 10 liters flow of water in rocks with contrasting temperatures is shown in Figure III-29.



**Figure III-29. Incremental NMR obtained by inversion of the relaxation curve on continuous fluid flow tests at initial state and after 10 liters.**

The C-HR-CF and C-CR-HF tests showed a shift of the peak to the left, a distribution that appeared to be more homogeneous (narrow distribution), and the major peak mode was at 53 and 49 ms, respectively. The room temperature test does not show a clear change in amplitude but a reduction in relaxation time with the major peak mode at 39 ms.

### III.2.4.5. Microstructural analysis with X-ray CT

The frequency of appearance of pore rays from 12 to 52  $\mu\text{m}$  is indicated in Figure III-30 for each sample, in intervals of 2  $\mu\text{m}$ . The larger sample size measured at the initial stage showed lower resolution and did not account for pores smaller than 8  $\mu\text{m}$  in radius.

Pores larger than a radius of 10  $\mu\text{m}$  represent 85, 45, and 55% of the total pore volume for the initial state, HR-CF test, and CR-HF test, respectively.

The porosity calculated by X-ray CT ( $\varphi_{\text{CT}}$ ) was 0.42% at the initial state. The pore volume of the HC-CF and CR-HF tests were higher due to the consideration of smaller radius. The comparison of the 2 samples showed a higher porosity by a factor of 2 for the CR-HF test.

The geometric parameters of the individual pores derived from the X-ray CT data are shown in Tableau III-5. The analysis of the 3D pore networks allowed us to evaluate potential changes in pore shapes. For the 3 samples analyzed, the sphericity (with the value 1 as a perfect sphere) of the pores was identical.

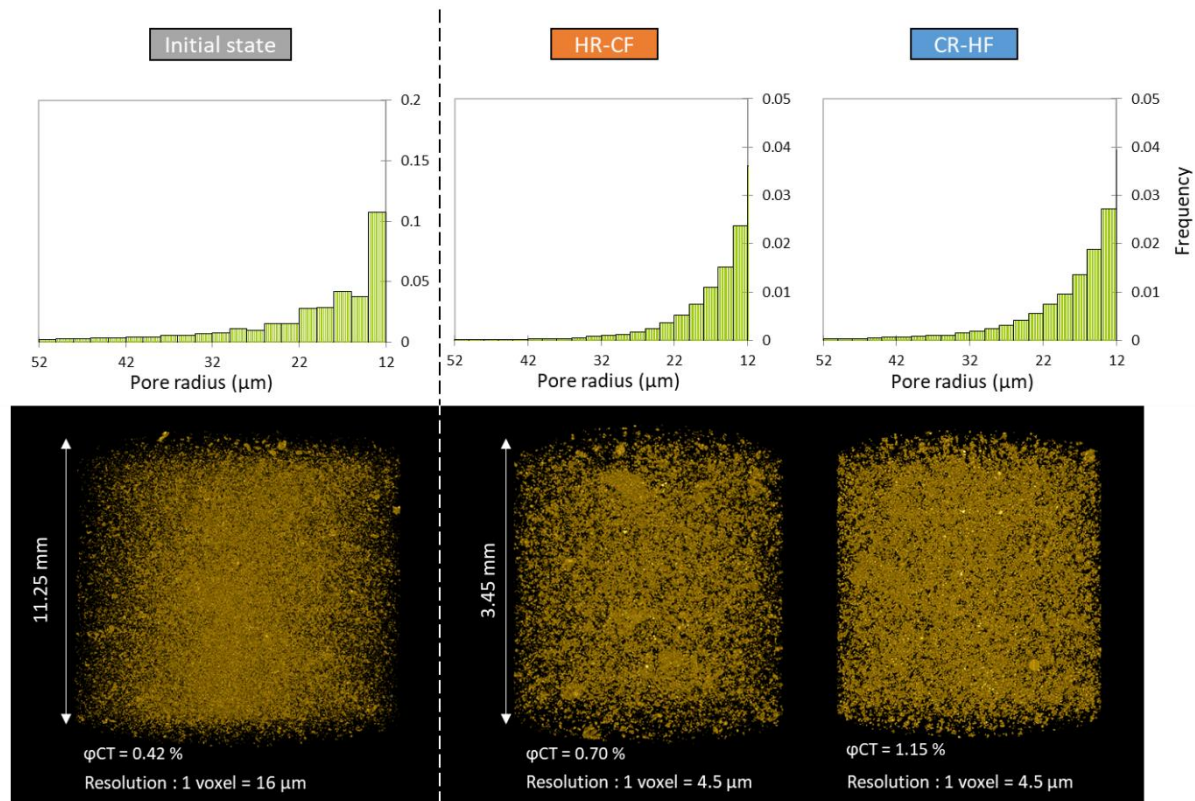


Figure III-30. Distribution of the pore radius ( $\mu\text{m}$ ) (distribution interval:  $2 \mu\text{m}$ ) and reconstruction of the 3D porous network.

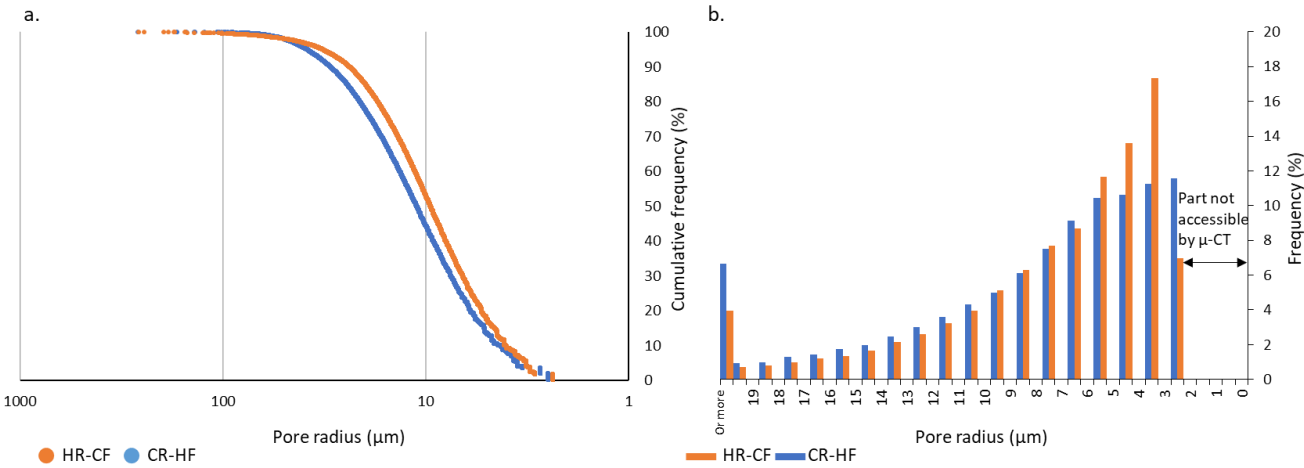
Tableau III-5. Geometrical parameters of individual pores derived from X-ray CT data.

	Diameter ( $\mu\text{m}$ )				Volume ( $\mu\text{m}^3$ )				Sphericity			
	min.	max.	Avg.	St.d.	min.	max.	Avg.	St.d.	min.	max.	Avg.	St.d.
Initial state (n = 132110)	17.9	578.9	36.9	26.0	1535.7	13174615	16883	99523	0.2	0.8	0.6	0.1
HR-CF (n = 88656)	4.7	800.1	15.6	13.1	21.6	8419074	1715	30797	0.1	0.8	0.6	0.1
CR-HF (n = 100834)	5.0	688.7	17.6	14.7	33.1	2613881	2479	16977	0.1	0.8	0.6	0.1

Min. minimal, Max. maximum, Avg. average, St.d. standard deviation

As shown in Figure III-31a, the X-ray CT method identifies large pores. However, the almost horizontal progression of the curve for radii greater than  $50 \mu\text{m}$  indicated that this pore volume was in the minority. It was observed that the 2 curves resulting from the contrasted temperature tests, the low resolution X-ray CT method identified smaller pores. It was also observed that the HR-CF test exhibited a greater quantity of pore with a radius of between 3 and 6. For all of the remaining pore sizes, the CR-HF test exhibited a greater quantity of pore (Figure III-31b).





**Figure III-31. a. Cumulative distribution of the pore radius of the total interparticle voids and distribution of the pore radius (µm) (distribution interval: 1 µm) between 0 and 20 µm for the HR-CF and CR-HF test.**

**III.2.5. DISCUSSION**

Chalk-water interactions have received considerable attention due to the weakening phenomena that can occur in certain reservoirs. This behaviour of chalk in contact to water results from numerous physico-chemical mechanisms such as modification of capillary forces, dissolution, compaction or adsorption pressure (Delage et al., 1996; Heggheim et al., 2005; Hellmann et al., 2002b; Newman, 1983; Risnes et al., 2003; Schroeder et al., 1998). In order to discuss the effects of the various tests on the chalk porous network, the detail of the petrographic parameters is listed in Tableau III-6. The end state corresponds to 150 cycles of capillary imbibition flow tests and 10 L of fluid circulated in continuous experiments.

Tableau III-6. Initial and final petrographic parameters.

	$D_v$	$D_e$	K (mD)	C ( $g \cdot m^{-2} \cdot s^{-1/2}$ )	$\phi_c$ (%)	$\phi_{MIP}$ (%)	$R_{MIP}$ ( $\mu m$ )	$R_{NMR}$ ( $\mu m$ )	$\phi_{X-ray CT}$ (%)	$R_{X-ray CT}$ ( $\mu m$ )
Initial state	0.00	0.00	2.28	448	39.56	38.33	0.277	1.22	0.42	18.47
HR-CF	0.11	0.12	1.90	401	39.51	40.92	<b>0.296</b>	1.31	0.70	7.82
CR-HF	0.09	0.09	<b>2.41</b>	<b>477</b>	39.78	38.46	<b>0.294</b>	1.17	1.15	8.79
R-F	0.12	0.10	<b>2.81</b>	<b>484</b>	38.80	39.18	<b>0.300</b>	1.32	-	-
TS	0.07	0.08	1.70	372	40.18	39.15	0.271	1.27	-	-
C-HR-CF	0.00	0.03	1.77	377	-	-	-	1.35	-	-
C-CR-HF	-0.03	0.04	2.26	428	-	-	-	1.31	-	-
C-R-F	-0.05	0.11	2.32	472	-	-	-	1.06	-	-

$D_e$  : Thermal damage factor calculated by the Young's modulus;  $D_v$ : Thermal damage factor calculated by the P-wave velocity; C: Capillary coefficient; K: Permeability;  $\phi_c$ : Connected porosity;  $\phi_{MIP}$ : Porosity calculated by mercury injection porosimetry;  $R_{MIP}$  ( $\mu m$ ): Median pore access radius;  $\phi_{X-ray}$ : porosity calculated by X-ray microtomography;  $R_{X-ray CT}$ : Pore size radii calculated X-ray microtomography.

It is known that chalk saturated with water is mechanically weaker than dry chalk (Duperret et al., 2005), and that its porous network deforms with each contact with water. This decrease in strength is attributed to the loss of cohesion due to the absorption of water on calcite surfaces. Dry, chalk tends to strengthen (Madland, 2005). The changes of  $D_e$  and  $D_v$  for the different heat treatments are shown in Tableau III-6. These two damage variables are able to reflect the changes in the internal damage of the rock specimen with thermal stress. The results show that the variation evaluated by Young's modulus and the speed of the P wave is similar. Regardless of the fluid circulation methods, the values of these two variables show little damage caused by the temperature contrast between the rock and the fluid. Two conclusions can be drawn from this; water weakening phenomena are not irreversible (Madland, 2005), and temperature contrast water flow tests did not significantly affect the porous network to induce internal damage.

Gutierrez et al. (2000) carried out an experimental study on the chalk-fluid interaction mechanisms and showed that the weakening phenomena are partly chemical in nature. Rhett, (1998) showed that possible organic coatings on the chalk surface seemed to protect portions of chalk from the weakening effect of brine and concluded that flooding of reservoirs would

degrade these protective coatings with the consequence of increased contact between water and calcite, which would lead to augmented compaction of the reservoir. In addition, some inhibitors, such as the presence of organic compounds can completely suppress precipitation (Lakshatanov et al., 2018). Although dissolution phenomena are sometimes taken into account, few studies have been carried out on the weakening by water from a purely chemical point of view, probably due to the very low solubility of calcite in pure water and low contact time. Most of the observations linking the weakening to the dissolution of calcite were made on experiments where the chalk was subjected to flooding of water or brine which was not in equilibrium with the calcite (Gutierrez et al., 2000; Madland et al., 2011; Nerموen et al., 2015). In this study, the water was in equilibrium with the chalk.

The study of temperature as an alteration factor can play an important role in revealing the basic mechanisms involving fluid-chalk interactions. In general, the increase in temperature tends to promote or reinforce certain mechanisms such as breakdown or chemical dissolution reaction. The dissolution kinetics of calcite are very temperature dependent (Lisabeth and Zhu, 2015). This difference may be related to the solubility of the chalk if chemical equilibrium has been established between the pore-filling fluid and the matrix. Indeed, the dissolution of chalk increases as the temperature decreases (Plummer and Busenberg, 1982).

### III.2.5.1. Hot rock-Cold fluid

Tests with rocks preheated to 80 °C and with cold water that circulated by capillary imbibition (HR-CF), continuous (C-HR-CF) and rapid cooling (TS) have shown a reduction in permeability, of 16, 22 and 26%, respectively. This reduction can be caused by recrystallization on the chalk surface of the  $\text{Ca}^{2+}$  and  $\text{CO}_3^{2-}$  ions saturating the fluid. This recrystallization would increase the size of the crystals (Fabricius, 2003). In contrast, recrystallization does not necessarily lead to a reduction in pore volume (Maliva and Dickson, 1992), as indicated by the measured porosity values.

For the 3 (hot rock-cold fluid) temperature contrast tests, the capillary coefficient decreases during the cycles. In addition, porosity and pore size measured in X-ray CT was lower than for the test of cold rock, circulated by hot water.

The consequences of closing the pore space with increasing temperature are not yet fully defined. In general, the decrease in porosity is explained by the increase in the wettability of

water on chalk (Anderson, 1987; Hamouda and Karoussi, 2008). However, the permeability calculations for this study were carried out at room temperature. Thermal expansion at the pore scale could also be responsible for pore closure (Katende et al., 2020). When heating to 80 °C the thermal expansion of the calcite grains will close the pores. The passage of cold water did not cause any dissolution (because the water was in equilibrium in the chalk).

At the end of each cycle, the chalk was dried and heated to 80 °C to perform a new cycle. During this drying / heating in the oven, dissolved ions (of the equilibrium fluid) in the grooves and pores may have precipitated at higher temperatures due to the decrease in water volume. When performing a new cycle, the flow of cold water would be slowed down. This could explain why increasing the number of cycles can lead to the decrease in permeability.

In the test C-HR-CF was even more reduced. Continuous fluid flow increases the likelihood that a grain will "detach" from its location and enter a pore of the porous network, thereby redistributing the pore space.

For chalks subjected to thermal shocks (TS) the main observation was the significant drop in permeability from the first cycle, a slight decrease in the size of access to the pore and, on the other hand, not a change in the size of the pores measured by NMR. Producing rapid cooling on a heated sample can cause compressive stresses in the center of the sample, thus closing the pores (Kim et al., 2014).

### III.2.5.2. Cold rock-Hot fluid

Total porosity was not affected by imbibition or continuous fluid flow tests, however an increase in water injection temperature (80 °C) may improve oil production (Hamouda and Karoussi, 2008). Indeed enhanced oil recovery (EOR) by hot water (or steam) in reservoirs can lead to increased oil recovery by improving water imbibition in the reservoir (Jabbari et al., 2017). In our case the permeability was slightly improved during the imbibition flow tests and remained the same for the continuous fluid flow.

X-ray CT measurements showed greater porosity and pore size than when circulating cold water.

There are a number of possible causes of increased fluid circulation. (1) When cooling samples to 8 °C, the dissolution processes could be greater. Indeed, if the samples were dried at 40 °C

before being cooled, residual water may remain, even after drying at 120 °C (Madland, 2005). The water present in the pores of the rock allowed the dissolution. On the other hand, with a high specific surface of approximately 2 g / cm<sup>3</sup>, this dissolution did not cause any damage. (2) The repeated action of wetting and drying together with the expansive force of water can represent a disruptive influence, especially in pore of a rock with a low tensile strength. For example, when the water temperature is raised from 0 °C to 60 °C, expansion of about 1.5% can take place and will exert pressure up to 52 Mpa. The expansion and contraction of water in narrow capillaries like chalk can produce pressure sufficient to disrupt its porous network (Bell, 2000).

### III.2.6. CONCLUSION

The effects of temperature and water circulation have been studied in different configurations. All the experiments led to the conclusion that the effects of cyclic water transfers by capillary action or continuously play a very minor role in the variations in pore volume. The most important conclusion that can be drawn from this study is the decrease in permeability during an injection of cold water into a hot rock. The anisotropic thermal expansion of calcite is the main mechanism for the variation of petrophysical parameters measured in this study when chalk is exposed to thermal cycling.

NMR measurements as a parameter for evaluating the size of the pores, is an alternative to the observation by thin section of chalk where certain facies are difficult to observe.

In summary, it has been shown that neither capillary transfer circulation cycles nor continuous transfer at low temperature (80 °C) demonstrate weakening effects.

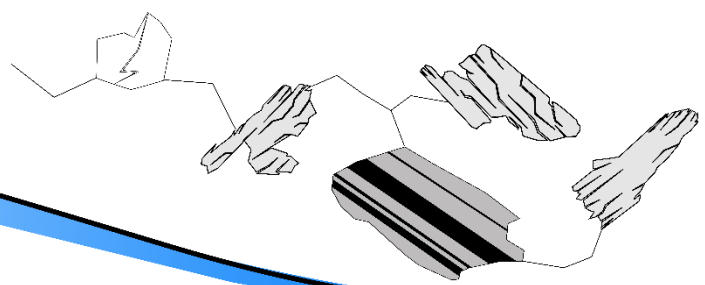
In accordance with the literature, the behavior of chalk and its weakening strongly depends on its water content. Monitoring of our dry samples did not show any pore collapse phenomenon.

The data acquired in this study did not allow to detect or verify exactly the impact of the dissolution on the changes of the porous networks. Even though the solubility of CaCO<sub>3</sub> is very low in water, and also decreases with increasing temperature, performing these same experiments with water not in equilibrium with chalk might give different results.





## IV. CHAPITRE : Comportement thermo- hydrique du granite





**Résumé étendu et conclusions principales de l'articles #3 « Évolution microstructurale des roches granitiques exposées à différents régimes thermiques analysés par thermographie infrarouge » et de l'article #4 « Étude expérimentale de l'effet des cycles de trempe sur les propriétés physico-chimiques des granites ».**

**Le granite** est considéré comme un constituant majeur de la croûte terrestre (Hans Wedepohl, 1995). Ses propriétés mécaniques sont influencées par ses caractéristiques pétrographiques et sa microstructure (Irfan, 1996; Lan et al., 2010; Tuğrul and Zarif, 1999). C'est un matériau relativement résistant avec une **faible porosité** de matrice (de l'ordre de 1% à quelques pourcents s'il est altéré). En raison de **l'hétérogénéité minérale** et de la **dilatation thermique différentielle** des minéraux, cette roche est très sensible aux effets de la température (Albissin and Sirieys, 1989; Berest and Vouille, 1988; Gómez-Heras et al., 2006; Vazquez et al., 2011). Au-delà d'un certain **seuil de température**, des microfissures irréversibles sont générées (Darot et al., 1992; Géraud et al., 1992; Lin, 2002; Meredith and Atkinson, 1985; Q. L. Yu et al., 2015) et influencent grandement la décomposition mécanique (Yilmaz et al., 2009).

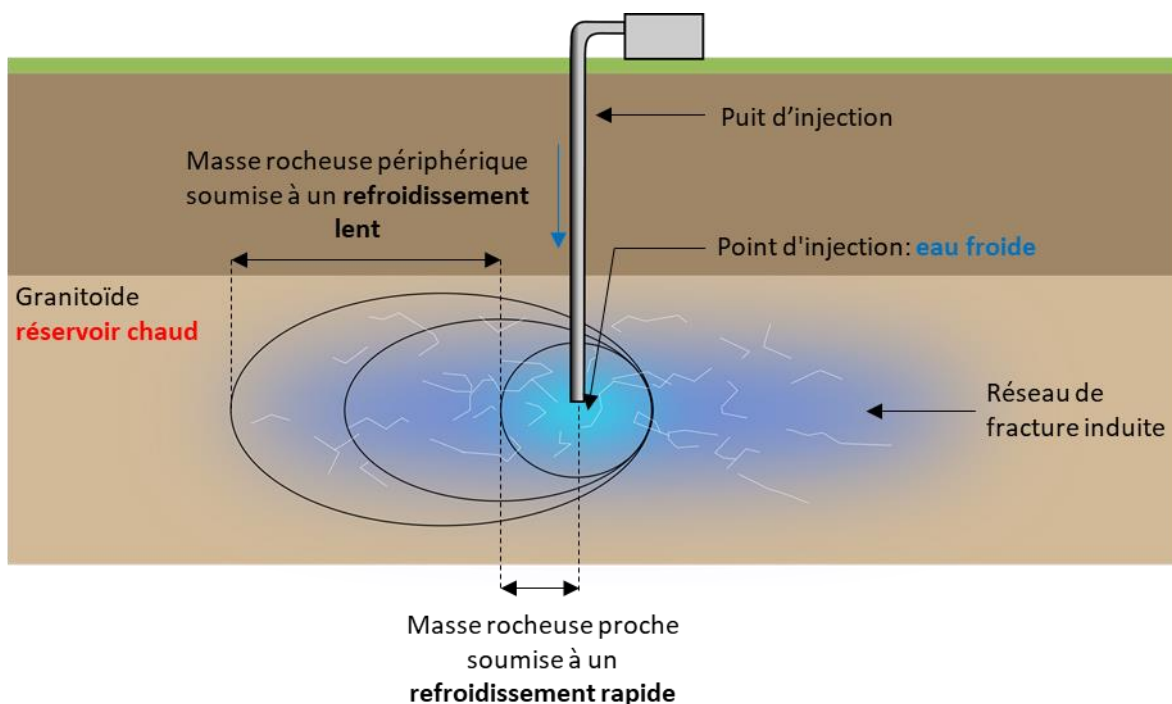
Parmi tous les paramètres influençant le comportement mécanique du granite, le rôle des **microfissures** est d'une grande importance (Alm et al., 1985; Ghasemi et al., 2020). La génération et la configuration des fissures dans les roches sont causées par différents processus et conditions (Kranz, 1983). Les facteurs pouvant favoriser la génération de nouvelles fissures ou la propagation de fissures préexistantes dans le granite peuvent être induits par contraintes thermiques (*e.g.* Géraud, 1994; Hall et al., 2008; Wang et al., 1989), chocs thermiques (*e.g.* Freire-Lista et al., 2016; Yu et al., 2020; Zhou et al., 2018), contraintes tectoniques (*e.g.* Borrelli and Gullà, 2017), ou la transition de phase  $\alpha / \beta$  des minéraux de quartz (Glover et al., 1995; Lin, 2002). La croissance des microfissures peut également avoir lieu lors d'une traction à la surface de l'échantillon pendant un refroidissement rapide (Kim et al., 2014).

Lors des tests thermiques expérimentaux en laboratoire, une faible **vitesse de chauffage** est requise pour s'assurer que les fissures induites dans le matériau résultent seulement de l'effet de la température et non pas du gradient thermique à travers l'échantillon. La vitesse de chauffe **inférieure à 5 °C / min** est considérée suffisamment faible pour éviter les chocs thermiques sur le granite (Chaki et al., 2008; Ding et al., 2016; Dwivedi et al., 2008; Homand-Etienne and Houpert, 1989; Huang et al., 2017; N. Li et al., 2019; Reuschlé et al., 2006; Shao

et al., 2015; Takarli and Prince-Agbodjan, 2008). Il a été démontré que le **temps de chauffage** est également un aspect important des conséquences du traitement thermique. Plus la durée de traitement est longue, plus les dégâts sont importants. Il est également souligné que les principaux dommages thermiques surviennent au cours des deux premières heures (Tang et al., 2019). Les fissures restent fermées lorsque les granites sont maintenus à la température à laquelle ils se sont formés. C'est lorsque l'échantillon préchauffé est refroidi à la température ambiante, que les changements microstructuraux sont générés (Homand-Etienne and Houpert, 1989).

La **vitesse de refroidissement** a une influence significative sur le comportement mécanique de la roche. En géothermie, par exemple, le réservoir profond peut subir des contraintes thermiques associées à des taux de refroidissement différents allant du refroidissement lent au choc thermique (Figure IV-1). Le premier scénario fait référence au refroidissement naturel qui peut avoir lieu dans les roches périphériques d'un puits d'injection. Le refroidissement lent de la masse rocheuse est généralement localisé sur une large zone. Dans le deuxième scénario, la méthode de refroidissement comprend principalement un refroidissement rapide par eau au niveau du point d'injection.

Par conséquent, l'injection d'un fluide froid dans la roche chauffée induit un fort gradient thermique qui développe de microfissures importantes près du point d'injection.



**Figure IV-1. Schéma des différents taux de refroidissement d'un réservoir chaud lors d'une injection de fluide.**

Pour évaluer le bon développement de cette application géologique, il est essentiel de suivre et de prévoir la microfissuration thermique, dépendante de la température dans la roche ainsi que les effets des différents traitements de refroidissement (refroidissement lent et trempé).

En raison de leur forte hétérogénéité minéralogique et texturale, les granites présentent des réactions différentes aux **cycles de contrainte thermique**. L'une des caractéristiques qui influence le plus la réponse thermique est la porosité. L'influence de la porosité lorsque ces roches sont exposées à **différents traitements thermiques** a fait l'objet d'un article. À cet effet, l'**article #3** : « **Evolution microstructurale des roches granitiques exposées à différents régimes thermiques analysés par thermographie infrarouge** », présente des expériences menées sur **quatre granitoïdes** sélectionnés par leur taille cristalline similaire, mais avec des proportions de minéraux différentes et des valeurs de porosité variables, allant de 1 à 6%. Deux types d'essais ont été réalisés :

- i) des cycles de chauffage progressifs de 90 °C à 130 °C pour déterminer le seuil critique d'endommagement thermique.
- ii) de la fatigue thermique avec cycles de chauffage-refroidissement lent jusqu'à 200 °C.

La porosité et les phénomènes de transport d'eau des échantillons ont été caractérisés avant et après chaque cycle par des **tests d'absorption capillaire d'eau couplé à de la thermographie infrarouge**. Cette technique a permis de suivre la migration des franges capillaires au cours du test et d'évaluer l'indice de vitesse de refroidissement. L'évaluation directe des dommages a été réalisée par porosimétrie par injection de mercure, microscopie optique polarisante et microscopie électronique à balayage.

L'évaluation des propriétés physico-chimiques du granite soumis à des cycles de trempé ont fait l'objet d'un second article. Dans cet **article #4** : « **Etude expérimentale de l'effet des cycles de trempé sur les propriétés physico-chimiques des granites** », quatre granites ont été préchauffés lentement à deux températures maximales cibles (200 et 400 °C) puis trempés dans l'eau à température ambiante 35 fois.

Pour étudier l'effet du cyclage thermique sur les propriétés physiques, des tests non-destructifs ont été utilisés (porosité de l'eau, tests d'absorption capillaire d'eau, vitesse de propagation des ondes P et S, relaxométrie par résonance magnétique nucléaire et microtomographie aux rayons X). L'analyse des granites a été réalisée en utilisant la fluorescence X, qui a fourni des informations sur les éléments majeurs et traces. Les interactions eau-granite ont été suivies en utilisant la spectrométrie de masse à plasma inductif (ICP-MS).

La variation de tous les paramètres mesurés indique la création de fissures avec la fatigue thermique. La porosité, l'absorption d'eau, la taille et le volume des fissures ont augmenté tandis que la vitesse des ondes P et S et le module de Young ont diminué. Un seul cycle de choc thermique pour des roches préchauffées à 400 °C a provoqué plus de dommages qu'après 35 cycles à 200 °C. À 400 °C, les dommages les plus importants ont été observés au cours des cinq premiers cycles. Ces changements étaient une conséquence directe de la propagation des microfissures induites par le fort gradient lors des essais de trempe. Pour les deux températures, les changements dépendaient des conditions d'altération initiales des granites. Les granites altérés ont montré la création ou la fermeture de fissures pendant la trempe, tandis que les dommages sur les roches saines étaient caractérisés par la création de microfissures intragranulaires. L'analyse des fluides expérimentaux a montré un enrichissement en K, Na et Ca dans la solution à la suite de la dissolution du K-feldspath, du plagioclase et de la dégradation du mica et des argiles, indépendamment des modifications physiques et mécaniques.

Il découle plusieurs **conclusions** des différents traitements thermiques issues des 2 articles. Un refroidissement lent et une trempe rapide ont induit des dommages aux échantillons de granite qui propagent des fissures inter et intragranulaires induites thermiquement.

Les contraintes induites pendant les processus de dilatation et de contraction thermique impliquées dans le chauffage et le **refroidissement lent** sont faibles jusqu'à un certain **seuil de microfissuration**. La combinaison de tous les résultats a permis d'établir un lien entre l'évolution de la température et la modification des réseaux poreux dans les granitoïdes. Les microfissures sont apparues distinctement à une température comprise entre **90 °C et 130 °C** pour les granitoïdes à forte porosité dont le rapport Quartz / Feldspath était proche de 1. En dessous de cette température seuil s'est produit une fermeture progressive des fissures et des

pores existants en raison de l'expansion thermique des minéraux. Pour des températures plus élevées, les granitoïdes à faible porosité développent des microfissures dès le premier cycle de chauffage. **La porosité** a alors montré un impact plus fort sur le comportement thermique que **l'effet de la minéralogie**. Les résultats obtenus par thermographie infrarouge ont permis de détecter les fortes variations de la microstructure.

Il a été démontré qu'un **refroidissement rapide** avec de l'eau sur des granites traités thermiquement induit des dommages plus importants que lors d'un **refroidissement lent** (Jin et al., 2019; Lam dos Santos et al., 2011; Li et al., 2020; Shao et al., 2014; W. Zhang et al., 2018). L'augmentation de la fissuration lors de ces **traitements de trempe** entraîne une réduction significative de la résistance, des paramètres élastiques du granite ainsi que des propriétés physiques en raison de l'augmentation de la densité des fissures (Li et al., 2020). De plus, l'effet du réchauffement-refroidissement cyclique conduit à une dégradation de la roche provoquée par la génération et le développement de microfissures (Dong et al., 2020; Kim et al., 2014; Xu and Sun, 2018; Zhu et al., 2020).

Comparé au refroidissement lent naturel, le **refroidissement par eau** peut induire des chocs thermiques intenses et soudains, induisant des contraintes de traction puis des microfissures à la surface de la roche. Au cours du processus de refroidissement par eau des granites préchauffés à **200 °C**, l'eau peut pénétrer dans les corps granitiques à travers les microfissures et les micropores, puis la force de cohésion entre les grains minéraux sera encore affaiblie, ce qui intensifiera la propagation et le développement des microfissures. Le refroidissement suivant entraîne un affaiblissement des propriétés petrophysiques grâce à l'augmentation de la fissuration.

La **connectivité hydrique** des échantillons à trempe rapide est toujours supérieure à celle des échantillons à refroidissement lent, ce qui démontre qu'un traitement de trempe rapide améliore la perméabilité du granite. Les microfissures intragranulaires au sein du feldspath K se sont propagées à travers les **granites à faible porosité initiale** entraînant des dommages plus importants à l'intérieur des cristaux et augmentant la connectivité hydraulique tandis que les **granites les plus altérés** ont expérimenté une augmentation de la microfissuration avec moins de connectivité.





## **IV.1. Article#3: Microstructural Evolution of Granitic Stones Exposed to Different Thermal Regimes Analysed by Infrared Thermography.**

Ce travail a été publié en ligne le 27 février 2021 dans la revue de rang A, *Engineering Geology* suivant la référence :

Junique<sup>1</sup>, T., Vazquez<sup>1</sup>, P., Géraud<sup>2</sup>, Y., Thomachot-Schneider<sup>1</sup>, C., & Sidibé<sup>1</sup>, H. (2021). Microstructural evolution of granitic stones exposed to different thermal regimes analysed by infrared thermography. *Engineering Geology*, 106057.

<sup>1</sup>GEGENAA EA 3795, University of Reims Champagne-Ardenne, 2, esplanade Roland Garros, 51100 Reims, France

<sup>2</sup>GeoRessources Laboratory UMR 7359, University of Lorraine, F54505 Vandoeuvre les Nancy

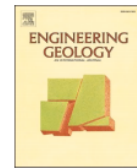




Contents lists available at ScienceDirect

Engineering Geology

journal homepage: [www.elsevier.com/locate/enggeo](http://www.elsevier.com/locate/enggeo)



## Microstructural evolution of granitic stones exposed to different thermal regimes analysed by infrared thermography.

T. Junique<sup>a, \*</sup>, P. Vázquez<sup>a</sup>, Y. Géraud<sup>b</sup>, C. Thomachot-Schneider<sup>a</sup>, H. Sidibé<sup>a</sup>

<sup>a</sup> GEGENAA EA 3795, University of Reims Champagne-Ardenne, 2, esplanade Roland Garros, 51100 Reims, France

<sup>b</sup> GeoResources Laboratory UMR 7359, University of Lorraine, F54505 Vandoeuvre les Nancy, France

### ARTICLE INFO

#### Keywords:

Thermal damage  
Granites  
Critical threshold  
Thermal fatigue  
Microcracks  
Infrared thermography

### ABSTRACT

Detailed knowledge of the behaviour of rocks under thermal stress is essential in a variety of fields such as the exploitation of oil and mineral resources, the geothermal sector, the storage of radioactive liquid waste, or even CO<sub>2</sub> capture and storage.

Granites are widely studied and exploited in these fields, and they show different reactions to high-temperature and thermal cycles due mainly to their high mineralogical and textural heterogeneity. One of the features that influences the most the thermal response is the porosity.

The objective of this study is to evaluate the influence of porosity when these rocks are exposed to different thermal treatments. For that purpose, experiments were carried out on four granitoids selected by their similar crystal size, but with variable mineral proportion and porosity values, ranging from 1 to 6%. Two kinds of tests were performed: i) progressive heating cycles from 90 °C to 130 °C to determine the critical threshold for thermal damage; ii) thermal fatigue with cycles of heating-cooling up to 200 °C.

The porosity and the water transport phenomena of the samples were characterised before and after each cycle by the monitoring of capillary water uptake coupled with infrared thermography. This technique allowed to follow the capillary fringe migration during the test and the evolution of the cooling rate index. The direct assessment of the damage was carried out by mercury injection porosimetry, optical polarising microscopy, and scanning electron microscopy.

The combination of all the results permitted to establish a link between the evolution of temperature and the modification of porous networks in granitoids. Microcracks appeared distinctly at a temperature between 90 °C to 130 °C for high porosity granitoids whose Quartz/Feldspar ratio was close to 1. For higher temperatures, the low porosity granitoids develop microcracks from the first heating cycle. The porosity then showed a stronger impact on thermal behaviour than the effect of the mineralogy. The results obtained from infrared thermography allowed to detect the strong variations in the microstructure.

### IV.1.1. INTRODUCTION

The effect of temperature on rock structures has been widely studied because of its common presence in many geological applications. Examples may be found in the field of ores, hydrocarbons, storage of nuclear waste or CO<sub>2</sub>, as well as in the geothermal resources, in which the energy is recovered thanks to the circulation of fluid through its porosity (faults, fractures and matrix) (Bai et al., 2018; Pandey et al., 2017; Parnell, 1988; Witherspoon et al., 1980). In the latter, the injection of cold water into hot rock is used to increase the transfer properties of the neighbouring rocks and causes a slow cooling of the peripheral rock mass (Isaka et al., 2018). These heating and cooling cycles alter the intact rock and thus, influence the fluid flow and in some occasions the stability of the well (Kumari et al., 2017a). The temperature of geothermal systems can be low temperature like 80 °C, but the global average temperature is around 200 °C (Breede et al., 2013; Olasolo et al., 2016). Granites are also prospected for geological disposal of radioactive waste, the containers used in deep storage can expose the surrounding rock masses to temperatures likely to degrade the rock microstructure (S. Chen et al., 2017). For the storage of high-level radioactive waste, the temperature in the canister surfaces must not exceed 100 °C (Hoekmark and Faeth, 2003). The temperature also has an impact on deep tunnels which can generate thermal stress on rocks surrounding tunnels, most of which do not exceed 130 °C (Chen et al., 2018).

The flow properties and the mechanical strength of the rocks are directly influenced by their microstructures. Recent studies have been conducted at pore-scale to characterise the physical parameters of the rock such as porosity, permeability, or elastic properties for natural strain (Chaki et al., 2008; Staněk and Géraud, 2019). The influence of the temperature is not yet well studied. Unravelling these physical parameters and the microstructures of the rock allows the understanding and the extrapolation to a large-scale system.

Granite is a material showing high mechanical strength with low matrix porosity and heterogeneous mineralogy, which makes it also very sensitive to the effects of temperature (Heuze, 1983). The differential mineral dilation, in most cases anisotropic (Berest and Vouille, 1988; Vázquez et al., 2011) may develop a microcracking (intergranular and intragranular) from a certain temperature threshold (Géraud et al., 1992). This critical temperature generates significant changes in physical properties. In general, microscopic observations show that microcracking often follows preferential directions, such as cleavage planes and

crystal boundaries in rocks with pre-existing microcracks, because less energy is needed to generate microcracking (Gómez-Heras et al., 2006). The ratio Quartz / Feldspar (Qz / F) plays a determinant role in the microstress development, and consequently in the decay of granite (Sajid and Arif, 2015; Sousa, 2013; Tuğrul and Zarif, 1999; Vazquez et al., 2015).

During heating procedures with gradual temperatures, most of the studies conclude that the temperature threshold corresponding to the beginning of microcracks development is about 120-130 °C (Darot et al., 1992; Guo et al., 2018; Lin, 2002). Geothermal systems operate on the principle of repetition of heating-cooling, and consequently, it becomes crucial to control the influence of the fatigue on the microstructure of the rock. In general, thermal fatigue in rocks leads to the propagation of pre-existing microcracks over cycling. Few works were done on the influence of fatigue thermal cycles on granite structures (Freire-Lista et al., 2016; Lin, 2002).

The main objective of this study is to assess the evolution of the granite pore network when these rocks are exposed in a geothermal system. Works on the thermal effects in relatively low geothermal temperature ranges (<200 °C) is scarce, as well as on damage during its long-term operation period. For that purpose, four granites, with similar mineralogy and crystal size but with different porosity values that ranged from 1 to 6%, were tested. Two different experiments were performed to determine the rock microcrack threshold by progressive heating cycles from 90 °C to 130 °C (EXP1) and to evaluate the thermal fatigue after five cycles at 200 °C (EXP2).

The samples were characterised in their healthy state and after each experiment by destructive and non-destructive methods such as Capillary Water Uptake Tests (CWUT), Infrared Thermography (IRT) monitoring, Mercury Injection Porosimetry (MIP), Optical Polarising Microscopy (POL), and Scanning Electron Microscopy (SEM).

### **IV.1.2. MATERIALS**

#### **IV.1.2.1. Geological settings**

Four types of granite were chosen due to their similar mineralogy and crystal size but their difference in alteration degree and consequently in porosity. Their commercial names are Albero (A), Gris Alba (GA), Golden Ski (GS), and Silvestre Moreno (SM). They all come from the

Iberian peninsula. The orientation of the (XYZ) axes was defined by the main crack system and the orientation of the mica plane in the quarry (Vazquez et al., 2011).

The four studied granites belong to the group of peraluminous syn- and post-kinematic granites. This group includes granites temporally related to processes of Hercynian crustal anatexis (Farias et al., 1987; Vera, 2004).

### IV.1.2.2. Granite description

The studied granites are shown in Figure IV-2, their main petrographic characteristics are introduced in Tableau IV-1. The petrographic characterisation (mineral proportion) was made with POL and crystal size was measured on the photographs at the macroscopic scale (Vazquez et al., 2018a).

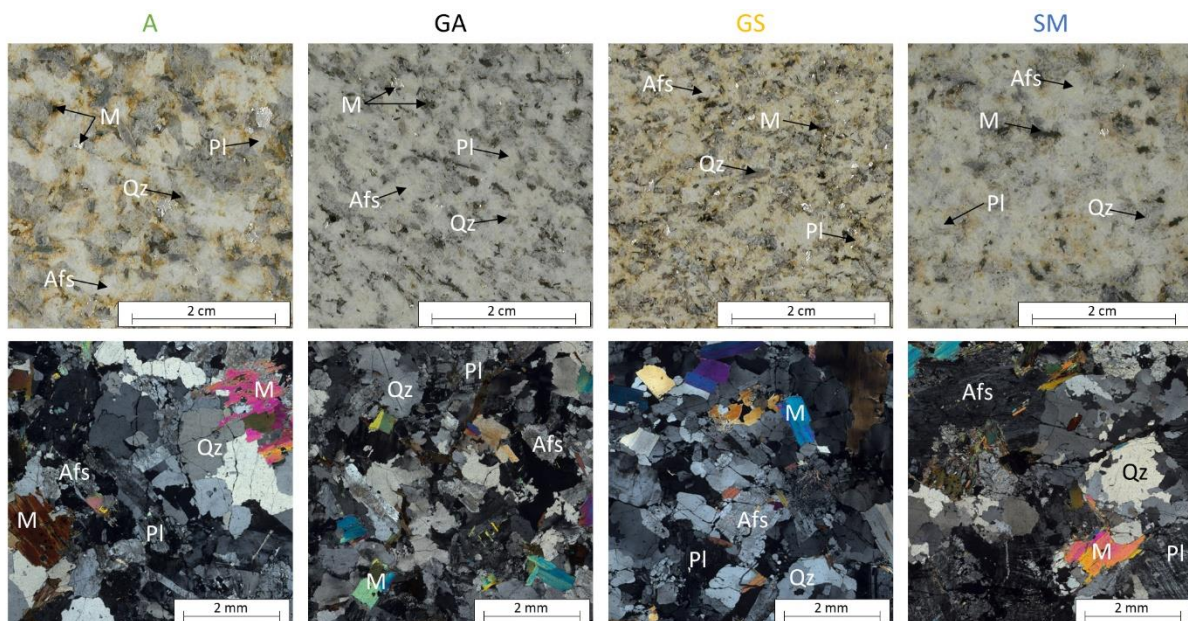


Figure IV-2. Macroscopic and microscopic photographs (Polarised light optical microscopy) of the studied granite: Albero (A); Gris Alba (GA); Golden Ski (GS); Silvestre Moreno (SM). (Qz: quartz; Afs: alkali feldspar; Pl: plagioclase; M: mica).

**Tableau IV-1. Main characteristics of the selected granitoids: Trade name, Mineral proportion, IUGS classification (Le Maitre, 2002), Qz / F ratio (Qz: Quartz; F: Alkali feldspar + Plagioclase) and crystal size (Vazquez et al., 2018a).**

Granite	Composition (%)					IUGS classification	Qz/F ratio	Macroscopical crystal size (mm)				
	Qz	Afs	Pl	M	Qz			Afs	Pl	M	Average	
A (Albero)	35	10	30	25	Granodiorite	0.88	5	5	6	4	5	
GA (Gris Alba)	23	37	23	17	Monzogranite	0.37	5	5	4	2	4	
GS (Golden Ski)	47	20	20	13	Monzogranite	1.18	4	4	4	2	4	
SM (Silvestre Moreno)	45	20	20	15	Monzogranite	1.13	4	5	7	4	5	

Qz: quartz; Afs: alkali feldspar; Pl: plagioclase; M: mica.

**Albero (A):** It is a homogeneous granodiorite with medium-fine crystal size (5 mm). It has the lowest alkali feldspar content among the four granites studied and a high proportion of mica (25%) with a similar proportion of muscovite and biotite. This granitoid is characterised by open transgranular microcracks.

**Gris Alba (GA):** It is a homogeneous monzogranite with a fine crystal size (4 mm). It has anhedral minerals and the boundaries between the quartz crystals are irregular. The proportion of muscovite / biotite minerals is about 2:1. The intergranular microcracks observed in this granite are located at the mica edges.

**Golden Ski (GS):** It is a homogeneous monzogranite with a fine crystal size (4 mm). Quartz and feldspars are subhedral and muscovite is euhedral. The muscovite has the largest crystal size and plagioclase the smallest. Its quartz content is higher than that of feldspars. Pre-existing microcracks are intergranular and are present in plagioclases. GS also has open transgranular microcracks.

**Silvestre Moreno (SM):** It is a homogeneous fine sized monzogranite (5 mm). After GS, this granite has the highest quartz proportion of the granitoids studied and proportions of feldspars and plagioclase are similar (20%). Plagioclases are the minerals with the largest size (up to 7 mm). As with A and GS, this granite has an initial alteration highlighted by intra-, inter- and transgranular microcracks (Vazquez et al., 2018).

An important parameter regarding the mineralogy is the Qz / F ratio. GA has a ratio Qz/F < 0.5, namely a granite rich in feldspar. Meanwhile, A, GS and SM have a similar proportion of both mineral types with values between 0.88 and 1.18. Porosity is the main differencing parameter

between these rocks. GA is considered as a fresh granite (porosity <2%, (Vazquez et al., 2018a)), with a grey pale colour. The granites A, GS, and SM show a yellow colour that indicates the presence of clays due to previous weathering and consequently a higher voids volume than the fresh rock. These three granites exhibit large intra-, inter-, and transgranular microcracks, giving them high water porosity for the granite range as well as high capillary transfer.

### IV.1.3. METHODOLOGY

#### IV.1.3.1. Heating set up

Two types of heating-cooling tests (EXP1 and EXP2) were performed on 2 samples of each granite with a rectangular prism shape of 10 mm × 40 mm × 40 mm in dimension. In addition, smaller samples of 10 mm × 10 mm × 15 mm (8 samples per granite type for EXP1 and 3 samples per granite type for EXP2) were also tested at the same time for further destructive analyses as MIP (Ritter and Drake, 1945), SEM (Fan et al., 2017). Two thin sections per granite were produced in the initial state and after heating to 200 °C for observations under POL (Freire-Lista et al., 2016; Jin et al., 2019).

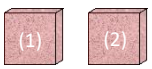


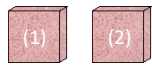
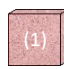
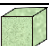
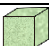


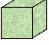




- EXP1: this test was conceived to determine the microcrack threshold of each granite. For this aim, 5 cycles of heating-cooling at an increasing temperature of 90 °C, 100 °C, 110 °C, 120 °C and 130 °C were undertaken. A climatic chamber "Vötsch VC3" ensured a low heating and cooling rate of 1 °C·min<sup>-1</sup> to avoid the microcracks formation due to a high-temperature gradient within the sample (Chaki et al., 2008; Dwivedi et al., 2008; Homand-Etienne and Houpert, 1989; Reuschlé et al., 2006; Takarli and Prince-Agbodjan, 2008). The target temperature was maintained for 2 hours to assure that the whole sample was completely heated with homogeneous temperature distribution (Chaki et al., 2008; Kumari et al., 2017a; Yin et al., 2015). It has been shown that heating time is also an important aspect of the consequences of the heat treatment. The longer temperature duration in the treatment, the greater the damage, but it is emphasised that the main thermal damage occurs within the first 2 hours (Tang et al., 2019). The microstructure evolution was assessed by CWUT and MIP after each cycle, SEM observations were also done at the initial and the final states.

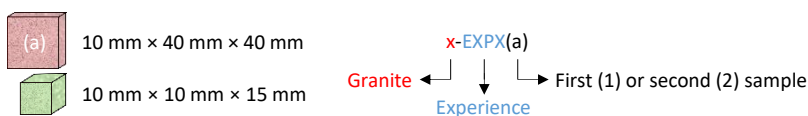
- EXP2: this second test aimed at knowing the effect of the thermal fatigue in microcracked rocks. For this purpose, a repetition of 5 heating cycles up to 200 °C was

performed. The heating process was carried out with a muffle furnace "Thermo scientific led M 110" with a heating gradient of  $5\text{ }^{\circ}\text{C}\cdot\text{min}^{-1}$  to promote microcracking (Ding et al., 2016; Huang et al., 2017; Kumari et al., 2017a; B. Li et al., 2019; Shao et al., 2015). The samples were thermally stabilised after 2 hours at  $200\text{ }^{\circ}\text{C}$ . For cooling, the specimens were left in the furnace to undergo slow cooling at a rate of  $0.5\text{-}1\text{ }^{\circ}\text{C}\cdot\text{min}^{-1}$ . CWUT was monitored by IRT after every cycle on one of the samples. SEM and POL observations were carried out on fresh rocks and after the first cycle ( $200(1)\text{ }^{\circ}\text{C}$ ).

The different cycles will be designated by the reference (Ref.) given in Tableau IV-2. The two size categories are represented by the red and green samples. From now on, the followed sample (red) will be called by the abbreviation of the granite (x), the corresponding experience, and the number of the sample (a), *i.e.* x-EXPX(a).

**Tableau IV-2. Specification of the measurement conditions for samples subjected to the two-heat treatments (EXP1 and EXP2). The red samples were used continuously through each EXP, while the green ones were used only once, due to the destructive nature of the measurements carried out.**

EXP1					EXP2					
Cycle	Ref.	CWUT	MIP	SEM	Cycle	Ref.	CWUT	IRT	MIP	SEM
0	Initial state	 x-EXP1(1) x-EXP1(2)			0	Initial state	 x-EXP2(1) x-EXP2(2)	 x-EXP2(1)	-	-
1	$90\text{ }^{\circ}\text{C}$			-	1	$200(1)\text{ }^{\circ}\text{C}$				
2	$100\text{ }^{\circ}\text{C}$			-	2	$200(2)\text{ }^{\circ}\text{C}$			-	-
3	$110\text{ }^{\circ}\text{C}$			-	3	$200(3)\text{ }^{\circ}\text{C}$			-	-
4	$120\text{ }^{\circ}\text{C}$			-	4	$200(4)\text{ }^{\circ}\text{C}$			-	-
5	$130\text{ }^{\circ}\text{C}$				5	$200(5)\text{ }^{\circ}\text{C}$		-		



Ref.: reference; CWUT: capillary water uptake tests; MIP: mercury injection porosimetry; SEM: scanning electron microscopy; IRT: infrared thermography.

### IV.1.3.2. Evaluation methods

Microstructural characteristics have been evaluated on the fresh rocks and the samples after heating as described in Tableau IV-2.

MIP was undertaken before and after the experiments with a Micromeritics Autopore IV 9500 on samples of 10 mm × 10 mm × 15 mm size: one sample per cycle and granite for EXP1 and one sample per granite after one and 5 cycles (200(1) °C and 200(5) °C) for EXP2. Thus, a total of 32 samples were measured. Mercury injection pressures ranged from 0.004 to 228 MPa, giving corresponding pore access radii of 180 to 0.003 μm, respectively.

A total of 12 samples were cut with an approximate size of 10 mm × 10 mm × 15 mm to be tested and studied directly under SEM to avoid the creation of additional microcracks from sawing after the heating. Observations under POL (Olympus BX51) and SEM (Hitachi TM-1000) were done on each granite and after being tested at 130 and 200(1) °C.

#### IV.1.3.2.1. Capillary water uptake tests (CWUT) and infrared thermography (IRT) monitoring experimental setup

For both experiments, capillary kinetics were measured on samples after each cycle to assess the modifications of the porous network due to thermal stresses. The capillary coefficient (C) was calculated based on the NF EN 1925, (1999) standard. After each heating cycle, the granites were thermally stabilised at 40 °C for 2h. Then, the samples were extracted from the climatic chamber and immediately submitted to a capillarity test with water at  $23 \pm 1$  °C, for both experiments. These tests were performed on two samples of each granite with dimensions of 10 mm × 40 mm × 40 mm and the same samples were used for every cycle within the same experience. The samples were suspended from an electronic precision balance, with a readability of 0.1 mg, using a hook and put into contact with distilled water from their bottom face with a fringe of about 1 mm (Figure IV-3). The weight was automatically recorded every 10 seconds on a control computer. The temperature of the room was kept at  $23 \pm 1$  °C. The test was carried out for 1 hour, time enough for all the granites to reach the stabilisation of the water uptake. Capillary kinetics are usually characterised by two phases (Hammecker et al., 1993; Hammecker and Jeannette, 1994). The first phase is the progressive

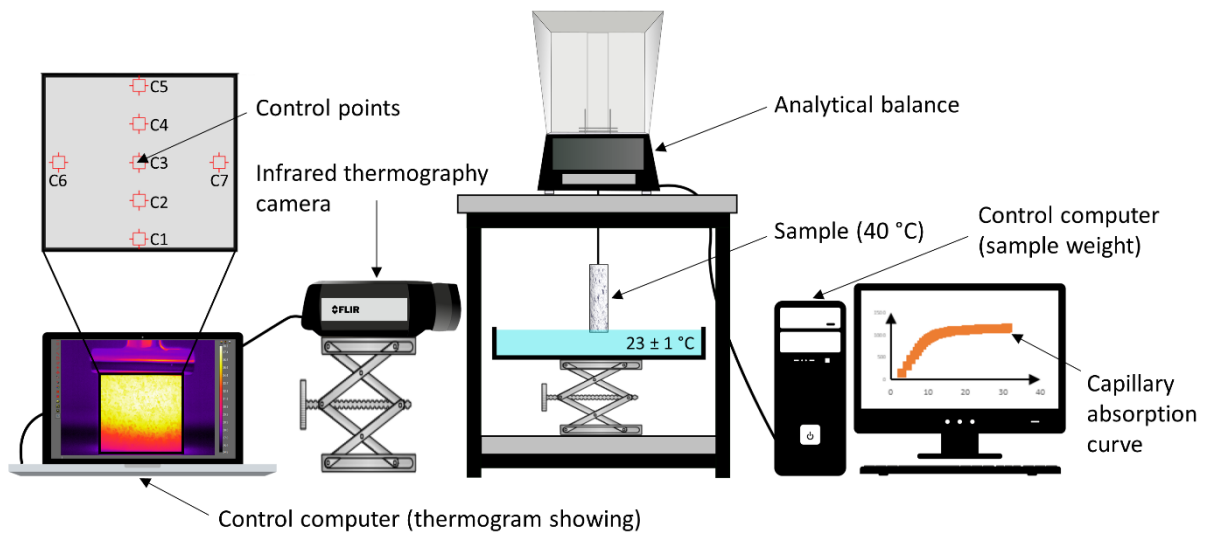


filling of the free porosity by the capillary forces of the water without external pressure applied. The slope of this curve that corresponds to the coefficient  $C$  ( $\text{g}\cdot\text{m}^{-2}\cdot\text{s}^{-1/2}$ ) (Roels et al., 2000) and depends on the porous network. The second phase, slower, begins after the break of slope and corresponds to the filling of the porous network by diffusion of water in the air.

The coefficient  $C$  was calculated for each sample, per cycle, to assess the water kinetic evolution and consequently the variations in the porous network. This test was carried out in two samples to verify the repeatability. For heterogeneous rocks with low porosity, the coefficients evolution of the two samples of each granite assessed individually were more relevant than an average and standard deviation to avoid smoothing of the mean and no longer perceive the changes.

Only for EXP2, IRT monitoring was used to evaluate the microcracking simultaneously to CWUT (Figure IV-3). The IRT camera used is a FLIR SC655, operating in wavelengths between 7.5 and 14  $\mu\text{m}$ . The detection temperature of the camera is comprised between -40 and 150 °C with a sensitivity of 0.1 °C. The detector is an uncooled array of microbolometers. The used IRT camera can build images using infrared radiation. The image size is 640 × 480 pixels, with a noise signal of about 40 mK. The recorded signal, called thermosignal (TS), depends on temperature and emissivity and is expressed in isothermal units (IU).

The cooling kinetics of the samples from 40 °C to room temperature was followed by IRT after each heating cycle. The thermal images show that the water spreading into the microstructure and propagating according to the physical characteristics of the material, leading to a possible evaluation of the porosity (Ludwig et al., 2018). The bottom part of the sample was cooled by the water rising by capillarity. The upper part of the sample was not affected by the capillary forces and was used to monitor the cooling by the air.



**Figure IV-3. Experimental setup of infrared thermography (IRT) monitoring of a sample submitted to capillary absorption.**

The temperature contrast between the rock and the water facilitated the IRT image assessment. This procedure made it possible to observe the progress of the water on the different samples since the rise of the water caused a cooling of the rock and different emissivity of the two media. In the experimental setup, the risks associated with the environmental variations were minimised. The temperature and humidity were monitored with a thermometer and a hygrometer. The experimental device was placed in a watertight tank which allowed to minimise evaporation phenomena as much as possible. Tests were performed in the darkness without artificial light.

The IRT camera was configured to record the thermal images at a rate of 1 frame every 10 seconds for 30 minutes and was activated 1 minute after the start of the experiment to avoid the wide signal variations during the calibrations due to the initial setup. Each image or thermogram of the whole face of each sample acquired during the experiment was processed by the FLIR RESEARCHIR software®. Each pixel of this thermogram corresponds to a specific temperature value. The interface allows placing control spots of  $3 \times 3$  pixels on the thermogram (C1 to C7, Figure IV-3). Five monitoring spots were placed vertically on the sample area, spaced 8 mm. Two spots were placed on the left and right side, centred vertically to observe the possible lateral variations. The "Temporal Plot" function allows us to have the evolution of the thermo-signal as a function of the acquisition time for each control spot.

To quantify the cooling rate, we used the cooling rate index (CRI) representing the temperature variation per unit of time. The CRI10 (calculated for the first 10 minutes of the test) was calculated according to the equation (IV. 1) on the 7 control spots of the thermograms and at each cycle. CRI10 index was described for the first time by Pappalardo et al. (2016) in the survey of rock masses as a reliable and best-suited index for the indirect quantification of porosity. According to Mineo and Pappalardo (2016), the cooling curves of a rock show their major evolution during the first 10 minutes, so that this interval was the one chosen for the CRI analysis. This parameter is inspired by Newton's law of cooling, which states that the heat loss of a body is proportional to the temperature difference between the sample and the environment. This law confirms that cooling is faster in the first minutes of the experiment due to the higher temperature difference between the sample and the air or the water. A fractured rock would cool down faster than a non-fractured one. Thus, this index allows to compare the temperature variation as a function of time of the 4 granites during heat treatment cycles and indirectly the microcrack evolution.

$$CRI10 = \frac{\Delta T}{\Delta t} = \frac{(T_{10}-T_0)}{(t_{10}-t_0)} \quad (IV. 1)$$

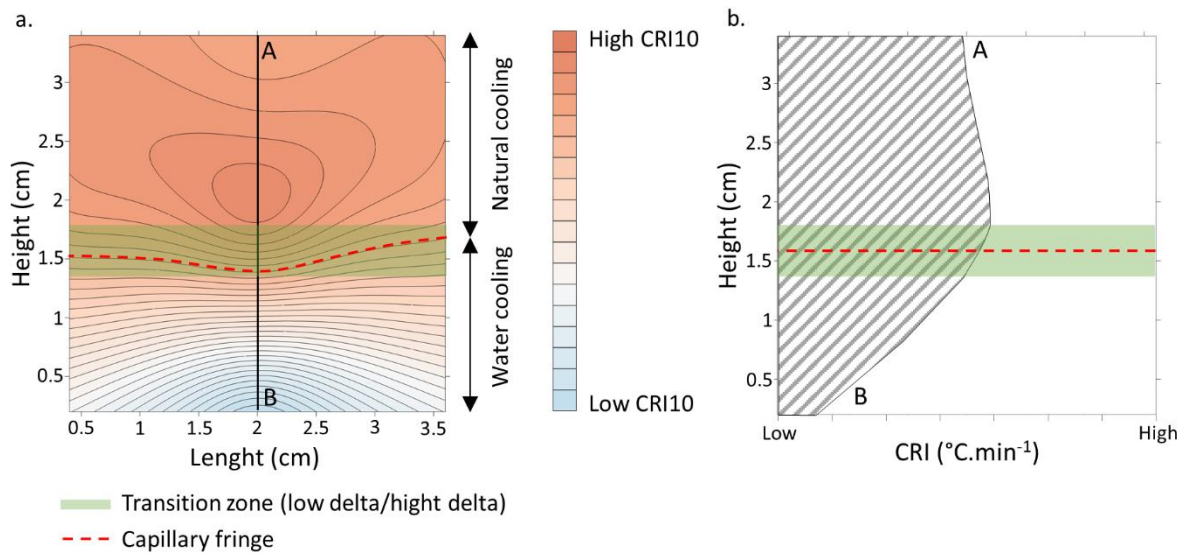
Where  $\Delta T$  is the variation in temperature between initial temperature ( $T_0$ ) and temperature after 10 minutes ( $T_{10}$ ) and  $\Delta t$  is the duration between the two temperature values, *i.e.* 10 min. High CRI10 values corresponded to a fast cooling and higher cracking than low values that represented a slow cooling.

The low porosity of the granites together with the evaporation and the air-environment makes it difficult to distinguish accurately the water limit of the capillary fringe with the naked eye and on the IRT images. The SURFER software<sup>®</sup> was used to facilitate the visualisation of the CRI10 and the capillary fringe on the surface of the samples. This software transformed the CRI10 data on grids in 2D by, in this case, the kriging method. Figure IV-4a shows the schematic distribution of CRI10 on the surface of a sample. The X and Y axes of the grids represented the dimensions of the sample in centimetres. For a time-lapse of 10 min, the placement of the isolines made it possible to detect the thermal contrast between wet and dry areas.

It has been considered 2 heat transfers: the air cooling and the water cooling. In both cases, the sample was at a temperature of 40 °C and the water and air about 20 °C lower.

- The air cooling on the top of the sample was quantified thanks to the C5 spot (the highest on the sample). Within the 10-minute time-lapse the capillary fringe of the water was not able to reach the C5 spot so that it did not influence the natural cooling of the rock at this point. In addition, this control spot was the closest to the upper surface, in which the temperature equilibrium was reached faster. Thus, the CRI10 (C5) values corresponded to the air-cooling velocity of the rock.
- The water cooling of the bottom of the sample was produced by CWUT. The bottom part showed slower cooling rates than the upper part due to its fast temperature decrease during the first-minute contact with the water. The diffusion of water in the sample resulted in isolines of low value, horizontal and close together (Figure IV-4a). The water cooling of the bottom of the sample was quantified by the C1 spot. Thus, the CRI10 (C1) measurement corresponded to the equilibrium research between the rock and the water temperature.

The vertical AB profile centred horizontally on the surface of the sample showed that CRI10 increase from bottom to top until reaching a plateau (Figure IV-4b). The break-in slope indicated the transition zone between the cooling by water and the natural cooling. The height of the capillary fringe was adjusted using isolines. This limit was represented by the red dashed line in Figure IV-4. The evolution of this height during the different thermal cycles corresponded to changes in the CWUT and thus in the microstructure of the rock. This parameter was used as comparative values between the cycles.



**Figure IV-4. a. Schematic representation of the cooling rate index (CRI10) on the surface of the samples. b. CRI10 values along the vertical profile AB. The red dotted line is positioned in the centre of this area. Its position is refined thanks to the isolines on the surface of the sample. Cooling rate index (CRI10) representing the temperature variation per unit of time (10 min).**

#### IV.1.4. RESULTS

The observations with the naked eye did not reveal any microcracks on the samples after the two treatments. The colour of A, GS, and SM has changed slightly with an accentuation of the reddish tone on the surface, mainly concentrated in the crystal boundaries at 200(5) °C due to the iron oxidation of clays (Vazquez et al., 2016). Clay minerals and phyllosilicates are more sensitive to heat and can be destabilised and undergo several transformations at high-temperatures (Hajpál and Török, 2004). Figure IV-5 shows the samples before and after EXP2.

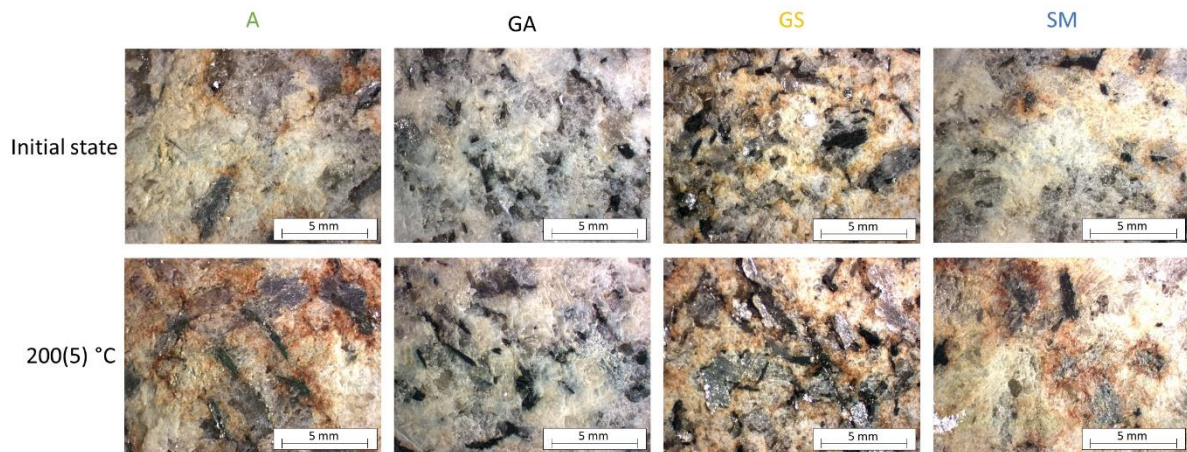


Figure IV-5. Sample surfaces before and after 5 cycles of heat treatment of EXP2. Albero (A); Gris Alba (GA); Golden Ski (GS); Silvestre Moreno (SM). Initially, the yellow-brown colour is due to feldspar weathering to clay minerals. A red colour change at crystal boundaries was observed at 200(5) °C due to the iron oxidation of those clays.

#### IV.1.4.1. Microstructural analysis

##### IV.1.4.1.1. Mercury intrusion porosimetry (MIP)

The analysis was carried out on the 4 granites before heat treatment and after each cycle of EXP1 (90, 100, 110, 120, and 130 °C) as well as for the first and last cycle of the EXP2 (200(1) °C and 200(5) °C). The porosity (%) measured by MIP of the samples after EXP1 and EXP2 are shown in Tableau IV-3.

Tableau IV-3. Total porosity determined by MIP (%) of the 4 granites before and after treatment at different temperatures. Underlined values mean lower values than the fresh rock, in bold the higher values and bold red the first higher value stated as the microcracking threshold.

	Initial state	EXP1					EXP2	
		Cycle 1 90 °C	Cycle 2 100 °C	Cycle 3 110 °C	Cycle 4 120 °C	Cycle 5 130 °C	Cycle 1 200(1) °C	Cycle 5 200(5) °C
A	5.43	<u>5.03</u>	<u>4.72</u>	<u>4.81</u>	<u>3.76</u>	<b>5.58</b>	<u>5.15</u>	<b>6.56</b>
GA	1.05	<u>0.87</u>	<u>0.95</u>	<u>0.96</u>	<u>0.95</u>	<u>0.80</u>	<b>1.59</b>	<b>1.39</b>
GS	3.77	<u>3.19</u>	<u>3.08</u>	<u>3.68</u>	<b>3.93</b>	<u>3.42</u>	<b>3.97</b>	<u>3.56</u>
SM	1.97	<b>2.30</b>	<b>1.98</b>	<b>2.44</b>	<b>2.25</b>	<b>2.01</b>	<b>2.12</b>	<b>2.16</b>

Through EXP1, three of the granites (A, GA, GS) experienced firstly a decrease in porosity. Three values (in bold red), at 130 °C for A, 120 °C for GS, and 90 °C for SM were higher than

the initial porosity and the preceding value. GA had not shown any increase in its porosity during EXP1.

Through EXP2, the general behaviour was an increase in porosity with high-temperatures, although value fluctuations indicated that crystal and microcracks adjustment was still taking place.

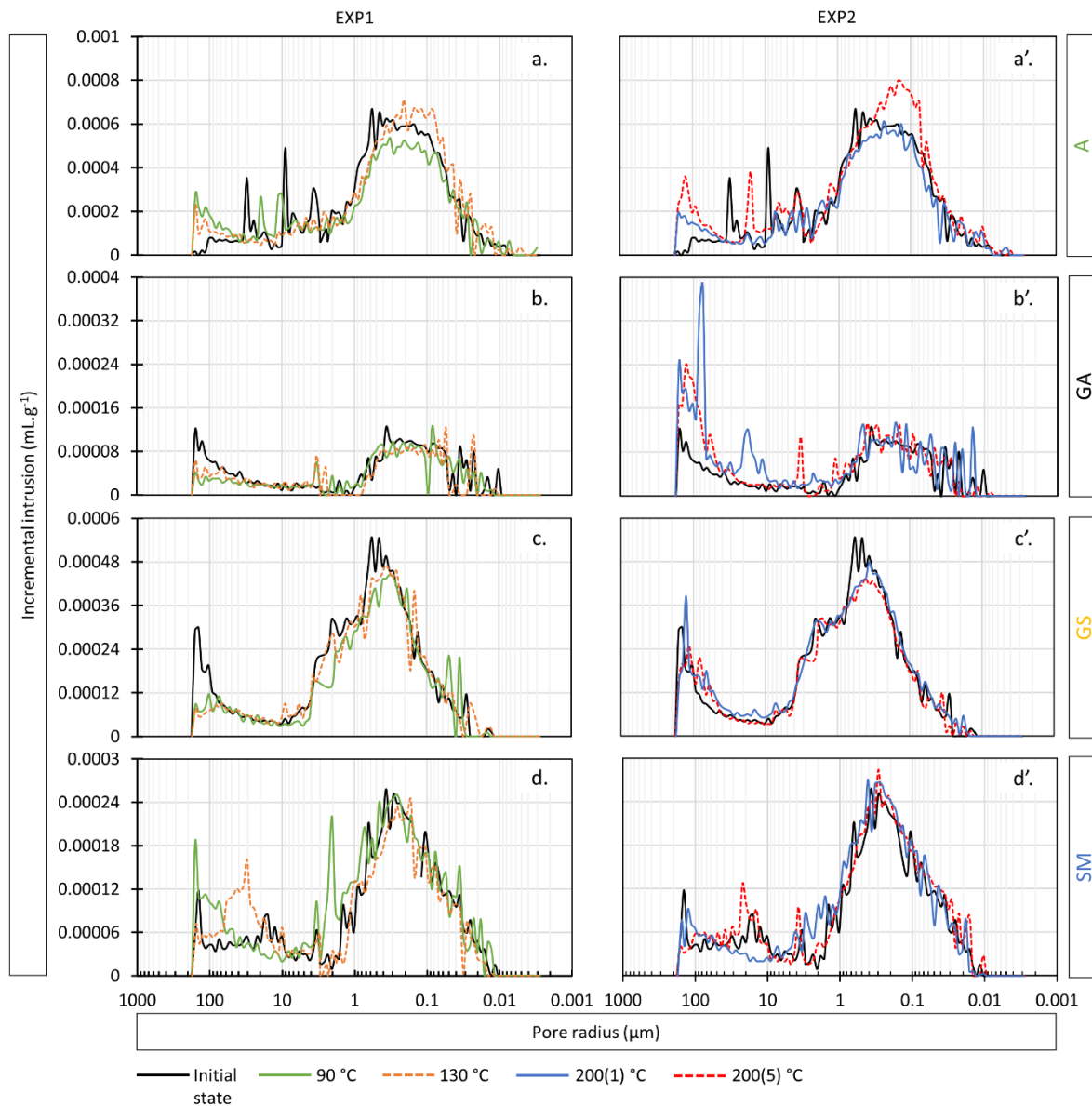


Figure IV-6. Pore access size distribution curves for EXP1 and EXP2. The curves show the granites tested at room temperature (initial state), 90 °C, 130 °C, 200(1) °C and 200(5) °C. (a-a') Albero, (b-b'), Gris Alba, (c-c') Golden Ski, (d-d') Silvestre Moreno.

The initial MIP curves of the four granites (Figure IV-6) can be divided into two parts: i) a main distribution between approximately 0.01  $\mu\text{m}$  and 1-10  $\mu\text{m}$  with unimodal shape; ii) and a heterogeneous distribution of the higher pore radii access.

EXP1:

A showed a main pore distribution in the range of 0.007 to 3  $\mu\text{m}$  (Figure IV-6a). The other well-defined subfamily with a heterogeneous distribution showing peaks at 5 and 31  $\mu\text{m}$ . There were variations between MIP yield curves for samples at the initial state and stressed at 90 °C and 130 °C. The main part of the curve showed a volume diminution at 90 °C then recovery at 130 °C. The heterogeneous peaks found at greater pore sizes vanished after heating.

GA is the lowest porous material. The main family curve is observed between 0.01 and 1  $\mu\text{m}$  with the value of higher intensity at 0.4  $\mu\text{m}$  (Figure IV-6b). The second family corresponded to a pore access radius from 31 to 157  $\mu\text{m}$ . The pore peak of the last family (about 100  $\mu\text{m}$ ) decreased from the first cycle. The last cycle was marked by the apparition of a threshold family around 1-3  $\mu\text{m}$ . The porous volume associated with the mean threshold family slightly decreased with temperature and redistribution of peaks for values under 0.1  $\mu\text{m}$  took place.

GS had a mean threshold family between 0.01 and 10  $\mu\text{m}$  and a heterogeneous family with a mode at 143  $\mu\text{m}$  (Figure IV-6c). The curve of the sample heated to 90 °C exhibited a volume reduction for the threshold between 0.2 and 3  $\mu\text{m}$ , slightly recovered at 130 °C. Furthermore, the large decrease of the pore volume associated with high pore radius sizes was observed from the first heating cycle.

SM showed its main pore family dispersed between about 0.01 and 2  $\mu\text{m}$  (Figure IV-6d). An increase in porosity at 90 °C was marked by the appearance of a peak centred at 2  $\mu\text{m}$  radius and a gradual increase of the pore volume thereof. At 130 °C, the main distribution did not differ from fresh results, while the pore volume accessible through threshold in the range 10-100  $\mu\text{m}$  increases.

EXP2:

For A, the first episode of heating at 200 °C (200(1) °C) induced a general reduction of the pore volume distributed through all the curve, although a redistribution was observed in pores greater than 34  $\mu\text{m}$  (Figure IV-6a'). At the end of EXP2, A showed an increase in porosity of



21% (up to 6.56%). On pores with an access radius greater than 1  $\mu\text{m}$ , the shift of some peaks and the volume increase towards a larger radius (110  $\mu\text{m}$ ) indicated a widening of the microcracks during the fifth heating cycle (200(5)  $^{\circ}\text{C}$ ).

For GA, a development of heterogeneities with heating was observed in the main threshold family (Figure IV-6b'). After the first cycle at 200  $^{\circ}\text{C}$ , significant pore radius microcracks formation centred at 18 and 74  $\mu\text{m}$  appeared, the latter softened during the fifth heating cycle. It was mainly the large accesses of the distribution that were concerned. Porosity values were in agreement with this increase.

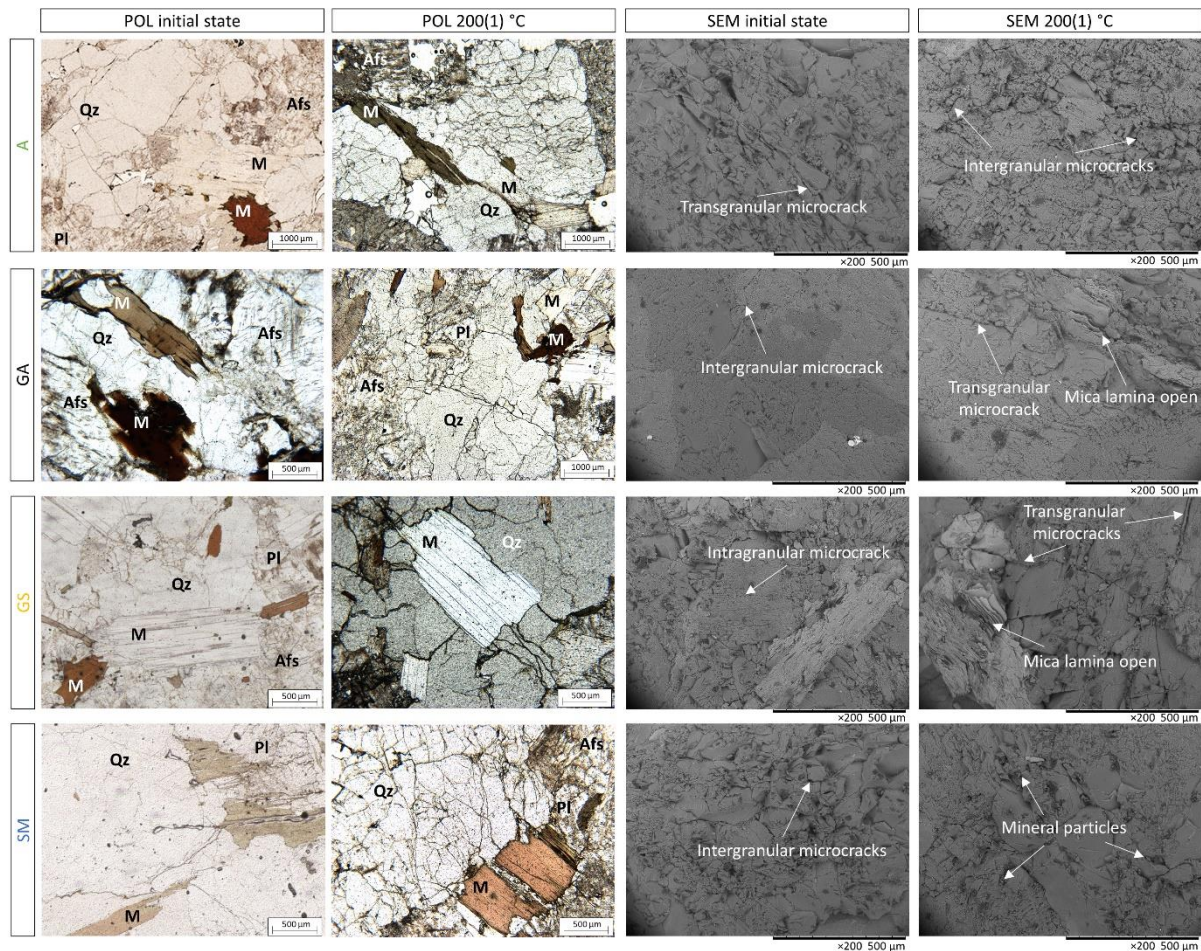
For GS, there was a decrease in the main area family, between 0.4 and 0.7  $\mu\text{m}$  at 200(1)  $^{\circ}\text{C}$  and between 0.2 and 0.7  $\mu\text{m}$  at 200(5)  $^{\circ}\text{C}$  (Figure IV-6c'). At 200(1)  $^{\circ}\text{C}$ , a peak between 6 and 126  $\mu\text{m}$  was formed and then softened at 200(5)  $^{\circ}\text{C}$ .

For SM, the distribution was very irregular over the entire pore radius range after the first heating cycle, then returned to close to the initial state at the end of the test (Figure IV-6d'). The porosity volume only increased slightly, also according to the curve variations.

### IV.1.4.1.2. Optical polarising microscopy (POL) and scanning electron microscopy (SEM)

The pre-existing microcracks present naturally in the granites were enhanced by the thermal effects. The observation and comparison of the microscopic images of the fresh and the heated up to 130  $^{\circ}\text{C}$  granites revealed little change, while at 200(1)  $^{\circ}\text{C}$ , the variations were slight although evident enough for description. Figure IV-7 shows microscopy images (POL and SEM) of fresh and thermally damaged granite, 200(1)  $^{\circ}\text{C}$ .

After heating, each mineral reacts differently to heat treatment. Thus, new-formed microcracks were observed on the surface of quartz crystals in A but especially in the less weathered granites GA and SM. Mica sheets were slightly raised due to thermal expansion and exhibited microcracking and a higher relief in GA and GS. Mineral particles were detached on the surface of the alkali feldspar crystals in SM.



**Figure IV-7. Optical polarising microscopy (POL) and scanning electron microscopy (SEM) illustrating the mineralogy (Qz: quartz; Afs: alkali feldspar; Pl: plagioclase; M: mica) and the microcracking of the four granites before and after one thermal treatment at 200 °C (200(1) °C). Albero (A), Gris Alba (GA), Golden Ski (GS), and Silvestre Moreno (SM).**

For A, the heated samples (200(1) °C) showed a crystal surface with a rougher appearance in SEM observations. Intragranular microcracks were already present in the quartz crystals and clearly developed when compared to the POL observations of a heated and fresh rock. The mica presented a slight opening. Microcracks had an average aperture of more than 10 µm after heating and did not present any particular orientation.

For GA, before the thermal treatment, the POL observations showed predominantly an intergranular microcracks network. The POL observations at 200(1) °C showed an increase of intergranular microcracks between the Afs-Pl limit, thus propagating microcracking along the boundaries of adjacent crystals. Notable intragranular microcracks were also present in quartz and alkali feldspar crystals. After one cycle at 200 °C, the pre-existing microcracks became

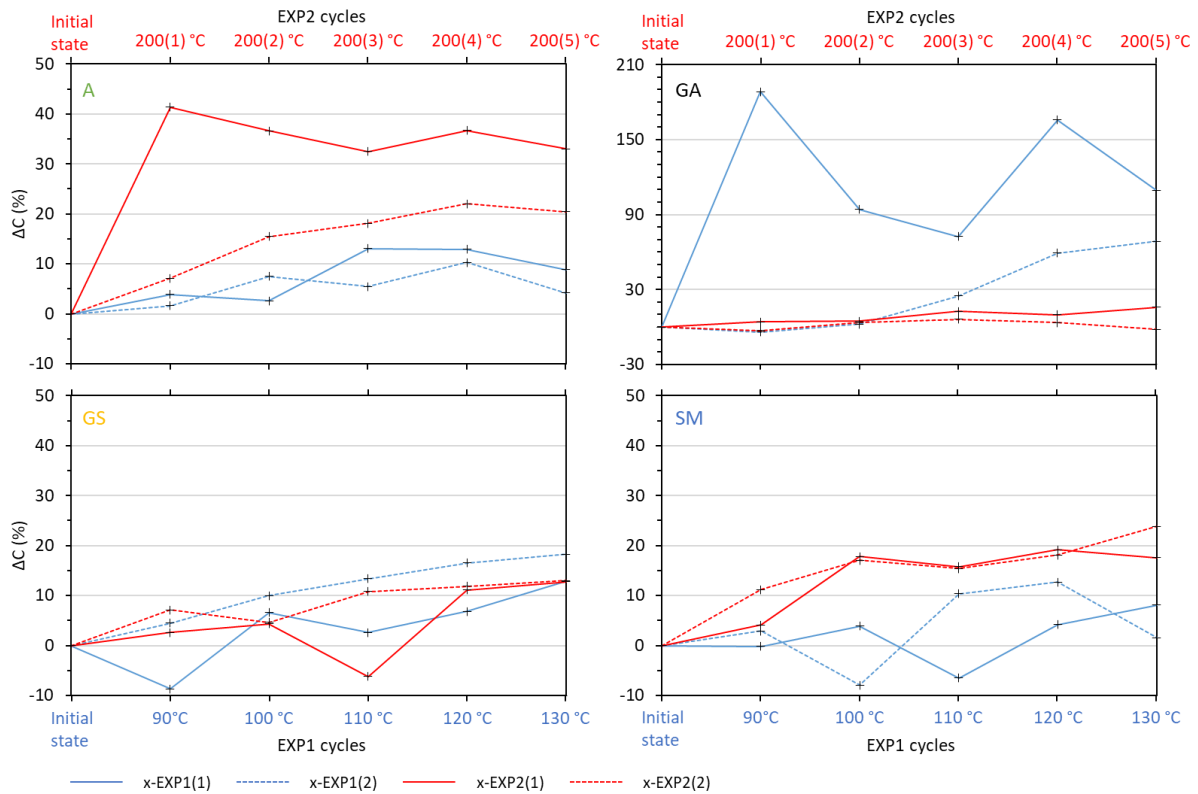
larger and slightly wider in diameter in SEM observations. Some intergranular microcracks are connected to long transgranular microcracks. The thermal expansion led to visible damage to the GA structure, especially on mica which had an increase in their roughness.

For GS, the POL observations showed a slight opening of mica. The SEM observations revealed that GS was marked by an initial alteration with a visible transgranular microcracking. This granite had pores larger than 30  $\mu\text{m}$  in diameter. After heating, many new microcracks had appeared especially in quartz crystals. Cleavage of mica was also altered, showing irregularities.

For SM, after treatment, the POL observations showed the development of an intragranular microcracking through quartz crystals as well as the advanced deterioration of mica. SM exhibited great diversity in the size and nature of the microcracks. There was also a detachment of microparticles on the surface of the pre-fractured sample at 200(1) °C.

### IV.1.4.1.3. Capillary coefficient (C)

The curves of Figure IV-8 represent the evolution of the capillary coefficient (C) concerning the cycles of the 2 experiments.



**Figure IV-8. Evolution of the capillary coefficient (C) during the 2 heat treatments (EXP1 in blue and EXP2 in red). The full line corresponds to sample 1 and the dotted line to sample 2.**

In general, for both experiments, the coefficient C increased with the thermal cycles. For A-EXP2(1) and GA-EXP1(1), the evolution was non-linear, influenced by a large variation during the first heating cycle. The redistribution of microcracks during the different experiments was noticeable by the non-linear variations of the coefficient C during cycles: some isolated low values and large variability of values between samples of the same granite. The initial heterogeneity of the sample may explain the differences between the acquired data.

### EXP1:

Overall, the samples experienced an increase in their coefficients C after heating. For A, the initial coefficients C of the two samples A-EXP1(1) and A-EXP1(2) were  $24.9$  and  $20.1 \text{ g}\cdot\text{m}^{-2}\cdot\text{s}^{-1/2}$  respectively. At,  $90^\circ\text{C}$  the variation was not very evident. The maximum values were reached at  $110^\circ\text{C}$  for sample A-EXP1 (1) with a coefficients C of  $28.2 \text{ g}\cdot\text{m}^{-2}\cdot\text{s}^{-1/2}$  and at  $120^\circ\text{C}$  for the other (A-EXP1 (2)) with a coefficient C of  $22.2 \text{ g}\cdot\text{m}^{-2}\cdot\text{s}^{-1/2}$ .

For GA, the initial coefficients C of the two samples GA-EXP1(1) and GA-EXP1(2) were  $1.8$  and  $2.1 \text{ g}\cdot\text{m}^{-2}\cdot\text{s}^{-1/2}$  respectively. This unaltered granite had the highest variability of coefficients C

during the cycles. The increase was high from the first cycle for the first sample (GA-EXP(1)) with a coefficients C of  $5.08 \text{ g}\cdot\text{m}^{-2}\cdot\text{s}^{-1/2}$ , while the C increase was gradual up to  $130 \text{ }^\circ\text{C}$  for the second sample GA-EXP(2) up to  $3.67 \text{ g}\cdot\text{m}^{-2}\cdot\text{s}^{-1/2}$  at the end of the treatment.

For GS, the initial coefficients C of the two samples GS-EXP1(1) and GS-EXP1(2) were 21.9 and  $19.0 \text{ g}\cdot\text{m}^{-2}\cdot\text{s}^{-1/2}$  respectively. At  $90 \text{ }^\circ\text{C}$ , there was a decrease for GS-EXP1(1) and no important change for the GS-EXP1(2). The maximum value was observed at  $130 \text{ }^\circ\text{C}$  with values of 24.7 and  $22.6 \text{ g}\cdot\text{m}^{-2}\cdot\text{s}^{-1/2}$  for GS-EXP1(1) and GS-EXP1(2) respectively.

For SM, the initial coefficients C of the two samples SM-EXP1(1) and SM-EXP1(2) were 9.7 and  $10.7 \text{ g}\cdot\text{m}^{-2}\cdot\text{s}^{-1/2}$  respectively. The trends in this granite with the increasing temperature were irregular, with a sharp decrease at  $110 \text{ }^\circ\text{C}$  for SM-EXP1(1) and at  $100 \text{ }^\circ\text{C}$  for the second one. The maximal coefficients C was observed at  $130 \text{ }^\circ\text{C}$  and  $120 \text{ }^\circ\text{C}$  with values of 10.5 and  $10.8 \text{ g}\cdot\text{m}^{-2}\cdot\text{s}^{-1/2}$  for SM-EXP1(1) and SM-EXP1(2), respectively.

EXP2:

The general trends after this test were a gradual increase in the C coefficient.

For A, an increase of C was measured on both samples. The first sample (A-EXP2(1)) increased after the first cycle from 13.2 to  $18.7 \text{ g}\cdot\text{m}^{-2}\cdot\text{s}^{-1/2}$  then nearly stabilised over the other four cycles. The coefficient C of the second sample (A-EXP2(2)) gradually increased until the fifth cycle ( $200(5) \text{ }^\circ\text{C}$ ) from 21.0 to  $25.3 \text{ g}\cdot\text{m}^{-2}\cdot\text{s}^{-1/2}$ .

For GA, the overall trend was an augmentation up to the third cycle ( $200(3) \text{ }^\circ\text{C}$ ). The coefficients C gained from 4.8 to  $5.4 \text{ g}\cdot\text{m}^{-2}\cdot\text{s}^{-1/2}$  for GA-EXP2(1) while it remained without variation for the other sample.

For GS, the capillary absorption of both samples changed similarly, except for the decrease in GS-EXP2(1) in the third cycle ( $200(3) \text{ }^\circ\text{C}$ ). Both samples showed a final increase of the same magnitude compared to their initial state.

For SM, the two samples showed a notable increase either during the first or second cycle. The coefficients C then remained stable around  $13\text{-}14 \text{ g}\cdot\text{m}^{-2}\cdot\text{s}^{-1/2}$  until the last cycle.

IV.1.4.2. Infrared thermography (IRT) monitoring of sample cooling

In EXP2, the CRI10 evolution of the air cooling was measured at the level of the control spot 5 (C5) and the water cooling at the level of control spot 1 (C1) (Figure IV-3 and Figure IV-9). The changes of CRI10 values were not linear through the cycles. However, the main trend revealed clearly a strong decrease of the CRI10 in A and a slight one in GS, while GA and SM experimented an increase.

The initial values of CRI10 (C5) were  $0.76 \text{ }^{\circ}\text{C}\cdot\text{min}^{-1}$  for A and  $0.82 \text{ }^{\circ}\text{C}\cdot\text{min}^{-1}$  for GS. GA and SM have intermediate values of  $0.77 \text{ }^{\circ}\text{C}\cdot\text{min}^{-1}$  and  $0.78 \text{ }^{\circ}\text{C}\cdot\text{min}^{-1}$ , respectively. The initial CRI10 (C1) was lower in the low porosity GA and SM ( $0.25 \text{ }^{\circ}\text{C}\cdot\text{min}^{-1}$ ) and higher in the high porosity A and GS ( $0.42 \text{ }^{\circ}\text{C}\cdot\text{min}^{-1}$ ).

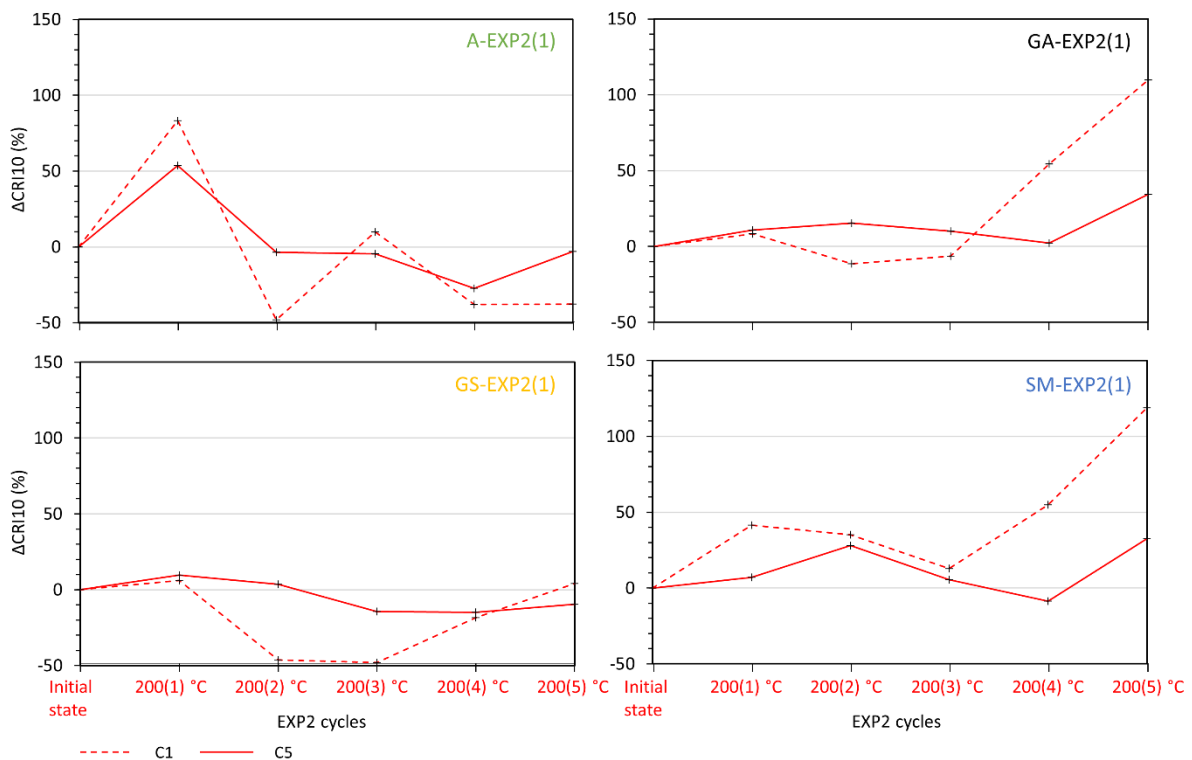


Figure IV-9. Evolution of the CRI10 measured at the top of the sample (air cooling-spot C5) and the bottom (water cooling-spot C1) through EXP2.

For A, the values through the cycles were the most heterogeneous. It was observed that the air cooling (C5) accelerated from the first heating cycle with an increase of about 50% to the value of  $1.17 \text{ }^{\circ}\text{C}\cdot\text{min}^{-1}$ . The CRI10 measured in the lower part of the sample (C1) also identified an increase of about 80% and reached a value of  $0.76 \text{ }^{\circ}\text{C}\cdot\text{min}^{-1}$ . The following cycle showed a

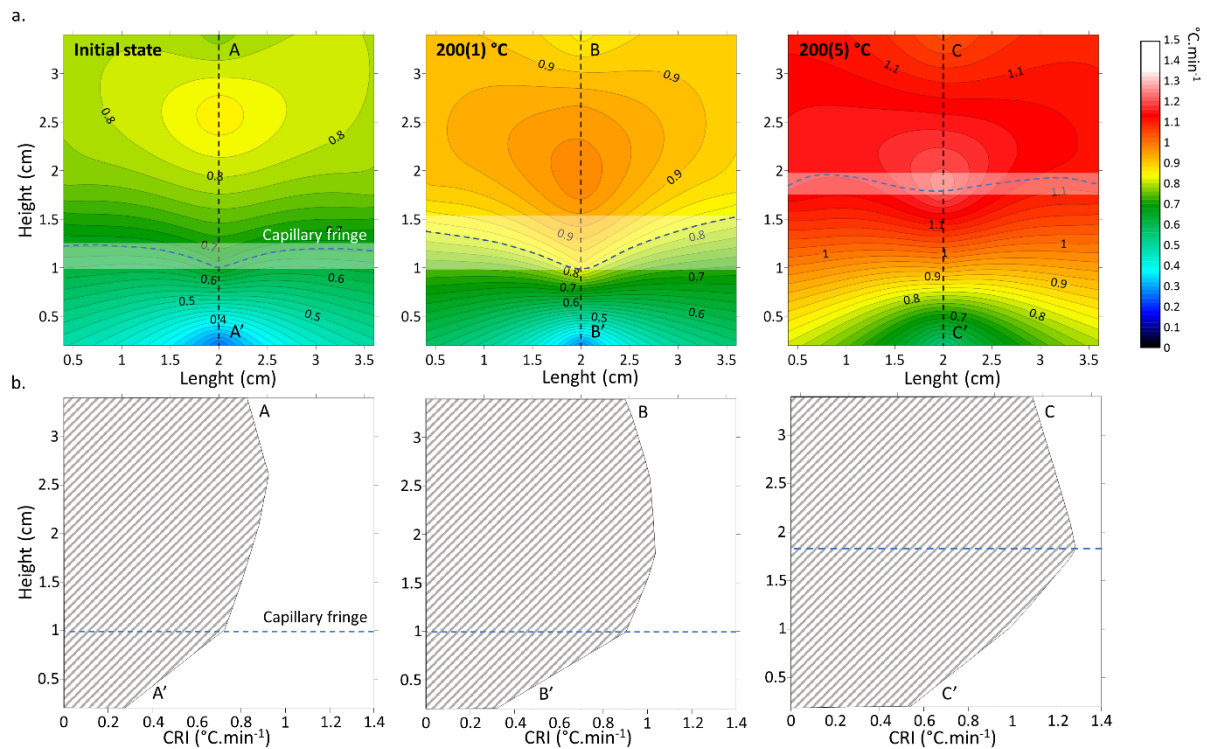
return to the original values of the CRI10 cooled down by air (C5) although there was a decrease of about 30% for the cycle at 200(4) °C. Water cooling showed a decrease to  $0.22 \text{ }^{\circ}\text{C}\cdot\text{min}^{-1}$  in the cycle 200 (2) °C, returns to the origin in the 200(3) °C cycle, and a decrease to  $0.26 \text{ }^{\circ}\text{C}\cdot\text{min}^{-1}$  (about 40%) in the last 2 cycles.

For GA, the final state showed a clear progression compared to the initial state. Whether for the top or the bottom of the sample, the CRI10 did not exceed variations of 15% during the first three cycles. The air cooling that took place at the top of the sample increased by about 30% with a final value of  $1.03 \text{ }^{\circ}\text{C}\cdot\text{min}^{-1}$ . It was during the fourth cycle that the water cooling increased to  $0.39 \text{ }^{\circ}\text{C}\cdot\text{min}^{-1}$  and during the last cycle, the CRI10 was twice its initial value with a value of  $0.53 \text{ }^{\circ}\text{C}\cdot\text{min}^{-1}$ .

For GS, variations in the air cooling were small. The most important changes were identified from cycle 3 marked by a decrease of about 10-15%. Water cooling decreased by about 50% ( $0.22 \text{ }^{\circ}\text{C}\cdot\text{min}^{-1}$ ) in cycle 2 and 3 and by 20% ( $0.34 \text{ }^{\circ}\text{C}\cdot\text{min}^{-1}$ ) in cycle 4.

For SM, air cooling increased in cycle 2 and 5, with an increase of 30%. The CRI10 in the lower part (C1) showed an increase of more than twice the initial value up to  $0.55 \text{ }^{\circ}\text{C}\cdot\text{min}^{-1}$  in the last cycle.

The mapping of the CRI10 distribution on the sample surface showed the air-water cooling contrast that was allowed to detect the capillary fringe. The example of GA is shown in Figure IV-10 in which a clear elevation of the capillary fringe was measured through the cycles. For the other granites, the change in the height of the capillary fringe (H) during EXP2 is shown in Figure IV-11.



**Figure IV-10. Example of CRI10 mapping (a) and associated profiles (b) obtained by infrared thermography (IRT) monitoring on GA before and after one thermal cycle at 200 °C (200(1) °C) and five thermal cycles (200(5) °C): the dot blue line corresponds to the transition zone and is assumed to correspond to the position of the capillary fringe.**

Before the thermal treatment, the capillary height of A was about 1.8 cm. For GA, this height was about 1 cm while GS and SM were in between.

A was marked by a general decreasing trend while for GA, the capillary fringe showed a gradual rise from approximately 1.0 cm to 1.8 cm after the last cycle. For SM and GS, the height of the fringe showed little variation and remained stable.



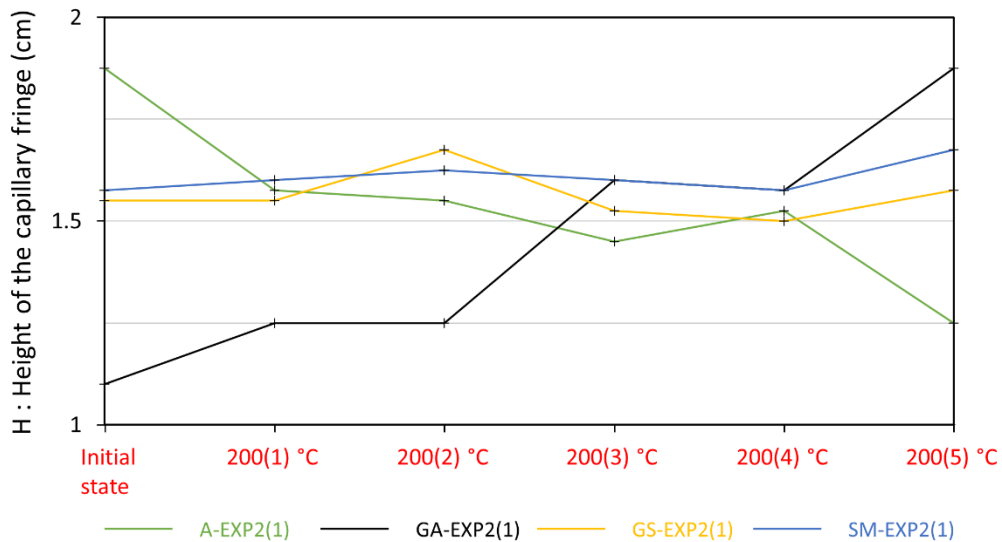


Figure IV-11. Height of the capillary fringe after the first 10 minutes (H) of capillary absorption of the four granites before and after thermal cycles at 200 °C (EXP2).

#### IV.1.5. DISCUSSION

The exposition of granitic rocks to high-temperatures causes an expansion of the rock-forming minerals and a microcrack development above a specific temperature threshold (Argandoña et al., 1985; Géraud et al., 1992; Gómez-Heras et al., 2006; Menéndez et al., 1999). This thermal behaviour depends mainly on two factors, mineralogy and porosity (Benavente et al., 2006; Freire-Lista et al., 2016; Houpert and Homand-Etienne, 1986; Miskovsky et al., 2004). Many researchers agree that the microcrack thermal threshold of granitoids often begins at a temperature of around 100-200 °C (Tableau IV-4).

Tableau IV-4. Some previous researches on the thermal microcracking threshold.

Author	Granite	Porosity (%)	Threshold (°C)
(Y.-L. Chen et al., 2017)	Fujian Province (China)	-	200-400
(Darot et al., 1992)	La Peyratte (France)	-	125
(Argandoña et al., 1985)	Gondomar granodiorite (Spain)	1.37	110-115
(Dwivedi et al., 2008)	Indian granite	0.8	65
(Fan et al., 2017)	Zhejiang Province (China)	-	200-400
(Gautam et al., 2018)	Jalore granite (India)	0.115	300
(Géraud et al., 1992)	Massif de la Borne-Pyrénées-Vendée (France)	0.48-2.3	50-200
(Guo et al., 2018)	Granodianite (China)	1.32	120-150
(Homand-Etienne and Houpert, 1989)	and Senones and Remiremont granite (France)	-	200-400

(Jansen et al., 1993)	Lac du Bonnet Granite (Canada)	0.24	80
(Jin et al., 2019)	Shandong province (China)	-	400-500
(Kumari et al., 2017a)	Strathbogie batholith (Australia)	1.16	400
(Lin, 2002)	Inada granite (Japan)	0.75	100-125
(Liu and Xu, 2014)	Qinling granite (China)	-	100-200
(Meredith and Atkinson, 1985)	Westerly granite (New England)	1	100-200
(Shao et al., 2015)	Strathbogie granite (Australia)	0.463	200-400
(Singh et al., 2015)	Bundelkhand granite (India)	-	400
(Sun et al., 2015)	Jining, Shandong (China)	0.88	300-400
(Takarli and Prince-Agbodjan, 2008)	-	0.68	105-200
(Yang et al., 2017)	Shandong province (China)	0.828	300-400
(Yin et al., 2015)	Laurentian granite (Canada)	0.64	100-250
(Q. L. Yu et al., 2015)	Dandong Liaoning Province (China)	-	100
(Zhao and Feng, 2019)	Lu gray granite (China)	-	200-300

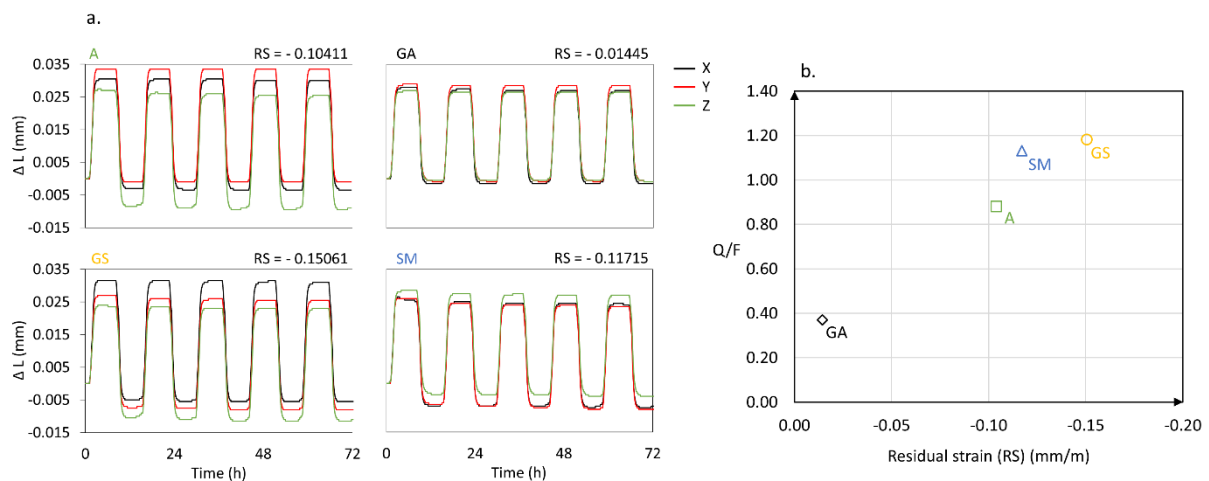
Before reaching the thermal threshold, the rock experimented a pore redistribution, defined by an opening and closing of the pre-existent microcracks or the development of new ones. (Géraud et al., 1992) observed the opening of pre-existent biotite and quartz boundaries between 50 and 100 °C. New microcracks were found between 60 °C and 90 °C by Guo et al. (2018) and Jansen et al. (1993) showed microcracking in their granite at temperatures above 80 °C. Dwivedi et al. (2008) observed pre-existing microcracks widening at 65 °C, followed by a closure at temperatures between 100 °C and 125 °C. Lin (2002) observed a microcracks widening threshold at temperatures between 100 °C and 125 °C. Most of the studies found a thermal threshold from 100 °C (Argandoña et al., 1985; Q. L. Yu et al., 2015). Takarli and Prince-Agbodjan (2008), suggested an increase of microcracking from 105 and 200 °C, according to also to many studies indicating that the critical temperature of granite microcracking takes place at higher temperatures, between 200 and 300 °C (Meredith and Atkinson, 1985; Sun et al., 2015; Yin et al., 2015).

Thermal fatigue is an important failure mechanism in granites. Freire-Lista et al. (2016) and Gómez-Heras et al. (2006) carried out several thermal cycles of continuous heating and cooling up to 105 °C to granitoids and showed that the thermal cyclic effect causes the generation of new microcracks and the fusion of pre-existing ones. Lin (2002) performed 5 to 9 cycles at the same peak temperature (from 200 to 600 °C) and observed that at a temperature of 200 °C all the microcracks are produced during the first two heating / cooling cycles and from 300 °C thermal microcracking continues developing.

**-The effect of mineralogy in granite behaviour**

One of the main reasons attributed to the generation of microcracks on poly-mineral rocks is the mismatching of the thermal expansion coefficients of different mineral crystals (Gómez-Heras et al., 2006). The thermal expansion of quartz is anisotropic ( $a_{11} = 14 \times 10^{-6} \cdot K^{-1}$  and  $a_{33} = 9 \times 10^{-6} \cdot K^{-1}$ ), unlike feldspar with a low and isotropic linear thermal expansion ( $a_{11} = 4.5 \times 10^{-6} \cdot K^{-1}$  and  $a_{33} = 4.5 \times 10^{-6} \cdot K^{-1}$ ) (Vázquez et al., 2015). Minerals dilate with temperature but sometimes they do not recover the original state after cooling, and the rock shows residual strain.

The linear thermal expansion measurements at 90 °C performed by Vázquez et al. (2011, 2015) on the same granites of this study help to understand the behaviour of these granites during those tests (Figure IV-12a). The four studied granites showed a permanent contraction after the first heating-cooling cycle, more notable for the weathered granites A, GS and SM. The direct relation between the Qz / F ratio and the residual strain of granites is shown in Figure IV-12b. Higher quartz content leads to higher residual strain independently of the porosity of the samples.



**Figure IV-12. a. Thermal dilation curve ( $\Delta L$ ) of the four granites submitted to heating-cooling cycles over a range of 20 to 90 °C. Residual strain (RS) expressed in mm / m. b. Relationship between the Qz / F ratio and average residual strain of A, GA, GS, and SM (Vázquez et al., 2010, 2011, 2015).**

### **-The effect of initial porosity in granite behaviour**

The initial porosity and the microcrack density can influence the thermal alteration of the granites. Tuğrul and Zarif (1999) found that the influence of textural characteristics on physical properties seems more important than mineralogy, and Vázquez et al. (2018) stated that only for sound granitoids with porosity under 2%, mineralogical features influence the rock behaviour. The mineral expansion of high porosity rocks intrudes on the voids and reduces the porosity (Géraud et al., 1992). When the rocks are held at the temperature the cracks generated at this temperature remain closed. During cooling, microstructural modifications can appear (Homand-Etienne and Houpert, 1989). If the thermal stress does not reach the microcracks threshold, the minerals will contract during cooling without generating microcracks. If the thermal stress exceeds the cohesion between the grains, the minerals by contracting generate microcracks (Dwivedi et al., 2008). The microcrack geometry (aperture, connection, tortuosity) may play a more important role in the hydric or thermal properties than the porosity volume itself. For this reason, granite detailed study of the pore distribution was carried out from MIP results. The threshold was defined for each granite and the pore access separating the macroporous and microporous domains was defined according to Figure IV-13, at 3  $\mu\text{m}$  for A, 1  $\mu\text{m}$  for GA, 10  $\mu\text{m}$  for GS and 2  $\mu\text{m}$  for SM, as mentioned in section IV.1.4.1.1 That facilitated to understand in which microcrack size domain the modifications observed in the total porosity took place.



Figure IV-13. Size distribution of the voids. On the top of each column, the porosity by MIP is detailed.

**EXP1: Determination of granite thermal threshold**

The low initial porosity of SM within the weathered granites, its high quartz (Qz) and mica content (Vazquez et al., 2015) and its residual strain suggest that the temperature required for a first closure of the pores could be less than 90 °C. Regarding the porosity values (MIP) of Tableau IV-3, SM is the granite that showed firstly an important increase of porosity considered as a thermal threshold. This occurred at 90 °C and produced mainly an increase in pore access radii over 2 μm (Figure IV-13). The capillary coefficient C of the samples varied slightly without a clear trend, although the closure of the pores at 100-110 °C took place that indicated the continuation of the redistribution phase. Beyond these temperatures, the coefficient C increased slightly. Heating to 110-120 °C would mark the new microcrack phase. This conclusion is in agreement with the increase in the connected porosity (> 2 μm) at 110 °C (Figure IV-13) that may lead to a more obvious microcracking.

In the second most weathered granite, GS, at 90 °C and 100 °C the total porosity and the radii larger than 10 μm decreased (Figure IV-13) in agreement with its residual strain, high Qz / F

ratio (Figure IV-12) and the variations in the capillary coefficient (Figure IV-8). Porosity by MIP indicates that the microcrack threshold was produced at 120 °C although the created space allowed a new closure during the last cycle. Capillary water uptake showed a progressive increase from 100 °C that implies the continuous crack in the tested samples.

The most weathered granite, A, showed contrary results in MIP and capillary coefficient. From the first heating cycle, a porosity around 100  $\mu\text{m}$  appeared, that favouring the progressive increase in water uptake by capillarity. Porosimetry showed a progressive closure up to 120 °C focused on the smaller pores and microcracks that do not affect greatly the capillary forces, explained by the quartz expansion in the existent fissures. A new microcracking was generated at 130 °C in the pore family under 3  $\mu\text{m}$ , so that the temperature range did not allow any pre-existing microcracks widening but possibly increased the open porosity thanks to the connection of previously closed discontinuities.

The results of the capillary water uptake tests of GA were not exactly coincident with MIP values. The coefficient C depends not only on the porosity volume but on the width and interconnection between microcracks. The water rises faster when the connections are larger, more numerous, and more uniformly distributed in the sample. MIP showed a microcrack closure through all the test explained by the low  $Q_z / F$  ratio (Vazquez et al., 2015). The slight expansion of the feldspar occupies the existent fissures and microcracks initially isolated, observed in the intergranular boundaries by microscopic methods, have merged to increase the vertical connections.

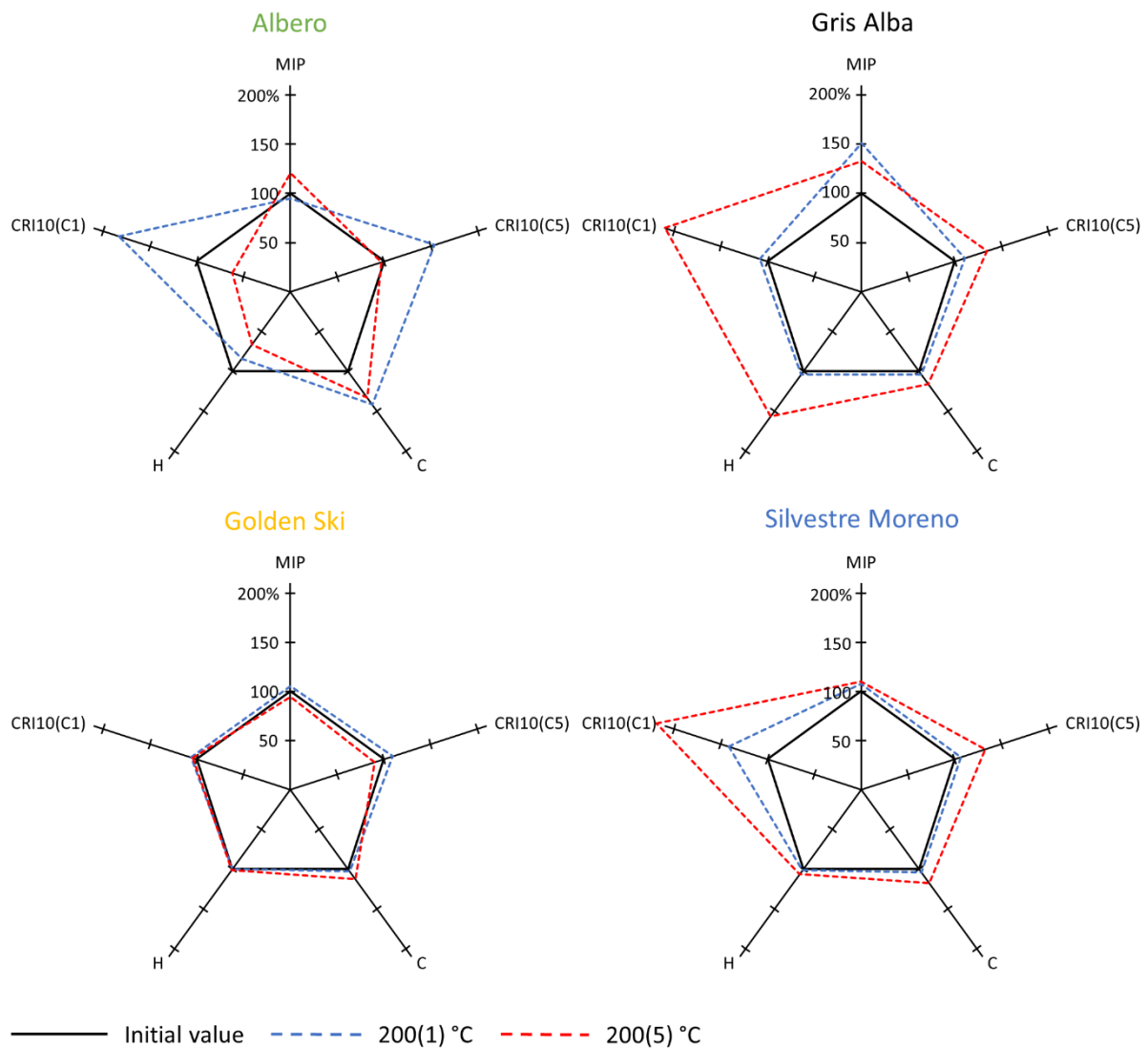
### **EXP2: Effect of thermal fatigue at 200 °C**

According to the porosity value change (Tableau IV-3), some rocks experimented a microcracking at 200 °C observed under SEM.

Granites with lower initial porosity (GA and SM) showed the greatest microcracking increase (Figure IV-14), in agreement with Simmons and Cooper (1978). The thermal fatigue in GA and SM leads to a progressive increase of microcracking measured by the different techniques. The damage caused by the first treatment at 200 °C confirmed a pore size augmentation beyond 1  $\mu\text{m}$  (Figure IV-13) that favoured a faster cooling (CRI). In GA, for the two tested samples, the coefficient C had a positive progression with temperature due to new

connections, in agreement with the increase in the height of the capillary fringe. SM showed good C repeatability for both samples with also a positive progression. The rest of pore-related properties showed an increase, which confirms an increase in microcracking with the thermal cycles.

High porosity and high mica content allowed a mineral expansion and contraction without a catastrophic failure of the rock. Thus, in the case of GS, that despite slight variations through the fatigue cycles, it can be said that the initial and final state of these granites remained similar (Figure IV-14). As the number of cycles increased, the porous network of GS has reorganised, avoiding major modifications. The small crystal size and the mica and clay content favoured the mineral adjustment.



**Figure IV-14. Diagram of the parameter evolution during EXP2: mercury intrusion porosimetry (MIP), the cooling rate index (CRI10 (C1); CRI10 (C5)) to spot C1 and C5, the capillary coefficient (C) and the height of the capillary fringe detected with an infrared thermography camera (H). Except for MIP, the parameters were measured on the same samples.**

A, showed the development of large microcracks that influence the CRI and caused a decrease in the height of the capillary fringe, while MIP remained constant. The capillary coefficient C increased as a result of the widening of the pre-existing intergranular microcracking observed with SEM. After the fatigue test, the bigger microcracks closed possibly by mineral expansion or / and clay remobilisation placed on the edge of pore walls, which did not, however, prevented the continuous circulation of water (Robert, 2004).



### IV.1.6. CONCLUSION

The heterogeneity of low porosity granites induces more dispersed results, while the trends are more similar for high porosity ones. The creation of microcracks and the thermal expansion of minerals are two contradictory phenomena in the evolution of porosity, leading to heterogeneous thermal behaviour. Several parameters are involved in the microcracking evolution with temperature. Thus, for a target temperature, some techniques may indicate an increase in the microcracks while others do not vary or show the contrary. High porosity granites fluctuate between microcracking closure and aperture, with some strong variations that can be considered as a thermal threshold between 90-130 °C. Low porosity granites do not show a thermal threshold at temperatures under 130 °C and only a microcrack closure is measured. However, that is also influenced by the low  $Q_z / F$  ration of this rock.

Thermal fatigue at a temperature of 200 °C shows the evolution of existent and / or generated microcracks. The lower porosity granites present an evident and progressive microcracking development from the very first heating cycle. Capillary coefficient increases with the repetition of the thermal cycles regardless of the affected pore family. The high porosity granites continue to show a redistribution of pre-existing microcracks through all the test and no signs of new microcracking.

Regarding the studied rocks, porosity shows a stronger impact on the thermal behaviour than the mineralogy. Nevertheless, for similar  $Q_z / F$  ratios, the lower porosity granites reach the thermal microcracking threshold earlier. Quartz allows to interpret the closure of the microcracking of granites with high porosity due to its higher thermal expansion. In addition, the low quartz content in the low porosity granite leads to a microcrack closing without microstress development, at low temperature. Mica accommodates the mineral expansion reducing microstresses and the consequent microcracking.

The IRT camera allows to calculate the cooling rate index. Water cooling is more important for granites with high initial porosity. The air cooling remains similar between the different granites. This parameter gives more confident results on the formation of greater microcracks. The image treatment provides a qualitative interpretation of the migration of the capillary fringe. The results show a good correlation with the capillary coefficient, validating this

method. These preliminary experiments confirm the utility of the IRT camera in the monitoring of the thermal behaviour of the granites that will help in the field of geothermal energy and nuclear waste storage.



## **IV.2. Article#4: Experimental Investigation of the Effect of Quenching Cycles on the Physico-chemical Properties of Granites.**

Ce travail a été publié en ligne le 31 août 2021 dans la revue de rang A, *Geothermics* suivant la référence :

Junique<sup>1</sup>, T., Vazquez<sup>1</sup>, P., Benavente<sup>2</sup>, D., Thomachot-Schneider<sup>1</sup>, C., & Géraud<sup>3</sup>, Y. (2021). Experimental Investigation of the Effect of Quenching Cycles on the Physico-chemical Properties of Granites. *Geothermics*, 102235.

<sup>1</sup>GEGENAA EA 3795, University of Reims Champagne-Ardenne, 2, esplanade Roland Garros, 51100 Reims, France

<sup>2</sup>Department of Earth and Environmental Sciences, University of Alicante, 03690 Alicante, Spain

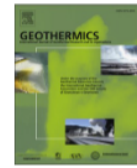
<sup>3</sup>GeoRessources Laboratory UMR 7359, University of Lorraine, F54505 Vandoeuvre les Nancy



Contents lists available at [ScienceDirect](https://www.sciencedirect.com)

Geothermics

journal homepage: [www.elsevier.com/locate/geothermics](https://www.elsevier.com/locate/geothermics)



## Experimental investigation of the effect of quenching cycles on the physico-chemical properties of granites

Thomas Junique<sup>a,\*</sup>, Patricia Vazquez<sup>a</sup>, David Benavente<sup>b</sup>, Céline Thomachot-Schneider<sup>a</sup>, Yves Géraud<sup>c</sup>

<sup>a</sup> GEGENAA EA 3795, University of Reims Champagne-Ardenne, 2, esplanade Roland Garros, 51100 Reims, France

<sup>b</sup> Department of Earth and Environmental Sciences, University of Alicante, 03690 Alicante, Spain

<sup>c</sup> GeoResources Laboratory UMR 7359, University of Lorraine, F54505 Vandœuvre-lès-Nancy, France

### ARTICLE INFO

#### Keywords:

Granites  
Thermal cycling  
Quenching  
Thermal cracking  
Microstructural analysis

### ABSTRACT

In this study, the physicochemical properties of granitic rocks subjected to quenching cycles were studied experimentally. Four granites of similar mineralogy but with different degrees of initial weathering (porosity between 1 and 6%) were slowly preheated at two peak temperatures (200 and 400 °C) and then quenched 35 times.

To study the effect of thermal cycling on the physical properties, non-destructive tests were used such as water porosity, capillary water absorption tests, P- and S- wave propagation velocities, nuclear magnetic resonance relaxometry, and X-ray micro-tomography. Chemical analysis of the granites was performed using X-ray fluorescence, which provided information on the major and trace elements. Water-granite interactions were followed using inductive plasma mass spectrometry (ICP-MS).

The variation of all the measured parameters indicates the creation of cracks with thermal fatigue. The porosity, water uptake, size, and volume of cracks increased while P- and S- wave velocity and Young's modulus decreased. At 200 °C, the changes were progressive up to ten cycles, from which the stress threshold was reached and only small readjustments took place. At 400 °C, the greatest damage was observed during the first five cycles. These changes were a direct consequence of the propagation of the microcracks induced by the strong gradient during the quenching tests. For both temperatures, the changes depended on the initial weathering conditions of the granites. Initially, weathered granites showed crack development or crack closure during quenching, meanwhile the damage on the sound rocks was characterized by the creation of intragranular microcracks.

The analysis of the experimental fluids showed enrichment in K, Na and Ca in the solution as consequence of the dissolution of K-feldspar, plagioclase and the degradation of mica and clays, independently of the physical and mechanical modifications.

### IV.2.1. INTRODUCTION

Recent environmental awareness is leading the world towards an ecological transition that requires exploring new renewable energy resources. Among them, geothermal energy is a clean, sustainable energy source with abundant reserves and with enormous potential for electricity generation, but its technical and geological feasibility must be well understood before any production. Enhanced Geothermal Systems (EGS) are man-made reservoirs created by drilling wells in a crystalline massif to access hot rocks in the earth's crust. The injection of cold water into the drilling of the EGS produces an overall rapid cooling of the neighbouring rocks. Hot water vapor reaching the surface turns a turbine to generate electricity. The water after being cooled is returned to the well, which subjects the well to repeated heating-cooling cycles (thermal cycles). These cycles allow to stimulate the geothermal energy reservoir. Thermal stimulation is a reservoir permeability enhancement technique prompted by injecting cold water into a reservoir at high temperature (Flores et al., 2005; Siratovich et al., 2011; Tarasovs and Ghassemi, 2012). The beneficial effect of this process is the initiation and propagation of hydraulic fractures created artificially in rocks of low thermal conduction and composed by minerals with high thermal dilation coefficient, such as granite (Kumari et al., 2018). Fluid flow is improved allowing increased thermal energy production. At the crystal scale, the changes in the geometry of the porous network induced by the mineral shape modification can increase or decrease the flow of fluid in the rock (Takarli and Prince-Agbodjan, 2008). The cracks formed in the reservoirs can expand and bring about changes in the physical and mechanical properties of the surrounding rocks. When the crack propagation reaches a certain degree, the stability of the well may change (Bérard and Cornet, 2003; Kumari et al., 2017b; Siratovich et al., 2016). In some areas of a granite reservoir, the thermal gradient can be high and reach  $100\text{ °C}\cdot\text{km}^{-1}$  (Baldeyrou et al., 2004). EGS are typically systems with temperatures of around  $200\text{ °C}$  (Olasolo et al., 2016) although some well temperatures, such as Northwest Geysers (California), are measured at  $400\text{ °C}$ . These geothermal systems present a great variety in their environment (temperature, hydrology, geomechanics or petrology) although granite is the primary source rock (Breede et al., 2013). Microcracking can start in granite at around  $100\text{-}120\text{ °C}$  (Junique et al., 2021; Lin, 2002) but most mineral crystals are micro-cracked at around  $400\text{ °C}$  (Chaki et al., 2008).

Granite is a low porous and strong material although very sensitive to the effects of temperature. The mineral composition of a granite, the size and grain distribution are major factors that greatly influence mechanical decomposition (Géraud, 1994; Gómez-Heras et al., 2006; Yilmaz et al., 2009). The increase in temperature will expand the granite minerals. This variation in volume will be different depending on the nature of the grains (Albissin and Sirieys, 1989; Berest and Vouille, 1988). This differential expansion may lead to irreversible microcracks (intergranular and intragranular), generated above a certain temperature threshold (David et al., 1999; Fredrich and Wong, 1986; Junique et al., 2021; Vazquez et al., 2011, 2015). For the most of the studies, the granites were heated to a given temperature although the monitoring experiments were carried out at room temperature after slow cooling down (Chaki et al., 2008; Gautam et al., 2018; Géraud and Gaviglio, 1990; Kant et al., 2017; Reuschlé et al., 2006; Xu et al., 2008). Some studies monitor the possible microcracking during heating by means of acoustic emission or P wave measurements (Glover et al., 1995; Griffiths et al., 2018). In recent years, more researches have been focused on property changes in the rock after experiencing rapid heating-cooling. For example, Pedras Salgadas granite initially heated to 200 °C exhibits a decrease in flexural strength when cooled with water after a cycle (Lam dos Santos et al., 2011). Wu et al. (2019) show that water-cooled samples exhibited a large decrease in P wave velocity and a large number of newly generated cracks on the sample surface. After having subjected a granite to a succession of 20 quenching cycles between 250 and 650 °C, it has been shown that the damage, followed by a decrease in the P wave velocity, increased with temperature and thermal shock cycles (Dong et al., 2020). Xu and Sun (2018), reported that wave velocity decreases as the temperature increases for the same quenching cycle and the wave velocity has a weaker relationship for more than five quenching cycles. Li et al. (2020) show on thermal shock cycles that the wave velocity and the elastic modulus decrease with an increase in temperature and that when the temperature is above 300 °C, the pre-existing microcracks expand and eventually develop into larger cracks. Yu et al. (2020) carried out 20 cycles of thermal shock at 300 °C and showed a progressive decrease in the peak strength and elastic modulus with increasing cycles.

Water penetrates into the pre-cracked granite through micropores and microcracks, which weakens the cohesive force between the crystals and intensifies the development of cracking (Kumari et al., 2017a). In addition, rapid cooling with water on heat-treated granites induces

greater damage than slow cooling, due to thermal gradient cracking (Isaka et al., 2018; Shao et al., 2014). Thus, the permeability of slowly cooled samples increases very weakly at 400 °C, 2.3 times at 500 °C and 35.6 times up to 600 °C while the permeability of fast quenching samples increases 2.9 times at 400 °C, 15.3 times at 500 °C, or even 79.3 times at 600 °C (Jin et al., 2019). The cracking development during these quenching treatments results in a significant reduction in the strength and elastic parameters of the granite as well as in the physical properties due to an augmentation of crack density (Kumari et al., 2017b; Li et al., 2020). Besides, the effect of cyclic heating-cooling leads to a degradation of rock prompted by the generation and development of micro-cracks (Dong et al., 2020; Kim et al., 2014; Xu and Sun, 2018; Zhu et al., 2020).

Geothermal reservoirs present different range of porosity due to damage (microcracks and alteration) (Surma and Géraud, 2003; Zeng et al., 2017) and the role of the initial microstructure on rock cracking is not clear. As a typical heterogeneous material, granites are prone to behave differently depending on their initial state of weathering. Furthermore, the generation of cracks increases the flow performance (Jin et al., 2019; Kumari et al., 2018; Siratovich et al., 2015). An estimate of permeability is therefore essential for applications in the exploitation of unconventional energy and must be correlated with its damage.

Under the thermal effect of quenching, various chemical changes take place in the internal composition of rocks. Many studies in the literature have followed the physical or mechanical properties of granite, however, only a few studies have incorporated the geochemical interaction into the characterisation of cracking processes (Alt-Epping et al., 2013; Baldeyrou et al., 2004; Wogelius et al., 2020). Chemical weathering studies after a fluid-rock interaction are often experiments performed on a single mineral phase, and few studies characterise total mineralogical changes in crystalline rocks (Drüppel et al., 2020; Schmidt et al., 2018).

The main objective of this study is to evaluate the evolution of the granite's void network when exposed to a succession of quenching and the influence of their initial microstructure. For that, four granites with similar mineralogy but with porosity values between 1 and 6% were tested. To obtain an accurate assessment of the sample evolution, a wide range of non-destructive techniques were used to characterise the microcracking distribution, elastic, mechanical and water transport properties, including water porosity, capillary water absorption tests, ultrasounds, nuclear magnetic resonance (NMR) relaxometry, and x-ray

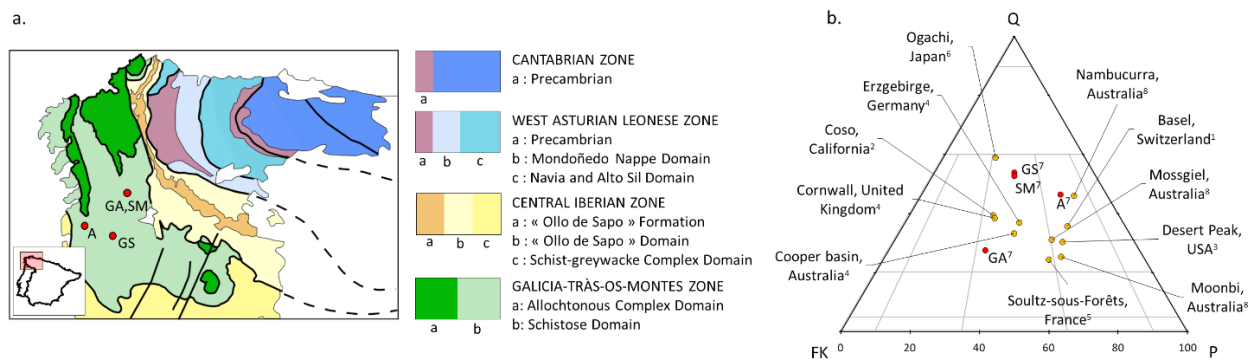


micro-tomography (X-ray CT). Finally, the geochemical interaction between water and minerals after thermal cycling was assessed using inductively coupled plasma mass spectrometry (ICP-MS).

## IV.2.2. MATERIALS

### IV.2.2.1. Characterisation of the outcrop samples: geological background

In this investigation, we selected Albero (A), Gris Alba (GA), Golden Ski (GS), and Silvestre Moreno (SM) granites from the Iberian Peninsula (Figure IV-15a) due to their similar mineralogy and crystal size and their difference in alteration degree and porosity. The ternary diagram compares the studied rocks with granites from Enhanced Geothermal System (EGS) around the world (Figure IV-15b).



**Figure IV-15. a. Geological and geographical settings of the Iberian granites studied within the diagram of the Macizo Ibérico: Albero (A), Gris Alba (GA), Golden Ski (GS), and Silvestre Moreno (SM) granites. b. Ternary diagram with quartz (Q), potassium feldspar (FK), and plagioclase (P) representing granites of this study (red) and granites from global EGS sites (yellow). (Alt-Epping et al., 2013<sup>1</sup>; Kovač et al., 2004<sup>2</sup>; Lutz et al., 2004<sup>3</sup>; Marshall et al., 2010<sup>4</sup>; Stussi et al., 2002<sup>5</sup>; Ueda et al., 2005<sup>6</sup>; Vazquez et al., 2018a<sup>7</sup>; Zhou et al., 2016<sup>8</sup>).**

The granites of this study come from quarries located in the Galician region (north-west of Spain) and the north of Portugal. The granites are located geologically in the Iberian massif and mostly structured during the Hercynian Orogenic Belt formation. All the rocks are post-kinematic and syn-kinematic Hercynian granites and they are located in the so-called Galicia-Trás-Os-Montes area (Farias et al., 1987). The region is sequentially organised into three groups according to their compositional characteristics and structural criteria (Vera, 2004): calc-alkaline syn-kinematic granites, peraluminous syn- and post-kinematic granites, and calc-

alkaline post-kinematic granites. The four studied granites belong to the group of Peraluminous syn and post-kinematic granites. This group includes granites temporally related to the processes of regional metamorphism and of Hercynian crustal anatexis. Albero is in Donón-Tomiño alignment which represents an elongated mass of about 56 km and 12 km wide with a small deformation that gives orientation to the minerals. This formation of longitudinal axis is parallel to the general directrices of the Hercynian in this region of Galicia. In 2004, the Geologic and Mining Spanish Institute (IGME, 2004a, 2004b) described the Gris Alba and Silvestre Moreno varieties as "very leucocratic two-mica granites". They are found in the Salvaterra-A Cañiza-Cerdedo alignment, which belongs to the Faro de Avión batholith. This massive elliptical shape measures about 7.5 km by 4 km. The Golden Ski variety places within the Salvaterra–A Cañiza–Cerdedo Alignment, which is an elongated granitic batholith with the longitudinal axis parallel to the general guidelines of the Hercynian in this area of Galicia.

### IV.2.2.2. Granite description

Binocular and microscopic views of the studied granites are shown in Figure IV-16. The petrographic characterisation (mineral proportion and crystal size) was produced by Vazquez et al. (2018a) by optical polarising microscopy and the main petrographic characteristics are presented in Tableau IV-5.

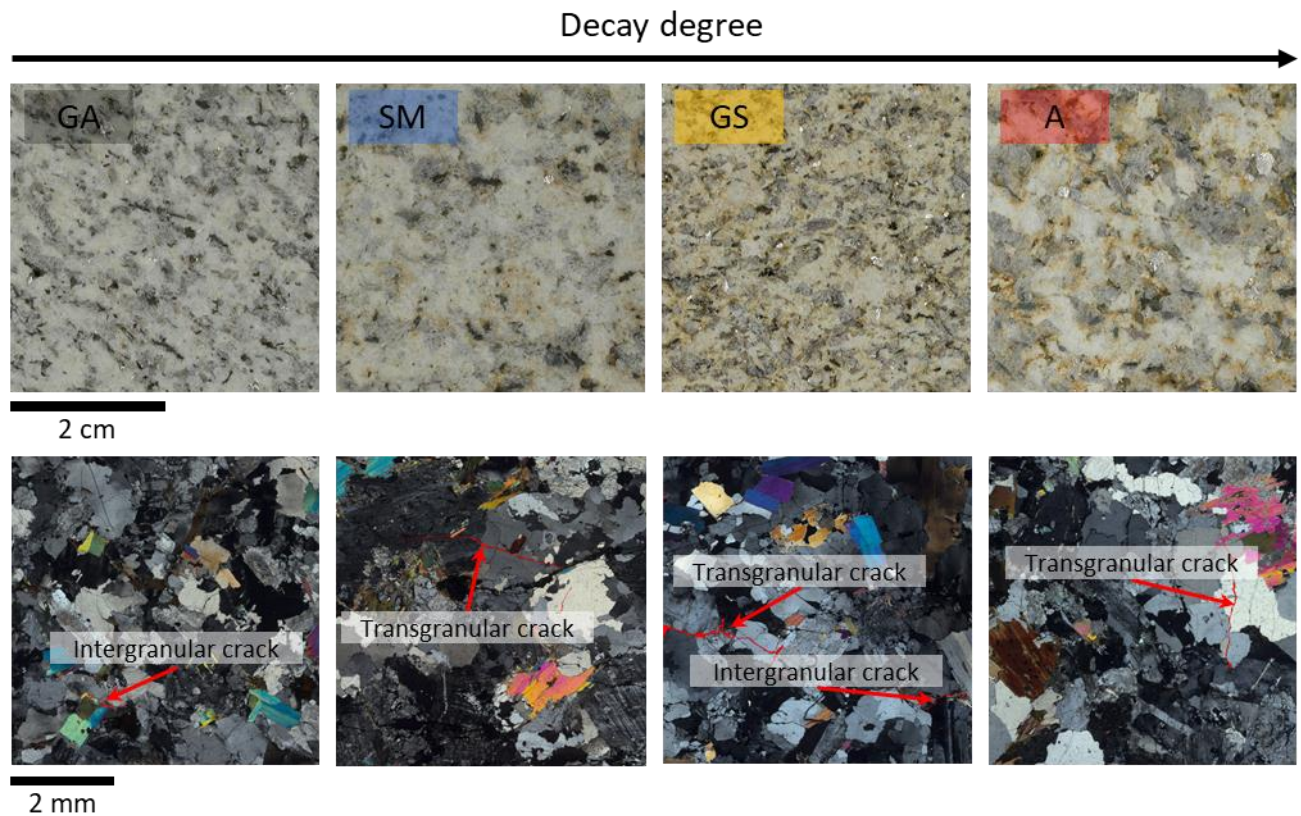


Figure IV-16. Macroscopic and microscopic photography of the studied granite: Gris Alba (GA), Silvestre moreno (SM), Golden ski (GS), and Albero (A).

Tableau IV-5. Characteristics of the selected granitoids. Trade name, mineral proportion (studied using optical polarisation microscopy), IUGS classification (Le Maitre, 2002) and the crystal size of the studied granites (Vazquez et al., 2018a). (Avg: Average; Q: quartz; FK: alkali feldspar; P: plagioclase; M: mica).

Stone	Composition (%)				IUGS classification	Crystal size (mm)				
	Q	FK	P	M		Q	FK	P	M	Avg.
<b>A</b>	35	10	30	25	Granodiorite	5	5	6	4	5
<b>GA</b>	23	37	23	17	Monzogranite	5	5	4	2	4
<b>GS</b>	47	20	20	13	Monzogranite	4	4	4	2	4
<b>SM</b>	45	20	20	15	Monzogranite	4	5	7	4	5

Albero (A): The yellowish hue found in the granite was due to a notable initial alteration and the presence of clay. Indeed, this granite was characterised by open transgranular cracks. It was a homogeneous granodiorite with medium-fine crystal (5 mm). It had the lowest alkali

feldspar content among the four granites studied and a high proportion of muscovite and biotite (25%). A contains elongated xenomorphic minerals orientated according to the foliation. Most boundaries were interpenetrated.

Gris Alba (GA): The intergranular cracks observed in this granite can be found mainly at the edge of the micas. It was a homogeneous monzogranite with fine crystal (4mm). It had anhedral minerals and the boundaries between the quartz crystals were irregular. The proportion of muscovite biotite minerals was about 2:1.

Golden Ski (GS): Pre-existing cracks were of intergranular nature and were present in plagioclases. GS also had open transgranular cracks. It was a homogeneous monzogranite with fine crystal (4 mm). Quartz and feldspars were subhedral and muscovite was euhedral. These were the muscovite crystals that have the largest crystal size and plagioclase the smallest crystal size. Quartz content was higher than that of feldspars which is 20% of plagioclases. This granite had an initial alteration characterised by the presence of clay.

Silvestre Moreno (SM): Like A and GS, this granite had an initial alteration indicated by the presence of intra, inter and transgranular cracks. It was a homogeneous monzogranite of small size (5 mm). These minerals were subidiomorphic. After GS, this granite had the highest quartz proportion of the granitoids studied. SM had the same proportion of feldspars and plagioclase (20%) as GS. Plagioclases were the minerals with the largest size (7 mm).

### **IV.2.3. METHODOLOGY**

#### **IV.2.3.1. Sampling and analytical procedure**

The experimental method was specifically designed to verify the impact of an abrupt change of temperature in the granites (Figure IV-17a) because there are not quenching standard tests.

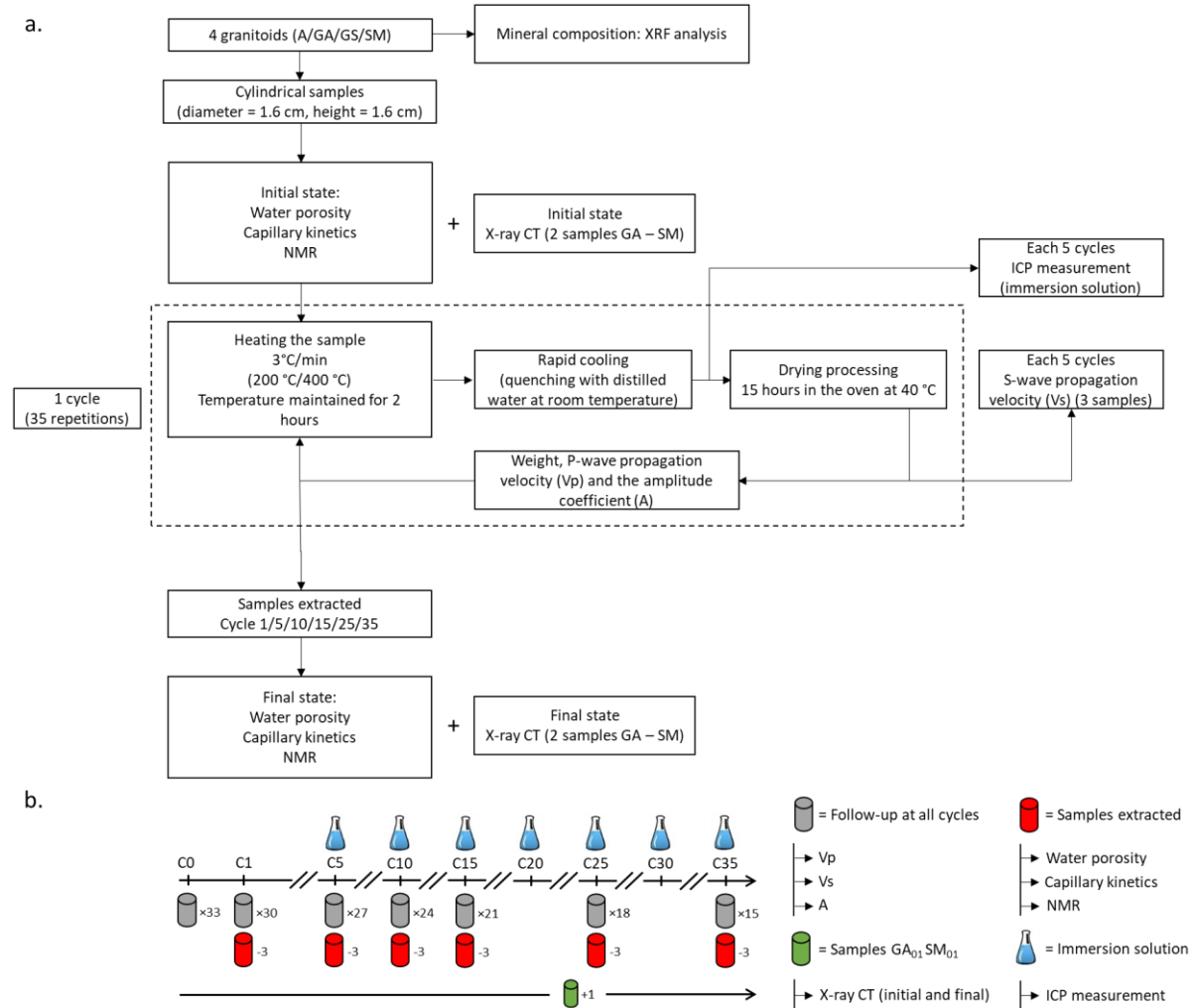


Figure IV-17. a. Experimental methodology. b. Detail of sampling during the cycles (C).

The samples are cylinders 1.6 cm in diameter (d) and 1.6 cm in height (h). A total of 33 samples per granite and per quenching test were used. A total of 3 samples per granite were removed on the 1 / 5 / 10 / 15 / 25 / 35 cycle for each quenching test. Samples of the purified water (5 ml) used during cooling was removed every 5 cycles for each quenching test (Figure IV-17b). The water samples taken will be analysed by inductively coupled plasma mass spectrometry (ICP-MS).

#### IV.2.3.2. Thermal treatment

The main goal was to study the influence of cyclic quenching on the mechanical and microstructural properties of granites. The samples were heated at a rate of 3 °C / min until the target temperature was reached. This heating rate was low enough to avoid thermal shocks on the granite and to ensure that induced microcracks were the direct response of temperature and not of the temperature gradient within the sample (Dwivedi et al., 2008; Li

et al., 2020; Zhu et al., 2020). Two heating temperatures (200 and 400 °C) were selected as average and maximum temperatures of existing geothermal systems (Breede et al., 2013). The temperature was kept constant for 2 hours to distribute the assigned temperature evenly (Tang et al., 2019). Cold distilled water (~25 °C) was then instantly inserted into the container containing the samples for 1 hour. This water was changed after each cycle. According to Zhang et al. (2018), the sample surface cooling time was about 10 and 25 min for the heating temperature of 200 and 400 °C. This cycle was repeated 35 times.

### IV.2.3.3. Physical property tests

#### IV.2.3.4. Water porosity

Connected porosity ( $\varphi_c$ ) is defined as the ratio of the volume of connected voids to the total volume of rock. In this study, the experimental protocol followed the standard (NF EN 1936, (2007)). It consists of obtaining the porosity using the triple mass method. The dried samples were weighed and placed in a desiccator where the pressure was gradually lowered with a vacuum pump to remove any air from the pores. The degassed distilled water was then gradually introduced until the samples were completely immersed. Once atmospheric pressure was restored, the samples were left in the water for 24 hours. The saturated mass and the hydrostatic mass of the samples were then recorded.

#### IV.2.3.5. Capillary coefficient

Capillarity on a natural stone is an intrinsic property and represents its ability to absorb water under the effect of capillary forces. This property is directly related to the porous network (size, pore shape, and network connection). The capillary coefficient (C) was calculated based on the NF EN 1925, (1999). The samples were dried at  $40 \pm 5$  °C before each test until their masses stabilised. The principle of experience is to put our porous solid in contact with distilled water. Capillary kinetics are usually characterised by two phases (Hammecker et al., 1993; Hammecker and Jeannette, 1994). The first phase is the progressive filling of the free porosity by the capillary forces of water without external pressure applied. The slope of this curve represents the capillary coefficient (Roels et al., 2000) that is the volume of water penetrated by capillarity into the rock per unit of square root of time according to the Washburn law ( $\text{g}\cdot\text{m}^{-2}\cdot\text{s}^{-1/2}$ ). The restitution curves of the water uptake tests give information about the porous

network (Benavente et al., 2015, 2002). The modification of the porous networks of the samples was only assessed through the variation of this parameter.

### IV.2.3.6. Elastic rock properties and deduced mechanical properties

P- and S-waves propagation velocities ( $V_p$  and  $V_s$  respectively) were measured to estimate dynamic mechanical rock properties. Moreover, the monitoring of the ultrasonic signal is effective in evaluating the characteristics of the pores of the rock because it depends mainly on the size, connectivity, and distribution of the pores, the lithology, and the bedding planes. Propagation velocities were measured using equipment for receiving non-transmitting signals (Panametrics-NDT 5058PR) coupled to an oscilloscope (TDS 3012B-Tektronix). The transducer frequency was centered on 2.5 MHz for P-waves and 1 MHz for S-waves. To ensure the transmission of ultrasonic energy between the transducers and the surface of the sample, a visco-elastic coupler was used. Constant pressure was systematically applied between the transducers and the sample. In this study, the P-wave velocity was measured on all the samples after each cycle of quenching.  $V_s$  was measured every 5 cycles on 3 samples for each test.

Dynamic Young's Modulus ( $E$ ) (IV.2) and Poisson's ratio ( $\nu$ ) (IV.3) were calculated as follows (Homand et al., 2000):

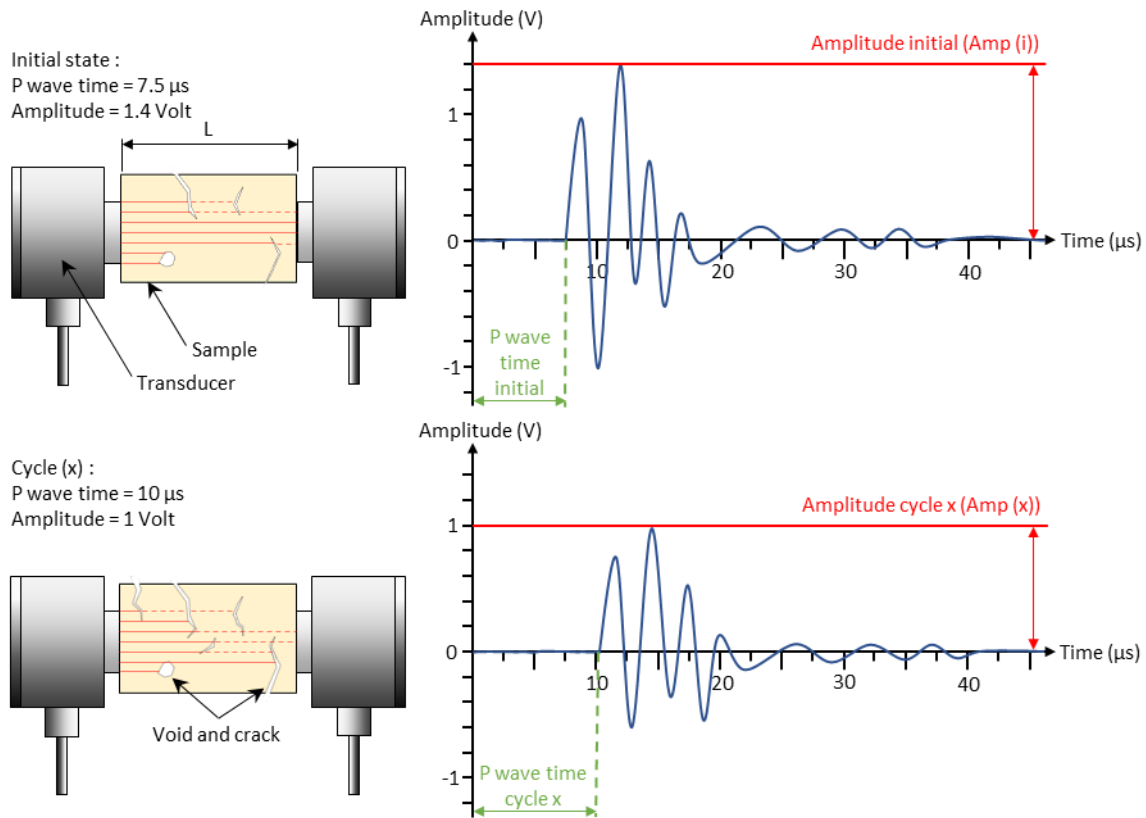
$$E = \rho \frac{V_p^2(1 + \nu)(1 - 2\nu)}{1 - \nu} \quad (\text{IV.2})$$

$$\nu = \frac{\frac{1}{2} - \left(\frac{V_s}{V_p}\right)^2}{1 - \left(\frac{V_s}{V_p}\right)^2} \quad (\text{IV.3})$$

Where  $\rho$  is the bulk density determined through direct measurement of dried weights and dimensions of samples.

In addition to  $V_p$  and  $V_s$ , the amplitude coefficient ( $A$ ) was obtained. It was defined as the ratio between the Amp ( $x$ ) and the Amp ( $i$ ). Amp is the maximum amplitude (in absolute values) measured in the waveform of the signal received: Amp ( $i$ ) corresponded to the value of the samples before the tests and Amp ( $x$ ) after each quenching test.

The quantification of this parameter allowed to estimate textural defects induced to the rock. The presence of an open fracture brings about a strong scattering of the ultrasonic waves and induces a decrease in coefficient A. The attenuation of the signal amplitude (Figure IV-18) depends on the textural characteristics of the rock and the individual defects but is less sensitive to crystal size and porosity as may be  $V_p$  (Martínez-Martínez et al., 2011).



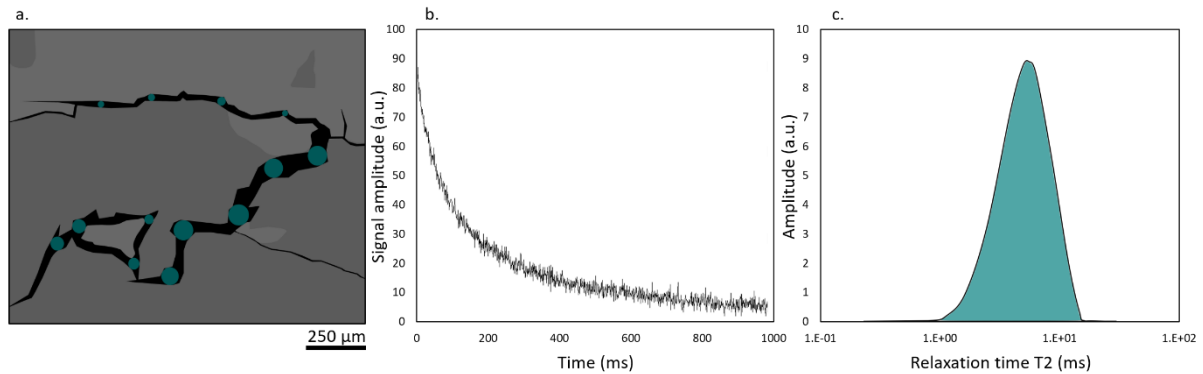
**Figure IV-18. Diagram of the transmission of ultrasonic waves with an example of signals received as a function of the degradation of the rock.**

#### IV.2.3.7. Nuclear Magnetic Resonance relaxometry

Nuclear magnetic resonance (NMR) is a fast, practical, and non-destructive tool for characterizing complex porous media. The NMR measurements were carried out on a set of 66 samples of each sound granitoid using a minispec mq-Series instrument. NMR is based on the decay by magnetisation of the hydrogen nucleus of water and useful for the deduction of certain information on the structure of pores (distribution pore) (Liu et al., 2017; Tian et al., 2020; Weng et al., 2018). The rock samples were vacuumed and saturated for 24 h and were then soaked in water for 24 h to fill the rock material with water. During the measurement, the sample was taken out from the water and instantly integrated into a hermetic support



before being placed in the NMR. That maintained the saturation during the whole measurements. The NMR method estimates the diameter which corresponds to the width between the porous walls (Figure IV-19).



**Figure IV-19. Summary of the use of NMR in the analysis of porous rocks. a. Diagram of the enlarged 2D X-ray CT view of the SM granite to visualise the cracks, the blue circles are detected by NMR. b. The transverse magnetisation decay curve (example of measurement on the SM granite). c. The transverse relaxation time (T2) distribution curve constructed by a mathematical inversion process (the curve reflects a distribution of pore, surface to volume ratios  $V / S$ ).**

The transverse relaxation time (T2) is measured with a Carr-Purcell-Meiboom-Gill (CPMG) sequence, at regular time intervals  $2\tau$  (or TE) of 100 μs. The transverse magnetisation decay curve (Figure IV-19b) is the sum of all decay signals generated by the protons in the sample. Dynamics Center software (Version: 2.5.5) was used to represent the distribution of relaxation times (the amplitudes  $A_i$  as a function of  $T2_i$ ) obtained through a mathematical transformation (Laplace inverse) (Figure IV-19c).

These are the surface effects and the physical properties that are used in nuclear magnetic relaxation in porous media. Each T2 is linked to the porous space of the sample, in particular the ratio / surface.

This link is transcribed in the equation (IV. 4) (Fleury, 1998), as follows:

$$\frac{1}{T2} = \frac{1}{T2b} + \rho \frac{S}{V} + \frac{1}{12} (TE\gamma G)^2 D \quad (IV. 4)$$

Where T2 represents the transverse relaxation time,  $\rho$  is the specific surface relaxivity (of the order of 1-30 μm·s<sup>-1</sup> for natural porous media). T2b represents the relaxation time of the fluid saturating the porous space (2700 ms for water at 30 °C), S is the surface and V the volume of

the pore considered, TE is the inter-echo time of the CPMG sequence; we set it at 100  $\mu$ s, G is the average local magnetic field gradient,  $\gamma$  is the gyromagnetic ratio and D is the auto-diffusion coefficient of the fluid. The term diffusion can be neglected in equation (IV. 4) because T2 is independent of the inter-echo time (very weak in this experiment).

The geometry of our pores must be hypothesised. In the monophasic case, the spherical pores have a surface ratio of:

$$\frac{S}{V} = \frac{3}{r} \quad (\text{IV. 5})$$

where r is the pore radius. If we consider that our pores are spherical, we simplified equation (IV. 6), as follows:

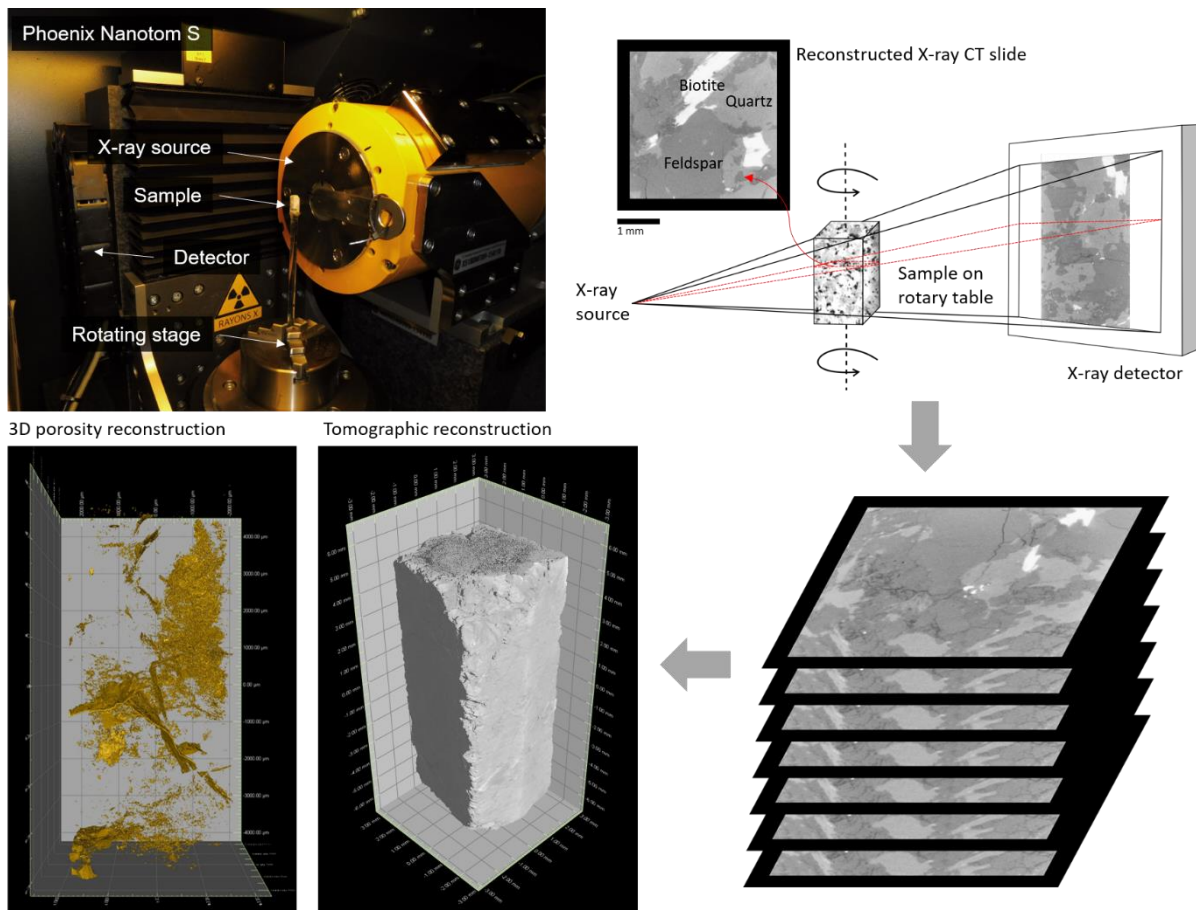
$$\frac{1}{T2} = \frac{1}{T2b} + \rho \frac{3}{r} \quad (\text{IV. 6})$$

The values of T2 were taken before and after cycling. Thus, the T2 distribution reflects the information on the pore size, the smaller the T2 value, the smaller the pore size.

### IV.2.3.8. X-ray micro-tomography

X-ray microtomography (X-ray CT) is a non-destructive technique that permits to visualise in 3 dimension the modifications of the porous network at high resolution, without sample preparation or chemical fixation. As a result, the natural characteristics of the mineralogical information and the porous network have been maintained. X-ray tomography imaging was performed on a Phoenix Nanotom S. A rectangular prisms of size 5 x 5 x 10 mm of the GA and SM granite were analyzed before and after 35 quench cycles. The X-ray tomography scan resolution was associated with the sample size. The resolution was about 1 voxel = 6  $\mu$ m. The maximum voltage that this microtomograph can supply is 180KV / 15W. An X-ray source generates beams which pass through the sample placed on a 360 ° rotating stage, leaving shadow projections on the detector and acquiring several 2D X-ray absorption images (Figure IV-20). The measurement of the x-ray attenuation is proportional to the local bulk density of the object if the chemical composition of the object is uniform. Density values are represented by grey levels, black is equivalent to air while white is set to the highest mineral density. In general, feldspar, quartz, and biotite minerals have average densities of 2560 kg·m<sup>3</sup>, 2648 kg·m<sup>3</sup>, and 3090 kg·m<sup>3</sup>, respectively. Therefore, biotite will appear in light colour on images

scanned by X-ray tomography, and quartz and feldspar minerals will have darker colours. The small difference in density between quartz and feldspar makes their identifications more difficult. The sectional images of the object are reconstructed and allow to create a full 3D representation of the samples. In geoscience, this technique has been widely implemented in studies (Fan et al., 2018; Géraud et al., 1999; Isaka et al., 2019; Kumari et al., 2018; Sepúlveda et al., 2020; Yun et al., 2013).



**Figure IV-20. Principle of X-ray microtomography going from image reconstruction to 3D visualisation.**

At the end of the acquisition process, the VGStudio MAX 2.2 © software (Volume Graphics) was used to perform the reconstruction and its qualitative and quantitative analysis. First, the volume defects associated with the acquisition were eliminated. Regions of Interest (ROI) were created respecting the capacity of the computer used and being the most representative of the entire sample. The same ROI was selected on the samples before and after treatment. The segmentation of the images allowed to separate the mineral phase from the crack porosity by attributing to each voxel of the image the corresponding phase according to its

shade of grey. The porosity values of the slides were strongly influenced by the choice of the binarisation threshold. For this reason, the adjustment parameters remained the same throughout all the analysis. Different properties of the voxels (volume, diameter, sphericity, etc.) were obtained using a flaw detection tool.

The heterogeneity of the distribution of microcracks along the z height was evaluated. From the porosity of the X-ray CT images of the cross-sections in x – y planes, the coefficient of variation called the coefficient of heterogeneity ( $U_z$ ) by (Fan et al., 2018) was calculated before and after the quenching test from equation (IV. 7):

$$U_z = \frac{1}{\underline{D}_{xy}} \sqrt{\frac{1}{n} \sum_{j=1}^n (D_{xy,j} - \underline{D}_{xy})^2} \quad (\text{IV. 7})$$

With  $D_{xy,j}$  denotes the porosity of the cross-section j and  $\underline{D}_{xy} = \frac{1}{n} \sum_{j=1}^n D_{xy,j}$  denote the mean porosity cross-section in the x-y plane. n is the number of X-ray CT images used for the analysis.

### IV.2.3.9. Chemical analysis

### IV.2.3.10. X-Ray Fluorescence and Inductively coupled plasma mass spectrometry analysis

The chemical analysis of the granites was performed using X-Ray Fluorescence (XRF) (Philips Magix Pro device), which provided information of major and trace elements.

The geochemical reactivity of the water-granite interaction was carried out by analysing the resulting / lixiviated water after one hour of water-quenching for each granite type and test every 5 cycles (Figure IV-17). The contents of dissolved Al, Ca, Fe, Mg, Mn, Na, K, and Ti were determined using Inductively coupled plasma mass spectrometry (ICP) (VG PQ-ExCell, THERMO ELEMENTAL). Nitric acid ( $\text{HNO}_3$ ) was added before analysis to stabilise the solutions.

## IV.2.4. RESULTS

The results of the initial physical properties of the selected stone are shown in Tableau IV-6.

**Tableau IV-6. Values of physical properties.  $\varphi_c$ : connected porosity C: capillary coefficient;  $V_p$ : P-wave propagation velocity; Amp: maximum amplitude of the P-waves;  $V_s$ : S-wave propagation velocity; E: Young's modulus and T2: transverse relaxation time.**

Stone	$\varphi_c$ (%)		C ( $g \cdot m^{-2} \cdot s^{-1/2}$ )		$V_p$ ( $m \cdot s^{-1}$ )		Amp (V)		$V_s$ ( $m \cdot s^{-1}$ )		E (GPa)		T2 (ms)	
	Avg.	St.d.	Avg.	St.d.	Avg.	St.d.	Avg.	St.d.	Avg.	St.d.	Avg.	St.d.	Avg.	St.d.
A	5.20	0.48	13.26	2.54	2526	322	$5.6 \times 10^{-04}$	$2.9 \times 10^{-04}$	1066	147	7.93	1.99	10.7	2.0
GA	1.19	0.35	2.39	0.45	3292	118	$8.0 \times 10^{-03}$	$4.1 \times 10^{-03}$	1549	94	17.22	2.07	38.8	4.0
GS	3.75	0.64	14.23	1.00	1758	197	$1.0 \times 10^{-03}$	$4.8 \times 10^{-04}$	889	149	5.30	1.69	25.0	2.8
SM	2.40	0.30	8.92	3.25	3951	308	$4.1 \times 10^{-03}$	$1.7 \times 10^{-03}$	1657	260	20.24	6.42	11.7	2.1

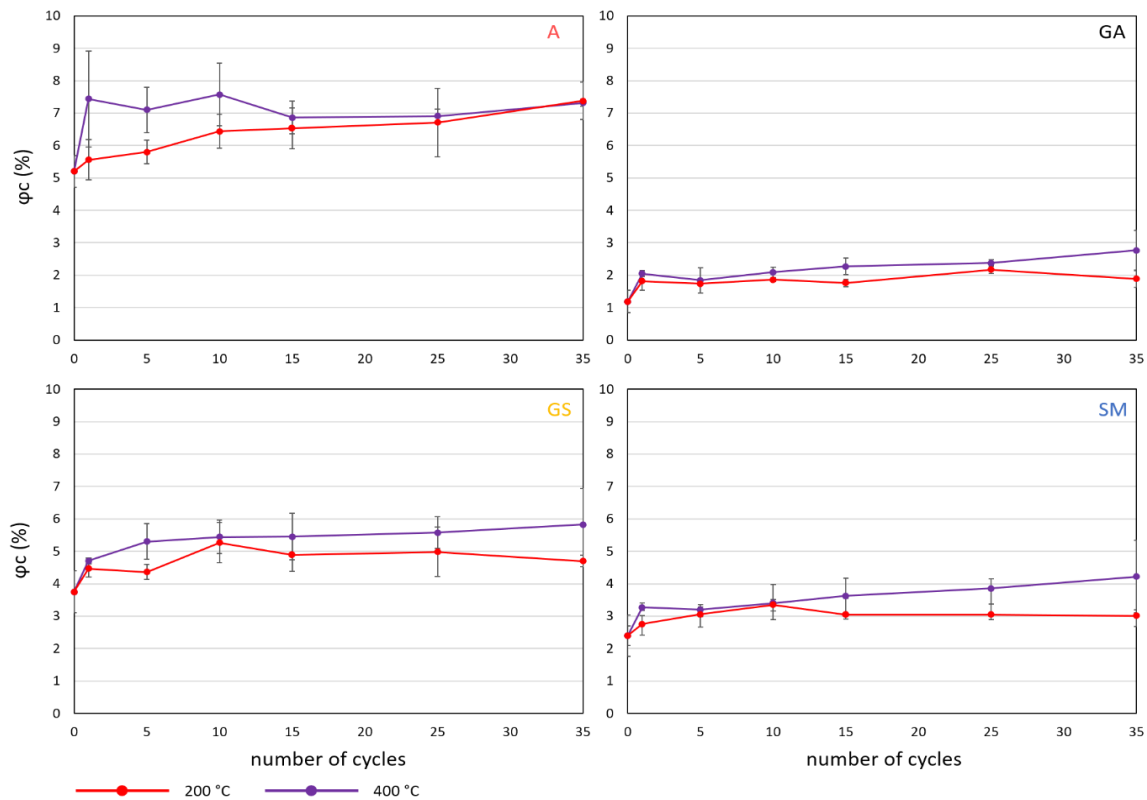
Avg. average, St.d. standard deviation

The degree of initial weathering of the four granites was assigned relative to their initial porosity.

Albero (A) will be referred to as a highly weathered granite with the highest porosity of 5.2%. Therefore, it showed low  $V_p$  and  $V_s$  values of about 2526 and 1066  $m \cdot s^{-1}$ , respectively. Gris Alba (GA) will be referred to as an unaltered granite with a low porosity of 1.2%. This granite showed the lowest values of the maximum amplitude of  $V_p$ . It showed the highest relaxation time T2 values. Golden Ski (GS) will be referred to as a moderately weathered granite with a porosity of 3.75%. It showed a highest C coefficient and lowest value of  $V_p$  and  $V_s$  of approximately 1758 and 889  $m \cdot s^{-1}$ , respectively, resulting in a low value of the elastic modulus E of 5.3 GPa. Silvestre Moreno (SM) will be referred to as a slightly weathered granite. It showed a porosity of around 2.4% and the highest  $V_p$ ,  $V_s$  and E values.

### IV.2.4.1. Connected porosity

The water porosity was calculated before the test and on the samples removed during the cycles (Figure IV-21).



**Figure IV-21. Relationship between the number of thermal cycles and the connected porosity ( $\phi_c$ ) for the two quenching tests at 200 °C and 400 °C.**

For each granite, the porosity showed an increasing trend with the quenching cycles, more remarkable after the first cycle, and greater when heated at 400 °C than at 200 °C. This increase was not monotonous for all granites. Indeed,  $\phi_c$  decreased slightly for A from the first to the fifth cycle at 400 °C for example.

For A, the cycles at 200 °C revealed that the  $\phi_c$  increased continuously with the number of cycles, with a change of 40% at the end of the test. At 400 °C, the  $\phi_c$  did not show any further increase after the first cycle, with an abrupt increase of also around 40%.

For GA, at 200 °C the  $\phi_c$  increased after cycle 1 and 25, with a variation of 60% at the end of the test. At 400 °C, after an abrupt increase during the first cycle,  $\phi_c$  grew continuously until the end of the test with a change of 130%.

For GS and SM, the curves of the cycles at 200 °C indicated 2 slopes, a first until cycle 10 with continuous increase and a second from cycle 10 to 35, which showed a stabilisation, with a final variation of 25% at the end of the test. The curves at 400 °C of these 2 granites showed

as for the rest of the rocks, an abrupt increase after the first cycle and a softer augmentation through the cycles, with a final increase of 55 and 75% for GS and SM respectively.

IV.2.4.2. Capillary coefficient

The capillary absorption curves lasted over 72 hours, where the capillary coefficient (C) was obtained after the first linear part of the curve. The rise of the capillary fringe was complete for A, GS, and SM. For the GA granite, the water weight gain curve showed several breaks in slope and the capillary fringe did not reach the top of the sample. This incomplete rise reflected the low porosity values as well as the poor interconnection between the multiple families of pores and cracks. Figure IV-22 represents the evolution of the coefficient C of each granite during the two quenching tests.

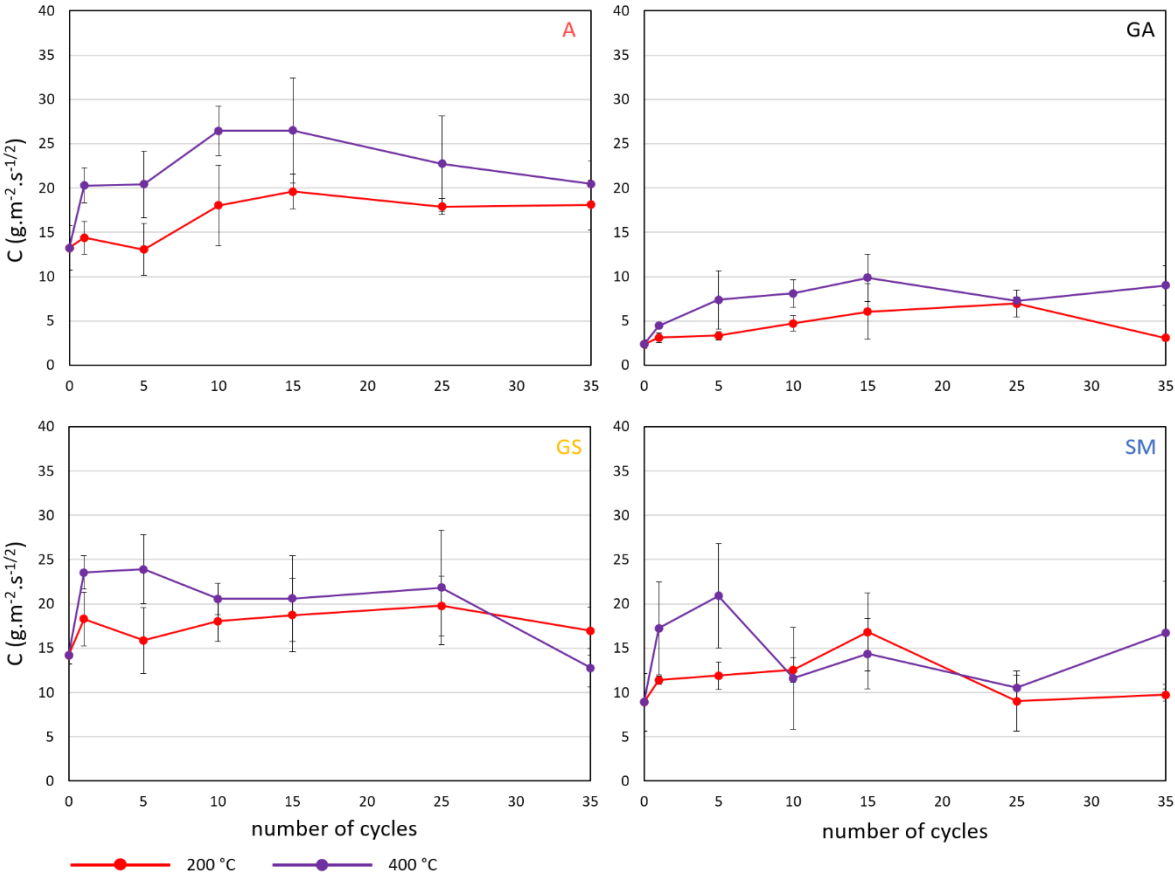


Figure IV-22. Relationship between the number of thermal cycles and the capillary coefficient (C) for the two quenching tests at 200 °C and 400 °C.

For both quenching tests, capillary water absorption increased from the first cycle for all granites. In general, the increase was greater for rocks heated at 400 °C.

For A, at cycle 15, the coefficient C reached its highest value for rocks preheated at 200 °C with an increase of about 50%, and at cycle 10 for rocks preheated at 400 °C with an increase of about 100%. It only took one cycle of the preheated rock at 400 °C to reach a rise of 50%. From cycle 15, the coefficient C decreased for the two quenching tests and ended at cycle 35 with a final increase of 35% for the tests at 200 °C and of 55% for the tests at 400 °C.

For GA, although the general increase was significant for both quenching tests, the progression was greater on rocks preheated at 400 °C. The C coefficient of rocks preheated at 200 °C increased by 200% in a linear trend until cycle 25. This increase was comparable to the increase observed during cycle 5 of rocks preheated at 400 °C. From cycle 15, the coefficient C of rocks preheated at 400 °C stabilised after an increase of about 310%.

For GS, the capillary water absorption showed an irregular progression for the two quenching tests after an abrupt increase after cycle 1. The coefficient C increased to a maximum of 40% at cycle 25 for the 200 °C tests and 70% at cycle 5 for the 400 °C tests.

For SM, the rocks preheated at 200 °C, the coefficient C increases by 80% after cycle 15. The coefficient remained stable from cycle 25. Rocks preheated at 400 °C increased significantly by 130% after cycle 5.

### IV.2.4.3. P- and S-waves velocities and dynamic elastic moduli

Figure IV-23 shows the variations of the average of P-waves propagation velocities ( $V_p$ ) and the attenuation coefficient (A) with the number of cycles. Each point corresponds to the average of the 18 samples measured from the initial state to cycle 35.

The granites preheated at 200 °C showed initially a gradual decrease in  $V_p$  with the number of cycles. A, GS, and SM exhibited a later stabilisation or even a slight recovery. Granites preheated at 400 °C showed a significant decrease in  $V_p$  after the first cycle, *i.e.* by approximately 26%, 15%, 23%, and 22% for A, GA, GS, and SM, respectively. Following this



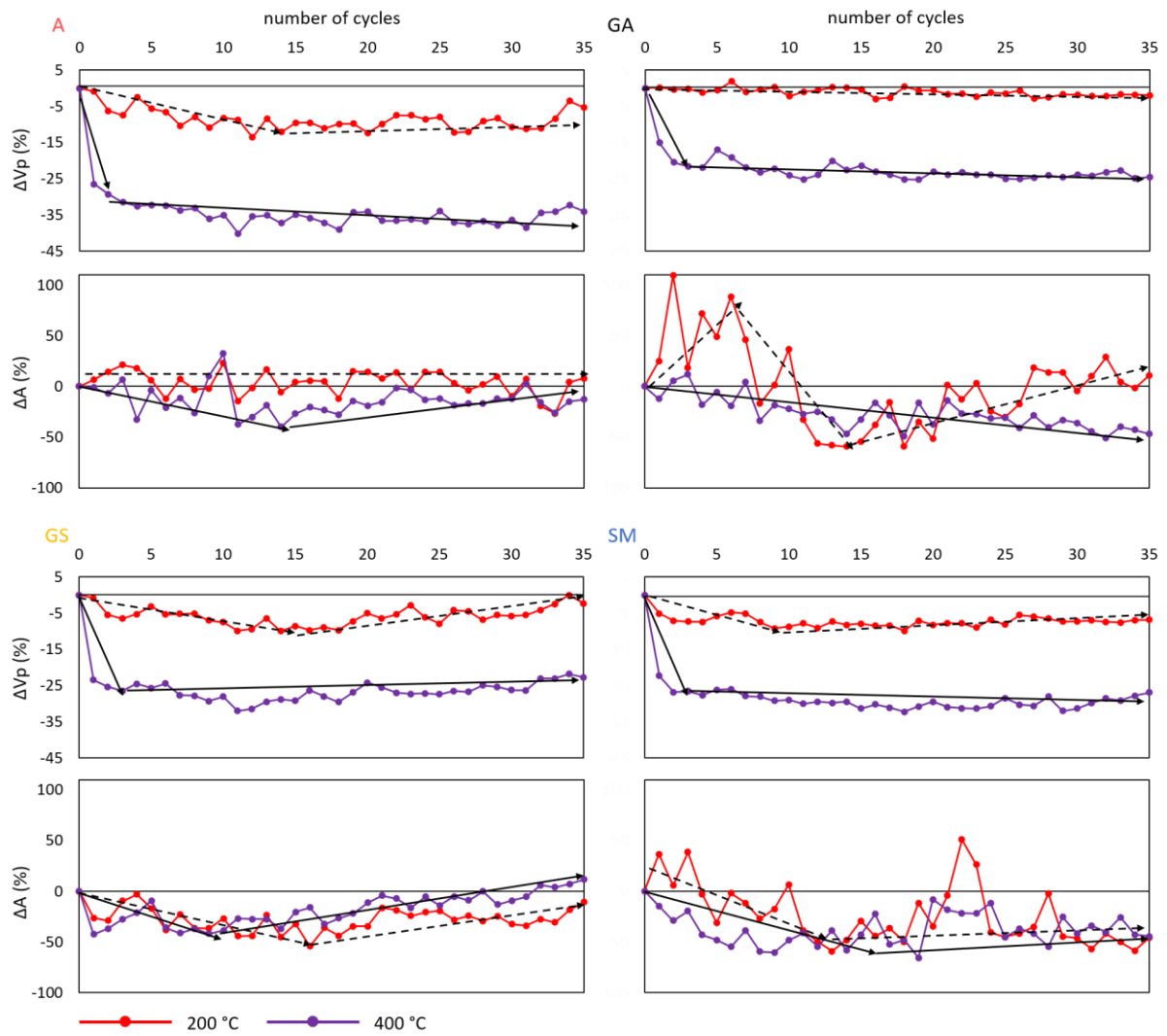
phase, the variations were smaller. The average rate of  $V_p$  decreased at cycle 35 by 34%, 25%, 23%, 27% for A, GA, GS, and SM, respectively.

For A,  $V_p$  gradually decreased by about 10% until cycle 14 at 200 °C, then remains stable. The coefficient A remained close to the initial value from the beginning at 200 °C. For 400 °C,  $V_p$  showed an overall decreasing trend with increasing cycles. The coefficient A decreased by about 40% after cycle 14 and then increased again.

For GA,  $V_p$  values did not show a significant variation, whereas coefficient A showed significant variation. The first cycles were marked by an increase followed by a decrease of about 60% after cycle 14 at 200 °C. The coefficient A increased again to reach the attenuation values of the initial wave. For 400 °C,  $V_p$  and the coefficient A decreased linearly up to cycle 35.

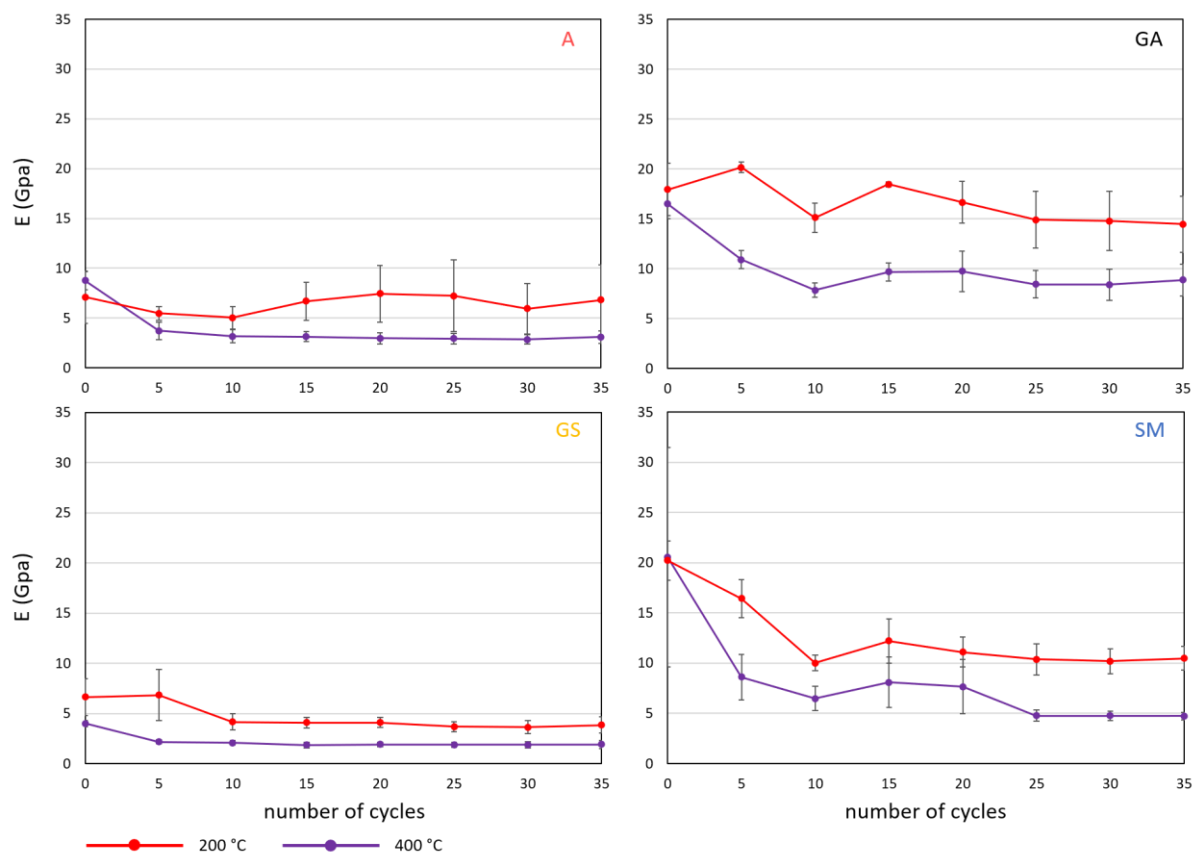
For GS,  $V_p$  decreased by approximately 10% until cycle 18 then gradually increased to reach the initial mean value again at cycle 33 at 200 °C. The coefficient A showed a similar trend with a decrease of approximately 50% after cycle 16, followed by an increase at 200 °C. For 400 °C, GS was the only one among the granites to have these  $V_p$  values which increased after the large falling after the first thermal shock cycles. The coefficient A also gradually increased after a decrease of about 40% after the first cycle.

For SM, a decrease of  $V_p$  of about 10% was observed after cycle 10, then a stable recovery to -7% of the initial value at 200 °C. After a balancing phase during the first 10 cycles, the coefficient A decreased by about 60% after cycle 13, then hovered around -40%. It is also noted that the values between samples had a high variability. For 400 °C, after a decrease at the first cycle,  $V_p$  remained between -20 and -30%. The coefficient A decreased by approximately 60% at cycle 17, then increased slightly.



**Figure IV-23. Relationship between the number of thermal cycles and the percentage change in the P-waves velocity ( $V_p$ ) and the amplitude coefficient (A) with the initial state. Solid and dashed black lines represent the trend for 200 °C and 400 °C, respectively.**

The changes of the elastic modulus (E) of granites after heating (200 °C and 400 °C) and treatment with water are shown in Figure IV-24.



**Figure IV-24. Relationship between the number of thermal cycles and the Young's Modulus (E) for the two quenching tests.**

For A, E decreased by approximately 20% from the first 5 cycles at 200 °C. Then, A remained stable around its initial value. For 400 °C, the values of E decreased significantly after 5 cycles, *i.e.* by about 60%, and then remained stable.

For GA, E showed an increase of 10% at cycle 5 then a decrease of 20% after cycle 35 at 200 °C. For 400 °C, the values of E decreased by 35% and 45% after 5 and 35 thermal treatments, respectively.

For GS, E remained stable after a 40% decrease after cycle 10 at 200 °C. For 400 °C, the values of E decreased by 45% and 50% at 400 °C after 5 and 35 thermal treatments, respectively.

For SM, E decreased by approximately 20% from the first 5 cycles at 200 °C and reached a decrease of 50% after cycle 35. For 400 °C, the values of E decreased by 60% and 80% at 400 °C after 5 and 35 thermal treatment, respectively.

#### IV.2.4.4. Nuclear Magnetic Resonance relaxometry

We compared quantitatively the microstructure evolution of the studied granites using the transverse relaxation time, T<sub>2</sub> (Figure IV-25).

The quenching test at 200 °C did not show any variation during the first cycle, although at the end of the test A and SM increased their T<sub>2</sub> values and showed a slightly greater amplitude. GA showed a slight decrease and GS shifted and reduced notably its signal (tighter cracks).

During the first cycle at 400 °C, A and SM evolve to similar values. GA kept a low signal amplitude before and after quenching and GS slightly decreased its amplitude. At the end of the test, A and SM slightly decreased their amplitudes but increased their T<sub>2</sub> values. GA and GS showed little change from their initial state.

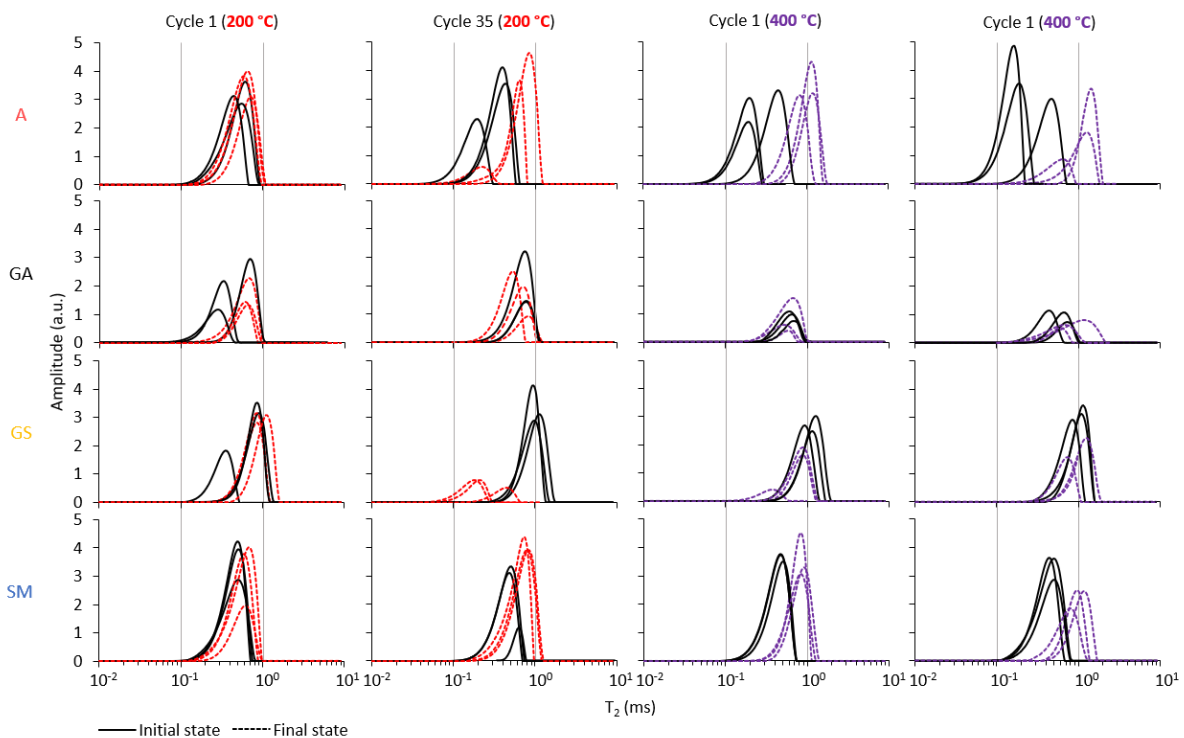


Figure IV-25. Evolution of the transverse relaxation time (T<sub>2</sub>) distribution curves after 1 and 35 cycles. The initial and final state corresponding to the same samples.

In summary, A and SM showed similar behaviour to quenching with a slight increasing evolution of the geometric mean of this T2 distribution at 200 °C and a significant evolution from the first's cycles at 400 °C (Figure IV-26). The general trend of GA does not show a clear change, and a slight decrease was still noted during cycles at 200 °C. Quenching at 200 °C on GS showed little change until cycle 15 and then decreased. Cycles at 400 °C showed an increasing phase up to cycle 5, and after stabilisation up to cycle 25, T2 values decreased.

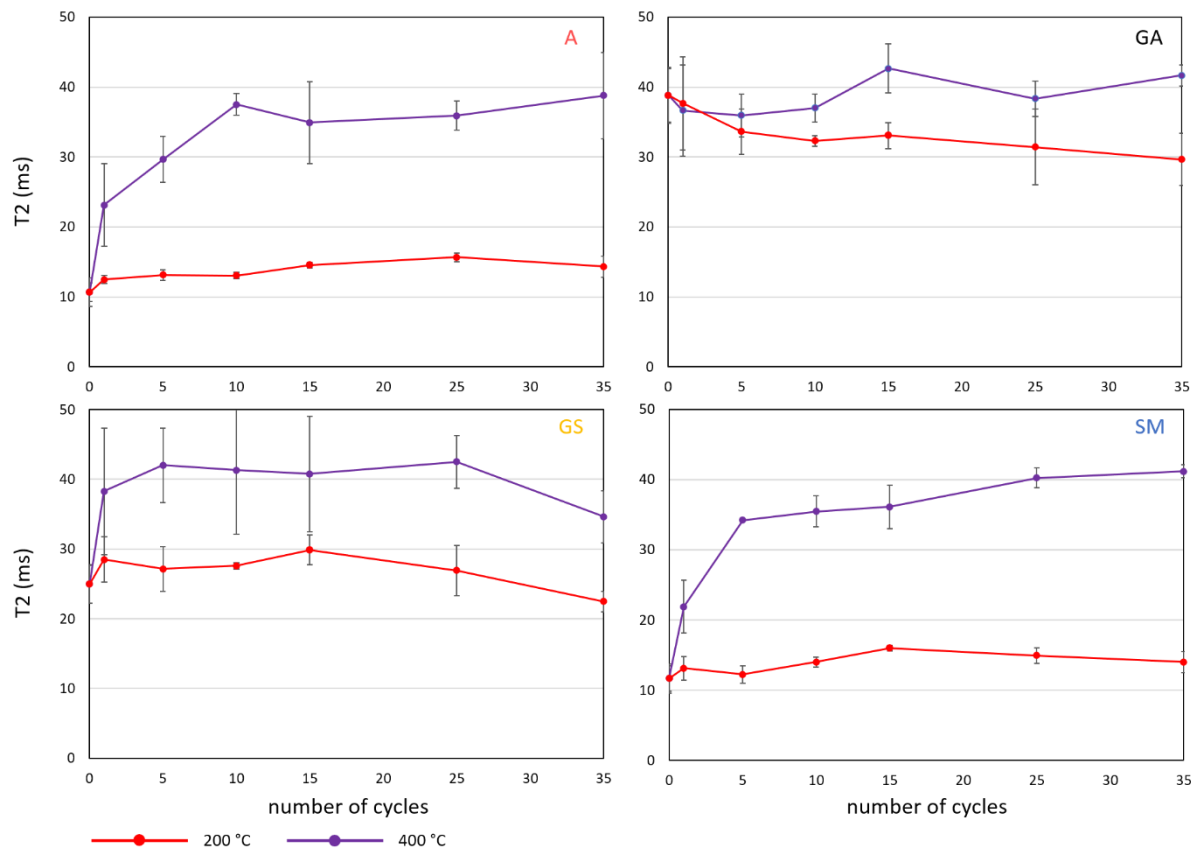


Figure IV-26. Relationship between the number of thermal cycles and the transverse relaxation time (T2) for the two quenching tests.

#### IV.2.4.5. Microstructural analysis with X-ray CT

GA and SM were assessed before and after 35 quenching cycles at 400 °C because their thermal sensitivity (Vazquez et al., 2018a) and also since their porosity and  $V_p$  values come closest to granites widely studied and subjected to high temperature treatments ( $V_p$  greater than  $3000 \text{ m}\cdot\text{s}^{-1}$  and a low porosity of close to 1% (W. Zhang et al., 2018). To establish the microcrack distribution of the studied rocks, three X-ray CT images of cross-sections in the x -

y planes along the z height were taken before and after the test at 400 °C, and they are shown in Figure 13. They exhibited significant microcracking at a resolution of 6 µm.

For GA, the initial state revealed mainly intra and intergranular microcracks in feldspars that sometimes are prolonged to quartz. After quenching cycles, the development of intergranular microcracks along the quartz-feldspar crystal boundaries were detected. Some of these cracks extended and formed intragranular cracks mainly in feldspars although also visible in quartz. As observed by Isaka et al. (2019), microcracks in granites preheated up at 400 °C seem to stop their progression when they encounter a crystal of biotite since the energy follow the path of the mica boundary. Indeed, very few microcracks were observed inside the biotite. Some showed their cleavage to open up after treatment (Figure IV-27).

For SM, the fresh rock revealed that the initial microcracking was more notable than in GA granite, with mainly long intragranular cracks that can be transformed into transgranular always through feldspars, and also a network of and short cracks as a result of feldspar alteration. After quenching test, the most remarkable change was the widening of pre-existent microcracks that prolonged as intragranular microcracks and that predominated over the creation of new ones. The mica was not attained by severe microcracking since the energy was absorbed and dissipated by their grain boundaries as in GA.

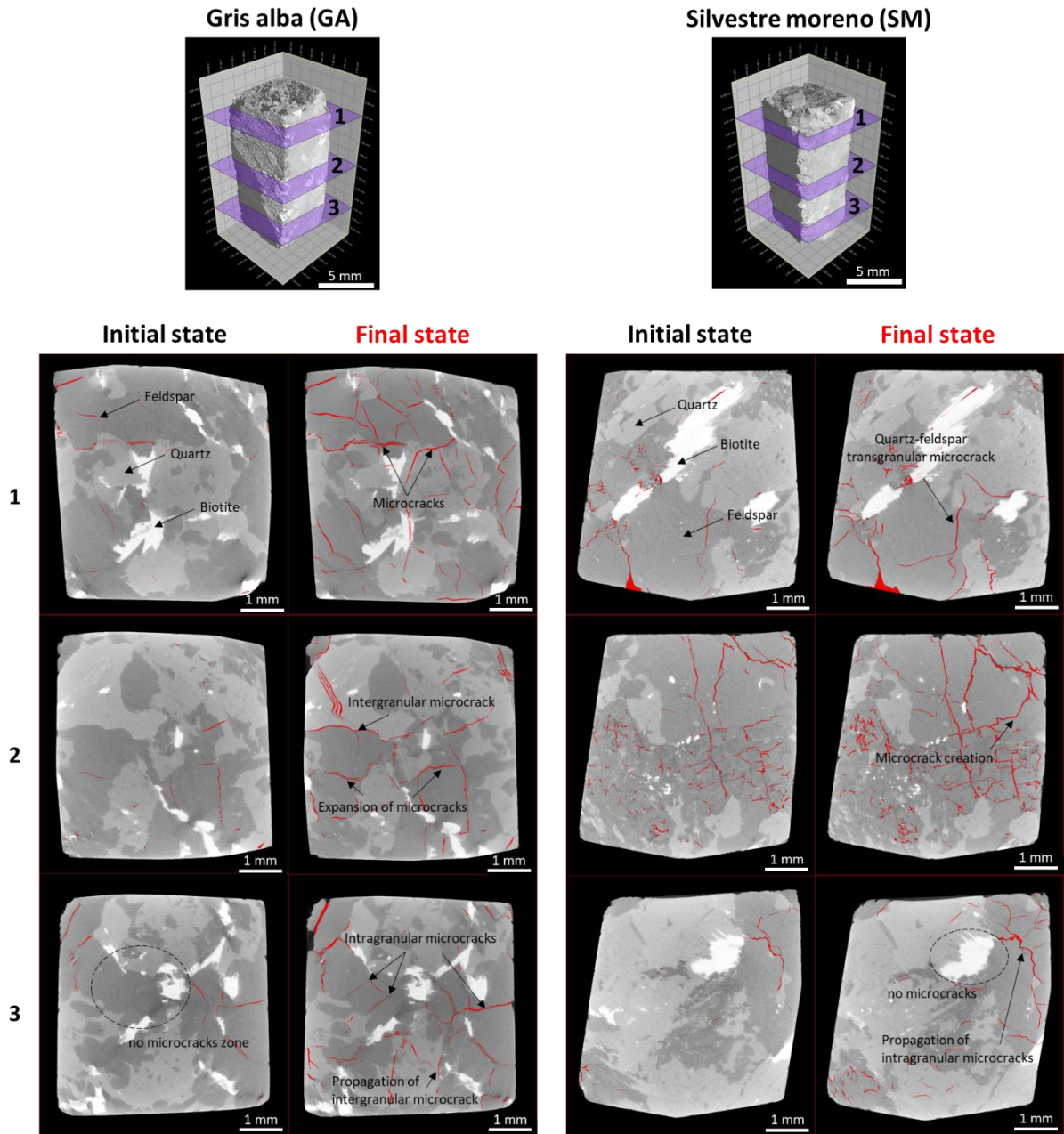


Figure IV-27. Horizontal X-ray CT slides of GA and SM initial and final state (cycle 35) for three different elevations. The pores and cracks are presented in red color.

From the volume analyse of the X-ray CT data, a quantification of the microcrack variation can be obtained (Figure IV-28). In general, the volume rendering of the porous networks showed that microcracks development were distributed evenly throughout the sample, before and after the tests so that the whole sample was affected by the quenching process. The porosity after treatment was 3.5 times greater for GA and 1.5 times for SM. The evolution in the degree of microcracking in the two granites increased the coefficient of heterogeneity (eq. IV. 7). At

the initial state, this coefficient was 65% for both GA and SM and it increased to 70% and 88%, respectively after 35 quenching cycles at 400 °C.

In detail, image processing allowed the cracks to be detected and segmented. The parameters of the porous network (pore volume, pore number and diameter) were quantified and they are shown in Figure IV-28.

For GA, a notable increase (325%) of the pore volume was observed after quenching from 1121 to 4766  $\mu\text{m}^3$  meanwhile the number of pores decreased by 13%. The quantification of the pore volume as a function of their diameter, represented in Figure IV-28b, showed the formation of large pores (greater than 800  $\mu\text{m}$ ) during the final state of quenching. The histogram (Figure IV-28c) showed the pore size distribution of GA before and after quenching. The frequency of pores increased for all pore class except the smallest between 6-10  $\mu\text{m}$ .

SM showed a smaller increase in pore volume (133%), with an average volume rising from 7175 to 16736  $\mu\text{m}^3$ . However, the number of pores was reduced more significantly with a value of 35% (Figure IV-28b'). The histogram (Figure IV-28c') evidence that pore diameters ranging from 6 to 15  $\mu\text{m}$  predominate in the sample. After heat treatment, the number of pores or cracks with a diameter greater than 10  $\mu\text{m}$  increased.



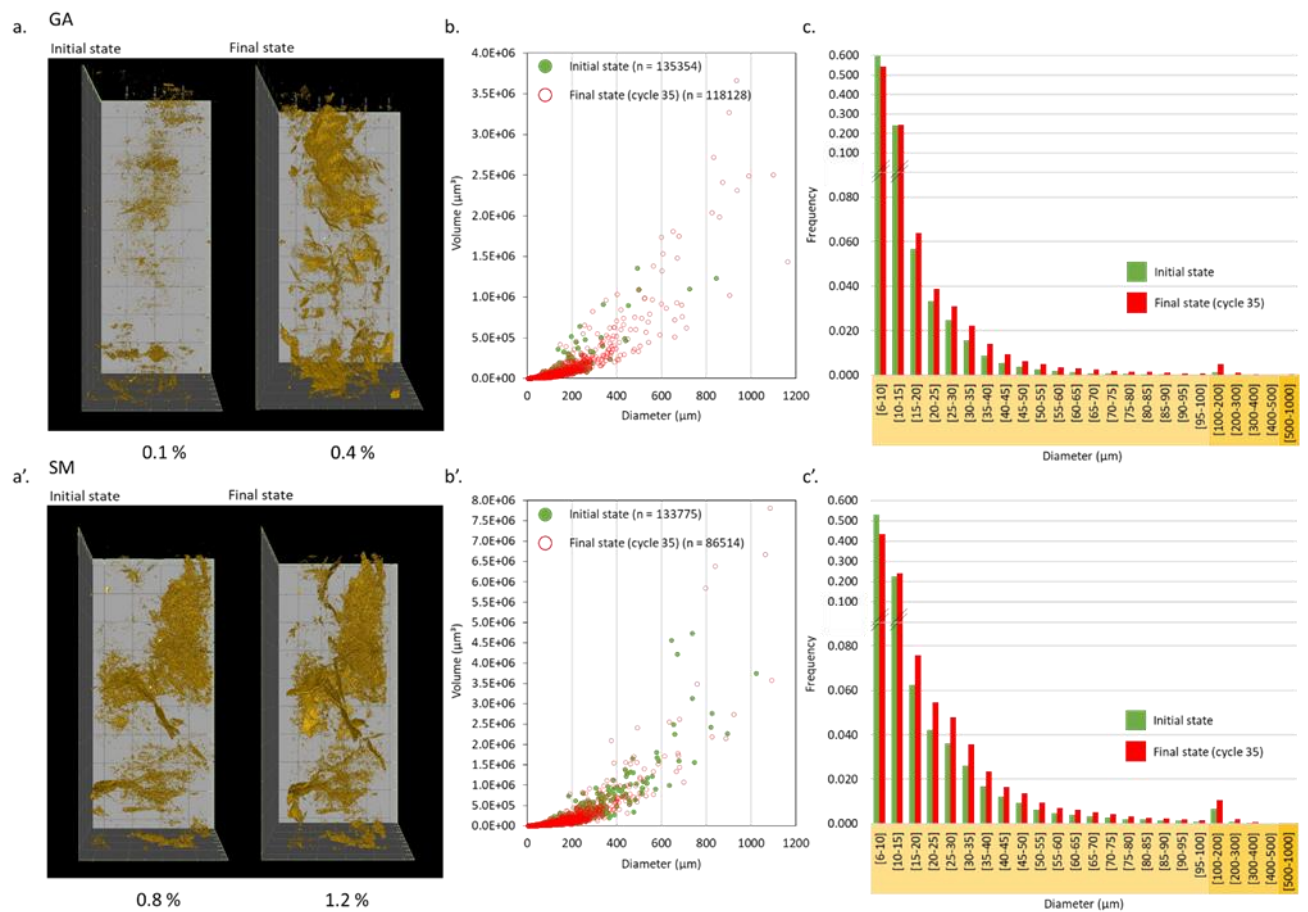


Figure IV-28. Qualitative and quantitative data extracted from X-ray CT measurements before and after the quenching test (cycle 35). a-a'. Reconstruction of the 3D porous network. b-b'. Relationship between volume and diameter of pores. c-c'. Pore size-frequency distribution.

#### IV.2.4.6. Mineral composition determined using XRF and chemical analysis of fluids

The granites in this study were mainly composed of quartz, K-feldspar, plagioclase, and micas. Tableau IV-7 shows the initial chemical composition of the granite samples determined by XRF, with slight variations between them.

**Tableau IV-7. Chemical composition of the major elements expressed in percent.**

	Na <sub>2</sub> O	MgO	Al <sub>2</sub> O <sub>3</sub>	SiO <sub>2</sub>	K <sub>2</sub> O	CaO	Fe <sub>2</sub> O <sub>3</sub>
A	2.50	0.50	13.85	74.09	4.97	1.12	1.26
GA	3.42	0.70	14.38	71.26	5.52	1.54	1.58
GS	2.99	0.34	13.88	74.26	5.21	0.79	1.49
SM	3.29	0.46	14.43	73.35	5.92	0.52	1.42

Mineralogical and chemical alteration processes were carried out thanks to the ability of water to access the rock matrix via micro-fractures (Wogelius et al., 2020). This process then allows to mobilise part of the natural radionuclides and other trace elements from the primary minerals of the rock matrix as they are degraded. Figure IV-29 showed the cumulative concentration of dissolved elements as a function of the cycles on the water used for cooling.

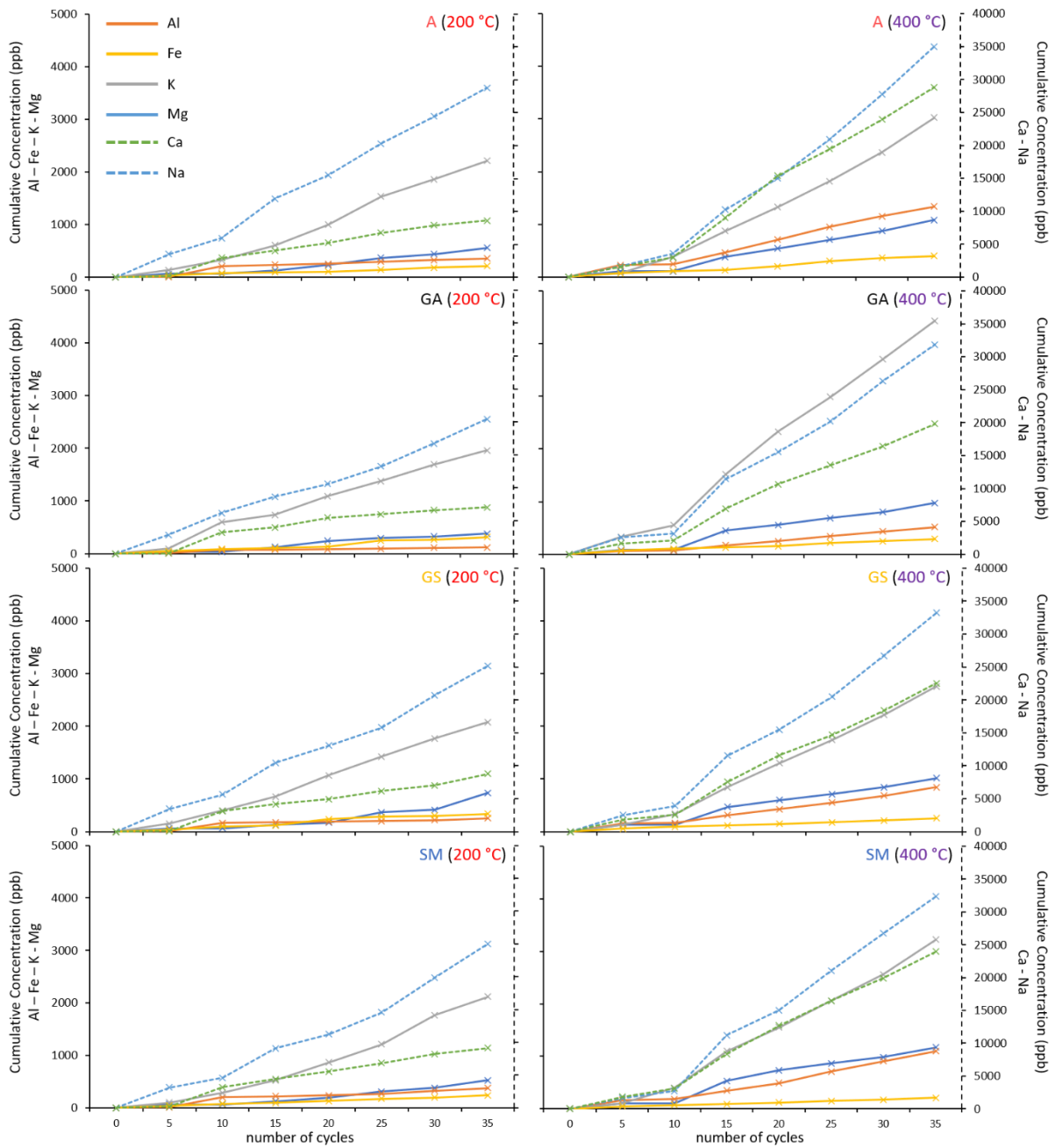


Figure IV-29. Cumulative curves of the concentration (ppb) in Al, Fe, K, Mg, Ca, and Na in the solutions as a function of the number of cycles for the two quenching tests.

ICP-MS analysis showed an increase in the release of minerals in the liquid phase during cycles, more intense at 400 °C. In cycles at 200 °C, all the elements were dissolved with an almost linear trend.

Tests at 400 °C showed an inflexion point after 10 cycles, from which the dissolution rate became faster and at the end of the experiment (cycle 35) the dissolution was greater than for the 200 °C tests.

### IV.2.5. DISCUSSION

Figure IV-30 relates the four main parameters (initial porosity  $\varphi_c$ , capillary coefficient  $C$ , maximum signal amplitude of ultrasonic waves  $Amp$ , P-wave velocity  $V_p$  and Young's modulus  $E$ ) used to judge the initial alteration of the granites in this study. The main observations are described below:

The unaltered granite (Gris Alba, GA) had the greatest value of ultrasonic wave amplitude, which resulted in a weakly attenuated ultrasonic signal compared to A, GS, and SM. Among all the granites, the unaltered granite exhibited the highest T2 values. This result was not apparently consistent with the porosity values, but the relaxation rate can be increased depending on the concentration and the mineralogical form of iron oxides for example (Keating and Knight, 2006) and the clay content can also reduce the pore size of weathered granite.

The slightly weathered granite (Silvestre Moreno, SM) had the highest Young's modulus values, which indicated high rigidity and a low amount of damage within the structure.

The moderately weathered granite (Golden Ski, GS) had the lowest mechanical properties and the highest capillary coefficient values. The capillary absorption coefficient was directly linked to the pore size and quantified the flow mechanisms influenced by the pore structure and the interconnectivity of the pores (Benavente et al., 2002; Cai and Yu, 2011; Çelik and Kaçmaz, 2016). The moderately weathered granite, the transverse relaxation time T2 values in NMR were the highest among the initially weathered granites, indicating a large pore size allowing good migration of the fluid.

The highly weathered granite (Albero, A) presented the largest pore volume. The ultrasonic wave attenuation of this granite was the highest, due to the individual microcracks distributed in the sample (Benavente et al., 2020). The low  $V_p$  values in the moderately and highly weathered granite were indicative of the high initial microcrack density.

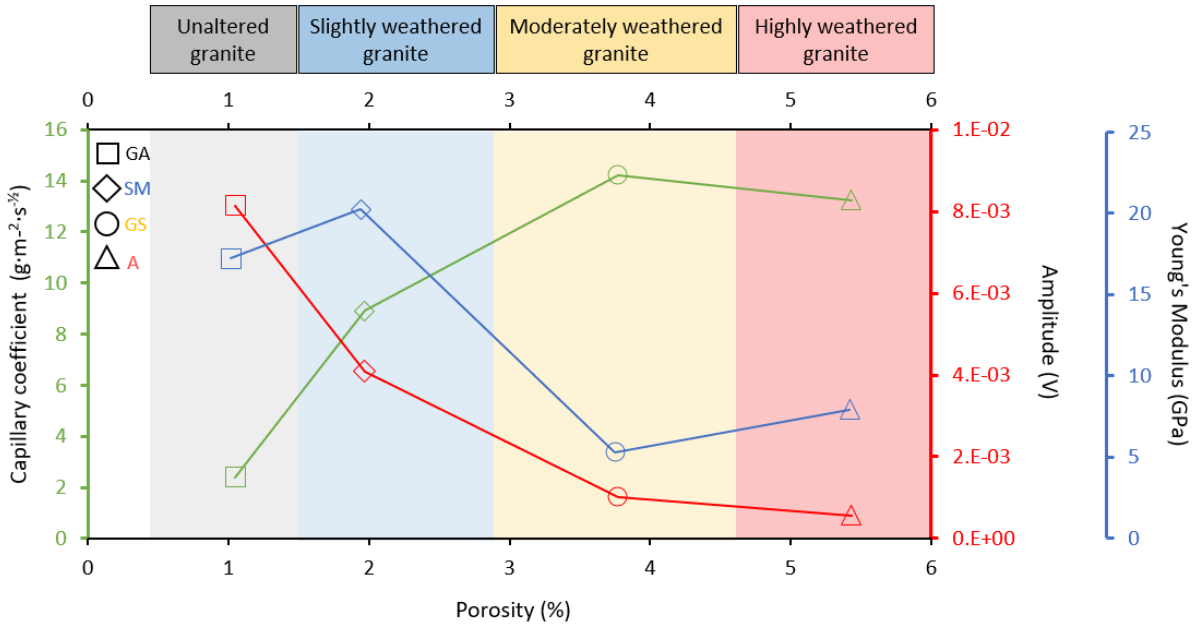


Figure IV-30. Relationship between the initial porosity of the granite and their capillary coefficient, maximum amplitude of the P-waves, and Young modulus.

IV.2.5.1. Effects of repeated quenching on damage

In geothermal engineering, extracting heat from deep rocks by injecting water into the well brings about a quenching process. The repetition of this operation can induce instability in the drilling at the expense of its profitability. The degree of cracking depends mainly on temperature and pressure stress, mineralogical composition, and particle size distribution (Freire-Lista et al., 2016). Due to this brutal thermal gradient during quenching, a thermal expansion occurs in the structure resulting in a thermal shock cracking (Kumari et al., 2018).

Quenching generally leads to tensile stress tangential to the surface of the rock. After a thermal shock, the damage near the surface is often greater than inside the sample (Fan et al., 2020). The damage to the surface of the granite sample may become more concentrated, resulting in nucleation of surface microcracks (Yu et al., 2020). The theoretical relationship exposed by Kim et al. (2014) allows estimating the maximum tangential tensile stress generated at the surface of the granites studied ( $\sigma_t \max$ ) (Tableau IV-8) :

$$\sigma_t = \frac{E\alpha \Delta T}{1 - \nu} \tag{IV.8}$$

where E was the average Young's modulus of samples Fast cooled from 200 or 400 °C,  $\alpha$  was the thermal expansion coefficient,  $\Delta T$  was the difference temperature, and  $\nu$  was the Poisson's

ratio. The calculations for the studied granites took the thermal expansion coefficients from Vazquez et al. (2011, 2015).

**Tableau IV-8. Maximum tangential tensile stress generated at the surface of the granites during the quenching after the two preheating treatments and experimental tensile strength test (Vazquez et al., 2018a<sup>1</sup>).**

	Mechanical properties: Tensile strength (MPa) <sup>1</sup>	$\sigma_t$ max (MPa)	
	25 °C	200 °C	400 °C
Unaltered granite	9.3	41.9	50.5
Slightly weathered granite	4.9	43.3	48.9
Moderately weathered granite	4.0	15.8	12.2
Highly weathered granite	4.4	16.3	22.1

The maximum tensile stresses that could be generated at the rock surface during quenching are much greater than the tensile strength of these granites measured experimentally at room temperature (Tableau IV-8; Vazquez et al., 2018a). Samples preheated at 400 °C and then immersed in cold water (25 °C) showed a maximum tensile stress greater than at 200 °C. For example, the maximum tensile stress of about 50 MPa could be generated at the surface of the unaltered granite. These values were sufficient to produce significant thermal cracking as observed by the measured properties and the images from X-ray CT (Figure IV-27).

The stress propagation from the surface to the interior of the sample, was directly related to the preheating temperature and the number of cycles. For both test, there was a fatigue threshold, that was the number of cycles from which the damage affected similarly the whole sample and the measured values were maintained or varied only slightly due mainly to crack redistribution. During repeated heating cycles, rocks can exhibit a stress memory effect, or the so-called Kaiser effect (Kaiser, 1953) which indicates that in order to sustain damage, a material must be subjected to stresses greater than those it has already experienced. This characteristic can be observed in many EGS sites during forced fluid injection operations (Maurer et al., 2020) and also under heat stress in the laboratory in a wide variety of rock types (Lavrov, 2003). For example, Yong and Wang (1980) have shown that there may be a

Kaiser effect on the Westerly Granite because during the heating process and at temperatures below the peak temperature of the previous cycle, very little acoustic emission occurred.

Figure IV-31 shows the parameter changes of quenching samples preheated at 200 °C and 400 °C with cycles. The damage variability was defined taking into account the initial standard deviation and the extreme values of all the granites. For rocks preheated to 200 °C, at least between ten and fifteen cycles of quenching were necessary to reach the stress threshold or Kaiser Effect, although certain properties and granites revealed a continuous progression of microcracking until the end of the test. Meanwhile for those rocks preheated to 400 °C, some definitive variations were observed from the very first cycle. The inadequacy of the thermal expansion coefficients of the different minerals prompted the generation of microcracks, causing significant damage to the granites (Jin et al., 2019; Sousa et al., 2005; Wu et al., 2019).

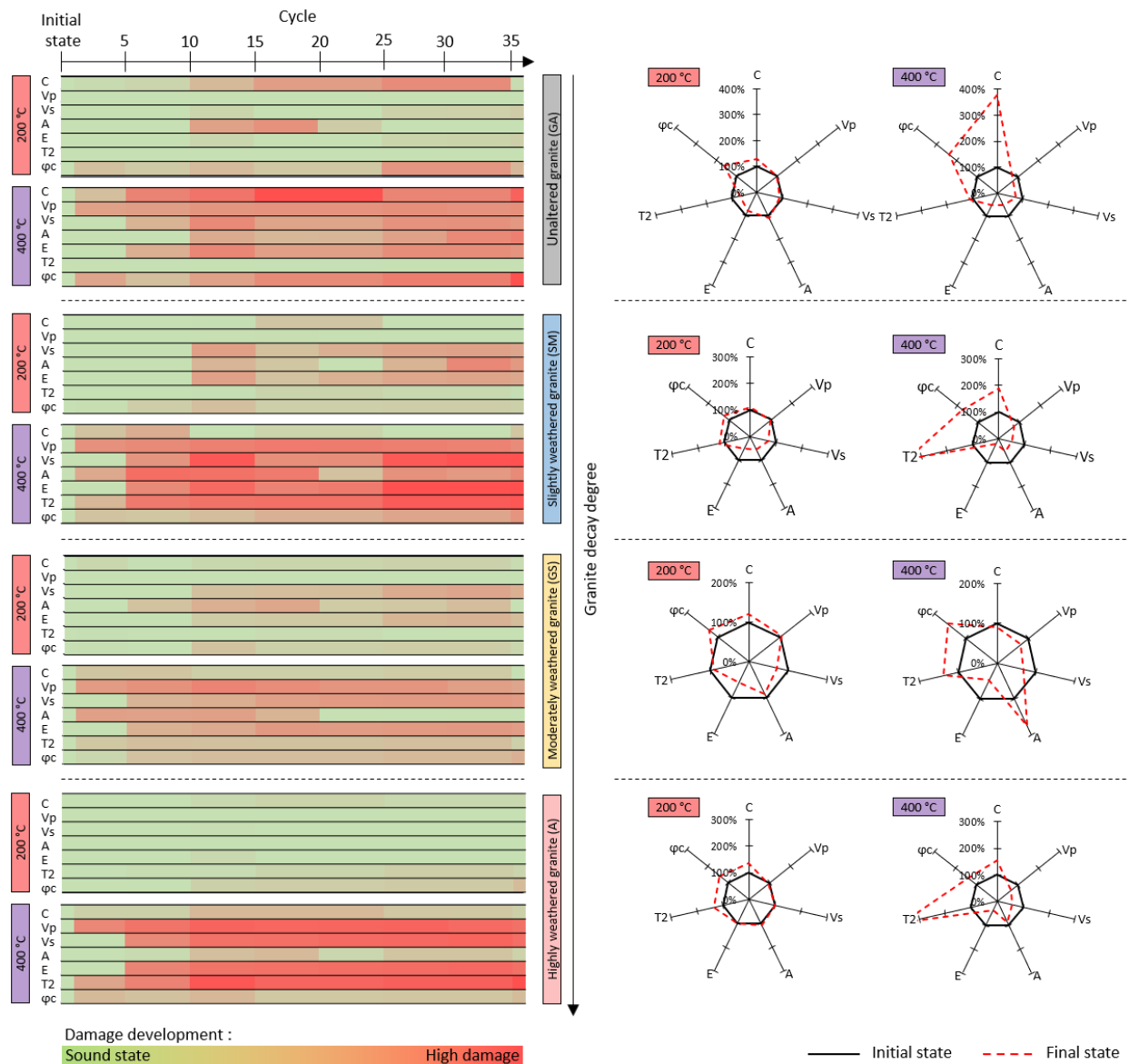


Figure IV-31. Evolution of the parameters measured for the two quenching tests. C: capillary coefficient;  $V_p$ : P-wave propagation velocity;  $V_s$ : S-wave propagation velocity; A: Amplitude coefficient; E: Young's modulus; T2: transverse relaxation time and  $\phi_c$ : Connected porosity.

Figure IV-32 relates the microstructural changes with the petrophysical properties measured. Two kind of behaviours can be differentiated in relation to the initial weathering.

The unaltered granite GA, showed at 200 °C, a progressive degradation until the end of the test. The main parameters affected were the porosity and the capillarity that indicated an increase in the volume and connectivity of the pores. The low initial porosity may influence the slight variation related to the mechanical parameters. At 400 °C, the change of these two parameters was enhanced and accompanied by a noticeable increase in the microcracking as



indirectly measured by ultrasounds. In agreement with Zhu et al. (2020),  $V_p$  showed an approximately 40% reduction at 400 °C after 30 quenching cycles with a significant decrease from the very first cycle. This behaviour agreed with the microcracking development observed in the figure 13, where X-ray CT also revealed a propagation mainly in intergranular cracks that enhanced connectivity (Figure IV-32).

The weathered granites showed a variation in microstructure due to crack propagation and opening, although without improving connectivity. The development of microcracking detected by ultrasound parameters and also observed by X-ray CT revealed a widening and propagation of transgranular microcracks that were not forcedly connected between them. For the three granites and both temperatures, 200 °C and 400 °C, connected porosity and capillary coefficient hardly changed. At 200 °C, noticeable changes were measured after 10 cycles, followed by stabilization. Albero, the most weathered granite hardly showed any variation. At 400 °C, a strong decrease in the dynamic and elastic parameters related to strength were measured from cycle 1 to 5. The small microcrack network observed in feldspars and the widening of long intragranular cracks may experiment readjustments during the rest of the cycles although without improving connectivity (Figure IV-32).

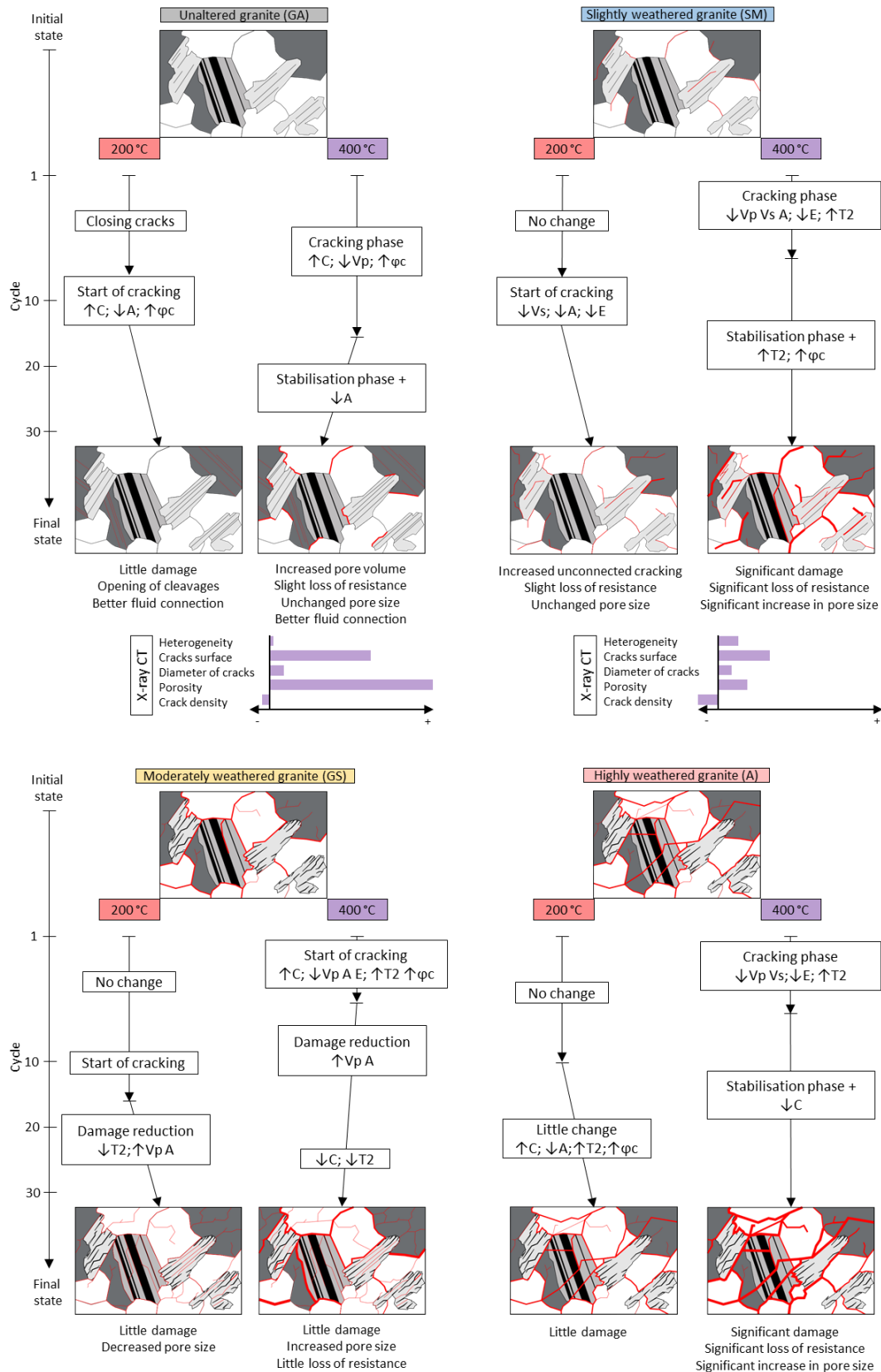


Figure IV-32. Synthesis of microstructural and observations.  $\uparrow$ : increase;  $\downarrow$ : decrease; C: capillary coefficient;  $V_p$ : P-wave propagation velocity;  $V_s$ : S-wave propagation velocity; A: Amplitude coefficient; E: Young's modulus;  $T_2$ : transverse relaxation time and  $\varphi_c$ : Connected porosity

### IV.2.5.2. Damage evaluation and permeability

With increasing crack density and increasing number of cycles, cracks can penetrate more easily, which improves permeability, on the other hand, the strong thermal gradient generated would tend to cause damage in the borehole.

Permeability is an important parameter that is generally used to describe the ability of the rock to allow the flow of fluids through its pores. The permeability ( $k$ ) was estimated from the Schlumberger-Doll Research (SDR) equation (IV. 9), based on the Kozeny-Carmen equation, as indicated in the following equation (Kenyon et al., 1988; Straley et al., 1997):

$$k = b\varphi^m(T2_{LM})^n \quad (\text{IV. 9})$$

Where  $\varphi$  is the porosity,  $T2_{LM}$  is the mean log of the T2 distribution, and  $b$ ,  $m$ , and  $n$  are empirically determined parameters. Each of the SDR parameters is expected to have a dependence on the lithology.

The porosity exponent  $m$  is associated with the Archie's formation resistivity factor (Chang et al., 1994). The exponent of the relaxation time  $n$  is associated with the grain size distribution (Dunn et al., 1999). For consolidated materials,  $m = 4$  and  $n = 2$  are the most commonly reported values (Knight et al., 2016; Ren et al., 2019). The constant  $b$  is considered to be dependent on the lithology and is related to the surface relaxivity  $\rho$ . It represents a practical calibration parameter to take into account these other properties independent of geological materials which are difficult to measure or quantify to obtain the best possible match for predicting permeability (Maurer and Knight, 2016). In petroleum applications, for  $m = 4$  and  $n = 2$ , the standard value of  $b$  is  $4 \text{ mD ms}^{-2} = 3.95 \times 10^{-9} \text{ m}^2 \cdot \text{s}^{-2}$  (Kenyon et al., 1995). We set these parameters for this study.

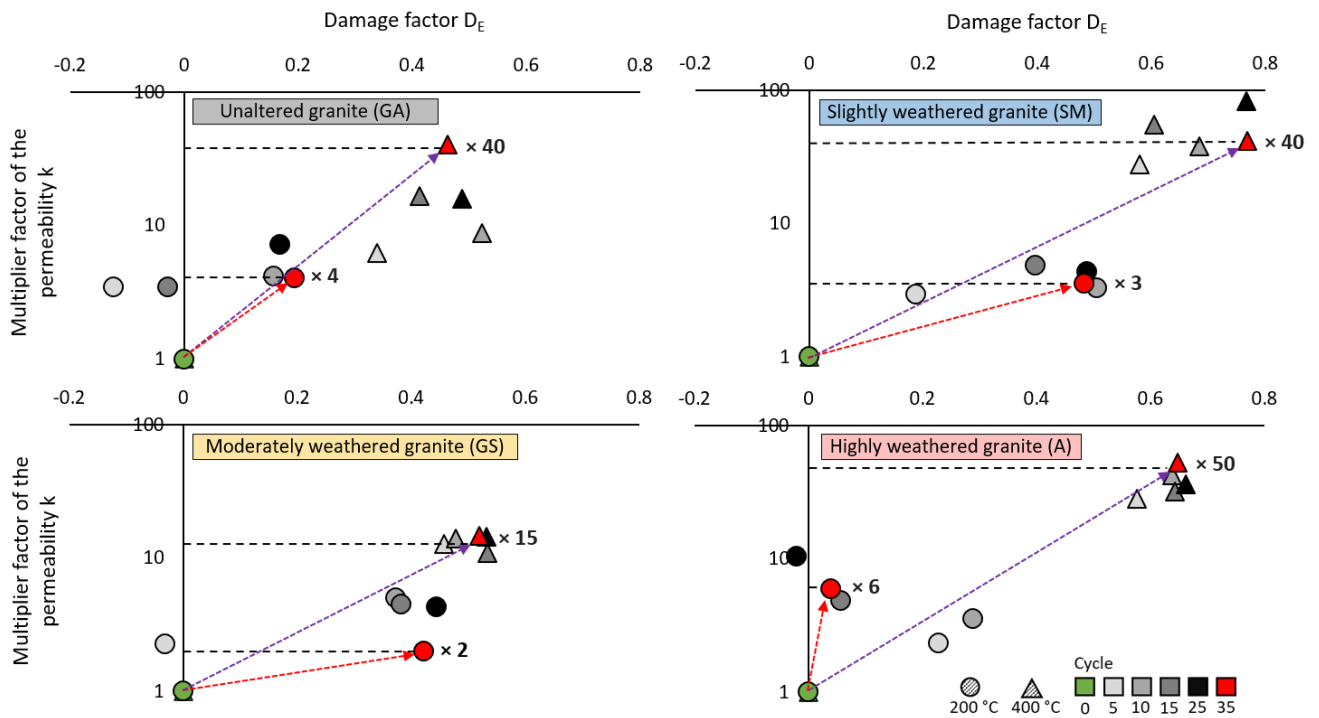
As indicated in section 5.1, the quenching cycles induce significant damage on the granite.

The thermal damage which is related to Young's modulus was thanks to the damage factor  $D_E(T)$  (Guo et al., 2018; Sha et al., 2020; W. Zhang et al., 2018), indicated in the following equation:

$$D_E(T) = 1 - \frac{E_t}{E_0} \quad (\text{IV. 10})$$

Where  $E_0$  and  $E_T$  are the values of the modulus of elasticity at room temperature, and temperature  $T$  (200 °C-400 °C), respectively. The application of this calculation was carried out at the two treatment temperatures and as a function of the number of cycles.

Figure IV-33 represents the evolution of the permeability  $k$  and the damage factor  $D_E$  as a function of the number of cycles. Each cycle represents the average of three samples.



**Figure IV-33. Evolution of the permeability  $k$  and the damage factor  $D_E$  as a function of the number of cycles. Samples preheated at 200 °C and 400 °C are represented by circles and triangles, respectively. The red and purple arrows represent the direction of the evolution of the 2 parameters. The base of arrows was positioned on the average value of 3 initial samples and having reached the average value of 3 samples of the final cycle.**

Thermally induced fractures have improved the permeability in all samples after 35 cycles at 400 °C. The critical temperature for which the permeability of granite significantly increases (Yangsheng Zhao et al., 2017) is set at 400 °C (Jin et al., 2019). Increasing crack density also leads to an increase in damage factor (Feng et al., 2020; Guo et al., 2018; Sha et al., 2020). The changes of  $E$  were smaller during the quenching test at 200 °C than at 400 °C. At the end of the 35 cycles of quenching of the samples at 400 °C, Young's modulus had decreased by 2.3, 1.6, 2.0, and 2.6 times that values compared to the thermal cycling performed at 200 °C for A,

GA, GS, and SM, respectively. If rocks heated at 200 °C still showed variability between cycles, on the other hand at 400 °C, the main changes were made during the first cycles.

At the end of the quenching tests, the permeability of the unaltered and slightly weathered granite was improved by a factor of approximately 5 at 200 °C and by a factor of 40 at 400 °C. At the same processing temperature, quenching shows more damage on the slightly weathered granite which could be due to its larger grain size (Shao et al., 2014).

The permeability of the moderately weathered granite was less affected by the quenching. Quenching cycles closed induced fractures after the first cycles following volumetric expansion (Barton, 2007), reducing hydraulic connections.

The 50-fold increase in permeability occurred after the first 5 thermal cycles for highly weathered granite and was accompanied by significant damage unlike quenching at 200 °C. This suggests that microcracks dominated the flow pathways through the sample.

### IV.2.5.3. Chemical analysis of fluids

The experimental fluids showed chemical element concentrations indicating signs of alteration of minerals present in the granite. The main reactive minerals were alkaline feldspars and clays. The increase of elements K and Al in the resulting water could be produced by the gradual alteration of alkali feldspar. In general, these 2 main elements resulting from water-granite rock interactions come mainly from the alteration of clays. They would be introduced into the fluid phase by the degradation of the surface of clay minerals such as smectite, illite, or kaolinite. K, Mg, Mn, Ti in the fluid came from biotite during the opening of the mica cleavages with temperature (Vazquez et al., 2015).

Ca can be found in the saturating fluid by the degradation and dissolution of plagioclases (Wogelius et al., 2020). Indeed, calcite-mineralised, transgranular, and intragranular microcracks were particularly frequent in plagioclase crystals, which generally show exsolution or zonation figures during their crystallisation. The composition of the water showed a slight increase in Fe. This enrichment may be due to iron degradation from biotite (Vazquez et al., 2016).

The K-feldspar-water interactions must lead to an increase in Al, Si, K, and Na in the fluid from 200 °C (Drüppel et al., 2020). Based on the ICP data, the increase of the concentration of all

the mentioned elements with the number of cycles for the two quenching tests could be attributed to the dissolution or mechanical deterioration of K-feldspar. It was noted that this dissolution kinetics was greater for rocks preheated at 400 °C. Feldspar crystals observed on X-ray CT showed intergranular and intragranular cracking.

The unaltered granite showed the highest K content during the final cycle at 400 °C. An evident intragranular microcrack was observed in K-feldspar which can go as far as coalescing with other intergranular microcracks (Figure IV-27). However, this high content can be interpreted by the high proportion of K-feldspar compared to other granites.

While the observed chemical alterations were independent of physical processes, minerals that underwent more physical deterioration also suffered more chemical alteration.

#### IV.2.5.4. Potential application of quenching in Enhanced Geothermal System (EGS) projects

Quenching of granite formations is closely linked to the implementation and the development of EGS projects. Stimulation of a rock reservoir by hydraulic fracturing from water at room temperature is often adopted to improve the porosity and permeability of the rock. The permeability obtained in this study was an estimate calculated from the NMR petrophysical data, used specifically as a comparison between four granites, while capillary imbibition testing was used as an estimator of rock degradation and conductivity index. It is inversely linked to the durability of stone (Benavente et al., 2004; Çelik and Kaçmaz, 2016; Fronteau, 2000; Sengun et al., 2014). Knowing the movement of water inside the rock is a simple way to assess the porosity of the rock (Fronteau et al., 2010). Benavente et al. (2015) show a strong relationship between the coefficient of water absorption by capillarity and water permeability.

The experimental results showed that whatever the granite tested, the effect of the thermal shock increased the permeability estimated by NMR and that the connectivity of the water by capillary imbibition could vary according to the type of granite.

In addition, the higher the temperature of the formation, the more the thermal stimulation will create cracks in the formation. The irreversible cracking stress was not always at 200 °C to generate the Kaiser effect, as for the sound granite GA. As a Kaiser effect was observed during heating to 400 °C and rapid cooling, it can be concluded that the improvement of the

permeability around the geothermal wells would be effective from the first cycles, but renewing the thermal stimulation would not be more beneficial. Indeed, heating the rock in repeated cycles without inducing cracking could induce a closure of the pre-existing microcracks with the expansion of the rock matrix. Thermal stimulation can be used to rapidly increase the permeability of rocks and thermal fatigue could potentially strengthen the rock mass or to remobilize the porous network.

The experimental data also showed that as the quenching progressed, fracturing increased which would lead to a decrease of the mechanical properties. Transcribed to the geothermal system, this observation means that if the thermal stress exceeds the equilibrium threshold of the surrounding deep rock system, zones of fragility could be created. The mechanisms involved during hydraulic stimulation could locally modify the stresses that could be at the origin of microseismicity, that may cause damage to local populations. Between June and July 2000, a hydraulic stimulation experiment took place at the EGS geothermal site in Soultz-sous-Forêts (Alsace, France) and more than 7,200 microseismic events were located in the range of magnitude  $-0.9$  to  $2.6$  (Cuenot et al., 2008). In 2006, the geothermal energy project in Basel (Switzerland) was stopped due to a seismic event of magnitude greater than  $2.0$  which caused some damage to buildings. Therefore, during hydraulic fracturing, it is necessary to ensure that the quenching only reaches the area dedicated to fracturing. It is therefore necessary to implement technologies such as thermal insulation of pipelines (Shen et al., 2020).

In this study, we focused on the effect of thermal cycling on the petrophysical properties of granite after quenching and hoped to contribute to the stability of boreholes when exploiting deep geothermal energy. All the tests were performed in an unconfined condition. However, geothermal reservoir rocks are subject to confinement pressure. Therefore, the behaviour of granite after quenching under these conditions requires further studies.

### **IV.2.6. CONCLUSION**

The study of quenching damage is essential to understand the fracturing on the permeability of the reservoir and therefore the life of a geothermal installation. In this work, the thermal shock behaviour of four granites with different initial properties was followed. From the results of the study, the following conclusions are drawn:

Strong correlations between the coefficient of capillarity, the P- S-wave propagation velocity, Young's modulus, and the porosity have been established. The size of the cracks measured with the NMR showed an increased with the number of cycles. Due to the different crystal structure of the 4 granites, the thermal stress limit threshold and the cracking morphology is different. If crack openings or closings occurred in weathered granites during thermal shocks, the size of the microcracks did not change in the sound granite but their density did. The change if the predicted permeability was a direct consequence of the propagation of microcracks induced by the strong gradient during quenching tests.

A single cycle of a thermal shock for rocks preheated at 400 °C prompted more damage than after 35 cycles at 200 °C. The propagation of pre-existing cracks was observed with X-ray CT and the enlargement of the size of the cracks with NMR, especially for granites with the smallest initial T2 value (A and SM).

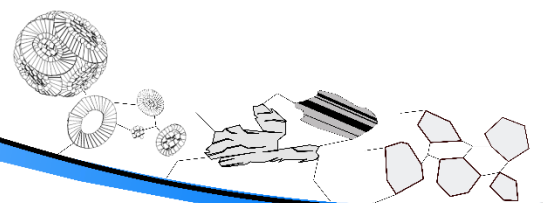
In the case of rapid quenching from 400 °C, intragranular microcracks within the K-feldspar propagated throughout the low initial porosity granites (the unaltered GA and the slightly weathered SM). For these less weathered granites, the expansion and contraction of the minerals lead to greater damage inside the crystals. The increase of connectivity improves the permeability while the more weathered granites experimented an increase of microcracking with less connectivity.

The chemical analysis of the fluids used for cooling served as clues of the mineralogical alteration and allowed the alteration processes to be evaluated. The water-granite rock interaction showed the dissolution of K-feldspar, plagioclase, and the degradation of clays, leading to an enrichment mainly in K, Na, and Ca in solution.





**V. CHAPITRE : Changements  
microstructuraux de 3 roches réservoirs :  
craie, granite et grès**



**Résumé étendu et conclusions principales de l'articles #5 « Utilisation de la thermographie infrarouge sur la mesure des changements microstructuraux des roches réservoirs induits par la température ».**

Une variation de température produit une modification de la microstructure de la roche en raison de la dilatation thermique minérale et de la déformation résiduelle. En fonction du cycle de température et de la texture, les micro-contraintes peuvent conduire au développement de fissures préexistantes ou à la création d'une nouvelle fissuration irréversible. L'effet de la température sur les roches réservoirs est un sujet important car il conditionne la perméabilité et l'écoulement du fluide.

En confrontant les résultats obtenus sur chaque roche et en introduisant les résultats obtenus sur le grès de Fontainebleau, il a été mis en évidence le rôle de la microstructure sur le **comportement thermique** et la **circulation de fluides par imbibition capillaire**.

Dans les chapitres précédents, il a été possible d'identifier les composants minéraux, les caractéristiques pétrographiques et pétrophysiques, qui peuvent jouer un rôle prépondérant dans les **propriétés de transport des fluides** dans la craie de Châlons puis dans les granitoïdes ibériques. Dans ce chapitre, la même **craie, 2 des 4 granites et un grès** sont les matériaux étudiés. Le **grès de Fontainebleau** a été intégré en raison de sa composition qui est faite uniquement de quartz, de sa granulométrie constante et de sa porosité intergranulaire. Cela a permis d'étudier les effets de la température sur la porosité et la microstructure indépendamment de tous les autres paramètres.

Lorsque ces différentes roches sont exposées à des températures élevées, trois questions sur leur comportement se posent. Quel est le seuil de fissuration irréversible ? Deuxièmement, lorsque les cycles de chauffage-refroidissement se répètent, quel est l'effet de la fatigue thermique ? Enfin, comment évolue l'écoulement par imbibition capillaire après différents traitements thermiques ?

Pour répondre à ces questions, les quatre roches de types réservoirs (craie, grès, granite sain, et granite altéré) ont été soumis à **deux régimes thermiques différents**. Le premier test a été conçu pour détecter le seuil de fissuration irréversible, et pour cela, les roches ont été soumises à un chauffage progressif (90, 100, 110, 120 et 130 °C). Le deuxième test consistait

à faire des cycles de chauffage jusqu'à 200 °C. La variation de microstructure a été évaluée au moyen d'un microscope électronique à balayage, de la porosimétrie au mercure et des tests d'absorption d'eau par capillaire. Le transfert d'eau lors des tests capillaires des roches, avant et après les tests, a été suivi grâce à la thermographie infrarouge. De plus, l'indice de vitesse de refroidissement, utilisé pour détecter le développement de fissures a été calculé. Les **roches ont été comparées** afin de comprendre les différences qui pourraient être relevées concernant leurs caractéristiques et **leurs propriétés initiales**. Les résultats de ces tests expérimentaux ont fait l'objet d'un article. Cet **article #5 : « Utilisation de la thermographie infrarouge sur la mesure des changements microstructuraux des roches réservoirs induits par la température »**, a permis de différencier les comportements par rapport au type de roche, avec la craie et le granite altéré moins sensibles aux contraintes thermiques qu'avec le granite sain et le grès.

Les résultats sur les propriétés de transport des fluides ont permis d'identifier les principaux chemins d'écoulement dans les roches à porosité granulaire et à porosité fissurale. La Figure V-11 illustre comment l'eau envahit chaque roche par imbibition capillaire dans les roches en ce qui concerne leurs structures minérales et poreuses.

Dans ce même chapitre, la thermographie infrarouge s'est à nouveau avérée être une technique indirecte très utile pour détecter la circulation d'eau à l'intérieur de la roche. Le suivi par IRT du transport des fluides dans des roches homogènes telles que le grès de Fontainebleau et la craie de Châlons peut être bien prédits. La structure homogène et interconnectée des roches granulaires a montré une montée homogène de la frange capillaire et un refroidissement de la pierre au fur et à mesure que les pores se remplissent. Les résultats obtenus pour des roches plus hétérogènes, telles que les granites, présentent un remplissage d'eau complexe. La prise d'eau se produit dans un premier temps dans les microfissures connectées, puis dans un second temps se poursuit dans les fissures transversales moins connectées à l'ensemble du réseau. La circulation de l'eau dans ces milieux poreux fissuraux est plus influencée par les composants minéraux et les autres caractéristiques pétrographiques que les roches granulaires.

Ces résultats préliminaires permettent de considérer l'IRT comme une technique prometteuse pour la caractérisation des roches, bien que des recherches supplémentaires soient

## Chapitre V : Changements microstructuraux de 3 roches réservoirs sous sollicitation thermique et circulation de fluide

---

nécessaires pour une interprétation plus précise des réseaux de fissures et de pores. Ceci pourrait généraliser cette méthode de description des propriétés de transport de fluides dans les géomatériaux.





## **V.1. Article #5: The Use of Infrared Thermography on the Measurement of Microstructural Changes of Reservoir Rocks Induced by Temperature.**

Ce travail a été publié en ligne le 8 janvier 2021 dans la revue de rang A, *Applied Sciences* suivant la référence :

Junique<sup>1</sup>, T., Vazquez<sup>1</sup>, P., Thomachot-Schneider<sup>1</sup>, C., Hassoun<sup>1</sup>, I., Jean-Baptiste<sup>1</sup>, M., & Géraud<sup>2</sup>, Y. (2021). The Use of Infrared Thermography on the Measurement of Microstructural Changes of Reservoir Rocks Induced by Temperature. *Applied Sciences*, 11(2), 559.

<sup>1</sup>GEGENAA EA 3795, University of Reims Champagne-Ardenne, 2, esplanade Roland Garros, 51100 Reims, France

<sup>2</sup>GeoRessources Laboratory UMR 7359, University of Lorraine, F54505 Vandoeuvre les Nancy



Article

## The Use of Infrared Thermography on the Measurement of Microstructural Changes of Reservoir Rocks Induced by Temperature

Thomas Junique <sup>1,\*</sup>, Patricia Vazquez <sup>1</sup>, Céline Thomachot-Schneider <sup>1</sup>, Issra Hassoun <sup>1</sup>, Mirlène Jean-Baptiste <sup>1</sup> and Yves Géraud <sup>2</sup>

<sup>1</sup> GEGENAA EA 3795, University of Reims Champagne-Ardenne 2, Esplanade Roland Garros, 51100 Reims, France; patricia.vazquez@univ-reims.fr (P.V.); celine.schneider@univ-reims.fr (C.T.-S.); issra.hassoun@etudiant.univ-reims.fr (I.H.); Mirlene.jean-baptiste@etudiant.univ-reims.fr (M.J.-B.)

<sup>2</sup> GeoRessources Laboratory UMR 7359, University of Lorraine, F54505 Vandoeuvre Les Nancy, France; yves.geraud@univ-lorraine.fr

\* Correspondence: thomas.junique@univ-reims.fr

**Abstract:** A variation of temperature produces a change in the microstructure of the rock due to the mineral thermal expansion and its residual strain. Depending on the temperature cycle and texture, microstresses may lead to the development of preexistent cracks or the creation of a new and irreversible cracking. The effect of temperature on reservoir rocks is an important topic since it conditions the permeability and the fluid flow. Two main questions arise from this: the first is if an irreversible cracking threshold is attained in the reservoir rocks at low temperature geothermal systems (around 100 °C); the second one is about the influence of thermal fatigue by the repetition of heating–cooling cycles on the different rock types. To answer these questions, four reservoir rocks (chalk, sandstone, fresh granite, and weathered granite) were submitted to two different thermal regimes. The first test was conceived to detect the irreversible cracking threshold, and for that, the rocks were submitted to progressive heating (90°, 100°, 110°, 120°, and 130 °C). The second test consisted of doing cycles of fast heating of the samples up to 200 °C. The microstructure variation was assessed by means of a scanning electron microscope, mercury porosimetry, and capillary water uptake combined with passive infrared thermography. Infrared thermography is an emerging tool in the field of rock study, used to detect water masses or determine thermal properties. The water transfer during the capillary tests of the rocks, before and after the tests, was monitored with this technique. In addition, the cooling rate index, a non-destructive parameter to detect cracking development, was calculated. The results made it possible to differentiate the behaviours in relation to the rock type, with a chalk and a weathered granite less susceptible to thermal stresses than a fresh granite and sandstone. In addition, infrared thermography resulted in being a very useful indirect technique to detect the changes on the surface, although they do not always correlate to the bulk microstructural changes.

**Keywords:** infrared thermography; reservoir rocks; thermal fatigue; thermal threshold; microstructure



**Citation:** Junique, T.; Vazquez, P.; Thomachot-Schneider, C.; Hassoun, I.; Jean-Baptiste, M.; Géraud, Y. The Use of Infrared Thermography on the Measurement of Microstructural Changes of Reservoir Rocks Induced by Temperature. *Appl. Sci.* **2021**, *11*, 559. <https://doi.org/10.3390/app11020559>

Received: 8 December 2020

Accepted: 5 January 2021

Published: 8 January 2021

**Publisher's Note:** MDPI stays neutral with regard to jurisdictional claims in published maps and institutional affiliations.

### V.1.1. INTRODUCTION

The influence of the temperature on the rock behaviour is studied in several geological domains such as petroleum extraction, geothermal activity, or storage of radioactive waste, and involve many rocks (Bai et al., 2018; Brehme et al., 2016; Nadah et al., 2009; Witherspoon et al., 1980). The researches show that high temperature changes the minerals and the void system of the rocks and the flow of the fluid in the rock may be enhanced or reduced (Andreassen, 2011; Heuze, 1983; Lion et al., 2005; Somerton et al., 1965; Takarli and Prince-Agbodjan, 2008).

The intensity of the modifications of the porous network is related to inherent stone characteristics such as mineralogy, texture, weathering degree (Sajid et al., 2016), and thermal regimes involving extreme temperatures and repetition cycles. Chalk, sandstone, and granite are reservoir rocks, and their properties and behaviours facing different temperatures and pressure are often compared due to their different porous network, that is high nano-microporosity for chalk, micro- macroporous distribution for sandstone, and low porosity of fissural type for granites.

Chalk is an interesting reservoir rock characterised by a large microporosity, with around 40% of void volume or even up to 50% for the North Sea Chalk (Faÿ-Gomord et al., 2016). The main features are its very rich to almost pure calcite composition and its reactivity to water. Despite the high and anisotropic thermal extension of calcite crystals, the high microporosity usually accommodates the expansion. Some authors show that heating, even at very high temperatures, does not modify the elastic parameters of the chalk but rather causes an extension of the elastic phase (Nadah et al., 2009). In the case of a fluid flow, chalk crystals are prone to dissolution or remobilisation, which creates a modification in chalk microstructure (Madland et al., 2011).

Sandstone (5-30%) is considered, due to its porosity, as a good reservoir rock and forms aquifers exploited as geothermal systems. The submission to high temperatures can trigger effects such as crushing of sand grains, fracturing, thermal expansion, or mineral cohesion rupture (Rosenbrand et al., 2014; Somerton et al., 1981; Wang and Dusseault, 2003), generating changes in permeability (Ding et al., 2016; Rosenbrand et al., 2014; Yang et al., 2017).

Granite is very sensitive to the effects of temperature due to its low porosity (from around 1% to a few% if weathered) and its mineral heterogeneity and its differential thermal expansion (Albissin and Sirieys, 1989; Berest and Vouille, 1988; Gómez-Heras et al., 2006; Vazquez et al., 2011). That may lead to the generation of irreversible microcracks beyond a certain temperature threshold (*e.g.* (Darot et al., 1992; Géraud et al., 1992; Lin, 2002; Meredith and Atkinson, 1985; Q. L. Yu et al., 2015). In addition, for fresh and low porosity granites, textural features such as Quartz / Feldspar ratio, mineral orientation, or crystal size become determinants in its behaviour (Janio de Castro Lima and Paraguassú, 2004; Vazquez et al., 2011, 2015, 2018a).

When a stone is exposed to high temperatures, two questions about its behaviour arise. Which is the threshold of irreversible cracking? And, when the heating-cooling cycles are repeated, what is the effect of thermal fatigue on the stones? Thus, the main aim of this study is to assess the microstructural variation of four rocks analogous to those found in hydrocarbons reservoirs or as geothermal energy sources submitted to different thermal regimes. For that purpose, two kinds of tests were performed: **TT**/ progressive heating cycles from 90 °C to 130 °C to determine the stone crack threshold and **TF**/ thermal fatigue with cycles of heating-cooling at 200 °C.

The rock microstructure was evaluated before, during, and after the tests by several methods. A microscopical evaluation by scanning electronic microscopy was carried out, to localise the new formed cracks. The variations of the bulk stone were carried out by mercury porosimetry. This technique gives information about the pore access distribution, which allows to compare the size and frequency of the rock pore access ratio before and after heating (Gómez-Heras et al., 2006; Zhang et al., 2016, 2017; Zhao et al., 2019).

To ensure the evolution continuity, capillary water uptake was also used to control the rock microstructure. This technique is non-destructive and allows to quantify indirectly the microcrack formation or variation in the same sample through the cycles (Benavente et al., 2002; Thomachot-Schneider et al., 2008; Vazquez et al., 2010). Capillary kinetics are related not only to porosity volume but also to pore width and connectivity, being complementary to mercury porosimetry.

New techniques are being developed for the study of rock state that can be applied in-situ, as the infrared thermography (IRT). This technique measures the thermal response of the outer layers of the materials.

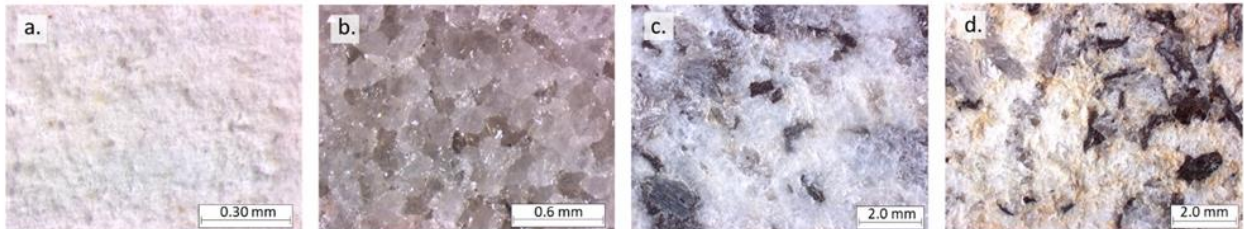
IRT allows to visualise the fluid flow, (Forestieri and Buergo, 2018; Ludwig et al., 2018; Fang Zhang et al., 2018) and to quantify the thermal kinetics of the rocks. They are directly related to porosity (Grinzato et al., 2004; Mineo and Pappalardo, 2016, 2019) or decay state (Thomachot-Schneider et al., 2019) and consequently, a heated stone will reach the temperature equilibrium with the environment faster with higher porosity.

The natural cooling of a rock can be expressed by the cooling rate index (CRI) following the works of (Pappalardo et al., 2016), and (Pappalardo and Mineo, 2017) that shows a direct correlation between the degree of fracturing and the cooling of the rock. Laboratory tests revealed a good correlation between the CRI during the first 10 minutes of cooling and the rock porosity, although for rocks with a porosity over 20% (Mineo and Pappalardo, 2016, 2019). This technique allows also to detect notable porosity variations given by the thermal behaviour of the outer layers, which may reflect the changes in the bulk microstructure. In addition, there may be a contrast between internal and external thermal damage in sandstone for example. It has been established that thermal stresses distributed in rock can induce tensile stresses in a thin region near the outside, producing microcracking, and compressive stresses in a large area in the middle, producing healing or closing of microcracks (Kim et al., 2014).

A specific aim of this study is to test the cooling rate index quantified by infrared thermography as a technique to determine the microstructural state of the selected rocks from their behaviour on the outer layers. In addition, the capillary water uptake was monitored with this technique. The objective is to know if this non-destructive technique can be applied accurately in the case of rock thermal degradation in rocks with different porosity distribution.

### V.1.2. MATERIALS

Four types of rocks analogs to those used in the fields of storage, geothermal energy, and hydrocarbon systems were chosen for this study: a chalk, a sandstone, a fresh granite, and a weathered granite (Figure V-1).



**Figure V-1. Selected rocks. Photographs made under a binocular microscope. a. Châlons chalk (CC); b. Fontainebleau sandstone (FS); c. Gris Alba granite (GA); d. Golden Ski granite (GS).**

**Châlons chalk (CC):** The chalk dated from the Upper Cretaceous, and belong to the Paris basin structure (France). Samples were extracted from the Grand Mont quarry (Saint-Germain-la-Ville, France).

From a mineralogical point of view, the Châlons chalk consisted almost exclusively of calcium carbonate ( $\text{CaCO}_3 > 98.5\%$ ).

**Fontainebleau Sandstone (FS):** The sandstone is dated from the Lower Oligocene and belongs to the Paris basin structure (France). Samples were extracted from the Fontainebleau quarry, (Fontainebleau, France). This rock has the particularity of being composed almost exclusively of quartz (>99%) with constant grain size, with a median diameter of about 300  $\mu\text{m}$  (Robert, 2004).

**Gris Alba Monzogranite (GA):** This rock belongs to the peraluminous syn and post-kinematic granites from the Galicia-tas-os-montes domain (Vera, 2004). It is temporally related to regional metamorphism and processes of Hercynian crustal anatexis. The granitoid was quarried in the Salvaterra–A Cañiza–Cerdedo alignment belonging to the Faro de Avión batholith (Galice, Spain). The study revealed a homogeneous monzogranite with a fine grain (2-5 mm). Quartz and plagioclase appeared in a similar proportion (around 25%) while alkali feldspar showed a higher proportion with almost 40%. The proportion of muscovite : biotite minerals is about 2 : 1 (Vazquez et al., 2018a).

**Golden Ski Monzogranite (GS):** Golden Ski is a peraluminous syn-kinematic granite that belongs also to the Galicia-Tras-os-montes Zone of the Iberian Massif. The samples were quarried close to the border between Galice (Spain) and Portugal. Similar to GA, this rock is located in the Salvaterra–A Cañiza–Cerdedo Alignment. GS is a homogeneous monzogranite with a fine grain (2-4mm). Quartz appeared in a proportion close to 50% of the stone, while alkali feldspar and plagioclase showed a similar quantity with around 20% each. Mica appeared similarly distributed, with 13% in total. Habits go from subhedral (feldspars) to euhedral (muscovite) with quartz showing irregular shape. This granite showed an initial alteration characterised by the presence of clay and yellow colour (Vazquez et al., 2018a).

### V.1.3. METHODOLOGY

#### V.1.3.1. Experimental Setup

The four stones were exposed to two different thermal tests, that were named Thermal Threshold Test (TT) and Thermal Fatigue Test (TF).

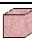















**Thermal Threshold Test (TT):** The first experiment aimed to determine if a crack threshold is produced for each rock at a geothermal low temperature. For this purpose, the samples were exposed to 5 cycles of progressive heating and cooling at 90 °C, 100 °C, 110 °C, 120 °C, and 130 °C. A climatic chamber "Vötsch VC3" was used to produce a low heating and cooling rate of 1 °C·min<sup>-1</sup>. This value was assigned to ensure that induced microcracks were the direct response of temperature and not the temperature gradient within the sample (Chaki et al., 2008; Dwivedi et al., 2008; Homand-Etienne and Houpert, 1989; Reuschlé et al., 2006; Takarli and Prince-Agbodjan, 2008). The temperature was maintained for 2 hours (Tang et al., 2019; Zhang et al., 2017) and the cooling was also performed at a low rate (1 °C·min<sup>-1</sup>) to avoid thermal shock.

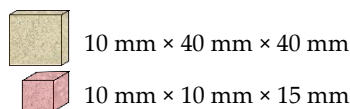
**Thermal Fatigue Test (TF):** The second experiment aimed at knowing the effect of thermal fatigue by temperature cycles. The samples went through 5 cycles of heating at 200 °C in a furnace "Thermo scientific led M 110" with a gradient of 5 °C·min<sup>-1</sup> to ensure the cracking (Ding et al., 2016; Huang et al., 2017; Kumari et al., 2017a; B. Li et al., 2019; Ozguven and Ozcelik, 2013). As in TT, the samples were maintained at the set temperature for 2 hours and the cooling down was slow with a rate of about 0.5-1 °C·min<sup>-1</sup>.

### V.1.3.2. Analysis of the Variations

Samples of each stone type were submitted to each test, with different dimensions in relation to the analytical approach (Tableau V-1): Scanning Electron Microscopy (SEM), Mercury Injection Porosimetry (MIP), or capillary uptake + IRT. Two samples of size 10 mm × 40 mm × 40 mm corresponded to those tested continuously through every cycle for the CWUT and one of them was monitored by IRT. A total of 32 samples of size 10 mm × 10 mm × 15 mm were used for MIP destructive measurements, one sample per cycle and stone for TT and one sample per stone after cycle one and five (200(1) °C and 200(5) °C) for TF. SEM observations were undertaken before and after the experiments on 16 samples of 10 mm × 10 mm × 15 mm size: on each initial stone and after being tested at 130 °C, 200(1) °C and 200(5) °C.

**Tableau V-1. Specification of the measurement conditions for samples subjected to the two thermal treatments: Threshold test (TT) and Thermal Fatigue test (TF).**

TT						TF					
Cycle	Temp.	CWUT	IRT	MIP	SEM	Cycle	Temp.	CWUT	IRT	MIP	SEM
0	Initial state					0	Initial state			-	-
1	90 °C				-	1	200(1) °C				
2	100 °C				-	2	200(2) °C			-	-
3	110 °C				-	3	200(3) °C			-	-
4	120 °C				-	4	200(4) °C			-	-
5	130 °C					5	200(5) °C				



Temp.: assigned temperature; CWUT: capillary water uptake tests; MIP: mercury injection porosimetry; SEM: scanning electron microscopy; IRT: infrared thermography.

#### 3.2.1. Scanning Electron Microscopy (SEM)

SEM images for the studied rocks were taken and assessed with a SEM Hitachi TM-1000. The porous space was quantified in the initial state as well as at 130 °C and 200(1) °C.

### V.1.3.3. Mercury Injection Porosimetry (MIP)

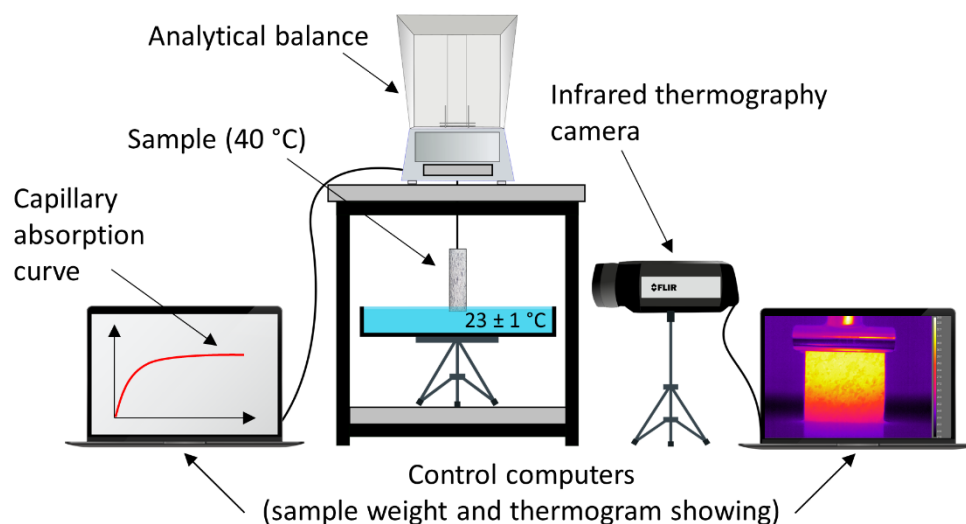
Mercury Injection Porosimetry (MIP) was determined with a Micromeritics AutoPore IV 950. The pressures applied were from 0 to 345 kPa measuring the pores of access radii ranging between 1.8 and 180  $\mu\text{m}$  for the low-pressure stage, and up to 228 MPa for the quantification of pores between 0.003 and 3  $\mu\text{m}$ .

### V.1.3.4. Capillarity Water Uptake

The samples were dried at  $40 \pm 5$   $^{\circ}\text{C}$  until constant weight before each test. Then, each sample was suspended from an electronic precision balance and put into contact with water in its bottom face at a depth of about 1 mm (Figure V-2). The weight was automatically recorded every 10 seconds on a control computer. The test was carried out for 1 hour, enough for all the samples to reach the stabilisation of the water uptake and the capillary coefficient (C) calculated from the obtained data. The temperature of the room was kept at  $23 \pm 1$   $^{\circ}\text{C}$ .

### V.1.3.5. IRT Monitoring

One of the two tested samples was monitored with IRT during the capillary water uptake test, that is one sample by rock type and cycle. The complete setup is shown in Figure V-2.



**Figure V-2. Experimental setup of capillary uptake controlled by automatic weight and IRT monitoring.**

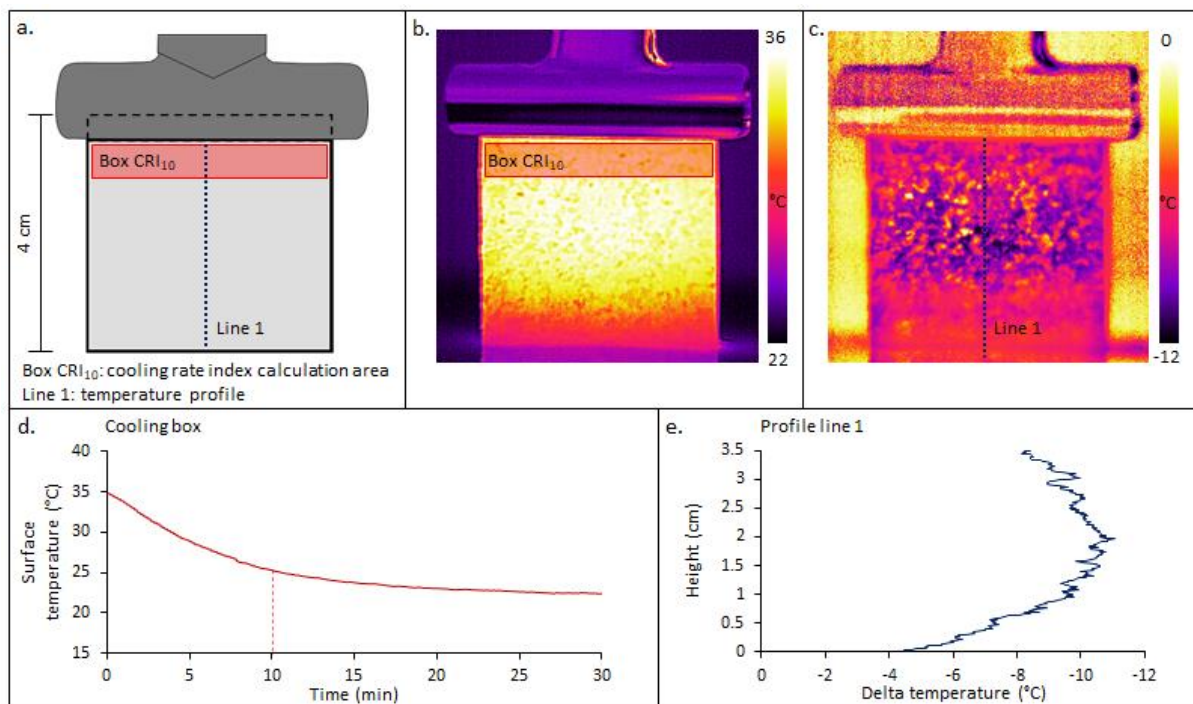
The monitoring was performed by a FLIR SC655 operating in wavelengths between 7.5 and 14  $\mu\text{m}$ . The detection temperature of this device is between -40 and 150  $^{\circ}\text{C}$  with a sensitivity of



0.1 °C. The detector is an uncooled array of microbolometers. The image size is 640 × 480 pixels and the noise signal is about 40 mK. The recorded signal is called thermosignal (TS) and it depends on temperature and emissivity, expressed in isothermal units (IU).

The risks associated with environmental variations were minimised (control of temperature and humidity, room lights off). The IRT camera recorded thermal images at a rate of 6 frames / minute for 30 minutes. The recordings were processed by the FLIR ResearchIR software.

Two informations were obtained from the IRT data: the monitoring of the wet fringe along the samples and the rock cooling rate index (CRI 10, (Pappalardo et al., 2016)), since the water rise did not reach the upper part of the samples during the first minutes, and the cooldown (from 40 °C to 23 °C) was done by exchange with the room temperature (Figure V-3a).



**Figure V-3. IRT setup. a. Schema of the sample and the measurements carried out. b. IRT image in false colour. c. Image after the application of a subtraction and an Advanced Plateau Equalisation (APE) scale. d. Cooling curves. e. Interpretation of the IRT image.**

### V.1.3.6. Wet fringe migration

The obtained IRT image during capillary water uptake revealed clearly the water presence on the rock (Figure V-3b). However, with the rock cooling, the wet fringe and the details of the image were less and less evident with time. For that reason, a subtraction filter was applied,

which produced images as the difference between the initial state and during the capillary test. In addition, an Advanced Plateau Equalisation (APE) scale was selected since it allowed to observe more details and contrast from the rock (Figure V-3c). A profile in the middle of the sample was plotted at different times to observe the water migration (Figure V-3e).

### V.1.3.7. Cooling rate index (CRI)

From the upper part of the sample (Figure V-3a, b), the "Temporal Plot" function of the software gives the thermosignal evolution with time. The calculation of CRI is as follows:

$$CRI = \frac{\Delta T}{\Delta t} = \frac{T_{10} - T_0}{t_{10} - t_0} \quad (V.1)$$

Where  $T_{10}$  is the temperature after 10 minutes of cooling,  $T_0$  the initial temperature,  $t_{10}$  and  $t_0$  are respectively the times with a lapse of around 10 minutes. In the case of chalk, with a very fast water absorption kinetics, the CRI was calculated for the first five minutes, before the water reaches the upper half. The data used were the cooling slopes related to the square root of time. High slope values corresponded to fast cooling and low values to a slow cooling (Figure V-3d).

## V.1.4. RESULTS

### V.1.4.1. Scanning Electron Microscopy Observations

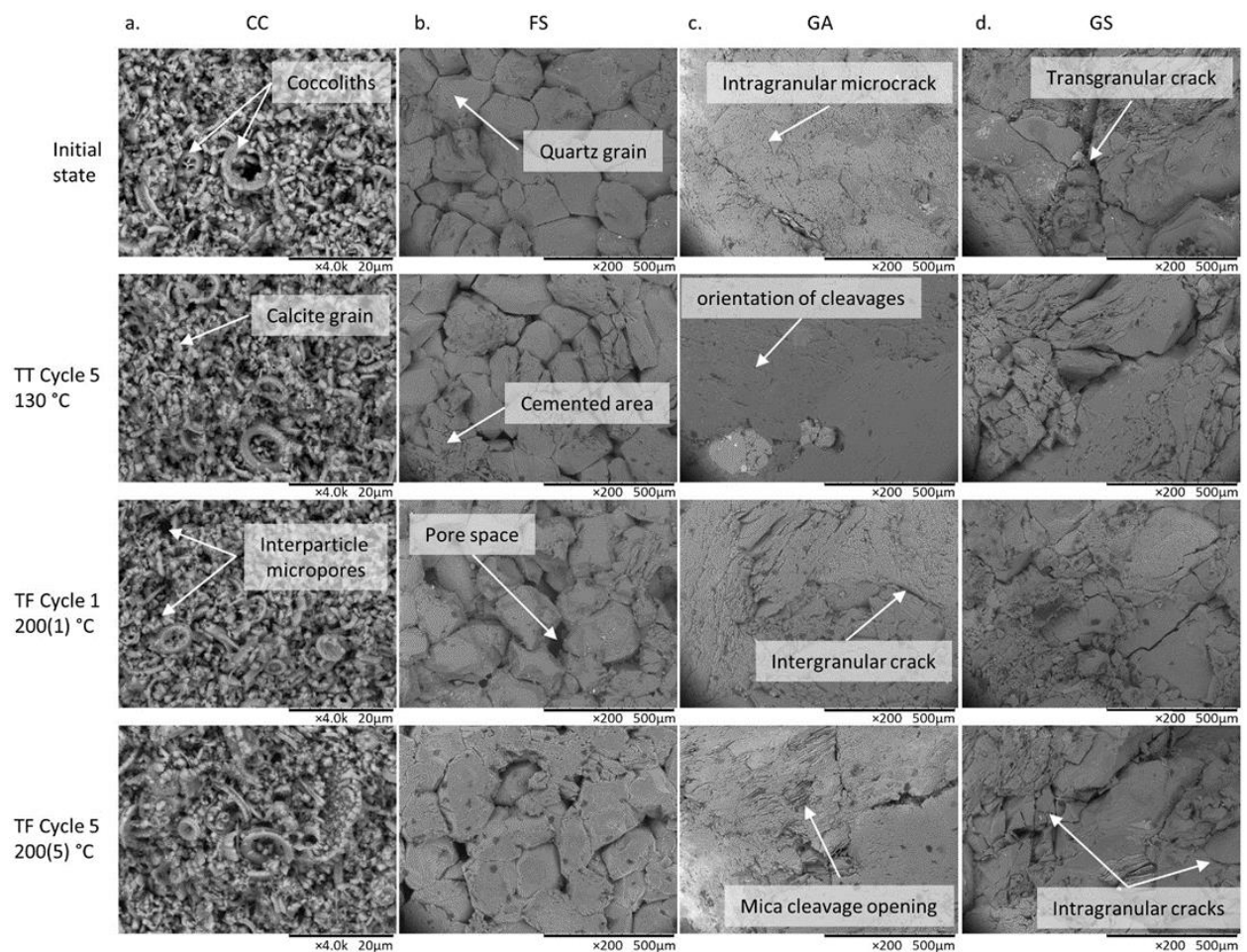
The porous network of the rocks before and after the main heating cycles viewed under SEM is shown in Figure V-4.

The Châlons chalk showed a homogeneous microporous network. The main components of the rock are well-preserved coccolith fragments of different shapes, although the majority are elliptical with no preferred orientation. The coccoliths length distribution was unimodal with a median of 4.2  $\mu\text{m}$  and an interquartile range of about 2  $\mu\text{m}$ . The contacts between the coccolith fragments were mainly punctic as well as between the micrites. The porosity was mainly composed of an interparticle microporosity inside the nanofossil cells (diameter < 1  $\mu\text{m}$ ). A few pores of around several microns in diameter have been observed. During the TT and TF test, the microtexture shows little major modification. The chalk surface at 200(5) °C appeared more irregular than the fresh samples, showing more grains clustered together and pore regions with enlarged intraparticle spaces.

The Fontainebleau sandstone presented different compactness, with some areas where the grains were strongly cemented. Clumps of grains were grouped and completely silicified. The crystals had a diameter between 100 and 300  $\mu\text{m}$ . The shape of the porous spaces consisted of networks of channels with widths that ranged from 5 to 30  $\mu\text{m}$ , although some could reach 60  $\mu\text{m}$ . This pore size was sufficient to allow correct hydraulic connectivity. Capillary rectilinear ends (less than 1  $\mu\text{m}$  in diameter) were found connecting the different channels of larger size. During the TT test, the rock showed some crushed crystals that invaded the intergranular porosity and the appearance of dispersed macropores, more numerous with higher temperatures (Figure V-4). During the TF test, the intergranular porosity changed in two ways, with closure and widening of boundaries, revealing a pore redistribution. Some crushed crystals were also present and intragranular microcracks became visible.

The Gris Alba granite showed predominantly intergranular cracks in the initial state. The grain size had a diameter between 4 and 6 mm (Vazquez et al., 2018a). The average crack width is about 8  $\mu\text{m}$  (Vazquez et al., 2010). After heating at 130 °C, the minerals increased in volume and the boundaries looked fused. Some pores of bigger size appeared, due to materials fracturing and material loss. The microcracks seemed angled, decreasing tortuosity, and improving connectivity. At 200 °C, new microcracking appeared on the rock surface, following grain boundaries with less than 1  $\mu\text{m}$  width. Mica showed a notable opening of the cleavage planes, and a material detachment was observed. The pre-existing cracks became larger and slightly wider in diameter.

The Golden Ski granite showed initially marked trans, inter, and intragranular microcracks, ranging in diameter from 5 to 50  $\mu\text{m}$ . The grain size had a diameter between 2 and 4 mm (Vázquez et al., 2018). After heating, minor variation was observed although new microcracks appeared especially in quartz grains. The cleavage of mica was also altered showing irregularities, even fractures that increased the roughness of the granite surface.



**Figure V-4. SEM observations of the Châlons chalk (a. CC), the Fontainebleau sandstone (b. FS), the Gris Alba granite (c. GA), and the Golden Ski granite (d. GS), in their initial state and after heating treatment. (TT: Threshold test and TF: Thermal fatigue test).**

#### V.1.4.2. Mercury Injection Porosimetry (MIP)

The connected porosity of the samples before and after the thermal tests is shown in Tableau V-2 and the variations in the pore radii access distribution in Figure V-5. During heating, the differential thermal expansion coefficients of the various mineral grains cause the generation of microcracks. When rocks are held at temperature, cracks generated at this temperature remain closed. During cooling, microstructural modifications can appear (Homand-Etienne and Houpert, 1989). If the microcrack threshold has not been reached, the minerals contracted during cooling without generating microcracks. If the thermal stress has been exceeded, microcracking occurred and increased the porosity (Dwivedi et al., 2008).

The Châlons chalk showed an initial porosity slightly lower than 40%, which consisted of a homogeneous microporous network with a unimodal distribution centred around 0.26  $\mu\text{m}$ . During the TT, the porosity increased slightly, between 7.5 and 11%, reflected by an increase in the modal peak intensity. That indicated an augmentation of the pore volume with the same size that the initial rock. After TF, the porosity increased by about 5% with no change in the pore access radii.

The Fontainebleau sandstone had a porosity of around 4% in its initial state, with a wide unimodal distribution centred on 1  $\mu\text{m}$ . The first cycle of the TT already revealed an increase in the porosity of approximately 11%, with also an evident change in the pore access radii larger than 1.5  $\mu\text{m}$ . The increase was not progressive along the cycles, although the maximal value was found at 130 °C, with more than 19% increase and a pore access threshold that shifted up to almost 2  $\mu\text{m}$ . In addition, a new family of bigger pores appeared from the very first heating cycle between 43 and 113  $\mu\text{m}$ . For the TF cycle 1, the microstructural variations were even more remarkable, with a strong increase of 35% of pore volume and a pore threshold increase up to 3  $\mu\text{m}$ . The fatigue (TF cycle 5) produced a slight opening of the microcracks at the end of the test, with an increase of 9% in porosity compared to the initial state and an increase to 2  $\mu\text{m}$  of the pore threshold.

The Gris Alba granite presented an initial porosity volume of 1.05% and showed two main distributions, a wide micropore family with pore access radii below 1  $\mu\text{m}$  and a macropore family starting from around 10  $\mu\text{m}$ . Through the TT, this rock showed a decrease in its pore volume of 17% at 90 °C and 25% at 130 °C. Figure V-5 exhibited a redistribution and a slight reduction in the micropore family, which could be due to the heating but also to the heterogeneity between the samples. Nevertheless, there was a clear decrease in the macroporous family for all the heating cycles. The TF test showed a great increase in the porosity, with 51% after the first cycle and 32% at the end. The microporous family exhibited a variation in the radii access proportion, without being possible to determine an increase or decrease graphically. A great increase in the pore access radii larger than 1  $\mu\text{m}$  was measured, with the apparition of new peaks and the development of voids around 100  $\mu\text{m}$ .

The Golden Ski granite had an initial porosity volume of 3.77%. This rock showed most of their pore access radii below 10  $\mu\text{m}$ , with a modal value around 0.5  $\mu\text{m}$ . Besides, it presented a

## Chapitre V : Changements microstructuraux de 3 roches réservoirs sous sollicitation thermique et circulation de fluide

macropore family with a modal peak measured around 150  $\mu\text{m}$ . During the TT test, this rock experimented fluctuations around the initial values, although for the temperatures of 90  $^{\circ}\text{C}$  and 130  $^{\circ}\text{C}$  a decrease of 15% and 10% respectively were measured. Figure V-5 revealed a slight decrease in the microporous family and a disappearance of the bigger peak area, as already observed in GA. The TF test did not produce a great microstructural change in pore volume, although Figure V-5 showed smoothing of the microporous family and differences between the cycles for the bigger pore area.

**Tableau V-2. Porosity MIP (%) of the 4 rocks before and after treatment at different temperatures (in blue, values lower than the initial value, in red, values higher than the initial value).**

	TT						TF	
	25 $^{\circ}\text{C}$	90 $^{\circ}\text{C}$	100 $^{\circ}\text{C}$	110 $^{\circ}\text{C}$	120 $^{\circ}\text{C}$	130 $^{\circ}\text{C}$	200(1) $^{\circ}\text{C}$	200(5) $^{\circ}\text{C}$
CC	37.93	42.61	37.69	39.81	40.44	40.95	40.05	40.35
FS	4.34	4.84	5.09	4.73	4.68	5.18	5.86	4.75
GA	1.05	0.87	0.95	0.96	0.95	0.80	1.59	1.39
GS	3.77	3.19	3.08	3.68	3.93	3.42	3.97	3.56

CC: Châlons chalk; FS: Fontainebleau sandstone; GA: Gris Alba granite; GS: Golden Ski granite;

TT: Threshold test; TF: Thermal fatigue test.

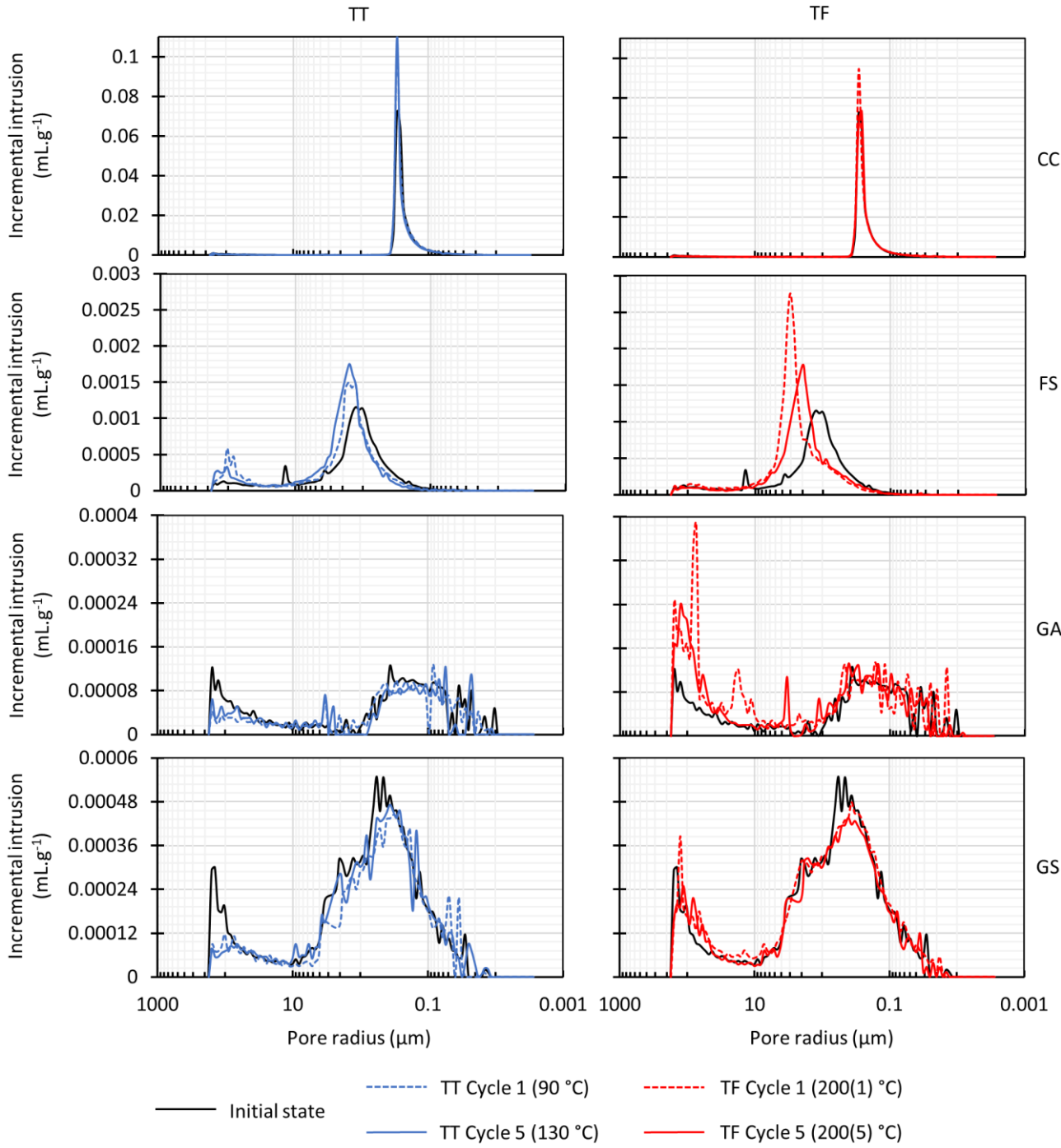


Figure V-5. Pore access size distribution curves of samples before and after the first heating cycle and at the end of the TT (Threshold test) and TF (Thermal fatigue test). CC: Châlons chalk; FS: Fontainebleau sandstone; GA: Gris Alba granite; GS: Golden Ski granite.

### V.1.4.3. Capillary Absorption

The capillary water uptake results showed that 1 hour was enough to calculate accurately the coefficient of capillarity. Tableau V-3 represents the change in the coefficient C relative to the weight increase per surface unit for the two samples of each stone and each cycle.

**Tableau V-3. Capillary coefficient (C) ( $\text{g}\cdot\text{m}^{-2}\cdot\text{s}^{-1/2}$ ) before and after heat treatments (in blue, values lower than the initial values, in red, values higher than the initial values).**

	TT						TF					
	25 °C	90 °C	100 °C	110 °C	120 °C	130 °C	25 °C	200(1) °C	200(2) °C	200(3) °C	200(4) °C	200(5) °C
CC	462	451	445	451	428	411	444	466	476	486	477	489
	345	339	356	363	350	335	396	416	416	417	347	330
FS	14.8	10.1	7.6	4.3	2.8	4.3	6.7	1.6	5.1	8.6	11.1	11.4
	21.7	13.3	15.4	16.8	15.5	14.6	6.5	7.7	6.9	6.1	5.7	6.5
GA	2.2	2.1	2.2	2.7	3.5	3.7	4.8	5.0	5.0	5.4	5.3	5.6
	5.5	4.2	5.2	4.8	4.7	4.8	5.0	4.9	5.2	5.3	5.2	4.9
GS	21.9	20.0	23.3	22.5	23.4	24.7	20.2	20.8	21.1	19.0	22.5	22.8
	19.1	19.9	21.0	21.6	22.2	22.6	23.5	25.2	24.6	26.1	26.3	26.6

CC: Châlons chalk; FS: Fontainebleau sandstone; GA: Gris Alba granite; GS: Golden Ski granite;

TT: Threshold test; TF: Thermal fatigue test.

The Châlons chalk showed the highest capillary coefficient with values that varied between 350 and 460  $\text{g}\cdot\text{m}^{-2}\cdot\text{s}^{-1/2}$  in accordance with its higher porosity combined with its unimodal microporous network. During the TT test, this rock hardly showed any variation for both samples, with a maximal decrease of 11% at 130 °C. During the TF test, the chalk behaved similarly, with almost no perceptible change and only a maximal reduction of 17% on the second sample.

The Fontainebleau sandstone presented an initial capillary coefficient between 7 and 22  $\text{g}\cdot\text{m}^{-2}\cdot\text{s}^{-1/2}$ . This high variability was explained by the compactness differences within the same block for this stone. For the TT, both samples showed a strong decrease in the capillary water uptake through all the heating cycles, with maximal values of 71% and 33% respectively. For the TF test, the progression of coefficient C showed different trends for each sample. The C of the first sample decreased by 77% after its first heating but finished with an increase of 70%. The second sample hardly showed any relevant change through the test.

For the Gris Alba Granite, the initial C coefficients were between 2.2 and 5.5  $\text{g}\cdot\text{m}^{-2}\cdot\text{s}^{-1/2}$  for the 2 samples tested. During the TT test, only the first sample showed an evident change, with a



progressive increase that finished with porosity 69% higher at the end of the experiment. The other sample fluctuated slightly without being considered significant. In the TF test, this rock hardly showed any variation for both samples, with only a slight increase of 15% for one of them at the end of the test.

The Golden Ski granite exhibited initial C coefficients between 19 and 24  $\text{g}\cdot\text{m}^{-2}\cdot\text{s}^{-1/2}$  respectively. During the TT test, the variations were very little, although a progressive increase with temperature was observed for both samples, with final increases of 12 and 18%. The TF test exhibited the same behaviour, a very slight progressive increase with cycles, and a maximal value of 13% at the end of the test.

### V.1.4.4. Wet Fringe

The wet fringe was observed and measured by the naked eye during the capillary test. IRT allowed to observe and quantify not only the wet fringe but also the water distribution within the outer layers of the studied stones. The main fact extracted from the IRT images was that porous and fissural rocks behaved differently. In both cases, three zones were defined (Figure V-6 and Figure V-7):

i) the wet zone, where the water filled the void system almost instantly and the temperature between the fluid and the rock equilibrated rapidly. The rock surface was wet.

ii) the capillary zone, an area of inner water migration evidenced by a homogeneous mineral cooling.

1. In the sedimentary stones, this zone was also observed by the naked eye as wet. The upper part of the capillary zone corresponded to the visible wet fringe.

2. In the granites, this zone was dry although a strong mineral cooling produced only by water effect was observed by IRT. The bottom part of the capillary zone corresponded to the visible wet fringe.

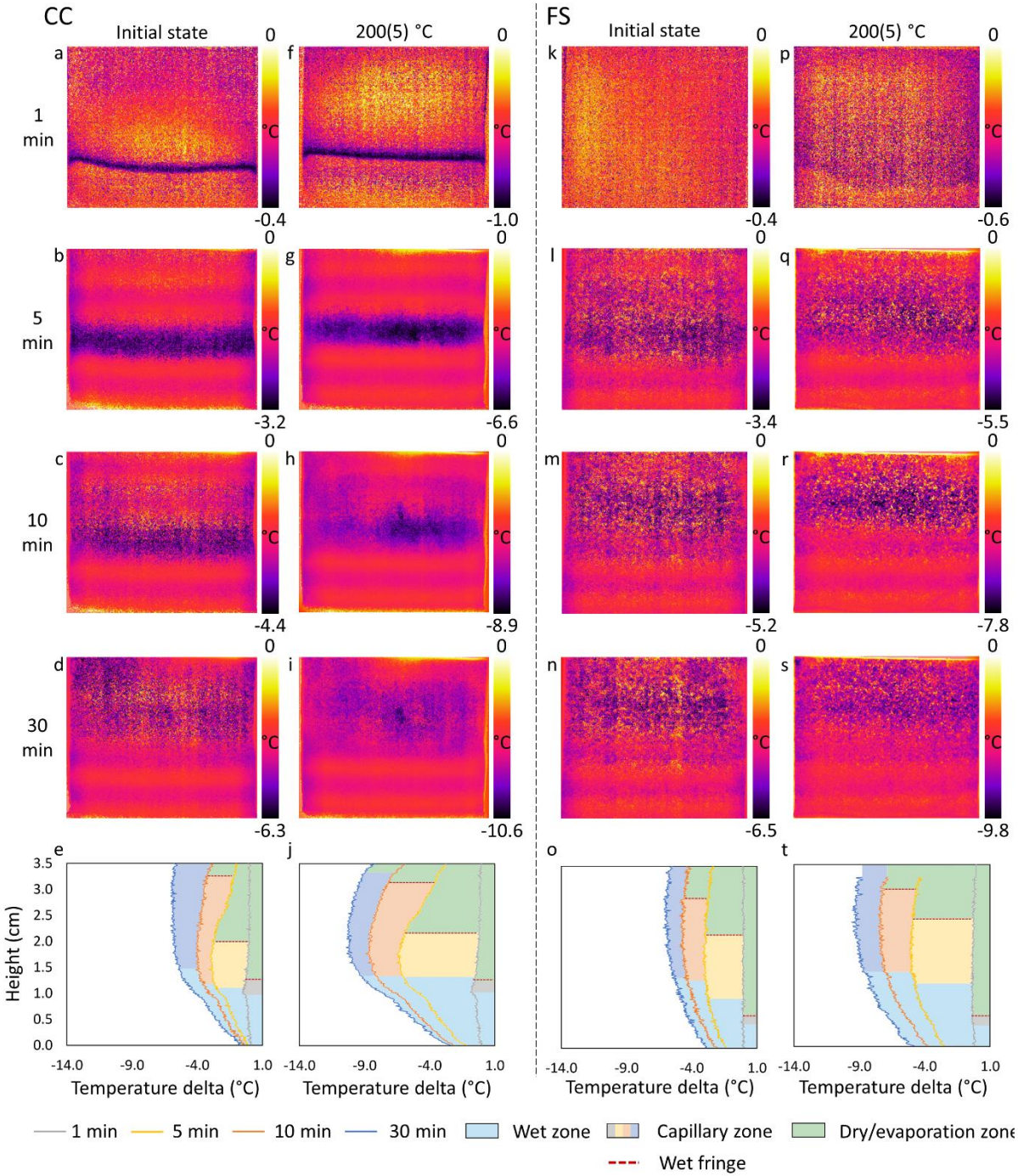
iii) the dry / evaporation zone, the upper part that was not invaded by water and cooled freely by air contact. In some cases, an evaporation zone when the water already reached the top of the sample.

Vertical profiles were graphed to delimit these zones at different times of the capillary water uptake test (Figure V-6 and Figure V-7).

Figure V-6 showed the three parts of the sedimentary stones behavior during capillary water uptake. A homogeneous wet zone that cooled fastly, a capillary zone marked by the distribution of the dark colour, and an upper dry zone in which the cooling took place at a moderate rate.

For the Châlons chalk, the IRT images revealed that for the fresh rock, after 1 minute of water contact, the wet fringe was a thin dark line at around 1 cm height (Figure V-6a). After 5 minutes, the wet zone was slightly spread at the mid-height of the sample, although the upper part of the dark line corresponded to the wet fringe observed visually around 2.2 cm. After 10 minutes, the water was well distributed in the whole sample in the IRT images (Figure V-6a-e) and also observed by the naked eye. At the end of TT, the IRT images were similar to those from the same time-lapse at the initial state, with a slight difference due to the increase of the capillary zone height after 5 minutes. The thermal profile graphed a faster cooling in the tested sample and an evaporation phase at the upper part. During the last cycle of the TF test (Figure V-6f-j), after 5 minutes, the wet fringe was measured slightly higher than the initial state and after 30 minutes, the sample saturation and an evaporation area were clearly observed.

The water behaviour in Fontainebleau sandstone is shown in Figure V-6k-t. After 1 minute, no changes were perceived on the IRT image. Nevertheless, at 5 minutes the wet fringe was clearly observed with the naked eye at around 2 cm, that in the IRT image included the wet zone (of about 0.5 cm) and the capillary moist zone (1.5 cm), in which the water circulated and advanced to the top with the time (Figure V-6o). In the TT test, the wet fringe appeared from minute 1, and its migration together with the rock cooling area to the upper part of the sample was observed. In the TF test (Figure V-6p-t), the wet zone rose higher and the cooling of the capillary area to the top of the sample at the end of the test was evident. The profiles were more homogeneous and smoother than the chalk ones, so the combination of the naked eye, the profiles, and the IRT images were needed to establish the interpretation of the water migration.



**Figure V-6.** Subtracted IRT images of CC (Châlons chalk) and FS (Fontainebleau sandstone) at their initial state (a–d; k–n) and after 5 cycles of TF (Thermal Fatigue test) (200(5) °C) (f–i; p–s) obtained by subtracting thermograms at 1, 5, 10, and 30 min from the initial state. Vertical temperature profiles are plotted from the IRT images (e,j,o,t).

Figure V-7 showed the three parts of granite behaviours. The wet zone presented homogeneous colours in the IRT image without mineral differentiation and an abrupt cooling

in the temperature profile. The capillary zone was defined as a smooth progression from the homogeneous wet zone to a zone with differential mineral cooling. The dry zone was clearly delimited during the first minutes in the IRT images. Afterward, air and water cooling were mixed and only the profiles helped to establish the limits.

The fresh Gris Alba granite exhibited in IRT a slight and homogeneous cooling after 1 minute. The vertical temperature profiles and the IRT images showed that the wet zone increased clearly from about 0.5 mm height at 5 min to around 1 mm at 30 min (Figure V-7a-j), in agreement with the wet fringe observed by the naked eye. The upper part of the capillary zone can be defined as the darkest band at the middle of the IRT image at 5 min, and despite the lack of visible moisture on the rock surface, the water possibly reached the top of the sample after 30 min, with regard to the cooling phenomena. During both TT and TF tests, the IRT images were similar to the fresh stone, although, after 5 min, the central area cooled by the water rise was better defined. The profiles showed a marked increase in the cooling rate and a bottom zone with more pronounced mineral differences.

The Golden Ski granite exhibited a comparable behaviour to GA, with a homogeneous cooling during the first minute (Figure V-7k). The wet zone was established approximately at the same height at 5 min and slightly higher at 10 and 30 min, also in agreement with visual observations. The capillary zone migrated to the top of the sample. At the end of TT and the TF test (Figure V-7p-t), the trend was the same, with a similar differential mineral cooling.

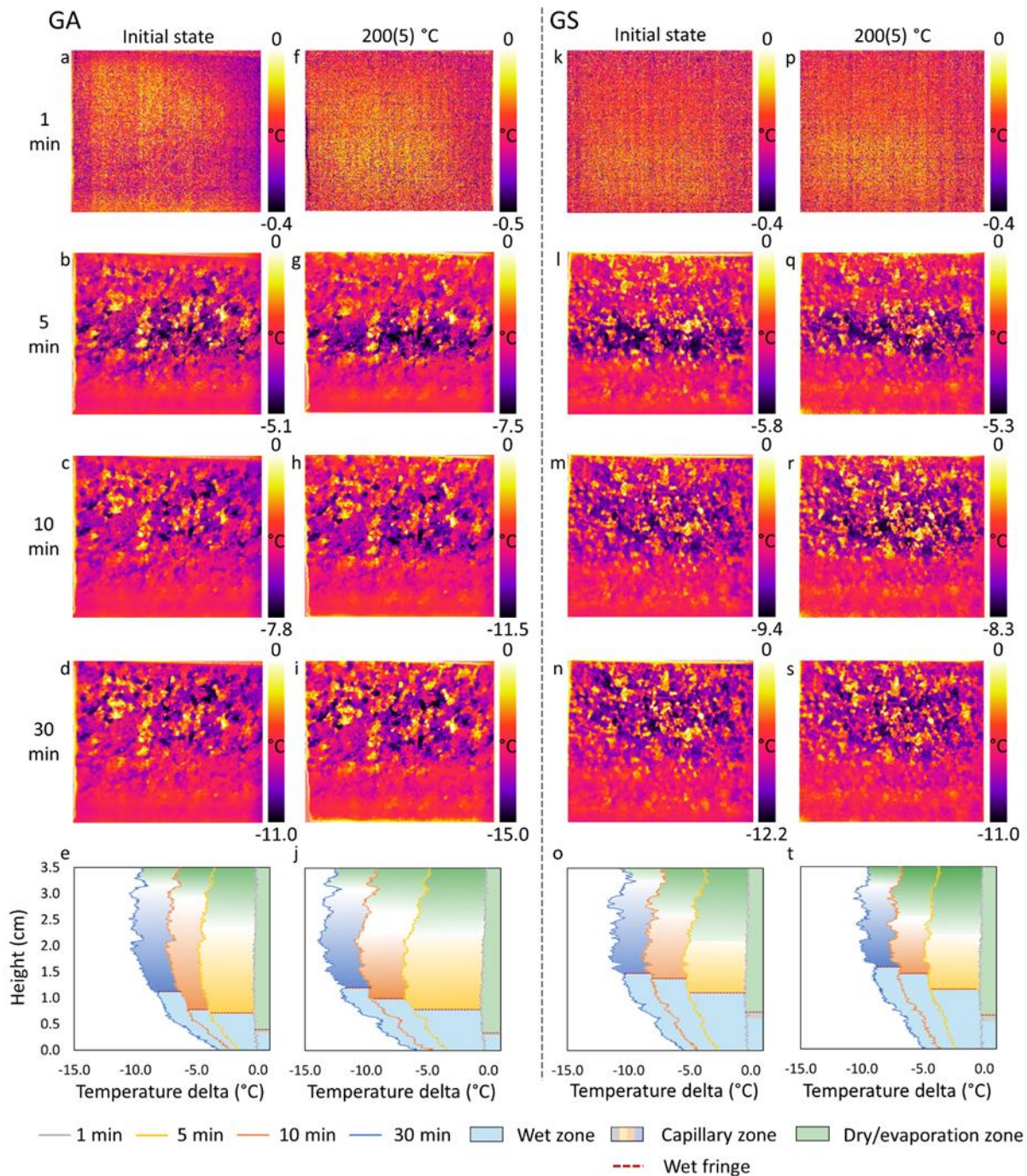


Figure V-7. Subtracted IRT images of GA (Gris Alba granite) and GS (Golden Ski granite) at their initial state (a–d; k–n) and after 5 cycles of TF (Thermal Fatigue test) (200(5) °C) (f–i; p–s) obtained by subtracting thermograms at 1, 5, 10, and 30 min from the initial state. Vertical temperature profiles are plotted from the IRT images (e,j,o,t).

#### V.1.4.5. Cooling Rate Index (CRI)

The CRI corresponded to the slope of the temperature average variation during the first 10 minutes of cooling according to (Mineo and Pappalardo, 2016). Because the CRI assesses the cooling of the dry zones, the average temperature was recorded in the upper part of the samples (Figure V-3). Only for the chalk where the capillary rise was very fast, the CRI was calculated during the first 5 minutes. Higher values of CRI meant fast cooling (Tableau V-4).

**Tableau V-4. Cooling Rate Indexes ( $^{\circ}\text{C}\cdot\text{min}^{-1}$ ) of the 4 rocks before and after treatment at different temperatures (in blue, values lower than the initial values, in red, values higher than the initial values).**

	TT						TF		
	25 $^{\circ}\text{C}$	90 $^{\circ}\text{C}$	100 $^{\circ}\text{C}$	110 $^{\circ}\text{C}$	120 $^{\circ}\text{C}$	130 $^{\circ}\text{C}$	25 $^{\circ}\text{C}$	200(1) $^{\circ}\text{C}$	200(5) $^{\circ}\text{C}$
CC (CRI5)	0.26	0.26	0.42	0.29	0.53	0.51	-	0.11	0.72
FS (CRI10)	0.43	0.62	0.57	0.59	0.75	0.86	-	0.48	0.71
GA (CRI10)	0.31	0.05	0.49	0.63	0.71	0.60	0.67	0.78	0.89
GS (CRI10)	0.90	0.56	0.71	0.70	0.71	0.64	0.77	0.83	0.68

CC: Châlons chalk; FS: Fontainebleau sandstone; GA: Gris Alba granite; GS: Golden Ski granite;  
TT: Threshold test; TF: Thermal fatigue test.

The Châlons Chalk showed the lowest cooling kinetics compared to all the stones. Despite its high porosity, the small pore sizes led to a very low thermal diffusivity of only  $0.59 \text{ mm}^2\cdot\text{s}^{-1}$  (Thermtest Thermal Conductivity Measurement & Testing Service, 2020). During the TT, the cooling rate increased up to double, which indicated a change of the surface properties. The variations through the TF also revealed an increase in the cooling velocity.

The Fontainebleau sandstone showed an initial CRI of intermediate value between the stones. The main parameters involved in its kinetics are the low porosity and the high quartz content that increase diffusivity in relation to a standard sandstone (diffusivity between  $1.13$  and  $1.67 \text{ mm}^2\cdot\text{s}^{-1}$ ) (Thermtest Thermal Conductivity Measurement & Testing Service, 2020). During the TT there was an increase of the cooling kinetics up to double of the initial values indicating a variation in outer layers porosity. The temperature was too low to produce a mineralogical change. On the other hand, the TF revealed an increase in the cooling velocities that confirmed the microstructural change.

The Gris Alba showed a low initial CRI, according to its low porosity and quartz content. A standard granite has a diffusivity of around  $1.13 \text{ mm}^2\cdot\text{s}^{-1}$  while a low porosity granite can have a lower one up to  $0.77 \text{ mm}^2\cdot\text{s}^{-1}$ . At the end of the TT test, the CRI values doubled, reaching the highest ones at  $120 \text{ }^\circ\text{C}$ . The fatigue at  $200 \text{ }^\circ\text{C}$  produced a slight increase in the cooling rate, although enough to ensure that a microcracking was taking place, at least on the surface.

The Golden Ski granite showed the highest CRI among the studied stones. That was probably due to its initial alteration with wide and long microcracks. A high permeability granite can reach diffusivity values of around  $1.77 \text{ mm}^2\cdot\text{s}^{-1}$ . During the TT, the CRI decreased for all the heating cycles, with a percentage of around -30% at the end of the test. The fatigue also led to a decrease of the cooling kinetics that implied an opposite behaviour than the rest of the rocks.

### V.1.5. DISCUSSION

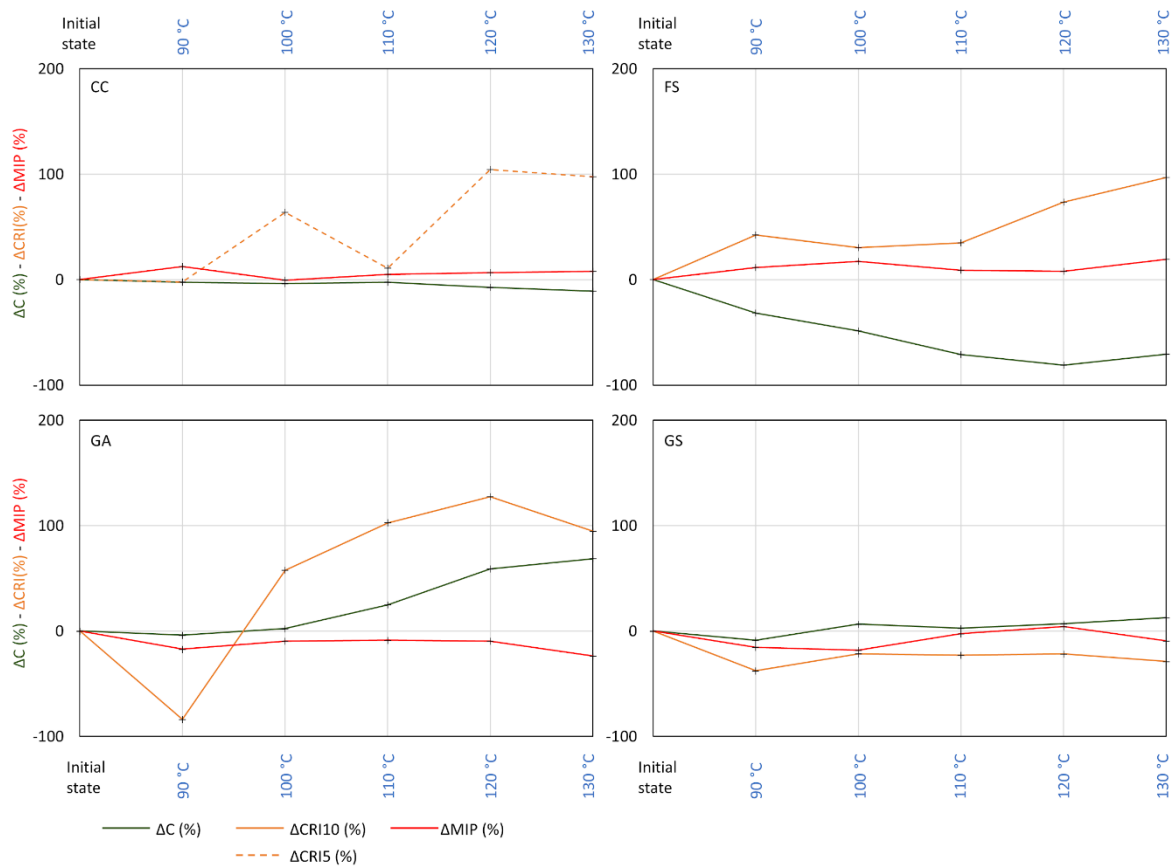
There are several parameters such as porosity, mineralogical composition, anisotropy, and granulometry that influence the thermal sensitivity of the rocks (Homand et al., 2000). In addition, other properties related to the porous network such as pore volume, pore access radii, tortuosity or connectivity, condition the water flow. During heating, the creation of microcracks and the thermal expansion of minerals are two contradictory phenomena in the evolution of the microstructure, and the variation of all the above mentioned parameters leads to differences in their thermal and hydric properties. The degree of cracking depends mainly on temperature and mechanical strains, mineralogical composition, and particle size distribution (Freire-Lista et al., 2016). In addition, it is possible that microcracks appear during the first cycles, even with a low heating rate ( $1 \text{ to } 2 \text{ }^\circ\text{C}\cdot\text{min}^{-1}$ ) (Tiskatine et al., 2017).

#### V.1.5.1. Thermal Threshold Test (TT)

The progressive heating of the selected stones up to  $130 \text{ }^\circ\text{C}$  produced changes more or less remarkable depending on the initial microstructure and composition quantified by MIP, Capillary water uptake, and CRI (Figure V-8).

The Châlons chalk (CC) is a microporous rock with a void volume of around 40%. That implies an easy readjustment of the calcite expansion during heating that avoids the microcrack

formation. Thus, very slight changes were observed in the properties related to their microstructure, that is capillary water absorption and MIP (Figure V-8).



**Figure V-8. Variations of the capillary coefficient (C), the cooling rate index (CRI), and the porosity (MIP) along the thermal threshold test (TT).**

Despite the calcite solubility, the interaction times between this mineral and water were too short during the tests to produce any chemical alteration on chalks (Megawati et al., 2015; Nermoen et al., 2016) or uniform dissolution between intergranular contacts (Madland, 2005). Most of the studies on the behaviour of chalk with increasing temperatures (around 100-130 °C) revealed that no mechanical variations were produced (Brignoli et al., 1994; Charlez et al., 1992; DaSilva et al., 1985; Nadah et al., 2009; Potts et al., 1988) although a few times, a slight variation of the elastic modulus was quantified (Brignoli et al., 1994; Hellmann et al., 2002b; Madland, 2005). However, the tensile forces on the outer layers during heating may produce weakness in some boundaries that may lead to a granular disaggregation or crushing on the surface (Kim et al., 2014). The SEM observations after treatment showed that the



porous structure of the chalk consisted of a more heterogeneous zone with the grouping of numerous particles in the same place. The surface roughness for natural chalk is on the order of only a few micrometers and cycles of wetting and drying can erode its surface (Weisbrod et al., 2000). This erosion was mainly due to the detachment of the particles. These observations suggest that the study of the surface roughness of the chalk is an important parameter for evaluating the cooling rate index (CRI) because it depends on the exchanges between the surface and the environment. An augmentation in roughness is a valuable hypothesis to explain the increase of the CRI after some heating cycles and capillary tests (Figure V-9a).

The Fontainebleau sandstone (FS) is composed mainly of quartz, a mineral with high and anisotropic thermal expansion. Microstructural variations through TT were observed with a slight increase in the pore volume and pore access radii under 140  $\mu\text{m}$  and a decrease in the capillary water uptake kinetics. Acoustic emission studies revealed microcracking in sandstones at temperatures as low as 65 °C (Vasin et al., 2006) and 100 °C (J. Yu et al., 2015) while (Jian-ping et al., 2010) discovered grain boundary cracking at temperatures under 125 °C. The trend of this microstructural variation is aleatory, with an increase in crack density measured by (Kim et al., 2020) and a decrease in porosity by (Hassanzadegan et al., 2014). Localisation, connectivity to porosity, and the opening of microcracks are important parameters in the analysis of fluid transfer (Dormieux et al., 2002). It has been observed that the water rises more slowly in the wider parts of the porous network of the Fontainebleau sandstone (Robert, 2004). The SEM images (Figure V-4) and the increase in the CRI (Figure V-8) helped to schematize the FS behaviour during the TT test (Figure V-9b). In its initial state, the flow of capillary water uptake was regular thanks to the homogeneous and continuous distribution of the entire pore volume. The size of the flow paths was small (radius centred about 1  $\mu\text{m}$ ) although pores of smaller size were present because of the strongly cemented areas locally. As described by Kim et al. (2014), a fine zone of microcracking on the outside of the samples (tensile stresses) and a thick zone of crack closure in the center (compressive stresses) can be observed on rocks following thermal stress. Between 90 and 130 °C, intergranular porosity healing may occur at the center of the sample in the compression zone, accentuated by the high thermal expansion of quartz (Skinner, 1966). This change led to a decrease in water absorption. The outer tensile zone readjusted the quartz grains and

widened the space between the grains. The presence of macropores increased the temperature exchanges with the external environment, that enhanced the cooling rate (CRI).

The Gris Alba (GA) is a fresh granite with low quartz content and low porosity. During heating, GA exhibited an increase in C and CRI, while the MIP showed a reduction of pores around 100  $\mu\text{m}$ . The SEM images (Figure V-4c) revealed a more compacted microstructure, with the disappearance or the fusion of microcracks that explained the MIP values, but also a crack redistribution with the connection of oriented microcracks, the cleavage opening of mica sheets, and the reduction of tortuosity (Figure V-9c), with the consequent augmentation of C. This higher connectivity and the mica opening influenced also positively the CRI. The opening of pre-existing cracks has already been characterised in granite at temperatures below 130 °C (Géraud et al., 1992; Jansen et al., 1993; Lin, 2002; Q. L. Yu et al., 2015). The MIP values nevertheless show a slight decrease in the pore volume after the first cycle. This pore closure at 90 °C was observed in particular with a reduction of the access larger than 10 microns. Thermal tests have been shown to induce more modification of the macroporosity than the microporosity for granites similar to GA (low porosity) (Freire-Lista et al., 2016).

The Golden Ski granite (GS) is a weathered granite with high cracking and clays. In addition, its high mica proportion helps to adapt to the stress produced during temperature rise. Due to this fact, few changes were observed in GS during TT, except for a slight decrease of the CRI, explained by the increase in the volume of certain minerals such as quartz, that may close the bigger microcracks

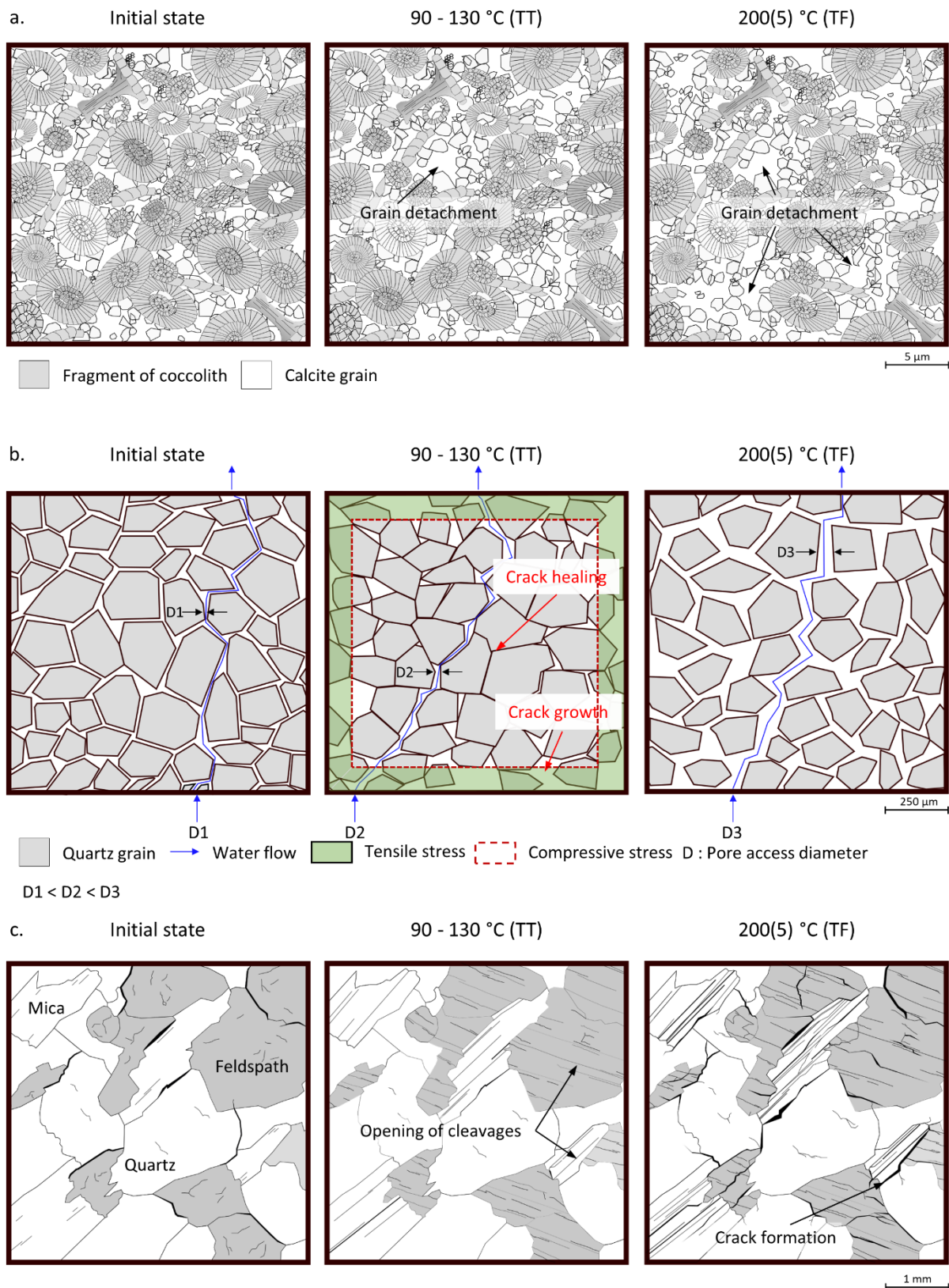


Figure V-9. Diagram of the evolution of the porous 2D network of the Châlons chalk (a), Fontainebleau sandstone (b), and Gris Alba (c) according to the temperature.

### V.1.5.2. Thermal Fatigue Test (TF)

The repetition of heating cycles (TF) showed fewer fluctuations than the TT, although some rocks were very sensitive to this thermal regime (Figure V-10).

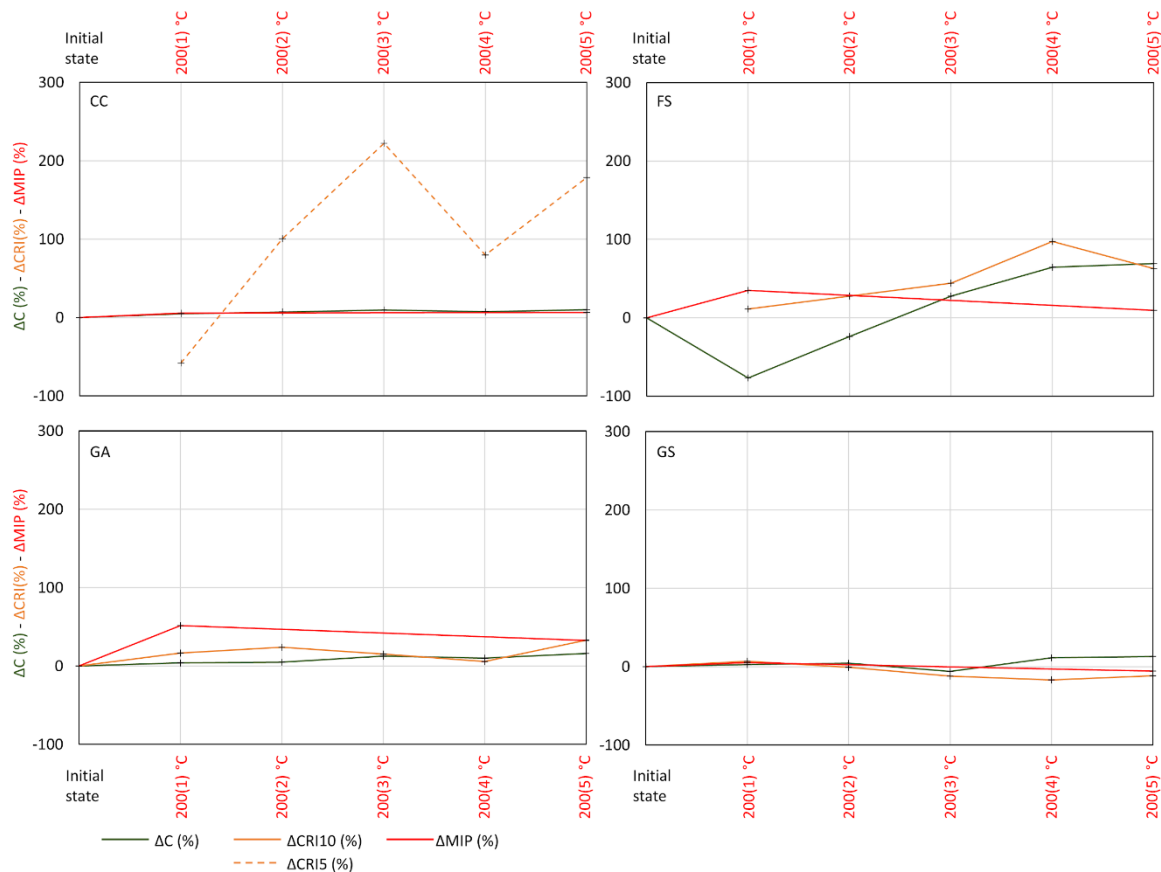
The behaviour of the chalk to the TF test was similar to the TT test, with no variations in its microstructure but a grain crushing and loss of material on the surface, which produced only an increase of the CRI (Figure V-9 and Figure V-10). During a temperature increase on chalk, the calcite observed at SEM is likely to expand freely (Somerton, 1992), however, none of these dilatations or mineralogical modifications have generated significant changes in the bulk microstructure of the chalk (Nadah et al., 2009).

The Fontainebleau sandstone (FS) showed a microstructural redistribution during the first heating at 200 °C, with an increase in porosity measured by MIP, and a decrease of C. Through the thermal fatigue, FS experienced better connectivity of the porosity thanks to the creation of intergranular cracks (Figure V-4) that lead to a higher C. Actually, the porous volume is connected in 3D with a larger intergranular matrix size than in the initial state (Figure V-9b). The big macropores and some grain detachment contributed to the augmentation of cooling velocities through the thermal cycles (Figure V-10).

From the very first heating at 200 °C, the Gris Alba granite (GA) showed a significant modification of its porous network, observed by SEM and quantified by MIP, with a more intense microcracking in feldspar (Freire-Lista et al., 2016) and an increase of the pore radius access greater than 100 µm. The pores with access radii greater than 10 µm constituted preferential flow paths during capillary water uptake. Nevertheless, they were not the largest part of the porous network of GA, which explained the little variation in C (Figure V-10). During the following heating cycles, all the properties as well as the observations did not show great changes, indicating that the first heating produced a great redistribution in the GA microstructure and that it was not affected by thermal fatigue.

Similarly to the TT test, the microstructural parameters of the Golden Ski granite (GS) hardly changed through the TF test, although for lower temperatures and fatigue of 30 cycles, an increase in porosity was reported (Vazquez et al., 2018a). Only the CRI experienced a decrease explained by a mineral expansion that closed the bigger cracks and clay remobilisation that

occluded some of the surface voids (Vazquez et al., 2011). The clays placed on the edge of the pore walls allowed the continuous water circulation (Robert, 2004) that was in agreement with the CRI and capillary results (Figure V-10).



**Figure V-10. Relationship between the capillary coefficient (C), the cooling rate index (CRI), and the MIP porosity for the thermal fatigue test (TF).**

### V.1.5.3. IRT as a tool to detect microstructural changes

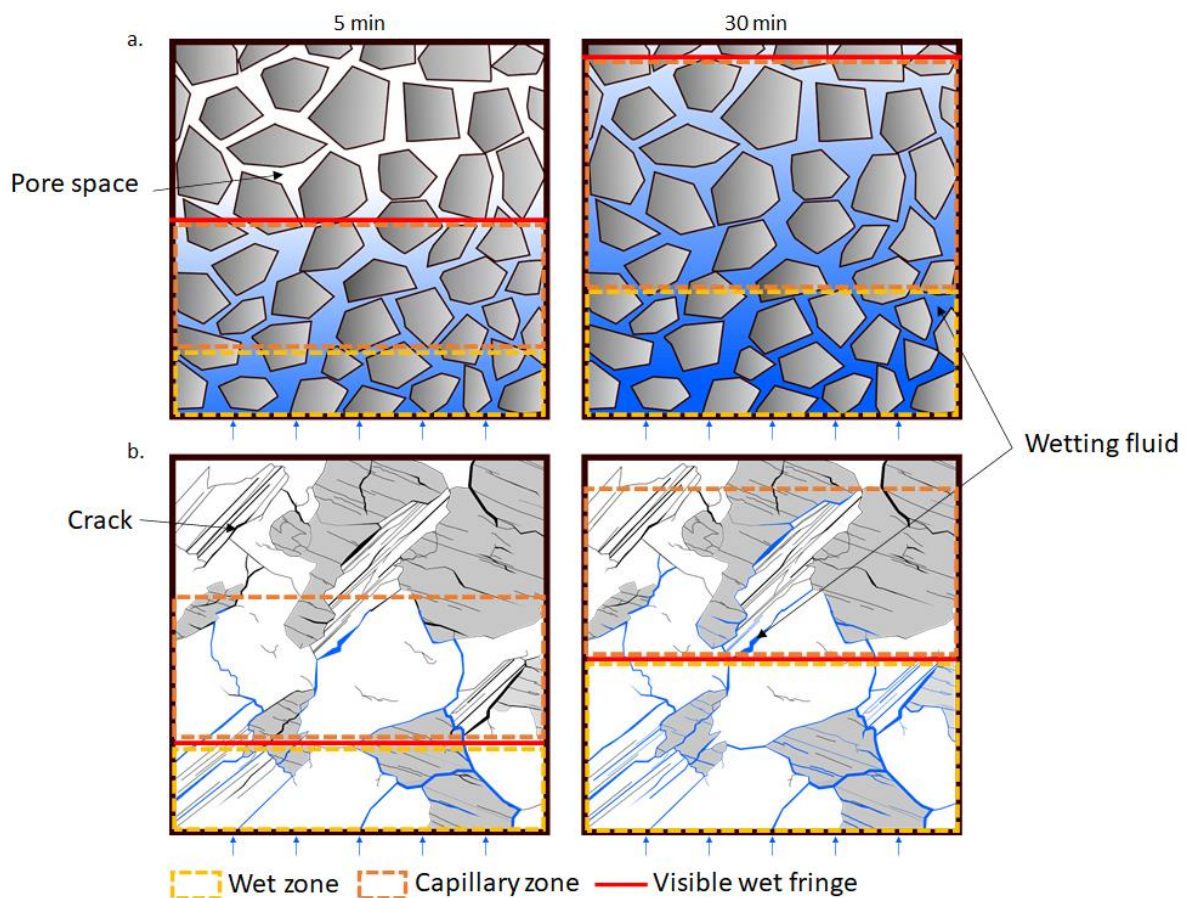
The capillary water uptake can be followed by IRT since the variation of emittance in wet porous materials allows the movement of water to be visualised on stone surfaces (Avdelidis and Moropoulou, 2004; Gayo and de Frutos, 1997). Regarding the fresh stones, the thermographs showed a correlation between porosity and water absorption by capillarity (Forestieri and Buergo, 2018; Ludwig et al., 2018), with a faster rise in the chalk, slower in the sandstone, and the granites with a stabilisation of the wet fringe at the middle of the samples.

The capillary water uptake test, and more precisely the penetration index, determined a bottom wet part, in which the water circulates, and an upper dry zone, separated by its

observable moist surface (wet fringe). The IRT monitoring made it possible to define these two visible zones, with different migration interpretations for porous and fissural rocks. During the first minutes, the water-rock interaction reached a very fast temperature equilibrium at the bottom part of the sample. From that, the void network controlled the wet fringe movement (Figure V-11).

For sedimentary rocks (Figure V-6e, j, o, t), the water contained in the pore system rose and occupied the pore space uniformly so that the wet fringe migrated according to the water filling, delimited by the upper part of the capillary zone (Figure V-11a). A better arrangement and connection of the grains favours the kinetics of internal migration of the fringe and the cooling by water. When the wet fringe reached the top, the sample compensated for the loss of water through evaporation.

Fissural rocks presented a heterogeneous pattern. The profiles in Figure V-7(e, j, o, t) and the visual observation revealed similar evolution for the wet zone and wet fringe. The interconnected cracks of the porous network became saturated from the first minutes. That included the wet zone and the capillary zone. The water saturation continued with the occupation of the transverse cracks, showing a heterogeneous migration of the wet fringe through the first 1.5 cm (Figure V-11b). Monitoring the rise in water by capillary using the IRT detects variations in the microstructure (cooling / variation of the wet fringe) but without quantification.



**Figure V-11. Fluid circulation in porous media. a. Granular rock. b. Polycrystalline rock.**

Infrared thermography also allowed to quantify the cooling rate index for the upper part of the sample, by simple exchange with the environment. This parameter is well correlated to porosity for stones with void volume over 10%, although with approximate values that allow only to divide in groups (10%, 15%, 20%) (Cernuschi, 2015; Mineo and Pappalardo, 2016, 2019). The studied rocks did not follow these statements. For fissural rocks and of special microporosity rock as chalk, the surface roughness and the microcrack connectivity will play a more important role than the porosity itself. The CRI of granite with 1% porosity and sandstone with 5% were similar, while the CRI of high microporous chalk was very low and the CRI of a weathered granite with the same porosity as the sandstone was three times.

The CRI varied during the heating cycles, although not in the same sense that the bulk microporosity. However, the changes on the network observed by SEM explained completely the cooling rate behaviour. That indicated that the CRI was not a probe of the small

development of microcracking within the rock but a good indicator of the damage to the outer layers, from which the temperature changes started.

### **V.1.6. CONCLUSION**

The comparison of four rocks with differences in mineralogy and porous networks submitted to increasing temperature and thermal fatigue tests was achieved using several methods including an innovative approach as infrared thermography.

The influence of temperature on the chalk microstructure was weak. Nevertheless, the instability of the particles and the loss of material increased the surface roughness and consequently the thermal exchange with the environment, translated by a rise in its cooling rates.

The progressive heating produced a compressive strain on the sandstones' core measured and observed as an internal closure of its porosity and tensile stress on the surface that increased the cooling rates. With fast and repetitive heating, this rock created an irreversible crack development measured and observed with all the techniques.

At the end of the thermal threshold tests, the fresh granite showed new intra- and intergranular oriented microcracks and cleavage opening, favouring the interconnection of the network and the fluid flow. Heating up to 200 °C only produced a slight microstructural change compensated by a mineral residual strain. The weathered granite showed fewer variations through the tests due to the clay and mica adaptation to the deformations.

Infrared thermography evidenced the variations produced by thermal stresses. The cooling rate index (CRI) did not correlate the stones to their bulk porosity although it gave information in agreement with the SEM observations about the surface changes.

The evolution of thermograms during water uptake made it possible to interpret two capillary diffusion mechanisms depending on the rock type. The homogeneous and interconnected structure of the granular rocks showed a homogeneous rise of the wet fringe and stone cooling as the pores were filled, that is the visible wet fringe corresponded to the water rise. The heterogeneous fissural media exhibited a complex water filling, in which the visible wet fringe was conditioned by a wet zone close to saturation and not by the height of the water



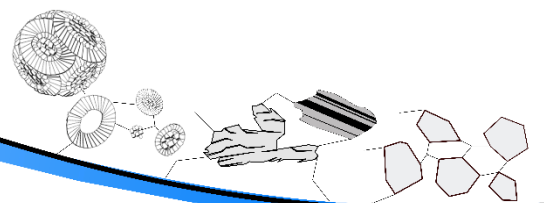
rise. The water uptake was carried out firstly in the connected microcracks, then in a second step, the filling of water continued in the transverse cracks less connected to the entire network. This filling marked the wet fringe evolution.

These preliminary results allow IRT to be considered as a promising technique for rock characterization, although more research is needed on CRI parameter and capillary water uptake for a more accurate interpretation of crack and pore networks.





# DISCUSSION GÉNÉRALE



Le **comportement des roches réservoirs en réponse à des sollicitations thermiques** est l'aspect principal étudié dans ce travail de thèse. Les gammes de température ont été choisies en fonction de différentes applications géologiques comme le stockage et l'entreposage de déchets radioactifs ou l'exploitation de ressources pétrolières ou géothermique. Nos travaux reposent sur une démarche expérimentale et fondamentale, et les résultats apportent de nouvelles idées pour des applications mais aussi pour le développement de nouveaux protocoles expérimentaux ou des axes de recherche pour des questions de stockage ou de gestion des ressources. Dans cette partie les résultats thermiques obtenus vont être appliqués au domaine du stockage de déchets radioactifs. Les tests de circulation d'eau dans la craie seront appliqués à l'activité pétrolière. Les tests de fatigues thermiques à différentes vitesses de refroidissement seront appliqués aux systèmes géothermiques. Enfin les différentes techniques laboratoire utilisé dans la description de l'évolution microstructurale seront discutées.

L'augmentation de la température d'une roche peut induire des phénomènes comme la **fermeture des pores** ou la création de **fissures en fonction de la nature de la roche mais aussi des conditions de sollicitation**. Ainsi différents comportements ont pu être décrits concernant l'évolution des structures du réseau poreux, des propriétés élastiques des roches et des circulations des fluides.

Le Tableau V-5 récapitule les principales conclusions des tests thermiques des **chapitres IV et V**.

### **Effet de l'élévation de la température de 90 à 130 °C appliqué au stockage et l'entreposage de déchets radioactifs :**

Plusieurs paramètres tels que la porosité, la composition minéralogique ou la granulométrie influencent le comportement thermique des roches. Des tests ont été effectués afin de déterminer si un **seuil de fissuration** existe à **basse température**. Avant d'atteindre ce seuil thermique, certaines roches montrent une redistribution des pores, définie par une **ouverture et une fermeture** des pores ou des microfissures préexistantes. L'analyse de la distribution de la taille d'accès aux pores montre que l'ouverture et la fermeture des pores / fissures n'étaient pas homogènes et que certaines familles de pore pouvaient être affectées alors que d'autres ne sont pas concernées.

Tableau V-5. Principales conclusions du comportement thermique des roches étudiées.

Nom de la roche	Chauffage croissant / refroidissement lent					Cycles thermiques à 200 °C		Cycles thermiques à 400 °C
	90 °C	100 °C	110 °C	120 °C	130 °C	Refroidissement lent	Refroidissement rapide	Refroidissement rapide
Granite Gris alba	↓ MP -----> Fermeture ↓ MP, μP					Fissuration au 1 <sup>er</sup> cycle Augmentation progressive lors de la fatigue thermique	Dommages légers Ouverture des clivages Meilleure connexion hydrique	Augmentation du volume des pores Taille des pores inchangée Meilleure connexion hydrique
Granite Silvestre Moreno	↑ MP, μP ★ -----> Succession d'ouvertures et de fermetures					Légère dégradation Réorganisation du réseau poreux	Augmentation de la fissuration non connectée Taille des pores inchangée	Dommages importants Diminution du module élastique Augmentation significative de la taille des pores
Granite Golden Ski	-----> ★ Fermeture ↓ MP, μP					Légère dégradation Réorganisation du réseau poreux	Dommages légers Diminution de la taille des pores	Dommages légers Augmentation de la taille des pores
Granite Albero	↑ MP -----> ★ Fermeture ↓ μP, nP					Faible variation de la microstructure	Dommages légers	Dommages importants Augmentation significative de la taille des pores
Craie de Châlons	-----> Absence de changement					Non réalisé		
Grès de Fontainebleau	↑ MP, μP ★ -----> Fermeture ↓ μP, nP							

Degré d'altération

Augmentation des dommages

★ Seuil de fissuration

MP : Macropore; μP : Micropore; nP : Nanopore

Chapitre 4    Chapitre 5

Les roches granitiques (matériaux peu poreux et peu perméables) sont considérées comme des roches hôtes potentielles pour l'ingénierie du **stockage des déchets nucléaires** (Wengang et al., 2008). L'augmentation de température induite par un stockage a une influence potentiellement négative, car à terme, la stabilité des excavations servant au dépôt sera affectée.

L'augmentation de la température dans une **gamme de 90 à 130 °C** peut être suffisante pour induire une contrainte thermique générant des microfissures.

Le **granite sain comme Gris alba (GA)**, ne montre aucun seuil de fissuration mais une fermeture des fissures pour des températures comprises entre 90 °C et 130 °C. Dans un projet d'ingénierie souterraine et dans cette plage de température les granites à faible porosité préserveraient leurs propriétés mécaniques et seraient les plus à même d'être utilisés. En revanche, lors des expériences, la circulation de l'eau par capillarité a été améliorée. En effet, les limites intergranulaires en s'ouvrant ont contribué à la connexion entre les fissures, l'ouverture des clivages du mica a pu également être observée. Dans le cadre du stockage de déchets radioactifs, cette amélioration de la connectivité hydrique pourrait créer des nouvelles voies d'écoulement des eaux souterraines et de migration des nucléides radioactifs, et par conséquent avoir un effet négatif.

Les **granites initialement altérés** montrent un seuil de fissuration critique pour les températures comprises entre 90 °C et 130 °C. Il a été fixé à 90, 120 et 130 °C pour SM, GS et A, respectivement. En augmentant la température, la pré-fissuration initiale contrôle le seuil de fissuration induit thermiquement. A 90 °C, le granite **Silvestre moreno (SM)**, de plus faible porosité initiale parmi les granites altérés, a montré tout d'abord une augmentation importante de la macro- microporosité. Avec l'augmentation de la température, ce granite a présenté des phases de redistribution du réseau poreux traduite par une succession d'ouvertures et de fermetures sans fissuration majeure supplémentaire. Jusqu'à 110 °C, le granite **Golden ski (GS)**, altéré à grain fin, a montré une fermeture de la macro- microporosité. Le seuil de fissuration s'est produit à 120 °C se matérialisant par une augmentation de sa porosité. A 130 °C, une nouvelle fermeture s'est opérée. Dès 90 °C, le granite **Albero (A)**, initialement le plus altéré, a vu sa macroporosité, et par conséquent sa capillarité, augmenter. La porosimétrie au mercure (MIP) a montré une fermeture progressive de la micro et nanoporosité jusqu'à 120 °C. Une nouvelle microfissuration s'est ensuite produite à 130 °C,

principalement dans la nanoporosité augmentant ainsi la porosité ouverte. Cependant, aucun élargissement de microfissures préexistantes n'a été observé. Contrairement au granite sain, la potentiel mise en place de déchets nucléaires dans des formations granitiques altérées, similaire à cette étude, serait à envisager plus prudemment.

En raison du procédé expérimental, le traitement thermique et la fracturation ont été effectués dans des conditions non confinées. En réalité, la masse rocheuse souterraine est soumise à une **pression de confinement**, ce qui a une influence importante sur la déformation de la roche. Les travaux d'Andersson et al. (2009) sur la paroi du pilier d'une masse rocheuse ou ceux, conduits en laboratoire par Wang et al. (2013), montrent que les effets de la fissuration thermique peuvent être considérablement réduits sous confinement. Ainsi, le seuil de fissure thermique induit dans les granites altérés pourrait alors être plus élevé en profondeur et ces contraintes induites seraient plus faibles jusqu'à 130 °C.

Avec la poursuite du développement des centrales nucléaires dans le monde et l'évolution des techniques de stockage, de nouveaux types des massifs rocheux susceptibles de stocker des déchets, comme les **roches carbonatées** (Tran et al., 2020), sont envisagés. Les résultats obtenus sur la **craie de Châlons** montrent que de très **légers changements** ont été observés lors de sollicitation thermique. Aucune déformation n'a généré un changement significatif dans la microstructure de la craie. Le réajustement des particules lors de la dilatation des grains de calcite a dû permettre d'éviter la formation de microfissures. En termes de comportement thermique, la craie répondrait favorablement au stockage de déchets radioactifs, néanmoins, la faible profondeur de ces formations et la grande circulation par capillarité des fluides pourrait rendre son développement problématique. La migration des radioéléments sur une longue échelle de temps ne serait pas assez retardée.

Les **grès** sont extrêmement sensibles à la chaleur. Les grès de Fontainebleau ont montré que leur perméabilité peut diminuer entre 90 et 130 °C. La dilatation thermique du quartz (Skinner, 1966) s'est avérée être la cause principale de la réduction de la perméabilité. Si un processus similaire se produisait dans un site de stockage de déchets nucléaires par exemple, la migration des radionucléides hors du site pourrait être considérablement réduite. En revanche, le grès n'est pas envisagé dans les formations de stockage pour l'instant.

**Effet de la circulation de d'eau à températures contrastées appliqué à l'activité pétrolière :**



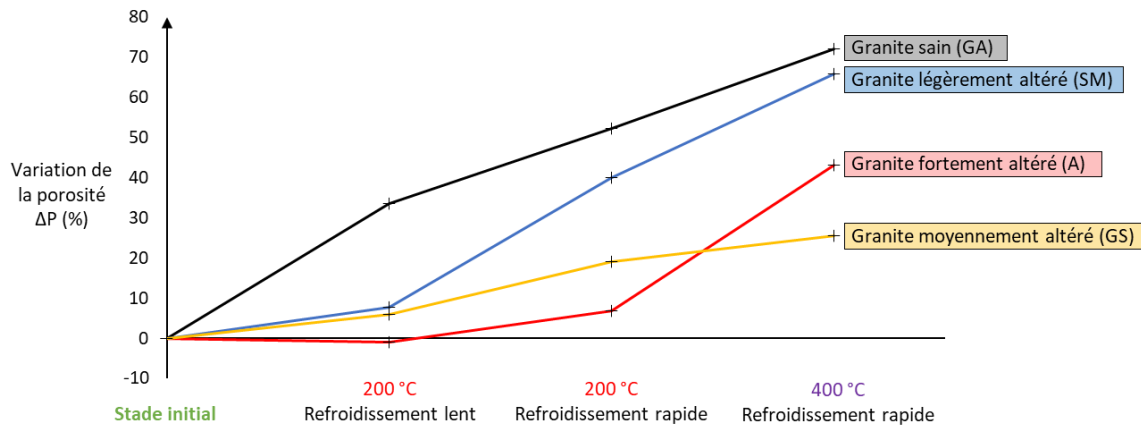
Dans les réservoirs carbonatés tels que **la craie**, l'injection d'eau ou les méthodes thermiques sont souvent utilisées dans la **récupération assistée du pétrole** (EOR). La température contrastée de l'eau et de la formation peut jouer un rôle majeur sur l'affaissement et l'effondrement des cavités souterraines. La réponse de la craie vis à vis d'un fluide injecté ou soumis à une contrainte thermique, comme une réduction de résistance mécanique, peut dépendre de différents mécanismes. En général, ils peuvent être classés en **mécanismes physiques et chimiques**. Dans cette thèse, il apparaît que l'écoulement de l'eau (chaude ou froide) à travers la craie provoque un réarrangement du réseau poreux, qui est observé par la variation des tests d'imbibition capillaire par l'eau. L'impact d'un cycle était faible et il a fallu reproduire la sollicitation pour observer un effet. Les observations faites à l'échelle des grains montrent de petits changements dans le volume, la forme et la taille des pores, impactant faiblement les propriétés élastiques et la perméabilité de la roche. Néanmoins, à long terme ces sollicitations pourraient modifier la rhéologie de la formation.

### **Effet de la fatigue thermique à différentes vitesses de refroidissement appliqué aux systèmes géothermiques améliorés :**

Les processus et les conséquences du refroidissement dans une formation chaude auront des effets différents entre un matériel monominéral, craie ou grès à porosité interparticulaire, et un matériel polyminéral à porosité fissurale comme le granite. Les tests de refroidissement rapide ont été focalisés sur le granite car cette roche est désignée comme étant la plus appropriée dans la mise en œuvre et le développement des projets de **systèmes géothermiques améliorés** (EGS) (Breede et al., 2013). La stimulation d'un réservoir par fracturation hydraulique à partir d'eau à température ambiante est souvent adoptée pour **améliorer la porosité et la perméabilité** de la roche. La température de ces réservoirs est généralement plus élevée que celle des réservoirs carbonatés, > 100 °C. Les EGS sont généralement des systèmes avec des températures d'environ 130-200 °C bien que certaines températures de puits soient supérieures et atteignent les 400 °C (Breede et al., 2013).

Les résultats expérimentaux de la fatigue thermique en laboratoire ont confirmé l'intérêt de la trempe à l'eau. Le **refroidissement** des granites traités dans l'eau est beaucoup plus rapide que dans l'air et provoque des chocs thermiques plus intenses qui se manifestent par une augmentation de la porosité totale (Figure V-12). L'augmentation de la porosité est d'autant plus forte que la température de chauffe est grande et que le refroidissement est rapide. Les

granites **sains à peu altérés** (GA et SM) présentent un plus fort endommagement que les granites **moyennement à fortement altérés**. Sur ces derniers, il a été montré que la **fatigue thermique** provoque un changement supplémentaire dans la microstructure des échantillons.



**Figure V-12. Évolution de la porosité des granites selon les différents traitements thermiques après 1 cycle.**

Lors du **refroidissement lent à 200 °C**, le granite sain (GA) a montré la plus forte augmentation de microfissuration. Les dommages causés par le premier traitement à 200 °C ont confirmé une augmentation de la taille des pores au-delà de 1  $\mu\text{m}$ . Le reste des propriétés liées aux pores ont montré une augmentation de la microfissuration après plusieurs cycles. La porosité élevée et une teneur élevée en mica **des granites altérés** (SM, GS et A) permettent une dilatation ou une contraction minérale sans rupture catastrophique. Ainsi, dans le cas du granite GS, hormis de légères variations au cours des cycles de fatigue, l'état initial et final de ces granites est resté similaire. Dans le granite A, les microfissures générées se sont fermées par réorganisation des grains lors de la dilatation-rétractation minérale associée ou non à la remobilisation des argiles.

Pendant la **phase de stimulation thermique** pour l'exploitation de l'énergie géothermique profonde, les roches chaudes du réservoir seront inévitablement soumises à des **changements cycliques rapides** de température. L'injection **rapide d'un fluide froid** induira le développement de microfissures importantes près du **point d'injection**. En conséquence, la zone impactée autour du puit d'injection pourra s'étendre et augmentera ainsi la circulation hydrique. La perméabilité obtenue dans cette étude était une estimation calculée à partir de données pétrophysiques RMN, utilisée spécifiquement comme comparaison entre les

granites. Les résultats expérimentaux ont montré que l'effet du choc thermique augmentait la **perméabilité de 2 à 6 fois pour les granites à 200 °C**, ce qui améliorerait potentiellement l'efficacité de l'extraction d'énergie géothermique.

En raison des structures différentes des 4 granites, le **seuil limite de contrainte thermique** et la **morphologie de fissuration sont également différents**. Les microfissures peuvent absorber de manière significative les déformations induites par les contraintes thermiques générées par la différence de dilatation des minéraux dès le **premier cycle thermique**. En effet, lorsque le chauffage est effectué à des températures égales ou supérieures à **400 °C**, la majeure partie des microfissures se forment dès les premiers cycles. L'absence de changement postérieur peut être attribuée à l'**effet Kaiser** (Kaiser, 1953) observé dans de nombreux sites EGS pendant les opérations d'injection (Maurer et al., 2020) et qui indique que pour subir des dommages, un matériau doit être soumis à des contraintes supérieures à celles qu'il a déjà connues.

L'espace créé par la **fissuration lors des premiers cycles** donne lieu à une dilatation moins contraintes des minéraux, ce qui permet à certains granites (en particulier GS) de voir leur porosité diminuer, leur  $V_p$  augmenter et leur taille de fissures diminuer. La fatigue thermique ne joue pas ici un rôle en tant que créateur de fissures, mais plutôt en tant que réorganisateur de la structure interne. Transcrite au système géothermique, **l'amélioration de la perméabilité autour des puits géothermiques** serait efficace dès les premiers cycles pour un réservoir à 400 °C, et le renouvellement de la stimulation thermique ne serait pas plus bénéfique.

Le granite le plus altéré initialement (A) a montré les dommages les plus importants lors des refroidissements rapides à 400 °C, estimé à partir du facteur de dommage calculé grâce au module de Young. Certains échantillons ont même cassé au cours des cycles de trempe. Compte tenu de la détérioration des propriétés physiques mesurées, un affaiblissant des propriétés mécaniques peut être envisagé autour du puits d'injection, pouvant aller jusqu'à provoquer une **potentielle instabilité de la paroi rocheuse**. Les mécanismes mis en jeu lors de la stimulation hydraulique modifient localement les contraintes qui peuvent être à l'origine de la micro sismicité pouvant causer des dommages aux populations locales (Cuenot et al., 2008; Shen et al., 2020). La meilleure configuration pour le développement d'un puit géothermique qui ressort de nos résultats, serait l'installation du puit d'injection dans une

formation granitique non altérée, permettant une stimulation thermique efficace, avec des formations granitiques plus altérées avoisinants le puit, évitant de potentielle instabilité.

### Détermination des meilleures techniques dans la description de l'évolution microstructurale :

Dans les **massifs rocheux**, la circulation de l'eau utilise principalement les réseaux de failles et de fractures, pour des déplacements rapides, toutefois le réseau matriciel peut avoir un rôle non négligeable si son volume et sa connectivité sont forts, mais aussi parce qu'il va localiser les processus d'échange chimique eau-roche, et qu'il peut induire des déplacements non négligeables si de grandes périodes de temps sont considérés. Par exemple, il a été montré qu'en quelques cycles un enrichissement en K, Na et Ca dans l'eau avait lieu à la suite de la dissolution du K-feldspath, du plagioclase et de la dégradation du mica et des argiles, lors des cycles de trempes du granite. Dans le cadre de ce travail, c'est ce réseau matriciel qui est considéré.

À l'échelle de la **matrice rocheuse**, cette circulation d'eau est conditionnée fondamentalement par la taille des vides, pores ou microfissures, leur géométrie et leur connectivité, ce qui va contrôler leur perméabilité. Par conséquent, une étude très détaillée du réseau poreux, de ses caractéristiques géométriques et de ses fonctionnalités hydrauliques est nécessaire.

Les principales caractéristiques des matériaux et propriétés liées au mouvement de l'eau à travers la matrice rocheuse de cette étude sont :

- la **porosité**, qui contrôlent la quantité d'eau que peut contenir la matrice rocheuse.
- les **éléments géométriques de cette porosité** : orientation, ouverture, dimensions et connectivité des pores et fissures, tortuosité, taille des accès aux pores et fissures.
- la **cinétique d'absorption capillaire, la migration de la frange capillaire et les paramètres liés à la porosité** : qui indiquent avec quelle facilité l'eau peut se déplacer à travers la matrice rocheuse et à quelle vitesse elle peut y accéder.

La procédure d'identification et de quantification de ces paramètres a regroupé plusieurs techniques dans cette thèse. Les méthodes sont complémentaires, notamment, du fait de leurs résolutions.

Pour la craie, l'auscultation ultrasonique des ondes P ( $V_p$ ), la porosité par injection de mercure (MIP) et la résonance magnétique nucléaire (RMN) forment une bonne combinaison afin d'obtenir suffisamment d'informations sur l'espace poreux. Les mesures MIP doivent, être utilisées en combinaison des mesures RMN et permettent de relier les gammes de rayons d'accès aux pores à celles de la taille des pores, respectivement. Les tests **d'absorption de l'eau par capillarité** ont été un moyen simple et efficace pour suivre l'évolution de la connectivité hydrique de la craie. Les images de **X-ray CT** ont fourni des informations sur les macropores uniquement. Pour envisager une caractérisation complète du réseau de pores avec une résolution nanoscopique les échantillons de craie nécessiteraient être de petite taille et ne seraient plus représentatifs de l'ensemble du réseau poreux.

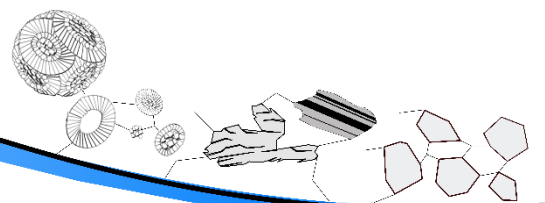
Pour le granite, la mesure des ondes ultrasonores ( $V_p$ ) a été utilisée comme **suivi quotidien**, étant donné son caractère non destructif, afin de détecter un changement majeur dans le réseau poreux. Les propriétés thermiques du granite se sont révélées être étroitement liées et sensibles à leur structure interne, et les vitesses  $V_p$  ont permis de suivre l'évolution de cette structuration tout en réalisant une mesure globale. De plus, **l'atténuation des ondes ultrasoniques** a été un paramètre sensible pour étudier le degré de détérioration du granite non altéré. En effet, si la vitesse  $V_p$  montre de faibles changements une fois que la fissuration majeure a été induite, le coefficient d'atténuation a montré plus de variation ; preuve que d'autres microfissures (probablement plus petites et peu ouvertes) pendant les cycles répétés sont tout de même générées. Un appareillage **automatisé** des **tests d'absorption de l'eau par capillarité** a garanti la précision de la mesure et a réduit les manipulations des échantillons de petite taille et de faible porosité. La forte influence de la présence d'ions paramagnétiques (Fe, Mn...) dans le granite peut perturber le **signal RMN** en raccourcissant les T2, et par conséquent, sous-estimer la taille réelle des pores. La **microtomographie** (X-ray CT) peut être utilisée en complément pour une description géométrique fine de l'espace poreux. Cette méthode offre la véritable distribution de tailles de pores avec une résolution micrométrique qui permet de quantifier efficacement l'évolution de la microfissuration avant et après traitement thermique pour les granites.

L'étude en laboratoire a démontré le potentiel de l'imagerie **thermographie infrarouge** comme nouvel outil non destructif et non invasif de suivi de l'état d'endommagement d'une roche. La thermographie infrarouge a mis en évidence les variations produites par les

contraintes thermiques. L'évolution des thermogrammes lors de la prise d'eau a permis d'interpréter deux mécanismes de diffusion capillaire selon le type de roche. Ce travail spécifique a constitué un des objectifs de cette thèse, à savoir la conception d'un dispositif permettant de suivre indirectement la porosité d'une roche et de visualiser l'écoulement du fluide.



# CONCLUSION GÉNÉRALE





L'objectif de cette thèse était de comparer les comportements thermique et hydrique de roches en développant une démarche expérimentale originale.

Cette étude a déterminé avec précision les caractéristiques du réseau poreux de la craie sélectionnée. Le volume poreux libre de la craie constitue l'essentiel de son volume poreux total. La taille d'accès aux pores est bien plus étroite que la taille réelle des pores. Les voies d'écoulement de l'eau sont nombreuses, bien interconnectées et la présence d'hétérogénéité n'affecte pas son cheminement.

Les effets de la température et de la circulation de l'eau sur la craie ont été étudiés dans deux configurations expérimentales (roche froide-eau chaude / roche chaude-eau froide). Bien que les modifications du volume et de la taille des pores étaient mineures, la microtexture a suffisamment été modifiée pour induire un cheminement différent des fluides à travers la roche. Lors d'une injection d'eau froide dans une roche chaude, la circulation d'eau par capillarité diminue et l'injection d'eau chaude dans une roche froide l'augmente légèrement.

Cette étude s'est concentrée également sur l'effet du cyclage thermique (chauffage lent suivi d'un refroidissement lent ou d'une trempe rapide) sur les propriétés pétrophysiques et hydriques du granite. La minéralogie et le stade d'altération initiale des granites sont les principaux facteurs de variations de leur microstructure et vont contrôler leurs réponses aux différentes sollicitations expérimentales.

Les granites à faible porosité et à faible teneur en quartz ne présentent pas de seuil de microfissuration à basse température (< 130 °C). Les microfissures apparaissent distinctement à des températures comprises entre 90 °C et 130 °C pour les granites à forte porosité et dont le rapport Quartz / Feldspath était proche de 1. Lors de la fatigue thermique à 200 °C, la porosité a un impact plus fort sur le comportement thermique que la minéralogie. Les granites de faible porosité présentent un développement important de la fissuration. Les granites à haute porosité montrent une redistribution des microfissures préexistantes.

L'augmentation de la fissuration lors des traitements de trempe entraîne une réduction des paramètres élastiques et une augmentation de la perméabilité. Dans les trempes à 200 °C, l'expansion et la contraction des minéraux entraînant des dommages plus importants à l'intérieur des grains augmentant la connectivité hydrique des granites à faible porosité. Les granites altérés ont montré une variation de microstructure marquée par la propagation et

l'ouverture des fissures, sans toutefois améliorer la connectivité. Dans les trempes à 400 °C, un seul cycle de choc thermique a provoqué plus de dommages qu'après 35 cycles à 200 °C. L'interaction eau-roche granitique a montré la dissolution du feldspath K, du plagioclase et la dégradation des argiles, conduisant à un enrichissement principalement en K, Na et Ca des fluides.

Des relations générales entre la structure minérale et poreuse des roches (craie, granite et grès) et leurs propriétés de transport de fluides ont été établies. La structure homogène et interconnectée des roches granulaires montre un transfert d'eau par capillarité et une montée de la frange capillaire homogène. Les milieux fissuraux hétérogènes présentent un remplissage d'eau complexe, dans lesquels les microfissures connectées réalisent la prise en eau initiale, puis dans un second temps, la saturation en eau se poursuit avec l'occupation des fissures transversales moins connectées à l'ensemble du réseau et montrant une migration hétérogène de la frange capillaire.

### **Perspectives :**

Suite à ces analyses, plusieurs perspectives émergent :

Les recherches futures devraient viser à caractériser le comportement couplé thermo-hydro-mécanique des différentes roches in-situ et sous confinement afin de s'approcher au plus près des conditions réelles des roches en profondeur.

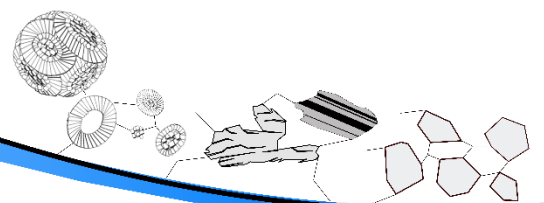
Il serait également intéressant de mesurer la perméabilité réelle mais aussi la perméabilité directement sous températures élevées.

Il est nécessaire de développer l'utilisation de la thermographie infrarouge comme outil de laboratoire utilisable dans la caractérisation non-destructive des transferts dans les roches à faible porosité. Une étude de cohérence de la répétabilité et l'établissement de valeurs clés est nécessaire pour mieux comprendre la fiabilité de cette technique et améliorer l'interprétation des données.

Enfin, à partir de données expérimentales récoltées dans cette étude, la modélisation numérique de la déformation des roches sous températures élevées et des propriétés de transfert associées permettrait d'étendre les conditions de traitement et d'approfondir la compréhension des phénomènes thermiques et hydriques.



# BIBLIOGRAPHIE



- Addis, M.A., **1989**. The Behaviour And Modelling of Weak Rocks. Presented at the ISRM International Symposium, International Society for Rock Mechanics and Rock Engineering, A.A. Balkema, Rotterdam, pp. 899–914.
- Addis, M.A., **1987**. Mechanisms of sediment compaction responsible for oil field subsidence (Thèse de doctorat). University of London, 580.
- Agar, J.G., Morgenstern, N.R., Scott, J.D., **1987**. Shear strength and stress-strain behaviour of Athabasca oil sand at elevated temperatures and pressures. *Can. Geotech. J.*; (Canada) 24:1. <https://doi.org/10.1139/t87-001>
- Alam, M.M., Fabricius, I.L., Prasad, M., **2011**. Permeability prediction in chalks. *AAPG Bulletin* 95, 1991–2014. <https://doi.org/10.1306/03011110172>
- Albissin, M.C., Sirieys, P., **1989**. Thermal Deformability of Rocks: Relation to Rock Structure. Presented at the ISRM International Symposium, International Society for Rock Mechanics and Rock Engineering.
- Allouc, J., Le Roux, J., **1995**. Mourmelon-le-Grand (133), Cartes géol. France (1/50000).
- Alm, O., Jaktlund, L.-L., Shaoquan, K., **1985**. The influence of microcrack density on the elastic and fracture mechanical properties of Stripa granite. *Physics of the Earth and Planetary Interiors, Special Issue Experiments in Solid State Physics Relevant to Lithospheric Dynamics* 40, 161–179. [https://doi.org/10.1016/0031-9201\(85\)90127-X](https://doi.org/10.1016/0031-9201(85)90127-X)
- Al-Naddaf, M., **2018**. A new automatic method for continuous measurement of the capillary water absorption of building materials. *Construction and Building Materials* 160, 639–643. <https://doi.org/10.1016/j.conbuildmat.2017.11.110>
- Alt-Epping, P., Diamond, L.W., Häring, M.O., Ladner, F., Meier, D.B., **2013**. Prediction of water–rock interaction and porosity evolution in a granitoid-hosted enhanced geothermal system, using constraints from the 5km Basel-1 well. *Applied Geochemistry* 38, 121–133. <https://doi.org/10.1016/j.apgeochem.2013.09.006>
- Anand, V., Hirasaki, G.J., **2007**. Diffusional Coupling Between Micro And Macroporosity For NMR Relaxation In Sandstones And Grainstones. *Petrophysics* 48, 289–307.
- Andersen, M.A., **1995**. Petroleum Research in North Sea Chalk. RF-Rogaland Research.
- Andersen, M.A., **1992**. The link between waterflood-induced compaction and rate-sensitive behaviour in a weak North Sea chalk, Deauville, France. 4th North Sea Chalk Symposium.
- Anderson, W.G., **1987**. Wettability Literature Survey Part 5: The Effects of Wettability on Relative Permeability. *J Pet Technol* 39, 1453–1468. <https://doi.org/10.2118/16323-PA>
- Andersson, J.C., Martin, C.D., Stille, H., **2009**. The Äspö Pillar Stability Experiment: Part II—Rock mass response to coupled excavation-induced and thermal-induced stresses. *International Journal of Rock Mechanics and Mining Sciences* 46, 879–895. <https://doi.org/10.1016/j.ijrmms.2009.03.002>
- Andreassen, K., **2011**. Temperature Influence on Rock Mechanical Properties: High-Porosity, Low-Cemented Chalk Technical University of Denmark, 147.
- Andreassen, K., Fabricius, I., **2010**. Biot critical frequency applied to description of failure and yield of highly porous chalk with different pore fluids. *Geophysics* 75. <https://doi.org/10.1190/1.3504188>
- Argandoña, V.G.R.D., Calleja, L., Montoto, M., **1985**. Determinación experimental del umbral de microfisuración térmica de la roca matriz o intact rock. *Trabajos de Geología* 15, 299–307. <https://doi.org/10.17811/tdg.15.1985.299-307>
- Avdelidis, N.P., Moropoulou, A., **2004**. Applications of infrared thermography for the investigation of historic structures. *Journal of Cultural Heritage* 5, 119–127. <https://doi.org/10.1016/j.culher.2003.07.002>

- Baechle, G.T., Colpaert, A., Eberli, G.P., Weger, R.J., **2008**. Effects of microporosity on sonic velocity in carbonate rocks. *The Leading Edge* 27, 1012–1018. <https://doi.org/10.1190/1.2967554>
- Bai, B., He, Y., Li, X., **2018**. Numerical study on the heat transfer characteristics between supercritical carbon dioxide and granite fracture wall. *Geothermics* 75, 40–47. <https://doi.org/10.1016/j.geothermics.2018.03.002>
- Baldeyrou, A., Surma, F., Fritz, B., **2004**. Geophysical and mineralogical impacts of fluid injection in a geothermal system: the Hot Fractured Rock site at Soultz-sous-Forêts, France. *Geological Society, London, Special Publications* 236, 355–367. <https://doi.org/10.1144/GSL.SP.2004.236.01.20>
- Baldeyrou, A., Vidal, O., Fritz, B., **2003**. Étude expérimentale des transformations de phase dans un gradient thermique : application au granite de Soultz-sous-Forêts, France. *Comptes Rendus Geoscience* 335, 371–380. [https://doi.org/10.1016/S1631-0713\(03\)00056-7](https://doi.org/10.1016/S1631-0713(03)00056-7)
- Ballif, J.-F., Guérin, H., Muller, J.-C., **1995**. *Éléments d'agronomie champenoise: connaissance des sols et de leur fonctionnement: rendzines sur craie et sols associés: esquisse géomorphopédologique*. Institut national de la recherche agronomique, Paris, 101.
- Barton, N., **2007**. Thermal over-closure of joints and rock masses and implications for HLW repositories. *Proc. of 11th ISRM Congress* 109–116.
- Beck, K., Al-Mukhtar, M., Rozenbaum, O., Rautureau, M., **2003**. Characterization, water transfer properties and deterioration in tuffeau: building material in the Loire valley—France. *Building and Environment, Building Stone Decay: Observations, Experiments and Modeling* 38, 1151–1162. [https://doi.org/10.1016/S0360-1323\(03\)00074-X](https://doi.org/10.1016/S0360-1323(03)00074-X)
- Bell, F.G., **1977**. A note on the physical properties of the chalk. *Engineering Geology* 11, 217–225. [https://doi.org/10.1016/0013-7952\(77\)90003-5](https://doi.org/10.1016/0013-7952(77)90003-5)
- Bell, F.G., **2000**. *Engineering properties of soils and rocks, fourth edition*. Blackwell Science, 475.
- Benavente, D., Galiana-Merino, J.J., Pla, C., Martínez-Martínez, J., Crespo-Jimenez, D., **2020**. Automatic detection and characterisation of the first P- and S-wave pulse in rocks using ultrasonic transmission method. *Engineering Geology* 266, 105474. <https://doi.org/10.1016/j.enggeo.2020.105474>
- Benavente, D., García del Cura, M.A., Fort, R., Ordóñez, S., **2004**. Durability estimation of porous building stones from pore structure and strength. *Engineering Geology* 74, 113–127. <https://doi.org/10.1016/j.enggeo.2004.03.005>
- Benavente, D., Lock, P., Ángeles García Del Cura, M., Ordóñez, S., **2002**. Predicting the Capillary Imbibition of Porous Rocks from Microstructure. *Transport in Porous Media* 49, 59–76. <https://doi.org/10.1023/A:1016047122877>
- Benavente, D., Martínez-Martínez, J., Jáuregui, P., Rodríguez, M.A., del Cura, M.A.G., **2006**. Assessment of the strength of building rocks using signal processing procedures. *Construction and Building Materials* 20, 562–568. <https://doi.org/10.1016/j.conbuildmat.2005.01.043>
- Benavente, D., Pla, C., Cueto, N., Galvañ, S., Martínez-Martínez, J., García-del-Cura, M.A., Ordóñez, S., **2016**. Response to ENGE07253 Discussion of: “Predicting water permeability in sedimentary rocks from capillary imbibition and pore structure” by D. Benavente et al., *Engineering Geology* (2015) [doi: 10.1016/j.enggeo.2015.06.003]. *Engineering Geology* 204, 123–125. <https://doi.org/10.1016/j.enggeo.2016.01.017>
- Benavente, D., Pla, C., Cueto, N., Galvañ, S., Martínez-Martínez, J., García-del-Cura, M.A., Ordóñez, S., **2015**. Predicting water permeability in sedimentary rocks from capillary imbibition and pore structure. *Engineering Geology* 195, 301–311. <https://doi.org/10.1016/j.enggeo.2015.06.003>
- Bera, B., Mitra, S.K., Vick, D., **2011**. Understanding the micro structure of Berea Sandstone by the simultaneous use of micro-computed tomography (micro-CT) and focused ion beam-scanning

- electron microscopy (FIB-SEM). *Micron* 42, 412–418. <https://doi.org/10.1016/j.micron.2010.12.002>
- Bérard, T., Cornet, F.H., **2003**. Evidence of thermally induced borehole elongation: a case study at Soultz, France. *International Journal of Rock Mechanics and Mining Sciences, Special Issue of the IJRMMS: Rock Stress Estimation ISRM Suggested Methods and Associated Supporting Papers* 40, 1121–1140. [https://doi.org/10.1016/S1365-1609\(03\)00118-7](https://doi.org/10.1016/S1365-1609(03)00118-7)
- Berckmans, A., Vandenberghe, N., **1998**. Use and potential of geothermal energy in Belgium. *Geothermics* 27, 235–242. [https://doi.org/10.1016/S0375-6505\(97\)10010-4](https://doi.org/10.1016/S0375-6505(97)10010-4)
- Berest, P., Bergues, J., Homand-Etienne, F., Troalien, J.P., Henry, J.P., Ikogou, S., **1989**. Comportement thermique et mécanique du grès de Fontainebleau. actes du colloque “bilan et perspectives du greco geomateriaux” 25-26 octobre 1989 - paris.
- Berest, P., Vouille, G., **1988**. Notions de base de la thermomécanique : La Thermomécanique des Roches. *Manuels et Méthodes, Brgm.* 328.
- Betson, M., Barker, J., Barnes, P., Atkinson, T., Jupe, A., **2004**. Porosity Imaging in Porous Media Using Synchrotron Tomographic Techniques. *Transport in Porous Media* 57, 203–214. <https://doi.org/10.1023/B:TIPM.0000038264.33451.4a>
- Blanton, T.L., **1981**. Deformation of Chalk Under Confining Pressure and Pore Pressure. *Society of Petroleum Engineers Journal* 21, 43–50. <https://doi.org/10.2118/8076-PA>
- Borrelli, L., Gullà, G., **2017**. Tectonic constraints on a deep-seated rock slide in weathered crystalline rocks. *Geomorphology* 290, 288–316. <https://doi.org/10.1016/j.geomorph.2017.04.025>
- Bossennec, C., Géraud, Y., Moretti, I., Mattioni, L., Stemmelen, D., **2018**. Pore network properties of sandstones in a fault damage zone. *Journal of Structural Geology* 110, 24–44. <https://doi.org/10.1016/j.jsg.2018.02.003>
- Bounenni, A., **2002**. Etude expérimentale de l'effet de l'endommagement sur la perméabilité des roches (Thèse de doctorat). Ecole des Ponts ParisTech, 220.
- Bourbie, T., Zinszner, B., 1985. Hydraulic and acoustic properties as a function of porosity in Fontainebleau Sandstone. *Journal of Geophysical Research: Solid Earth* 90, 11524–11532. <https://doi.org/10.1029/JB090iB13p11524>
- Bousquié, P., **1979**. Texture et porosité de roches calcaires relations avec perméabilité, ascension capillaire, gélimité, conductivité thermique (Thèse de Troisième Cycle). Université Pierre et Marie Curie (Paris), 191.
- Breede, K., Dzebisashvili, K., Liu, X., Falcone, G., **2013**. A systematic review of enhanced (or engineered) geothermal systems: past, present and future. *Geothermal Energy* 1, 4. <https://doi.org/10.1186/2195-9706-1-4>
- Brehme, M., Blöcher, G., Cacace, M., Kamah, Y., Sauter, M., Zimmermann, G., **2016**. Permeability distribution in the Lahendong geothermal field: A blind fault captured by thermal–hydraulic simulation. *Environmental Earth Sciences* 75, 1088. <https://doi.org/10.1007/s12665-016-5878-9>
- Brigaud, B., Vincent, B., Durllet, C., Deconinck, J.-F., Jobard, E., Pickard, N., Yven, B., Landrein, P., **2014**. Characterization and origin of permeability–porosity heterogeneity in shallow-marine carbonates: From core scale to 3D reservoir dimension (Middle Jurassic, Paris Basin, France). *Marine and Petroleum Geology* 57, 631–651. <https://doi.org/10.1016/j.marpetgeo.2014.07.004>
- Brignoli, M., Santarelli, F.J., Righetti, C., **1994**. Capillary phenomena in an impure chalk. Presented at the Rock Mechanics in Petroleum Engineering, Society of Petroleum Engineers, 837. <https://doi.org/10.2118/28135-MS>
- Buitrago, A., Alejandro, J., **2015**. Efecto de la temperatura en las propiedades mecánicas y petrofísicas de formaciones de crudo pesado. Escuela de Procesos y Energía.

- Burchette, T.P., **2012**. Carbonate rocks and petroleum reservoirs: a geological perspective from the industry. Geological Society, London, Special Publications 370, 17–37. <https://doi.org/10.1144/SP370.14>
- Cai, C., Li, G., Huang, Z., Shen, Z., Tian, S., Wei, J., **2014**. Experimental study of the effect of liquid nitrogen cooling on rock pore structure. *Journal of Natural Gas Science and Engineering* 21, 507–517. <https://doi.org/10.1016/j.jngse.2014.08.026>
- Cai, J., Yu, B., **2011**. A Discussion of the Effect of Tortuosity on the Capillary Imbibition in Porous Media. *Transport in Porous Media* 89, 251–263. <https://doi.org/10.1007/s11242-011-9767-0>
- Catalli, F., Rinaldi, A.P., Gischig, V., Nespoli, M., Wiemer, S., **2016**. The importance of earthquake interactions for injection-induced seismicity: Retrospective modeling of the Basel Enhanced Geothermal System. *Geophysical Research Letters* 43, 4992–4999. <https://doi.org/10.1002/2016GL068932>
- Çelik, M.Y., Kaçmaz, A.U., **2016**. The investigation of static and dynamic capillary by water absorption in porous building stones under normal and salty water conditions. *Environmental Earth Sciences* 75, 307. <https://doi.org/10.1007/s12665-015-5132-x>
- Cernuschi, F., **2015**. Can TBC porosity be estimated by non-destructive infrared techniques? A theoretical and experimental analysis. *Surface and Coatings Technology* 272, 387–394. <https://doi.org/10.1016/j.surfcoat.2015.03.036>
- Chabart, M., Pinson, S., Bernon, N., **2012**. Atlas du potentiel très basse énergie des aquifères de la région Champagne-Ardenne (Rapport final No. BRGM:RP-60024-FR), 120.
- Chaki, S., Takarli, M., Agbodjan, W.P., **2008**. Influence of thermal damage on physical properties of a granite rock: Porosity, permeability and ultrasonic wave evolutions. *Construction and Building Materials* 22, 1456–1461. <https://doi.org/10.1016/j.conbuildmat.2007.04.002>
- Chang, D., Vinegar, H.J., Morriss, C., Straley, C., **1994**. Effective Porosity, Producing Fluid And Permeability In Carbonates From Nmr Logging. Presented at the SPWLA 35th Annual Logging Symposium, OnePetro.
- Charlez, P., Heugas, O., Shao, J.F., **1992**. Effect of temperature on mechanical properties of chalk. Joint Chalk Research Program, Deauville, France.
- Chen, G., Wang, J., Li, J., Li, T., Zhang, H., **2018**. Influence of Temperature on Crack Initiation and Propagation in Granite. *International Journal of Geomechanics* 18, 04018094. [https://doi.org/10.1061/\(ASCE\)GM.1943-5622.0001182](https://doi.org/10.1061/(ASCE)GM.1943-5622.0001182)
- Chen, S., Yang, C., Wang, G., **2017**. Evolution of thermal damage and permeability of Beishan granite. *Applied Thermal Engineering* 110, 1533–1542. <https://doi.org/10.1016/j.applthermaleng.2016.09.075>
- Chen, Y., Wu, X., Zhang, F., **1999**. Experiments on thermal fracture in rocks. *Chinese Science Bulletin* 44, 1610–1612. <https://doi.org/10.1007/BF02886103>
- Chen, Y.-L., Wang, S.-R., Ni, J., Azzam, R., Fernández-steeger, T.M., **2017**. An experimental study of the mechanical properties of granite after high temperature exposure based on mineral characteristics. *Engineering Geology* 220, 234–242. <https://doi.org/10.1016/j.enggeo.2017.02.010>
- Chicco, J.M., Vacha, D., Mandrone, G., **2019**. Thermo-Physical and Geo-Mechanical Characterization of Faulted Carbonate Rock Masses (Valdieri, Italy). *Remote Sensing* 11, 179. <https://doi.org/10.3390/rs11020179>
- Chrysochoos, A., Chezeaux, J.-C., Caumon, H., **1989**. Analyse thermomécanique des lois de comportement par thermographie infrarouge. *Revue de Physique Appliquée* 24, 215–225. <https://doi.org/10.1051/rphysap:01989002402021500>



- Coulon, M., Lamotte, D.F. de, **1988**. Les craies éclatées du secteur d'Omey (Marne, France) ; le résultat d'une brechification par fracturation hydraulique en contexte extensif. *Bulletin de la Société Géologique de France IV*, 177–185. <https://doi.org/10.2113/gssgfbull.IV.1.177>
- Cuenot, N., Dorbath, C., Dorbath, L., **2008**. Analysis of the Microseismicity Induced by Fluid Injections at the EGS Site of Soultz-sous-Forêts (Alsace, France): Implications for the Characterization of the Geothermal Reservoir Properties. *Pure and Applied Geophysics* 165, 797–828. <https://doi.org/10.1007/s00024-008-0335-7>
- Darot, M., Gueguen, Y., Baratin, M.-L., **1992**. Permeability of thermally cracked granite. *Geophysical Research Letters* 19, 869–872. <https://doi.org/10.1029/92GL00579>
- DaSilva, F., Sarda, J.P., Schroeder, C., **1985**. Mechanical behavior of chalks, Second North Sea Chalk Symposium, Book II, Stavanger. Norway, 88.
- Datcu, S., Ibos, L., Candau, Y., Matteï, S., **2005**. Improvement of building wall surface temperature measurements by infrared thermography. *Infrared Physics & Technology* 46, 451–467. <https://doi.org/10.1016/j.infrared.2005.01.001>
- David, C., Menéndez, B., Darot, M., **1999**. Influence of stress-induced and thermal cracking on physical properties and microstructure of La Peyratte granite. *International Journal of Rock Mechanics and Mining Sciences* 36, 433–448. [https://doi.org/10.1016/S0148-9062\(99\)00010-8](https://doi.org/10.1016/S0148-9062(99)00010-8)
- De Kock, T., Boone, M.A., De Schryver, T., Van Stappen, J., Derluyn, H., Masschaele, B., De Schutter, G., Cnudde, V., **2015**. A Pore-Scale Study of Fracture Dynamics in Rock Using X-ray Micro-CT Under Ambient Freeze–Thaw Cycling. *Environmental Science & Technology* 49, 2867–2874. <https://doi.org/10.1021/es505738d>
- De Simone, S., Vilarrasa, V., Carrera, J., Alcolea, A., Meier, P., **2013**. Thermal coupling may control mechanical stability of geothermal reservoirs during cold water injection. *Physics and Chemistry of the Earth* 64, 117–126. <https://doi.org/10.1016/j.pce.2013.01.001>
- Delage, P., Schroeder, C., Cui, Y.-J., **1996**. Subsidence and capillary effects in chalks, in: ISRM International Symposium. Balkema, Torino, Italy, pp. 1291–1298.
- Dessandier, D., Antonelli, F., Rasplus, L., **1997**. Relations entre mineralogie et milieu poreux de la craie tuffeau (bassin de Paris, France). *Bulletin de la Société Géologique de France* 168, 741–749.
- Ding, Q.-L., Ju, F., Mao, X.-B., Ma, D., Yu, B.-Y., Song, S.-B., **2016**. Experimental Investigation of the Mechanical Behavior in Unloading Conditions of Sandstone After High-Temperature Treatment. *Rock Mechanics and Rock Engineering* 49, 2641–2653. <https://doi.org/10.1007/s00603-016-0944-x>
- Dong, Z., Sun, Q., Zhang, W., Xu, C., **2020**. Thermal damage of granite after thermal shock cycle. *Géotechnique Letters* 10, 168–173. <https://doi.org/10.1680/jgele.19.00062>
- Dormieux, L., Molinari, A., Kondo, D., **2002**. Micromechanical approach to the behavior of poroelastic materials. *Journal of the Mechanics and Physics of Solids* 50, 2203–2231. [https://doi.org/10.1016/S0022-5096\(02\)00008-X](https://doi.org/10.1016/S0022-5096(02)00008-X)
- Drüppel, K., Stober, I., Grimmer, J.C., Mertz-Kraus, R., **2020**. Experimental alteration of granitic rocks: Implications for the evolution of geothermal brines in the Upper Rhine Graben, Germany. *Geothermics* 88, 101903. <https://doi.org/10.1016/j.geothermics.2020.101903>
- Dunn, K., LaTorraca, G.A., Bergman, D.J., **1999**. Permeability relation with other petrophysical parameters for periodic porous media. *Geophysics* 64, 470–478. <https://doi.org/10.1190/1.1444552>
- Dunn, K., Bergman, D.J., LaTorraca, G.A., **2002**. Nuclear Magnetic Resonance: Petrophysical and Logging Applications. Elsevier, 312.
- Duperret, A., Taibi, S., Mortimore, R.N., Daigneault, M., **2005**. Effect of groundwater and sea weathering cycles on the strength of chalk rock from unstable coastal cliffs of NW France. *Engineering Geology* 78, 321–343. <https://doi.org/10.1016/j.enggeo.2005.01.004>

- Duric, N., **2013**. Geothermal potentiality of the North-East part of Republika Srpska - Bosnia and Herzegovina. Presented at the 13th SGEM GeoConference on science and technologies in geology, exploration and mining, pp. 171–178. <https://doi.org/10.5593/SGEM2013/BA1.V2/S02.023>
- Dvorkin, J., Alabbad, A., **2019**. Velocity–porosity–mineralogy trends in chalk and consolidated carbonate rocks. *Geophysical Journal International* 219, 662–671. <https://doi.org/10.1093/gji/ggz304>
- Dwivedi, R.D., Goel, R.K., Prasad, V.V.R., Sinha, A., **2008**. Thermo-mechanical properties of Indian and other granites. *International Journal of Rock Mechanics and Mining Sciences* 45, 303–315. <https://doi.org/10.1016/j.ijrmms.2007.05.008>
- Eberli, G.P., Baechle, G.T., Anselmetti, F.S., Incze, M.L., **2003**. Factors controlling elastic properties in carbonate sediments and rocks. *The Leading Edge* 22, 654–660. <https://doi.org/10.1190/1.1599691>
- Engstrøm, F., **1992**. Rock mechanical properties of Danish North Sea chalk, in: *Fourth North Sea Chalk Symposium*, Deauville, 62.
- Fabricius, I.L., **2003**. How burial diagenesis of chalk sediments controls sonic velocity and porosity. *AAPG Bulletin* 87, 1755–1778. <https://doi.org/10.1306/06230301113>
- Fabricius, I.L., Borre, M.K., **2007**. Stylolites, porosity, depositional texture, and silicates in chalk facies sediments. *Ontong Java Plateau – Gorm and Tyra fields, North Sea. Sedimentology* 54, 183–205. <https://doi.org/10.1111/j.1365-3091.2006.00828.x>
- Fan, L.F., Gao, J., Du, X., Wu, Z., **2020**. Spatial gradient distributions of thermal shock-induced damage to granite. *Journal of Rock Mechanics and Geotechnical Engineering* 12, 917–926. <https://doi.org/10.1016/j.jrmge.2020.05.004>
- Fan, L.F., Gao, J.W., Wu, Z.J., Yang, S.Q., Ma, G.W., **2018**. An investigation of thermal effects on micro-properties of granite by X-ray CT technique. *Applied Thermal Engineering* 140, 505–519. <https://doi.org/10.1016/j.applthermaleng.2018.05.074>
- Fan, L.F., Wu, Z.J., Wan, Z., Gao, J.W., **2017**. Experimental investigation of thermal effects on dynamic behavior of granite. *Applied Thermal Engineering* 125, 94–103. <https://doi.org/10.1016/j.applthermaleng.2017.07.007>
- Farias, P., Gallastegui, G., González Lodeiro, F., Marquínez, J., Martín Parra, L.M., Martínez Catalán, J.R., Pablo Maciá, J. de, Rodríguez Fernández, L.R., **1987**. Aportaciones al conocimiento de la litoestratigrafía y estructura de Galicia Central. *Memórias da Faculdade de Ciências, Universidade do Porto* 1, 411–431.
- Faÿ-Gomord, O., Soete, J., Davy, C.A., Janssens, N., Troadec, D., Cazaux, F., Caline, B., Swennen, R., **2017**. Tight chalk: Characterization of the 3D pore network by FIB-SEM, towards the understanding of fluid transport. *Journal of Petroleum Science and Engineering* 156, 67–74. <https://doi.org/10.1016/j.petrol.2017.05.005>
- Faÿ-Gomord, O., Soete, J., Katika, K., Galaup, S., Caline, B., Descamps, F., Lasseur, E., Fabricius, I.L., Saïag, J., Swennen, R., Vandycke, S., **2016**. New insight into the microtexture of chalks from NMR analysis. *Marine and Petroleum Geology* 75, 252–271. <https://doi.org/10.1016/j.marpetgeo.2016.04.019>
- Fellner, M., Supancic, P., **2002**. Thermal Shock Failure of Brittle Materials. *Key Engineering Materials* 223, 97–106. <https://doi.org/10.4028/www.scientific.net/KEM.223.97>
- Feng, G., Wang, X., Wang, M., Kang, Y., **2020**. Experimental investigation of thermal cycling effect on fracture characteristics of granite in a geothermal-energy reservoir. *Engineering Fracture Mechanics* 235, 107180. <https://doi.org/10.1016/j.engfracmech.2020.107180>

- Feng, Z., Zhao, Y., Zhang, Y., Wan, Z., **2018**. Real-time permeability evolution of thermally cracked granite at triaxial stresses. *Applied Thermal Engineering* 133, 194–200. <https://doi.org/10.1016/j.applthermaleng.2018.01.037>
- Fleury, M., **1998**. Caractérisation de structures poreuses par relaxométrie RMN. *Revue de l'Institut Français du Pétrole* 53, 489–493. <https://doi.org/10.2516/ogst:1998041>
- Flores, M., Davies, D.R., Couples, G.D., Palsson, B., **2005**. Stimulation of geothermal wells, can we afford it? Presented at the World Geothermal Congress 2005, p. 8.
- Folk, R.L., **1974**. Petrology of sedimentary rocks. Hemphill Publishing Company.
- Forestieri, G., Buergo, M.Á. de, **2018**. Infrared Thermography technique (IRT) for the evaluation of the hydric behavior of building stones. *Acta IMEKO* 7, 20–23. [https://doi.org/10.21014/acta\\_imeko.v7i3.559](https://doi.org/10.21014/acta_imeko.v7i3.559)
- Foucault, A., Raoult, J.-F., **2010**. Dictionnaire de Géologie - 7e édition. Dunod.
- Fredrich, J.T., Wong, T., **1986**. Micromechanics of thermally induced cracking in three crustal rocks. *Journal of Geophysical Research: Solid Earth* 91, 12743–12764. <https://doi.org/10.1029/JB091iB12p12743>
- Freire-Lista, D.M., Fort, R., Varas-Muriel, M.J., **2016**. Thermal stress-induced microcracking in building granite. *Engineering Geology* 206, 83–93. <https://doi.org/10.1016/j.enggeo.2016.03.005>
- Fronteau, G., **2000**. Comportements tégénétiques des principaux calcaires de Champagne-Ardenne : en relation avec leur facies de dépôt et leur séquençage diagénétique (Thèse de doctorat). Reims, 296.
- Fronteau, G., Moreau, C., Thomachot-Schneider, C., Barbin, V., **2010**. Variability of some Lutetian building stones from the Paris Basin, from characterisation to conservation. *Engineering Geology, Natural stones for historical monuments, testing, durability and provenance* 115, 158–166. <https://doi.org/10.1016/j.enggeo.2009.08.001>
- Frykman, P., **2001**. Spatial variability in petrophysical properties in Upper Maastrichtian chalk outcrops at Stevns Klint, Denmark. *Marine and Petroleum Geology* 18, 1041–1062. [https://doi.org/10.1016/S0264-8172\(01\)00043-5](https://doi.org/10.1016/S0264-8172(01)00043-5)
- Gao, Z., Hu, Q.-H., **2012**. Using spontaneous water imbibition to measure the effective permeability of building materials. *Special Topics & Reviews in Porous Media - An International Journal* 3, 209–213. <https://doi.org/10.1615/SpecialTopicsRevPorousMedia.v3.i3.20>
- Garcia, J., Walters, M., Beall, J., Hartline, C., Pingol, A., Pistone, S., Wright, M., **2012**. Overview of the northwest geysers EGS demonstration project. Presented at the Thirty-Seventh Workshop on Geothermal Reservoir Engineering, Stanford California, pp. 1–11.
- Gautam, P.K., Verma, A.K., Jha, M.K., Sharma, P., Singh, T.N., **2018**. Effect of high temperature on physical and mechanical properties of Jalore granite. *Journal of Applied Geophysics* 159, 460–474. <https://doi.org/10.1016/j.jappgeo.2018.07.018>
- Gayo, E., de Frutos, J., **1997**. Interference filters as an enhancement tool for infrared thermography in humidity studies of building elements. *Infrared Physics & Technology* 38, 251–258. [https://doi.org/10.1016/S1350-4495\(97\)00025-X](https://doi.org/10.1016/S1350-4495(97)00025-X)
- Géraud, Y., **1994**. Variations of connected porosity and inferred permeability in a thermally cracked granite. *Geophysical Research Letters* 21, 979–982. <https://doi.org/10.1029/94GL00642>
- Géraud, Y., Gaviglio, P., **1990**. Textural changes in granites submitted to artificial heating: porosity and density variations as functions of the temperature. *Comptes Rendus de l'Académie des Sciences. Serie 2* 310, 1681–1686.
- Géraud, Y., Mazerolle, F., Raynaud, S., **1992**. Comparison between connected and overall porosity of thermally stressed granites. *Journal of Structural Geology, Mechanical Instabilities in Rocks and Tectonics* 14, 981–990. [https://doi.org/10.1016/0191-8141\(92\)90029-V](https://doi.org/10.1016/0191-8141(92)90029-V)

- Géraud, Y., Tournier, B., Mazerolle, F., **1999**. Detection of porosity and mineralogical variations in geological materials: radiological density measured by CT scan. *Proceedings of the International Symposium on Imaging Applications in Geology Geovision 99*, 109–112.
- Ghasemi, S., Khomehchiyan, M., Taheri, A., Nikudel, M.R., Zalooli, A., **2020**. Crack Evolution in Damage Stress Thresholds in Different Minerals of Granite Rock. *Rock Mechanics and Rock Engineering* 53, 1163–1178. <https://doi.org/10.1007/s00603-019-01964-9>
- Gibb, F.G.F., **2000**. A new scheme for the very deep geological disposal of high-level radioactive waste. *Journal of the Geological Society* 157, 27–36. <https://doi.org/10.1144/jgs.157.1.27>
- Gibeaux, S., Vázquez, P., De Kock, T., Cnudde, V., Thomachot-Schneider, C., **2018**. Weathering assessment under X-ray tomography of building stones exposed to acid atmospheres at current pollution rate. *Construction and Building Materials* 168, 187–198. <https://doi.org/10.1016/j.conbuildmat.2018.02.120>
- Glover, P.W.J., Baud, P., Darot, M., Meredith, P.G., Boon, S.A., LeRavalec, M., Zoussi, S., Reuschlé, T., **1995**.  $\alpha/\beta$  phase transition in quartz monitored using acoustic emissions. *Geophysical Journal International* 120, 775–782. <https://doi.org/10.1111/j.1365-246X.1995.tb01852.x>
- Gómez-Heras, M., Smith, B.J., Fort, R., **2006**. Surface temperature differences between minerals in crystalline rocks: Implications for granular disaggregation of granites through thermal fatigue. *Geomorphology* 78, 236–249. <https://doi.org/10.1016/j.geomorph.2005.12.013>
- Gommesen, L., Fabricius, I.L., Mukerji, T., Mavko, G., Pedersen, J.M., **2007**. Elastic behaviour of North Sea chalk: A well-log study. *Geophysical Prospecting* 55, 307–322. <https://doi.org/10.1111/j.1365-2478.2007.00622.x>
- Gräf, V., Jamek, M., Rohatsch, A., Tschegg, E., **2013**. Effects of thermal-heating cycle treatment on thermal expansion behavior of different building stones. *International Journal of Rock Mechanics and Mining Sciences* 64, 228–235. <https://doi.org/10.1016/j.ijrmms.2013.08.007>
- Grant, M., Donalds, I.G., Bixley, P.F., **1982**. *Geothermal Reservoir Engineering*. Academic Press, New York, 378.
- Griffiths, L., Lengline, O., Heap, M., Baud, P., Schmittbuhl, J., **2018**. Thermal Cracking in Westerly Granite Monitored Using Direct Wave Velocity, Coda Wave Interferometry, and Acoustic Emissions. *Journal of Geophysical Research: Solid Earth* 123, 2246–2261. <https://doi.org/10.1002/2017JB015191>
- Grinzato, E., Marinetti, S., Bison, P.G., Concas, M., Fais, S., **2004**. Comparison of ultrasonic velocity and IR thermography for the characterisation of stones. *Infrared Physics & Technology, Workshop on Advanced Infrared Technology and Application* 46, 63–68. <https://doi.org/10.1016/j.infrared.2004.03.009>
- Guo, L.-L., Zhang, Y.-B., Zhang, Y.-J., Yu, Z.-W., Zhang, J.-N., **2018**. Experimental investigation of granite properties under different temperatures and pressures and numerical analysis of damage effect in enhanced geothermal system. *Renewable Energy* 126, 107–125. <https://doi.org/10.1016/j.renene.2018.02.117>
- Gutierrez, M., Øino, L.E., Høeg, K., **2000**. The effect of fluid content on the mechanical behaviour of fractures in chalk. *Rock Mechanics and Rock Engineering* 33, 93–117.
- Hajpál, M., Török, Á., **2004**. Mineralogical and colour changes of quartz sandstones by heat. *Environmental Geology* 46, 311–322. <https://doi.org/10.1007/s00254-004-1034-z>
- Hall, K., Guglielmin, M., Strini, A., **2008**. Weathering of granite in Antarctica: II. Thermal stress at the grain scale. *Earth Surface Processes and Landforms* 33, 475–493. <https://doi.org/10.1002/esp.1617>
- Hammecker, C., Jeannette, D., **1994**. Modelling the capillary imbibition kinetics in sedimentary rocks: Role of petrographical features. *Transp Porous Med* 17, 285–303. <https://doi.org/10.1007/BF00613588>

- Hammecker, C., Mertz, J.-D., Fischer, C., Jeannette, D., **1993**. A geometrical model for numerical simulation of capillary imbibition in sedimentary rocks. *Transp Porous Med* 12, 125–141. <https://doi.org/10.1007/BF00616976>
- Hamouda, A.A., Karoussi, O., **2008**. Effect of Temperature, Wettability and Relative Permeability on Oil Recovery from Oil-wet Chalk. *Energies* 1, 19–34. <https://doi.org/10.3390/en1010019>
- Hans Wedepohl, K., **1995**. The composition of the continental crust. *Geochimica et Cosmochimica Acta* 59, 1217–1232. [https://doi.org/10.1016/0016-7037\(95\)00038-2](https://doi.org/10.1016/0016-7037(95)00038-2)
- Hassanzadegan, A., **2013**. Thermomechanical and poromechanical behavior of Flechtinger sandstone. (Thèse de doctorat). Université technique de Berlin, 109. <https://doi.org/10.14279/DEPOSITONCE-3569>
- Hassanzadegan, A., Blöcher, G., Milsch, H., Urpi, L., Zimmermann, G., **2014**. The Effects of Temperature and Pressure on the Porosity Evolution of Flechtinger Sandstone. *Rock Mechanics and Rock Engineering* 47, 421–434. <https://doi.org/10.1007/s00603-013-0401-z>
- Headon, J., Banks, D., Waters, A., Robinson, V.K., **2009**. Regional distribution of ground temperature in the Chalk aquifer of London, UK. *Quarterly Journal of Engineering Geology and Hydrogeology* 42, 313–323. <https://doi.org/10.1144/1470-9236/08-073>
- Heggheim, T., Madland, M.V., Risnes, R., Austad, T., **2005**. A chemical induced enhanced weakening of chalk by seawater. *Journal of Petroleum Science and Engineering* 46, 171–184. <https://doi.org/10.1016/j.petrol.2004.12.001>
- Hellmann, R., Gaviglio, P., Renders, P., Gratier, J.P., Bekri, S., Adler, P.M., **2002a**. Experimental pressure solution compaction of chalk in aqueous solutions. Part 2. Deformation examined by SEM, porosimetry, synthetic permeability, and X-ray computerized tomography, *Water-Rock interactions, ores deposits, and Environmental Geochemistry: The Geochemical Society Special publication* 153.
- Hellmann, R., Renders, P.J., Gratier, J.P., Guiguet, R., **2002b**. Experimental pressure solution compaction of chalk in aqueous solutions. Part 1. Deformation behavior and chemistry. *Water-rock interactions, ore deposits, and environmental geochemistry: A tribute to David A. Crerar* 7, 129–152.
- Heugas, O., Charlez, P., **1990**. Mechanical effect of the water injection on Ekofisk chalk, in: *Third North Sea Chalk Symposium*, Copenhagen.
- Heuze, F.E., **1983**. High-temperature mechanical, physical and Thermal properties of granitic rocks— A review. *International Journal of Rock Mechanics and Mining Sciences & Geomechanics Abstracts* 20, 3–10. [https://doi.org/10.1016/0148-9062\(83\)91609-1](https://doi.org/10.1016/0148-9062(83)91609-1)
- Hirschwald, J., **1908**. Die Prüfung der natürlichen Bausteine auf ihre Wetterfeständigkeit. W. Ernst & Sohn.
- Hjuler, M.L., Fabricius, I.L., **2009**. Engineering properties of chalk related to diagenetic variations of Upper Cretaceous onshore and offshore chalk in the North Sea area. *Journal of Petroleum Science and Engineering* 68, 151–170. <https://doi.org/10.1016/j.petrol.2009.06.005>
- Hoekmark, H., Faeltz, B., **2003**. Thermal dimensioning of the deep repository. Influence of canister spacing, canister power, rock thermal properties and nearfield design on the maximum canister surface temperature (No. SKB-TR--03-09). Swedish Nuclear Fuel and Waste Management Co, 79.
- Homand, F., Duffaut, P., Bérest, P., Billiaux, D., Boulon, M., Cornet, F., David, C., Durville, J.L., Gentier, S., Giraud, A., Ghoreychi, M., Henry, J.P., Kondo, D., Londe, P., Pellet, F., Pigué, J.P., Sarda, J.P., Shao, J.F., Souley, M., **2000**. Manuel de mécanique des roches - tome 1 Fondements, Ecole des Mines de Paris, 265.

- Homand-Etienne, F., Houpert, R., **1989**. Thermally induced microcracking in granites: characterization and analysis. *International Journal of Rock Mechanics and Mining Sciences & Geomechanics Abstracts* 26, 125–134. [https://doi.org/10.1016/0148-9062\(89\)90001-6](https://doi.org/10.1016/0148-9062(89)90001-6)
- Hounsfield, G.N., **1972**. A method of and apparatus for examination of a body by radiation such as X- or gamma-radiation. British Patent No. 1,283,915.
- Houpert, R., Homand-Etienne, F., **1986**. Données récentes sur le comportement des roches en fonction de la température. P. Berest. Ph. Weber (die), *La thermomécanique des roches, Manuels et méthodes* 304–312.
- Huang, Y.-H., Yang, S.-Q., Tian, W.-L., Zhao, J., Ma, D., Zhang, C.-S., **2017**. Physical and mechanical behavior of granite containing pre-existing holes after high temperature treatment. *Archives of Civil and Mechanical Engineering* 17, 912–925. <https://doi.org/10.1016/j.acme.2017.03.007>
- Hurlimann, M.D., Helmer, K.G., Latour, L.L., Sotak, C.H., **1994**. Restricted Diffusion in Sedimentary Rocks. Determination of Surface-Area-to-Volume Ratio and Surface Relaxivity. *Journal of Magnetic Resonance, Series A* 111, 169–178. <https://doi.org/10.1006/jmra.1994.1243>
- IGME, **2004a**. Mapa de rocas y minerales industriales de Galicia. Orense-Verín (17–27). E. 1:200.000.
- IGME, **2004b**. Mapa de rocas y minerales industriales de Galicia. Pontevedra-A Guarda (16–26). E. 1:200.000.
- Ioannou, I., Andreou, A., Tsikouras, B., Hatzipanagiotou, K., **2009**. Application of the Sharp Front Model to capillary absorption in a vuggy limestone. *Engineering Geology* 105, 20–23. <https://doi.org/10.1016/j.enggeo.2008.12.008>
- Irfan, T.Y., **1996**. Mineralogy, fabric properties and classification of weathered granites in Hong Kong. *Quarterly Journal of Engineering Geology and Hydrogeology* 29, 5–35. <https://doi.org/10.1144/GSL.QJEGH.1996.029.P1.02>
- Isaka, B.L.A., Gamage, R.P., Rathnaweera, T.D., Perera, M.S.A., Chandrasekharam, D., Kumari, W.G.P., **2018**. An Influence of Thermally-Induced Micro-Cracking under Cooling Treatments: Mechanical Characteristics of Australian Granite. *Energies* 11, 1338. <https://doi.org/10.3390/en11061338>
- Isaka, B.L.A., Ranjith, P.G., Rathnaweera, T.D., Perera, M.S.A., Kumari, W.G.P., **2019**. Influence of long-term operation of supercritical carbon dioxide based enhanced geothermal system on mineralogical and microstructurally-induced mechanical alteration of surrounding rock mass. *Renewable Energy* 136, 428–441. <https://doi.org/10.1016/j.renene.2018.12.104>
- Jabbari, H., Afsari, K., Rabiei, M., Monk, A., **2017**. Thermally-induced wettability alteration from hot-water imbibition in naturally fractured reservoirs—Part 1: Numerical model development & 1D models. *Fuel* 208, 682–691. <https://doi.org/10.1016/j.fuel.2017.07.016>
- Jaeger, J., Cook, N., Zimmerman, R., **2007**. *Fundamental of Rock Mechanics*. John Wiley & Sons, 488. <https://doi.org/10.1017/CBO9780511735349>
- Janio de Castro Lima, J., Paraguassú, A.B., **2004**. Linear thermal expansion of granitic rocks: influence of apparent porosity, grain size and quartz content. *Bull Eng Geol Environ* 63, 215–220. <https://doi.org/10.1007/s10064-004-0233-x>
- Jansen, D.P., Carlson, S.R., Young, R.P., Hutchins, D.A., **1993**. Ultrasonic imaging and acoustic emission monitoring of thermally induced microcracks in Lac du Bonnet granite. *Journal of Geophysical Research: Solid Earth* 98, 22231–22243. <https://doi.org/10.1029/93JB01816>
- Japsen, P., Bruun, A., Fabricius, I.L., Rasmussen, R., Vejrbæk, O.V., Pedersen, J.M., Mavko, G., Mogensen, C., Høier, C., **2004**. Influence of porosity and pore fluid on acoustic properties of chalk: AVO response from oil, South Arne Field, North Sea. *Petroleum Geoscience* 10, 319–330. <https://doi.org/10.1144/1354-079303-586>

- Jeanne, P., Rutqvist, J., Dobson, P.F., **2017**. Influence of injection-induced cooling on deviatoric stress and shear reactivation of preexisting fractures in Enhanced Geothermal Systems. *Geothermics* 70, 367–375. <https://doi.org/10.1016/j.geothermics.2017.08.003>
- Ji, Y., Baud, P., Vajdova, V., Wong, T. -f, **2012**. Characterization of Pore Geometry of Indiana Limestone in Relation to Mechanical Compaction. *Oil & Gas Science and Technology – Revue d'IFP Energies nouvelles* 67, 753–775. <https://doi.org/10.2516/ogst/2012051>
- Ji, Y., Hall, S.A., Baud, P., Wong, T., **2015**. Characterization of pore structure and strain localization in Majella limestone by X-ray computed tomography and digital image correlation. *Geophysical Journal International* 200, 701–719. <https://doi.org/10.1093/gji/ggu414>
- Jian-ping, Z., He-ping, X., Hong-wei, Z., Su-ping, P., **2010**. SEM in situ investigation on thermal cracking behaviour of Pingdingshan sandstone at elevated temperatures. *Geophysical Journal International* 181, 593–603. <https://doi.org/10.1111/j.1365-246X.2010.04532.x>
- Jin, P., Hu, Y., Shao, J., Zhao, G., Zhu, X., Li, C., **2019**. Influence of different thermal cycling treatments on the physical, mechanical and transport properties of granite. *Geothermics* 78, 118–128. <https://doi.org/10.1016/j.geothermics.2018.12.008>
- Johnson, J.P., Rhett, D.W., Siemers, W.T., **1988**. Rock Mechanics Of The Ekofisk Reservoir In The Evaluation Of Subsidence. Presented at the Offshore Technology Conference, Offshore Technology Conference. <https://doi.org/10.4043/5621-MS>
- Josse, J., Husson, F., **2016**. missMDA: a package for handling missing values in multivariate data analysis. *Journal of Statistical Software* 70, 1–31.
- Junique, T., Vázquez, P., Géraud, Y., Thomachot-Schneider, C., Sidibé, H., **2021**. Microstructural evolution of granitic stones exposed to different thermal regimes analysed by infrared thermography. *Engineering Geology* 286, 106057. <https://doi.org/10.1016/j.enggeo.2021.106057>
- Kaiser, J., **1953**. Erkenntnisse und Folgerungen aus der Messung von Geräuschen bei Zugbeanspruchung von metallischen Werkstoffen. *Archiv für das Eisenhüttenwesen* 24, 43–45. <https://doi.org/10.1002/srin.195301381>
- Kant, M.A., Ammann, J., Rossi, E., Madonna, C., Höser, D., Rohr, P.R. von, **2017**. Thermal properties of Central Aare granite for temperatures up to 500°C: Irreversible changes due to thermal crack formation. *Geophysical Research Letters* 44, 771–776. <https://doi.org/10.1002/2016GL070990>
- Katende, A., Lu, Y., Bungler, A., Radonjic, M., **2020**. Experimental quantification of the effect of oil based drilling fluid contamination on properties of wellbore cement. *Journal of Natural Gas Science and Engineering* 79, 103328. <https://doi.org/10.1016/j.jngse.2020.103328>
- Keating, K., Knight, R., **2012**. The effect of spatial variation in surface relaxivity on nuclear magnetic resonance relaxation rates Spatially variable surface relaxivity. *Geophysics* 77, E365–E377. <https://doi.org/10.1190/geo2011-0462.1>
- Keating, K., Knight, R., **2006**. A laboratory study to determine the effect of iron oxides on proton NMR measurements. *Geophysics* 72, E27–E32. <https://doi.org/10.1190/1.2399445>
- Kelly, S., El-Sobky, H., Torres-Verdín, C., Balhoff, M.T., **2016**. Assessing the utility of FIB-SEM images for shale digital rock physics. *Advances in Water Resources, Pore scale modeling and experiments* 95, 302–316. <https://doi.org/10.1016/j.advwatres.2015.06.010>
- Kenyon, B., Kleinberg, R., Straley, C., Gubelin, G., Morriss, C., **1995**. Nuclear magnetic resonance imaging - technology for the 21st century. *Oilfield Review* 7, 19–33.
- Kenyon, W.E., **1997**. Petrophysical Principles of Applications of NMR Logging. *The Log Analyst* 38.02.
- Kenyon, W.E., Day, P.I., Straley, C., Willemsen, J.F., **1988**. A Three-Part Study of NMR Longitudinal Relaxation Properties of Water-Saturated Sandstones. *SPE Formation Evaluation* 3, 622–636. <https://doi.org/10.2118/15643-PA>

- Keszthelyi, D., Dysthe, D.K., Jamtveit, B., **2016**. Compaction of North-Sea Chalk by Pore-Failure and Pressure Solution in a Producing Reservoir. *Frontiers in Physics* 4. <https://doi.org/10.3389/fphy.2016.00004>
- Kiers, H.A., **1997**. Weighted least squares fitting using ordinary least squares algorithms. *Psychometrika* 62, 251–266.
- Kim, B.-C., Chen, J., Kim, J.-Y., **2020**. Relation between crack density and acoustic nonlinearity in thermally damaged sandstone. *International Journal of Rock Mechanics and Mining Sciences* 125, 104171. <https://doi.org/10.1016/j.ijrmms.2019.104171>
- Kim, K., Kemeny, J., Nickerson, M., **2014**. Effect of Rapid Thermal Cooling on Mechanical Rock Properties. *Rock Mechanics and Rock Engineering* 47, 2005–2019. <https://doi.org/10.1007/s00603-013-0523-3>
- Kleinberg, R.L., Farooqui, S.A., Horsfield, M.A., **1993**. T1/T2 Ratio and Frequency Dependence of NMR Relaxation in Porous Sedimentary Rocks. *Journal of Colloid and Interface Science* 158, 195–198. <https://doi.org/10.1006/jcis.1993.1247>
- Kleinberg, R.L., Flaum, C., Griffin, D.D., Brewer, P.G., Malby, G.E., Peltzer, E.T., Yesinowski, J.P., **2003**. Deep sea NMR: Methane hydrate growth habit in porous media and its relationship to hydraulic permeability, deposit accumulation, and submarine slope stability. *Journal of Geophysical Research: Solid Earth* 108. <https://doi.org/10.1029/2003JB002389>
- Klinkenberg, L.J., **1941**. The Permeability Of Porous Media To Liquids And Gases. Presented at the Drilling and Production Practice, American Petroleum Institute, p. 318.
- Knight, R., Walsh, D.O., Butler, J.J., Grunewald, E., Liu, G., Parsekian, A.D., Reboulet, E.C., Knobbe, S., Barrows, M., **2016**. NMR Logging to Estimate Hydraulic Conductivity in Unconsolidated Aquifers. *Groundwater* 54, 104–114. <https://doi.org/10.1111/gwat.12324>
- Kovač, K., Moore, J., Mcculloch, J., Ekart, D., **2004**. Geology and Mineral Paragenesis Study Within the Coso-EGS Project. Presented at the Twenty-Ninth Workshop on Geothermal Reservoir Engineering Stanford University, Stanford, California.
- Kranz, R.L., **1983**. Microcracks in rocks: A review. *Tectonophysics, Continental Tectonics: Structure, Kinematics and Dynamics* 100, 449–480. [https://doi.org/10.1016/0040-1951\(83\)90198-1](https://doi.org/10.1016/0040-1951(83)90198-1)
- Kranz, R.L., **1979**. Crack growth and development during creep of Barre granite. *International Journal of Rock Mechanics and Mining Sciences & Geomechanics Abstracts* 16, 23–35. [https://doi.org/10.1016/0148-9062\(79\)90772-1](https://doi.org/10.1016/0148-9062(79)90772-1)
- Kruschwitz, S., Halisch, M., Dlugosch, R., Prinz, C., **2020**. Toward a better understanding of low-frequency electrical relaxation — An enhanced pore space characterization. *Geophysics* 85, MR257–MR270. <https://doi.org/10.1190/geo2019-0074.1>
- Kumari, W.G.P., Ranjith, P.G., Perera, M.S.A., Chen, B.K., **2018**. Experimental investigation of quenching effect on mechanical, microstructural and flow characteristics of reservoir rocks: Thermal stimulation method for geothermal energy extraction. *Journal of Petroleum Science and Engineering* 162, 419–433. <https://doi.org/10.1016/j.petrol.2017.12.033>
- Kumari, W.G.P., Ranjith, P.G., Perera, M.S.A., Chen, B.K., Abdulatov, I.M., **2017a**. Temperature-dependent mechanical behaviour of Australian Strathbogie granite with different cooling treatments. *Engineering Geology* 229, 31–44. <https://doi.org/10.1016/j.enggeo.2017.09.012>
- Kumari, W.G.P., Ranjith, P.G., Perera, M.S.A., Shao, S., Chen, B.K., Lashin, A., Arifi, N.A., Rathnaweera, T.D., **2017b**. Mechanical behaviour of Australian Strathbogie granite under in-situ stress and temperature conditions: An application to geothermal energy extraction. *Geothermics* 65, 44–59. <https://doi.org/10.1016/j.geothermics.2016.07.002>
- Lakshmanov, L.Z., Okhrimenko, D.V., Karaseva, O.N., Stipp, S.L.S., **2018**. Limits on Calcite and Chalk Recrystallization. *Crystal Growth & Design* 18, 4536–4543. <https://doi.org/10.1021/acs.cgd.8b00537>



- Lam dos Santos, J.P., Rosa, L.G., Amaral, P.M., **2011**. Temperature effects on mechanical behaviour of engineered stones. *Construction and Building Materials* 25, 171–174. <https://doi.org/10.1016/j.conbuildmat.2010.06.042>
- Lan, H., Martin, C.D., Hu, B., **2010**. Effect of heterogeneity of brittle rock on micromechanical extensile behavior during compression loading. *Journal of Geophysical Research: Solid Earth* 115. <https://doi.org/10.1029/2009JB006496>
- Laplace, P.S., **1806**. *Traité de Mécanique Céleste*. Eds. Courcier, Paris.
- Lavrov, A., **2003**. The Kaiser effect in rocks: principles and stress estimation techniques. *International Journal of Rock Mechanics and Mining Sciences* 40, 151–171. [https://doi.org/10.1016/S1365-1609\(02\)00138-7](https://doi.org/10.1016/S1365-1609(02)00138-7)
- Law, R., **2010**. Geothermal systems in the Chalk of the south east of England: methods of predicting thermal transport in a fractured aquifer (Thèse de doctorat). University of Birmingham, 231.
- Le Maitre, R.W., **2002**. International Union of Geological Sciences (IUGS). *Igneous Rocks: A Classification and Glossary of Terms*, 236.
- Le Roux, A., **1973**. Texture et comportement des craies. La Craie. *Bulletin de Liaison des Laboratoires des Ponts et Chaussées* 49–53.
- Li, B., Ju, F., Xiao, M., Ning, P., **2019**. Mechanical stability of granite as thermal energy storage material: An experimental investigation. *Engineering Fracture Mechanics* 211, 61–69. <https://doi.org/10.1016/j.engfracmech.2019.02.008>
- Li, C., Hu, Y., Meng, T., Jin, P., Zhao, Z., Zhang, C., **2020**. Experimental study of the influence of temperature and cooling method on mechanical properties of granite: Implication for geothermal mining. *Energy Science & Engineering* 8, 1716–1728. <https://doi.org/10.1002/ese3.627>
- Li, H., Zhang, J., **2018**. Well log and seismic data analysis for complex pore-structure carbonate reservoir using 3D rock physics templates. *Journal of Applied Geophysics* 151, 175–183. <https://doi.org/10.1016/j.jappgeo.2018.02.017>
- Li, L., Shikhov, I., Zheng, Y., Hermann Arns, C., **2014**. Experiment and simulation on NMR and electrical measurements on Liège Chalk. *Diffusion fundamentals* 22, 1–7.
- Li, N., Zhang, S.C., Ma, X.F., Zou, Y.S., Cao, T., **2019**. Experimental Research on the Effect of Cold Water Injection on the Mechanical Properties and Brittleness of Granite in HDR. Presented at the 53rd U.S. Rock Mechanics/Geomechanics Symposium, American Rock Mechanics Association.
- Liaw, H.-K., Kulkarni, R., Chen, S., Watson, A.T., **1996**. Characterization of fluid distributions in porous media by NMR techniques. *AIChE Journal* 42, 538–546. <https://doi.org/10.1002/aic.690420223>
- Lin, W., **2002**. Permanent strain of thermal expansion and thermally induced microcracking in Inada granite. *Journal of Geophysical Research: Solid Earth* 107, ECV 3-1. <https://doi.org/10.1029/2001JB000648>
- Lin, W., Tadai, O., Takahashi, M., Sato, D., Hirose, T., Tanikawa, W., Hamada, Y., Hatakeda, K., **2015**. An Experimental Study on Measurement Methods of Bulk Density and Porosity of Rock Samples. *Journal of Geoscience and Environment Protection* 03, 72. <https://doi.org/10.4236/gep.2015.35009>
- Linoir, D., **2014**. Les horizons d'accumulations carbonatées (HAC) en Champagne-Ardenne ; répartition régionale, caractérisation et conséquences sur les transferts hydriques (Thèse de doctorat). Université de Reims Champagne-Ardenne, 385.
- Lion, M., Skoczylas, F., Ledesert, B., **2005**. Effects of heating on the hydraulic and poroelastic properties of bourgogne limestone. *International Journal of Rock Mechanics and Mining Sciences* 42, 508–520. <https://doi.org/10.1016/j.ijrmms.2005.01.005>

- Lipin, V., Trufanov, D., **2019**. Effect of chalk thermal treatment mode on its strength. *Journal of Mining Institute* 236, 210–215. <https://doi.org/10.31897/pmi.2019.2.210>
- Lisabeth, H.P., Zhu, W., **2015**. Effect of temperature and pore fluid on the strength of porous limestone: chemomechanical weakening of limestone. *Journal of Geophysical Research: Solid Earth* 120, 6191–6208. <https://doi.org/10.1002/2015JB012152>
- Liu, C., Deng, H., Wang, Y., Lin, Y., Zhao, H., **2017**. Time-Varying Characteristics of Granite Microstructures after Cyclic Dynamic Disturbance Using Nuclear Magnetic Resonance. *Crystals* 7, 306. <https://doi.org/10.3390/cryst7100306>
- Liu, S., Xu, J., **2014**. Mechanical properties of Qinling biotite granite after high temperature treatment. *International journal of rock mechanics and mining sciences* 71, 188–193. <https://doi.org/10.1016/J.IJRMMS.2014.07.008>
- Lord, C.J., Johlman, C.L., Rhett, D.W., **1998**. Is Capillary Suction a Viable Cohesive Mechanism in Chalk? Presented at the SPE/ISRM Rock Mechanics in Petroleum Engineering, Society of Petroleum Engineers. <https://doi.org/10.2118/47310-MS>
- Loveless, S., Pluymaekers, M., Lagrou, D., De Boever, E., Doornenbal, H., Laenen, B., **2014**. Mapping the Geothermal Potential of Fault Zones in the Belgium-Netherlands Border Region. *Energy Procedia, European Geosciences Union General Assembly 2014, EGU Division Energy, Resources & the Environment (ERE) 59, 351–358.* <https://doi.org/10.1016/j.egypro.2014.10.388>
- Lu, J., Wang, K., Qu, M.-L., **2020**. Experimental determination on the capillary water absorption coefficient of porous building materials: A comparison between the intermittent and continuous absorption tests. *Journal of Building Engineering* 28, 101091. <https://doi.org/10.1016/j.job.2019.101091>
- Lucas, R., **1918**. Ueber das Zeitgesetz des kapillaren Aufstiegs von Flüssigkeiten. *Kolloid-Zeitschrift* 23, 15–22. <https://doi.org/10.1007/BF01461107>
- Ludwig, N., Rosina, E., Sansonetti, A., **2018**. Evaluation and monitoring of water diffusion into stone porous materials by means of innovative IR thermography techniques. *Measurement* 118, 348–353. <https://doi.org/10.1016/j.measurement.2017.09.002>
- Luong, **1990**. Infrared thermovision of damage processes in concrete and rock. *Engineering Fracture Mechanics, Special Issue Fracture and Damage of Concrete and Rock* 35, 291–301. [https://doi.org/10.1016/0013-7944\(90\)90207-W](https://doi.org/10.1016/0013-7944(90)90207-W)
- Lutz, S., Robertson-Tait, A., Morris, C., **2004**. Stratigraphic relationships in Mesozoic basement rocks at the Desert Peak East EGS area, Nevada. Presented at the Twenty-Ninth Workshop on Geothermal Reservoir Engineering Stanford, University, Stanford, California.
- Ma, H., **2014**. Mercury intrusion porosimetry in concrete technology: tips in measurement, pore structure parameter acquisition and application. *Journal of Porous Materials* 21, 207–215. <https://doi.org/10.1007/s10934-013-9765-4>
- Madland, M.V., **2005**. Water weakening of chalk: A mechanistic study. University of Stavanger, Norway.
- Madland, M.V., Hiorth, A., Omdal, E., Megawati, M., Hildebrand-Habel, T., Korsnes, R.I., Evje, S., Cathles, L.M., **2011**. Chemical Alterations Induced by Rock-Fluid Interactions When Injecting Brines in High Porosity Chalks. *Transport in Porous Media* 87, 679–702. <https://doi.org/10.1007/s11242-010-9708-3>
- Maget, P., Rambaud, D., **1980**. Possibilités géothermiques de la région Champagne-Ardenne-II. Etude hydrogéologique des sites. *BRGM* 80, 120.
- Maliva, R.G., Dickson, J. a. D., **1992**. Microfacies and Diagenetic Controls of Porosity in Cretaceous/Tertiary Chalks, Eldfisk Field, Norwegian North Sea. *AAPG Bulletin* 76, 1825–1838. <https://doi.org/10.1306/BDF8AE2-1718-11D7-8645000102C1865D>

- Marshall, V., Van Zyl, J., Bryan, S., Uysal, T., Gasparon, M., **2010**. Comparative petrology and geochemistry of high heat-producing granites in Australia and Europe, in: Weber, R.D., Gurgenci, H. (Eds.), *Proceedings of the 2010 Australian Geothermal Energy Conference*. Presented at the Australian Geothermal Energy Conference, Geoscience Australia, Australia, pp. 41–47.
- Martínez-Martínez, J., Benavente, D., García-del-Cura, M.A., **2011**. Spatial attenuation: The most sensitive ultrasonic parameter for detecting petrographic features and decay processes in carbonate rocks. *Engineering Geology* 119, 84–95. <https://doi.org/10.1016/j.enggeo.2011.02.002>
- Mata, C., **2001**. Experimental study and mechanical modelling of the effects of water-driving in an oil saturated chalk. Application to the petroleum industry; Etude expérimentale et modélisation mécanique des effets du balayage à l'eau dans une craie saturée d'huile. Application à l'industrie pétrolière.
- Maurer, J., Knight, R., **2016**. Models and methods for predicting hydraulic conductivity in near-surface unconsolidated sediments using nuclear magnetic resonance. *Geophysics* 81, D503–D518. <https://doi.org/10.1190/geo2015-0515.1>
- Maurer, V., Gaucher, E., Grunberg, M., Koepke, R., Pestourie, R., Cuenot, N., **2020**. Seismicity induced during the development of the Rittershoffen geothermal field, France. *Geothermal Energy* 8. <https://doi.org/10.1186/s40517-020-0155-2>
- Megawati, M., Madland, M.V., Hiorth, A., **2015**. Mechanical and physical behavior of high-porosity chalks exposed to chemical perturbation. *Journal of Petroleum Science and Engineering* 133, 313–327. <https://doi.org/10.1016/j.petrol.2015.06.026>
- Megawati, M., Madland, M.V., Hiorth, A., **2012**. Probing pore characteristics of deformed chalk by NMR relaxation. *Journal of Petroleum Science and Engineering* 100, 123–130. <https://doi.org/10.1016/j.petrol.2012.11.001>
- Menéndez, B., David, C., Darot, M., **1999**. A study of the crack network in thermally and mechanically cracked granite samples using confocal scanning laser microscopy. *Physics and Chemistry of the Earth, Part A: Solid Earth and Geodesy* 24, 627–632. [https://doi.org/10.1016/S1464-1895\(99\)00091-5](https://doi.org/10.1016/S1464-1895(99)00091-5)
- Meola, C., **2007**. A new approach for estimation of defects detection with infrared thermography. *Materials Letters* 61, 747–750. <https://doi.org/10.1016/j.matlet.2006.04.120>
- Meredith, P.G., Atkinson, B.K., **1985**. Fracture toughness and subcritical crack growth during high-temperature tensile deformation of Westerly granite and Black gabbro. *Physics of the Earth and Planetary Interiors* 39, 33–51. [https://doi.org/10.1016/0031-9201\(85\)90113-X](https://doi.org/10.1016/0031-9201(85)90113-X)
- Mertz, J.-D., **1991**. Structures de porosité et propriétés de transport dans les grès, *Sciences Géologiques. Mémoire*, 90, 170. Institut de Géologie – Université Louis-Pasteur.
- Meyer, A.G., Nourani, M., Stemmerik, L., **2019**. Description of chalk microporosity via automated mathematical morphology on scanning electron microphotographs. *Petroleum Geoscience*, 386–399. <https://doi.org/10.1144/petgeo2019-018>
- Meyer, K., Lorenz, P., Böhl-Kuhn, B., Klobes, P., **1994**. Porous solids and their characterization methods of investigation and application. *Crystal Research and Technology* 29, 903–930. <https://doi.org/10.1002/crat.2170290702>
- Mineo, S., Pappalardo, G., **2019**. InfraRed Thermography presented as an innovative and non-destructive solution to quantify rock porosity in laboratory. *International Journal of Rock Mechanics and Mining Sciences* 115, 99–110. <https://doi.org/10.1016/J.IJRMMS.2019.01.012>
- Mineo, S., Pappalardo, G., **2016**. The Use of Infrared Thermography for Porosity Assessment of Intact Rock. *Rock Mechanics and Rock Engineering* 49, 3027–3039. <https://doi.org/10.1007/s00603-016-0992-2>

- Mineo, S., Pappalardo, G., Rapisarda, F., Cubito, A., Di Maria, G., **2015**. Integrated geostructural, seismic and infrared thermography surveys for the study of an unstable rock slope in the Peloritani Chain (NE Sicily). *Engineering Geology* 195, 225–235. <https://doi.org/10.1016/j.enggeo.2015.06.010>
- Miskovsky, K., Duarte, M.T., Kou, S.Q., Lindqvist, P.-A., **2004**. Influence of the mineralogical composition and textural properties on the quality of coarse aggregates. *Journal of Materials Engineering and Performance* 13, 144–150. <https://doi.org/10.1361/10599490418334>
- Monjoie, A., Schroeder, C., **1989**. Caractéristiques mécaniques de craies du Crétacé supérieur. Presented at the Journée craie, pp. 00–01.
- Müter, D., Sørensen, H.O., Jha, D., Harti, R., Dalby, K.N., Suhonen, H., Feidenhans'l, R., Engstrøm, F., Stipp, S.L.S., **2014**. Resolution dependence of petrophysical parameters derived from X-ray tomography of chalk. *Applied Physics Letters* 105, 043108. <https://doi.org/10.1063/1.4891965>
- Nadah, J., **2010**. Valorisation d'une craie du Nord de la France en assise de chaussée routière (Thèse de doctorat). Ecole Centrale de Lille, 214.
- Nadah, J., Bignonnet, F., Davy, C.A., Skoczylas, F., Troadec, D., Bakowski, S., **2013**. Microstructure and poro-mechanical performance of Haubourdin chalk. *International Journal of Rock Mechanics and Mining Sciences* 58, 149–165. <https://doi.org/10.1016/j.ijrmms.2012.11.001>
- Nadah, J., Skoczylas, F., Bakowski, S., **2009**. Effet de la temperature sur le comportement mecanique d'une craie du Nord de la France, in: Congrès Français de Mécanique. AFM, Maison de la Mécanique, 39/41 rue Louis Blanc-92400 Courbevoie.
- Nermoen, A., Korsnes, R.I., Aursjø, O., Madland, M.V., Kjørslevik, T.A.C., Østensen, G., **2016**. How Stress and Temperature Conditions Affect Rock-Fluid Chemistry and Mechanical Deformation. *Frontiers in Physics* 4. <https://doi.org/10.3389/fphy.2016.00002>
- Nermoen, A., Korsnes, R.I., Hiorth, A., Madland, M.V., **2015**. Porosity and permeability development in compacting chalks during flooding of nonequilibrium brines: Insights from long-term experiment. *Journal of Geophysical Research: Solid Earth* 120, 2935–2960. <https://doi.org/10.1002/2014JB011631>
- Newman, G.H., **1983**. The Effect of Water Chemistry on the Laboratory Compression and Permeability Characteristics of Some North Sea Chalks. *Journal of Petroleum Technology* 35, 976–980. <https://doi.org/10.2118/10203-PA>
- NF EN 1925, **1999**. Méthodes d'essai pour pierres naturelles - Détermination du coefficient d'absorption d'eau par capillarité.
- NF EN 1936, **2007**. Méthodes d'essai de la pierre naturelle - Détermination de la densité réelle et de la densité apparente et de la porosité totale et ouverte.
- NF EN 14066, **2013**. Méthodes d'essai pour les pierres naturelles - Détermination de la résistance au vieillissement accéléré par choc thermique.
- Nguyen, H.D., **2009**. Influence des interactions eau-roche sur le comportement à long terme de cavités souterraines dans la craie (Thèse de doctorat).
- Okabe, H., Blunt, M.J., **2007**. Pore space reconstruction of vuggy carbonates using microtomography and multiple-point statistics. *Water Resources Research* 43. <https://doi.org/10.1029/2006WR005680>
- Olasolo, P., Juárez, M.C., Morales, M.P., D'Amico, S., Liarte, I.A., **2016**. Enhanced geothermal systems (EGS): A review. *Renewable and Sustainable Energy Reviews* 56, 133–144. <https://doi.org/10.1016/j.rser.2015.11.031>
- Ozguven, A., Ozcelik, Y., **2013**. Investigation of some property changes of natural building stones exposed to fire and high heat. *Construction and Building Materials, 25th Anniversary Session for ACI 228 – Building on the Past for the Future of NDT of Concrete* 38, 813–821. <https://doi.org/10.1016/j.conbuildmat.2012.09.072>

- Pandey, S.N., Chaudhuri, A., Kelkar, S., **2017**. A coupled thermo-hydro-mechanical modeling of fracture aperture alteration and reservoir deformation during heat extraction from a geothermal reservoir. *Geothermics* 65, 17–31. <https://doi.org/10.1016/j.geothermics.2016.08.006>
- Pappalardo, G., Mineo, S., **2017**. Investigation on the mechanical attitude of basaltic rocks from Mount Etna through InfraRed Thermography and laboratory tests. *Construction and Building Materials* 134, 228–235. <https://doi.org/10.1016/j.conbuildmat.2016.12.146>
- Pappalardo, G., Mineo, S., Zampelli, S.P., Cubito, A., Calcaterra, D., **2016**. InfraRed Thermography proposed for the estimation of the Cooling Rate Index in the remote survey of rock masses. *International Journal of Rock Mechanics and Mining Sciences* 83, 182–196. <https://doi.org/10.1016/j.ijrmms.2016.01.010>
- Parnell, J., **1988**. Migration of biogenic hydrocarbons into granites: a review of hydrocarbons in British plutons. *Marine and Petroleum Geology* 5, 385–396. [https://doi.org/10.1016/0264-8172\(88\)90032-3](https://doi.org/10.1016/0264-8172(88)90032-3)
- Perkins, T.K., Gonzalez, J.A., **1985**. The effect of thermoelastic stresses on injection well fracturing. *Society of Petroleum Engineers Journal* 25:1, 78–88. <https://doi.org/10.2118/11332-PA>
- Plummer, L.N., Busenberg, E., **1982**. The solubilities of calcite, aragonite and vaterite in CO<sub>2</sub>-H<sub>2</sub>O solutions between 0 and 90°C, and an evaluation of the aqueous model for the system CaCO<sub>3</sub>-CO<sub>2</sub>-H<sub>2</sub>O. *Geochimica et Cosmochimica Acta* 46, 1011–1040. [https://doi.org/10.1016/0016-7037\(82\)90056-4](https://doi.org/10.1016/0016-7037(82)90056-4)
- Poiseuille, J.L., **1844**. Recherches experimentales sur le mouvement des liquides dans les tubes de tres-petits diametres. Imprimerie Royale.
- Potts, D.M., Jones, M.E., Berget, O.P., **1988**. Subsidence above the Ekofisk oil reservoirs 113–127.
- Poulsen, S.E., Balling, N., Bording, T.S., Mathiesen, A., Nielsen, S.B., **2017**. Inverse geothermal modelling applied to Danish sedimentary basins. *Geophysical Journal International* 211, 188–206. <https://doi.org/10.1093/gji/ggx296>
- Purcell, W.R., **1949**. Capillary Pressures - Their Measurement Using Mercury and the Calculation of Permeability Therefrom. *Journal of Petroleum Technology* 1, 39–48. <https://doi.org/10.2118/949039-G>
- R: The R Project for Statistical Computing [WWW Document], **2020**. URL <https://www.r-project.org/> (accessed 11.24.20).
- Rao, Q., Wang, Z., Xie, H., Xie, Q., **2007**. Experimental study of mechanical properties of sandstone at high temperature. *Journal of Central South University of Technology* 14, 478–483. <https://doi.org/10.1007/s11771-007-0311-x>
- Raynal, J., **2005**. Mesure de la masse volumique de l'eau interfoliaire dans les smectites ; application aux courbes capillaires. *Revue Française de Géotechnique* 69–76. <https://doi.org/10.1051/geotech/2005110069>
- Regnet, J.B., Robion, P., David, C., Fortin, J., Brigaud, B., Yven, B., **2015**. Acoustic and reservoir properties of microporous carbonate rocks: Implication of micrite particle size and morphology. *Journal of Geophysical Research: Solid Earth* 120, 790–811. <https://doi.org/10.1002/2014JB011313>
- Rehbinder, P.A., Lichtman, V., **1957**. Effect of surface active media on strains and rupture in solids, in: *Proceedings of the Second International Congress of Surface Activity*. Butterworths, pp. 563–580.
- Ren, S., Parsekian, A.D., Zhang, Y., Carr, B.J., **2019**. Hydraulic Conductivity Calibration of Logging NMR in a Granite Aquifer, Laramie Range, Wyoming. *Groundwater* 57, 303–319. <https://doi.org/10.1111/gwat.12798>

- Reuschlé, T., Gbaguidi Haore, S., Darot, M., **2006**. The effect of heating on the microstructural evolution of La Peyratte granite deduced from acoustic velocity measurements. *Earth and Planetary Science Letters* 243, 692–700. <https://doi.org/10.1016/j.epsl.2006.01.038>
- Rezaee, M.R., Jafari, A., Kazemzadeh, E., **2006**. Relationships between permeability, porosity and pore throat size in carbonate rocks using regression analysis and neural networks. *Journal of Geophysics and Engineering* 3, 370–376. <https://doi.org/10.1088/1742-2132/3/4/008>
- Rhett, D.W., **1998**. Ekofisk Revisited: A New Model of Ekofisk Reservoir Geomechanical Behavior. Presented at the SPE/ISRM Rock Mechanics in Petroleum Engineering, OnePetro, 367. <https://doi.org/10.2118/47273-MS>
- Rhett, D.W., **1990**. Long term effects of water injection on strain in North Sea chalks, in: Proc. 3rd North Sea Chalk Symp., Copenhagen.
- Richard, J., **2014**. Large-scale mass transfers related to pressure solution creep–faulting interactions in mudstones: driving processes and impact of lithification degree. *Tectonophysics* 612–613, 40–55. <https://doi.org/10.1016/j.tecto.2013.11.034>
- Richard, J., **2008**. Mass transfers and volume changes related to pressure solution–fracturing interactions in carbonate rocks: Example of the Oligocene deformation of the Coniacian chalk from the Omev area (Paris Basin, France). *Journal of Structural Geology* 30, 1300–1313. <https://doi.org/10.1016/j.jsg.2008.07.003>
- Richard, J., **1996**. L’alteration des craies de champagne : de l’analyse de terrain aux traceurs géochimiques (Thèse de doctorat). Reims, 240.
- Richard, J., Coulon, M., Gaviglio, P., **2002**. Mass transfer controlled by fracturing in micritic carbonate rocks. *Tectonophysics* 350, 17–33. [https://doi.org/10.1016/S0040-1951\(02\)00079-3](https://doi.org/10.1016/S0040-1951(02)00079-3)
- Richard, J., Coulon, M., Gaviglio, P., Ramseyer, K., **1997**. L’hydrofracturation: une déformation tectonique à haut potentiel diagénétique. Exemple des craies hydrofracturées de la région d’Omev (Bassin de Paris, France). *Comptes Rendus de l’Académie des Sciences - Series IIA - Earth and Planetary Science* 325, 359–366. [https://doi.org/10.1016/S1251-8050\(97\)81384-5](https://doi.org/10.1016/S1251-8050(97)81384-5)
- Richard, J., Sizun, J.P., Machhour, L., **2007**. Development and compartmentalization of chalky carbonate reservoirs: The Urgonian Jura-Bas Dauphiné platform model (Génissiat, southeastern France). *Sedimentary Geology* 198, 195–207. <https://doi.org/10.1016/j.sedgeo.2006.12.003>
- Rios, E.H., Figueiredo, I., Moss, A.K., Pritchard, T.N., Glassborow, B.A., Domingues, A.B.G., Azeredo, R.B. de V., **2016**. NMR permeability estimators in ‘chalk’ carbonate rocks obtained under different relaxation times and MICP size scalings. *Geophysical Journal International* 206, 260–274. <https://doi.org/10.1093/gji/ggw130>
- Risnes, R., **2001**. Deformation and yield in high porosity outcrop chalk. *Physics and Chemistry of the Earth, Part A: Solid Earth and Geodesy* 26, 53–57. [https://doi.org/10.1016/S1464-1895\(01\)00022-9](https://doi.org/10.1016/S1464-1895(01)00022-9)
- Risnes, R., Flaageng, O., **1999**. Mechanical Properties of Chalk with Emphasis on Chalk-Fluid Interactions and Micromechanical Aspects. *Oil & Gas Science and Technology - Rev. IFP* 54, 751–758. <https://doi.org/10.2516/ogst:1999063>
- Risnes, R., Haghghi, H., Korsnes, R.I., Natvik, O., **2003**. Chalk-fluid interactions with glycol and brines. *Tectonophysics* 370, 213–226. [https://doi.org/10.1016/S0040-1951\(03\)00187-2](https://doi.org/10.1016/S0040-1951(03)00187-2)
- Risnes, R., Madland, M.V., Hole, M., Kwabiah, N.K., **2005**. Water weakening of chalk— Mechanical effects of water–glycol mixtures. *Journal of Petroleum Science and Engineering* 48, 21–36. <https://doi.org/10.1016/j.petrol.2005.04.004>
- Ritter, H.L., Drake, L.C., **1945**. Pressure Porosimeter and Determination of Complete Macropore-Size Distributions. *Pressure Porosimeter and Determination of Complete Macropore-Size*

- Distributions. *Industrial & Engineering Chemistry Analytical Edition* 17, 782–786. <https://doi.org/10.1021/i560148a013>
- Robert, R., **2004**. Analytical characterization of porous geomaterials: reference assessment in some sedimentary rocks (Thèse de doctorat). Humboldt University, Berlin, 249.
- Roduit, N., **2007**. JMicroVision : un logiciel d'analyse d'images pétrographiques polyvalent. University of Geneva, 129. <https://doi.org/10.13097/archive-ouverte/unige:468>
- Roels, S., Carmeliet, J., Hens, H., Elsen, J., **2000**. Microscopic analysis of imbibition processes in oolitic limestone. *Geophysical Research Letters* 27, 3533–3536. <https://doi.org/10.1029/1999GL008471>
- Røgen, B., Fabricius, I.L., Japsen, P., Høier, C., Mavko, G., Pedersen, J.M., **2005**. Ultrasonic velocities of North Sea chalk samples: influence of porosity, fluid content and texture. *Geophysical Prospecting* 53, 481–496. <https://doi.org/10.1111/j.1365-2478.2005.00485.x>
- Røgen, B., Gommessen, L., Fabricius, I.L., **2001**. Grain size distributions of chalk from image analysis of electron micrographs. *Computers & Geosciences, Geological Applications of Digital Imaging* 27, 1071–1080. [https://doi.org/10.1016/S0098-3004\(00\)00159-X](https://doi.org/10.1016/S0098-3004(00)00159-X)
- Rosenbrand, E., Haugwitz, C., Jacobsen, P.S.M., Kjølner, C., Fabricius, I.L., **2014**. The effect of hot water injection on sandstone permeability. *Geothermics* 50, 155–166. <https://doi.org/10.1016/j.geothermics.2013.09.006>
- Rosenholtz, J.L., Smith, D.T., **1949**. Linear thermal expansion of calcite, var. Iceland spar, and Yule marble. *American Mineralogist* 34, 846–854.
- Saiag, J., **2016**. Caractérisation des hétérogénéités sédimentaires et pétrophysiques d'un réservoir carbonaté microporeux: le cas de la Craie (Crétacé supérieur, Bassin de Paris) (Thèse de doctorat). Dijon, 405.
- Sajid, M., Arif, M., **2015**. Reliance of physico-mechanical properties on petrographic characteristics: consequences from the study of Utlā granites, north-west Pakistan. *Bulletin of Engineering Geology and the Environment* 74, 1321–1330. <https://doi.org/10.1007/s10064-014-0690-9>
- Sajid, M., Coggan, J., Arif, M., Andersen, J., Rollinson, G., **2016**. Petrographic features as an effective indicator for the variation in strength of granites. <https://doi.org/10.1016/J.ENGCEO.2016.01.001>
- Saki, M., Siahpoush, S., Khaz'ali, A.R., **2020**. A new generalized equation for estimation of sandstone and carbonate permeability from mercury intrusion porosimetry data. *Journal of Petroleum Exploration and Production Technology*. <https://doi.org/10.1007/s13202-020-00900-w>
- Sausse, J., Jacquot, E., Fritz, B., Leroy, J., Lespinasse, M., **2001**. Evolution of crack permeability during fluid–rock interaction. Example of the Brézouard granite (Vosges, France). *Tectonophysics* 336, 199–214. [https://doi.org/10.1016/S0040-1951\(01\)00102-0](https://doi.org/10.1016/S0040-1951(01)00102-0)
- Schmidt, R.B., Bucher, K., Stober, I., **2018**. Experiments on granite alteration under geothermal reservoir conditions and the initiation of fracture evolution. *European Journal of Mineralogy* 30, 899–916. <https://doi.org/10.1127/ejm/2018/0030-2771>
- Schroeder, C., **2002**. Du coccolithe au réservoir pétrolier: approche phénoménologique du comportement mécanique de la craie en vue de sa modélisation à différentes échelles (Thèse de doctorat). University of Liege, 173.
- Schroeder, C., **1995**. Le Pore Collapse : aspect particulier de l'interaction fluide-squelette dans les craies ? Presented at the international du Groupement belge de mécanique des roches, Brussels.
- Schroeder, C., Bois, A.-P., Maury, V., Halle, G., **1998**. Water/Chalk (or Collapsible Soil) Interaction: Part II. Results of Tests Performed In Laboratory On Lixhe Chalk to Calibrate Water/Chalk Models. Presented at the SPE/ISRM Rock Mechanics in Petroleum Engineering, Society of Petroleum Engineers. <https://doi.org/10.2118/47587-MS>

- Sengun, N., Demirdag, S., Akbay, D., Ugur, I., Altindag, R., Akbulut, A., **2014**. Investigation of the relationships between capillary water absorption coefficients and other rock properties of some natural stones, V, in: Global Stone Congress. pp. 22–25.
- Sepúlveda, J., Arancibia, G., Molina, E., Gilbert, J.P., Duda, M., Browning, J., Roquer, T., Morata, D., Ahrens, B., Bracke, R., **2020**. Thermo-mechanical behavior of a granodiorite from the Liquiñe fractured geothermal system (39°S) in the Southern Volcanic Zone of the Andes. *Geothermics* 87, 101828. <https://doi.org/10.1016/j.geothermics.2020.101828>
- Sha, S., Rong, G., Chen, Z., Li, B., Zhang, Z., **2020**. Experimental Evaluation of Physical and Mechanical Properties of Geothermal Reservoir Rock after Different Cooling Treatments. *Rock Mechanics and Rock Engineering* 53, 4967–4991. <https://doi.org/10.1007/s00603-020-02200-5>
- Shao, S., Ranjith, P.G., Wasantha, P.L.P., Chen, B.K., **2015**. Experimental and numerical studies on the mechanical behaviour of Australian Strathbogie granite at high temperatures: An application to geothermal energy. *Geothermics* 54, 96–108. <https://doi.org/10.1016/j.geothermics.2014.11.005>
- Shao, S.S., Wasantha, P.L., Ranjith, P.G., Chen, B., **2014**. Effect of cooling rate on the mechanical behavior of heated Strathbogie granite with different grain sizes. *International Journal of Rock Mechanics & Mining Sciences* 70, 381–387. <https://doi.org/10.1016/j.ijrmms.2014.04.003>
- Shen, Y., Hou, X., Yuan, J., Xu, Z., Hao, J., Gu, L., Liu, Z., **2020**. Thermal deterioration of high-temperature granite after cooling shock: multiple-identification and damage mechanism. *Bulletin of Engineering Geology and the Environment* 79, 5385–5398. <https://doi.org/10.1007/s10064-020-01888-7>
- Shitrit, O., Hatzor, Y.H., Feinstein, S., Palchik, V., Vinegar, H.J., **2016**. Effect of kerogen on rock physics of immature organic-rich chalks. *Marine and Petroleum Geology* 73, 392–404. <https://doi.org/10.1016/j.marpetgeo.2016.03.023>
- Simmons, G., Cooper, H.W., **1978**. Thermal cycling cracks in three igneous rocks. *International Journal of Rock Mechanics and Mining Sciences & Geomechanics Abstracts* 15, 145–148. [https://doi.org/10.1016/0148-9062\(78\)91220-2](https://doi.org/10.1016/0148-9062(78)91220-2)
- Simon, D.E., Coulter, G.R., King, G., Holman, G., **1982**. North Sea Chalk Completions- A Laboratory Study. *Journal of Petroleum Technology* 34, 2 531-2 536. <https://doi.org/10.2118/10395-PA>
- Sing, K.S.W., **1985**. Reporting physisorption data for gas/solid systems with special reference to the determination of surface area and porosity (Recommendations 1984). *Pure and Applied Chemistry* 57, 603–619. <https://doi.org/10.1351/pac198557040603>
- Singh, B., Ranjith, P.G., Chandrasekharam, D., Viète, D., Singh, H.K., Lashin, A., Al Arifi, N., **2015**. Thermo-mechanical properties of Bundelkhand granite near Jhansi, India. *Geomechanics and Geophysics for Geo-Energy and Geo-Resources* 1, 35–53. <https://doi.org/10.1007/s40948-015-0005-z>
- Siratovich, P., Sass, I., Homuth, S., Bjornsson, A., **2011**. Thermal Stimulation of Geothermal Reservoirs and Laboratory Investigation of Thermally Induced Fractures. *Transactions - Geothermal Resources Council* 35, 1529–1535.
- Siratovich, P.A., Heap, M.J., Villeneuve, M.C., Cole, J.W., Kennedy, B.M., Davidson, J., Reuschlé, T., **2016**. Mechanical behaviour of the Rotokawa Andesites (New Zealand): Insight into permeability evolution and stress-induced behaviour in an actively utilised geothermal reservoir. *Geothermics* 64, 163–179. <https://doi.org/10.1016/j.geothermics.2016.05.005>
- Siratovich, P.A., Villeneuve, M.C., Cole, J.W., Kennedy, B.M., Bégué, F., **2015**. Saturated heating and quenching of three crustal rocks and implications for thermal stimulation of permeability in geothermal reservoirs. *International Journal of Rock Mechanics and Mining Sciences* 80, 265–280. <https://doi.org/10.1016/j.ijrmms.2015.09.023>
- Siwak, J.-M., **1994**. Comportement et modélisation de la craie (Thèse de doctorat). Lille 1.



- Skinner, B.J., **1966**. Thermal expansion. *Mem. Geol. Soc. Amer.* 97, 76–96.
- Somerton, W.H., **1992**. *Thermal Properties and Temperature-Related Behavior of Rock/Fluid Systems*. Elsevier Science Ltd, Amsterdam ; New York.
- Somerton, W.H., Janah, A.H., Ashqar, P.I., **1981**. Thermal Expansion Of Fluid Saturated Rocks Under Stress. Presented at the SPWLA 22nd Annual Logging Symposium, Society of Petrophysicists and Well-Log Analysts.
- Somerton, W.H., Mehta, M.M., Dean, G.W., **1965**. Thermal Alteration of Sandstones. *Journal of Petroleum Technology* 17, 589–593. <https://doi.org/10.2118/907-PA>
- Sousa, L.M.O., **2013**. The influence of the characteristics of quartz and mineral deterioration on the strength of granitic dimensional stones. *Environmental Earth Sciences* 69, 1333–1346. <https://doi.org/10.1007/s12665-012-2036-x>
- Sousa, L.M.O., Suárez del Río, L.M., Calleja, L., Ruiz de Argandoña, V.G., Rey, A.R., **2005**. Influence of microfractures and porosity on the physico-mechanical properties and weathering of ornamental granites. *Engineering Geology* 77, 153–168. <https://doi.org/10.1016/j.enggeo.2004.10.001>
- Staněk, M., Géraud, Y., **2019**. Granite microporosity changes due to fracturing and alteration: secondary mineral phases as proxies for porosity and permeability estimation. *Solid Earth* 10, 251–274. <https://doi.org/10.5194/se-10-251-2019>
- Straley, C., Rossini, D., Vinegar, H., Tutunjian, P., Morriss, C., **1997**. Core Analysis By Low-field Nmr. *The Log Analyst* 38, 84–94.
- Stussi, J.-M., Cheilletz, A., Royer, J.-J., Chervremont, P., Feraud, G., **2002**. The hidden monzogranite of Soultz-sous-Forêts (Rhine Graben, France). *Mineralogy, petrology and genesis* 45–64.
- Sulak, A.M., Danielsen, J., **1988**. Reservoir Aspects Of Ekofisk Subsidence. Presented at the Offshore Technology Conference, Offshore Technology Conference. <https://doi.org/10.4043/5618-MS>
- Sun, Q., Zhang, W., Xue, L., Zhang, Z., Su, T., **2015**. Thermal damage pattern and thresholds of granite. *Environmental Earth Sciences* 74, 2341–2349. <https://doi.org/10.1007/s12665-015-4234-9>
- Sun, X., Xu, H., He, M., Zhang, F., **2017**. Experimental investigation of the occurrence of rockburst in a rock specimen through infrared thermography and acoustic emission. *International Journal of Rock Mechanics and Mining Sciences* 93, 250–259. <https://doi.org/10.1016/j.ijrmms.2017.02.005>
- Surma, F., Géraud, Y., **2003**. Porosity and Thermal Conductivity of the Soultz-sous-Forêts Granite. *Pure and applied geophysics* 160, 1125–1136. <https://doi.org/10.1007/PL00012564>
- Sylte, J.E., Thomas, L.K., Rhett, D.W., Bruning, D.D., Nagel, N.B., **1999**. Water Induced Compaction in the Ekofisk Field. Presented at the SPE Annual Technical Conference and Exhibition, Society of Petroleum Engineers. <https://doi.org/10.2118/56426-MS>
- Takarli, M., Prince-Agbodjan, W., **2008**. Temperature Effects on Physical Properties and Mechanical Behavior of Granite: Experimental Investigation of Material Damage. *JAI* 5, 1–13. <https://doi.org/10.1520/JAI100464>
- Tang, Z.C., Sun, M., Peng, J., **2019**. Influence of high temperature duration on physical, thermal and mechanical properties of a fine-grained marble. *Applied Thermal Engineering* 156, 34–50. <https://doi.org/10.1016/j.applthermaleng.2019.04.039>
- Tarasovs, S., Ghassemi, A., **2012**. On the role of thermal stress in reservoir stimulation. *Proceedings: Thirty-Seventh Workshop on Geothermal Reservoir Engineering*.
- Taylor, S.C., Hall, C., Hoff, W.D., Wilson, M.A., **2000**. Partial Wetting in Capillary Liquid Absorption by Limestones. *Journal of Colloid and Interface Science* 224, 351–357. <https://doi.org/10.1006/jcis.2000.6732>
- Thermtest Thermal Conductivity Measurement & Testing Service [WWW Document], **2020**. Thermtest Inc. URL <https://thermtest.com/> (accessed 12.3.20).

- Thiry, M., Ayrault, M.B., Grisoni, J.-C., **1988**. Ground-water silicification and leaching in sands: Example of the Fontainebleau Sand (Oligocene) in the Paris Basin. *GSA Bulletin* 100, 1283–1290. [https://doi.org/10.1130/0016-7606\(1988\)100<1283:GWSALI>2.3.CO;2](https://doi.org/10.1130/0016-7606(1988)100<1283:GWSALI>2.3.CO;2)
- Thiry, M., Maréchal, B., **2001**. Development of Tightly Cemented Sandstone Lenses in Uncemented Sand: Example of the Fontainebleau Sand (Oligocene) in the Paris Basin. *Journal of Sedimentary Research* 71, 473–483. <https://doi.org/10.1306/2DC40956-0E47-11D7-8643000102C1865D>
- Thomachot-Schneider, C., **2002**. Modifications de propriétés pétrophysiques de grès soumis au gel ou recouverts “d’encroûtements noirs vernissés” (Thèse de doctorat). Strasbourg 1, 253.
- Thomachot-Schneider, C., Gommeaux, M., Fronteau, G., **2008**. Modifications of the porous network of sandstone accompanying the formation of black varnish. *Environmental geology* 56, 571–582. <https://doi.org/10.1007/s00254-008-1443-5>
- Thomachot-Schneider, C., Gommeaux, M., Lelarge, N., Conreux, A., Mouhoubi, K., Bodnar, J.-L., Vázquez, P., **2016**. Relationship between Na<sub>2</sub>SO<sub>4</sub> concentration and thermal response of reconstituted stone in the laboratory and on site. *Environmental Earth Sciences* 75, 762. <https://doi.org/10.1007/s12665-016-5388-9>
- Thomachot-Schneider, C., Vázquez, P., Gommeaux, M., Lelarge, N., Conreux, A., Drothière, X., Mouhoubi, K., Bodnar, J.-L., **2019**. Thermal response of building stones contaminated with salts. *Construction and Building Materials* 226, 331–344. <https://doi.org/10.1016/j.conbuildmat.2019.07.127>
- Tian, W.-L., Yang, S.-Q., Elsworth, D., Wang, J.-G., Li, X.-Z., **2020**. Permeability evolution and crack characteristics in granite under treatment at high temperature. *International Journal of Rock Mechanics and Mining Sciences* 134, 104461. <https://doi.org/10.1016/j.ijrmmms.2020.104461>
- Timur, A., **1972**. Nuclear Magnetic Resonance Study Of Carbonate Rocks. Presented at the SPWLA 13th Annual Logging Symposium, Society of Petrophysicists and Well-Log Analysts.
- Timur, A., **1969**. Pulsed Nuclear Magnetic Resonance Studies of Porosity, Movable Fluid, and Permeability of Sandstones. *Journal of Petroleum Technology* 21, 775–786. <https://doi.org/10.2118/2045-PA>
- Tiskatine, R., Oaddi, R., Ait El Cadi, R., Bazgaou, A., Bouirden, L., Aharoune, A., Ihlal, A., **2017**. Suitability and characteristics of rocks for sensible heat storage in CSP plants. *Solar Energy Materials and Solar Cells* 169, 245–257. <https://doi.org/10.1016/j.solmat.2017.05.033>
- Tomašić, I., Lukić, D., Peček, N., Kršinić, A., **2011**. Dynamics of capillary water absorption in natural stone. *Bulletin of Engineering Geology and the Environment* 70, 673–680. <https://doi.org/10.1007/s10064-011-0355-x>
- Tran, E.L., Reimus, P., Klein-BenDavid, O., Teutsch, N., Zavarin, M., Kersting, A.B., Weisbrod, N., **2020**. Mobility of Radionuclides in Fractured Carbonate Rocks: Lessons from a Field-Scale Transport Experiment. *Environ. Sci. Technol.* 54, 11249–11257. <https://doi.org/10.1021/acs.est.0c03008>
- Tuğrul, A., Zarif, I.H., **1999**. Correlation of mineralogical and textural characteristics with engineering properties of selected granitic rocks from Turkey. *Engineering Geology* 51, 303–317. [https://doi.org/10.1016/S0013-7952\(98\)00071-4](https://doi.org/10.1016/S0013-7952(98)00071-4)
- Ueda, A., Kato, K., Ohsumi, T., Yajima, T., Ito, H., Kaieda, H., Metcalfe, R., Takase, H., **2005**. Experimental studies of CO<sub>2</sub>-rock interaction at elevated temperatures under hydrothermal conditions. *Geochemical Journal* 39, 417–425. <https://doi.org/10.2343/geochemj.39.417>
- Uribe-Patiño, J.A., Alzate-Espinosa, G.A., Arbeláez-Londoño, A., **2017**. Geomechanical aspects of reservoir thermal alteration: A literature review. *Journal of Petroleum Science and Engineering* 152, 250–266. <https://doi.org/10.1016/j.petrol.2017.03.012>

- Urmos, J., Wilkens, R.H., **1993**. In situ velocities in pelagic carbonates: New insights from Ocean Drilling Program Leg 130, Ontong Java Plateau. *Journal of Geophysical Research: Solid Earth* 98, 7903–7920. <https://doi.org/10.1029/93JB00013>
- Vasin, R.N., Nikitin, A.N., Lokajicek, T., Rudaev, V., **2006**. Acoustic emission of quasi-isotropic rock samples initiated by temperature gradients. *Izvestiya, Physics of the Solid Earth* 42, 815–823. <https://doi.org/10.1134/S1069351306100053>
- Vazquez, P., Acuña, M., Benavente, D., Gibeaux, S., Navarro, I., Gomez-Heras, M., **2016**. Evolution of surface properties of ornamental granitoids exposed to high temperatures. *Construction and Building Materials* 104, 263–275. <https://doi.org/10.1016/j.conbuildmat.2015.12.051>
- Vazquez, P., Alonso, F.J., Esbert, R.M., Ordaz, J., **2010**. Ornamental granites: Relationships between p-waves velocity, water capillary absorption and the crack network. *Construction and Building Materials, Special Issue on Fracture, Acoustic Emission and NDE in Concrete (KIFA-5)* 24, 2536–2541. <https://doi.org/10.1016/j.conbuildmat.2010.06.002>
- Vazquez, P., Sánchez-Delgado, N., Carrizo, L., Thomachot-Schneider, C., Alonso, F.J., **2018a**. Statistical approach of the influence of petrography in mechanical properties and durability of granitic stones. *Environmental Earth Sciences* 77, 287. <https://doi.org/10.1007/s12665-018-7475-6>
- Vazquez, P., Sartor, L., Thomachot-Schneider, C., **2018b**. Influence of substrate and temperature on the crystallization of KNO<sub>3</sub> droplets studied by infrared thermography. *Progress in Earth and Planetary Science* 5, 75. <https://doi.org/10.1186/s40645-018-0229-y>
- Vazquez, P., Shushakova, V., Gómez-Heras, M., **2015**. Influence of mineralogy on granite decay induced by temperature increase: Experimental observations and stress simulation. *Engineering Geology* 189, 58–67. <https://doi.org/10.1016/j.enggeo.2015.01.026>
- Vazquez, P., Siegesmund, S., Alonso, F.J., **2011**. Bowing of dimensional granitic stones. *Environmental Earth Sciences* 63, 1603–1612. <https://doi.org/10.1007/s12665-010-0882-y>
- Vera, J.A., **2004**. *Geología de España*. SGE-IGME.
- Vincent, B., Fleury, M., Santerre, Y., Brigaud, B., **2011**. NMR relaxation of neritic carbonates: An integrated petrophysical and petrographical approach. *Journal of Applied Geophysics* 74, 38–58. <https://doi.org/10.1016/j.jappgeo.2011.03.002>
- Vlcek, J., **1982**. Determination of emissivity with imaging radiometers and some emissivities at  $\lambda = 5 \mu\text{m}$ . *Photogrammetric Engineering and Remote Sensing*, 609–614.
- Voake, T., Nermoen, A., Korsnes, R.I., Fabricius, I.L., **2019**. Temperature cycling and its effect on mechanical behaviours of high-porosity chalks. *Journal of Rock Mechanics and Geotechnical Engineering* 11, 749–759. <https://doi.org/10.1016/j.jrmge.2018.11.010>
- Wang, H.F., Bonner, B.P., Carlson, S.R., Kowallis, B.J., Heard, H.C., **1989**. Thermal stress cracking in granite. *Journal of Geophysical Research: Solid Earth* 94, 1745–1758. <https://doi.org/10.1029/JB094iB02p01745>
- Wang, Q., Ji, S., Sun, S., Marcotte, D., **2009**. Correlations between compressional and shear wave velocities and corresponding Poisson's ratios for some common rocks and sulfide ores. *Tectonophysics* 469, 61–72. <https://doi.org/10.1016/j.tecto.2009.01.025>
- Wang, X.-Q., Schubnel, A., Fortin, J., Guéguen, Y., Ge, H.-K., **2013**. Physical properties and brittle strength of thermally cracked granite under confinement. *Journal of Geophysical Research: Solid Earth* 118, 6099–6112. <https://doi.org/10.1002/2013JB010340>
- Wang, Y., Dusseault, M.B., **2003**. A coupled conductive-convective thermo-poroelastic solution and implications for wellbore stability. *Journal of Petroleum Science and Engineering (Amsterdam)* 38, 187–198. [https://doi.org/10.1016/S0920-4105\(03\)00032-9](https://doi.org/10.1016/S0920-4105(03)00032-9)
- Wardlaw, N.C., McKellar, M., **1981**. Mercury porosimetry and the interpretation of pore geometry in sedimentary rocks and artificial models. *Powder Technology* 29, 127–143. [https://doi.org/10.1016/0032-5910\(81\)85011-5](https://doi.org/10.1016/0032-5910(81)85011-5)

- Washburn, E.W., **1921**. Note on a Method of Determining the Distribution of Pore Sizes in a Porous Material. *Proceedings of the National Academy of Sciences of the United States of America* 7, 115–116.
- Watson, K., **1975**. Geologic applications of thermal infrared images. *Proceedings of the IEEE* 63, 128–137. <https://doi.org/10.1109/PROC.1975.9712>
- Weibel, R., Olivarius, M., Vosgerau, H., Mathiesen, A., Kristensen, L., Nielsen, C.M., Nielsen, L.H., **2020**. Overview of potential geothermal reservoirs in Denmark. *Netherlands Journal of Geosciences* 99, e3. <https://doi.org/10.1017/njg.2020.5>
- Weisbrod, N., Nativ, R., Adar, E.M., Ronen, D., Ben-Nun, A., **2000**. Impact of coating and weathering on the properties of chalk fracture surfaces. *Journal of Geophysical Research: Solid Earth* 105, 27853–27864. <https://doi.org/10.1029/2000JB900295>
- Weng, L., Wu, Z., Li, X., **2018**. Mesodamage Characteristics of Rock with a Pre-cut Opening Under Combined Static–Dynamic Loads: A Nuclear Magnetic Resonance (NMR) Investigation. *Rock Mechanics and Rock Engineering* 51, 2339–2354. <https://doi.org/10.1007/s00603-018-1483-4>
- Wengang, L., Geology (China), B.R.I. of U., Ju, W., Hongwei, Z., Pengfei, J., Chunhe, Y., **2008**. Coupled thermo-mechanical analysis of granite for high-level radioactive waste repository Presented at academic seminar on waste underground disposal, Dunhuang (China), pp. 589.
- Wennberg, O.P., Casini, G., Jahanpanah, A., Lapponi, F., Ineson, J., Wall, B.G., Gillespie, P., **2013**. Deformation bands in chalk, examples from the Shetland Group of the Oseberg Field, North Sea, Norway. *Journal of Structural Geology* 56, 103–117. <https://doi.org/10.1016/j.jsg.2013.09.005>
- Wennberg, O.P., Wall, B.G., Sæther, E., Jounoud, S., Rozhko, A., Naumann, M., **2018**. Fractures in Chalks and Marls of the Shetland Group in the Gullfaks Field, North Sea. Presented at the 80th EAGE Conference and Exhibition 2018, European Association of Geoscientists & Engineers, pp. 1–5. <https://doi.org/10.3997/2214-4609.201801488>
- Westphal, H., Surholt, I., Kiesl, C., Thern, H.F., Kruspe, T., **2005**. NMR Measurements in Carbonate Rocks: Problems and an Approach to a Solution. *Pure and applied geophysics* 162, 549–570. <https://doi.org/10.1007/s00024-004-2621-3>
- Witherspoon, P.A., Nelson, P., Doe, T., Thorpe, R., Paulsson, B., Gale, J., Forster, C., **1980**. Rock Mass Characterization for Storage of Nuclear Waste in Granite. *IEEE Transactions on Nuclear Science* 27, 1280–1290. <https://doi.org/10.1109/TNS.1980.4331008>
- Wogelius, R.A., Milodowski, A.E., Field, L.P., Metcalfe, R., Lowe, T., van Veelen, A., Carpenter, G., Norris, S., Yardley, B., **2020**. Mineral reaction kinetics constrain the length scale of rock matrix diffusion. *Scientific Reports* 10, 8142. <https://doi.org/10.1038/s41598-020-65113-x>
- Wu, J.-H., Lin, H.-M., Lee, D.-H., Fang, S.-C., **2005**. Integrity assessment of rock mass behind the shotcreted slope using thermography. *Engineering Geology* 80, 164–173. <https://doi.org/10.1016/j.enggeo.2005.04.005>
- Wu, Q., Weng, L., Zhao, Y., Guo, B., Luo, T., **2019**. On the tensile mechanical characteristics of fine-grained granite after heating/cooling treatments with different cooling rates. *Engineering Geology* 253, 94–110. <https://doi.org/10.1016/j.enggeo.2019.03.014>
- Xu, C., Sun, Q., **2018**. Effects of quenching cycle on tensile strength of granite. *Géotechnique Letters* 8, 165–170. <https://doi.org/10.1680/jgele.18.00053>
- Xu, X., Gao, F., Shen, X., Xie, H., **2008**. Mechanical characteristics and microcosmic mechanisms of granite under temperature loads. *Journal of China University of Mining and Technology* 18, 413–417. [https://doi.org/10.1016/S1006-1266\(08\)60086-3](https://doi.org/10.1016/S1006-1266(08)60086-3)
- Yang, S.-Q., Ranjith, P.G., Jing, H.-W., Tian, W.-L., Ju, Y., **2017**. An experimental investigation on thermal damage and failure mechanical behavior of granite after exposure to different high

- temperature treatments. *Geothermics* 65, 180–197. <https://doi.org/10.1016/j.geothermics.2016.09.008>
- Yilmaz, N., Karaca, Z., Goktan, R.M., Akal, C., **2009**. Relative brittleness characterization of some selected granitic building stones: Influence of mineral grain size. *Construction and Building Materials* 23, 370–375. <https://doi.org/10.1016/j.conbuildmat.2007.11.014>
- Yin, T., Li, X., Cao, W., Xia, K., **2015**. Effects of Thermal Treatment on Tensile Strength of Laurentian Granite Using Brazilian Test. *Rock Mechanics and Rock Engineering* 48, 2213–2223. <https://doi.org/10.1007/s00603-015-0712-3>
- Yong, C., Wang, C., **1980**. Thermally induced acoustic emission in westerly granite. *Geophysical Research Letters* 7, 1089–1092. <https://doi.org/10.1029/GL007i012p01089>
- Young, T., **1805**. III. An essay on the cohesion of fluids. *Philosophical Transactions of the Royal Society of London* 95, 65–87. <https://doi.org/10.1098/rstl.1805.0005>
- Yousef, A.A., Al-Saleh, S.H., Al-Kaabi, A., Al-Jawfi, M.S., **2011**. Laboratory Investigation of the Impact of Injection-Water Salinity and Ionic Content on Oil Recovery From Carbonate Reservoirs. *SPE Reservoir Evaluation & Engineering* 14, 578–593. <https://doi.org/10.2118/137634-PA>
- Yu, J., Chen, S., Chen, X., Zhang, Y., Cai, Y., **2015**. Experimental investigation on mechanical properties and permeability evolution of red sandstone after heat treatments. *Journal of Zhejiang University-Science A* 16, 749–759. <https://doi.org/10.1631/jzus.A1400362>
- Yu, P., Pan, P.-Z., Feng, G., Wu, Z., Zhao, S., **2020**. Physico-mechanical properties of granite after cyclic thermal shock. *Journal of Rock Mechanics and Geotechnical Engineering* 12, 693–706. <https://doi.org/10.1016/j.jrmge.2020.03.001>
- Yu, Q.L., Ranjith, P.G., Liu, H.Y., Yang, T.H., Tang, S.B., Tang, C.A., Yang, S.Q., **2015**. A Mesostructure-based Damage Model for Thermal Cracking Analysis and Application in Granite at Elevated Temperatures. *Rock Mechanics and Rock Engineering* 48, 2263–2282. <https://doi.org/10.1007/s00603-014-0679-5>
- Yun, T.S., Jeong, Y.J., Kim, K.Y., Min, K.-B., **2013**. Evaluation of rock anisotropy using 3D X-ray computed tomography. *Engineering Geology* 163, 11–19. <https://doi.org/10.1016/j.enggeo.2013.05.017>
- Zeng, Y., Tang, L., Wu, N., Cao, Y., **2017**. Analysis of influencing factors of production performance of enhanced geothermal system: A case study at Yangbajing geothermal field. *Energy* 127, 218–235. <https://doi.org/10.1016/j.energy.2017.03.100>
- Zhang, Fang, Zhang, X., Li, Y., Tao, Z., Liu, W., He, M., **2018**. Quantitative description theory of water migration in rock sites based on infrared radiation temperature. *Engineering Geology* 241, 64–75. <https://doi.org/10.1016/j.enggeo.2018.05.006>
- Zhang, Fan, Zhao, J., Hu, D., Skoczylas, F., Shao, J., **2018**. Laboratory Investigation on Physical and Mechanical Properties of Granite After Heating and Water-Cooling Treatment. *Rock Mechanics and Rock Engineering* 51, 677–694. <https://doi.org/10.1007/s00603-017-1350-8>
- Zhang, L., Mao, X., Lu, A., **2009**. Experimental study on the mechanical properties of rocks at high temperature. *Science in China Series E: Technological Sciences* 52, 641–646. <https://doi.org/10.1007/s11431-009-0063-y>
- Zhang, W., Sun, Q., Hao, S., Yang, L., **2016**. Experimental study of the effect of thermal damage on resistivity and mechanical properties of sandstone. *Acta Geodynamica et Geomaterialia* 13.2, 185–192. <https://doi.org/10.13168/AGG.2015.0056>
- Zhang, W., Sun, Q., Zhang, Y., Xue, L., Kong, F., **2018**. Porosity and wave velocity evolution of granite after high-temperature treatment: a review. *Environmental Earth Sciences* 77, 350. <https://doi.org/10.1007/s12665-018-7514-3>
- Zhang, W., Sun, Q., Zhu, S., Wang, B., **2017**. Experimental study on mechanical and porous characteristics of limestone affected by high temperature. *Applied Thermal Engineering* 110, 356–362. <https://doi.org/10.1016/j.applthermaleng.2016.08.194>

- Zhao, F., Sun, Q., Zhang, W., **2019**. Fractal analysis of pore structure of granite after variable thermal cycles. *Environmental Earth Sciences* 78, 677. <https://doi.org/10.1007/s12665-019-8703-4>
- Zhao, P., Feng, Z., **2019**. Thermal Deformation of Granite under Different Temperature and Pressure Pathways. *Advances in Materials Science and Engineering* 2019, 7869804. <https://doi.org/10.1155/2019/7869804>
- Zhao, Yixin, Zhu, G., Dong, Y., Danesh, N.N., Chen, Z., Zhang, T., **2017**. Comparison of low-field NMR and microfocus X-ray computed tomography in fractal characterization of pores in artificial cores. *Fuel* 210, 217–226. <https://doi.org/10.1016/j.fuel.2017.08.068>
- Zhao, Yangsheng, Feng, Z., Zhao, Yu, Wan, Z., **2017**. Experimental investigation on thermal cracking, permeability under HTHP and application for geothermal mining of HDR. *Energy* 132, 305–314. <https://doi.org/10.1016/j.energy.2017.05.093>
- Zhou, C., Remoroza, A.I., Shah, K., Doroodchi, E., Moghtaderi, B., **2016**. Experimental study of static and dynamic interactions between supercritical CO<sub>2</sub>/water and Australian granites. *Geothermics* 64, 246–261. <https://doi.org/10.1016/j.geothermics.2016.05.007>
- Zhou, C., Wan, Z., Zhang, Y., Gu, B., **2018**. Experimental study on hydraulic fracturing of granite under thermal shock. *Geothermics* 71, 146–155. <https://doi.org/10.1016/j.geothermics.2017.09.006>
- Zhu, Z., Tian, H., Chen, J., Jiang, G., Dou, B., Xiao, P., Mei, G., **2020**. Experimental investigation of thermal cycling effect on physical and mechanical properties of heated granite after water cooling. *Bulletin of Engineering Geology and the Environment* 79, 2457–2465. <https://doi.org/10.1007/s10064-019-01705-w>

---

## **Comportement des roches sous sollicitations thermiques et circulation de fluides (FLUTE)**

---

L'objectif général de FLUTE est d'optimiser l'extraction et le stockage des ressources naturelles et de minimiser les risques pour une meilleure connaissance des roches encaissantes. L'objectif spécifique de FLUTE est d'approfondir la connaissance des variations texturales de roches types dans les domaines du stockage, de la géothermie et des hydrocarbures (craie, grès, granite) soumises à des sollicitations thermiques. Les variations de température peuvent conduire à une fracturation des roches qui va dépendre de leur minéralogie et de leur texture. Si à cette fracturation s'ajoute la circulation de fluides à différentes températures, les variations texturales subies par les roches modifient leurs propriétés de transfert et donc leur fonctionnement. Ce projet se fonde sur une expérimentation innovante menée à petite échelle sur les processus de déformation, fracturation et dissolution de roches dans des conditions similaires à celles des domaines de stockage ou de géothermie. L'originalité de ce projet réside dans i) l'utilisation des techniques d'imagerie pour l'étude de matériaux peu utilisés sur les roches, et ii) l'étude des variations texturales des roches soumises à des circulations de fluides avec des températures contrastées.

---

Mots-clés : Sollicitation thermique, roches réservoir, analyses pétrophysiques, milieux poreux, fissuration.

---

## **Rock behaviour under thermal stresses and fluid flow (FLUTE)**

---

The main objective of FLUTE is to optimize the extraction and storage of natural resources and to minimize the risks for a better knowledge of the host rocks. The specific objective of FLUTE is to deepen the knowledge of the textural variations of type rocks of the Grand Est region in the fields of storage, geothermal energy and hydrocarbons (chalk, sandstone, granite) subjected to thermal stresses. Temperature variations can lead to rock fracturing which will depend on their mineralogy and texture. If this fracturing is added to the circulation of fluids at different temperatures, the textural variations undergone by the rocks modify their transfer properties and thus their functioning. This project is based on an innovative experimental part conducted on a small scale on the processes of deformation, fracturing and dissolution of rocks under conditions similar to those of the storage or geothermal domains. The originality of this project lies in (i) the use of imaging techniques for the study of other materials that have never been used on rocks before, and (ii) the study of textural variations of rocks subjected to fluid flows with contrasting temperatures.

---

Keywords : Thermal stress, reservoir rocks, petrophysical analyzes, porous media, cracking.

---

**Discipline** : : SCIENCES DE L'UNIVERS

**Spécialité** : Géosciences de l'environnement

---

Université de Reims Champagne-Ardenne

GEGENAA – EA 3795

51100 REIMS - FRANCE

